# Design, modeling, and analysis of piezoelectric energy harvesters

Khazaee, Majid

*Publication date:*
2021

*Document Version*
Publisher's PDF, also known as Version of record

# DESIGN, MODELING, AND ANALYSIS OF PIEZOELECTRIC ENERGY HARVESTERS

**BY**
**MAJID KHAZAEE**

DISSERTATION SUBMITTED 2021

AALBORG UNIVERSITY
DENMARK

# DESIGN, MODELING, AND ANALYSIS OF PIEZOELECTRIC ENERGY HARVESTERS

A PH.D. THESIS

by

Majid Khazaee

AALBORG UNIVERSITY
DENMARK

Dissertation submitted

.

Dissertation submitted: 30 March 2021

PhD supervisor: Associate Prof. Alireza Rezaniakolaei,
Aalborg University

Ph.D. Co-supervisor: Professor Lasse Rosendahl,
Aalborg Universi

PhD committee: Associate Professor Mads Pagh Nielsen (chairman)
Aalborg University

Professor Elie Lefeuvre
University of Paris-Sud

Associate Professor Jan Høgsberg
Technical University of Denmark

PhD Series: Faculty of Engineering and Science, Aalborg University

Department: Department of Energy Technology

ISSN (online): 2446-1636
ISBN (online): 978-87-7210-924-4

Published by:
Aalborg University Press
Kroghstræde 3
DK – 9220 Aalborg Ø
Phone: +45 99407140
aauf@forlag.aau.dk
forlag.aau.dk



Printed in Denmark by Rosendahls, 2021

# CV

Majid Khazaee received his B.Sc. and M.Sc. in Aerospace Engineering from Tehran Polytechnic (Amirkabir University of Technology) in Tehran, Iran, in 2013 and 2015. During his B.Sc. and M.Sc., he worked in vibration modeling, experimental vibration tests, analysis, and machine and structural health monitoring. Before starting his Ph.D., he worked for three years as a Vibration Engineer in the R&D section.

He is currently pursuing his Ph.D. studies in the Department of Energy Technology, Aalborg University (AAU) in Denmark. His research interests include:

- Piezoelectric energy-harvesting module modeling.
- Piezoelectric energy-harvesting system design.
- Assessment of vibration-based renewable energy harvesting.
- Applied mathematical modeling of engineering problems.
- Finite element formulation derivation and modification.
- Structural and vibration modeling and analysis.

# ENGLISH SUMMARY

A movement toward the regenerative energy harvester has been started for scavenging the wasted energy from the environment and structures in the hope to fabricate self-powered electronic devices. Kinetic motion is present in any natural and environmental actions, making kinetic energy harvesting a popular topic. Among different energy harvesting mechanisms, piezoelectricity is one of the leading technologies because of its simple conversion mechanism, relatively high power density, and easy integration into the various systems. A piezoelectric energy harvester (PEH) is a beam consists of piezoelectric materials, substrate shim, bonding adhesive, and added mass. Despite many research studies in Piezoelectric Vibration Energy Harvesting (PVEH), there are still challenges in this field.

There are still struggles for correctly modeling harvesters in complex shapes and under "real" vibration excitation. Furthermore, the power generation's sensitivity to the PEH components, especially the bonding layer, needs further investigation. As a perplex parameter, the damping coefficient determination requires accurate and straightforward approaches and a systematic method to investigate the sources and importance of different energy dissipation mechanisms in PEHs. Because of numerous available vibration sources, finding new applications and designing enhanced PEHs need constant research. In this Ph.D. thesis, the primary goals are to provide a comprehensive modeling technique, explore the influential parameters on the power generation, and develop and test PEHs for some practical vibration sources.

A comprehensive finite element (FE) method is proposed on the modeling techniques that tackle the critical issues in the current FE and analytical models. The presented FE model is applicable for a wide range of PEH designs, including multi-layered composites, thick plates, variable thickness, and non-uniform piezoelectric patches. The FE method presents a united matrix formulation that can accommodate the classical (classical plate theory, first and third-order shear deformation theory) and advanced Carrera's Unified Formulation (CUF). Moreover, the analytical beam model is developed to understand the electromechanical coupling in PEHs better and study the interaction of optimum electric load, resonant frequency, and excitation frequency. By sensitivity analysis of electromechanical-coupled resonant frequency, recommendations for the resonant matching designs are proposed. Besides, the transient voltage signal from harmonic excitations is investigated.

The damping, bonding layer, substrate shim in unimorph, and tip mass effects are experimentally investigated to analyze different PEH power output parameters. The bonding layer material can cause variations in the peak and root mean square (RMS) power generation. The substrate shim positively affects the unimorph power generation as it deviates the neutral axis from the piezo-layer mid-plane. Tip mass increases the power generation due to the beam deflection increase and reduces the

resonant frequency, which can be used as a tuning factor for the resonant matching design. Damping mechanisms in PEH beams are comprehensively investigated. Two damping determination methods are presented, which can extract the damping coefficient from only the piezoelectric voltage measurements without extra response measurements.

Different harvester configurations are investigated for different applications in the PVEH applications. Typical resonant design from the ordinary rectangular beams, the trapezoid beams, variable-thickness piezoelectric layer, and composite energy harvesters are presented and discussed. The energy harvesting from the DC motor is experimentally measured. The power generation from the water pump is calculated using the experimental acceleration data made on a water pump. As one application for the PVEH, a conceptual design for autonomous condition monitoring is proposed and applied for a water pump. Composite energy harvesters with variable piezo-fiber directions are investigated and integrated into a harvester setting for broadband energy harvesting.

This Ph.D. project is successfully presented the FE modeling technique for piezoelectric energy harvesters, which can be applied to a wide range of piezoelectric configurations. The experimental validations for these models prove the accuracy of the FE method. Sensitivity analyses are carried out to study the power output dependency to the different structural parameters. Moreover, experimental-based straightforward methods are presented for the damping coefficient determination. These damping determination methods are employed to study the damping mechanisms systematically. Finally, the development of piezoelectric energy harvesters is carried out for a series of practical applications, namely the water pump, DC motor, and car vibration. The feasibility of a remote autonomous condition monitoring system based on PEH is also investigated.

# DANSK RESUME

Der er startet en bevægelse mod den regenerative energihøster til at benytte den energi i omgivelser, som går til spild i håb om at fremstille selvdrevne elektroniske enheder. Kinetisk bevægelse findes i eventuelle naturlig og miljømæssig bevægelser, hvilket gør høstning af kinetisk energi, et populært emne. Blandt forskellige mekanismer til energihøstning er piezoelektrisk en af de førende teknologier, på grund af dens enkle konverteringsmekanisme, relativt højt effekttæthed og nem integration i de forskellige systemer. En piezoelektriske energihøster (PEH) er en bjælke, der består af piezoelektriske materialer, underlagsskinne, klæbemiddel og ekstra masse. På trods af mange forskningsundersøgelser i den Piezoelectriske Vibration Energi Høst (PVEH) er der stadig udfordringer på dette område.

Der er stadig mange udfordringer forbundet med korrekt modellering af høstmaskiner i komplekse former og under "ægte" vibrations anslag. Derudover skal el-produktionens følsomhed over for PEH-komponenterne, især bindingslaget, undersøges nærmere. Som en kompleks-parameter kræver bestemmelsen af dæmpningskoefficienten nøjagtige og ligefremme fremgangsmåder og en systematisk metode til at undersøge kilderne og betydningen af forskellige energispredningsmekanismer i PEH'er. På grund af adskillige tilgængelige vibrationskilder er konstant forskning nødvendigt for at finde nye applikationer og konstruere forbedrede PEH'er. Primære mål i denne Ph.d. afhandling er at tilvejebringe en omfattende modelleringsteknik, udforske de indflydelsesrige parametre på ølproduktionen, udvikle og afprøve PEH'er for nogle praktiske vibrationskilder.

Med hensyn til modelleringsteknikker foreslås en omfattende FE-metode (FE), som kan håndtere de kritiske problemer, der findes i de nuværende FE og analytiske modeller. Den præsenterede FE-model kan anvendes til en lang række PEH-design, herunder kompositter i flere lag, tykke plader, variabel tykkelse og ikke-ensartede piezoelektriske pletter. FE-metoden præsenterer en forenet matrixformulering, der kan rumme den klassiske (klassiske pladeteori, første og tredje ordens forskydningsdeformationsteori) og avanceret Carreras Unified Formulation (CUF). Desuden er den analytiske strålemodel udviklet for at forstå den elektromekaniske kobling i PEH'er bedre og studere interaktionen mellem optimal elektrisk belastning, resonansfrekvens og anslagsfrekvens. Ved følsomhedsanalyse af elektromekanisk koblet resonansfrekvens foreslås anbefalinger til resonansmatchende design. Desuden undersøges det transiente spændingssignal fra harmoniske anslager.

I forbindelse med analysen af forskellige PEH-effektudgangsparametre undersøges dæmpnings-, bindingslag, substratbelægning i unimorf og spidsmassevirkninger eksperimentelt. Bindingslagsmaterialet kan forårsage variationer i produktionen begge to i spids (peak) og kvadratrod af gennemsnitlig kvadratafvigelse (root mean

square -RMS). Substratskinnet påvirker den uniforme energiproduktion positivt, da det afviger den neutrale akse fra piezo-lagets midler plane. Tipmasse øger kraftgenerering på grund af forøgelse af bjælkes nedbøjning og reducerer resonansfrekvensen. Dette kan bruges som en indstillingsfaktor til resonansmatchende design. Derudover undersøges dæmpningsmekanismer i PEH-bjælker grundigt og to bestemmelsesmetoder til dæmpning præsenteres, som kun kan udtrække dæmpningskoefficienten fra de piezoelektriske spændingsmålinger uden ekstra responsmålinger.

I forhold til PVEH-applikationer undersøges forskellige høstkonfigurationer for forskellige applikationer. Typisk resonansdesign fra de almindelige rektangulære bjælker, trapezbjælkerne, det piezoelektriske lag med variabel tykkelse og høstmaskiner med komposit energi præsenteres og diskuteres. Energihøstningen fra jævnstrømsmotoren måles eksperimentelt. Derudover beregnes energiproduktionen fra vandpumpen ved hjælp af de eksperimentelle accelerationsdata, der er lavet på en vandpumpe. Som en applikation til PVEH foreslås et konceptuelt design til autonom tilstandsovervågning og anvendes til en vandpumpe. Høstmaskiner med sammensat energi med variabel piezo-fiberretning undersøges og integreres i en høstmaskine indstilling til bredbåndsenergihøstning.

I denne ph.d. projektet præsenteres en succesfuld FE-modelleringsmetode til piezoelektriske energihøster, som kan anvendes til en lang række piezoelektriske konfigurationer. De eksperimentelle valideringer for denne FE-model beviser nøjagtigheden af FE-metoden. Følsomhedsanalyser udføres for at undersøge afhængigheden af effektudgang til de forskellige strukturelleforhold. Desuden præsenteres eksperimentelle baserede enkle metoder til bestemmelse af dæmpningskoefficienten. Disse dæmpningsbestemmelsesmetoder anvendes til systematiske undersøgelse af dæmpningsmekanismerne. Endelig udføres udviklingen af piezoelektriske energihøster til en række praktiske anvendelser, nemlig vandpumpe, jævnstrømsmotor og bilvibrationer. Muligheden for et eksternt autonomt tilstandsovervågningssystem baseret på PEH undersøges også.

# PREFACE

As a collection of papers, this dissertation is submitted to the Doctoral School of Engineering and Science at Aalborg University in partial fulfillment of the requirement for the Danish Ph.D. degree. This collection covers the research activities from June 2018 until March 2021. This Ph.D. project has been conducted under Associate Prof. Alireza Rezaniakolaei and Prof. Lasse Rosendahl's supervision at the Department of Energy Technology at Aalborg University.

# ACKNOWLEDGEMENTS

"Ah, my Beloved, fill the Cup that clears
Today of past Regrets and future Fears-
Tomorrow? – Why, Tomorrow I may be Myself with Yesterday's Seven Thousand year" (Omar Khayyam 1048-1131, Iran).

ای دوست بیا تا غم فردا نخوریم  وین یکدم عمر را غنیمت شمریم
فردا که ازین دیر فنا درگذریم  با هفت هزار سالگان سر بسریم

حکیم عمر خیام

I would like to say thank you to my supervisors, Prof. Alireza Rezaniakolaei and Prof. Lasse Rosendahl, for their endless support during this project and for giving me the vision for my future profession.

I also would like to express my gratitude to Prof. John E. Huber from the University of Oxford for helping me during my research visit as a mentor and as a teacher.

Finally, yet importantly, I would like to thank my wife, Mastideh, who has walked with me along this road; without her, I could not be this successful. I also would like to thank my family, for their endless unrequited kindliness, and to my friends, my second family, and I would not be this happy without you.

To my mother, Shahrbanou.

# THESIS DETAIL AND PUBLICATIONS

Thesis title: Design, modeling and analysis of piezoelectric energy harvesters

Ph.D. Student: Majid Khazaee

Supervisor: Assoc. Professor Alireza Rezaniakolaei, Aalborg University

Co-supervisor: Prof. Lasse Rosendahl, Aalborg University.

The research outcomes of this Ph.D. thesis are derived from the following papers, completed during this Ph.D. degree period. These papers are attached as appendices.

[1] Khazaee, M., Rezaniakolaei, A., & Rosendahl, L. (2019). Effect of damage and support damping mechanisms on unimorph piezoelectric energy harvester. Journal of Vibration and Control, 25(18), 2409-2422.

[2] Khazaee, M., Rezaniakolaei, A., & Rosendahl, L. (2019, July). A proof for looking differently into damping modeling in piezoelectric energy harvesting systems. In 26th International Congress on Sound and Vibration. The International Institute of Acoustics and Vibration (IIAV).

[3] Khazaee, M., Rezaniakolaei, A., & Rosendahl, L. (2019). On the effect of driving amplitude, frequency and frequency-amplitude interaction on piezoelectric generated power for MFC unimorph. In 26th International Congress on Sound and Vibration (pp. T07-RS03). Canadian Acoustical Association.

[4] Khazaee, M., Rezaniakolaie, A., Moosavian, A., & Rosendahl, L. (2019). A novel method for autonomous remote condition monitoring of rotating machines using piezoelectric energy harvesting approach. Sensors and Actuators A: Physical, 295, 37-50.

[5] Khazaee, M., Rosendahl, L., & Rezaniakolaei, A. (2020). A comprehensive electromechanically coupled model for non-uniform piezoelectric energy harvesting composite laminates. Mechanical Systems and Signal Processing, 145, 106927.

[6] Khazaee, M., Rezaniakolaie, A., & Rosendahl, L. (2020). A broadband macro-fiber-composite piezoelectric energy harvester for higher energy conversion from practical wideband vibrations. Nano Energy, 76, 104978.

[7] Khazaee, M., Huber, J. E., Rosendahl, L., & Rezaniakolaei, A. (2021). The investigation of viscous and structural damping for piezoelectric energy harvesters using only time-domain voltage measurements. Applied Energy, 285, 116427.

[8] Khazaee, M., Rezaniakolaei, A., & Rosendahl, L. (2021). An experimental study to determine damping of piezoelectric harvesters using transient analysis of unified electromechanical voltage equation. Energy Conversion and Management, 227, 113567.

[9] Khazaee, M., Rezaniakolaei, A., & Rosendahl, L., "An optimum practical piezoelectric energy-harvesting device for energy scavenging from car vibration", To Be Submitted.

[10] Khazaee, M., Rezaniakolaei, A., & Rosendahl, L., "Power generation from a DC motor at defect-free and misaligned shaft conditions by piezoelectric energy harvester attached to the shaft bearing", To Be Submitted.

In addition to these papers, the following paper has been completed:

Khazaee, M., Rezaniakolaei, A., & Rosendahl, L. (2019). An experimental study on macro Piezoceramic fiber composites for energy harvesting. In Materials Science Forum (Vol. 951, pp. 3-8). Trans Tech Publications Ltd.

# TABLE OF CONTENTS

# TABLE OF FIGURES

# CHAPTER 1. BACKGROUND AND BEYOND

"*If you want to find the secrets of the universe, think in terms of energy, frequency, and vibration*" Nikola Tesla

## 1.1. INTRODUCTION TO PIEZOELECTRIC ENERGY HARVESTING (PEH)

With advancements in electronic development, the power consumption of small electronic devices has been reduced substantially [1]. Table 1-1 gives an overview of the small electronics' power consumption. The power consumption for communication applications is tens of mW for continuous operation; however, this power consumption can be reduced using intermittent operation. For medical applications, like hearing aid and heart pacemakers, the power consumption is in the range of µW. The voltage range for these applications lies within 2 to 4 V.

| Device | Power | Current | Voltage |
|---|---|---|---|
| ZigBee | 60mW peak | 20 mA | 3.0 V |
| Apple Watch | 52mW avg | 13.8 mA | 3.76 V |
| Bluetooth 4.0 | 45 mW peak | 15 mA | 2.0-3.6 V |
| GPS Tracker | Intermittent | Intermittent | 3.0 V |
| Hearing Aid | 1 mW avg | 0.67 mA | 1.4 V |
| Heart Pacemaker | 33 µW avg | 13 µA | 2.5 V |
| Analog Wrist Watch | 2.8 µW avg | 1.0 µA | 2.8 V |
| Timer | 88 nW | 35 nA | 2.5 V |

Table 1-1. The power consumption of small electronics [2].

The reduction in power consumption enabled researchers to seek new renewable energy sources that make these small electronic devices free from the power supply, battery, and wires. With the renewable energy sources from the environment, the systems' lifetime can be improved, self-powered systems are achievable, wiring difficulties can be eliminated, and more importantly, having access to inaccessible locations becomes possible [3], [4].

Fig. 1-1 presents the power density (power normalized to the device volume) and normalized power density (power density normalized to the square input acceleration)

for three energy harvesting technologies (electrostatic, piezoelectric, and electromagnetic) in the typical environmental frequency range (below 200 Hz). The power density for piezoelectric energy harvesting is better than electrostatic and electromagnetic, especially at higher frequencies. Piezoelectricity normalized power density is 10 to 100 $\mu W/cm^3/g^2$ for below 50 Hz frequencies and between 1 to 10 $mW/cm^3/g^2$ for above 50 Hz frequencies. The piezoelectric power generation is in the range of the required power for small electronic devices, so that using piezoelectric energy harvesting for autonomous devices is feasible. The piezoelectric voltage generation ranges from 0.01 to 20 V [5], which is suitable for many small electronic devices, including those mentioned in Table 1-1.

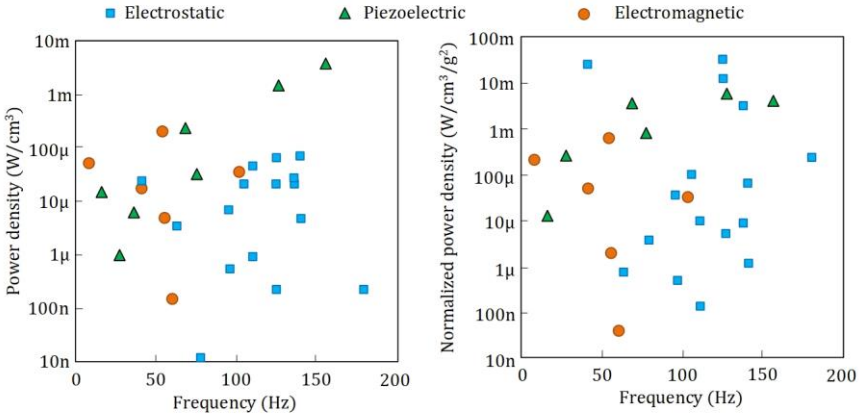


Fig. 1-1. Power density and normalized power density for different energy harvesting technologies (electrostatic, piezoelectric, and electromagnetic) [2].

Piezoelectricity benefits from advantageous priorities over the other energy harvesting technologies, including direct mechanical conversion to electrical [6], high practical power density [1], easy integration into the various systems [7], matured manufacturing methods [8]. Piezoelectric devices can be manufactured in various sizes, from micro-scale to centimeter scale. Thus, piezoelectric energy harvesting has been a focus for many researchers, and the number of publications in this area has been considerably increasing during recent years, see Fig. 1-2.

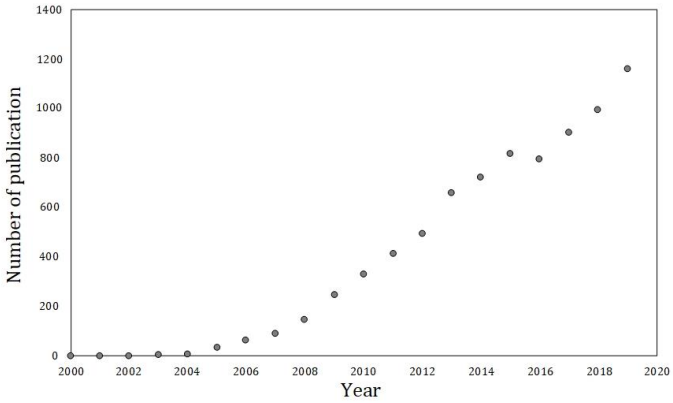


Fig. 1-2. Number of publications in piezoelectric energy harvesting [9].

Piezoelectric materials are a type of smart materials. Smart materials *change their physical properties in a specific manner in response to a stimuli input*. Piezoelectric materials are also categorized as a class of ferroelectric materials. Ferroelectric materials exhibit spontaneous polarization when no external electric field is present. Piezoelectric materials can be polarized by applying mechanical stress (without applying an external electrical field).

Polycrystalline ceramic, as one of the most common crystal structures, has microscopic randomly oriented poled units, see Fig. 1-3 (a). However, as their poling directions are random, the macroscopic scale's net polarization is weak or null. If the crystal structure is subjected to a strong electrical field, the random polarization direction will be aligned in the electrical field direction, see Fig. 1-3 (b). The crystal in this condition is called macroscopically polarized, and the net polarization is not weak. Fig. 1-3 shows the polycrystalline ceramic structure before, during, and after the polarization. Once the polarization is accomplished, the piezoelectric material is poled, and this polarization remains after the external field removal, see Fig. 1-3 (c).

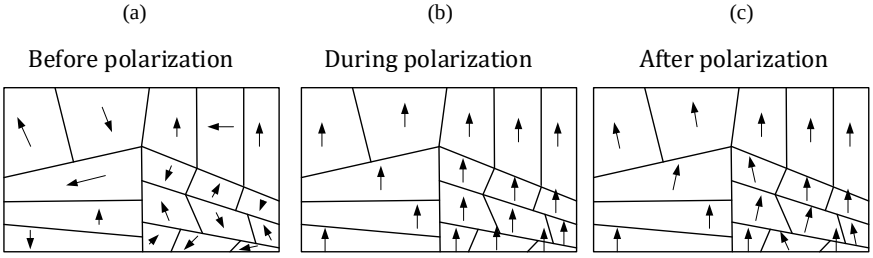


Fig. 1-3. Polycrystalline ceramic structure, (a) before, (b) during, and (c) after polarization.

Piezoelectricity is a dual-way property. Direct piezoelectricity is the electrical field generation due to the mechanical stress (sensor or generator), while reverse piezoelectricity is the mechanical deformation due to the external electrical field (actuator or motor). For the energy harvesting application, the direct piezoelectricity effect is of interest see Fig. 1-4. In direct piezoelectricity, the electrical charges are displaced by applying a mechanical deformation, generating a voltage difference. The mechanical deformation direction will impose the generated voltage direction. For continuous voltage generation, the mechanical deformation shall vary over time.

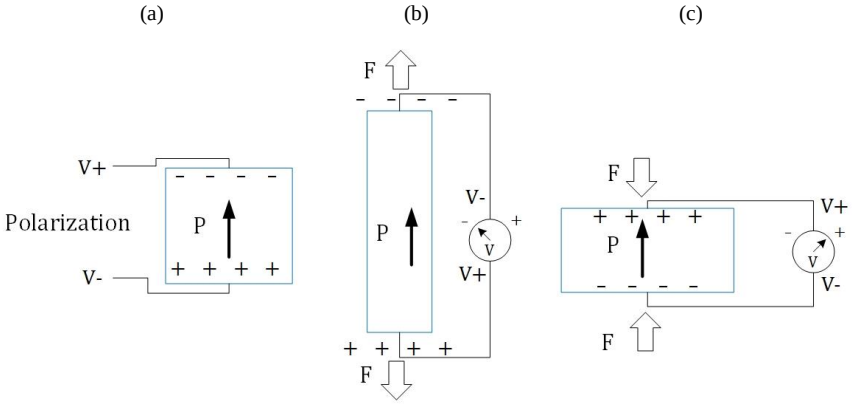


Fig. 1-4. The demonstration of direct piezoelectric effect (sensing), (a) polarization, (b) piezoelectric stretched, and (c) the piezoelectric compressed.

Piezoelectric harvester operates in 33-mode or 31-mode depending on the direction of mechanical deformation and polarization. The harvester operates in 33-mode if the mechanical deformation and polarization directions are the same, while for the 31-mode, the polarization and mechanical deformation direction are perpendiculars. Fig. 1-5 (a) and (b) show the 33-mode and 31-mode.

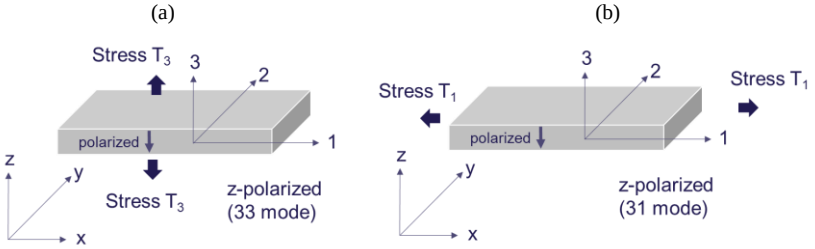


Fig. 1-5. Piezoelectric harvester operation mode, (a) 33-mode harvester, and (b) 31 mode.

Fig. 1-6 shows two examples of piezoelectric beams under loading. In Fig. 1-6 (a), a vertical force bends the piezoelectric beam, which creates stress in the length direction while the poling direction is through the thickness; thus, the bender acts as the 31-mode harvester. If the force is applied lengthwise, and the piezoelectric material has lengthwise polarization due to the interdigitated electrodes, as shown in Fig. 1-6 (b), the beam serves as a 33-mode harvester.

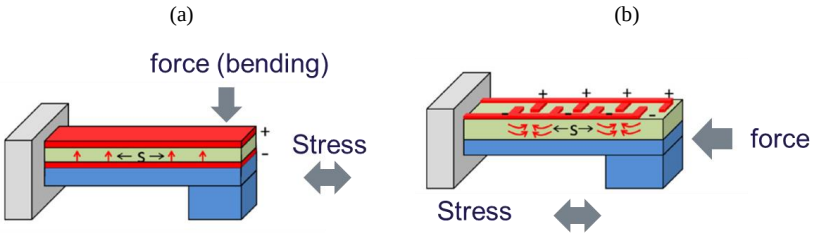


Fig. 1-6. Examples of piezoelectric beams under different loading, (a) bending load and 31-mode, and (b) axial load and 33-mode [10].

An energy-harvesting beam can have one or two piezoelectric layers called unimorph or bimorph, respectively. Typically, the piezoelectric layer is attached to a substrate shim or a host structure. The unimorph is less stiff and has a lower natural frequency. On the other hand, the bimorph generates more power than the unimorph as it has two piezoelectric layers. Fig. 1-7 (a) and (b) demonstrate the unimorph and bimorph, respectively.

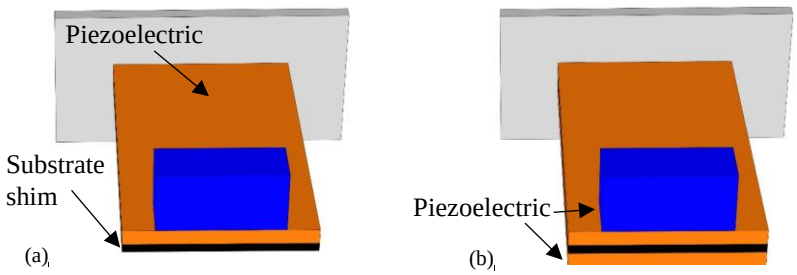


Fig. 1-7. (a) Unimorph harvester: one piezoelectric layer, and (b) bimorph harvester: two piezoelectric layers.

## 1.2. PIEZOELECTRIC COEFFICIENTS

This subsection will briefly present the significant piezoelectric coefficients.

- Piezoelectric charge coefficient ($d$)

The piezoelectric charge coefficient shows the induced strain ($S$) under an external electrical field ($E$), as shown in Eq. (1.1),

$$S = dE. \tag{1.1}$$

*d* coefficient is important for actuators as it demonstrates the mechanical deformation under a particular electrical field.

By considering the elastic relationship between strain ($S$) and stress ($T$),

$$T = QS = \underbrace{Qd}_{e} E = eE. \quad (e = Qd) \tag{1.2}$$

where $Q$ is the elastic constant.

There is also an alternative way to express coefficients *d* and *e*, as given by:

$$D = dT. \tag{1.3}$$

$$D = eS. \tag{1.4}$$

where $D$ is the electric displacement field.

- Piezoelectric voltage coefficient ($g$)

The piezoelectric voltage coefficient calculates the generated electrical field ($E$) under external mechanical stress ($T$), as shown in Eq. (1.5).

$$E = -gT \tag{1.5}$$

$g$ coefficient is important for sensors (energy harvesting) as this is a measure for the output voltage under mechanical stress.

By considering the elastic relationship, the piezoelectric voltage coefficient can also be given by:

$$E = -hS \ , \quad h = Qg. \tag{1.6}$$

- Permittivity (dielectric) constant ($\varepsilon$)

The permittivity constant relates the electric displacement field ($D$) to the electrical field ($E$) as given by:

$$D = \varepsilon E \tag{1.7}$$

By the permittivity constant definitions, the relationship between the piezoelectric voltage and charge constants can be expressed by:

$$g = \frac{d}{\varepsilon} \tag{1.8}$$

- Coupling factor ($K$)

The coupling factor is defined as

$$K^2 = \frac{\text{Extracted electrical charge}}{\text{Applied mechanical energy}} \tag{1.9}$$

The extracted electrical energy is $\frac{1}{2}\varepsilon E^2$ and the applied mechanical energy is $\frac{1}{2}ST$. Therefore, the coupling factor is,

$$K^2 = \frac{\frac{1}{2}\varepsilon E^2}{\frac{1}{2}ST} = \frac{\varepsilon \times (gT)^2}{(T/Y) \times T} = \varepsilon g^2 Y. \tag{1.10}$$

As can be seen from Eq. (1.10), the coupling factor depends on the piezoelectric voltage coefficient, the permittivity constant, and the elastic modulus.

- Electromechanical coupling factor ($k$)

The electromechanical coupling factor illustrates the generated charge from a mechanical deformation under a specific vibration mode.

For the lengthwise vibration (33-mode), transverse vibration (31-mode), and shear vibration (15-mode), the electromechanical coupling coefficients are defined by [11]:

$$k_{33} = d_{33}/(\varepsilon_{33}^S Q_{33}^E)^{\frac{1}{2}}. \tag{1.11a}$$

$$k_{31} = d_{31}/(\varepsilon_{33}^S Q_{11}^E)^{\frac{1}{2}} \tag{1.11b}$$

$$k_{15} = d_{15}/(\varepsilon_{11}^S Q_{55}^E)^{\frac{1}{2}} \tag{1.11c}$$

- Piezoelectric effect on the elastic modulus

For piezoelectric materials subjected to mechanical deformation, in addition to the mechanical stresses, a piezoelectric polarization is generated.

The elastic stress is given by $T_e = QS$.

According to Eq. (1.4), the piezoelectric polarization is given by $D = eS$. This polarization will create an electrical field of $E = \frac{D}{\varepsilon}$ according to Eq. (1.7). This electrical field then will create mechanical stress of $T_p = eE = e\frac{eS}{\varepsilon} = \frac{e^2S}{\varepsilon}$.

Thus, the resultant mechanical stress by applying a mechanical strain can be expressed by:

$$T = T_e + T_p = QS + eE = \left(Q + \frac{e^2}{\varepsilon}\right)S. \quad (1.12)$$

As can be seen from Eq. (1.12), the piezoelectric effect increases the structure's stiffness.

- Piezoelectric effect on the dielectric constant

Like the elastic modulus, the piezoelectricity also affects the dielectric constant. If an electrical field is applied to a piezoelectric material, an electric displacement field is created, and a mechanical strain due to the piezoelectric coupling.

The electric displacement field is $D = \varepsilon E$.

The mechanical strain due to the electrical field is $S = dE$. This mechanical strain causes an electric displacement field $D_p = eS$ according to Eq. (1.4).

Thus, the total electric displacement field can be expressed by:

$$D = D + D_p = \varepsilon E + edE = (\varepsilon + ed)S. \quad (1.13)$$

## 1.3. TYPICAL PIEZOELECTRIC MATERIALS

There is a wide range of piezoelectric materials, from natural to synthetic materials. Four types of piezoelectric materials have been extensively used in energy harvesting applications, namely Piezoceramic, Piezo polymer, Piezo composite, and piezoelectric single crystals. These four will be introduced in this subsection. Fig. 1-8 (a) to (c) shows the Piezoceramic, Piezo polymer, and the piezo composite.

Piezoceramic materials have a good piezoelectric property, so they have been frequently used for energy harvesting. They have low cost, good conversion coupling, high elastic modulus, high density, and brittle. They can tolerate their weight, but they

are solely used alone because they are very brittle and stiff. Lead Zirconate Titanate (PZT) is a popular and widespread member of Piezoceramic materials, with different PZT-5A and PZT-5H.

Piezoelectric single ceramic has single crystalline structures, with a highly ordered orientation of positive and negative ions [7]. PMN-PT and PZN-PT are two common single crystal materials. Comparing with Piezoceramic, the single ceramic materials have a better piezoelectric conversion, high permittivity, and low elastic modulus.

Piezo polymers are flexible materials with a low piezoelectric property. Nevertheless, they have a lightweight, low elastic modulus and highly flexible. Polyvinylidene difluoride (PVDF) is the most common member of piezo polymers. PVDF cannot tolerate its weight, so a host structure is essential for the PVDF materials.

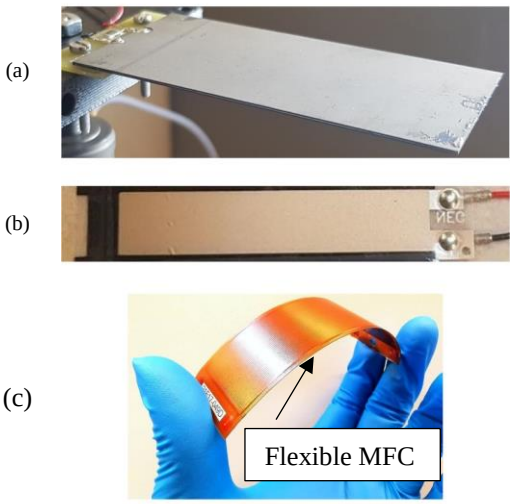


Fig. 1-8. Three common piezoelectric materials, (a) Piezoceramic, (b) Piezo polymer, and (c) piezo composite.

Table 1-2 shows the properties of these four types of piezoelectric materials. The coupling factor in 33-mode for the single ceramic materials is approximately 90%, which is the highest among these materials. Overall, the single ceramic materials have the best performance, and the PVDF materials have the lowest energy conversion. Overall, the MFC coupling factor is considerably better than the PVDF, still lower than the Piezoceramic.

| | PVDF | PZT-5A | PMN-PT (single crystal) | MFC |
|---|---|---|---|---|
| Density ($kg/m^3$) | 1800 | 7800 | 8120 | 5440 |
| Relative permittivity $\varepsilon/\varepsilon_0$ | 12 | 1800 | 4753 | 1600 |
| $d_{31}$ ($10^{-12}$ C/N) | -23 | -190 | -646 | -170 |
| $g_{31}$ ($10^{-3}$ Vm/N) | -216 | -11.6 | -15.36 | -12.0 |
| $K_{31}$ | 0.19 | 0.35 | 0.46 | 0.25 |
| $d_{33}$ ($10^{-12}$ C/N) | 30 | 390 | 1285 | 400 |
| $g_{33}$ ($10^{-3}$ Vm/N) | 340 | 24 | 30.55 | 28.2 |
| $K_{33}$ | 0.13 | 0.72 | 0.89 | 0.59 |
| Y (Gpa) | 8.5 | 52 | 20.4 | 30.3 |
| Mechanical quality factor $Q=1/\zeta$ | 3-10 | 80 | 150 | |
| Curie Temp (ºC) | 150 | 200 | 90 | 150 [12] |

Table 1-2. Comparing material properties between Piezoceramic (PZT and single ceramic), polymer-based piezoelectric, and composite piezoelectric materials [13].

Fig. 1-9 compares the power output from Piezoceramic and single ceramic materials. The efficiency of single-crystal materials is considerably higher than the PZT performance [14]. The better performance of single crystals exists in both on-resonance and off-resonance excitations [14].

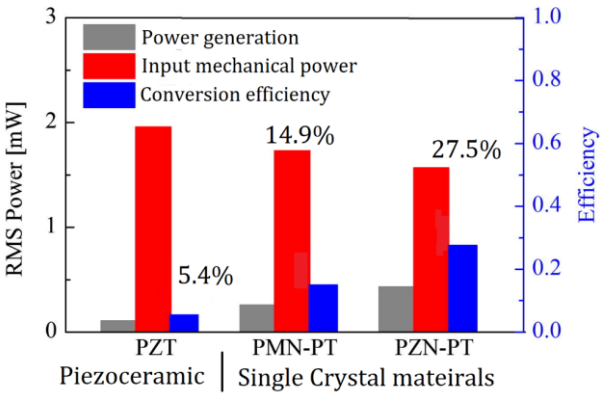


Fig. 1-9. Power output and efficiency comparison between PZT ceramic and PMN-PT and PZN-PT single crystals [14].

## 1.4. TYPICAL PIEZOELECTRIC BENDERS FOR ENERGY HARVESTING

For many practical applications, including human motion, environmental vibrations, and industrial sources, the working frequency span is below 200 Hz see Table 1-3. This frequency span is a low-frequency category, and therefore, the focus for the piezoelectric harvesters is the low-frequency designs.

| Category | Frequency span |
|---|---|
| Human walking and running | 0 to 5 Hz |
| Human motion | 5 to 15 Hz |
| Automobiles' vibration | 15 to 50 Hz |
| Household appliances | 50 to 200 Hz |
| Industrial vibration | 200 Hz |

Table 1-3. The working frequency range for different vibration sources [15].

The cantilevered beam is one of the most widely used configurations in piezoelectric energy harvesting because it undergoes high deformation under vibration and therefore is suitable for power generation. The cantilevered beam also has a relatively low working frequency, suitable for low-frequency energy harvesting. Fig. 1-10 shows a typical energy harvester under the base excitation. The beam under the base excitation experiences bending deformation. One way of applying the base excitation is to attach the clamp box to a vibration shaker. Besides, a force transducer, an accelerometer, or a laser displacement sensor may be employed for measuring the input vibration characteristics. Fig. 1-10 illustrates the typical instrumentation of a shaker test on the piezoelectric cantilevered beam.

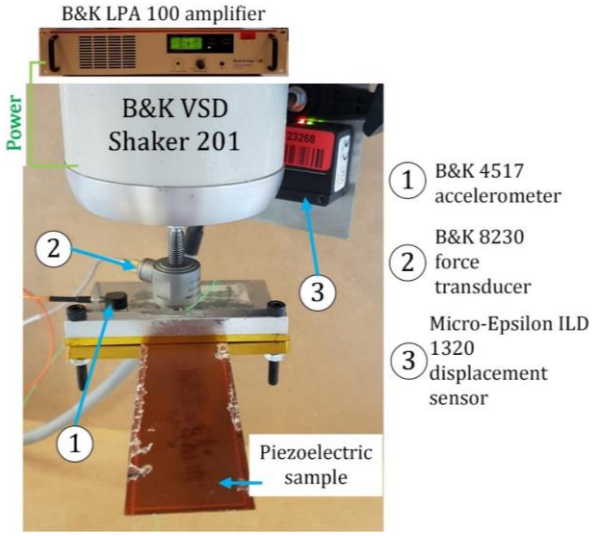


Fig. 1-10. A typical experimental setup for the piezoelectric energy harvester under the clamped-free boundary condition [16].

As a typical performance of the piezoelectric bender, the voltage response of a unimorph beam (Fig. 1-11 (a)) under harmonic excitation is shown in Fig. 1-11 (b). The input vibration has a harmonic form, so the output voltage has a harmonic shape, and the voltage output is AC. However, in many practical cases, the AC voltage will be connected to a full-bridge rectifier to transform the AC voltage to an always-positive voltage.

As the output piezoelectric voltage depends on the beam vibration, the excitation frequency that affects the beam vibration will also influence the voltage generation. The voltage output for harmonic excitations with a 0-70 Hz frequency range is shown in Fig. 1-11 (c). As can be seen from Fig. 1-11 (c), the voltage output is negligible firstly but sharply rises to a peak value at a specific frequency called "*resonant frequency*". At the resonant frequency, the bender deflection is maximum, which will therefore generate the maximum voltage.

An electrical resistance load is often attached to the piezoelectric beam so that the current flows. In no-load condition (open-circuit or infinity load), the voltage is maximum but no current flows, so the power generation is zero. When the load is close to zero (short-circuit condition), the current flow is maximum, but there will be no voltage difference, so the power generation is zero. An "*optimum electrical*" load gives the maximum power output (Fig. 1-11 (d)), which should be found for piezoelectric energy harvesting.

These basic introductory definitions for the resonant frequency and optimum load will be comprehensively developed in the following chapters.

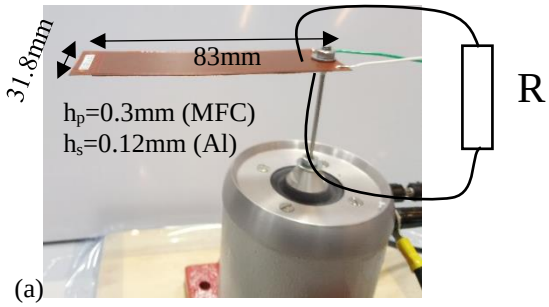


(a)

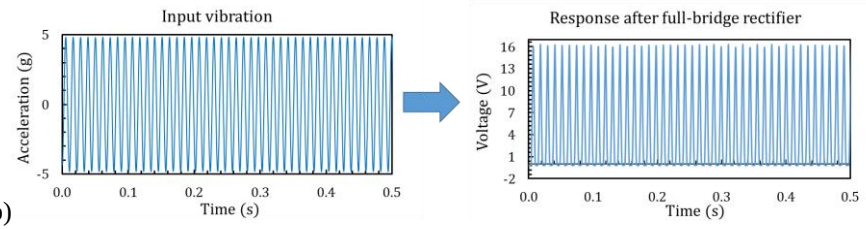


(b)

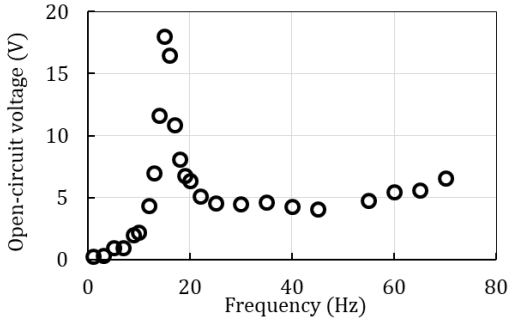


(c)

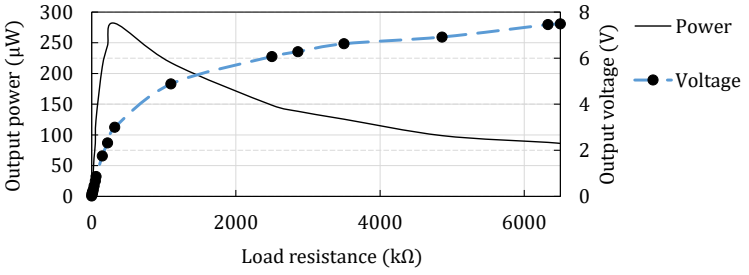


(d)

Fig. 1-11. (a) A piezoelectric unimorph with one MFC under the base excitation, (b) the voltage response over frequency, and (c) resonant voltage and power outputs versus electrical load resistance [17].

The clamping in the cantilever configuration can be done in different ways. One way can be using a clamp bar that keeps the energy harvester by tightening screws, or the energy harvester is attached to a medium plate by adhesive, and then the medium plate is joined to the base plate by screws. Fig. 1-12 (a) shows these two clamping types. It is also typical to add a tip mass so that the beam deformation increases. Fig. 1-12 (b) shows an added tip mass attached to a piezoelectric beam.

(a)

(b)

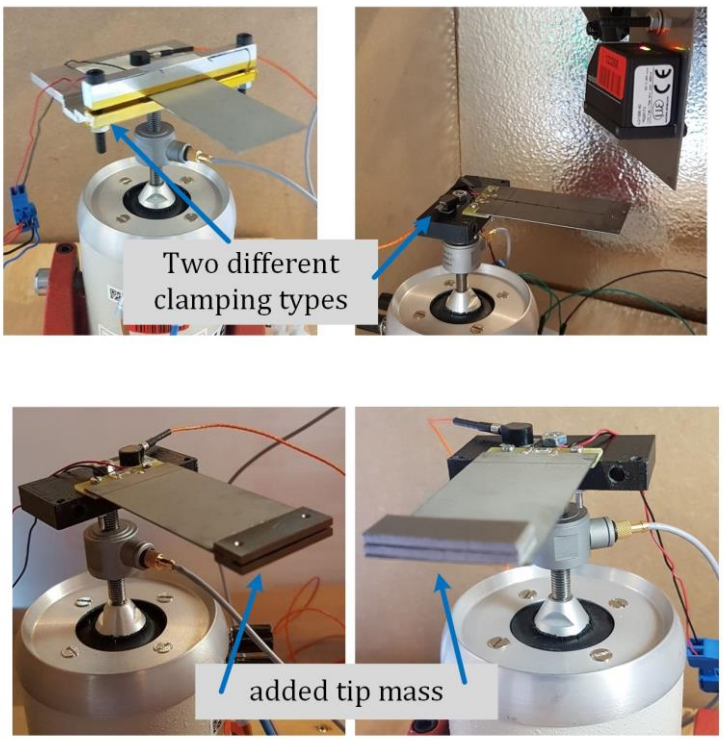


Fig. 1-12. The demonstrations of different (a) clamping types and (b) added tip mass connection.

In many practical cases, an energy harvester may comprise more than one piezoelectric beam to improve the power output performance. The multi-beam energy harvesters can have multiple beams with different piezoelectric materials, Fig. 1-13 (a), or substrate shims, Fig. 1-13 (b). Since each beam has an optimal frequency range, the two beams' combined performance is improved over the frequency range. Fig. 1-13 (c) illustrates a typical power output for a two-beam energy harvester.

(a)

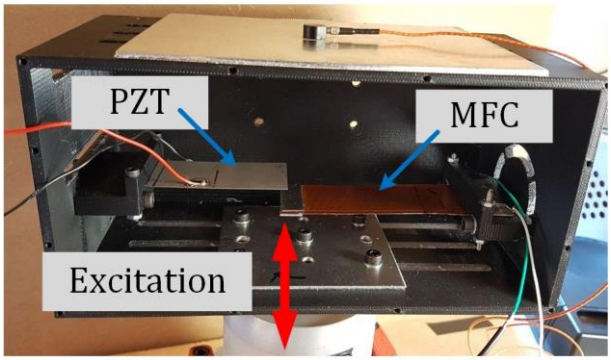


(b)

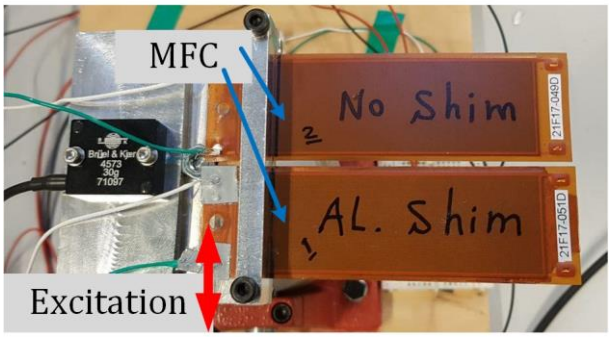


(c)

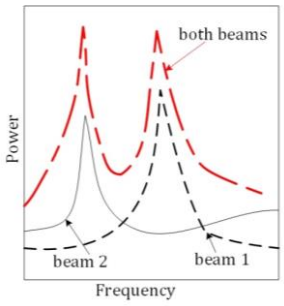


Fig. 1-13. Two-beam energy harvesters under the same base excitation, (a) one PZT and one MFC sample in one energy harvesting box, (b) two MFCs attached to one clamping box, and (c) a typical response from the two-beam harvester.

## 1.5. PIEZOELECTRIC VIBRATION ENERGY HARVESTER (PVEH): STATE-OF-THE-ART

According to Scopus, piezoelectricity has been a significant focus for energy harvesting research, with more than 1000 research articles annually. Thus, there are

also vast review articles addressing the piezoelectric energy harvesting, from design, material, and application perspectives [1], [7], [9], [10], [15], [18]–[29].

Sodano and coworkers [25] reviewed the energy harvesting by piezoelectric materials in 2004. In addition to the harvesters' fundamental vibration, they also studied the electrical circuit, electrical damping, and storage. [25]. Later, in a paper by Anton and Sodano [26], Sodano and his team presented a review paper on piezoelectric energy harvesting focusing on mechanical and electrical modulations for improving power generation performance. Ten years later, in 2019, Safaei, Sodano, and Anton [24] reviewed piezoelectric energy harvesting by reporting the recent advancements in material science and electrical circuits as well as a comprehensive presentation of different piezo-harvester designs.

In 2021, Sezer and Koc [9] reviewed the most recent advancements in piezoelectric material developments and presented a comprehensive review of the different piezoelectric harvesters from different vibration sources.

The following subsection, state-of-the-art piezoelectric energy harvesting, its challenges, and the leading-edge solutions for these challenges, will be reviewed.

## 1.5.1. A BRIEF SURVEY ON THE PVEH FROM DIFFERENT VIBRATION SOURCES

### 1.5.1.1 Environmental forces

As one of the available environmental forces, the air force has been extensively used for piezoelectric energy harvesting. Wind energy can be a substantial source of energy, as it has been shown that a wind speed of 4.6 m/s can approximately generate 0.35 mW power using a T-shape harvester with piezo-patches [30].

Aircraft is one potential vibration source experiencing structural vibration during the flight. The aircraft vibration has been used for piezoelectric energy harvesting. Energy harvesting from unmanned aerial vehicles (UAV) [31], wing-box [32], and composite wing surface [33] are some research examples.

The wind turbine blade will experience mechanical strain during the turbine operation. This strain energy can be used for piezoelectric energy harvesting [34]. It is suggested that the stored electrical energy from piezoelectricity made on the wind turbine blade's stored energy is sufficient for wireless sensor nodes [35].

Fluids (other than air) can also create energy sources for energy harvesting. Rain [36] and ocean wave [37] energy are two familiar energy sources by water. In an actual rain, it has been shown that in an actual rain in an 18 $cm^2$ surface area, 6.9 μJ/min

energy can be stored from an actual rain [38]. The power output from ocean waves is considerably high at the 30 W range [37].

#### 1.5.1.2 Car, road, and bridge

The vibration in a traffic tunnel wall can reach 7 $m/s^2$ from a passing car to more than 20 $m/s^2$ for the induced vibration by a truck [39]. This kinetic energy source is often wasted. The excitation frequencies from the tunnel are in the range of kilo-Hz. It has been experimentally shown that power of 2.43 mW is generated from the pavement road from a 1200 N axel passing with 60 km/h [40]. The power generation from a 6×6 $in^2$ prototype with four Φ8mm×t8mm piezoelectric discs is estimated to be 1080 W h of RMS energy per year [41].

In addition to the structural vibration, the moving car itself can be another vibration source. By designing a flexible piezoelectric composite and attaching it to the tire surface, a 380.2 μJ energy per tire revolution has been generated, equivalent to 1.37 $\mu W/mm^3$ [42]. The car suspension system can also be a potential energy source for power generation in the range of Watts [43].

The piezoelectric energy harvesting from car and road can be used to power car wireless sensors [42], smart tires [44], and smart roads [45] for the future.

Peigney and Siegert [46] showed that the traffic-induced bridge vibration could be used for designing a wireless sensor for low-duty cycle structural health monitoring.

#### 1.5.1.3 Floor and building

Walking can cause the floor to be excited by a considerable force. Therefore, floors can be designed to accommodate piezoelectric harvesters for power generation.

A 63-kg pedestrian by a soft step can generate approximately 10 V and 0.18 A [47].

A floor tile with 150×150 $mm^2$ has been designed and showed that for one step from a 68-kg man, 0.12 mW RMS power has been generated, which was enough to turn on sixty chip LED [48].

It has been estimated that for an educational building at Macquarie University in Sydney, by 3.1% piezoelectric coverage, 1.1 MW h/year can be generated [49].

#### 1.5.1.4 Train and railway

A considerable vibration is induced into the railway by a moving train. The moving train is a moving load, and a particular modeling type is required for this type of analysis. Zhang et al. [50] presented a modeling technique for a piezoelectric

cantilevered beam subjected to a moving load. The train-induced acceleration is in the range of 600 m/s$^2$ and lasts for approximately 20 seconds at one point in the rail [39]. Wischke and coworkers estimated that energy of 395 µJ per train could be stored [39].

For the railway energy harvesting, the patch and stack-box designs have been proposed by Wang and coworkers [51], and it has been calculated that 85.6 mJ and 21.88 mJ energy can be stored from the patch and stack designs.

Amini et al. [52] presented a complete study on the power output from multiple moving loads and showed that power in the range of 1mW could be generated for velocities above 30 m/s.

#### 1.5.1.5 Industrial vibration

The vibration induced in the pipe by a moving flow can also be regarded as a kinetic energy source. One issue for applying piezo-materials is that the piezoelectric patches should be flexible. Thus, the Piezoceramic patches cannot be attached to the pipe surface. The development of MFC materials for PVEH from pipes was demonstrated with a demo that generated power above 3 mW/N$^2$ [53].

Motors, which inevitably emits vibration due to their rotating shaft, typically have a high acceleration level with relatively moderate excitation frequency. Different conversion mechanisms can be employed for the PEH from motor vibration. Direct attachment of piezoelectric beam to the motor case [54] is the most straightforward design; nevertheless, the vibration level might be low at some working conditions. Another solution can be to use the shaft rotating motion as a base excitation, as shown in Fig. 1-14 [55]. In addition to the rotation motion design, the shaft rotation motion can be converted to a linear motion, and that this linear motion excites the piezoelectric beam, as illustrated in Fig. 1-15 [56]. Another way to use the rotation motion as a beam excitation force is to apply magnets, as shown in Fig. 1-16 [57].

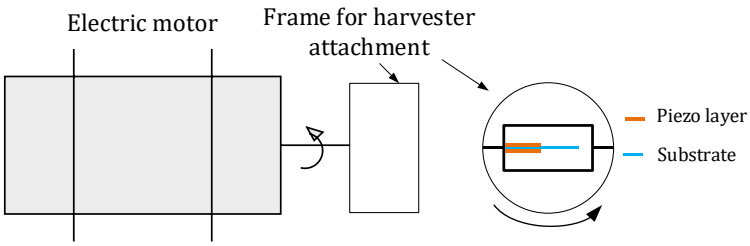


Fig. 1-14. Piezo-beam for rotation energy harvesting with the application on the motor [55]

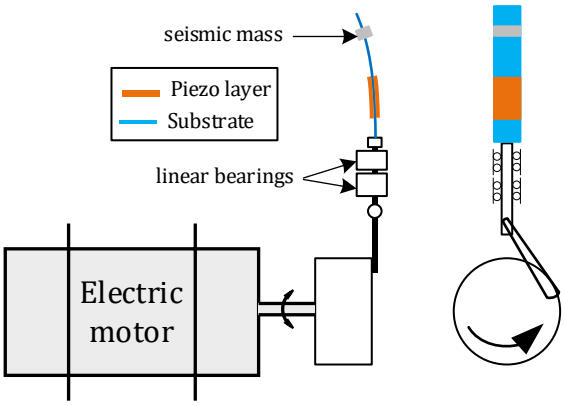


Fig. 1-15. Converting rotation motion to linear motion for parametric excitation of piezoelectric beams [56].

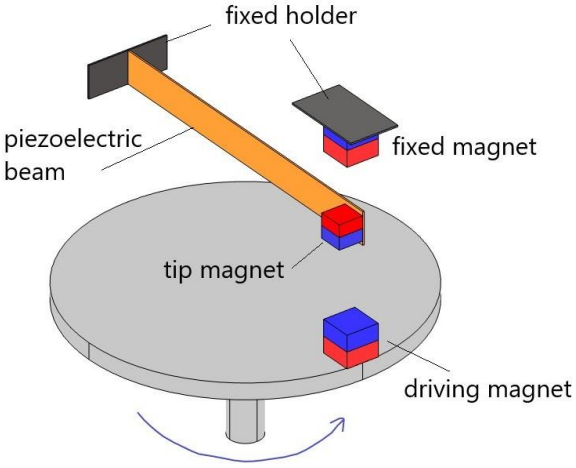


Fig. 1-16. Using the magnetic force in a rotating shaft to excite the piezoelectric beam by tip force [57].

### 1.5.1.6 Kinetic energy from living sources

The human body is an excellent source of various energy types. Moreover, the human body may need to have implants or biomedical sensors for health purposes. Fig. 1-17 illustrates a schematic of some implanted medical electronic devices [58]. Therefore, the human body can be an excellent power generation source and a customer for the power. Therefore, many studies have focused on the body as an energy-harvesting source.

Typical, the medical implants need power around 100μW (with a lifetime of 10 years), and specifically for the pacemakers, the required power is within 10μW range (with a lifetime of 5 years) [59]. Human motion and activities can be kinetic energy sources with available power output in the range of mW to W, as illustrated in Table 1-4. Thus, from a power consumption point of view, having self-powered implanted medical devices is possible. Dagdeviren and coworkers [60] demonstrated a series of practical demonstrations of the energy harvesters using biofuel cells, thermoelectric generators, triboelectric generators, and piezoelectric generators. Their study focused on the harvesters that can be implanted. For the on-body energy harvesters, Roundy and Trolier-McKinstry [61] reviewed different energy-harvesting technologies, including the piezoelectricity, for the on-body applications.

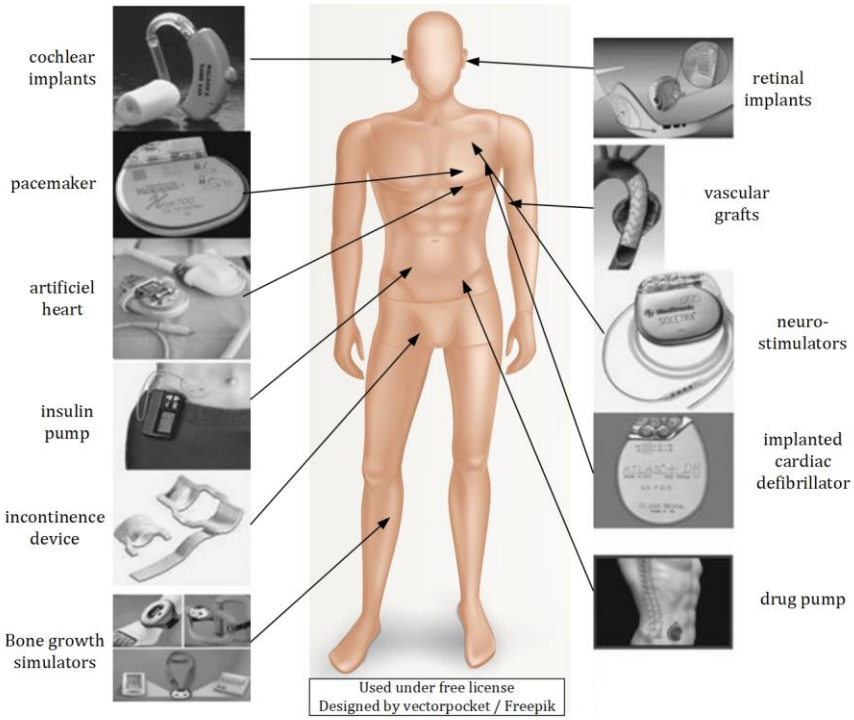


Fig. 1-17. The various implanting medical devices [58]

| Activity | Available electrical power | Available energy per motion |
|---|---|---|
| Blood flow [62] | 0.37 W | 0.37 J |
| Exhalation [62] | 0.4 W | 2.4 J |
| Breath [62] | 0.091-0.42 W | 0.5- 2.5 J |
| Upper limbs [62] | 0.33-1.5 W | 1.5-6.7 J |
| Typing by fingers [62] | 0.76- 2.1 mW | 143- 266 µJ |
| Walk [62] | 5- 8.4 W | 8.3- 14.0 J |
| Stepping- Heel strike [63] | 2-20 W | 1-5 J |
| Stepping- ankle [63] | 66.8 W | 33.4 J |
| Knee [64] | 4.8 mW | |

Table 1-4. Estimation of available power and energy from human motion [62], [63]

Platt et al. [65] explored the use of PZT bulk elements in a knee implant toward the use of autonomous biosensors. Furthermore, a vast number of studies focused on human walking motions for power generation, and they showed that considerable power could be generated from human walking. Examples of studies on the power generation from human walking are Fan et al. [66], Wang et al. [67], and Hwang et al. [48]. Fan et al. [66] could successfully design a piezoelectric harvester by which an RMS voltage output of 1.64 V can be produced when the walking speed is 8 km/h. Besides, kinetic energy from jaw motion [68] has been converted to electrical energy by a flexible piezoelectric strap.

Moreover, several practical devices have been tested on animals for future body applications. A flexible PVDF film was warped around a pig ascending aorta in one study, and a voltage of 1.5V has been generated [69]. Furthermore, a PZT-based thin film is integrated into the soft tissues for being attached to the heart, lung, and diaphragm of cows and sheep [70]. Their study showed that a power density of 1.2 µW/cm$^2$ could be produced from PZT materials [70]. Furthermore, a flexible thin-film PMN-PT harvester with 1.7×1.5 cm$^2$ could generate an 8.2 V voltage from the rat heart [71].

## 1.5.2. GENERAL TECHNIQUES FOR PVEH MODELING

### 1.5.2.1 Constitutive equations for piezoelectric materials

IEEE standard on piezoelectricity has introduced the linear piezoelectricity equations from the first law of thermodynamics and the electric enthalpy density [72], as given by:

$$T_{ij} = Q^E_{ijkl} S_{kl} - e_{kij} E_k \tag{1.14}$$

$$D_i = e_{ikl}S_{kl} + \varepsilon_{ik}^{S}E_k \tag{1.15}$$

wherein *T* is the stress tensor, *S* is the strain tensor, *E* is the electrical field, *e* is the piezoelectricity coupling coefficients, *Q* is the stiffness constants, *D* is the electrical displacement tensor, and $\varepsilon$ is the piezoelectric permittivity constant.

The IEEE piezoelectricity standard also has presented different piezoelectric constitutive equations and the relationships between the piezoelectric coupling coefficients. Eq. (1.16) and Eq. (1.17) show another alternative form of the piezoelectric constitutive equations.

$$S_{ij} = Q_{ijkl}^{E}T_{kl} + d_{kij}E_k \tag{1.16}$$

$$D_i = d_{ikl}S_{kl} + \varepsilon_{ik}^{T}E_k \tag{1.17}$$

Joshi [73] introduced the nonlinear constitutive equations for piezoelectric materials by employing the thermodynamic Gibbs potential function, as shown by Eq. (1.18) and Eq. (1.19).

$$S_{ij} = Q_{ijlm}^{E}T_{lm} + d_{ijn}E_n + \frac{1}{2}Q_{ijlmpq}^{E}T_{lm}T_{pq} + \frac{1}{2}d_{ijnr}E_nE_r + \kappa_{ijlmn}T_{lm}E_n \tag{1.18}$$

$$D_k = d_{klm}S_{lm} + \varepsilon_{kn}^{T}E_n + \frac{1}{2}\kappa_{ijlmn}T_{lm}T_{pq} + \frac{1}{2}\varepsilon_{knr}^{T}E_nE_r + d_{klmn}T_{lm}E_n \tag{1.19}$$

As can be seen from Eq. (1.18) and Eq. (1.19), nonlinear terms exist in the constitutive equations.

Wang and Gross [74] have developed the constitutive equations for bimorph piezoelectric bender with a substrate. Their formulation considers the voltage, point-load, moment at the beam end, and uniform load.

Nguyen et al. [75] have developed the constitutive equations for two types of piezoelectric harvesters, 31-mode by the top and bottom electrodes (TBE) and 33-mode by interdigitated electrodes (IDE).

#### 1.5.2.2 Linear models

In the linear models, the constitutive piezoelectric equations and the strain-deformation relationships are linear. Therefore, the material and geometrical

nonlinearities are not considered in the linear models. A great deal of piezoelectric modeling techniques has been developed in the linear framework.

### Single-degree-of-freedom (SDOF) models

In 1996, Williams and Yates [76] presented a mass-spring-damper model to illustrate a micro-electric generator's performance focusing on the electromagnetic generator. This model has not been developed for the piezoelectric purpose, and therefore the material electromechanical coupling behavior is not present in the model.

Plat et al. [65] have developed an SDOF model with the electromechanical coupling (from the linear constitutive equations) and extracted the steady-state response under the harmonic excitation.

DuToit et al. [77] investigated an SDOF model considering the electromechanical coupling effects. Using this SDOF model, they obtained the optimal conditions (frequency and electrical load) for the optimum power generation. They also showed that the piezoelectric voltage generation affects the beam stiffness. The DuToit SDOF model can provide a correct platform for sensitivity analysis of power output and structural analysis. Nevertheless, finding the equivalent dynamic properties of the piezoelectric beam for the SDOF model is an issue.

Therefore, some researchers employed the beam models to provide correlation factors so that the SDOF model is correlated to the beam models, such as [78]. Shu and Lien presented an SDOF model with correlation factors from the Rayleigh-Ritz approximation [79].

Luschi and coworkers [80] have recently provided a global reduced one-dimension beam model for piezoelectric beams under different beam dimensions, e.g., narrow enough beams and beams with a very-thin piezoelectric layer and wide beams.

### Beam distributed models

In 1999, Li and coworkers [81] presented the bending moment of a PZT-brass unimorph considering the electromechanical coupling.

DuToit and coworkers [77] presented an analytical model for the unimorph and bimorph beams using the generalized Hamilton's principle. Later, DuToit and Wardle [82] presented the experimental verification for their analytical beam model by testing a PZT-5A bimorph. According to their experimental data, the beam analytical model under-predicts the mechanical response and the power output at the resonance or near resonance.

Erturk and Inman in 2008 [83] critically reported issues in piezoelectric beam modeling and provided solutions for these issues. Erturk and Inman, in another study [84], presented a distributed beam model based on Euler-Bernoulli's beam theory.

This study [84] presented detailed explanations about the power output, electromechanically coupled responses, and power-load relationships. Later, Erturk and Inman [85] expanded their model to bimorphs (parallel and series connections) and carried out experimental data verifications.

In the distributed beam models, the equations of motion are often developed based on the modal coordination so that for solving the equations, a summation over all the modal modes (in theory, from one to infinity) is required. However, if the piezoelectric beam vibrates with a frequency around its first natural frequency, the first mode contribution is substantially more vital than the other modes' contributions; therefore, the distributed beam models can be reduced to single-mode equations. Liao and Sodano [86] introduced a reduced-order model using the analytical transverse vibration of beams. Banerjee and Roy [87] developed a 1D reduced-order electromechanical coupled model for the piezoelectric beams.

The previously mentioned models have been developed for conventional 31-mode harvesters. Ajitsaria and coworkers [88] investigated unimorph benders' performance with interdigitated electrodes by developing a theoretical model for this unimorph type.

Kim and coworkers [89] thoroughly studied the effect of added tip mass on the piezoelectric beams by employing the distributed beam model.

Lumentut and Howard [90] provided an analytical beam model for both bending and axial vibration excitations, focusing on developing various frequency response functions. Their model has good agreement with the experimental data.

Many material and geometrical properties are required for modeling the piezoelectric harvester based on the beam models that may be incorrect or inaccessible. Therefore, for making the beam models straightforward, Kim and coworkers [91] provided a reduced-order beam model that the modeling parameters can be simply obtained by the geometry and the modal data from the experiment.

The distributed beam models for trapezoid harvesters differ from the rectangular ones, which have been generally assumed for the model development. Muthalif and Nordin [92], Xie and coworkers [93], and Kherbeet and coworkers [94] have developed the analytical beam models for the tapered beam configurations.

Most of the work on piezoelectric beam modeling has been derived from the Euler-Bernoulli beam theory. Banerjee and Roy [95] presented a Timoshenko-like beam model by taking the shear mode into account.

Paknejad and coworkers [96] developed an analytical solution for the piezoelectric bimorph beams with a composite center shim.

Wang and Wang [97] developed a beam model with a partially covered piezoelectric layer and the tip mass for the nanoscale and considering the flexoelectric effect. They showed that if the piezoelectric layer's thickness is less than 1000 nm, the flexoelectric effect becomes significant, influencing the output voltage.

Zhang and coworkers [50] investigated a piezoelectric bimorph attached to a bridge and developed a beam model under a moving harmonic load.

Mallouli and Chouchane [98] provided an analytical beam model for piezoelectric harvesters with the macro fiber composite (MFC), which has the interdigitated electrodes.

Zhou and Zhao [99] have recently revisited the classical beam approach for modeling the piezoelectric energy harvesters and provided a comprehensive archive of the beam models.

In the previous methods, the boundary condition is considered chiefly clamped-free. If the boundary condition is changed, the piezoelectric beam formulation shall be modified as well. Lu and coworkers [100] presented a beam model for two-span piezoelectric energy harvesters and investigated this energy harvester type.

### 2-D Finite element models

Conventional and straightforward beam configurations can be solvable analytically by the beam models. However, for the beam complex configurations, providing analytical solutions is not possible. Besides, only the simple deformation theories can be applied in the beam models; otherwise, finding the solutions would be complex. Finite element (FE) models are powerful numerical models for solving the partial differential equations (PDEs) under the boundary conditions (BCs).

In the FE method, the piezoelectric domain is divided into small elements, and the PDEs are developed for the small element. Next, by assembling the PDEs, a matrix representation of the PDEs over all the elements is obtained. This matrix equation will be solved after applying the BCs.

Many researchers on the FE model for piezoelectric materials were devoted to the actuator-sensor applications in a composite multi-layered structure, not energy harvesting applications. The works by Hossack and Hayward [101], Lam and coworkers [102], Reddy [103], and Azzouz and coworkers [104] are among the FE models for the piezoelectric sensor or actuator applications. Later, studies have been carried out for the FE analysis for the piezoelectric energy-harvesting applications, including the works by Yaman [105], Moradi-Dastjerdi et al. [106], Lezgy-Nazargah and coworkers [107], and Marqui-Junior and coworkers [108].

Different plate theories can be employed for the FE formulation. Fig. 1-18 shows a category of different plate theories based on the beam deformations' assumptions. In the classical methods, the beam deformation in the thickness is null, so that the beam displacement through the thickness is constant. In the classical methods, classical plate laminate theory (CLPT) does not consider the shear stresses. While the shear deformation theories consider the shear stresses, the out-of-plane stresses are not continuous in the classical methods as the mechanical properties in the thickness are not continuous. Here, the advanced theories appear as a tool for satisfying the inter-laminar continuity.

The FE works on the piezoelectric energy harvesters have developed based on the classical theories. For instance, the studies [105], [108] use the classical plate theory, and the study [106] uses the high order shear deformation theory, but in all of these studies, the deformation in the thickness is null. On the other hand, the studies that used advanced theories, like [109], [110], have not been developed for energy harvesting applications.

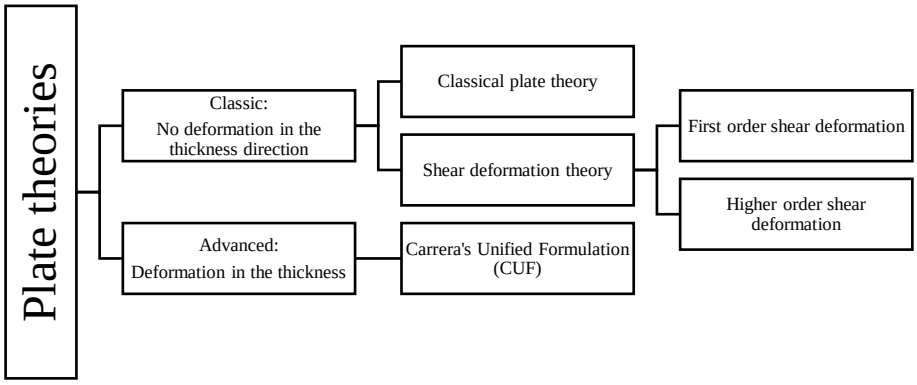


Fig. 1-18. Different plate theories for structural analysis of piezoelectric materials.

### 1.5.2.3 Nonlinear models

The piezoelectric energy harvester is typically designed to work in the resonant for the highest possible electrical power conversion. The resonant operation can cause a sizeable mechanical strain, as the deformation will be substantial at the resonance. If the mechanical strain becomes substantial, elastic nonlinearities can occur, as demonstrated by Priya et al. [111] for soft and hard PZTs.

Many of the developed models for the piezoelectric energy harvesters are obtained in the linear framework. Nevertheless, nonlinearities can occur for the high strain conditions. Abdelkefi and coworkers [112] developed a nonlinear distributed beam

model for the 31-mode harvester considering the geometric, inertia, and piezoelectric material nonlinearities. According to their conclusions, the PZT has a nonlinear softening behavior, and the nonlinearity can affect the voltage generation performance depending on the effective nonlinear coefficient. It has also shown that if the piezoelectric beam exhibits nonlinear behavior, using the single-mode approximation leads to misleading conclusions. Besides, Abdelkefi and coworkers [113] also developed a nonlinear distributed beam model for a piezoelectric beam under the length-wise vibration excitation.

Mam and coworkers [114] investigated the nonlinearity from large-deflection and piezoelectric material nonlinearity for the piezoelectric beams with transverse and axial base excitations.

Firoozy and coworkers [115] presented a nonlinear beam model for a piezoelectric beam with a proof mass and showed that attaching a massive proof mass will change the system behavior from linear to nonlinear, causing changes in the power generation and optimal frequency and load conditions.

### 1.5.3. CHALLENGES AND PERFORMANCE OF THE PVEHS

#### 1.5.3.1 Resonant frequency tuning

One of the challenges for piezoelectric energy harvesting is that they generate low power on the off-resonant. Therefore, the harvester should be designed so that its natural frequency matches the excitation frequency. Therefore, PVEH designs that can adopt the harvester's natural frequency without changing the harvester configurations are advantageous.

Considering a piezoelectric beam in the simply supported boundary condition, applying a preload and using a mobile mass can be used for frequency tuning. The preload can reduce the harvester's natural frequency up to 24%, which can also partially increase the power output even though it also increases the damping coefficient [116]. A mobile mass can provide an automatic resonant tuning for a range of approximately 40 Hz [117]. Even though these techniques can lead to resonant frequency tuning, the energy harvester with simply supported boundary conditions has higher resonance than the clamped-free boundary conditions. This may hinder the use of these harvesters for human motions and environmental forces.

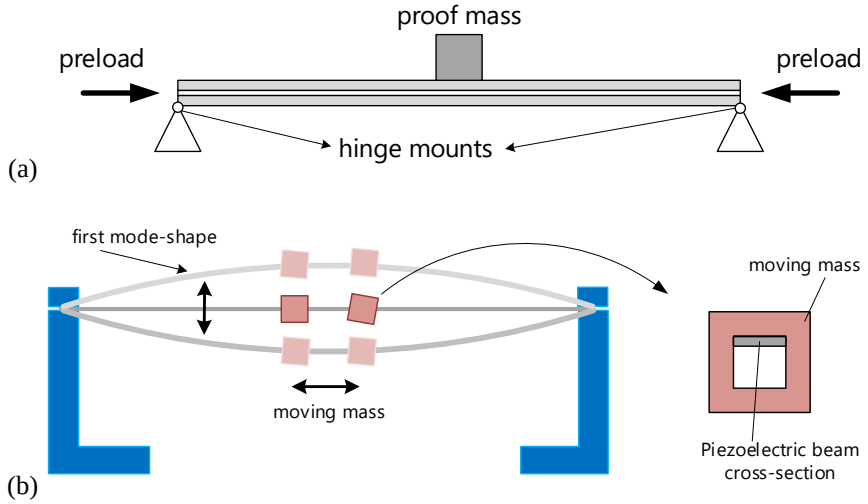


Fig. 1-19. Frequency tuning in simply supported beams, (a) the use of preload [116], and (b) the use of mobile mass for the automatic tuning [117].

Using nonlinear mechanisms for resonant tuning is another option. The nonlinear mechanisms can be applied by a direct mechanical nonlinearity (a stopper plate, for example) or nonlinear couplings, like magnetic forces. With a spring-plate combination in the bottom and stopper-plate on top, the resonant frequency can be tuned by adjusting the gap between these plates [118]. Using magnetic forces and adjusting the magnets' gap, the resonant frequency can be tuned [119]. In the non-linear stopper and spring plates, the resonant frequency is tuned within the 150 Hz range [118], and for the magnetic design, the resonant frequency is tuned within the 40 Hz range [119].

As mentioned before, the resonant frequency for the above resonant tuning is more than 40 Hz, which may be significant for some applications. Another method is adjusting the added mass position along a polymer-based large substrate [120], as demonstrated in Fig. 1-20. This approach can provide resonant frequencies in the range of 10 Hz.

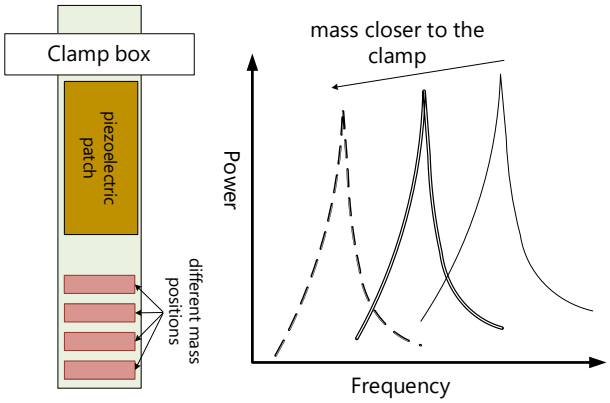


Fig. 1-20. The use of added mass position as a resonant tuning parameter [120].

### 1.5.3.2 Narrowband power output

As Fig. 1-11 (b) demonstrated a typical voltage output made on a piezoelectric beam, the power generation will decrease meaningfully by a slight variation in the excitation frequency. For the smaller damping coefficient becomes, the power frequency response will have narrower bandwidth. This narrow bandwidth will reduce piezoelectric harvesters' efficiency, as the source excitation frequency may slightly change, which will cause a considerable power reduction. Thus, a wide range of PEH studies has focused on providing broadband power generation. These techniques can be broadly categorized into four groups:

- Group 1: Magnetic force [66], [119], [121]–[126]

Using the magnetic force has been one approach for providing a coupling between the mechanical vibration and the magnetic force. Attaching magnets to the beam tip will provide a magnetic force, which will create broadband power outputs. The magnets can be simple permanent magnets, coils with an electromagnetic field, or oscillatory magnets. Fig. 1-21 (a) and (b) show the permanent magnet use in two different configurations.

| (a) | (b) |
|---|---|

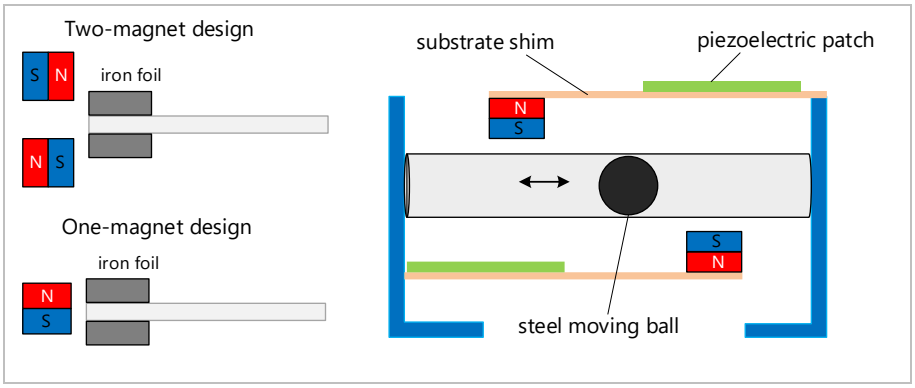


Fig. 1-21. Improving the power bandwidth by (a) the use of one or two magnets by Li and Thomsen [122], and (b) the use of a magnet and a rolling steel ball by Fan and coworkers [66].

The power generation performances of permanent magnets in the fixed and oscillatory configurations are compared with the standard linear harvester performance in Fig. 1-22. Comparing the standard and fixed permanent magnets in Fig. 1-22 (a) and Fig. 1-22 (b) shows that the power bandwidth is slightly improved, but the peak power is reduced. This power reduction can be due to preventing the beam vibration by the magnet force. Nevertheless, the oscillatory magnet design improved both the peak power and the bandwidth power.

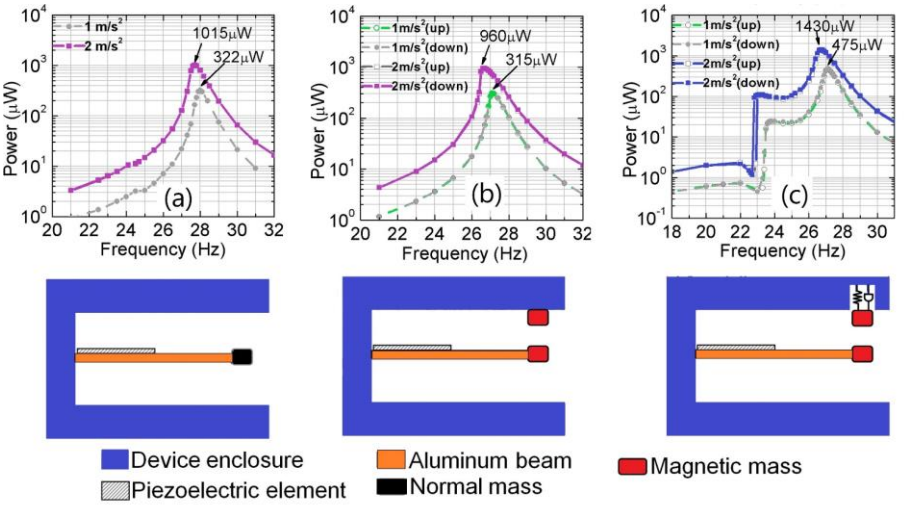


Fig. 1-22. A comparison between the power outputs in (a) standard PVEH design, (b) fixed magnets, and (c) oscillatory magnet mass [121].

- Group 2: Stoppers [127]–[132]

Adding one or two mechanical stoppers at the beam tip can also provide a broadband power frequency response. The mechanical stopper can be a piezoelectric beam [127] or a rigid stopper [129]. The power output over the frequency range for a piezoelectric harvester with a beam stopper is shown in Fig. 1-23 [127], showing that the power bandwidth is increased from a few Hertz to 25-35 Hertz. The stopper mechanism and the magnetic forces can form a combined version for broadband energy harvester [128].

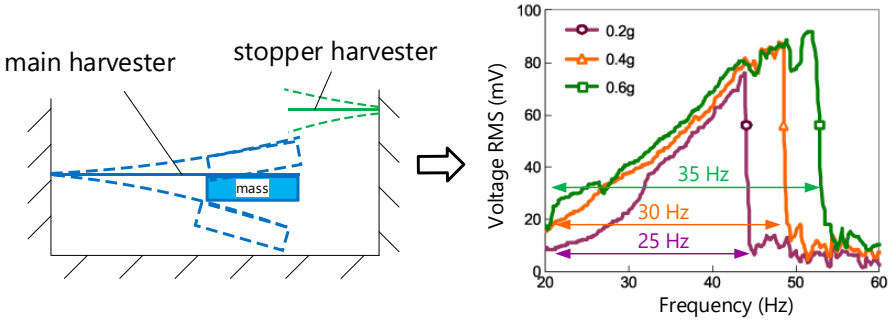


Fig. 1-23. The power output from a piezoelectric beam with another piezo-beam stopper [127].

- Group 3: Multi-modal beams [119], [133]–[136]

Another group of designs for providing broadband energy harvester is to use multiple beams attached to one base. Such energy harvesters with multiple beams have been shown in Fig. 1-13. By attaching several harvesting beams, a wider range of frequencies can be covered and reach broadband power performance. One example of the multi-modal beams is shown in Fig. 1-24 [136].

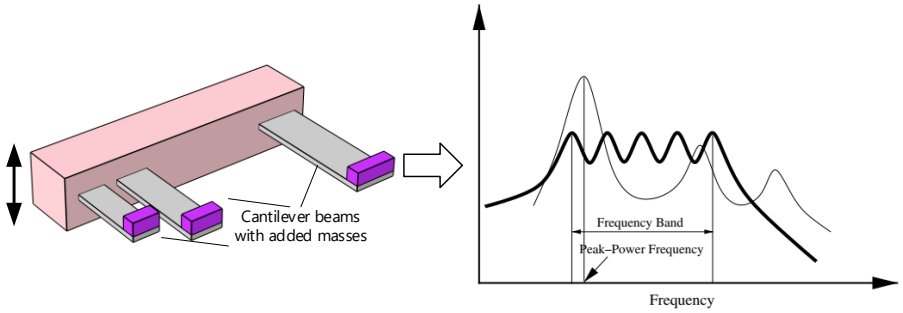


Fig. 1-24. A multi-beam energy harvester design with its power output [136].

- Group 4: Impact-driven forces [137]–[141]

When an energy harvester is subjected to an impact, it vibrates with its natural frequency. Regardless of the excitation frequency, each impact excites the beam with its natural frequency; therefore, a wider power bandwidth can be expected in the impact-driven designs. Fig. 1-25 shows an energy harvester with two piezoelectric beams excited with the impact from a sliding mass [141]. Jacquelin and coworkers [141] showed that this energy-harvesting design benefits from a wider power bandwidth.

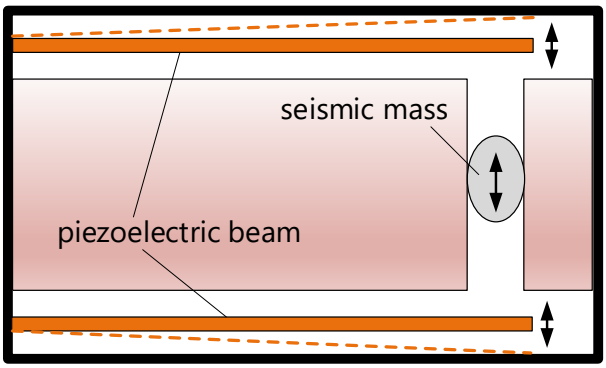


Fig. 1-25. An energy harvester based on the impact force [141].

### 1.5.3.3 Mechanical damping

Damping has a negative role on the power generation by piezoelectric energy harvesters as it dissipates the mechanical energy. The drop in the power output versus the mechanical damping ratio is substantial, as can be seen from Fig. 1-26. For instance, increasing the damping ratio from 1% to 2% will reduce the power from 2mW to 0.85mW [142].

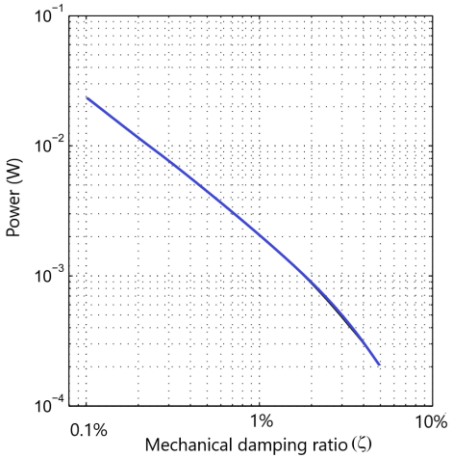


Fig. 1-26. The piezoelectric power output is a function of the mechanical damping ratio [142].

As can be seen from Fig. 1-27 (a), the mechanical damping depends on the beam width, according to Dayou and coworkers [143]. Therefore, they suggested that splitting the beam into three splits will increase the power output due to the damping reduction. The power increase of beam splitting is shown in Fig. 1-27 (b).

(a) (b)

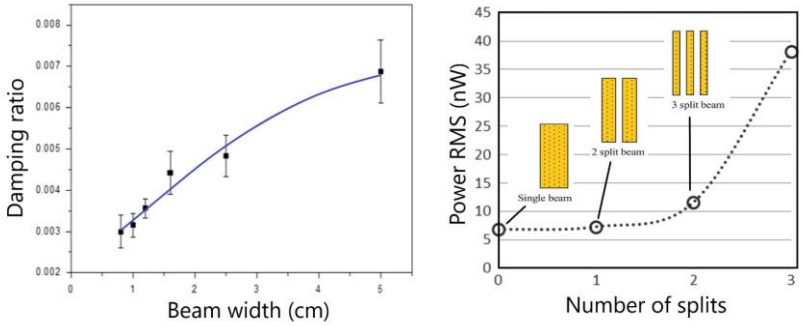


Fig. 1-27. The influence of beam width on the mechanical damping, (a) beams with reduced width, (b) damping ratio versus the beam width, and (c) the power output improvement by splitting the beam [143].

For the piezoelectric beams that vibrate in the surrounding fluid, the fluid resistance force is a factor that prevents the beam vibration. In other words, the fluid resistance force dissipates the kinetic energy. The fluid resistance force is called viscous damping. This viscous damping depends on the excitation amplitude and the

surrounding fluid [144], as can be seen from Fig. 1-35 (a). The effect of surrounding fluid on the power generation can be seen in Fig. 1-35 (b). The bimorph vibrating in oil generates considerably lower power than that of vibrating in the air.

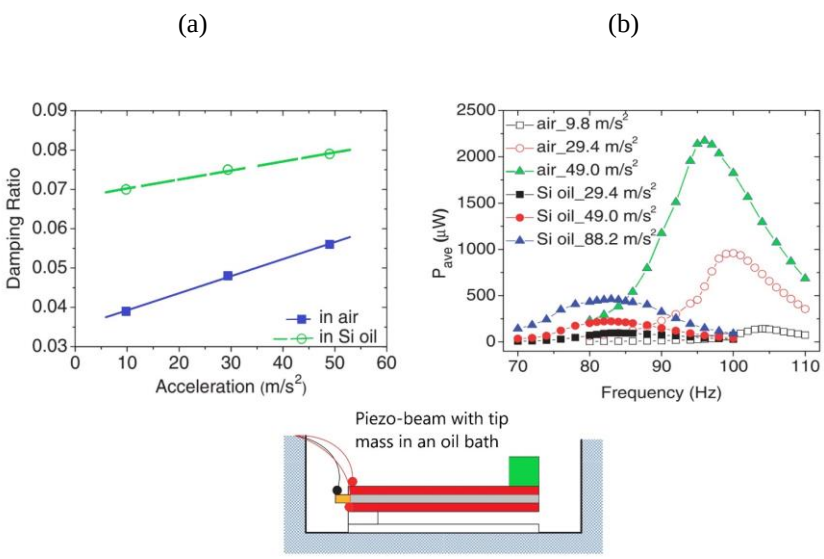


Fig. 1-28. (a) The damping ratio is a function of excitation acceleration for the bimorph vibration in air and oil and (b) the power frequency response for different vibrating conditions [144].

One way to quantify the effect of viscous air damping on the PEH performance is to study the power generation in a vacuum surrounding. This study has been carried out by Elfrink and coworkers [145]. They showed a considerable power rise from the PEH when it is vibrating in the vacuum, showing that the effect of viscous damping can be reduced if the piezoelectric sample is inserted into a vacuum-package.

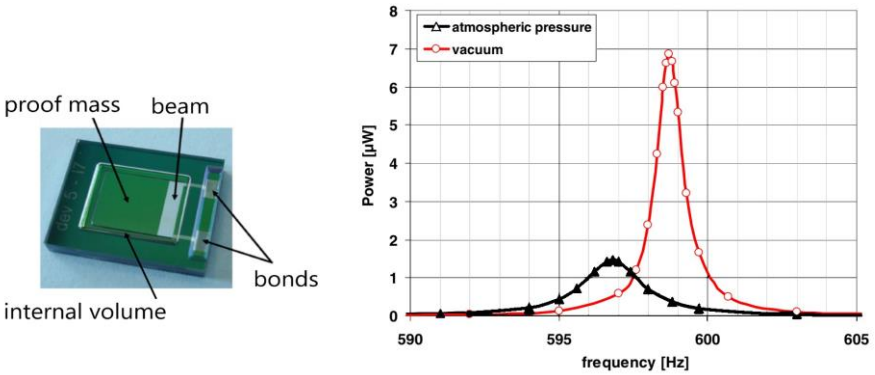


Fig. 1-29. The power increase of piezoelectric sample using the vacuum-package [145].

In addition to the viscous damping, internal energy dissipation is also another damping mechanism. According to Baker et al. [146] and Crandall [147], which considered structural damping due to acoustic radiation loss, internal damping is maximum at a frequency called relaxation frequency. In Crandall's study [147], it was shown that by adding a strip of damping tape to an aluminum plate, internal damping changes with an order of six, indicating the importance of adding viscoelastic materials on structural damping. Baker et al. [146] showed that structural damping has a negligible dependency on the vibration amplitude for thin benders.

### 1.5.3.4 Fragility of Ceramics

Ceramics, Piezoceramic, and single crystals have excellent piezoelectric properties, yet they suffer from fragility and inflexibility. Sessler in 1981 [148] reported that piezoelectricity exists in the PVDF polymer. Nevertheless, the low piezoelectric coupling coefficients in the PVDF are an issue. Thus, many efforts have been focused on proving flexible piezoelectric samples with an excellent piezoelectric conversion.

One of the solutions is to manufacture composite materials with piezoelectric fibers. Two of the widely used piezo-composites are Piezoelectric Fiber Composite (PFC) and Macro Fiber Composite (MFC). The PFC has cylindrical fibers, while the MFC has rectangular fibers. In both of them, the Piezo-fibers are aligned and embedded into a polymer resin. Therefore, these composites become more flexible, but their power generation performance diminishes [7].

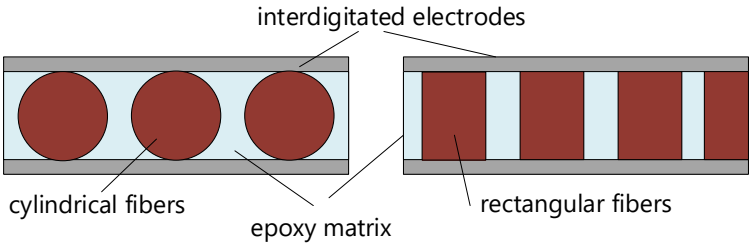


Fig. 1-30. The illustration of Piezo-composites, (a) Piezoelectric Fiber Composite (PFC), and (b) Macro Fiber Composite (MFC) [149]

Crossley and Kar-Nayaran [150] discussed the thin-film flexible Nanogenerators based on piezoelectric nanofibers. Using piezoelectric particles to form a piezoelectric composite layer with interdigitated electrodes is investigated by Sun and coworkers [151].

3D printing using the polymer PVDF can also manufacture the flexible composite piezoelectric structures [152]. A highly flexible piezoelectric sample made from PVDF sandwiched between aluminum substrates is developed for energy harvesting from human vessels [69].

Another solution, developed by Hwang and coworkers [71], is to manufacture a thin film ceramic and then attach it onto a flexible substrate. Hwang and coworkers fabricated the flexible piezo-harvester from PMN-PT single crystal to harvest energy from the external heart wall [71].

A flexible type of materials for piezoelectric energy harvesting is recently developed from the pomelo fruit membrane [153]. This piezoelectric generator's performance is low compared to the other materials, but this material is bio-waste and sustainable.

#### 1.5.3.5 Temperature effect

The temperature harms the piezoelectric performance. Above the Curie temperature, the piezoelectric materials will be depolarized and lose their conversion ability. Between the room temperature and the Curie temperature, the temperature also affects the piezoelectric voltage generation.

For the Piezo-composites, the MFC [12] and PFC [154], the conversion mechanism has the best performance around 20$^{o}$C, and after this temperature, the power generation is expected to decrease. In another study in Ref. [155], it is observed that for the Piezoceramic PZT-5A, increasing the temperature will reduce the voltage output. For higher excitation forces, the voltage reduction due to the temperature becomes more severe.

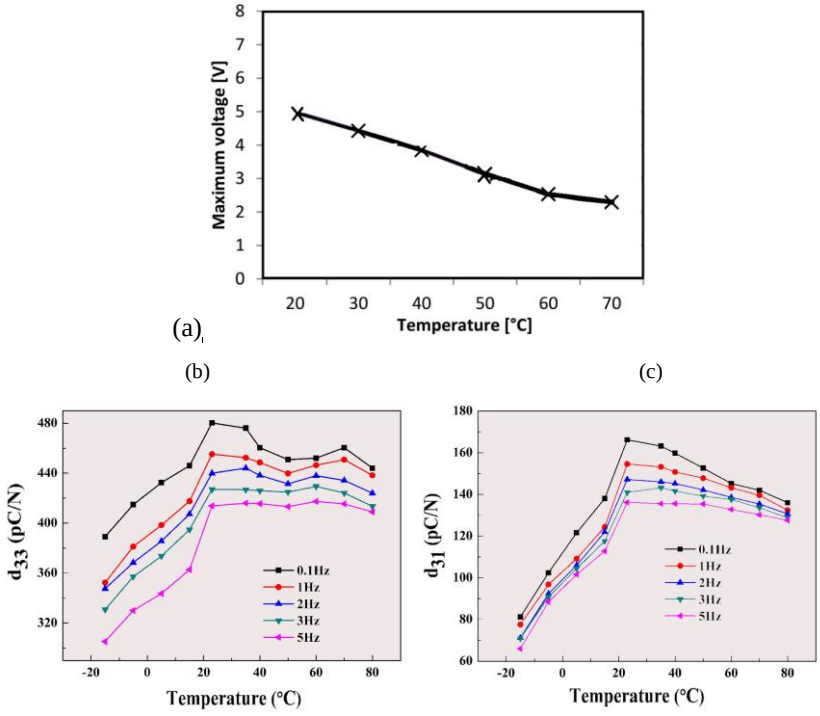


Fig. 1-31. The temperature effect on the Piezo composites, (a) voltage output from a Macro Fiber Composite (MFC) sample [12], (b) $d_{33}$, and (c) $d_{31}$ coefficients for Piezoelectric Fiber Composite (PFC) [154].

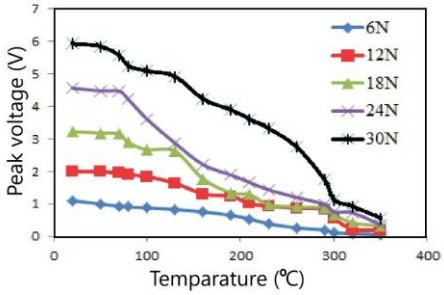


Fig. 1-32. The effect of temperature on the voltage output from PZT-5A [155].

The piezoelectric composite made from the piezoelectric particles in the polyimide matrix has demonstrated excellent performance at high temperatures [151], as shown in Fig. 1-33.

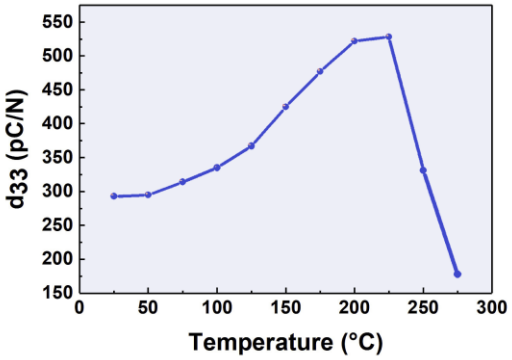


Fig. 1-33. The improved performance of the piezoelectric composite made from piezo-particles and polyimide matrix [151].

### 1.5.3.6 Long-term use of PVEHs

The discussion about the long-term use of piezoelectric harvesters has recently drawn attention. There is a low number of studies on the fatigue performance of PVEHs. Nevertheless, as PVEHs aims to provide a long-term power source, their long-term performance shall be considered. Salzar and coworkers [156] have recently reviewed the fatigue behavior of piezoelectric materials for energy-harvesting applications.

The MFC fatigue behavior can be more difficult because, generally, composites' fatigue behavior is challenging. Therefore, there are more studies on the MFC behavior study than other materials.

The MFC composite with PZT fibers after around 1 million cycles experiences a drop in the power generation and a shift in the resonant frequency, as shown in Fig. 1-34 (a) [157]. Therefore, this frequency shift should be considered if the resonant matching design is considered. Besides, in Ref. [157], it has been observed that the MFC layer in tension has more severed power degradation than the compressed MFC, as shown in Fig. 1-34 (b). The severe power degradation in the tension-layer is because of the initiation of Micro-cracks, which has been observed experimentally [157].

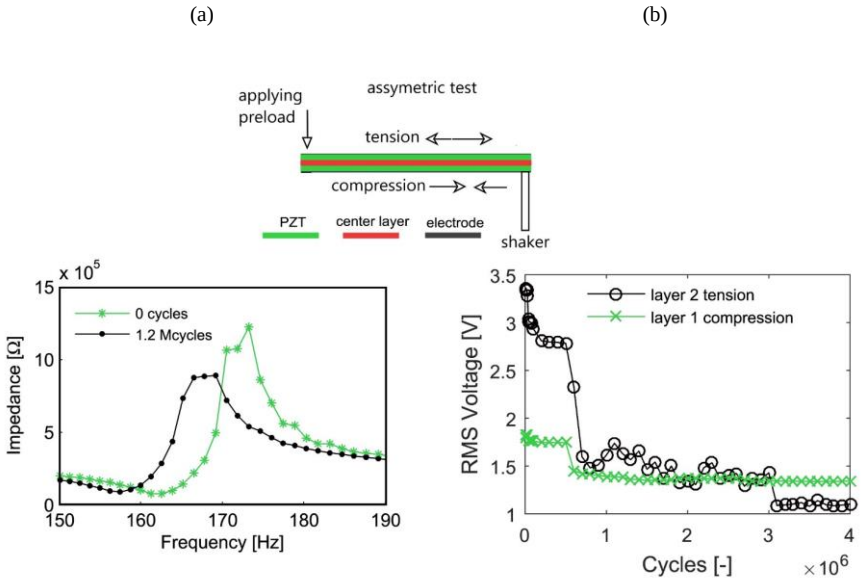


Fig. 1-34. The fatigue behavior of MFC with PZT fibers (a) frequency shift and (b) the voltage output for the compression and tension layers [157]

Ref. [158] investigated the MFC's fatigue behavior with single-crystal fibers (soft and hard single crystals). In both samples, after 1 million cycles, the power variation initiates. Nevertheless, the power degradation for the soft single crystal fibers is more severe [158]. This outcome can be seen in Fig. 1-35 (a) and (b).

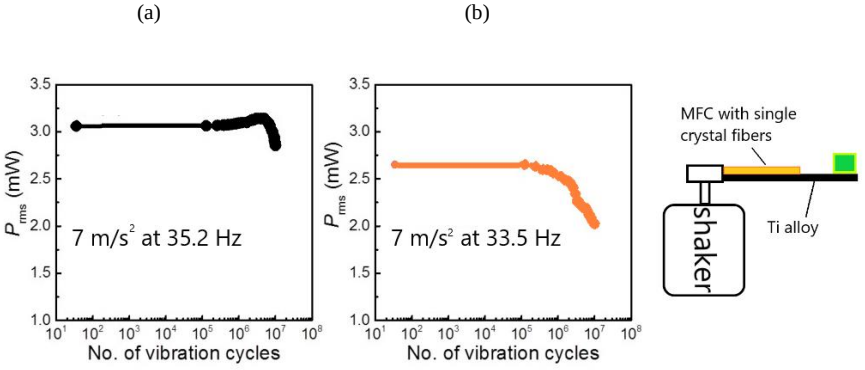


Fig. 1-35. The power output during a fatigue test for MFCs (a) hard single crystal fiber and (b) soft single-crystal fiber [158].

Another study about the MFC fatigue behavior, the voltage output, surface strain, and natural frequency is analyzed over a cyclic loading [159]. In the first 0.5 million

cycles, first, a drop in the voltage experienced, but afterward, again, the voltage value is slightly recovered. The resonant frequency constantly reduces during the cyclic load in contrast to the strain where it increases constantly. According to Ref. [159], if the acceleration level is below 6 m/s$^2$, the voltage degradation is negligible, as shown in Fig. 1-36 (c).

(a) (b)

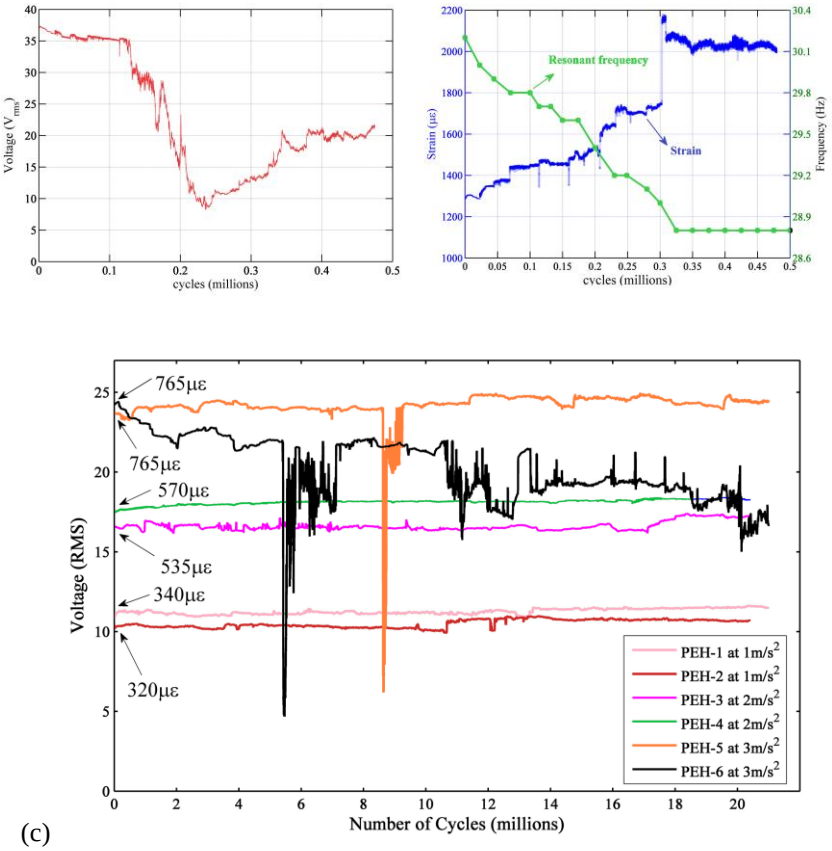


(c)

Fig. 1-36. The fatigue behavior of the MFC, (a) the voltage for 0.5 million cycles, (b) the resonant frequency and strain for 0.5 million cycles, and (c) the voltage for different strain levels during 20 million cycles [159].

Ref. [160] compared the fatigue behavior of PVDF, MFC, and PZT materials for three different tip mass ratios. The power output made from these materials over the cyclic load is shown in Fig. 1-37 [160]. PVDF does not demonstrate power reduction due to the fatigue, while there is a power reduction for the MFC and PZT. The MFC fatigue

behavior is abnormal compared to the PZT. For 10% and 30% tip mass ratios, the power output remains relatively constant, while for the 20% tip mass ratio, the power is reduced over time. There is power degradation for all tip mass ratios for the Quick Pack sample (with PZT layers); especially for the larger tip mass ratio, the power reduction increases.

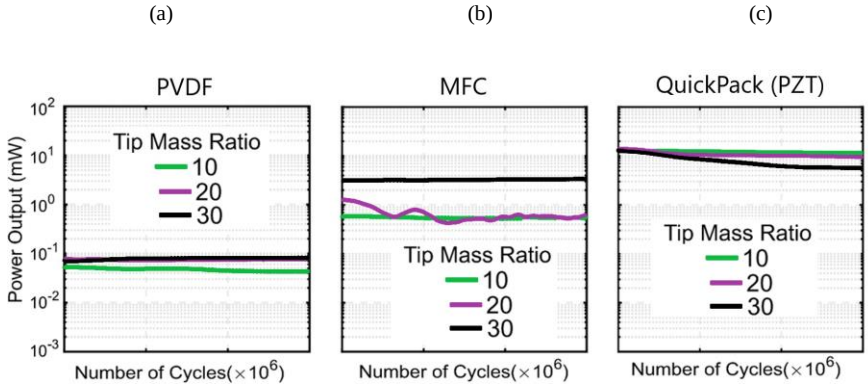


Fig. 1-37. The voltage degradation for three different tip mass ratios for (a) PVDF, (b) MFC, and (c) Quick Pack made of PZT [160].

Yang and Zu [14] showed that the fatigue performance of the single crystals PMN-PT and PZN-PT is more substantial than the PZT.

In some applications, there is a need to insert the piezoelectric beam into a package box. This packaging box will reduce the power output according to Ref. [145], as demonstrated in Fig. 1-38.

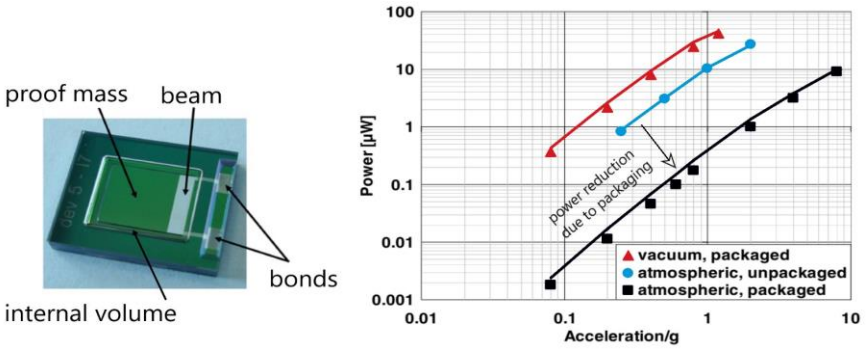


Fig. 1-38. The performance of piezoelectric energy harvester under atmospheric packaging box [145]

## 1.6. OBJECTIVES

As a general objective, this Ph.D. thesis aims to progress the state-of-the-art in piezoelectric energy harvesting. By this project, the following objectives are elaborated:

1. Modeling of piezoelectric energy harvesters (PEHs):
    a. Presenting a comprehensive finite element model by which a wide range of piezoelectric harvester configurations can be analyzed.
    b. Accommodating the advanced plate theories with shear-stress considerations in the FE model.
    c. Accommodating the viscous and structural damping mechanisms in the FE modeling.
    d. Presenting a layered model for the piezoelectric multi-layer composite materials.
    e. Developing a unified electromechanically coupled equation for the voltage output toward better electrical and mechanical modulations of piezoelectric energy harvesters.
    f. Demonstrating the correlation between the simple spring-damper-mass, distributed beam, and FE methods.

2. Parameter investigation for the PEHs
    a. Clarifying the role of substrate and bonding layer on the power generation
    b. The tip-mass effect on the power output, resonant frequency, and viscous air damping
    c. Developing straightforward methods for the determination of damping in a simple experimental setup
    d. Illustrating the role of different damping mechanisms on the total damping
    e. Demonstrating the role of structural damping
    f. Investigating the viscous air damping under different piezo-beam excitations

3. Applications of the PEHs
    a. Exploring the possible vibration energy sources for the PVEH
    b. Investigation of piezoelectric energy harvesters with simple configurations that can be easily adopted into motors
    c. Comparing the performance of different materials in the energy harvesting
    d. Developing and investigating the remote condition monitoring as a significant possible application of the PVEH
    e. Investigating different approaches for the resonant frequency matching method.
    f. Analyzing and developing power management systems so the output power by PEH can power small electronic devices.
    g. Optimizing PEHs from composite material toward better power generation performance.

h. Improving the power generation from practical vibration sources by geometry and material modulations.

## 1.7. THESIS OUTLINE

The thesis is structured with the following chapters.

*Chapter 2* presents these thesis contributions to the modeling techniques for the piezoelectric energy-harvesting beams. The SDOF method with an equivalent beam approach for structural modeling of unimorph and bimorph is reported. The distributed beam model is revisited to present a unified electromechanically coupled equation for the voltage, which is then the transient response under the harmonic motion is reported for the beam model. Finally, a comprehensive FE method for non-uniform variable thickness beams using the advanced plate theories is reported. A sideline subsection is dedicated to the layer-wised modeling of the MFC.

*Chapter 3* presents this thesis's contributions to the sensitivity analysis of different elements in a piezoelectric beam. The substrate structure, the added tip mass, and the contact layer are studied.

*Chapter 4* contributes to the damping determination methods in piezoelectric harvesters from only the voltage measurement outputs. Moreover, the contributions of different mechanisms in energy dissipation are investigated.

*Chapter 5* presents the contributions of this thesis to the design of practical piezoelectric energy harvesters. One application of piezoelectric energy harvesting, the autonomous condition monitoring system, is studied in detail. The resonant matching design is investigated. Moreover, a multi-beam trapezoid configuration with improved strain contours is presented as a way for broadband power generation.

*Chapter 6* summarizes the thesis's main contributions and comments on future research directions.

# CHAPTER 2. PIEZOELECTRIC ENERGY HARVESTER (PEH) MODELS

This chapter aims to present the methods for modeling piezoelectric energy harvesters. Two of the typical 31-mode energy harvesters are unimorph and bimorph energy beams. In the unimorph harvester, one piezoelectric layer is attached to a substrate shim, as shown in Fig. 2-1 (a); in the bimorph harvester, two piezoelectric layers are attached to the substrate shim, as shown in Fig. 2-1 (b). A proof mass may be added to the beam tip to generate more power output in either of them.

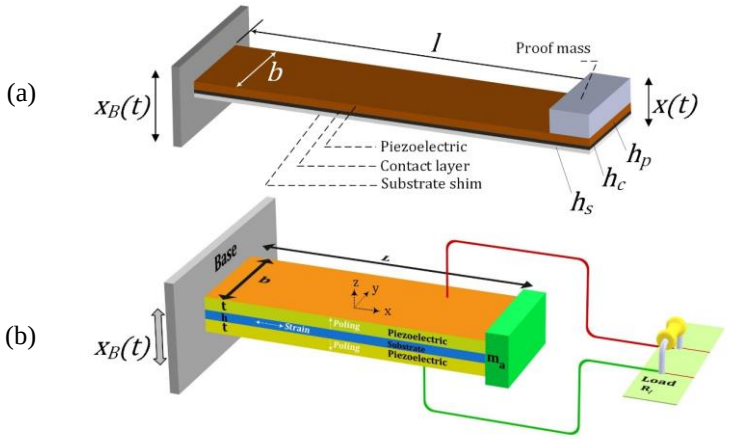


Fig. 2-1. Typical energy harvesting beams, (a) unimorph [161] and (b) bimorph [4]

This chapter presents different models for modeling piezoelectric energy harvesters derived from the previously published papers. Single-Degree-of-Freedom (SDOF) method is rewritten from Ref. [161], the beam distributed model is rewritten from Ref. [4], [162], finite element model is rewritten according to Ref. [163], and the modeling for Macro-fiber Composite (MFC) energy harvester is rewritten according to Ref. [164].

## 2.1. THE DESCRIPTION OF BENCHMARK EXAMPLE

Throughout this section, for validation and sensitivity analysis, a benchmark example is used. The experimental data for this benchmark example has been reported by Erturk and Inman [165]. Researchers have extensively used this benchmark example for the model validations [32], [162], [163].

The benchmark example is a bimorph piezoelectric beam with 0.012 kg added tip mass, consisting of two PZT-5A piezo layers with a brass center shim. Table 2-1 presents the benchmark example's geometries and the material properties for the piezo layers and the substrate brass shim.

| | | | |
|---|---|---|---|
| Length of the beam (mm) | 50.8 | Width of the beam (mm) | 31.8 |
| Tip mass, (kg) | 0.012 | Damping (experimentally measured) | 2.7% |
| Substrate shim (brass) | | | |
| density ($kg/m^3$) | 9000 | Young's modulus (GPa) | 105 |
| thickness (mm) | 0.14 | | |
| Piezoelectric layer (PZT-5A) | | | |
| Density ($kg/m^3$) | 7800 | thickness- each layer (mm) | 0.26 |
| $c_{11}^{E}$(GPa) | 66.0 | $e_{13}$ ($C/m^2$) | -15.9 |
| Permittivity ($F/m$) | 1.593×10-8 | | |

Table 2-1. The geometries and material properties for the benchmark example [165].

## 2.2. SINGLE-DEGREE-OF-FREEDOM MODEL (SDOF)

This section deals with the Single-Degree-of-Freedom (SDOF) model for piezoelectric beams. DuToit model is employed as the base method for this section. However, this method has some limitations, which will be discussed during the method presentation. Some tips will be provided during the model derivation to overcome the method limitations.

DuToit model is an electromechanically coupled model that represents a piezoelectric beam with an SDOF vibration system. In the DuToit model, electrical and mechanical equations are not separated and assumed coupled. The electromechanical-coupled model is the correct model for piezoelectric materials [83], as piezoelectricity is a material characteristic. DuToit model [77], as shown in Fig. 2-2 (a), comprises a piezoelectric mass with internal resistance $R_p$ connected to a load resistor $R_l$. In this model, the entire structure is piezoelectric and, therefore, electromechanically coupled.

This model has the following advantages and disadvantages.

Advantages:

- Simple method requiring a small number of variables and easy to implement
- Representing the proper electromechanical behavior of piezoelectric materials
- Useful for both 31 and 33 mode energy harvesters

- Considered the backward piezoelectric effect; able to demonstrate the open-circuit and short-circuit condition effects on the structural response
- Giving analytical function for the output voltage and power facilitate finding the optimum electrical load
- Can accommodate the added tip mass

Disadvantages:

- Too much simplification for the structural modeling (material, layup, and geometry)
- Not applicable to complex structures of the PVEHs
- A rough estimation of the natural frequency

For the electrical equivalent circuit, the piezoelectric material is modeled as capacitance ($C_P$) and resistance ($R_P$) in series connection, see Fig. 2-2 (b). The scale of internal piezoelectric resistance is >$10^9$, which is large to the external load ($R_l$<1MΩ); therefore, it can be neglected. According to DuToit et al. [77], [82], the capacitance of a piezoelectric layer is defined as a function of the permittivity constant $\varepsilon^s$, piezoelectric surface area $A_p$, and the piezoelectric thickness $h_p$ by:

$$C_p = \varepsilon_{31}^s A_p / h_p \tag{2.1}$$

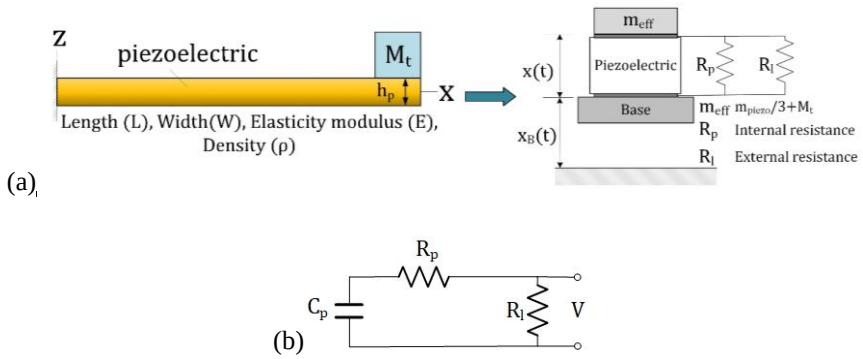


Fig. 2-2. (a) DuToit SDOF model for PVEHs and (b) electrical circuit for the PVEH

The DuToit model can be used for 31 (bending) and 33 (extension) mode energy harvesters. Therefore, the piezoelectric coefficient "$d$" should be inserted according to the mode of vibration. In this section, the 31-mode harvester is considered, thus, $d_{31}$ is inserted into the model.

The vibration equation for a non-piezoelectric SDOF vibration system is [166]:

$$\ddot{x}(t) + 2\zeta_m \omega_n \dot{x}(t) + \omega_n^2 x(t) = -\ddot{x}_B(t) \tag{2.2}$$

Wherein mechanical viscous damping coefficient and natural frequency are respectively $\zeta_m$ and $\omega_n$. $\zeta_m$ usually is extracted from experiments, but $\omega_n$ can be extracted either by experiment or analytical modeling. Different methods estimate $\omega_n$ with different accuracies.

However, if the vibrating element is piezoelectric, a backward piezoelectric effect should be added to the mechanical vibration equation due to piezoelectricity. DuToit et al. estimate the coupling effect with $\theta = \omega_n^2 d_{31}$ [77], [82].

Ref. [77], [82] assumed that the piezoelectric element is the only vibrating element, while in many practical cases, the piezoelectric element is attached to a substrate. To accommodate the unimorph design, α coefficient is introduced as the ratio of the piezoelectric layer mass to the total beam mass, i.e., $\alpha = m_{\text{piezo}}/m_{\text{beam}}$. If the energy harvester is only piezoelectric layer, then α=1.

Consequently, the equations of motion for this system under base excitation can be expressed [77], [161]:

$$\ddot{x}(t) + 2\omega_n \zeta_m \dot{x}(t) + \omega_n^2 x(t) - \alpha\theta V(t) = -\ddot{x}_B(t) \tag{2.3}$$

$$R_l m_{\text{eff}} \theta \dot{x}(t) + R_l C_p \dot{V}(t) + V(t) = 0 \tag{2.4}$$

$x$, $V$ and $\ddot{x}_B$ represent the displacement field, output voltage, and base acceleration, respectively. Besides, the effective harvester mass and piezoelectric coupling factor for the harvester are respectively $m_{\text{eff}}$ and $d$. $m_{\text{eff}}$ is the effective mass of the piezoelectric layer because of the electromechanical coupling. $m_{\text{eff}}$ and $\omega_n$ are given by [77]:

$$m_{\text{eff}} = m_{\text{piezo}}/3 + M_t \tag{2.5}$$

$$\omega_n = \sqrt{C_{31}^E A_p / m_{\text{eff}} h_p} \tag{2.6}$$

wherein $C_{31}^E$ is the elastic modulus in the 31 direction under the constant electric field.

By solving the first-order differential equation for voltage (Eq.(2.4)), it can be shown that generated voltage can be expressed as:

$$V(t) = -\frac{m_{\text{eff}}\theta}{C_p} e^{-\frac{t}{C_p R_l}} \int_0^t e^{\frac{s}{C_p R_l}} \dot{x}(s) ds \tag{2.7}$$

As can be seen from Eq. (2.7), the voltage output has a time constant of $\frac{1}{C_p R_l}$ analogous to RC circuits, and a dependency to the velocity because of $\dot{x}(s)$. However, $\dot{x}(s)$ is coupled with voltage output because of the backward piezoelectric effect, see Eq. (2.3). Therefore, these equations should be solved simultaneously. 0

If the base excitation is a harmonic signal $\ddot{x}_B(t) = \ddot{X}_B e^{j\omega_1 t}$, then the steady-state displacement is also a harmonic function with the same frequency but with complex magnitude such as $x(t) = Xe^{j\omega_1 t}$. By substituting these expressions into Eq. (2.3) and (2.7), the output voltage per acceleration unit is

$$\frac{V(t)}{\ddot{X}_B} = \frac{jR_l m_{\text{eff}} \omega_1 \theta}{\left(1 + jR_l\omega_1 C_p\right)(\omega_n^2 - \omega_1^2 + j2\zeta_m\omega_1\omega_n) + j\alpha R_l m_{\text{eff}}\theta^2\omega_1} e^{j\omega_1 t} \tag{2.8}$$

Because of the capacitance in the piezoelectric electrical circuit, the voltage output is a complex parameter, and the measured voltage is the magnitude of this complex parameter. Besides, from Eq. (2.8), $e^{j\omega_1 t}$ indicates that the steady state voltage is harmonic, similar to the base excitation. The voltage magnitude per unit acceleration can be expressed by:

$$\left|\frac{V(t)}{\ddot{X}_B}\right| = \frac{R_l m_{\text{eff}} \omega_1 \theta}{\sqrt{\begin{array}{c}\left(\omega_n^2 - \omega_1^2 - 2\zeta_m\omega_n\omega_1^2 R_l C_p\right)^2 + \\ \left(2\zeta_m\omega_1\omega_n + R_l\omega_1 C_p(\omega_n^2 - \omega_1^2) + \alpha R_l m_{\text{eff}}\theta^2\omega_1\right)^2\end{array}}} \tag{2.9}$$

By defining a new electromechanical coupling factor $k_e^2 = \frac{e_{31}^2}{C_{31}^E \varepsilon_{31}^S}$, a dimensionless frequency $\Omega = \omega_1/\omega_n$, and $r = R_l C_p \omega_n$ [77], the displacement, voltage, and power ($|p(t)| = \frac{1}{R_l}|V(t)|^2$) normalized to the acceleration can be expressed with:

$$\left|\frac{x(t)}{\ddot{X}_B}\right| = \frac{\sqrt{1 + (r\Omega)^2}}{\omega_n^2\sqrt{[1 - (1 + 2\zeta_m r)\Omega^2]^2 + [(1 + \alpha k_e^2)r\Omega + 2\zeta_m\Omega - r\Omega^3]^2}} \tag{2.10}$$

$$\left|\frac{V(t)}{\ddot{X}_B}\right| = \frac{m_{\text{eff}} R_l d_{31} \omega_n \Omega}{\sqrt{[1-(1+2\zeta_m r)\Omega^2]^2 + [(1+\alpha k_e^2) r\Omega + 2\zeta_m \Omega - r\Omega^3]^2}} \tag{2.11}$$

$$\left|\frac{P(t)}{\ddot{X}_B{}^2}\right| = \frac{(1/\omega_n) m_{\text{eff}} r k_e^2 \Omega^2}{[1-(1+2\zeta_m r)\Omega^2]^2 + [(1+\alpha k_e^2) r\Omega + 2\zeta_m \Omega - r\Omega^3]^2} \tag{2.12}$$

DuToit model estimates the harvester's natural frequency in the simplest way, which is only valid for a single piezoelectric layer, not for unimorph and bimorph harvesters. This inaccurate natural frequency estimation can lead to inaccurate power estimations, as $\omega_n$ appears in both voltage and power equations, see Eq. (2.11) and (2.12). There are two ways to eliminate this issue. One is to extract the natural frequency from experiments, and the other is to estimate the natural frequency using the Equivalent Beam Method (EBM), as demonstrated in subsection 2.2.1.

As shown from power output in Eq.(2.12), apart from a piezoelectric harvester's physical properties, output voltage depends on load resistance and excitation frequency for a given excitation magnitude. Therefore, it is of great interest to find the optimum load ($R_{\text{opt}}$) and resonant frequencies ($\omega_{\text{reson.}}$) that give the maximum power. The optimal conditions can be extracted by differentiating the power output equation.

- For obtaining the optimum electrical load: $\frac{\partial}{\partial R_l}(|p(t)|) = 0 \rightarrow R_l = R_{\text{opt}}$.

$$R_{\text{opt}} = \frac{1}{C_p \omega_n} \frac{\Omega^4 + (4\zeta_m^2 - 2)\Omega^2 + 1}{\Omega^6 + \left(4\zeta_m^2 - 2(1+k_e^2)\right)\Omega^4 + (1+k_e^2)^2\Omega^2} \tag{2.13}$$

The optimum load not only depends on the piezoelectric electrical features ($k_e^2$ and $C_p$), it depends on the mechanical properties ($\omega_n$ and $\zeta_m$) and excitation frequency ($\Omega$).

The optimum load is plotted against the excitation frequency ($\Omega$) and the mechanical damping ($\zeta_m$) in Fig. 2-3. Four damping coefficient values, i.e. $\zeta_m$=1%, 2.5%, 5%, and 10%, and a range of excitation frequencies $0.2 < \Omega < 2$ is plotted. As it can be seen from Fig. 2-3, the optimum load has a great dependency on the excitation frequency over the whole range. On the other hand, the damping coefficient influence on the optimum load is prominent at two peak frequencies, but the rest of the frequency range

does not considerably influence the optimum load. These frequencies will be described in detail in the next paragraph. As these frequencies lead to the highest power generation, then it can be concluded that the damping coefficient has a considerable effect on the optimum load selection.

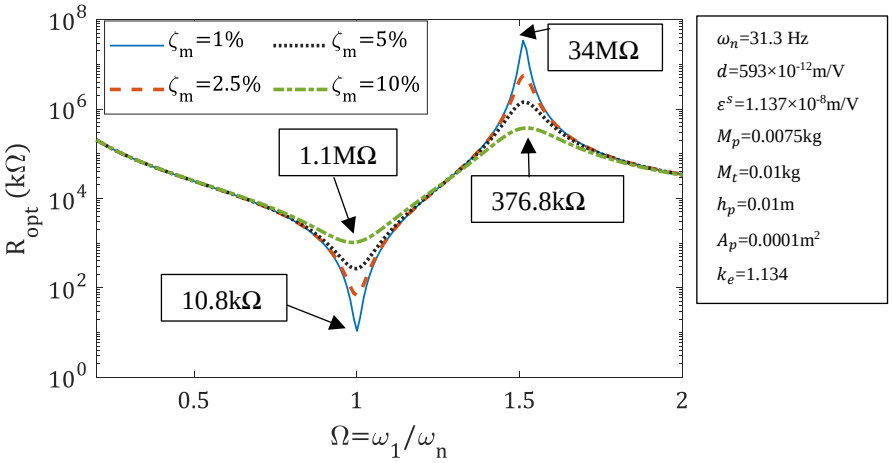


Fig. 2-3. Optimum load as a function of excitation frequency and damping coefficient in SDOF DuToit model.

- For obtaining the resonant excitation frequency: $\frac{\partial}{\partial\Omega}(|p(t)|) = 0 \rightarrow \Omega = \Omega_{\text{reson.}}$.
  After the partial differential, it can be shown that the resonant frequency depends on the electrical load (because of the backward piezoelectric effect). Therefore, there is a coupling between the optimum resonant frequency and the optimum load. Here two special load conditions are considered, i.e., short-circuit and open-circuit.
  At short-circuit condition: $R_l \rightarrow 0$,
  $\Omega_{sc} = 1, \omega_1 = \omega_n = \sqrt{C_{31}^E A_p / m_{\text{eff}} h_p}$.

  At open-circuit condition: $R_l \rightarrow \infty$,
  $\Omega_{oc} = \sqrt{1 + k_e^2} = \sqrt{C_{31}^D A_p / m_{\text{eff}} h_p}$.
  ($C_{31}^D$: elastic modulus in the presence of electrical displacement)

  According to these resonant frequencies, the coupling coefficient also can be calculated by:

$$k_e^2 = (\Omega_{oc}/\Omega_{sc})^2 - 1 \tag{2.14}$$

Power output over the excitation frequency range of 0.2< Ω<2 is shown in Fig. 2-4 for a range of small to large electrical loads. When the electrical load is in the range of hundred to kilo Ohms, the peak power is at a frequency range $\Omega_{sc} \cong 1$, which is close to the pure structural natural frequency of the beam. While the load increases to Mega Ohms, the peak power occurs at $\Omega_{oc} \cong 1.52$. Therefore, it can be concluded that the frequency at which the power is maximum depends on the electrical load.

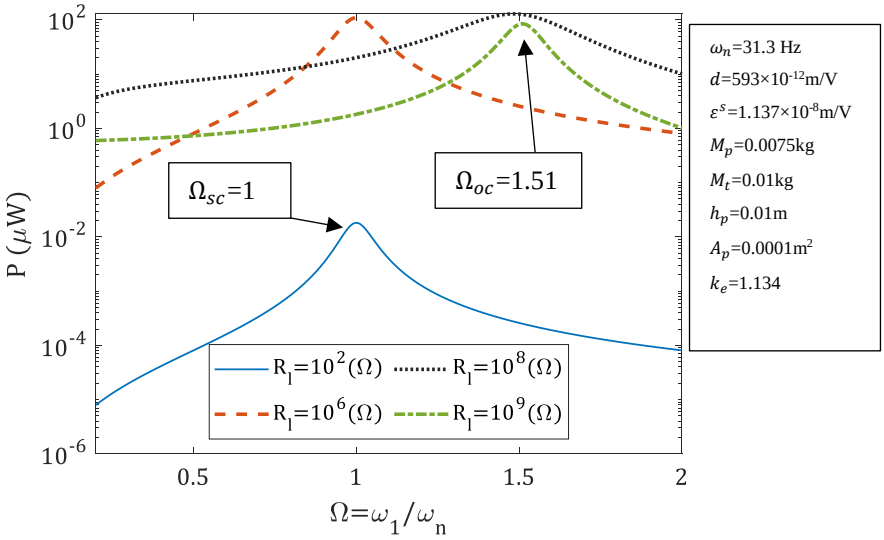


Fig. 2-4. The power output versus the excitation frequency and load in the SDOF DuToit model.

### 2.2.1. EQUIVALENT BEAM METHOD (EBM) FOR NATURAL FREQUENCY APPROXIMATION

As described before, the DuToit model uses a simple approach for natural frequency estimation. The Equivalent Beam Method (EBM) is introduced to improve the natural frequency estimation. The EBM method was introduced by Yi et al. [167]. An advantage of the Yi approach is that it also accommodates the added tip mass effect on the natural frequency.

According to Yi et al. [167], the beam's natural frequency can be estimated by estimating the piezoelectric beam's effective stiffness and mass. They linked the effective stiffness to the effective spring constant at the beam tip, which can be

expressed by the bending stiffness, width, and length of the beam given by Eq. (2.15). The effective mass is also estimated from the effective beam mass at bending and the added tip mass, as given in Eq. (2.16).

$$K_{\text{eff}} = \frac{3b\mathcal{D}_B}{L^3} \tag{2.15}$$

$$M_{\text{eff}} = 0.236M_{\text{beam}} + M_t \tag{2.16}$$

wherein $\mathcal{D}_B$ is the bending stiffness.

Consequently, the natural bending frequencies can be obtained by:

$$\omega_n^2 = \lambda_n^2\sqrt{0.236/3}\sqrt{\frac{K_{\text{eff}}}{M_{\text{eff}}}} \tag{2.17}$$

wherein $\lambda_n$ is the eigenvalue constant for the bending modes. Specifically, $\lambda_n$ are the roots for the equation: $\cos(\lambda_n)\cosh(\lambda_n) = -1$. For the first five modes, these coefficients are: $\lambda_1$=1.875, $\lambda_2$=4.694, $\lambda_3$=7.855, $\lambda_4$=10.996, and $\lambda_5$=14.137 [168].

The bending modulus per unit length can be expressed with:

- For piezoelectric only sheet

$$\mathcal{D}_B = \int_{-h_p/2}^{h_p/2} Q_{11_p}^E z^2 dz = \frac{1}{12} Q_{11_p}^E h_p^3 \tag{2.18}$$

$$M_{\text{beam}} = \rho_p LBh_p$$

- For unimorph harvester (piezoelectric layer and substructure shim)

$$\mathcal{D}_B = \int_{-h_s}^{0} Q_{11_s}(z - z_{nt})^2 dz + \int_{0}^{h_p} Q_{11_p}^E (z - z_{nt})^2 dz$$
$$= \frac{Q_{11_p}^{E\,2} h_p^4 + Q_{11_s}^{\ 2} h_s^4 + 2Q_{11_p}^E Q_{11_s} h_p h_s \left(2h_p^2 + 2h_s^2 + 3h_p h_s\right)}{12\left(Q_{11_s} h_s + Q_{11_p}^E h_p\right)} \tag{2.19}$$

$$M_{\text{beam}} = LB\left(\rho_s h_s + \rho_p h_p\right)$$

- For bimorph harvester (two piezoelectric layers and substructure shim)

$$\mathcal{D}_B = \int_{-h_p-\frac{h_s}{2}}^{-\frac{h_s}{2}} Q_{11_p}^E z^2 dz + \int_{-\frac{h_s}{2}}^{\frac{h_s}{2}} Q_{11_s} z^2 dz + \int_{\frac{h_s}{2}}^{\frac{h_s}{2}+h_p} Q_{11_p}^E z^2 dz = \frac{1}{12}\left(Q_{11_p}^E\left(8h_p^3 + 6h_p h_s^2 + 12h_p^2 h_s\right) + Q_{11_s} h_s^3\right) \quad (2.20)$$

$$M_{\text{beam}} = LB\left(\rho_s h_s + 2\rho_p h_p\right)$$

## 2.3. DISTRIBUTED BEAM MODEL

In the distributed beam model, the piezoelectric beam is analyzed using beam theories, and an analytical model can be obtained for the mechanical and electrical responses. Here, the beam equation of motion based on the Euler-Bernoulli beam theory is employed.

### 2.3.1. MECHANICAL VIBRATION EQUATION

Fig. 2-5 presents the piezoelectric beams and the associated parameters. The presented method here considers both unimorph and bimorph beams. These two configurations are shown respectively in Fig. 2-5 (a) and (b). The beam shall be investigated as a bending problem, requiring the neutral axis to be determined, as the z distance is measured from this axis. The front-view and thicknesses are shown in Fig. 2-5 (c).

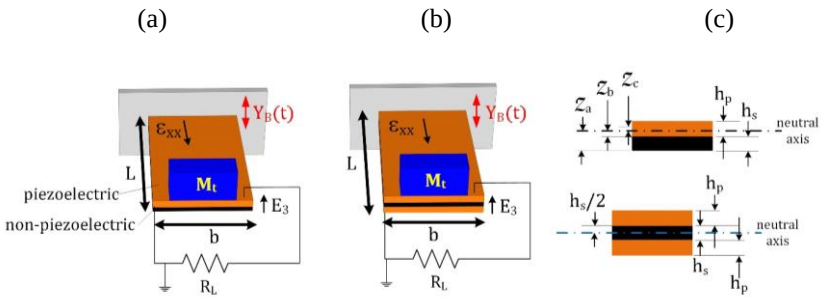


Fig. 2-5. The piezoelectric beams with added tip mass and their parameters for developing distributed beam model, (a) unimorph, (b) bimorph, and (c) thicknesses in front-views. ($L$: length, $b$: width, $h$: thickness, $\varepsilon_{xx}$: axial strain, $E_z$: electrical field, $Y_B(t)$: base excitation) [162].

Fig. 2-6 shows the steps for deriving the distributed beam model. It starts with the equation of motion (based on Euler-Bernoulli theory), followed by stresses-strain and strain-deformation relationships. These relationships transform the equation of motion to a differential equation between the beam deformation, external acceleration, and material properties. To solve this differential equation for the beam deformation, the physical coordination is transformed to the modal coordination, and the beam deformation is expressed as the summation of the vibration modes. The modal expression will give a series of the decoupled second-order differential equation, which their solution is known.

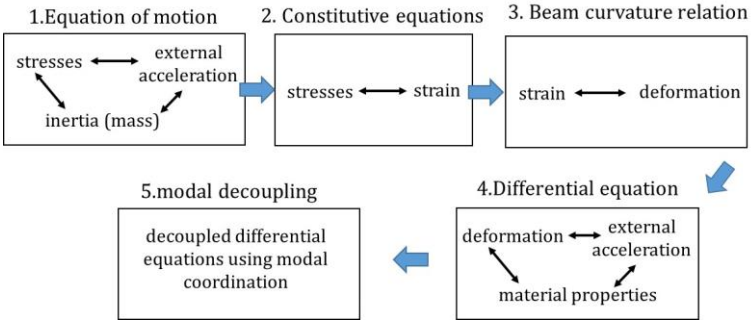


Fig. 2-6. Five steps for obtaining the distributed beam model.

The motion equation can be obtained using the beam's free diagram (see Timoshenko [168]). By considering the Euler-Bernoulli beam theory, the beam equation of motion can be given by [96]:

$$\frac{\partial^2 \mathrm{M}(x,t)}{\partial \mathrm{x}^2} + \mathcal{C}_a \frac{\partial \mathrm{w}(x,t)}{\partial \mathrm{t}} + m^* \frac{\partial^2 \mathrm{w}(x,t)}{\partial \mathrm{t}^2} = -(m^* + M_t) \frac{\mathrm{d}^2 \mathrm{Y}_B(t)}{\mathrm{dt}^2} \tag{2.21}$$

wherein $\mathrm{M}(x,t)$ is the bending moment, $m^*$ is the effective mass per unit length, and $\mathcal{C}_a$ is the viscous damping coefficient. The bending moment, created by the axial stress due to the beam deformation, can be expressed by:

$$\mathrm{M}(x,t) = \int (\mathrm{T}: \text{axial stress}) dA \tag{2.22a}$$

If the beam width is constant, then $dA = bdz$, and the bending moment yields to;

$$\xrightarrow{\text{constant width}} \mathrm{M}(x,t) = b \int_{-\frac{\text{thickness}}{2}}^{\frac{\text{thickness}}{2}} (\mathrm{T}: \text{axial stress}) dz \tag{2.22b}$$

The bending moment for the unimorph and bimorph then can be given by [162]:

$$\mathrm{M}(x,t) = -b\left(\int_{-\mathcal{Z}_a}^{-\mathcal{Z}_b} T_{xx}^s \, z dz + \int_{-\mathcal{Z}_b}^{0} T_{xx}^p \, z dz + \int_{0}^{\mathcal{Z}_c} T_{xx}^p \, z dz\right) \tag{2.22c}$$

Unimorph

$$\mathrm{M}(x,t) = -b\left(\int_{-h_p-\frac{h_s}{2}}^{-\frac{h_s}{2}} T_{xx}^p \, z dz + \int_{-\frac{h_s}{2}}^{\frac{h_s}{2}} T_{xx}^s \, z dz + \int_{\frac{h_s}{2}}^{\frac{h_s}{2}+h_p} T_{xx}^p \, z dz\right) \tag{2.22d}$$

Bimorph

The superscripts "$p$" and" $s$" represent the piezoelectric and substrate properties, respectively.

The constitutive equations will relate the stress in piezoelectric and substrate layers and the strain. As the strain is linked to the beam curvature, it can only be directly estimated from the beam deformation. The constitutive equation for piezoelectric and substrate (non-piezoelectric) layers are different because electromechanical coupling exists in piezoelectric materials. The constitutive equations for piezoelectric and substrate layers are given by [162]:

$$T_{xx}^{p} = \bar{c}_{11}^{E}\varepsilon_{xx} - \bar{e}_{31}E_z \; ; \; T_{xx}^{s} = Y_s\varepsilon_{xx} \tag{2.23}$$

By applying the base excitation $Y_B(t)$, the beam will deform with the deformation shape $w(x,t)$, as shown in Fig. 2-7. Using Euler-Bernoulli beam theory, in the linear framework, the axial strain can be expressed by the beam curvature, as given by:

$$\varepsilon_{xx} = -z\frac{\partial^2 \mathrm{w}(x,t)}{\partial \mathrm{x}^2} \tag{2.24}$$

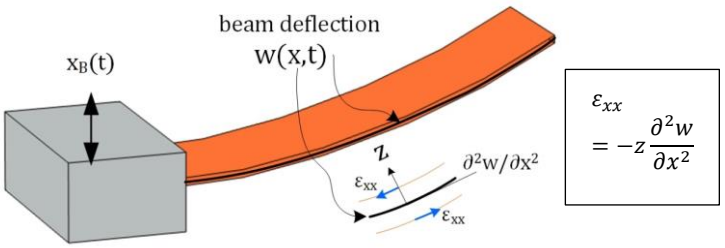


Fig. 2-7. Beam deformation and axial strains because of the beam base excitation.

By substituting the constitutive equations Eq. (2.23) and strain-curvature equation Eq. (2.24) into the equation of motion, the beam equation of motion can be expressed with the beam deformation and material properties as given by Eq. (2.25) [162]:

$$\begin{aligned} YI\frac{\partial^4 \mathrm{w}(x,t)}{\partial \mathrm{x}^4} + \mathcal{C}_a\frac{\partial \mathrm{w}(x,t)}{\partial \mathrm{t}} + m^*\frac{\partial^2 \mathrm{w}(x,t)}{\partial \mathrm{t}^2} \\ + \mathcal{P}\mathrm{V_R}(t)\left(\frac{d\delta(x)}{dx} - \frac{d\delta(x-L)}{dx}\right) \\ = -(m^* + M_t)\frac{\mathrm{d}^2 \mathrm{Y}_B(t)}{\mathrm{dt}^2} \end{aligned} \tag{2.25}$$

$YI$ is the beam stiffness, and $\mathcal{P}$ is the piezoelectric coupling factor. These parameters are summarized in Table 2-2 for both unimorph and bimorph beams.

For solving the partial differential equation in Eq. (2.25), the method of variable separation will be assumed. The generalized coordination is assumed the modal modes because they are known for a wide range of problems and have physical meaning. It is considered that the beam deformation is a summation of all vibration

modes, but their contributions in the solution are unknown, which should be solved through the differential equation. The beam deformation is given by:

$$\sum_{i=1}^{\infty} \phi_i(x)\eta_i(t) \tag{2.26}$$

wherein $\phi_i(x)$ are the modal modes and $\eta_i(t)$ are their contributions in the summation. Until now, no assumption regarding the boundary conditions has been made. The boundary conditions are introduced to the solution by assuming suitable modal modes, i.e. $\phi_i$-s. Therefore, the modal modes $\phi_i$ should satisfy the cantilevered boundary conditions and also accommodate the added tip mass effect. The four boundary conditions are given by:

(i) $w(x=0,t)=0 \rightarrow \phi_i(x=0)=0$

(ii) $w'(x=0,t)=0 \rightarrow \phi_i'(x=0)=0$

(iii) $w''(x=L,t)=0 \rightarrow \phi_i''(x=L)=0$ (2.27)

(iv) $w'''(x=L,t)=0 \rightarrow \phi_i'''(x=L)=0$

The cantilevered beams' mode shapes have been previously presented, as shown in Eq. (2.28) [169].

$$\phi_i(x) = \chi_i\left[cosh\frac{\lambda_i}{L}x - cos\frac{\lambda_i}{L}x + \alpha_i\left(sinh\frac{\lambda_i}{L}x - sin\frac{\lambda_i}{L}x\right)\right] \tag{2.28}$$

wherein

$\lambda_i$ is the root of $1+\cos\lambda_i\cosh\lambda_i+\lambda_i\frac{M_t}{m^*L}(\cos\lambda_i\sinh\lambda_i-\sin\lambda_i\cosh\lambda_i)=0$ and

$\alpha_i$ is given by $\alpha_i=\frac{\sin\lambda_i-\sinh\lambda_i+\lambda_i\frac{M_t}{m^*L}[\cos\lambda_i-\cosh\lambda_i]}{\cos\lambda_i+\cosh\lambda_i-\lambda_i\frac{M_t}{m^*L}[\sin\lambda_i-\sinh\lambda_i]}$.

Because mode shapes are not unique, it is of interest to normalize them to the mass. This mass normalization is achieved by setting the coefficient $\chi_i$ to a value that satisfies $\int_0^L m^*\phi_i^2(x)\,dx + M_t\phi_i^2(L) = 1$.

Therefore, using the modal coordination, the equation of motion yields to:

$$YI\sum_{i=1}^{\infty}\phi_i^{(4)}(x)\eta_i(t)+\mathcal{C}_a\sum_{i=1}^{\infty}\phi_i(x)\dot{\eta}_i(t)+m^*\sum_{i=1}^{\infty}\phi_i(x)\ddot{\eta}_i(t)+\mathcal{P}\mathrm{V_R}(t)\left(\frac{d\delta(x)}{dx}-\frac{d\delta(x-L)}{dx}\right)=-(m^*+M_t)\ddot{\mathrm{Y}}_B(t). \tag{2.29}$$

From Eq. (2.28), $\phi_i^{(4)}(x)=\left(\frac{\lambda_i}{L}\right)^4\phi_i(x)$. Eq. (2.29) is multiplied by $\phi_j(x)$ from the right-hand side, and integrated from 0 to L, as given by:

$$\begin{aligned}&YI\sum_{i=1}^{\infty}\left[\int_0^L\left(\frac{\lambda_i}{L}\right)^4\phi_i(x)\phi_j(x)dx\right]\eta_i(t)+\\&\mathcal{C}_a\sum_{i=1}^{\infty}\left[\int_0^L\phi_i(x)\phi_j(x)dx\right]\dot{\eta}_i(t)+\\&m^*\sum_{i=1}^{\infty}\left[\int_0^L\phi_i(x)\phi_j(x)dx\right]\ddot{\eta}_i(t)+\mathcal{P}\mathrm{V_R}(t)\frac{d\phi_j(x)}{dx}-\frac{d\phi_j(x-L)}{dx}\Big|_0^L=\\&-\left(m^*\int_0^L\phi_j(x)dx+M_t\int_0^L\phi_j(x)dx\right)\ddot{\mathrm{Y}}_B(t).\end{aligned} \tag{2.30}$$

The modal orthogonality characteristic states that $\int_0^L\phi_i(x)\phi_j(x)\,dx=\delta_{ij}$. Therefore, Eq. (2.30) is simplified to:

$$\begin{aligned}&\frac{YI}{m^*}\left(\frac{\lambda_n}{L}\right)^4\eta_n(t)+\frac{\mathcal{C}_a}{m^*}\dot{\eta}_n(t)+\ddot{\eta}_n(t)+\mathcal{P}\frac{d\phi_n(x)}{dx}\Big|_0^L\mathrm{V_R}(t)=\\&-\left(m^*\int_0^L\phi_n(x)dx+M_t\phi_n(L)\right)\ddot{\mathrm{Y}}_B(t),\quad\text{where } n\text{=1 to }\infty.\end{aligned} \tag{2.31}$$

The definition of natural frequency and damping coefficient, as given by Eq. (2.32), is applied to standardize the formulation.

$$\omega_n=\left(\frac{\lambda_i}{L}\right)^2\sqrt{\frac{YI}{m^*}}\quad,\quad\frac{\mathcal{C}_a}{m^*}=2\zeta_n\omega_n \tag{2.32}$$

With these definitions, along with the new defined coupling coefficient $\Upsilon$, and the excitation coefficient $\sigma$ (see Table 2-2), the electromechanical vibration equation becomes:

$$\ddot{\eta}_n(t)+2\zeta_n\omega_n\dot{\eta}_n(t)+\omega_n^2\eta_n(t)+\Upsilon\mathrm{V_R}(t)=-\sigma_n\ddot{\mathrm{Y}}_B(t),\ n\text{=1 to }\infty \tag{2.33}$$

| Parameter | Unimorph | Bimorph |
|---|---|---|
| $YI$ | $b/3\,[Y_s(Z_b^3 - Z_a^3) + \bar{c}_{11}^E(Z_c^3 - Z_b^3)]$. | $2b/3\left[Y_s\, h_s^3/8 + \bar{c}_{11}^E\left(\left(h_p + h_s/2\right)^3 - h_s^3/8\right)\right]$. |
| $\mathcal{P}$ | $-\frac{\bar{e}_{31}b}{2h_p}[Z_c^2 - Z_b^2]$ | $\frac{\bar{e}_{31}b}{2h_p}\left[h_s^2/4 - \left(h_p + h_s/2\right)^2\right]$ |
| $m^*$ | $b(h_p + h_s)$ | $b(2h_p + h_s)$ |
| $\sigma_n$ | $m^*\int_0^L \phi_n(x)dx + M_t\phi_n(L)$ | |
| $\Upsilon_n$ | $\mathcal{P}\left(\frac{d\phi_n(x)}{dx}\Big\|_{x=L}\right)$ | |

Table 2-2. Summary of the defined parameters for the vibration equation of piezoelectric beams

### 2.3.2. ELECTRICAL CIRCUIT EQUATION

For assessing the electrical equations, it should be noted that only the electrical displacement in z (or 3) directions is non-zero due to the poling direction, see Fig. 2-5. According to Gauss's law, the current through each piezoelectric layer is given by:

$$\mathrm{I}(t) = \frac{\mathrm{d}}{\mathrm{d}t}\oiint D_3(t)dA = \Sigma \mathrm{V_R}(t) \tag{2.34}$$

wherein $D_3$ is the electrical displacement in 3-direction, and $\Sigma$ is the circuit admittance. As only a purely resistance is connected to the piezoelectric layer, the admittance is $\Sigma = 1/\mathrm{R}_l$.

$D_3$ can be related to the mechanical stress and electric field using the piezoelectric constitutive equation, as given by [96]:

$$D_3(t) = \bar{e}_{31}\varepsilon_{xx}(t) + \bar{\epsilon}_{33}E_3(t) \tag{2.35}$$

wherein $\bar{\epsilon}_{33}$ is the permittivity constant at constant strain (the plane-stress), which is obtained from the permittivity constant ($\epsilon_{33}^T$) at constant stress by $\bar{\epsilon}_{33} = \epsilon_{33}^T - e_{31}^2/(\bar{c}_{11}^E)^2$[165].

$E_3$ can be estimated by assuming a constant electrical field through the piezoelectric thickness, as can be expressed with:

$$E_3(t) = -\frac{\mathrm{V_R}(t)}{h_p} \tag{2.36}$$

$\varepsilon_{xx}$ in Eq. (2.35) is the average strain on the piezoelectric layer. $\varepsilon_{xx}$ is obtained from Eq. (2.24) and assuming $z$ to be the mid-plane of the piezoelectric layer. For the bimorph $z_p = \left(h_s + h_p\right)/2$, and for the unimorph $z_p = \mathcal{Z}_c$, see Fig. 2-5.

Substituting the axial strain and the electrical field, the derivative of Eq. (2.35) is given by:

$$\frac{\mathrm{d}D_3(t)}{\mathrm{dt}} = -z_p \bar{e}_{31} \frac{\partial^3 \mathrm{w}(x,t)}{\partial \mathrm{t}\, \partial \mathrm{x}^2} - \frac{\bar{\epsilon}_{33}}{h_p} \frac{d\mathrm{V_R}(t)}{dt} \tag{2.37}$$

Substituting Eq. (2.37) into Eq. (2.34), the electrical equation becomes:

$$\frac{\mathrm{V_R}(t)}{R_l} = -b \int_0^L \left[ z_p \bar{e}_{31} \frac{\partial^3 \mathrm{w}(x,t)}{\partial \mathrm{t}\, \partial \mathrm{x}^2} + \frac{\bar{\epsilon}_{33}}{h_p} \frac{d\mathrm{V_R}(t)}{dt} \right] dx$$

Or

$$\frac{\mathrm{V_R}(t)}{R_l} + \frac{\bar{\epsilon}_{33} bL}{h_p} \frac{d\mathrm{V_R}(t)}{dt} = -b z_p \bar{e}_{31} \overbrace{\int_0^L \frac{\partial^3 \mathrm{w}(x,t)}{\partial \mathrm{t}\, \partial \mathrm{x}^2} dx}^{A} \tag{2.38}$$

Now, term A is approximated using the modal expansion (presented in Eq. (2.26)), as given by:

$$A = \int_0^L \frac{\partial^3 \mathrm{w}(x,t)}{\partial \mathrm{t}\, \partial \mathrm{x}^2} dx = \sum_{n=1}^{\infty} \left( \frac{d\phi_n(x)}{dx} \Big]_0^L \right) \dot{\eta}_n(t) \tag{2.39}$$

Thus, the electrical equation yields to [4]

$$\frac{\mathrm{V_R}(t)}{R_l} + \underbrace{\frac{\bar{\epsilon}_{33} bL}{h_p}}_{C_P} \frac{d\mathrm{V_R}(t)}{dt} = \underbrace{-b z_p \bar{e}_{31} \sum_{n=1}^{\infty} \left( \frac{d\phi_n(x)}{dx} \Big]_0^L \right) \dot{\eta}_n(t)}_{I_p(t) = \sum_{n=1}^{\infty} \Lambda_n \dot{\eta}_n(t)} \tag{2.40}$$

Eq. (2.40) is analogous to Kirchhoff's current equation for an RC circuit. Therefore, the term associated with the voltage derivative is called the capacitance $C_P$ and the right-hand side of the equation is similar to a current source $I_p(t)$ due to piezoelectric effect.

Eq. (2.40) is derived for only one piezoelectric layer. If the energy harvester consists of more than one layer, an effective circuit can be found for either series or parallel

connections. Khazaee et al. [162] presented the effective circuit for bimorph under the parallel and series connections, as shown in Fig. 2-8 (a) and (b), respectively. The effective electrical resistances for the series and parallel connections are $R_{\text{eff}}=R_l$ and $R_{\text{eff}}=2R_l$, respectively. Besides, the effective capacitance for the series and parallel connections are $C_{\text{p,eff}}=C_p/2$ and $C_{\text{p,eff}}=C_p$, respectively [165]. Therefore, the general electrical equation yields

$$\frac{\mathrm{V_R}(t)}{R_{\text{eff}}}+C_{\text{p,eff}}\frac{d\mathrm{V_R}(t)}{dt}=\sum_{n=1}^{\infty}\Lambda_n\dot{\eta}_n(t) \tag{2.41}$$

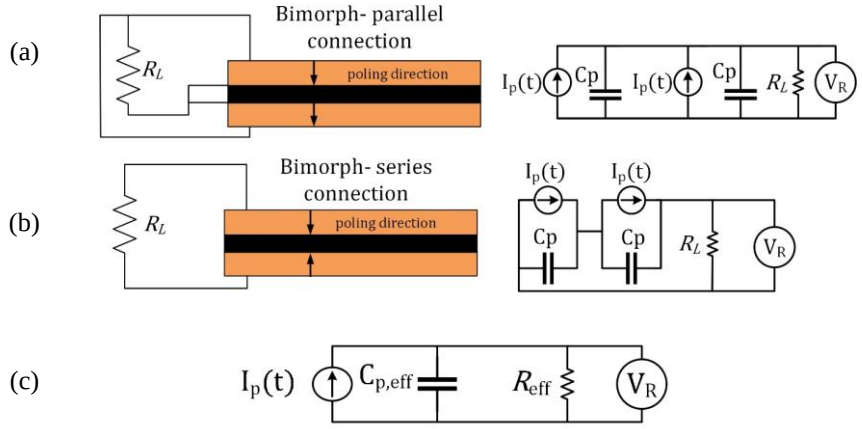


Fig. 2-8. (a) The electrical circuit for bimorph in parallel connection, (b) electrical circuit for bimorph in series connection, and (c) effective circuit for vases (a) and (b) [162].

Table 2-3 presents the summary of the defined variables for the electrical equation Eq. (2.41).

| Parameter | Unimorph | Bimorph |
|---|---|---|
| $\Lambda_n$ | $-Z_c\bar{e}_{31}b\left(\frac{d\phi_n(x)}{dx}\right]_0^L$ | $-\frac{(h_s+h_p)}{2}\bar{e}_{31}b\left(\frac{d\phi_n(x)}{dx}\right]_0^L$ |
| $C_{P,\text{eff}}$ | $\frac{\bar{\epsilon}_{33}bL}{h_p}$ | • series: $\frac{\bar{\epsilon}_{33}bL_T}{2h_p}$<br>• parallel: $\frac{\bar{\epsilon}_{33}bL_T}{h_p}$ |
| $R_{\text{eff}}$ | $R_l$ | • series: $R_l$<br>• parallel: $2R_l$ |

Table 2-3. Summary of the defined parameters for the electrical circuit equation

## 2.3.3. STEADY-STATE SOLUTION

The steady-state solution for the pair of electromechanical equations for piezoelectric beams is the focus of this subsection. These equations are given again here.

$$\ddot{\eta}_n(t) + 2\zeta_n\omega_n\dot{\eta}_n(t) + \omega_n^2\eta_n(t) + \Upsilon \mathrm{V}_\mathrm{R}(t) = -\sigma_n\ddot{\mathrm{Y}}_B(t),\ n\text{=1 to } \infty \tag{2.33}$$

$$\frac{\mathrm{V}_\mathrm{R}(t)}{R_\mathrm{eff}} + C_{\mathrm{p,eff}}\frac{d\mathrm{V}_\mathrm{R}(t)}{dt} = \sum_{n=1}^{\infty}\Lambda_n\dot{\eta}_n(t) \tag{2.41}$$

### Harmonic base excitation

Like SDOF steady-state solution, a base excitation of $Y_B(t) = \ddot{Y}_B\cos(\omega t)$ is considered. In this excitation, the mechanical response will be $\eta_n(t) = \bar{\eta}_n\cos(\omega t)$ and the voltage response will be $\mathrm{V}_\mathrm{R}(t) = \overline{\mathrm{V}}_\mathrm{R}\cos(\omega t)$. The only difference is that $\bar{\eta}_n$ and $\overline{\mathrm{V}}_\mathrm{R}$ are complex variables because of the mechanical damping and the capacitance constant. Therefore, the steady-state responses have the following relationships.

$$(\omega_n^2 - \omega^2 + j2\zeta_n\omega_n\omega)\bar{\eta}_n + \gamma_n\overline{\mathrm{V}}_\mathrm{R} = -\sigma_n\ddot{\mathrm{Y}}_B \tag{2.42}$$

$$\left(\frac{1}{R_\mathrm{eff}} + j\mathrm{C}_{P,\mathrm{eff}}\omega_r\right)\overline{\mathrm{V}}_\mathrm{R} = \sum_{n=1}^{\infty} j\omega\Lambda_n\bar{\eta}_n \tag{2.43}$$

By elimination method, the voltage and mechanical responses can be obtained, as given by:

$$\overline{\mathrm{V}}_\mathrm{R} = \frac{\sum_{n=1}^{\infty} j\omega\Lambda_n\sigma_n\alpha_n}{\frac{1}{R_\mathrm{eff}} + j\omega\mathrm{C}_{P,\mathrm{eff}} + j\omega\sum_{n=1}^{\infty}\Lambda_n\gamma_n\alpha_n}\ddot{\mathrm{Y}}_B \tag{2.44}$$

$$\bar{\eta}_n = \alpha_n\ddot{\mathrm{Y}}_B\left[\sigma_n - \gamma_n\frac{\omega\sum_{n=1}^{\infty} j\Lambda_n\sigma_n\alpha_n}{\frac{1}{R_\mathrm{eff}} + j\omega\mathrm{C}_{P,\mathrm{eff}} + j\omega\sum_{n=1}^{\infty}\Lambda_n\gamma_n\alpha_n}\right] \tag{2.45}$$

where $\alpha_n$ the non-coupled frequency response function (FRF), which is given by [166]:

$$\alpha_{n,\omega} = \frac{1}{\omega_n^2 - \omega^2 + j(2\zeta_n\omega_n\omega)} \tag{2.46}$$

The power output can be obtained by the $\mathrm{P_R}(t) = \left(\mathrm{V_R}(t)\right)^2 / R_l$.

The presented solutions in Eq. (2.44) and Eq. (2.45) contain an indefinite number of modes, i.e., $n$=1 to ∞. Using higher number of modes generates results that are more accurate even though the computational cost will be higher. It is common to present the single-mode approximation outputs [165] because less computational time is required and accurate. Fig. 2-9 shows the single-mode approximation accuracy in the benchmark example's voltage and power output performance. It can be seen that the single-mode approximation has good agreement with the multi-mode response, and the error does not exceed 1%.

(a)

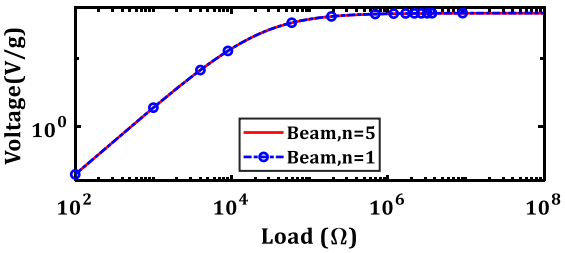


(b)

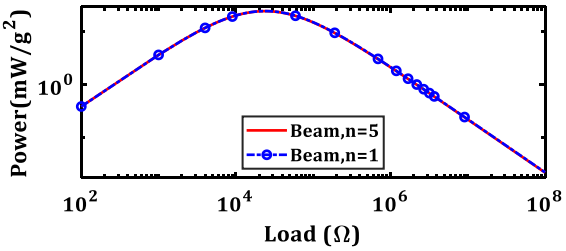


Fig. 2-9. Comparison between the single-mode and multi-mode voltage and power outputs from the distributed beam model for the benchmark example (differences between the solutions for the voltage and power are 0.5% and 1.0%, respectively).

The benchmark example is investigated for the steady-state voltage and power outputs versus the excitation frequency and electrical load, as shown in Fig. 2-10 in a frequency range containing the natural beam frequency and an electrical range from small to large values. It can be seen that the voltage increases from 0 to open-circuit voltage at large loads. Besides, the voltage output is maximum at a specific frequency called *"resonant frequency"*. This resonant frequency also depends on the electrical load due to the backward piezoelectric feature because the generated voltage will

induce additional stiffness to the piezoelectric beam. Fig. 2-10 (a) shows the shift in the resonant frequency due to the electrical load. The same behavior was also shown in Fig. 2-4 for the SDOF DuToit model. This shift in the resonant frequency becomes critically essential for the resonant matching design.

The power output is shown in Fig. 2-11 (b) illustrates that two conditions should be met for the maximum power generation: the resonant frequency excitation and the optimum load connection. A significant result from the zoomed-in view in Fig. 2-10 (b) is that the resonant frequency and the optimum load are linked to each other because of the dual coupling between the electrical and the mechanical physics in a piezoelectric beam. The same dependency was observed in Fig. 2-3 for the SDOF DuToit model. Subsection 2.3.4 will try to investigate this dual-way relationship with more details.

(a)

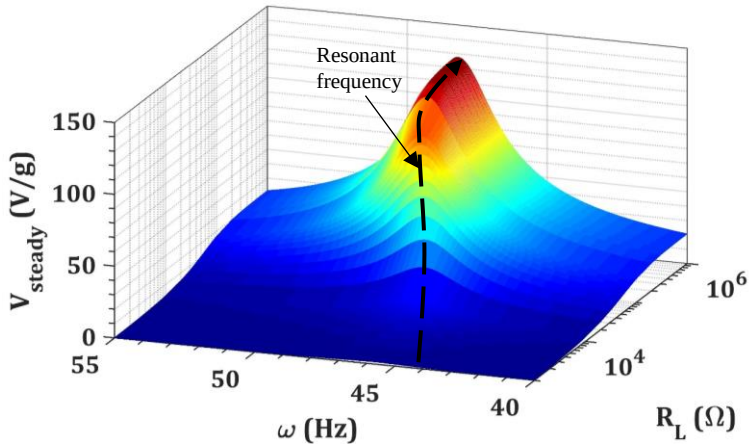

(b)

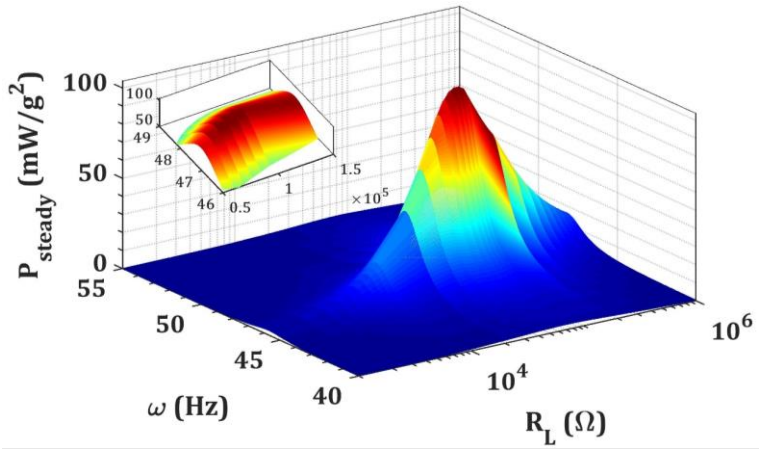


Fig. 2-10. (a) Voltage and (b) power outputs versus the electrical load and excitation frequency for the benchmark example [162].

### General (deterministic) base excitation

Next, if it is considered that the input base excitation is not a pure harmonic load, however, it can be discretized into a series of harmonic functions using the Fourier Transform. Therefore, the input base excitation should be *absolutely integrable*, i.e. $\int_{-\infty}^{+\infty}|Y_B(t)|dt < \infty$, or, for the discrete base excitation signals, $\sum_{-\infty}^{+\infty}|Y_B(t)| < \infty$.

Let assume that the base excitation is expressed by the Fourier Transform, given by,

$$Y_B(t) = \frac{1}{2\pi}\int_{-\infty}^{\infty}\hat{Y}_B(\omega)e^{j\omega t}d\omega\,, \qquad \hat{Y}_B(\omega) = \int_{-\infty}^{\infty}Y_B(t)e^{-j\omega t}dt \tag{2.47}$$

In practical vibration sources, $\hat{Y}_B(\omega)$ has significant components in the frequency span for a wide range of frequencies, and each frequency excites the harvester beam, which will eventually generate a voltage. For instance, Fig. 2-11 shows the time domain and the Fast Fourier Transform (FFT) acceleration for a diesel car moving on the bumpy highway. In this example, the acceleration between 20 to 40 Hz is higher than the other frequencies and has a peak at 30Hz.

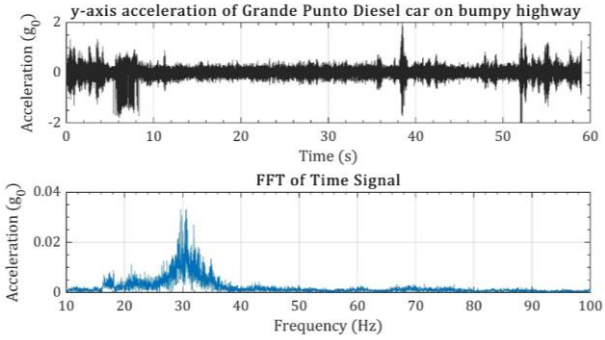


Fig. 2-11. Time domain and FFT of the car acceleration data for a Grande Punto car on a bumpy highway [170].

Then, by considering all frequencies' superposition effect, the voltage and power outputs from the piezoelectric beam can be extracted by summing the outputs from all the frequencies. Therefore, the mechanical response and voltage output, and power output can be obtained by:

$$\eta_n(t) = \int_{-\infty}^{\infty} \eta_{n,\omega}(t)d\omega = \int_{-\infty}^{\infty} \bar{\eta}_{n,\omega} e^{j\omega t} d\omega \cong \sum_{r=-\infty}^{\infty} \bar{\eta}_{n,\omega_r} . e^{j\omega_r t}$$
$$\mathrm{V_R}(t) = \int_{-\infty}^{\infty} V_{R,\omega}(t)d\omega = \int_{-\infty}^{\infty} \bar{V}_{R,\omega} e^{j\omega t} d\omega \cong \sum_{r=-\infty}^{\infty} \overline{\mathrm{V}}_{\mathrm{R},\omega_r} . e^{j\omega_r t} \quad (2.48)$$

wherein $\bar{\eta}_{n,\omega_r}$ and $\overline{\mathrm{V}}_{\mathrm{R},\omega_r}$ are the mechanical and electric responses at each frequency step, obtained from the solutions in Eq. (2.44) and Eq. (2.45). Thus, the mechanical response and the voltage output for the general base excitation are given by:

$$\eta_n(t) = \sum_{r=-\infty}^{\infty} \alpha_{n,\omega} \hat{Y}_B(\omega_r) \left[ \sigma_n - \gamma_n \frac{\omega_r \sum_{n=1}^{\infty} j\Lambda_n \sigma_n \alpha_{n,\omega_r}}{\frac{1}{R_{\mathrm{eff}}} + j\omega_r \mathrm{C}_{P,\mathrm{eff}} + j\omega_r \sum_{n=1}^{\infty} \Lambda_n \gamma_n \alpha_{n,\omega_r}} \right] . e^{j\omega_r t} \quad (2.49)$$

$$\mathrm{V_R}(t) = \sum_{r=-\infty}^{\infty} \frac{\hat{Y}_B(\omega_r)\omega_r \sum_{n=1}^{\infty} j\Lambda_n \sigma_n \alpha_{n,\omega_r}}{\frac{1}{R_{\mathrm{eff}}} + j\omega_r \mathrm{C}_{P,\mathrm{eff}} + j\omega_r \sum_{n=1}^{\infty} \Lambda_n \gamma_n \alpha_{n,\omega_r}} . e^{j\omega_r t} \quad (2.50)$$

Fig. 2-12 shows the results of power estimation of the benchmark piezoelectric beam for the car vibration by applying Eq. (2.50). Fig. 2-12 (a) consists of two curves, namely the car acceleration FFT and the power response function of the piezoelectric beam per square unit acceleration with $R_l$=24kΩ. As can be seen from Fig. 2-12 (a), the car acceleration FFT has a peak at 30Hz while the piezoelectric energy harvester has a resonant peak around 47Hz. The output power can be obtained by multiplying the square acceleration FFT to the power frequency response, given in Fig. 2-12 (b). As can be seen from Fig. 2-12 (b), there are two maximums in the output power. One is due to the car acceleration peak, while the other is due to the piezoelectric resonant frequency. Because the beam dimensions have not been optimized for the frequency matching, two weak peaks exist in the power spectrum. However, if one designs the energy-harvesting beam for a specific application, there will be one strong peak in the power spectrum. This PVEH design will be demonstrated in Chapter 5.

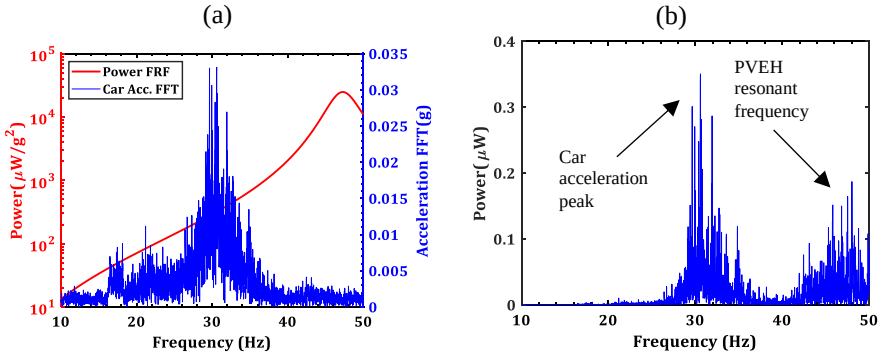


Fig. 2-12. The power analysis for the benchmark example by assuming the car vibration data from Fig. 2-11, (a) the power frequency response function (FRF) and the acceleration FFT of the car vibration, and (b) the estimation of power output for the benchmark example by the car vibration simulation.

### 2.3.4. A UNIFIED ELECTROMECHANICAL COUPLED VOLTAGE EQUATION

As described previously, the voltage is dependent on the load and the excitation frequency. For the maximum power generation, the harvester should be excited by the resonant frequency, and an optimum load shall be connected. Previous models present two coupled equations, one for the mechanical vibration and one for the electrical circuit. In this section, a unified voltage equation will be presented that has the electromechanical coupling effect. This equation has been reported in Ref. [162]. This unified voltage equation presents the transient harmonic response in subsection 2.3.5 and damping determination in subsection 4.2. The single-mode approximation will be employed (shown in Fig. 2-9 that this will not influence the accuracy).

For obtaining a unified voltage equation, a relationship between the mechanical response $\eta_n(t)$ and the voltage output $\mathrm{V_R}(t)$ should be found from Eq. (2.41). The mechanical response should then be replaced by the voltage output, which makes Eq. (2.33) an equation that contains only the voltage.

Finding a relationship between $\eta_n(t)$ and $\mathrm{V_R}(t)$ (from Eq. (2.41)) is not possible generally because of the time derivatives in this equation. However, under certain circumstances, this direct link can be found. These two conditions are 1) open-circuit condition, 2) harmonic excitation with any electrical load.

*1) Open-circuit condition ($R_l \to \infty$,):* As there is no current flow in the piezoelectric in open-circuit condition, the term $(1/R_{\mathrm{eff}})$ vanishes in the Eq. (2.41), and therefore,

$$C_P \frac{d\mathrm{V_R}(t)}{dt} = \sum_{n=1}^{\infty} \Lambda_n \dot{\eta}_n(t) \xrightarrow{\int dt} C_P \mathrm{V_R}(t) = \sum_{n=1}^{\infty} \Lambda_n \eta_n(t)$$
$$\xrightarrow{\text{single-mode}} \eta_n(t) = \frac{C_{\mathrm{p,eff}}}{\Lambda_n} \mathrm{V_{OC}}(t) \tag{2.51}$$

By substituting Eq. (2.51) into the mechanical vibration equation Eq. (2.33) [162], the unified voltage equation can be given by,

$$\ddot{\mathrm{V}}_{\mathrm{OC}}(t) + 2\zeta_n \omega_n \dot{\mathrm{V}}_{\mathrm{OC}}(t) + \underbrace{\left(\omega_n^2 + \frac{\Upsilon_n \Lambda_n}{C_{\mathrm{p,eff}}}\right)}_{\omega_{\mathrm{nc}}^2\text{: coupled resonant frequency}} \mathrm{V_{OC}}(t) = \sigma_n \frac{\Lambda_n}{C_{\mathrm{p,eff}}} \ddot{Y}_B(t). \tag{2.52}$$

The beam natural frequency is now replaced by the coupled resonant frequency $\omega_{\mathrm{nc}}^2$ in Eq. (2.52), which has the electromechanical coefficients of the harvester.

*2) Harmonic excitation with $R_l$ load:* In this case, the term $R_l$ remains, but using the harmonic excitation assumption, the time derivatives in Eq. (2.41) can be analytically applied. Therefore, the relationship between the mechanical response $\eta_n(t)$ and the voltage output $\mathrm{V_R}(t)$ can be shown by:

$$\eta(t) = \frac{\mathrm{V_R}(t)}{\Gamma_n(\omega)} \tag{2.53}$$

wherein $\Gamma(\omega)$ is given by,

$$\Gamma_n(\omega) = \frac{\Lambda}{\sqrt{\left(\frac{1}{R_{\text{eff}}\omega}\right)^2 + {C_P}^2}} \tag{2.54}$$

Consequently, the unified voltage equation can be shown to be,

$$\ddot{\mathrm{V}}_{\mathrm{R}}(t) + 2\zeta_n\omega_n\dot{\mathrm{V}}_{\mathrm{R}}(t) + \underbrace{\left(\omega_n^2 + \Upsilon_n\Gamma_n(\omega)\right)}_{\omega_{\mathrm{nc}}^2}\mathrm{V}_R(t) = \sigma_n\Gamma_n\ddot{Y}_B(t) \tag{2.55}$$

Thus, an electromechanical-coupled natural frequency is defined by:

$$\omega_{\mathrm{nc}} = \sqrt{\omega_n^2 + \Upsilon_n\Gamma_n(\omega)},\ \omega\text{: excitation frequency} \tag{2.56}$$

Eq. (2.52) is valid for all the excitation types in the open-circuit condition, but Eq. (2.55) is valid for only harmonic excitations but in connection with any electrical load.

To validate the correctness of the electromechanical-coupled natural frequency, the natural and the open-circuit resonant frequencies using this method are compared with the experimental values in Ref [165]. The considered energy harvester is the benchmark example. Table 2-4 presents these comparisons, which shows a good agreement between the results, and therefore, the unified voltage equation can predict the resonant variation concerning the electrical load.

| | $\omega_n$ (Hz) | $\omega_{\mathrm{nc}}$ at open-circuit (Hz) |
|---|---|---|
| Present method | 45.74 | 48.2 |
| Erturk and Inman experiments [165] | 45.6 | 48.4 |
| Difference | +0.2% | -0.4% |

Table 2-4: Comparing the natural frequency and the open-circuit resonant frequency for the benchmark example (experiment by Erturk and Inman [165]).

Fig. 2-13 illustrates the coupled resonant frequency sensitivity concerning the excitation frequency and the electrical load. The typical optimum range of the electrical loads and the resonant excitation is indicated in Fig. 2-13. Fig. 2-13 (a) shows that the ratio $\frac{\omega_{\mathrm{nc}}}{\omega_{\mathrm{n}}}$ increases by increasing the electrical load, which is correct for all the excitation frequencies. According to Fig. 2-13 (b), the ratio $\frac{\omega_{\mathrm{nc}}}{\omega_{\mathrm{n}}}$ is close to 1 in the small loads and reaches to a maximum at large load. Fig. 2-13 (b) shows that

the ratio $\frac{\omega_{nc}}{\omega_n}$ is frequency-insensitive for small and large loads. However, for the typical optimum load ranges, there is sharp jump in the $\frac{\omega_{nc}}{\omega_n}$ curves. Typical $\frac{\omega_{nc}}{\omega_n}$ value for the practical electrical loads in the resonant excitation design is 1.025 [162].

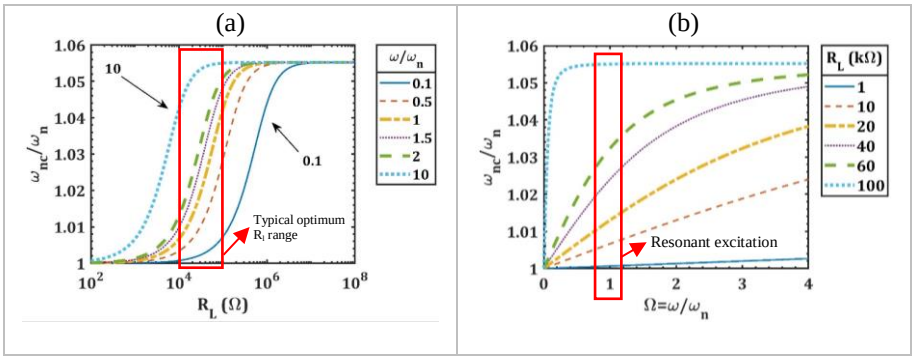


Fig. 2-13. The coupled resonant frequency is a function of the excitation frequency and the electrical load connection for the benchmark example [162].

## 2.3.5. TRANSIENT RESPONSE TO A HARMONIC EXCITATION

The transient response of the voltage equation to a harmonic excitation will be developed in this subsection. The transient voltage response has some beneficial characteristics for the piezoelectric damping extraction and the power output estimation under the varying excitation signals. This method is presented by Khazaee et al. [162].

A harmonic excitation is considered as the base excitation $\ddot{Y}_B(t) = \bar{Y}_B\omega^2\cos(\omega t)$. At harmonic excitations, Eq. (2.52) is a particular case (open-circuit) for the general case Eq. (2.55). Therefore, the focus will be on developing the transient solution for Eq. (2.55), and the presented solution will be valid for Eq. (2.52) as well.

Eq. (2.55) is a non-homogeneous second-order differential equation, which its solution is well known. The solution for Eq. (2.55), as given in Eq. (2.57), contains a general (transient) solution and a particular (forced or steady-state) solution.

$$V_R(t) = V_{trans}e^{-\zeta_n\omega_n t}sin(\omega_{dc}t + \phi) + V_{steady}\cos(\omega t - \theta) \qquad (2.57)$$

where the parameters for this solution are given by [162]:

$$V_{\text{trans}} = -\kappa V_{\text{steady}},\ \phi = \tan^{-1}\frac{\omega_d \cos\theta}{\zeta_n\omega_n\cos\theta+\omega\sin\theta}, \tag{2.58a}$$

$$V_{\text{steady}} = \frac{\sigma\Gamma\bar{Y}_B\omega^2}{\sqrt{\left(\omega_n^2+\Upsilon\Gamma-\omega^2\right)^2+(\zeta_n\zeta\omega_n\omega)^2}},\ \theta = \tan^{-1}\frac{2\zeta_n\omega_n\omega}{\omega_n^2+\Upsilon\Gamma-\omega^2}. \tag{2.58b}$$

wherein $\kappa = \frac{\cos\theta}{\sin\phi}$.

Besides, $\omega_{\text{dc}}$ is the damped coupled resonant frequency, and given by:

$$\omega_{\text{dc}} = \omega_n\sqrt{1-\zeta_n^2+\frac{\Upsilon\Gamma}{\omega_n^2}}. \tag{2.59}$$

The angles $\theta$ and $\phi$ and coefficient $\kappa$ are plotted against the frequency ratio for 2.7% and 10% damping coefficients. $\phi$ and $\theta$ have a 90º shift. For under resonant excitation $\Omega$<1 $\phi = 90-\theta$ and for over resonant excitation $\phi = -90-\theta$. The ratio between the transient and the steady-state solution, i.e., $\kappa$, depends on $\theta$ and $\phi$. $\kappa$ is plotted in Fig. 2-14 against the frequency ratio for 2.7% and 10% damping coefficients. According to Fig. 2-14, $\kappa$ is 1 for $\Omega\leq1$ and is -1 for $\Omega$>1. Therefore, the harmonic transient response in Eq. (2.57) can be simplified to [162]:

$$V_{\text{R}}(t) \cong V_{\text{steady}}\left(-\not{f}(\Omega)e^{-\zeta\omega_n t}sin(\omega_{\text{dc}}t+\phi)+\cos(\omega t-\theta)\right). \tag{2.60}$$

wherein $\not{f}(\Omega) = \begin{cases}1 & \Omega\leq1\\ -1 & \Omega>1\end{cases}$.

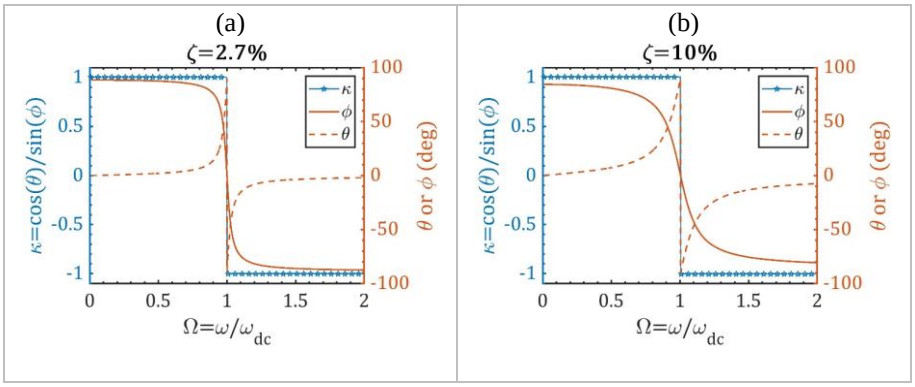


Fig. 2-14. The coefficients $\kappa$, $\theta$ and $\phi$ for different excitation

To investigate the unified voltage equation, the output voltage for the benchmark example using the unified voltage equation is plotted in Fig. 2-15 against the experimental data [165] for $R_l$=1 kΩ and 6.7 kΩ. A good agreement can be seen among the analytical and the experimental data for both electrical loads.

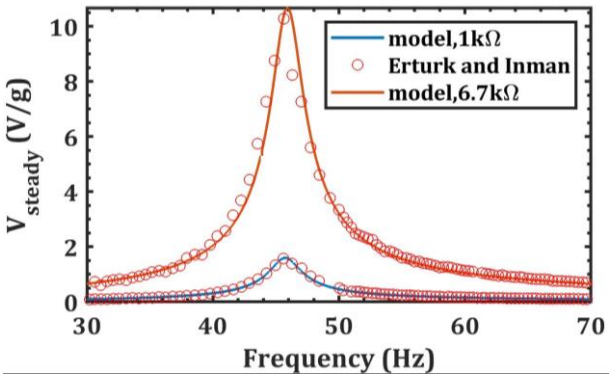


Fig. 2-15. The experimental validation of the voltage versus frequency (the experiment by Erturk and Inman [165]) for the benchmark example [162].

## 2.4. FINITE ELEMENT (FE) MODEL

This section presents the finite element (FE) model for the piezoelectric beams developed by Khazaee et al. [163]. This FE model has the following advantaging features:

- High order deformation theory is considered for relating the strains to the deformations.
- Carrera's advanced formulation (CUF) is employed for the displacement fields, which means that the deformation through the thickness is not constant.
- Shear stresses are considered.
- Two-dimensional formulations with variable thickness are obtained.
- The energy harvester can be non-uniform with partially covered by piezoelectric layers.
- Contact layer effect and a viscous-structural combined damping model are proposed.
- Added mass connected to the harvester is considered.
- The model is electromechanically coupled considering the backward piezoelectric effect.
- The model is general for any type of excitation. However, the formulations are also presented for the base excitation as the most applicable condition.

Fig. 2-16 shows a general non-uniform piezoelectric beam with added tip mass under the base excitation.

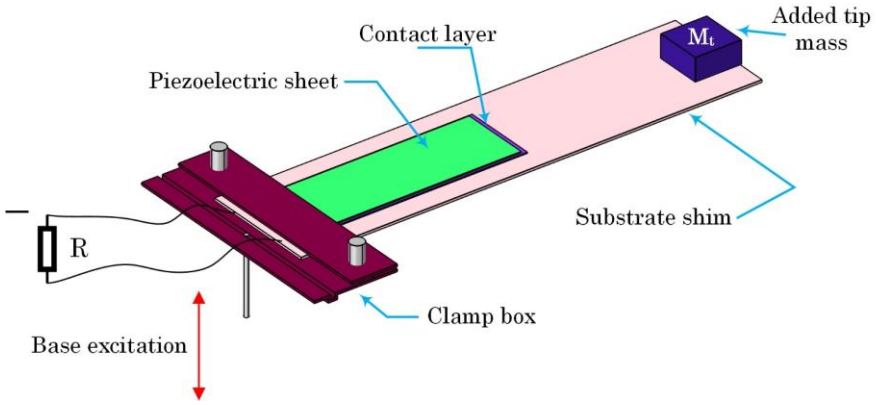


Fig. 2-16. The illustration of a typical piezoelectric beam is considered for the FE model [163].

The derivation of the FE model has five steps, which are:

1. Constitutive equations: It will be derived by considering the orthotropic material model for the piezoelectric and substrate layer.
2. Strains and displacements relationships: The Carrera's Unified Formulation (CUF) and the Third Shear Deformation Theory (TSDT) will be used to find the relationships between the strains and beam displacements.
3. Finite discretization and spatial approximation: The energy harvester domain will be discretized into small elements, and the spatial approximation for each element will be given.
4. The equation of motion: It will be derived according to the extended Hamilton's principle.
5. Differential equations' derivation: The differential equations will be obtained for each small element. Numerical methods for the element matrices' calculations will be given.

The nomenclature for the parameters used in this formulation can be found in Appendix E.

### 2.4.1. CONSTITUTIVE EQUATIONS

It is considered that the material model for the piezoelectric and the substrate is the orthotropic material, while for the contact layer is the isotropic material. In the orthotropic material model, transformations in the principal coordination are assumed, as shown in Fig. 2-17. The linear material model is considered for all three material types.

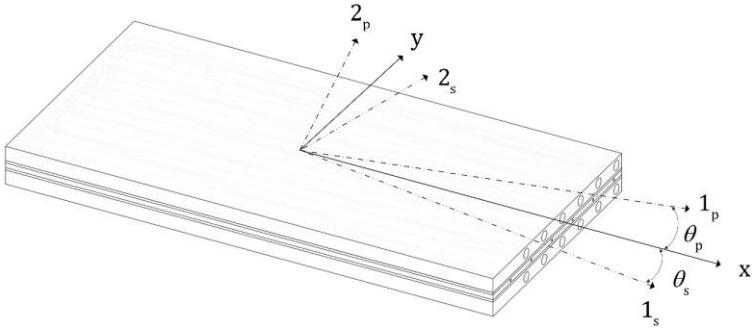


Fig. 2-17. The transformation of principal coordination for the piezoelectric and substrate layers [163].

The constitutive equation (the stress-strain relationship) for the piezoelectric material as a linear orthotropic material, for the substrate layer as a linear orthotropic material, and the contact layer as linear isotropic material are [163]

$$\begin{aligned} T_p &= [\bar{Q}]_p S - [\bar{e}]\mathcal{E} \quad \text{Piezoelectric layer} \\ T_s &= [\bar{Q}]_s S \quad \text{Substrate shim} \\ T_c &= [Q]_c S \quad \text{Contact layer} \end{aligned} \tag{2.61}$$

where $T$ is the stress tensor, $S$ is the strain tensor, $\mathcal{E}$ is the electric field, $[\bar{Q}]$ is the stiffness matrix, and $[\bar{e}]$ is the piezoelectric coupling matrix. The components of these matrices and tensors are:

$$T = \begin{Bmatrix} \sigma_{xx} \\ \sigma_{yy} \\ \sigma_{yz} \\ \sigma_{xz} \\ \sigma_{xy} \end{Bmatrix}, S = \begin{Bmatrix} \varepsilon_{xx} \\ \varepsilon_{yy} \\ \gamma_{yz} \\ \gamma_{xz} \\ \gamma_{xy} \end{Bmatrix}, \mathcal{E} = \begin{Bmatrix} \mathcal{E}_x \\ \mathcal{E}_y \\ \mathcal{E}_z \end{Bmatrix},$$

$$[\bar{Q}] = \begin{bmatrix} \bar{Q}_{11} & \bar{Q}_{12} & 0 & 0 & \bar{Q}_{16} \\ \bar{Q}_{12} & \bar{Q}_{22} & 0 & 0 & \bar{Q}_{26} \\ 0 & 0 & \bar{Q}_{44} & \bar{Q}_{45} & 0 \\ 0 & 0 & \bar{Q}_{45} & \bar{Q}_{55} & 0 \\ \bar{Q}_{16} & \bar{Q}_{26} & 0 & 0 & \bar{Q}_{66} \end{bmatrix}, [\bar{e}] = \begin{bmatrix} 0 & 0 & \bar{e}_{31} \\ 0 & 0 & \bar{e}_{32} \\ 0 & 0 & \bar{e}_{36} \\ \bar{e}_{14} & \bar{e}_{24} & 0 \\ \bar{e}_{15} & \bar{e}_{25} & 0 \end{bmatrix}. \tag{2.62}$$

wherein $\sigma_i$ are the axial stresses, $\tau_{ij}$ are shear stresses, $Q_{ij}$ are the stiffnesses, $\varepsilon_i$ are the axial strains, $\gamma_{ij}$ are the shear strains, $e_{ij}$ are the piezoelectric coefficient, and $\mathcal{E}_i$ are the electric field.

The electric constitutive equation for the piezoelectric material is given by [163]

$$D = \begin{Bmatrix} D_x \\ D_y \\ D_z \end{Bmatrix} = \begin{bmatrix} 0 & 0 & \bar{e}_{14} & \bar{e}_{15} & 0 \\ 0 & 0 & \bar{e}_{24} & \bar{e}_{25} & 0 \\ \bar{e}_{31} & \bar{e}_{32} & 0 & 0 & \bar{e}_{36} \end{bmatrix} \begin{Bmatrix} \varepsilon_{xx} \\ \varepsilon_{yy} \\ \gamma_{yz} \\ \gamma_{xz} \\ \gamma_{xy} \end{Bmatrix} + \begin{bmatrix} \bar{\epsilon}_{11} & \bar{\epsilon}_{12} & 0 \\ \bar{\epsilon}_{12} & \bar{\epsilon}_{22} & 0 \\ 0 & 0 & \bar{\epsilon}_{33} \end{bmatrix} \begin{Bmatrix} \mathcal{E}_x \\ \mathcal{E}_y \\ \mathcal{E}_z \end{Bmatrix}, \tag{2.63}$$

$$D = [\bar{e}]^t S + [\bar{\epsilon}^s]\mathcal{E}.$$

wherein the permittivity matrix in physical coordination is denoted by $[\bar{\epsilon}^s]$.

The overbar symbol indicates that the material properties are in physical coordination. The relationship between the principal coordination (1-2 coordination) and the physical coordination (x-y coordination) can be found in Appendix E.

For the 3-1 mode energy harvester, the poling direction is only in the z-direction, and, therefore, the electrical field can be estimated from the voltage between the two electrode surfaces, which is:

$$\mathcal{E} = \begin{Bmatrix} 0 \\ 0 \\ -V/h_p \end{Bmatrix} = \begin{bmatrix} 0 \\ 0 \\ \frac{-1}{h_p} \end{bmatrix} V = \{A_e\}_{3\times 1} V. \tag{2.64}$$

## 2.4.2. STRAINS AND DISPLACEMENT RELATIONSHIPS

In the FE model for a piezoelectric beam, the beam area is divided into small elements. The 31-mode energy harvester undergoes bending, and therefore each element has a 2-D deformation shape. According to the assumption for the plate deformations, there are different plate theories. Fig. 2-18 presents different plate theories' characteristics, and Fig. 2-19 illustrates different deformation shapes. The present FE model uses the advanced theories with the TSDT plate model.

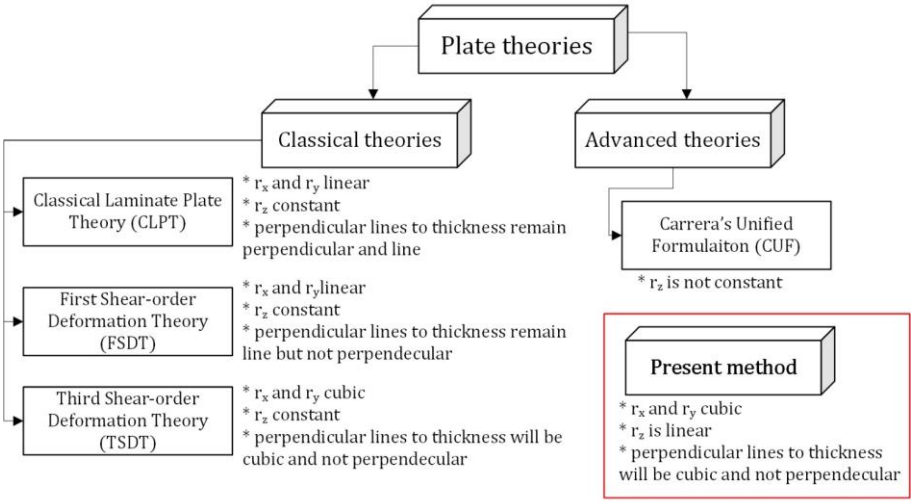


Fig. 2-18. Different plate theories, classical (CLPT, FSDT, and TSDT) and advanced (CUF) plate theories.

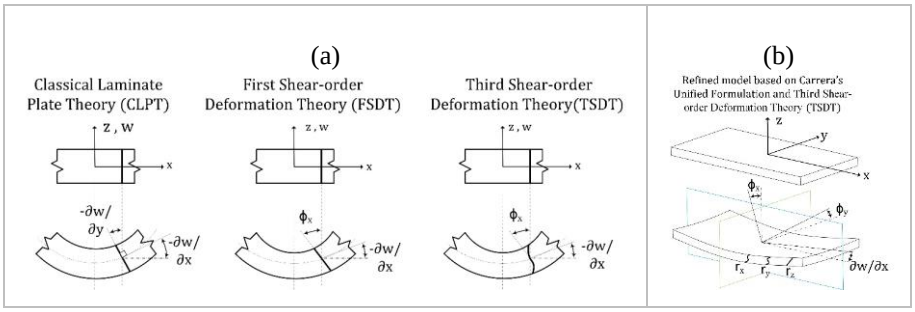


Fig. 2-19. (a) The plate deformations for classical plate theories, and (b) the present model based on Carrera's unified formulation and the TSDT approximations [163].

According to the assumptions, the displacement field for an element can be given by:

$$r = \begin{Bmatrix} r_x(x,y,z,t) \\ r_y(x,y,z,t) \\ r_z(x,y,z,t) \end{Bmatrix} = \begin{Bmatrix} 0 \\ 0 \\ w \end{Bmatrix} + z \begin{Bmatrix} \frac{5}{4}\phi_x + \frac{1}{4}w_{,x} \\ \frac{5}{4}\phi_y + \frac{1}{4}w_{,y} \\ \mathcal{W} \end{Bmatrix} - \mathcal{C}_1 z^3 \begin{Bmatrix} \frac{5}{4}\phi_x + \frac{5}{4}w_{,x} \\ \frac{5}{4}\phi_y + \frac{5}{4}w_{,y} \\ 0 \end{Bmatrix}. \tag{2.65}$$

where $\mathcal{C}_1 = \frac{4}{3h^2}$ ($h$ is the total beam thickness). Moreover, $z$ is the distance to the neutral axis. The above formulation is a general formulation that can accommodate all the advanced and classical theories, including CLPT, FSDT, and TSDT.

The strain tensor now can be calculated from the displacement field by

$$S=\begin{Bmatrix}\varepsilon_{xx}\\ \varepsilon_{yy}\\ \gamma_{yz}\\ \gamma_{xz}\\ \gamma_{xy}\end{Bmatrix}=\begin{Bmatrix}r_{x,x}\\ r_{y,y}\\ r_{y,z}+r_{z,y}\\ r_{x,z}+r_{z,x}\\ r_{x,y}+r_{y,x}\end{Bmatrix}=\begin{Bmatrix}0\\ 0\\ \frac{5}{4}\phi_y+\frac{5}{4}w_{,y}\\ \frac{5}{4}\phi_x+\frac{5}{4}w_{,x}\\ 0\end{Bmatrix}+$$
$$z\begin{Bmatrix}\frac{5}{4}\phi_{x,x}+\frac{1}{4}w_{,xx}\\ \frac{5}{4}\phi_{y,y}+\frac{1}{4}w_{,yy}\\ \mathcal{W}_{,y}\\ \mathcal{W}_{,x}\\ \frac{5}{4}\phi_{x,y}+\frac{5}{4}\phi_{y,x}+\frac{1}{2}w_{,xy}\end{Bmatrix}-3\mathcal{C}_1z^2\begin{Bmatrix}0\\ 0\\ \frac{5}{4}\phi_y+\frac{5}{4}w_{,y}\\ \frac{5}{4}\phi_x+\frac{5}{4}w_{,x}\\ 0\end{Bmatrix}- \tag{2.66}$$
$$\mathcal{C}_1z^3\begin{Bmatrix}\frac{5}{4}\phi_{x,x}+\frac{5}{4}w_{,xx}\\ \frac{5}{4}\phi_{y,y}+\frac{5}{4}w_{,yy}\\ 0\\ 0\\ \frac{5}{4}\phi_{x,y}+\frac{5}{4}\phi_{y,x}+\frac{5}{2}w_{,xy}\end{Bmatrix}.$$

## 2.4.3. DISCRETIZATION AND SPATIAL APPROXIMATION

By Finite Element Method (FEM) analysis, a complicated structure is divided into small elements, and therefore a finite element mesh is formed. Then the equations of motion are applied for each element. In a typical piezoelectric structure, there are layer-wised elements in the finite element mesh. One way to deal with this is to compute an equivalent element that contains all layers' structural stiffness properties. According to the plate theory that will be used, each node has six mechanical degrees of freedom (DOFs). Because of the piezoelectricity, each element has one voltage DOF. As there are six DOFs per node, a high number, element shapes with small node numbers can be used. Here, 4-node quadrilateral elements will be considered. Fig. 2-20 shows the finite element mesh, the multi-layer element, and the equivalent element with its DOFs.

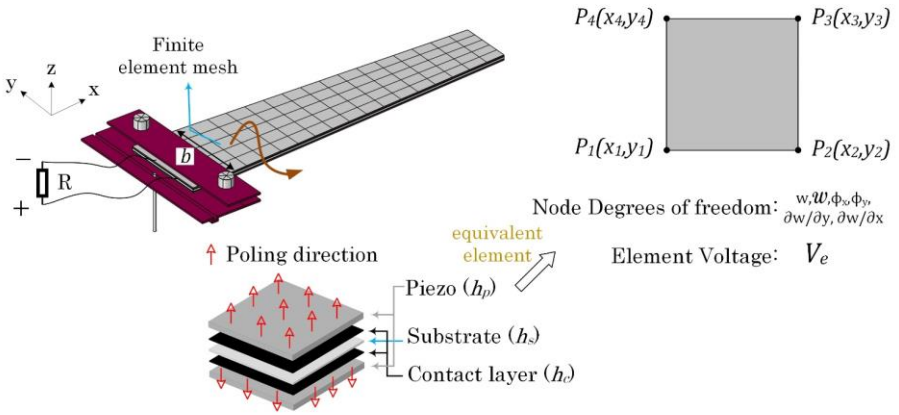


Fig. 2-20. The finite element mesh illustration, a typical layered element, and the equivalent element [163].

The DOFs for each node are given by

$$\text{DoF}_{p\text{th node}} = \left[w^p \; w^p_{,x} \; w^p_{,y} \; \phi^p_{,x} \; \phi^p_{,y} \; \mathcal{W}^p\right]^t. \tag{2.67}$$

Note the DOFs' order, as in matrix assembling for all the elements; this order should be kept.

Similar to the modal expansion method in the distributed beam model, spatial approximations should be inserted instead of $w(x,y,t)$, $\mathcal{W}(x,y,t)$, $\phi_x(x,y,t)$, and $\phi_y(x,y,t)$. As in the strain equation in Eq. (2.66), there is the second derivation of $w$, the shape functions for $w$ should be continuous differentiable in the order of three. Besides, the shape functions for $\mathcal{W}$, $\phi_x$, and $\phi_y$ need to be differentiable in the order of two. Therefore, the Hermite shape functions ($\Lambda_i(x,y)$) will be used for $w$, and the Lagrangian shape functions ($\psi_i(x,y)$) will be used for $\mathcal{W}$, $\phi_x$, and $\phi_y$. These spatial approximations are given by:

$$\begin{aligned}
\phi_x(x,y,t) &\approx \textstyle\sum_{i=1}^{4} X_i^e(t)\psi_i(x,y),\\
\phi_y(x,y,t) &\approx \textstyle\sum_{i=1}^{4} Y_i^e(t)\psi_i(x,y),\\
w(x,y,t) &\approx \textstyle\sum_{i=1}^{12} \Delta_i^e(t)\Lambda_i(x,y),\\
\mathcal{W}(x,y,t) &\approx \textstyle\sum_{i=1}^{4} \Xi_i^e(t)\psi_i(x,y).
\end{aligned} \tag{2.68}$$

The shape functions $\psi_i(x,y)$ and $\Lambda_i(x,y)$ can be given by [163]:

$$[\psi] = [\psi_1 \cdots \psi_4] = \underbrace{\{1 \;\; x \;\; y \;\; xy\}}_{\{N\}} \underbrace{\begin{bmatrix} 1 & x_1 & y_1 & x_1y_1 \\ 1 & x_2 & y_2 & x_2y_2 \\ 1 & x_3 & y_3 & x_3y_3 \\ 1 & x_4 & y_4 & x_4y_4 \end{bmatrix}^{-1}}_{[X]} = \{N\}[X]^{-1}, \tag{2.69}$$

$[\Lambda] = [\Lambda_1 \cdots \Lambda_{12}] = \{P\}[Z]^{-1}$, where

$$\{P\} = \{1 \;\; x \;\; y \;\; x^2 \;\; xy \;\; y^2 \;\; x^3 \; x^2y \;\; xy^2 \;\; y^3 \;\; x^3y \;\; xy^3\},$$

$$[Z] = \begin{bmatrix} \begin{bmatrix} \{P\} \\ \{P\}_{,x} \\ \{P\}_{,y} \end{bmatrix}_{(x_1,y_1)} & \begin{bmatrix} \{P\} \\ \{P\}_{,x} \\ \{P\}_{,y} \end{bmatrix}_{(x_2,y_2)} & \begin{bmatrix} \{P\} \\ \{P\}_{,x} \\ \{P\}_{,y} \end{bmatrix}_{(x_3,y_3)} & \begin{bmatrix} \{P\} \\ \{P\}_{,x} \\ \{P\}_{,y} \end{bmatrix}_{(x_4,y_4)} \end{bmatrix}^T. \tag{2.70}$$

The displacement and the strain vectors in Eq. (2.65) and Eq. (2.66) shall be presented using these spatial approximations. Since a numerical integration shall be carried out on each element volume, the matrix relations for the displacement and strain vectors will be presented in a separate matrix form so the volume integration can be implemented separately for reducing the computation time.

The displacement vector is given by

$$r(x,y,z,t) = \begin{Bmatrix} \frac{5}{4}(z - \mathcal{C}_1 z^3) \sum_{i=1}^{4} X_i^e(t)\psi_i + \left(\frac{1}{4}z - \frac{5}{4}\mathcal{C}_1 z^3\right) \sum_{i=1}^{12} \Delta_i^e(t)\Lambda_{i,x} \\ \frac{5}{4}(z - \mathcal{C}_1 z^3) \sum_{i=1}^{4} Y_i^e(t)\psi_i + \left(\frac{1}{4}z - \frac{5}{4}\mathcal{C}_1 z^3\right) \sum_{i=1}^{12} \Delta_i^e(t)\Lambda_{i,y} \\ z\sum_{i=1}^{4} \Xi_i^e(t)\psi_i(x,y) + \sum_{i=1}^{12} \Delta_i^e(t)\Lambda_i \end{Bmatrix} = [A_m(z)]_{3\times 6}[B_m(x,y)]_{6\times 24}\{\chi^e(t)\}_{24\times 1} \tag{2.71}$$

where the element DOF vector is $\chi^e$ and $[A_m]$ and $[B_m]$ are the two auxiliary matrices. These parameters are given by:

$$\{\chi^e(t)\} = \{X_1^e \;\cdots\; X_4^e \;\; Y_1^e \;\cdots\; Y_4^e \;\; \Xi_1^e \cdots \Xi_4^e \;\; \Delta_1^e \;\cdots\; \Delta_{12}^e\}^t, \tag{2.72a}$$

$$[A_m(z)] = \begin{bmatrix} \frac{5}{4}(z - \mathcal{C}_1 z^3) & 0 & 0 & 0 & \left(\frac{1}{4}z - \frac{5}{4}\mathcal{C}_1 z^3\right) & 0 \\ 0 & \frac{5}{4}(z - \mathcal{C}_1 z^3) & 0 & 0 & 0 & \left(\frac{1}{4}z - \frac{5}{4}\mathcal{C}_1 z^3\right) \\ 0 & 0 & z & 1 & 0 & 0 \end{bmatrix} \tag{2.72b}$$

$$[B_m(x,y)] = \begin{bmatrix} [\psi] & [0] & [0] & [0] \\ [0] & [\psi] & [0] & [0] \\ [0] & [0] & [\psi] & [0] \\ [0] & [0] & [0] & [\Lambda] \\ [0] & [0] & [0] & [\Lambda]_{,x} \\ \underbrace{[0]}_{1\times4} & \underbrace{[0]}_{1\times4} & \underbrace{[0]}_{1\times4} & \underbrace{[\Lambda]_{,y}}_{1\times12} \end{bmatrix} = \begin{bmatrix} \{N\}[X]^{-1} & [0] & [0] & [0] \\ [0] & \{N\}[X]^{-1} & [0] & [0] \\ [0] & [0] & \{N\}[X]^{-1} & [0] \\ [0] & [0] & [0] & \{P\}[Z]^{-1} \\ [0] & [0] & [0] & \{P\}_{,x}[Z]^{-1} \\ [0] & [0] & [0] & \{P\}_{,y}[Z]^{-1} \end{bmatrix} \tag{2.72c}$$

Similarly, the strain vector is presented as the product of two auxiliary matrices and the DOF vector, as given by

$$\begin{aligned} &S(x,y,z,t) \\ &= \begin{Bmatrix} \frac{5}{4}(z-\mathcal{C}_1z^3)\sum_{i=1}^{4} X_i^e(t)\psi_{i,x} + \left(\frac{1}{4}z - \frac{5}{4}\mathcal{C}_1z^3\right)\sum_{i=1}^{12}\Delta_i^e(t)\Lambda_{i,xx} \\ \frac{5}{4}(z-\mathcal{C}_1z^3)\sum_{i=1}^{4} Y_i^e(t)\psi_{i,y} + \left(\frac{1}{4}z - \frac{5}{4}\mathcal{C}_1z^3\right)\sum_{i=1}^{12}\Delta_i^e(t)\Lambda_{i,yy} \\ z\sum_{i=1}^{4}\Xi_i^e(t)\psi_{i,y} + \frac{5}{4}(1-3\mathcal{C}_1z^2)\left(\sum_{i=1}^{4} Y_i^e(t)\psi_i + \sum_{i=1}^{12}\Delta_i^e(t)\Lambda_{i,y}\right) \\ z\sum_{i=1}^{4}\Xi_i^e(t)\psi_{i,x} + \frac{5}{4}(1-3\mathcal{C}_1z^2)\left(\sum_{i=1}^{4} X_i^e(t)\psi_i + \sum_{i=1}^{12}\Delta_i^e(t)\Lambda_{i,x}\right) \\ \frac{5}{4}(z-\mathcal{C}_1z^3)\sum_{i=1}^{4} X_i^e(t)\psi_{i,y} + \frac{5}{4}(z-\mathcal{C}_1z^3)\sum_{i=1}^{4} Y_i^e(t)\psi_{i,x} + 2\left(\frac{1}{4} - \frac{5}{4}\mathcal{C}_1z^3\right)\sum_{i=1}^{12}\Delta_i^e(t)\Lambda_{i,xy} \end{Bmatrix} \\ &= [A_k(z)]_{5\times13}[B_k(x,y)]_{13\times24}\{\chi^e(t)\}_{24\times1} \end{aligned} \tag{2.73}$$

wherein the auxiliary matrices are presented below.

$$[A_k(z)] = \begin{bmatrix} 0 & 0 & \frac{5}{4}(z-\mathcal{C}_1z^3) & 0 & 0 & 0 \\ 0 & 0 & 0 & 0 & 0 & \frac{5}{4}(z-\mathcal{C}_1z^3) \\ 0 & \frac{5}{4}(1-3\mathcal{C}_1z^2) & 0 & 0 & 0 & 0 \\ \frac{5}{4}(1-3\mathcal{C}_1z^2) & 0 & 0 & 0 & 0 & 0 \\ 0 & 0 & 0 & \frac{5}{4}(z-\mathcal{C}_1z^3) & \frac{5}{4}(z-\mathcal{C}_1z^3) & 0 \end{bmatrix}$$

$$\begin{bmatrix} 0 & 0 & 0 & 0 & 0 & \left(\frac{1}{4}z - \frac{5}{4}\mathcal{C}_1z^3\right) & 0 \\ 0 & 0 & 0 & 0 & 0 & 0 & \left(\frac{1}{4}z - \frac{5}{4}\mathcal{C}_1z^3\right) \\ 0 & z & 0 & 0 & 0 & 0 & 0 \\ z & 0 & 1+\frac{5}{4}(1-3\mathcal{C}_1z^2) & 0 & 0 & 0 & 0 \\ 0 & 0 & 0 & 0 & 2\left(\frac{1}{4} - \frac{5}{4}\mathcal{C}_1z^3\right) & 0 & 0 \end{bmatrix} \tag{2.74a}$$

$$[B_k(x,y)] = \begin{bmatrix} [\psi] & [0] & [0] & [0] \\ [0] & [\psi] & [0] & [0] \\ [\psi]_{,x} & [0] & [0] & [0] \\ [0] & [\psi]_{,x} & [0] & [0] \\ [\psi]_{,y} & [0] & [0] & [0] \\ [0] & [\psi]_{,y} & [0] & [0] \\ [0] & [0] & [\psi]_{,x} & [0] \\ [0] & [0] & [\psi]_{,y} & [0] \\ [0] & [0] & [0] & [\Lambda]_{,x} \\ [0] & [0] & [0] & [\Lambda]_{,y} \\ [0] & [0] & [0] & [\Lambda]_{,xy} \\ [0] & [0] & [0] & [\Lambda]_{,xx} \\ \underbrace{[0]}_{1\times4} & \underbrace{[0]}_{1\times4} & \underbrace{[0]}_{1\times4} & \underbrace{[\Lambda]_{,yy}}_{1\times12} \end{bmatrix} = \begin{bmatrix} \{N\}[X]^{-1} & [0] & [0] & [0] \\ [0] & \{N\}[X]^{-1} & [0] & [0] \\ \{N\}_{,x}[X]^{-1} & [0] & [0] & [0] \\ [0] & \{N\}_{,x}[X]^{-1} & [0] & [0] \\ \{N\}_{,y}[X]^{-1} & [0] & [0] & [0] \\ [0] & \{N\}_{,y}[X]^{-1} & [0] & [0] \\ [0] & [0] & \{N\}_{,x}[X]^{-1} & [0] \\ [0] & [0] & \{N\}_{,y}[X]^{-1} & [0] \\ [0] & [0] & [0] & \{P\}_{,x}[Z]^{-1} \\ [0] & [0] & [0] & \{P\}_{,y}[Z]^{-1} \\ [0] & [0] & [0] & \{P\}_{,xy}[Z]^{-1} \\ [0] & [0] & [0] & \{P\}_{,xx}[Z]^{-1} \\ [0] & [0] & [0] & \{P\}_{,yy}[Z]^{-1} \end{bmatrix} \tag{2.74b}$$

### 2.4.4. DERIVATION OF FE FORMULATION FOR ONE ELEMENT

The equation of motion for the piezoelectric beam should now be developed. In the first step, the FE formulation is developed on one element. The equation of motion here is derived from Hamilton's principle.

Hamilton's principle does not include electrical work and potential. Nevertheless, a generalized Hamilton's principle was developed for the piezoelectric domains [108]. According to the generalized Hamilton's principle, the definite integral

$$I = \int_0^{t_0} [(\mathrm{KE} - \mathrm{PE} + W_e) + W_E]dt \tag{2.75}$$

is stationary regardless of the path along with the integration is calculated. Therefore, the variation of $I$ is 0, i.e., $\delta I = 0$. This feature is used to derive the equation of motion.

The kinetic energy, the inertial energy for all the layers in the piezoelectric beam, is given by:

$$\mathrm{KE} = \int_{V_s} \frac{1}{2}\dot{r}^t \mu_s \dot{r} d\mathcal{V}_s + \int_{V_c} \frac{1}{2}\dot{r}^t \mu_c \dot{r} d\mathcal{V}_c + \int_{V_p} \frac{1}{2}\dot{r}^t \mu_p \dot{r} d\mathcal{V}_p \tag{2.76a}$$

The potential energy, the elastic energy stored in the material, is given by:

$$\mathrm{PE} = \int_{V_s} \frac{1}{2} S^t T_s d\mathcal{V}_s + \int_{V_c} \frac{1}{2} S^t T_c d\mathcal{V}_c + \int_{V_p} \frac{1}{2} S^t T_p d\mathcal{V}_p \tag{2.76b}$$

The electrical energy, the energy caused by electric charge transfer, is given by:

$$W_e = \int_{V_p} \frac{1}{2} \mathcal{E}^t D d\mathcal{V}_p \tag{2.76c}$$

The external work by the external mechanical work and the electric charge is given by:

$$W_E = \delta r_E . f_E + \delta \Phi_e q_e \tag{2.76d}$$

By inserting these expressions into Eq. (2.75), $\delta I = 0$ yiels to [163]:

$$\begin{aligned}\delta I = \int_0^{t_0}\Bigg[\delta\{\chi\}^t\Bigg[&\int_{\mathcal{V}_s}[B_m]^t[A_m]^t\mu_s[A_m][B_m]\{\ddot{\chi}^e\}d\mathcal{V}_s+\int_{\mathcal{V}_c}[B_m]^t[A_m]^t\mu_c[A_m][B_m]\{\ddot{\chi}^e\}d\mathcal{V}_c\\&+\int_{\mathcal{V}_p}[B_m]^t[A_m]^t\mu_p[A_m][B_m]\{\ddot{\chi}^e\}d\mathcal{V}_p+\int_{\mathcal{V}_s}[B_k]^t[A_k]^t[\bar{Q}]_s[A_k][B_k]\{\chi^e\}d\mathcal{V}_s\\&+\int_{\mathcal{V}_c}[B_k]^t[A_k]^t[Q]_c[A_k][B_k]\{\chi^e\}d\mathcal{V}_c+\int_{\mathcal{V}_p}[B_k]^t[A_k]^t[\bar{Q}]_p[A_k][B_k]\{\chi^e\}d\mathcal{V}_p\\&-\int_{\mathcal{V}_p}[B_k]^t[A_k]^t[\bar{e}][A_e]v_e d\mathcal{V}_p-f_E\Bigg]\\&+\delta\{\Phi\}\Bigg[\int_{\mathcal{V}_p}[A_e]^t[\bar{e}]^t[A_k][B_k]\{\chi^e\}d\mathcal{V}_p+\int_{\mathcal{V}_p}[A_e]^t[\bar{\varepsilon}^s][A_e]v_e d\mathcal{V}_p+q_e\Bigg]\Bigg]dt\\&=0\end{aligned}\tag{2.77}$$

Setting $\delta\{\chi\}^t$=0 and $\delta\{\Phi\}$=0, two sets of equations will be obtained. The equation obtained by $\delta\{\chi\}^t$=0 is the mechanical vibration equation and the one obtained by $\delta\{\Phi\}$=0 is the electrical circuit equation. Some standard definitions are employed in order to present the FE equations in the standard form. These standard matrix definitions are the mass matrix, the stiffness matrix, piezoelectric coupling matrix, capacitance scalar. These are given by [163]:

Mass: $[m^e]=\sum_{\sigma=s,c,p}\lambda_\sigma\int_{V_\sigma}[B_m]^t[A_m]^t\mu_\sigma[A_m][B_m]d\mathcal{V}_\sigma$ (2.78a)

Stiffness: $\left[k^e_{qq}\right]=\sum_{\sigma=s,c,p}\lambda_\sigma\int_{V_\sigma}[B_k]^t[A_k]^t[\bar{Q}]_\sigma[A_k][B_k]d\mathcal{V}_\sigma$ (2.78b)

Electromechanical coupling: $\left[k^e_{q\phi}\right]=\lambda_p\int_{V_p}[B_k]^t[A_k]^t[\bar{e}][A_e]d\mathcal{V}_p$ (2.78c)

Capacitance scalar: $k^e_{\phi\phi}=\lambda_p\int_{V_p}\{A_e\}^t[\bar{\varepsilon}^s]\{A_e\}d\mathcal{V}_p$ (2.78d)

In Eq. (2.78a) to Eq. (2.78d), the coefficient $\lambda_\sigma$ controls if a material is present in the multi-layered finite element mesh. $\lambda_\sigma$ equals to one if the piezoelectric and contact layers are present in the multilayered element.

Using the matrix definitions in Eq. (2.78a) to Eq. (2.78d), the equations for one nominal element can be given by:

$$[m^e]\{\ddot{\chi}^e\} + \left[k_{qq}^e\right]\{\chi^e\} - \left[k_{q\phi}^e\right]v_e = \{f_E^e\} \tag{2.79a}$$

$$\left[k_{q\phi}^e\right]^t\{\chi^e\} + q_e + k_{\phi\phi}^e v_e = 0 \tag{2.79b}$$

$\{f_E^e\}$ is the external vibration force acting on the piezoelectric beam. In this FE formulation, any mechanical force can be applied by inserting the force vector's proper DOF. One type of input force, which is very common in energy harvesting, is base excitation. In the base excitation, the beam is attached to the piezoelectric base. The effective force under the base excitation is due to the structure inertia in the transverse direction (z).

$$\{f_E^e\} = \int_{Ap} [\Lambda]^t\left(-m^*\ddot{Y}_B\right)dA + [\Lambda]^t|_{@(L,0)}M_t \tag{2.80}$$

This effective force for the base excitation can also be approximated from the beam distributed model. This approach will be introduced when the global finite element matrices are obtained by assembling the element matrices.

In Eq. (2.78a) to Eq. (2.78d), there are integrations over the element volume. According to the thickness properties of the layers, the volume element for different layers is given by:

$$\begin{aligned}
\left(d\mathcal{V}_p\right)_{lower} &= \int_{\frac{-h_s}{2}-h_c-h_p}^{\frac{-h_s}{2}-h_c} dz \int_{A_\mathrm{p}} d\mathrm{xdy}\ , \\
(d\mathcal{V}_c)_{lower} &= \int_{-h_s/2-h_c}^{-h_s/2} dz \int_{A_\mathrm{c}} d\mathrm{xdy}\ , \\
d\mathcal{V}_s &= \int_{-h_s/2}^{+h_s/2} dz \int_{A_\mathrm{s}} d\mathrm{xdy}\ , \\
(d\mathcal{V}_c)_{upper} &= \int_{h_s/2}^{h_s/2+h_c} dz \int_{A_\mathrm{c}} d\mathrm{xdy}\ , \\
\left(d\mathcal{V}_p\right)_{upper} &= \int_{h_s/2+h_c}^{h_s/2+h_c+h_p} dz \int_{A_\mathrm{p}} d\mathrm{xdy}.
\end{aligned} \tag{2.81}$$

Obtaining analytical solutions for these integrations becomes time-consuming; instead, the numerical method as an alternative solution is preferred. One integration will be investigated as an example, and the rest of the integrations can be calculated accordingly. As in the matrix representations, matrices are break into z-only and x-y matrices; therefore, the volumetric integration can be break into an integration over the are times the integration over the thickness, as illustrated in Eq. (2.82).

$$\int_{V_p} [B_m(x,y)]^t [A_m(z)]^t \mu_p [A_m(z)][B_m(x,y)] dV_p$$
$$= \int_{A_p} [B_m(x,y)]^t \left[ \int_{-z_p}^{z_p} [A_m(z)]^t \mu_p [A_m(z)] dz \right] [B_m(x,y)] dA_p \quad (2.82)$$

The integration over the area for a quadrilateral element can be obtained using the Gaussian integration. However, the original Gaussian integration is for rectangular shapes. Thus, a modification should be made before applying the Gaussian numerical integration rule. To do so, Ref. [163] suggested that the element area become divided into three subdomains, and then the Gaussian integral can be applied easily. Fig. 2-21 shows this element division for a general quadrilateral element. The details for the Gaussian integration rule can be found in Appendix E.

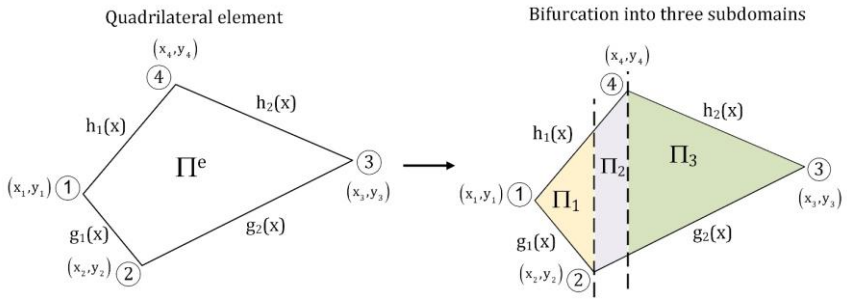


Fig. 2-21. The illustration of the element area bifurcation into three subdomains [163].

## 2.4.5. MATRIX ASSEMBLING AND FE MODEL FOR THE WHOLE DOMAIN

Once the FE matrices for all the elements have been calculated, the global FE matrices should be calculated by assembling the element FE matrices. This assembly should be carried out according to the degrees of freedom in the element (element DOFs). The global mass, stiffness, electromechanical coupling matrices are denoted by $[M]$, $[K_{qq}]$, and $[K_{q\phi}]$, respectively. The assembled external force vector is also denoted by $[F_E]$.

Some assumptions should be made to form the general matrix assembling process. These assumptions are:

1. Damping matrix: The damping matrix is introduced in the general matrix equations. The proportional Rayleigh damping is one the most common damping model in vibration systems, which has been used by many studies in vibration and also in energy harvesting [108], [163], [171]. The source of damping can be

structural and viscous damping. Viscous air damping depends on the velocity, while structural damping is due to the material. Therefore, these two damping types are different, requiring different models to represent them. Here, both damping mechanisms are considered, but the structural and viscous damping's contribution shall be determined before extracting these damping coefficients. More information about the damping mechanisms contribution will be given in Chapter 4. The viscous and structural damping matrices are denoted by $[C]$ and $[H]$, respectively, and are given by:

$$[C] = \beta_1[M] + \beta_2\left[K_{qq}\right] \tag{2.83a}$$

$$[H] = \gamma\left[K_{qq}\right] \tag{2.83b}$$

wherein $\beta_1$, $\beta_2$, and $\gamma$ are the damping matrix coefficients, which should be determined based on the experimental data. Assuming that the viscous damping ratios at frequency $f_1$ are $\zeta_1$, the viscous damping coefficient at frequency $f_2$ is $\zeta_2$, and the structural damping is $\eta_n$, then the damping matrix coefficients become:

$$\beta_1 = 4\pi f_1 f_2 \frac{\zeta_1 f_2 - \zeta_2 f_1}{f_2^2 - f_1^2}, \beta_2 = \frac{1}{\pi}\frac{\zeta_2 f_2 - \zeta_1 f_1}{f_2^2 - f_1^2}, \eta_n = \gamma \tag{2.84}$$

2. Special consideration for the electrodes:
Commonly, the piezoelectric layers are covered by a negligible thickness electrode on both sides. These electrodes impose certain conditions on the global matrixes.r
The voltage difference in all the elements is the same, which is equal to the voltage difference between the electrodes. Thus, a single value for piezoelectric voltage, denoted by $V_p$ is assumed.
The coupling matrix $\left[K_{q\phi}\right]$ should be modified into a new coupling matrix $\left[\widetilde{K}_{q\phi}\right]$ in order to consider the electrode coverage because the adjacent elements cannot have different voltages. All the coupling values at all electrode elements should be summed up for each mechanical DOF's coupling parameter. Thus,

$$\left[\widetilde{K}_{q\phi}\right] = \left[K_{q\phi}\right]\{\mathrm{diag}(I_{N_e})\} \text{ or } \left(\widetilde{K}_{q\phi}\right)_{j\in[1,n]} = \sum_{k=1}^{N_e}\left(K_{q\phi}\right)_{jk} \tag{2.85}$$

The general capacitive coefficient is the summation of the capacitive for all the elements, as given by:

$$K_{\phi\phi} = \left(\sum_{i=1}^{N_e} k_{\phi\phi}^{e}\right) \tag{2.86}$$

3. Electrical load:
The transferred charge from the piezoelectric element is introduced into the electrical equation. However, this transferred charge shall be related to the voltage. Therefore, the electrical equation, Eq. (2.79b), is differentiated concerning $t$, which is given by

$$\left[k_{q\phi}^{e}\right]^{t}\{\dot{\chi}^{e}\} + \underbrace{\dot{q}_{e}}_{=v_e/R} + k_{\phi\phi}^{e}\dot{v}_{e} = 0 \tag{2.87}$$

The time derivative of extracted charge is current, which according to Ohm's law, can be expressed by $\dot{q}_e = v_e/R$.

4. Parallel and series connections:

The FE equations have been developed by considering only one piezoelectric layer. However, in the bimorph beams with two piezoelectric layers, these equations should be modified as two electrical connections are available. The electromechanical coupling and the capacitance should be modified for two piezoelectric layers as they have been calculated for a single piezo layer.
In the parallel connection, the effective capacitance and coupling matrix are equal to the summation of that for the bottom and upper piezoelectric layers. On the other hand, in the series connection, the effective capacitance is half of the single-layer capacitance, and the effective coupling matrix is equal to that of a single piezo layer. In equation form

$$\text{Parallel: } \mathrm{K}_{\phi\phi_{\mathrm{eff}}} = \mathrm{K}_{\phi\phi_{\mathrm{lower}}} + \mathrm{K}_{\phi\phi_{\mathrm{upper}}},\ \left[K_{q\phi}\right]_{\mathrm{eff}} = \left[K_{q\phi}\right]_{\mathrm{lower}} + \left[K_{q\phi}\right]_{\mathrm{upper}} \tag{2.88a}$$

$$\text{Series: } \mathrm{K}_{\phi\phi_{\mathrm{eff}}} = \mathrm{K}_{\phi\phi_{\mathrm{lower}}}/2,\ \left[K_{q\phi}\right]_{\mathrm{eff}} = \left[K_{q\phi}\right]_{\mathrm{lower}} \tag{2.88b}$$

5. Added mass:
The added mass can be easily accommodated by updating the mass matrix. Note that the stiffness matrix does not change provided that the added mass is stiff enough compared to the piezoelectric beam. If the added mass is placed at the $i$

-th node in the FE mesh, then the following matrix is added to the $i$-the node DOFs,

$$\begin{array}{c} \overbrace{\phantom{6i-5}}^{\text{DOFs}} \\ \begin{matrix} 6i-5 \\ 6i-4 \\ 6i-3 \\ 6i-2 \\ 6i-1 \\ 6i \end{matrix} \end{array} \begin{bmatrix} M_t & 0 & 0 & 0 & 0 & 0 \\ 0 & 0 & 0 & 0 & 0 & 0 \\ 0 & 0 & 0 & 0 & 0 & 0 \\ 0 & 0 & 0 & 0 & 0 & 0 \\ 0 & 0 & 0 & 0 & I_{xx} & 0 \\ 0 & 0 & 0 & 0 & 0 & I_{yy} \end{bmatrix} \quad \begin{matrix} M_t\text{: added tip mass} \\ I_{xx} \text{ and } I_{yy}\text{: the moments of inertia} \end{matrix} \tag{2.89}$$

6. Force term:

   Various types of input forces can be applied to the FE problem using the force term. Overall, the force term for point loads can be expressed by $[F_E] = \bar{F}.\{\mathcal{T}\}$, where $\bar{F}$ is the total point load at a certain point on the beam surface, and the vector $\{\mathcal{T}\}$ contains the DOF of this applying load.
   For the case of base excitation, the base excitation creates an inertial force at all the elements. Therefore, the force term for all the elements shall be calculated. Then, the element force vectors shall be assembled to form the general force term. There is another simple way to consider the base excitation. A single force replaces the force term for all the elements at the beam tip, and the single force term contains a sufficient mass of the beam $m_{\text{eff}}$. For base excitation, the single point approximation is given by:

$$\bar{F} = m_{\text{eff}}\ddot{Y}_B, \text{ where } m_{\text{eff}} = \mu_1\left(\frac{m_{\text{beam}}}{3} + M_t\right) \quad (\mu_1 \text{ in [83]}) \tag{2.90}$$

By considering the above discussions, the global FE equations for piezoelectric energy harvesters are given by:

$$[M]\{\ddot{\chi}\} + [C]\{\dot{\chi}\} + \left(\left[K_{qq}\right] + j[H]\right)\{\chi\} - \left[\tilde{K}_{q\phi}\right]V_p = [F_E] \tag{2.91a}$$

$$\left[\tilde{K}_{q\phi}\right]^t\{\dot{\chi}\} + V_p\ /\mathrm{R} + K_{\phi\phi}\dot{V}_p = 0 \tag{2.91b}$$

### 2.4.6. STEADY-STATE SOLUTION

The response to a harmonic load of $[F_E] = \bar{F}e^{j\omega t}.\{\mathcal{T}\}$ ($\omega$ is the frequency) is of interest. In this case, the mechanical and voltage responses are also harmonic functions with the same frequency, which can be expressed by $\{\chi\} = \{\hat{\chi}\}e^{j\omega t}$ and $V_p = \hat{V}_p e^{j\omega t}$. However, $\{\hat{\chi}\}$ and $\hat{V}_p$ are complex values because of the capacitance and the damping in the equations of motion. The steady-state solution can be found by inserting these expressions into Eq. (2.91a) and Eq. (2.91b). The complex values of the mechanical and voltage responses are given by Eq. (2.92a) and (2.92b), respectively.

$$\{\hat{\chi}\} = [\hbar(\omega)][F_E] \tag{2.92a}$$

$$\hat{V}_p = j\omega\left(1/_R + j\omega K_{\phi\phi}\right)^{-1}\left[\tilde{K}_{q\phi}\right]^t[\hbar(\omega)]\{\hat{F}_e\} \tag{2.92b}$$

In Eq. (2.92a) and (2.92b), $[\hbar(\omega)]$ is the coupled transfter function between the mechanical displacement and the mechanical force vector, as given by:

$$[\hbar(\omega)] = \Big((-\omega^2 + j\omega\beta_1)[M] + \big(1 + j(\gamma + \omega\beta_2)\big)\big[K_{qq}\big] + j\omega\big(1/_R + j\omega K_{\phi\phi}\big)^{-1}\big[\tilde{K}_{q\phi}\big]\big[\tilde{K}_{q\phi}\big]^t\Big)^{-1} \tag{2.93}$$

If the base excitation is the applying vibration, then $\bar{F} = m_{\text{eff}}\ddot{Y}_B$, thus, the amplitude of the mechanical response and the output voltage is given by:

$$\left|\frac{\{\hat{\chi}\}}{\ddot{Y}_B}\right| = m_{\text{eff}}[\hbar(\omega)]\{\mathcal{T}\}. \tag{2.94a}$$

$$\left|\frac{\hat{V}_p}{\ddot{Y}_B}\right| = m_{\text{eff}}j\omega\left(1/_R + j\omega K_{\phi\phi}\right)^{-1}\left[\tilde{K}_{q\phi}\right]^t[\hbar(\omega)]\{\mathcal{T}\}. \tag{2.94b}$$

The output power can also be expressed with:

$$\left|\frac{P(t)}{\left(\ddot{Y}_B\right)^2}\right| = \frac{m_{\text{eff}}^2}{R}\left(\left|\frac{j\omega\left({}^{1}/_{R}+j\omega K_{\phi\phi}\right)^{-1}\left[\widetilde{K}_{q\phi}\right]^t}{\begin{pmatrix}(-\omega^2+j\omega\beta_1)[M]+\left(1+j(\gamma+\omega\beta_2)\right)\left[K_{qq}\right]+\\ j\omega\left({}^{1}/_{R}+j\omega K_{\phi\phi}\right)^{-1}\left[\widetilde{K}_{q\phi}\right]\left[\widetilde{K}_{q\phi}\right]^t\end{pmatrix}}\{\mathcal{T}\}\right|\right)^2 \quad (2.95)$$

Once the steady-state response is obtained, one can extract the mechanical strain and stresses and the FE domain's electrical displacements. The following steps lead to the extraction of these parameters [163]:

1. The element responses $\{\hat{\chi}^e\}$ shall be extracted from the global responses $\{\hat{\chi}\}$. Afterward.
2. The element deformation vector is calculated by:

$$\hat{r}(x,y,z) = \left\{\hat{r}_x \;\; \hat{r}_y \;\; \hat{r}_z\right\}^t = [A_m(z)][B_m(x,y)]\{\hat{\chi}^e\} \quad (2.96a)$$

3. The strain vector is calculated by:

$$\hat{S}(x,y,z) = \left\{\,\hat{\varepsilon}_{xx}\;\hat{\varepsilon}_{yy}\;\;\hat{\gamma}_{yz}\;\;\hat{\gamma}_{xz}\;\;\hat{\gamma}_{xy}\right\}^t = [A_k(z)][B_k(x,y)]\{\hat{\chi}^e\} \quad (2.96b)$$

4. The electrical displacement vector is calculated by:

$$\widehat{D} = \left\{\widehat{D}_x \;\; \widehat{D}_y \;\; \widehat{D}_z\right\}^t = [\bar{e}]^t\,\hat{S}(x,y,z) + [\bar{\varepsilon}^s]\left\{0 \;\; 0 \;\; -1/h_p\right\}\widehat{V}_p \quad (2.96c)$$

5. The stresses for the piezoelectric, contact, and substrate layers are calculated by:

$$\begin{aligned}\hat{T}_p &= [\bar{Q}]_p\hat{S}(x,y,z) - [\bar{e}]\left\{0 \;\; 0 \;\; -1/h_p\right\}\widehat{V}_p,\\ \hat{T}_s &= [\bar{Q}]_s\hat{S}(x,y,z),\\ \hat{T}_c &= [Q]_c\hat{S}(x,y,z).\end{aligned} \quad (2.96d)$$

## 2.4.7. COMPARISON OF THE FE RESULTS

This subsection presents the results from the presented FE model with the literature and the experimental data. Two cases are considered: One is the bimorph harvester without the tip mass, the other is the bimorph harvester with a tip mass.

### 2.4.7.1 For a bimorph harvester

This bimorph harvester was first presented by Erturk and Inman [5] for model validation. This example was later employed by Akbar and Curiel-Sosa [32] for model verification. Here this example is used for comparing the undamped natural frequencies and the open-circuit resonant frequencies using this study and the other modeling methods.

This example is a bimorph piezoelectric beam with aluminum substrate and without tip mass. Table 2-5 presents the properties of this example.

| Description | Piezoelectric | Substrate |
|---|---|---|
| Material | PZT-5A | Aluminum |
| Length (mm) | L= 30 | |
| Width (mm) | b=5 | |
| Thickness (mm) | 0.15 (each) | 0.05 |
| Density ($kg/m^3$) | See Table 2-1 | 2700 |
| Elastic modulus (GPa) | | 62.3 |
| Poisson's ration | | 0.33 |

Table 2-5. The geometries and material properties for the bimorph example.

The comparisons between the natural and coupled resonant frequencies for the first three bending modes are given in Table 2-6 and Table 2-7. As shown in Table 2-6, the first mode's present FE results have a negligible difference from the other analytical models. However, for the 2nd and 3rd modes, this difference becomes immense. The FE model considers the shear stresses, and therefore, extra stiffness due to the shear stresses can be expected.

Table 2-7 shows how the resonant frequencies can change due to the short and open circuit conditions. The short-circuit and open-circuit resonant frequencies are denoted by $f_r^{sc}$ and $f_r^{oc}$, respectively. There are good agreements between the present model with the analytical Erturk-Inman beam model. In both cases, due to the large electrical load connection, $f_r^{oc}$ is greater than $f_r^{sc}$. The ratio of $\frac{f_r^{oc}}{f_r^{sc}}$ for both modeling approaches are the same. One impressive result is that the ratio of $\frac{f_r^{oc}}{f_r^{sc}}$ for the 2nd and 3rd becomes

smaller, indicating that the effect of load on the resonant frequency for higher modes becomes negligible.

| Vibration mode | Undamped natural frequency (Hz) | | | |
|---|---|---|---|---|
| | Beam analytical | Akbar-Curiel Sosa [32] | | Present FE [163] |
| | Erturk-Inman [5] | Beam analytical | Finite element | TSDT approx. |
| 1st bending | 185.1 | 185.1 | 187 | 185.9 |
| 2nd bending | 1159.8 | 1160.1 | 1162.3 | 1174.4 |
| 3rd bending | 3247.6 | 3248.3 | 3238.5 | 3356.4 |

Table 2-6. Comparing the undamped natural frequencies for the bimorph example [163].

| | 1st bending | | 2nd bending | | 3rd bending | |
|---|---|---|---|---|---|---|
| | $f_r^{sc}$ | $f_r^{oc}$ | $f_r^{sc}$ | $f_r^{oc}$ | $f_r^{sc}$ | $f_r^{oc}$ |
| Erturk-Inman [5] | 185.1 | 191.1 | 1159.7 | 1171.6 | 3245.3 | 3254.1 |
| Finite Element [163] | 185.9 | 191.3 | 1174.4 | 1186.4 | 3356.4 | 3368.0 |
| Difference between Erturk-Inman and present FE | 0.4% | 0.1% | 1.25% | 1.25% | 3.31% | 3.38% |
| $\frac{f_r^{oc}}{f_r^{sc}} \cong$ | 1.03 | | 1.01 | | 1.004 | |

Table 2-7. Comparing the short-circuit resonant frequencies and open-circuit resonant frequencies for the bimorph example [163].

### 2.4.7.2 For the benchmark example (a bimorph harvester with tip mass)

Here, the present FE results for the benchmark example are compared with the experimental data provided by Erturk-Inman [165]. The benchmark example is a bimorph energy harvester with a tip mass, and their properties were given in subsection 2.1.

According to Table 6 in Ref. [163], the present FE model predicts the short-circuit fundamental natural frequency of 45.69 Hz, which is 0.2% greater than the experimental value of 45.6 Hz.

The comparison between the natural frequencies from different plate theories is given in Table 2-8. In Table 2-8, the error (ER) in percent is calculated concerning the advanced CUF-TSDT method. Overall, the CLPT method's accuracy is lower than the other methods, in a way that the 3rd bending mode has a 13% difference compared to the CUF method. The difference between the classical method using the FSDT and

TSDT with the advanced method TSDT is slight, less than 0.5%. It can be concluded that the CLPT plate theory is not suitable for a comprehensive analysis, and at least the first shear deformation theory (FSDT) shall be employed. Besides, it can be settled that for the thin-layered piezoelectric energy harvesters, using the advanced method by high-order shear deformation theory generated similar results with the classic method considering the shear deformation theories.

| Mode number and type | Classic method | | | | | | Advance method (CUF) |
|---|---|---|---|---|---|---|---|
| | CLPT | ER (%) | FSDT | ER (%) | TSDT | ER (%) | TSDT |
| 1st Bending | 45.008 | -1.49 | 45.703 | 0.03 | 45.687 | 0.00 | 45.687 |
| 1st Torsion | 318.841 | -24.80 | 424.206 | 0.05 | 423.592 | -0.09 | 423.987 |
| 2nd Bending | 500.121 | -4.10 | 521.556 | 0.01 | 521.233 | -0.05 | 521.482 |
| 2nd Torsion | 1138.693 | -21.86 | 1458.357 | 0.08 | 1454.942 | -0.15 | 1457.174 |
| 3rd Bending | 1286.336 | -13.35 | 1486.863 | 0.16 | 1483.320 | -0.08 | 1484.453 |
| 4th Bending | 2183.624 | -6.42 | 2335.924 | 0.10 | 2332.049 | -0.06 | 2333.486 |
| 3rd Torsion | 2444.333 | -19.80 | 3052.329 | 0.15 | 3041.001 | -0.22 | 3047.853 |
| 5th Bending | 2490.304 | -22.05 | 3211.723 | 0.53 | 3190.174 | -0.15 | 3194.821 |

Table 2-8. The comparison between the natural frequencies in (Hz) from different plate theories [163].

The voltage response and the beam tip velocity from the present FE method are compared with the Erturk-Inman experiments, as depicted in Fig. 2-22 (a) and (b), respectively. These comparisons are given for three resistive loads, i.e., 1kΩ, 6.7 kΩ, and 100 kΩ. Overall, there are fair agreements between the experimental data and the FE model outcomes; however, some comments about the differences can be made.

First, the correlation among the voltage data is better than among the tip velocity data. This fact can be due to the lower accuracy of the mechanical response measurements. Overall, the devices for measuring the voltage are capable of measuring in mV scales. However, the experimental error for the tip velocity measurements can be higher due to the senor error, stand error, and recording system error. Besides, since the piezoelectric layer is covered with the electrode, the output voltage is a surface-integration parameter, while the tip velocity is a local parameter, and therefore, more sensitive.

Second, in both voltage and tip velocity curves, the electrical load increases the resonant frequency, and the FE model captures this effect well.

Third, in the tip velocity curve, increasing the electrical load first reduces the tip velocity; however, when the load becomes enormous, the tip velocity increases again, yet smaller than the short-circuit tip velocity.

(a)

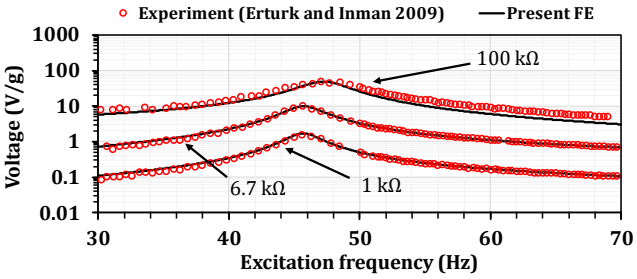


(b)

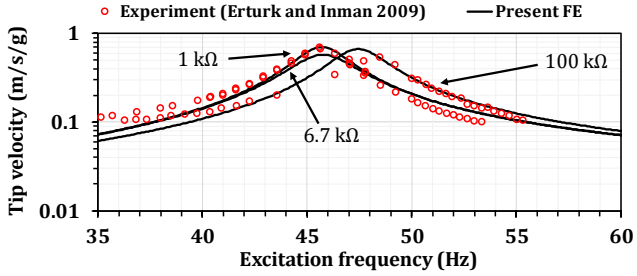


Fig. 2-22. The comparison of the (a) voltage and (b) beam tip velocity between the results from the present FE and the experimental data (Erturk and Inman [108]) [163].

## 2.5. MACRO-FIBER COMPOSITE ENERGY HARVESTER MODELING

This subsection briefly presents the modeling of the macro-fiber composite (MFC). This approach for modeling the MFC is based on the FE and is derived from Ref. [164] (see Appendix F).

In Ref. [164], a piezoelectric bimorph harvester with a composite substrate and two MFC layers is modeled with the high-order-advanced-element FE method. This biomorph is shown in Fig. 2-23 (a). The steps for discretization, spatial approximation, matrix derivation, and solution are the same as the FE approach described in subsection 2.4. The only difference here is to find the equivalent element for a layered MFC. The MFC has seven layers, one active layer, two electrode layers, two acrylic layers, and two Kapton layers, as shown in Fig. 2-23 (b). The substrate layer is usually a metal layer; however, as a general case, it is considered that the

substrate is also a composite layer with fiber orientation $\theta_s$, as shown in Fig. 2-23 (c). The active layer itself, shown in Fig. 2-23 (d), is a composite lamina with PZT rectangular cross-section fibers with a fiber orientation $\theta_p$. These rotations in the fibers for the substrate and the active layer are tools for modifying the resonant frequency and the power output. These will be discussed in the application section.

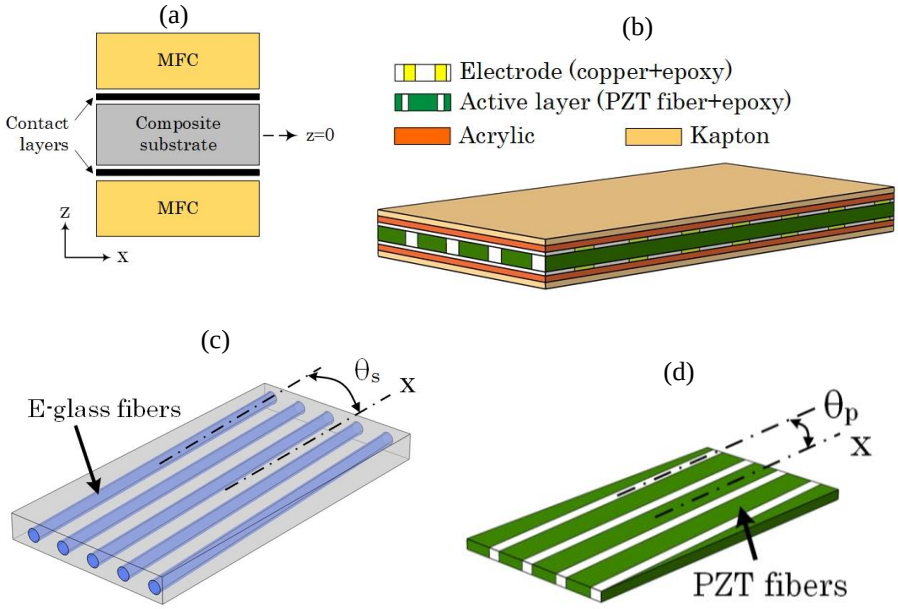


Fig. 2-23. (a) a bimorph beam with two MFCs, (b) the MFC and its layers, (c) the composite substrate with a typical E-glass fiber, and (d) the active piezoelectric layer in the MFC [164].

Mixing and transformation rules for obtaining the material properties at different conditions should be presented. Besides, specific material properties for each layer in the MFC need to be reported. These pieces of information will be given in the following subsections.

### 2.5.1. MIXING RULES FOR THE COMPOSITE LAMINATE

The electrode layer and the active layer in the MFC and the substrate layer are composite laminate, for which the micromechanical equivalent properties can be obtained using the mixing rules. If "1" denotes the direction in length, "2" denotes the direction in width, the superscript "f" denotes the fiber, the superscript "m" denotes the matrix, and "$v_f$" denotes the fiber volume fraction, the engineering material properties in the "1" and "2" direction are given by [172]:

$$E_1 = \mathcal{V}_f E_1^f + \left(1 - \mathcal{V}_f\right) E^m \tag{2.97a}$$

$$\frac{1}{E_2} = \frac{\mathcal{V}_f}{E_2^f} + \frac{1 - \mathcal{V}_f}{E^m} \tag{2.97b}$$

$$v_{12} = \mathcal{V}_f v_{12}^f + \left(1 - \mathcal{V}_f\right) v_{12}^m \tag{2.97c}$$

$$\frac{1}{G_{12}} = \frac{\mathcal{V}_f}{G_{12}^f} + \frac{1 - \mathcal{V}_f}{G^m} \tag{2.97d}$$

$$G_{13} = \mathcal{V}_f G_{13}^f + \left(1 - \mathcal{V}_f\right) G^m \tag{2.97e}$$

$$\frac{1}{G_{23}} = \frac{\mathcal{V}_f}{G_{23}^f} + \frac{1 - \mathcal{V}_f}{G^m} \tag{2.97f}$$

As the active layer is a composite material, assigning the PZT coupling material properties to the active layer coupling properties is not correct. The piezoelectric properties for the active layer can be extracted by the mixing rules, as given by [173]:

$$d_{31} = \frac{1}{E_1} \mathcal{V}_f d_{31}^p E_1^p \tag{2.98a}$$

$$d_{32} = -d_{31}^p v_{12} + \mathcal{V}_f d_{31}^p E_1^p \left(1 + v_{12}^p\right) \tag{2.98b}$$

$$\epsilon_{33} = \mathcal{V}_f \epsilon_{33}^p \tag{2.98c}$$

## 2.5.2. TRANSFORMATION RULES FOR THE MATERIAL PROPERTIES

A fiber orientation different from zero will change the stiffness properties for all the layers and the active layer's piezoelectric properties. It should be noted that the fiber rotation in the PZT and substrate are arbitrary and denoted by $\theta_p$ and $\theta_s$. Besides, $\theta$=90º for the MFC electrode layer according to the manufacturer's datasheet.

If $[Q_{ij}]$ and $[\bar{Q}_{ij}]$ are the stiffness matrices in the principal and physical coordinates, respectively, the relationships between their components can be given by [103]:

$$\begin{aligned}
\bar{Q}_{11} &= Q_{11}\cos^4\theta + 2(Q_{12}+2Q_{66})\sin^2\theta\cos^2\theta + Q_{22}\sin^4\theta \\
\bar{Q}_{12} &= (Q_{11}+Q_{22}-4Q_{66})\sin^2\theta\cos^2\theta + Q_{12}(\sin^4\theta+\cos^4\theta) \\
\bar{Q}_{22} &= Q_{11}\sin^4\theta + 2(Q_{12}+2Q_{66})\sin^2\theta\cos^2\theta + Q_{22}\cos^4\theta \\
\bar{Q}_{16} &= (Q_{11}-Q_{12}-2Q_{66})\sin\theta\cos^3\theta + (Q_{11}-Q_{12}+2Q_{66})\sin^3\theta\cos\theta \\
\bar{Q}_{26} &= (Q_{11}-Q_{12}-2Q_{66})\sin^3\theta\cos\theta + (Q_{11}-Q_{12}+2Q_{66})\sin\theta\cos^3\theta \\
\bar{Q}_{66} &= (Q_{11}+Q_{22}-2Q_{12}-2Q_{66})\sin^2\theta\cos^2\theta + Q_{66}(\sin^4\theta+\cos^4\theta) \\
\bar{Q}_{44} &= Q_{44}\cos^2\theta + Q_{55}\sin^2\theta \\
\bar{Q}_{45} &= (Q_{55}-Q_{44})\cos\theta\sin\theta \\
\bar{Q}_{55} &= Q_{55}\cos^2\theta + Q_{44}\sin^2\theta
\end{aligned} \tag{2.99}$$

The material properties for the piezoelectric layer due to the $\theta$-rotation are given by [103]:

$$\begin{aligned}
\bar{e}_{31} &= e_{31}\cos^2\theta + e_{32}\sin^2\theta \\
\bar{e}_{32} &= e_{31}\sin^2\theta + e_{32}\cos^2\theta \\
\bar{e}_{36} &= (e_{31}-e_{32})\sin\theta\cos\theta \\
\bar{e}_{14} &= (e_{15}-e_{24})\sin\theta\cos\theta \\
\bar{e}_{24} &= e_{24}\cos^2\theta + e_{15}\sin^2\theta \\
\bar{e}_{15} &= e_{15}\cos^2\theta + e_{24}\sin^2\theta \\
\bar{e}_{25} &= (e_{15}-e_{24})\sin\theta\cos\theta
\end{aligned} \tag{2.100}$$

$$\begin{aligned}
\bar{\epsilon}_{11} &= \epsilon_{11}\cos^2\theta + \epsilon_{22}\sin^2\theta \\
\bar{\epsilon}_{22} &= \epsilon_{11}\sin^2\theta + \epsilon_{22}\cos^2\theta \\
\bar{\epsilon}_{12} &= (\epsilon_{11}-\epsilon_{22})\sin\theta\cos\theta \\
\bar{\epsilon}_{33} &= \epsilon_{33}
\end{aligned}$$

### 2.5.3. MATERIAL PROPERTIES FOR THE MFC SUBLAYERS

Accurate MFC modeling is a challenge because there are many sublayers that their material properties shall be inserted into the model. Many of these material properties are not given explicitly by the manufacturer's datasheet. Therefore, the equivalent properties for the sublayers shall be calculated from the raw material properties. The

seven sublayers' properties are derived from Ref. [173]–[175] and are given in Table 2-9. The small fiber volume fraction in the electrode layer can be due to the light weightiness and flexibility design criteria. On the other hand, the high volume fraction in the active layer should be due to the necessity for high power generation; yet 0.14% epoxy volume creates flexibility in the active layer.

| Properties | Active layer | Electrode layer | Acrylic layer | Kapton layer |
|---|---|---|---|---|
| Fiber volume fraction $v_f$ | 0.86 | 0.24 | — | — |
| Layer thickness (μm) | 177.8 | 17.78 | 12.7 | 25.4 |
| Fiber material | PZT-5A | Copper | — | — |
| Matrix material | Epoxy | Epoxy | — | — |

Table 2-9. The MFC sublayers' properties [173]–[175].

Six different materials are used in the MFC, ranging from PZT to viscoelastic epoxy. The PZT material is considered orthotropic, while epoxy, copper, acrylic, and Kapton are considered isotropic materials. Material properties for these six materials are given in Table 2-10.

| Properties | PZT fibers | Epoxy | Copper | Acrylic | Kapton |
|---|---|---|---|---|---|
| Young's modulus (GPa) | $E_1$=53<br>$E_2$=61 | 3.378 | 117.2 | 2.7 | 2.5 |
| Shear modulus (GPa) | $G_{12}$=12<br>$G_{23}$=22.6<br>$G_{13}$=22.6 | 1.33 | 44.7 | 1.0 | 0.93 |
| Poisson's ratio | $v_{12}$=0.384<br>$v_{23}$=0.35 | 0.27 | 0.31 | 0.35 | 0.34 |
| Density (g/cm3) | 7.75 | 1.4 | 8.96 | 1.185 | 1.42 |
| Coupling charge constants (pC/N) | $d_{31}$=-167.28<br>$d_{32}$=-167.28 | — | — | — | — |
| Dielectric constants (nF/m) | $1850\varepsilon_0$ | — | — | — | — |

Table 2-10. The material properties for the materials in the MFC sublayers [164].

## 2.5.4. COMPARISON WITH THE EXPERIMENTS

Using the mixing rules and the sublayer material properties, the FE model outcomes adopted for the MFC are compared with the experimental results. Fig. 2-24 (a) shows the experimental setup, an unimorph piezoelectric harvester with the MFC undergoing harmonic base excitation. Fig. 2-24 (b) shows the natural frequency comparison between the FE model and the experiment, 205.7 Hz and 197.5 Hz. A 4% error exists in the natural frequency comparison. The power output is compared with the

experiments Fig. 2-24 (c) as a frequency ratio function, where the frequency ratio is the excitation frequency divided by the natural frequency. The FE model results are given in two states, one undamped without damping matrix and the other with the damping model. The proportional damping coefficients are extracted using the model's correlation to the experiment based on the peak power. Fig. 2-24 (c) shows that the resonant occurs at approximately $\Omega \approx 1.016$ for both the experiments and the FE results. The undamped FE model's peak power is substantially overestimated, while the FE power curve matches perfectly with the experimental data using the FE damped model.

(a)

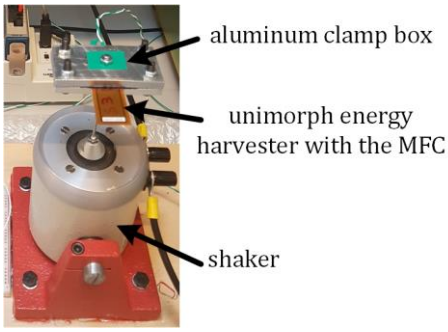


(b)

| | 1st natural frequency (Hz) |
|---|---|
| Experiment [161] | 197.5 |
| FE model [164] | 205.7 |
| Difference | +4% |

(c)

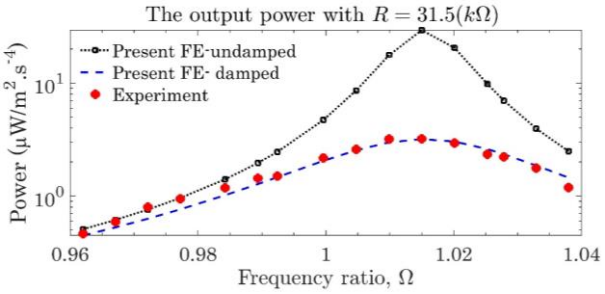


Fig. 2-24. (a) Experimental setup: A cantilevered unimorph piezoelectric beam with the MFC, (b) the comparison of the natural frequencies, and (c) the comparison of output power between the FE model in undamped and damped model with the experiments [164].

## 2.5.5. COMPARISON WITH FE COMMERCIAL SOFTWARE

In this subsection, the current FE model's output is compared for a trapezoid piezoelectric bimorph beam. These results are given from Ref. [164].

The trapezoid energy harvesting beam has two PZT-5A piezo layers attached to an E-glass fiber unidirectional composite with 50μm epoxy contact layers. Fig. 2-25 shows this piezoelectric beam. The material properties for the substrate composite and the contact layers are given by t. The piezoelectric active layer's layerwise characteristics, the substrate composite, and the contact layers are given in Table 2-12.

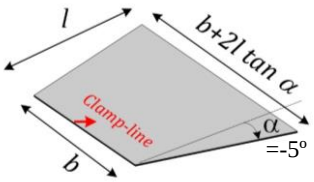


Fig. 2-25. The trapezoid piezoelectric bimorph with E-glass unidirectional substrate and two PZT-5A piezo layers [164].

| Properties | E-glass fibers | Contact layer |
|---|---|---|
| Young's modulus (*GPa*) | *E*=30 | 1.05 |
| Shear modulus (*GPa*) | *G*=30 | 0.40 |
| Poisson's ratio | *v*=0.32 | 0.3 |
| Density ($g/cm^3$) | 2.540 | 1.4 |

Table 2-11. The properties of the E-glass fibers and the contact layer for the bimorph shown in Fig. 2-25.

| Properties | Active layer | Substrate layer | Electrode layer | Contact layer |
|---|---|---|---|---|
| Length (*mm*) | 100 | | | |
| Width (*mm*) | 100 | | | |
| Fiber direction $\theta$ (*deg*) | $\theta_p$=10 | $\theta_s$=30 | 90 | — |
| Layer thickness ($\mu m$) | 177.8 | 150.0 | 17.78 | 50.0 |
| Fiber material | PZT-5A | E-glass $v_f$=60% | Copper | — |
| Matrix material | Epoxy | Epoxy | Epoxy | — |

Table 2-12. The layerwise characteristics considered for the bimorph shown in Fig. 2-25.

The first three modes for this bimorph harvester are shown in Fig. 2-26 (a). The first mode is the bending mode, and the second and third modes are bending-torsion modes. The 1st mode, which is the bending mode, does not considerably vary concerning the element numbers. In contrast, the 2nd and third modes require a fine mesh to generate accurate natural frequencies. There is good agreement between the present FE model and the COMSOL® software results in all three modes. Note that

for an accurate FE model in all the modes, approximately 300 elements are required. Nevertheless, for energy harvesting applications, the bending mode is of great interest. Therefore, for energy harvesting applications, Khazaee et al. [164] only used a 24-element mesh, which is accurate enough for the 1st bending mode.

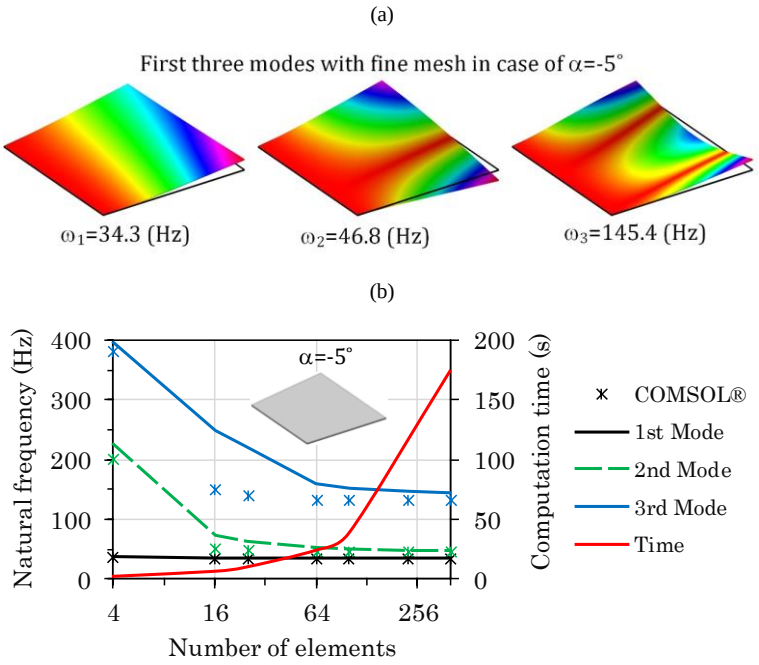


Fig. 2-26. (a) the first three modes using COMSOL®, and (b) The natural frequency comparisons for the first three modes between COMSOL® and the FE model at different element numbers [164].

## 2.6. COMPARISON BETWEEN THE SDOF, DISTRIBUTED AND FE METHODS

The natural frequencies and the output voltage and power for the benchmark example are compared against each other for comparing the Single-Degree-of-Freedom (SDOF), analytical beam, and the finite element methods.

Table 2-13 illustrates the first and second mode natural frequencies using the SDOF, beam, and FE models and the first experimentally obtained natural frequency. In the first mode, the FE natural frequency is the closest value to the experiment. Nevertheless, the error for the first mode is less than 1%. For the second mode, however, the SDOF model gives an incorrect value, and the beam model result has a 3.7% error. Therefore, the SDOF and beam models are not accurate for estimating the natural frequencies in higher modes.

| | SDOF $\omega_n$(Hz) | Beam $\omega_n$(Hz) | FE $\omega_n$(Hz) | Experiment $\omega_n$(Hz) [108] |
|---|---|---|---|---|
| Mode I (Variation) | 45.17 (0.43Hz) | 45.73 (0.13Hz) | 45.69 (0.09Hz) | 45.6 |
| Mode II | 282.27 | 541.24 | 521.73 | - |

Table 2-13. The comparison of the first and second mode natural frequencies between SDOF, Beam, and FE methods.

The voltage and power outputs from the SDOF, beam, and FE models under the resonant excitation are compared in Fig. 2-27 (a) and Fig. 2-27 (b). Overall, while the beam and FE method results are similar, the SDOF behavior has considerable differences. From Fig. 2-27 (a), the open-circuit voltage of the SDOF, for instance, is notably lower than the other methods' results. The optimum load for the maximum power in Fig. 2-27 (b) shows that the SDOF method will give an inaccurate optimum load, even though the peak power can be similar to the beam and FE peak power. Thus, estimation of the optimum load based on SDOF is not accurate. Besides, the output voltage from the FE method is slightly lower than the beam model.

Nevertheless, this difference becomes smaller in the electrical load range of $10^4$ to $10^5$ Ω. This range of loads is within the optimum loads for many piezoelectric beams. Therefore, the beam model gives accurate results in the optimum conditions, even though the open-circuit and short-circuit conditions slightly overestimate the power.

(a)

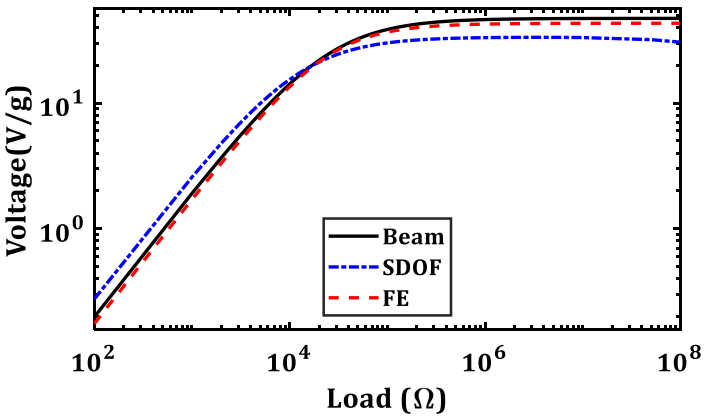

(b)

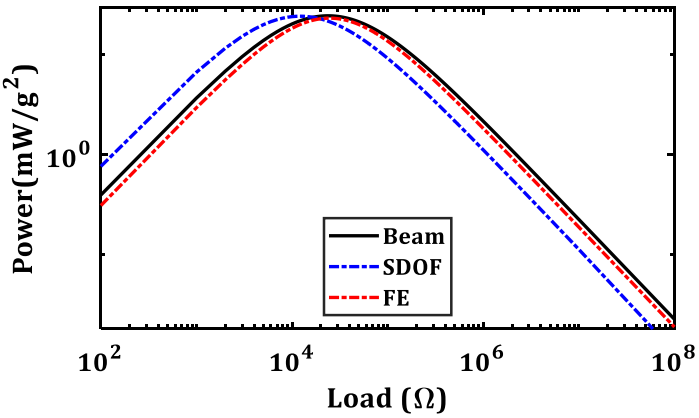


Fig. 2-27. (a) Voltage and (b) power outputs versus electrical load under the resonant excitation using the SDOF, beam, and FE models.

## 2.7. LARGE DEFLECTION NON-LINEARITY

In the linear framework, the beam tip deflection is also doubled by doubling the base excitation amplitude. The voltage is doubled, and the output power is multiplied by $2^2$ for all three models in Chapter 2. Also, in the linear framework, the beam's natural frequency is independent of excitation magnitude. However, this independence is not valid in reality, and for the large beam deflections, the large deflection non-linearity will occur.

Ref. [176] carried out tests on a small unimorph beam with a single MFC. The voltage output from the unimorph was measured over a range of frequencies for three different excitation amplitudes. Fig. 2-28 shows the experimental setup from Ref. [176].

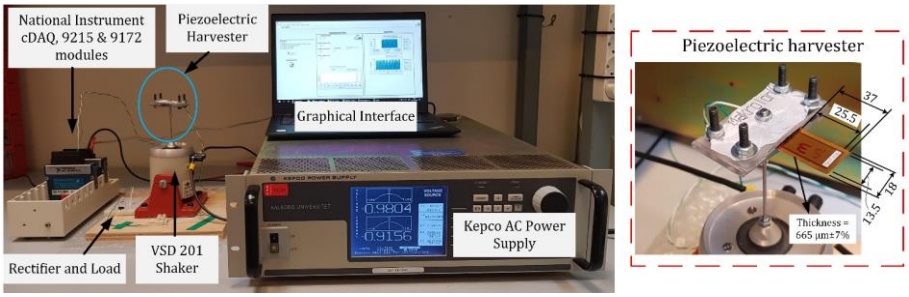


Fig. 2-28. The experimental setup on a small MFC unimorph for illustrating the large deflection nonlinearity [176].

The power output for three different excitation amplitudes, 0.1, 0.2, and 0.25V shaker input signal, is shown in Fig. 2-29. Each test is repeated two times. As expected, Fig. 2-29 shows that the output power increases by increasing the base excitation amplitude. Besides, Fig. 2-29 indicates that the resonant frequency reduces by increasing the base excitation, from 219 Hz to 214 Hz. Since the electrical load is constant at all the tests, the resonant frequency reduction is due to the damping increase or the natural frequency reduce, because $\omega_d = \omega_n\sqrt{1-\zeta_m^2}$. The damping increase should be extremely high to cause such a reduction in the resonant frequency, which is not realistic. Therefore, the resonant frequency reduction is due to the natural frequency reduction.

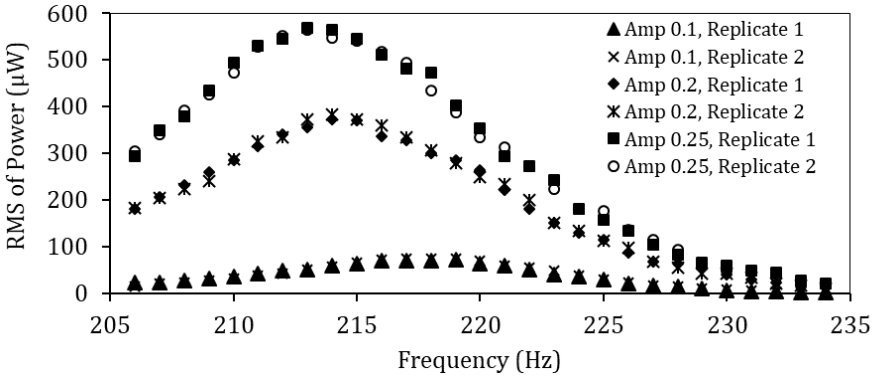


Fig. 2-29. The output power for three different harmonic excitation amplitudes with a 31.5kΩ resistance load (the test setup shown in Fig. 2-28 [176].)

Fig. 2-30 shows how the natural frequency reduces by increasing the base excitation. As can be seen, at $\frac{Y}{Y_0} = 2.5$, the natural frequency is reduced by a factor of 0.972. This natural frequency reduction illustrates that this unimorph has a softening behavior.

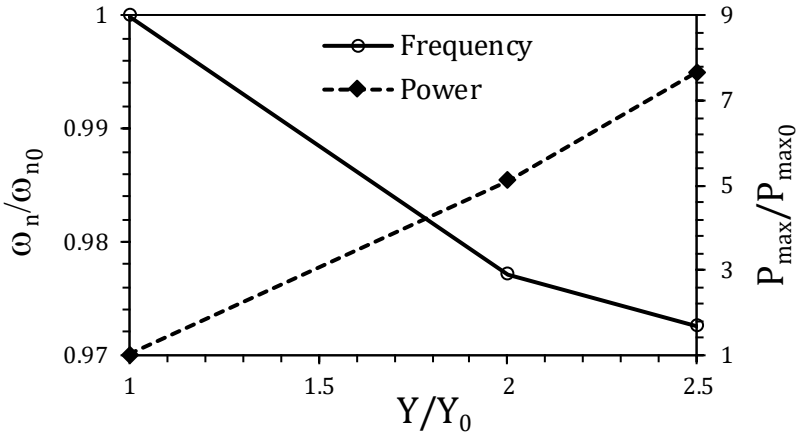


Fig. 2-30. The natural frequency and power output variation as a function of base excitation amplitude [176].

# CHAPTER 3. FURTHER INVESTIGATION OF SOME PEHS' CHARACTERISTICS

A piezoelectric beam has some sub-components, substrate shim, the added mass, and the contact layer, as depicted in Chapter 2, that affect the system's vibration characteristics (modal parameters) and the output power. This chapter introduces investigations about these parameters' effects on the natural frequency and power generation.

## 3.1. SUBSTRATE SHIM

The purpose of adding a substrate shim in the piezoelectric beam is to provide a substructure for the piezoelectric layers, which are often fragile and substantially stiff. These subsection results are derived from Ref [16], where a piezoelectric MFC unimorph is subjected to shock-based base excitations for the vibration and power performance analyses. Further details about the test configurations can be found in Ref. [16].

The substrate shim changes the natural frequency as it adds stiffness to the system. Fig. 3-1 compares the first bending mode between the No-Shim and Alu-Shim samples over a range of different base excitations. In this example, the substrate shim and contact layer increase the natural frequency by a factor of 20%, from an average of 16 Hz to 22 Hz.

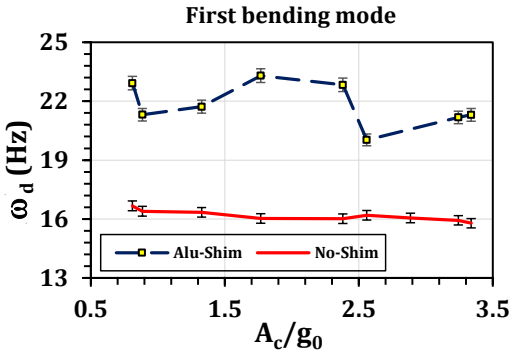


Fig. 3-1. The substrate's effect on the first bending mode for the piezoelectric MFC unimorph [16].

The voltage generation from a single MFC layer and a unimorph consisting of a MFC and an aluminum substrate is compared. The MFC has a thickness of 0.3mm, and the substrate shim is 0.12mm aluminum.

Fig. 3-2 compares the voltage outputs under a shock-excitation for the piezoelectric beam with and without the substrate shim. The Alu-Shim sample's peak voltage is approximately 1.6V, which is four times greater than the 0.4V for the No-Shim sample, illustrating the positive effect of the aluminum shim on the voltage generation. The zoomed-in view in Fig. 3-1 an interesting outcome because high-frequency (over 100Hz) fluctuations can be seen in the No-Shim sample, while these variations are not visible for the Alu-Shim sample. Besides, the voltage response in the Alu-Shim is damped out faster than the No-Shim sample.

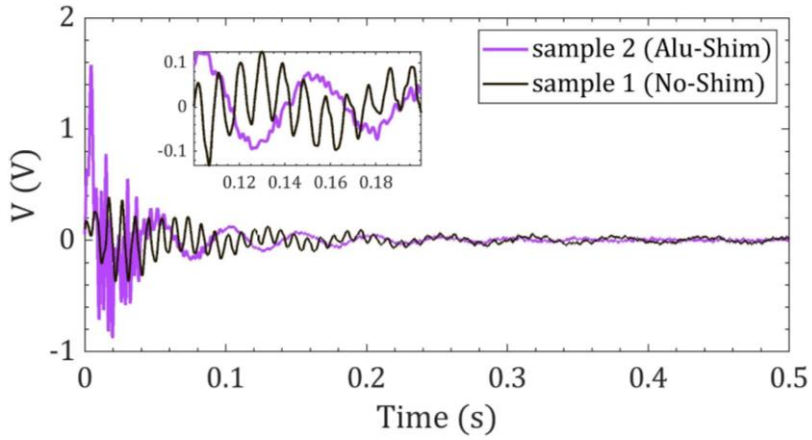


Fig. 3-2. The voltage response of a piezoelectric MFC unimorph under the 1.77g0 ($g_0$=9.81m/$s^2$) shock-based excitation with and without a substrate shim [16].

Fig. 3-3 illustrates the effect of substrate shim on the voltage generation under the stochastic DC motor vibration. The With-Shim sample generates the voltage two times larger than only the MFC layer. According to Fig. 3-2 and Fig. 3-3, the substrate shim increases the voltage output in both shock-based and stochastic vibration excitations.

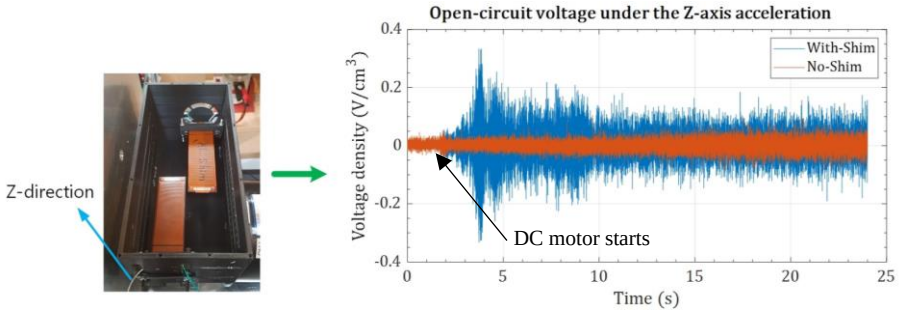


Fig. 3-3. The voltage response comparison between the No-Shim and With-Shim samples under the vibration from a DC motor [177]

In the piezoelectric MFC sample, the substrate shim increases the voltage generation substantially for both shock-excitation and practical stochastic vibration, proving that the substrate layer has a substantial positive effect. The same results about the positive effect of the substrate layer have been observed by Hong and coworkers [178]. The reason behind this is due to the neutral axis position in the bender [178]. As shown in Fig. 3-4, adding the substrate shim will deviate the neutral plane from the piezoelectric mid-plane, which will affect the charge distributions so that the resultant charge output becomes large.

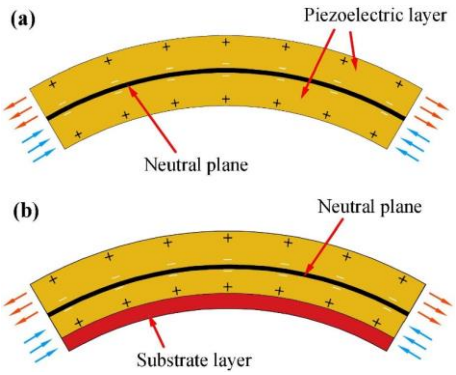


Fig. 3-4. The neutral axis position for (a) a piezoelectric layer without the substrate shim and (b) a piezoelectric layer with the substrate shim [178]

## 3.2. ADDED TIP MASS

A tip mass is often added to the piezoelectric energy harvester in the piezoelectric energy harvester design. This subsection investigates the effect of the added mass on the systems' vibration.

Table 3-1 shows the natural frequency variations when a 4.2g added tip mass is introduced, 80% mass of the No-Shim sample, and 58% mass of the Alu-Shim sample. It can be seen that the added tip mass reduces the first natural frequency by 50%, which is a substantial reduction. The added tip mass causes a 72% reduction for the second-mode natural frequency, which is even more significant than the first mode's natural frequency reduction.

| Description | $\overline{\omega}_d$(Hz) | | Frequency ratio |
|---|---|---|---|
| | no tip mass | 4.2g tip mass | |
| No-Shim sample | | | |
| - first mode | 16.2±0.4 | 8.2±0.2 | 0.51 |
| - second mode | 108.6±3.5 | 78.0±3.6 | 0.72 |
| Alu-Shim sample | | | |
| - first mode | 21.3±0.7 | 10.8±0.5 | 0.51 |

Table 3-1. The natural frequencies' variation due to the added tip mass [16].

It has been shown by many researchers that the added tip mass enhances the voltage generation by piezoelectric harvesters. The outcomes of the experiments, as shown in Fig. 3-5, also prove this statement. The tip mass increases the output voltage considerably in both No-Shim and Alu-Shim samples. This increase for the Alu-Shim sample is from 0.9V to 1.4V, while for the No-Shim sample is from 0.1V to 0.6V. Thus, the added tip mass increases the No-Shim sample's voltage more prominent because the No-Shim sample is less stiff, and the tip mass causes more significant tip deflection than the Alu-Shim sample. Since the No-Shim sample is more flexible than the Alu-Shim, the added tip mass vibration endures for a longer time, as shown in Fig. 3-5.

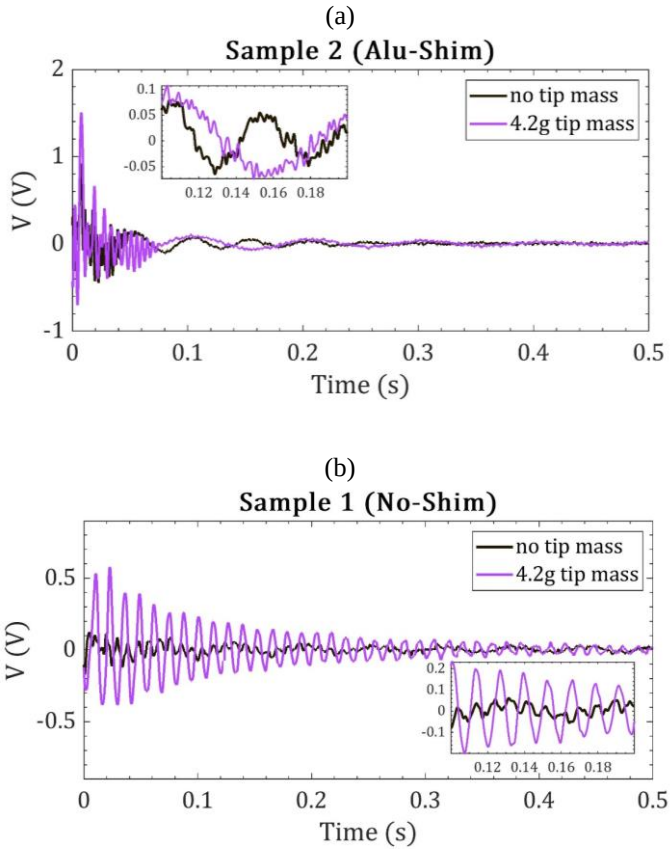


Fig. 3-5. The effect of added tip mass on the voltage for the piezoelectric MFC unimorph subjected to a $0.88g_0$ shock excitation (a) with substrate shim and (b) without substrate shim [16].

Fig. 3-5 only compares the voltage output for one shock excitation. The comparison between the voltages is repeated for a range of different shock excitations, shown in Fig. 3-6. It is still valid that the added tip mass increases the peak voltage considerably for both the No-Shim and Alu-Shim samples.

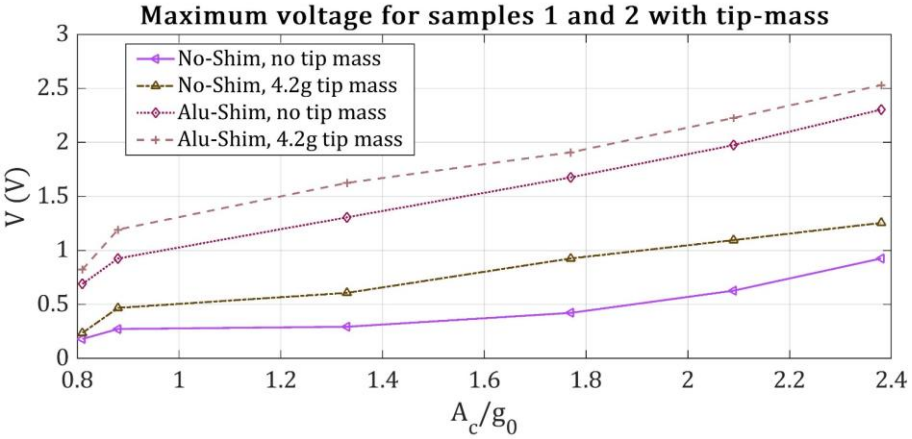


Fig. 3-6. The tip mass effect on the voltage (peak voltage) for No-Shim and Alu-Shim samples over a range of shock base excitations [16].

Under the shock excitation, the RMS of the output power is more important than the peak power. Thus, the power RMS plotted in Fig. 3-7 compares the power RMS to add tip mass. Overall, by increasing the shock excitation amplitude, the effect of tip mass becomes more significant. Besides, the increase in the power for the No-Shim sample is more significant than the Alu-Shim sample. The tip mass induces extra tip deflection due to its inertia, and if the beam is less stiff, the extra tip deflection becomes more extensive, which consequently increases the output power. In the No-Shim sample, the vibration damps out slower, and therefore, the power RMS will also be more prominent.

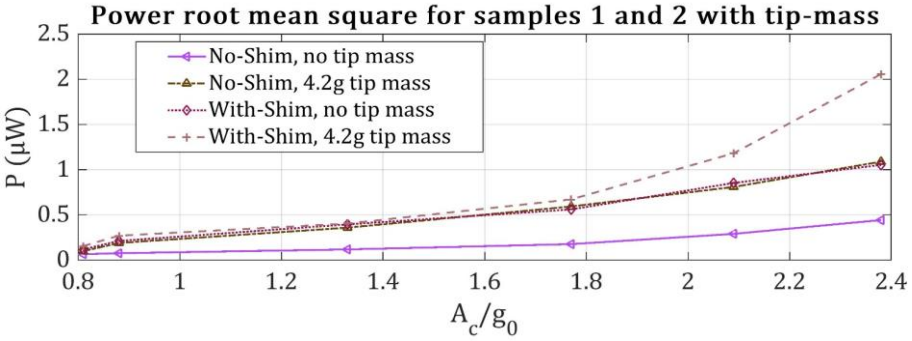


Fig. 3-7. The tip mass effect on the power RMS for Alu-Shim and No-Shim samples over a range of shock excitations [16].

## 3.3. CONTACT LAYER

The contact layer is an inseparable part of a piezoelectric beam because the piezoelectric beam is made of different layers, which need to be joined. However, the contact layer effects are often neglected. In this subsection, the numerical and experimental results are presented for pointing out the contact layer effect.

First, numerically, the contact layer's effect in an energy harvester with two piezoelectric layers is investigated using the presented FE model in subsection 2.4. The geometries of the energy harvester are given in Fig. 3-8. The power output versus the harmonic excitation frequency is shown in Fig. 3-8. The contact layer 0μm, which is not valid in a real case, leads to the highest power output. However, by increasing the thickness of the contact layer, the peak power output drops. The contact layer shifts the resonant frequency to the right because it adds stiffness to the beam.

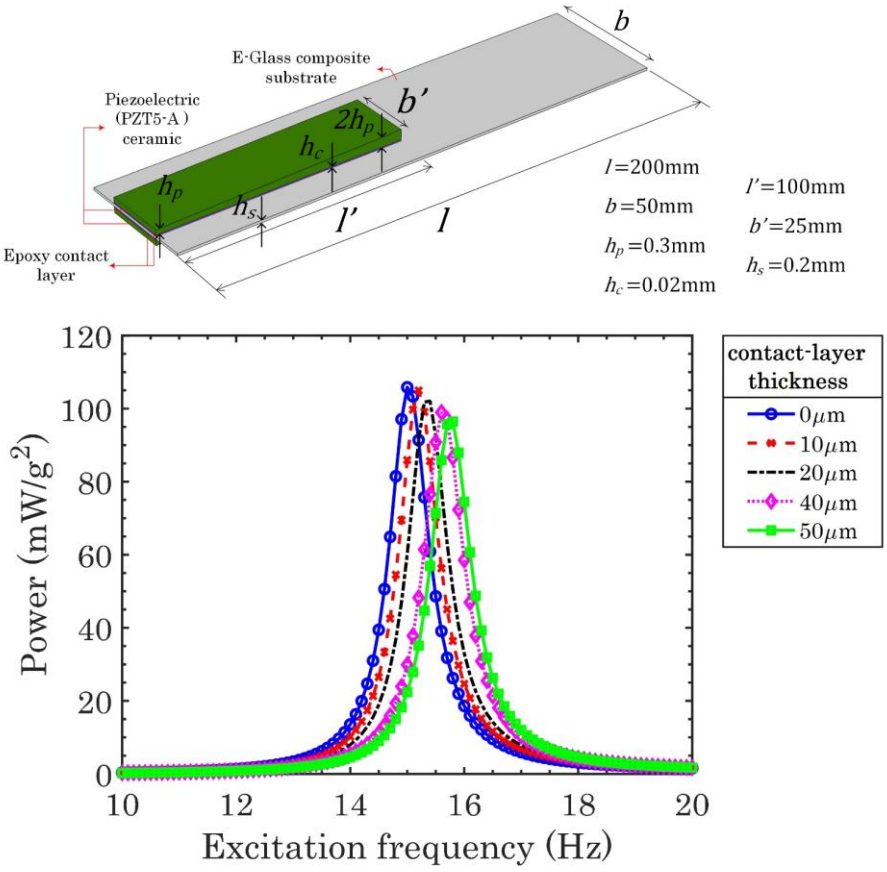


Fig. 3-8. The effect of contact layer thickness on the power output under harmonic excitations using the FE model [163].

For further investigation, the experimental voltages from the unimorph beams with different contact layers from Ref. [16] are presented in Fig. 3-9. The base excitation is shock excitation; therefore, the voltage response has a peak voltage and then damps out. Thus, for comparisons, both voltage peak and RMS are plotted in Fig. 3-9. The sample with the thinnest contact layer generates the highest voltage peak and the voltage RMS. The sample with a 1200µm contact layer, on the other hand, generates the smallest voltage output.

In addition to the peak voltage changes due to the contact layer, the voltage RMS varies substantially with different contact layers. Therefore, it can be concluded that the contact layer not only changes the peak voltage but also changes the decaying response.

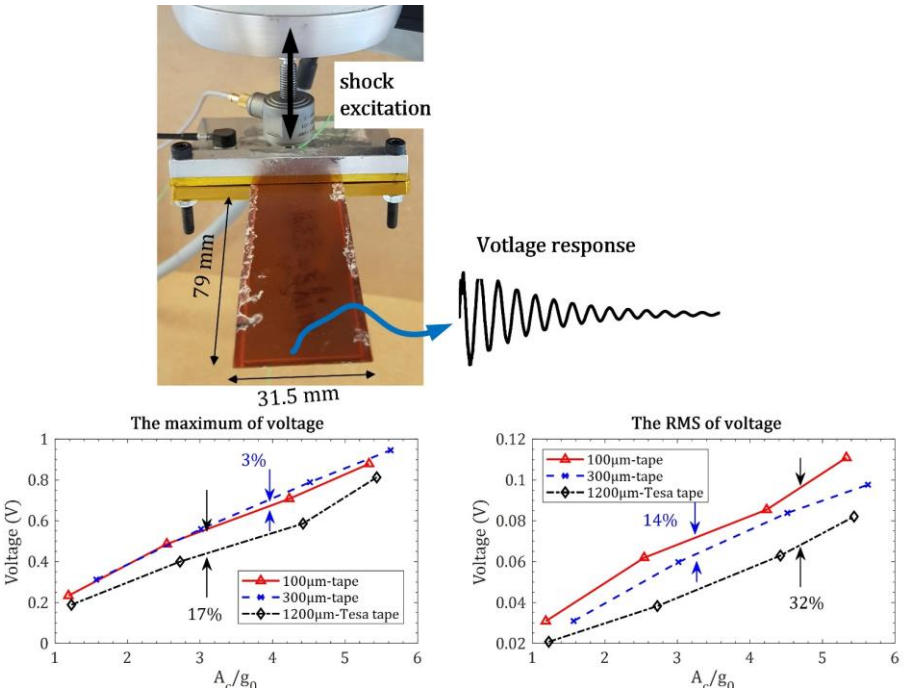


Fig. 3-9. Experimental investigation for the contact layer effect on the voltage output from the large unimorph with the MFC under the shock-based base excitation [16].

The numerical and experimental results prove that the contact layer effect is not negligible if the thickness is not small. The contact layer effect depends on its thickness and material. Less contact layer thickness gives better power generation performance. Nevertheless, the manufacturing process affects the contact layer thickness substantially. For instance, Fig. 3-10 shows two different energy harvesters; one built in the laboratory, Fig. 3-10 (a), while the other is a commercially

manufactured product, Fig. 3-10(b). As can be seen, the unimorph built in the laboratory has a considerable contact layer thickness because controlling a thin thickness of the epoxy is difficult.

On the other hand, in the commercial bimorph beam, the contact layer has a negligible constant. Thus, for the energy harvester manufacturers by advanced treatment, the contact layer thickness may be eliminated. However, if the piezoelectric composite beam is built in the laboratory and by hand, the contact layer thickness will be inevitably in the range of 100µm, which affects the piezoelectric performance. The damping effect of the contact layer is investigated in detail in Chapter 4.

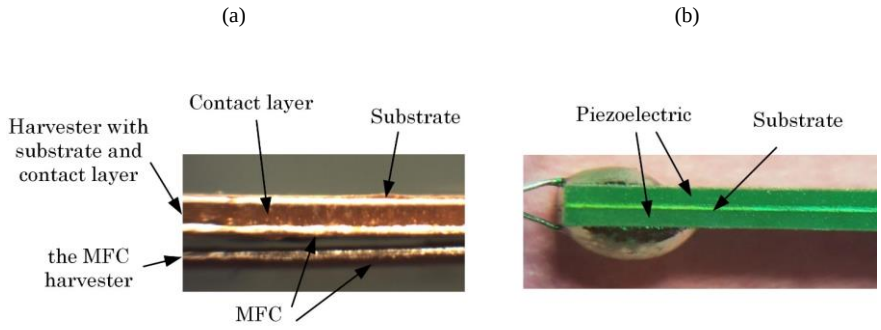


Fig. 3-10. (a) A unimorph beam without substrate and a unimorph beam with substrate and contact layer manufactures in the Aalborg University laboratory and (b) a bimorph beam commercially manufacture.

# CHAPTER 4. DAMPING IN PEHS

The power output from piezoelectric energy harvesters also depends on the damping, among other factors. A piezoelectric beam is a composite beam vibrating in the surrounding fluid, often has mechanical support. Energy dissipation in such a piezoelectric beam can have different reasons. These different energy dissipation sources, as shown in Fig. 4-1, are:

- Viscous airflow force: When the beam is vibrating in the air, the airflow force resistance applies a resistance force against the beam surface.
- Squeeze force: The force created by the airflow against a fixed wall generates a squeezing force against the beam vibration.
- Internal energy dissipation: Any energy dissipation inside the piezoelectric beam due to acoustic emissions, heat flux, and viscoelasticity, is categorized as internal energy dissipation.
- Support loss: When the piezoelectric beam is clamped or has mechanical supports, energy will be lost through the support.
- Damage damping: If any imperfection occurred between the piezoelectric beam layers, this damage could cause energy dissipation.

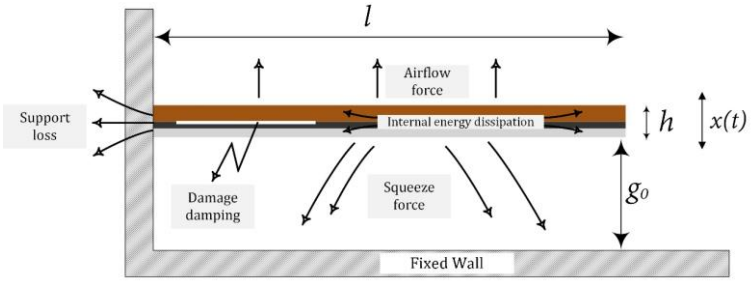


Fig. 4-1. Energy dissipation sources in a piezoelectric beam during the vibration [161]

These energy dissipation sources depend on many parameters and can be different for different piezoelectric beams. Quantifying these energy dissipation sources can help to understand the nature of damping in piezoelectric energy harvesters. The following subsections try to present methods for determining the damping coefficient and quantify different damping mechanisms.

## 4.1. SUPPORT LOSS AND DEBONDING DAMPING MECHANISMS

This subsection presents the support loss damping and the debonding damping results, which have been derived from Ref. [161].

### 4.1.1. EXPERIMENT SETUP

The experimental setup for obtaining the power output response over the frequency is given in Fig. 4-2 [161]. The piezoelectric sample, clamped by a clamp box, is subjected to harmonic excitations by the V201 shaker controlled by the NI 9215 module. The NI 9263 module measures the output voltage. Consequently, the output power is measured using Ohm's law.

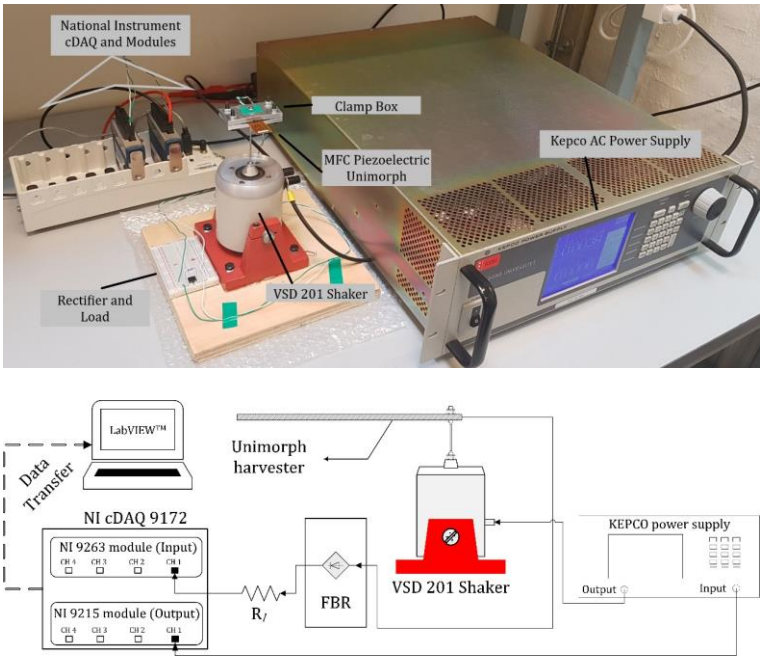


Fig. 4-2. Experimental setup for the support and damage damping mechanisms [161]

Fig. 4-3 shows the piezoelectric samples' dimensions in this study. Piezoelectric beams are unimorph beams with MFC and 0.12mm-thickness aluminum substrate, which are joined together with epoxy adhesive. Besides, there is a thickness difference between the pristine and the debonded samples due to the bonding layer, affecting the damping coefficient. Typically, having greater thickness can cause a structural damping increase. For debonding effect study, the MFC size was selected to be large so that the debonding effect can be seen clearly.

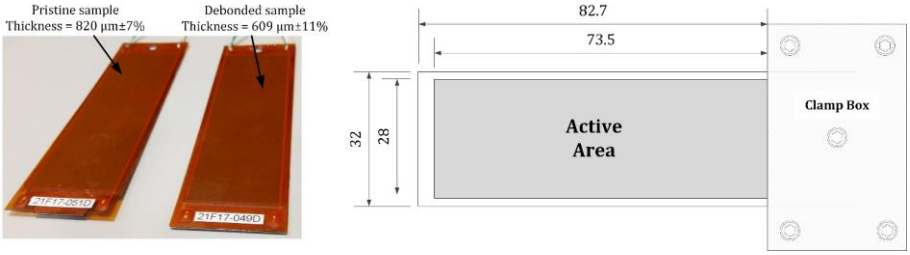


Fig. 4-3. The piezoelectric samples (pristine and debonded) were tested with the dimensions [161].

Fig. 4-4 (a) shows the experimental samples used for assessing the support loss damping. Again, the piezoelectric beams are unimorph samples with the MFC and the 0.12-mm-thickness aluminum substrate. Fig. 4-4 (b) and (c) show the piezoelectric sample connected to two different clamp boxes, one aluminum clamp box, and one plastic clamp box. In both of these boxes, four screws are used to clamp the beam.

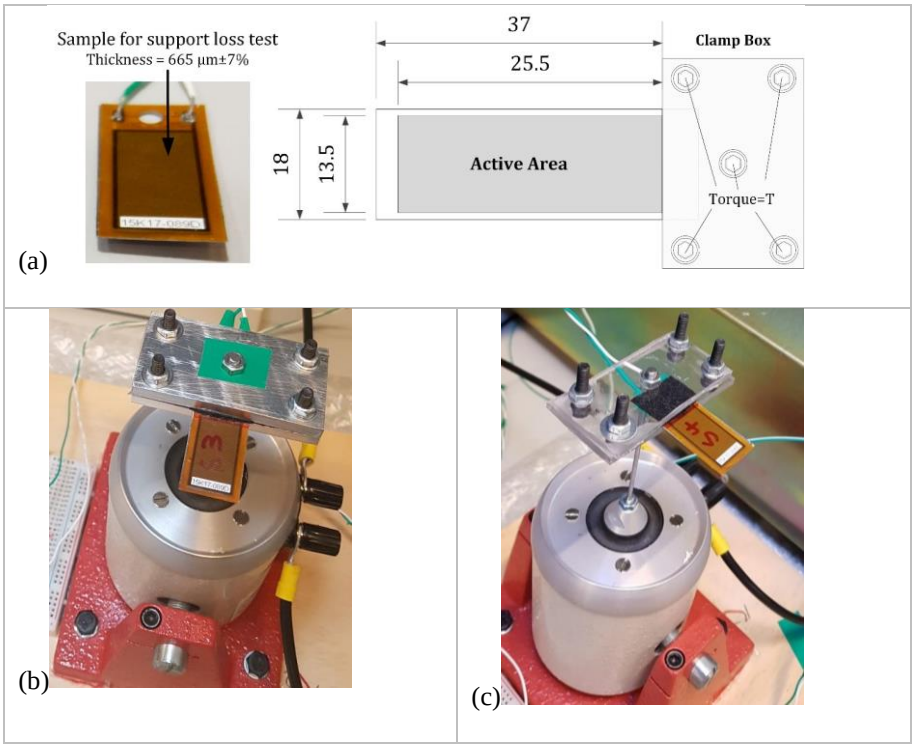


Fig. 4-4. The piezoelectric sample tested at different support conditions for measuring the support loss, (a) sample with the dimensions, (b) the aluminum clamp box, and (c) the plastic clamp box [161].

### 4.1.2. ANALYSIS METHOD

The analysis method relies on the SDOF method and model correlation. It has the following steps:

a. The piezoelectric beam is modeled using the SDOF method. The power output then will be:

$$\left|\frac{P(t)}{\ddot{X}_B{}^2}\right| = \frac{(1/\omega_n)m_{\text{eff}}rk_e^2\Omega^2}{[1-(1+2\zeta_m r)\Omega^2]^2+[(1+\alpha k_e^2)r\Omega+2\zeta_m\Omega-r\Omega^3]^2} \tag{2.12}$$

The power output model in Eq. (2.12) is based on the SDOF simple model. However, some critical parameters are extracted based on the experiments so that the model becomes accurate.

b. Natural frequency ($\omega_n$) will be obtained through the experimentally obtained frequency response function, e.g., power output FRF.
c. A model correlation is performed between the analytical SDOF model and the experimental so that the damping coefficient is updated until the resonant power outputs from the experiment and the model match.

Fig. 4-5 shows the SDOF model correlation using the resonant peak difference minimization by model correlation using the above steps (a)-(c). As can be seen from Fig. 4-5, there is good agreement between the analytical and experimental data after the correlation; however, there are some differences in the power response bandwidth of the experimental data and the analytical SDOF model. This SDOF model is simple, but the model updating using the SDOF is less time-consuming and more effortless. Besides, this study aims to track the damping variation relatively due to the support loss and damage damping, so having an acceptable accurate damping model is not the critical need in this study.

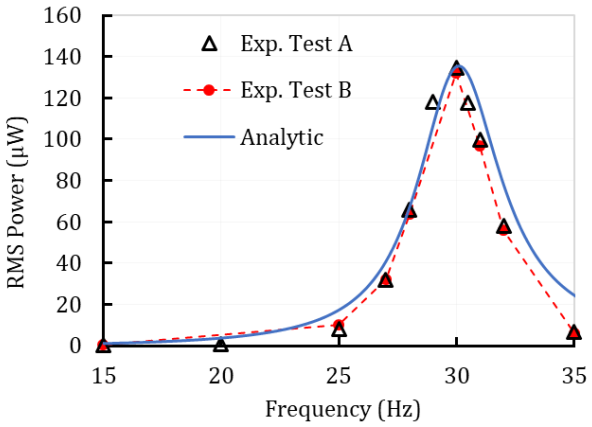


Fig. 4-5. The SDOF model correlation using experimental data by updating the damping coefficient [161].

### 4.1.3. SUPPORT LOSS DAMPING

Fig. 4-6 illustrates the variation of power over frequency for different clamp boxes with different tightening torques. If the torque for the clamp box is varied, the output power is also changed. The clamp box material also affects the output power; using the plastic clamp box leads to higher power generation.

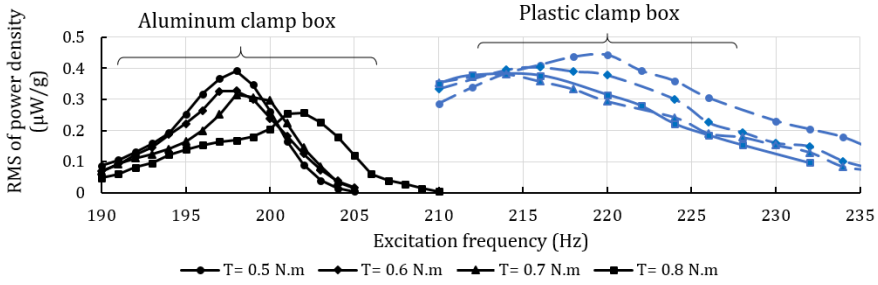


Fig. 4-6. The power output over the frequency range for the aluminum and plastic clamp boxes with different tightening torques [161].

The natural frequencies between the plastic and aluminum clamp configurations for a torque range of 0.5-0.8N.m are presented in Fig. 4-7. The sample's natural frequency with a plastic clamp is 8.2% higher than that for the sample with an aluminum clamp.

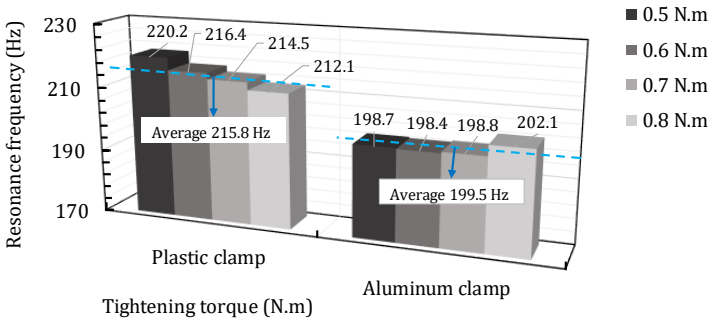


Fig. 4-7. The natural frequency comparison between the aluminum and plastic clamp configurations with different tightening torques [161].

The power output for different support clamp conditions is shown in Fig. 4-8 (a). There is an evident variation in the power output between the plastic and aluminum clamp box; the piezoelectric sample with plastic clamp has higher power generation. Besides, for both clamp boxes, by increasing the tightening torque, the power output reduces. The tightening torque is increased from an initial value to the final value and then reduced to its initial value for the plastic clamp box to ensure that the variation is repeatable. There is a good agreement between the power outputs in changing the tightening torque despite some minor variations.

Fig. 4-8 (b) illustrates the identified damping coefficient that the model correlation approach has obtained. Overall, it can be concluded that applying more pressure on the clamp box by the screws will increase friction in the support and therefore increase the damping coefficient. It also indicates that the aluminum clamp box leads to higher support loss.

(a)

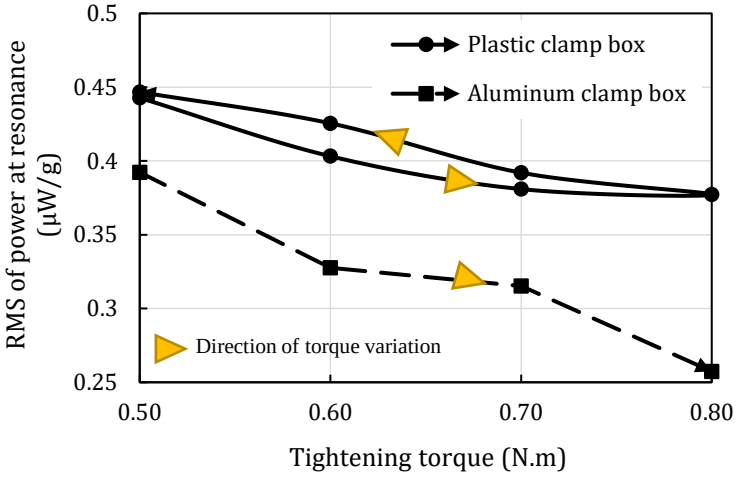


(b)

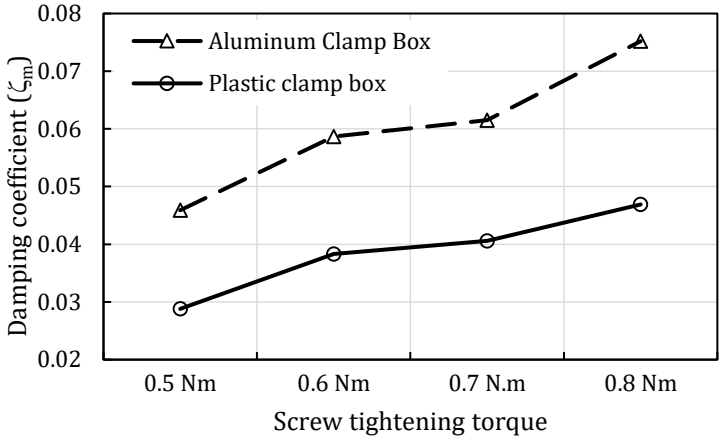


Fig. 4-8. (a) The power outputs from different clamp support conditions and (b) the identified damping for different clamp support conditions [161].

### 4.1.4. DEBONDING DAMPING

Debonding in the contact layer can be a phenomenon that occurs during manufacturing techniques or aging. Here, the performance of a piezoelectric beam is investigated due to the debonding in the contact layer. Fig. 4-9 shows the sample with the debonding area. This debonding area was created without any control on its boundaries to resemble a real debonding.

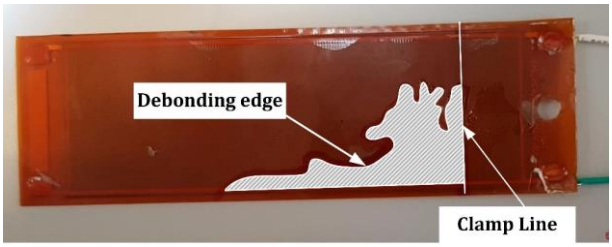


Fig. 4-9. The deboned sample with the debonding area [161].

The power output FRFs for the pristine and the debonded samples are shown in Fig. 4-10. There are two peak frequencies in the power FRF. It can be seen that the resonant power drops significantly due to the debonding with more than 40% power drop in the first bending mode frequency. Moreover, the peak frequencies are also reduced by approximately 20%. Hence, this debonding has a significant effect on both the resonant frequency and the power output; therefore, the piezoelectric beam performance would considerably change. In this clamped-free boundary condition, the strains close to the clamp box are substantially larger than other areas. Therefore, most of the power output in a piezoelectric cantilever is generated from the clamp line regions. This debonding area is located in the region close to the clamp line, leading to significant influences on the piezoelectric beam performance.

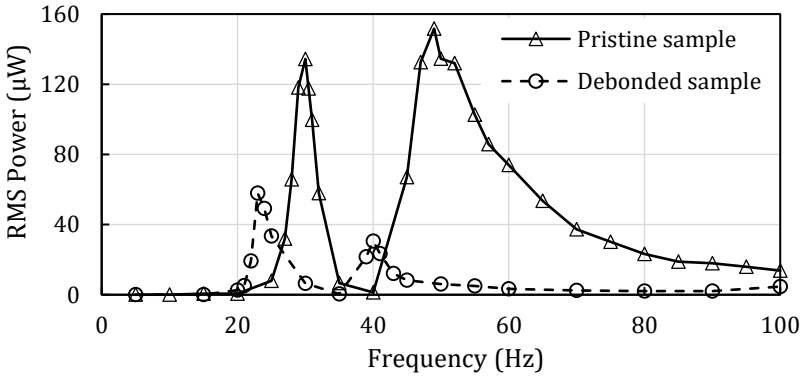


Fig. 4-10. The power FRF for the pristine (undamaged) and debonded samples [161].

As discussed in the analysis method, the analytical model power will be updated by updating the damping coefficient so that the peak power outputs match, and it is assumed that this identified damping is the correct damping value for the piezoelectric beam. Fig. 4-11 shows the performance of the model correlation. It can be seen that the analytical model power is matched with the experimental peak power for the updated damping coefficient. The resultant identified damping is also shown in Fig. 4-11 for the undamaged and the debonded samples. The damping coefficient in the

debonded sample is considerably greater than that of the undamaged sample. Therefore, this debonding will increase the damping coefficient.

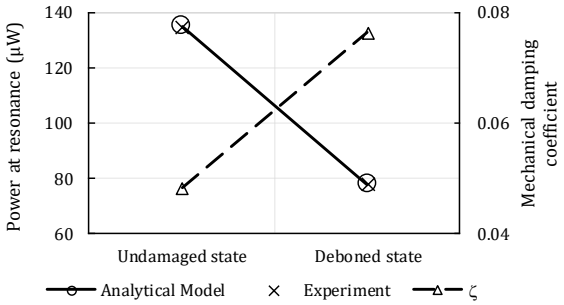


Fig. 4-11. The identified damping coefficient for the undamaged and deboned samples using the power output correlations [161].

* The fluid-structure damping is different between the undamaged and debonded samples because of their different thicknesses.

Table 4-1 summarizes the comparisons of the performance parameters between the undamaged and debonded samples. Overall, the debonding reduces the power output by 41%, reduces the natural frequency by 23%, and increases the damping coefficient. The damage-induced damping coefficient is almost responsible for one-third of the total damping.

| Parameter | Undamaged | Debonded |
|---|---|---|
| Active area ($cm^2$) | 20.58 | 17.49 |
| RMS resonant power (μW) | 132 | 77.9 |
| Resonant frequency (Hz) | 30 | 23 |
| $\zeta_m$ (Correlated value) | 4.83E-02 | 7.65E-02 |
| $\zeta_{Fluid\text{-}Structure}$* [161] | 7.90E-04 | 1.24E-03 |
| $\zeta_{Structural}$ [28] | 5.00E-07 | 5.00E-07 |
| $\zeta_{Support}$ ($=\zeta_m - \zeta_{Fluid\text{-}Structure} - \zeta_{Structural}$) | 4.75E-02 | 4.75E-02 |
| $\zeta_{Damage}$ ($=\zeta_m - \zeta_{Fluid\text{-}Structure} - \zeta_{Structural} - \zeta_{Support}$) | - | 2.78E-02 |

* The fluid-structure damping is different between the undamaged and debonded samples because of their different thicknesses.

Table 4-1. Comparing power output, resonant frequency, and the damping coefficient between the undamaged and debonded sample [161].

## 4.2. HTVR METHOD FOR DAMPING DETERMINATION

The damping is a sensitive parameter depending on many influential parameters, including the boundary conditions and the manufacturing process. Therefore, it is of great interest to present simple methods to quickly and reliably determine the damping coefficient. One method for the damping determination for the piezoelectric beams is the harmonic transient voltage response (HTVR) method [162], which uses only the voltage measurements made on piezoelectric beams; no pre-knowledge about the system is needed. This subsection presents the HTVR method and its performance for the damping determination according to Ref. [162].

### 4.2.1. HTVR METHOD PRESENTATION

HTVR has four main steps, as shown in Fig. 4-12.

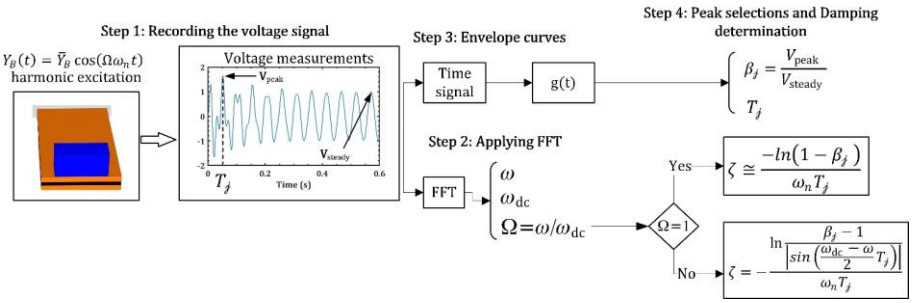


Fig. 4-12. The four main steps for the HTVR method [162].

The first step is to apply a harmonic base excitation to the piezoelectric beam and measure the transient voltage response. It is critically important that the voltage response be measured from the zero conditions. A sample of the measured transient voltage is shown in Fig. 4-12.

The second step is to apply the Fast Fourier Transform (FFT) to the measured signal. By this, the excitation frequency and the damped natural frequency can be obtained. Because the voltage is measured from the zero conditions, the response also contains the natural frequency information because it is evident in the transient response. Fig. 4-13 shows that how the FFT can reveal the dominant frequencies in the voltage response.

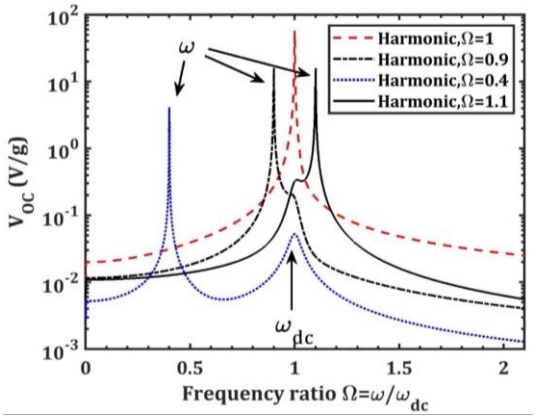


Fig. 4-13. The FFT of the voltage signal determines the excitation and the damped natural frequency [162].

The third step is to obtain the envelope curves for the transient voltage response. The transient voltage response equation was investigated in subsection 2.3.5. The transient voltage response has specific patterns for specific excitation frequency ratios. In two specific excitations, a straightforward analytical equation can be derived for the voltage envelope curve. These two conditions are (I) resonant excitation, Ω=1 and (II) under or near-resonant excitations, Ω<1 or Ω ≈1. The voltage transient response and the envelope curve for these two categories are shown in Fig. 4-14. In these two cases, the envelope curves are given by:

Case one (Ω=1) $\quad g(t) = V_{steady}(1 - e^{-\zeta\omega_n t})$, for all $t$ (4.1)

Case two (Ω<1 or Ω ≈1) $\quad g(t) = V_{steady}(1 + e^{-\zeta\omega_n t}) sin\left(\frac{\omega_{dc}-\omega}{2}t\right)$, for t $< \frac{1}{\tau}$ (4.2)

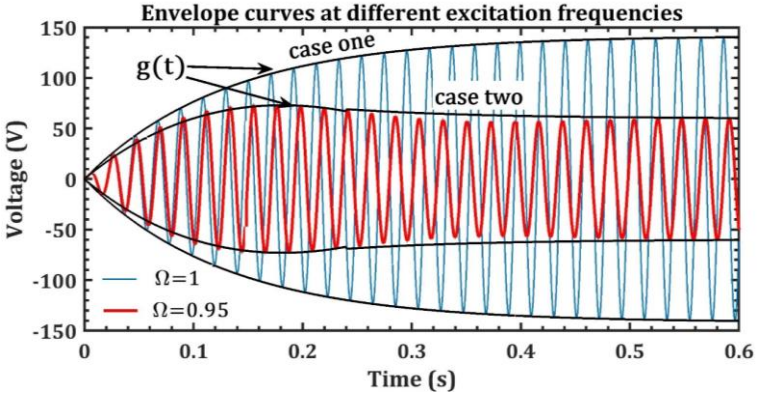


Fig. 4-14. The envelope curves for the transient voltage response at the two excitation cases [162].

The last step is to select the transient peaks and the steady-state value, and by using the envelope curve equations, calculate the damping coefficient. Fig. 4-15 shows the transient peaks and the steady-state value for a resonant excitation case. The damping coefficient can be determined from the ratio of the peaks. If $\beta_j$ is the ratio of the transient peak at a time $T_j$ to the steady-state value, as given by:

$$\beta_j = \frac{V_{\text{peak}}\big|_{@T_j}}{V_{\text{steady}}} \tag{4.3}$$

, then the damping coefficient can be given by:

Case one (Ω=1)

$$\zeta = \frac{-ln(1-\beta_j)}{\omega_n T_j} \tag{4.4}$$

Case two (Ω<1 or Ω ≈1)

$$\zeta = -\frac{\ln\dfrac{\beta_j - 1}{\left|sin\left(\dfrac{\omega_{\text{dc}} - \omega}{2} T_j\right)\right|}}{\omega_n T_j} \tag{4.5}$$

One should note that for case two, the transient peak should be located in the early stage no later than $\tau = \zeta\omega_n$, e.g., $T_j < \frac{1}{\tau}$.

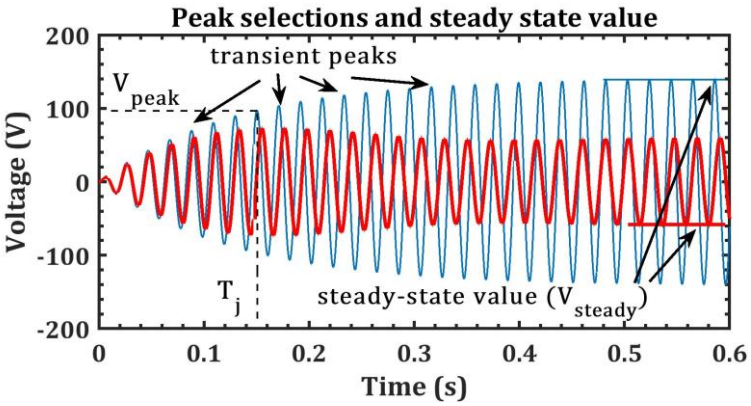


Fig. 4-15. The illustration of the transient peaks and the steady-state value [162].

## 4.2.2. EXPERIMENTAL VERIFICATION FOR THE HTVR METHOD

Experimental data is used to assess the performance of the HTVR method for the damping determination. The experiments are carried out on a unimorph piezoelectric beam with the MFC. Fig. 4-16 (a) to (c) illustrate the experimental setup and the piezoelectric sample dimensions.

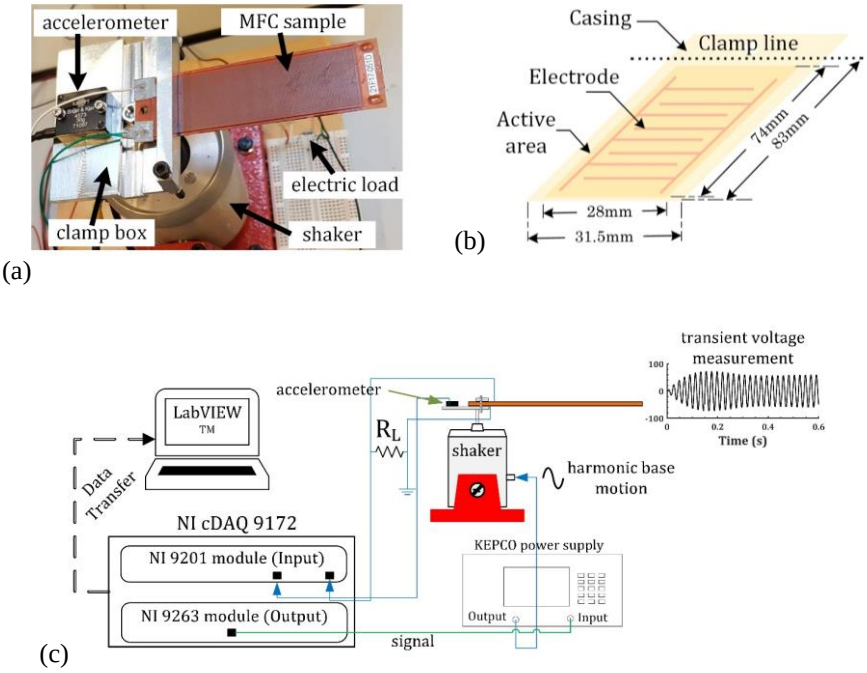


Fig. 4-16. (a) the experimental setup, (b) the piezoelectric sample with its dimension, and (c) the devise setup for the excitation and the measurement [162].

The piezoelectric sample is excited with 14-Hz and 15-Hz sinusoidal base excitations, and the HTVR method is applied to the voltage response for the damping determination.

The voltage transient response and the FFT transform of the voltages are shown in Fig. 4-17 (a) and (b), respectively. The transient and the steady-state zones are also given in Fig. 4-17 (a). Besides, the dominant frequencies in the voltage response can be seen from the FFT plots in Fig. 4-17 (b)

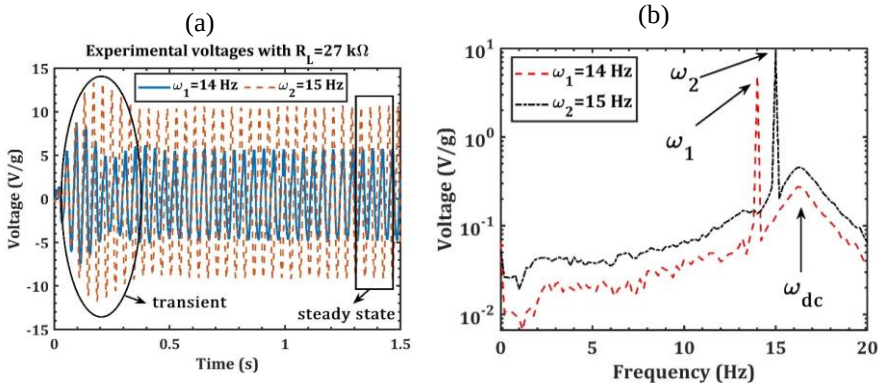


Fig. 4-17. (a) The transient voltage response under the 14Hz and 15Hz harmonic excitations and (b) applying the FFT on the transient voltage responses [162].

By applying the HTVR method to the transient voltage responses, the damping coefficients can be determined. Table 4-1 shows the parameters associated with applying the HTVR and the identified damping coefficient. According to the HTVR results, the identified damping in 14Hz and 15Hz excitations are in good agreement with each other.

| | $T_1$ (ms) | $V(T_1)$ (V/g) | $V_{\text{steady}}$ (V/g) | $\frac{V(T_1)}{V_{\text{steady}}}$ | $\zeta$ (%) |
|---|---|---|---|---|---|
| ω = 14 Hz | 95.6 | 8.629 | 5.95 | 1.45 | 4.38 |
| ω = 15 Hz | 171.0 | 13.29 | 10.1 | 1.32 | 4.82 |

Table 4-2. The identified damping coefficients from the 14Hz and 15Hz harmonic excitations using the HTVR [162].

Having the damping from the HTVR, the optimum electrical load is obtained from the analytical formula given by [179]:

$$R_{\text{L}}^{\text{opt}} = \frac{1}{\omega C_P} \frac{2\zeta}{\sqrt{4\zeta^2 + \left(\frac{\bar{e}_{31}{}^2}{\bar{c}_{11}^E \bar{\varepsilon}_{33}}\right)^2}} \tag{4.6}$$

For the understudy MFC unimorph, the analytical and experimentally obtained optimum load is given in Table 4-3. The difference between the experiment and the optimum analytical load is 25kΩ. However, this difference maybe is less in reality because the selective loads in the experiments are discrete.

| | Analytical by Eq.(4.6) | Experiment [162] | Difference |
|---|---|---|---|
| $R_{\mathrm{L}}^{\mathrm{opt}}$ | 25 kΩ | 27 kΩ | 7.4% |

Table 4-3. The comparison of the optimum analytical load with the experiments.

### 4.2.3. ACCURACY EVALUATION FOR THE HTVR METHOD

This subsection assesses the HTVR method's accuracy under different circumstances and compares the HTVR against other damping determination methods. The benchmark example in subsection 2.1 is used for the investigations.

#### 4.2.3.1 Comparison with the other methods

Here, the benchmark example is investigated by the HTVR method, and the HTVR results are compared with the results from the half-power bandwidth [180] and logarithmic decay [166] methods.

The half-power bandwidth method needs the steady-state FRF response (see Fig. 4-18 (a)), while the logarithmic decay curve needs the transient response to an impact or shock excitation (see Fig. 4-18(b)).

The damping coefficient from the half-power bandwidth method is:

$$\zeta \cong \frac{\Delta\omega}{2\omega_{dc}} = \frac{2.4}{2 \times 48.25} = 2.49\%$$

Besides, the damping coefficient from the decay curve method using the first two peaks is:

$$\zeta = \frac{1}{\sqrt{1 + \left( \frac{2\pi}{\frac{1}{N} \ln \frac{V_{\mathrm{peak}-1}}{V_{\mathrm{peak}-N}}} \right)^2}} = 2.37\%$$

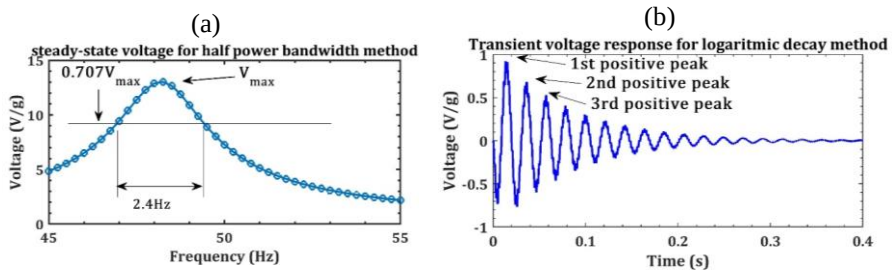


Fig. 4-18. (a) The steady-state voltage response for the half-power bandwidth method and (b) the transient response for the logarithmic decay method [162].

Table 4-4 presents the identified damping coefficients from the HTVR, half-power bandwidth, and the logarithmic decay methods. According to the results in Table 4-4, the HTVR method gives the best damping coefficient values.

| Method | Determined damping coefficient | Exact damping coefficient | Error (%) |
|---|---|---|---|
| HTVR method ($\Omega \approx 1$) | 2.71% | 2.7% | 0.0 |
| HTVR method ($\Omega = 0.9$) | 2.64% | | 2.2% |
| half-power bandwidth method | 2.49% | | 7.8% |
| logarithmic decay method- N=2 | 2.37% | | 12.2% |
| logarithmic decay method- N=3 | 2.98% | | 10.4% |

Table 4-4. The damping coefficient determination using different methods [162].

### 4.2.3.2 Effect of the excitation frequency

The HTVR method requires that the structure be excited with a harmonic force. Then, it will be essential to explore the effect of the excitation frequency on the HTVR damping results. Therefore, the transient responses for the benchmark example under different harmonic excitations are considered inputs to the HTVR, as shown in Fig. 4-19.

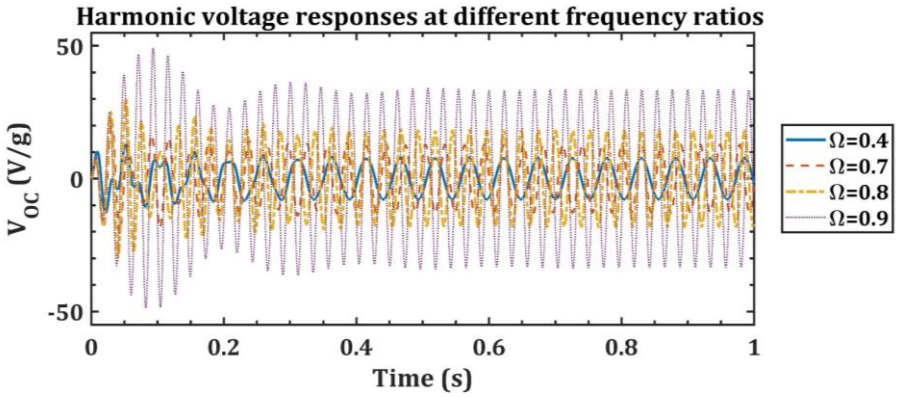


Fig. 4-19. The transient voltage responses for the benchmark example under different harmonic excitations [162].

The analysis of these transient voltages using the HTVR is given in Table 4-5. According to the HTVR results, the HTVR has the most accurate results for resonant excitations. Besides, the near-resonant excitations leave the accurate results with a 2.2% error. Nevertheless, the HTVR error for the damping determination never exceeds 5%, which is a low accuracy compared to the other damping methods [181].

| | $T_1$ (ms) | $V(T_1)$ (V/g) | $V_{\text{steady}}$ (V/g) | $\zeta$ | Exact $\zeta$ value | Error |
|---|---|---|---|---|---|---|
| $\Omega = 0.4$ | 52.01 | 13 | 7.8 | 2.57% | 2.7% | 4.8% |
| $\Omega = 0.7$ | 30.81 | 22.53 | 12.82 | 2.82% | | 4.4% |
| $\Omega = 0.8$ | 52.21 | 30.07 | 18.06 | 2.58% | | 4.4% |
| $\Omega = 0.9$ | 93.41 | 49.04 | 33.41 | 2.64% | | 2.2% |
| $\Omega = 1.0$ | 502.9 | 125.30 | 127.83 | 2.71% | | 0.3% |

Table 4-5. The effect of the excitation frequency on the identified damping coefficient using the HTVR method [162].

#### 4.2.3.3 Effect of the added white noise

As the HTVR investigates the time voltage responses, the noise can pollute the data and hinder HTVR performance. Thus, the effect of adding 2% and 5% white noise to the transient voltage response is investigated here.

Fig. 4-20 illustrates the identified damping coefficient from the time voltage signals polluted with the white noise. As can be expected, adding the white noise will increase the damping identification error. However, the HTVR method still accurately identifies the damping for the near-resonant or low-frequency excitations.

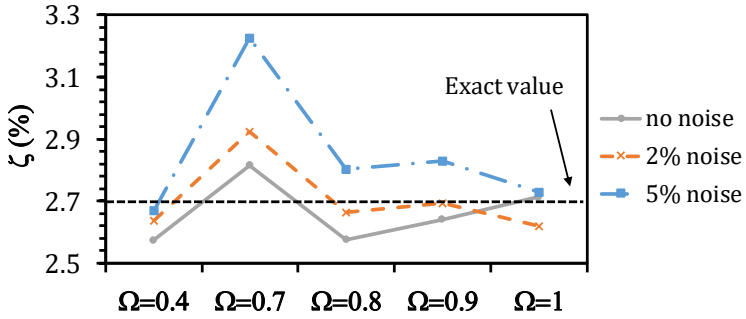


Fig. 4-20. The effect of adding white noise to the identified damping by the HTVR method [162].

## 4.3. MODIFIED STFR METHOD FOR DAMPING DETERMINATION

The modified STFR (Short-Term Fourier transform and Resampling) is derived based on the STFR method in Ref. [182] that has been used for the modal analysis of non-piezoelectric structures. Some modifications have been added to the primary STFR method so that the modified STFR has more capabilities to filter unwanted data and provide a more accurate curve fitting process.

In the STFR (main and the modified versions), the structure response to an impulse, shock, or shock-based excitation is required. In the primary STFR method, the response should be measured from the structure by a sensor. Nevertheless, in the modified STFR, which is derived for the PVEHs, there is no need for extra response measurements, and only the decaying voltage response is measured. Fig. 4-21 shows a typical decaying voltage response made on a piezoelectric sample.

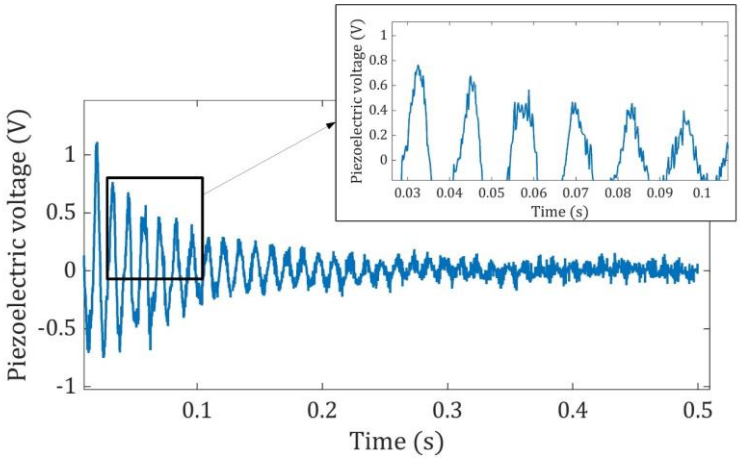


Fig. 4-21. A typical decaying response of the PVEH to a shock-based excitation [16].

Fig. 4-22 shows the modified STFR process for the damping determination. The approach has five main steps, which will be discussed in detail.

*Step 1. Response measurement and segmentation*

The voltage response is measured after an excitation, impulse, or shock-based type applied to the beam. It is considered that the voltage is measured with a sampling rate of $F_s$ with the total data points of $N_s$. Thus, the duration of the measured voltage signal is $\frac{N_s}{F_s}$. The voltage sequence $V[k]$ is denoted by

$$V[k] = V(t = k\Delta T) \quad \text{for } 0 \le k \le N_s - 1 \tag{4.7}$$

wherein $\Delta T = 1/F_s$ is the time-step and $k$ is the sample number.

An impulse force excites the structure in all the frequency range from zero to infinity (in ideal condition). Therefore, the measured response $V[k]$ contains the effects of not only the first mode but also from higher modes. Therefore, ideally, the STFR method can be applied to extract higher mode modal parameters, e.g., $V[k] = \sum_{i=1}^{N} V^i[k]$.

According to the transient voltage response presented in subsection 2.3.5, the voltage response to an initial impulse condition can be given by:

$$V^i[k] = A_i e^{-\zeta_i \overline{\omega}_{n,i}(k\Delta T)} \sin\left(\overline{\omega}_{d,i}(k\Delta T) + \theta_i\right) \tag{4.8}$$

Therefore, the envelope curves have an equation of $A_i e^{-\zeta_i \overline{\omega}_{n,i}(k\Delta T)}$, and the peaks lye in this envelope curve.

The original sequence $V[k]$ is divided into $U$ segments to form a decay curve from these segments. As the result of segmentation, the number of data points at each segment is $N_w = N_s/U$. The segmented voltage signal is expressed by:

$$V_u[w] = V(t = (uN_w + w)\Delta T)\mathcal{H}(w, N_w), \qquad 0 \le w \le N_w - 1 \tag{4.9}$$

$\mathcal{H}(w, N_w)$ is the symmetric Hann function of $N_w$ length to ensure smooth corners in the segmented signal.

An average time is assigned to each segment, as given by:

$$t_m[u] = uN_w\Delta T + \frac{N_w}{2}\Delta T \tag{4.10}$$

The FFT on the segmented signal is denoted by:

$$\hat{V}_u[n] = \sum_{w=0}^{N_w-1} \big(V\big(t = (uN_w + w)\big)\Delta T\big)e^{-j2\pi\frac{nw}{N_w}} \tag{4.11}$$

*Step 2. Resampling and Short-Term FFT*

Reducing the total data points by segmenting will reduce the frequency resolution, and therefore the accuracy for the natural frequency determination becomes less. A resampling and zero-padding process are carried out to improve the frequency resolution. The resampling is performed by a factor of $d$, and the zero-padding with a factor of $b$. Thus, the frequency resolution becomes $\Delta\omega_{n,d} = \frac{2\pi F_S U}{bdN_s}$.

The decay curve in the modified STFR is formed based on the peaks obtained from applying the FFT on all the samples, Short-Term Fourier Transform (STFT). Therefore, the FFT should be applied on each resampled segmented signal, as expressed by:

$$\hat{V}_{u,d}[n] = \sum_{p=0}^{N_b-1} \big(V\big(t = (uN_w + w)\big)d\Delta T\big)e^{-j2\pi\frac{np}{N_b}} \tag{4.12}$$

A scaling process shall be carried out to scale up the resampled FFT ($\hat{V}_{u,d}[n]$) to the original segmented FFT ($\hat{V}_u[n]$) because the resampling and zero-padding change the number of data points.

*Step 3. Extract peak from the STFT*

For the frequency range of interest, at each resampled segment, the (local) maximum is searched in the FFT signal $\hat{V}_{u,d}[n]$. The local maximum for the *i*-th modal mode is denoted by $\hat{V}_{\max,i}[u]$. In other words, $\hat{V}_{\max,i}[u]$-s are the peaks in the $\hat{V}_{u,d}[n]$ for the *i*-th mode. The location of the peaks (resonances) in the frequency span is also stored in the $\omega_{d,i}[u]$.

*Step 4. Curve fitting on the peaks*

After extracting the local maximums at each resampled segmented signal, the peak values can be plotted over the segmented time $t_m[u]$ to form the decaying curve. According to the exponential form of the envelope curves ($A_i e^{-\zeta_i\overline{\omega}_{n,i}(k\Delta T)}$), the peak values have the exponential scale representation. Rather than performing an exponential curve fitting, a linear curve fitting between the segment time and the peak logarithmic value will be performed so that all the peak data points have the same weight in the least-square curve fitting. The linear relationship between the logarithmic peak values over the times is given by:

$$\log\left(\hat{V}_{\max,i}[u]\right) = \log A_i - \delta_i t_m[u] \tag{4.13}$$

Therefore, $\delta_i$, the slope of the logarithmic peak values over time is obtained from the STFR method.

*Step 5. Modal parameter extraction*

The damped natural frequency for the *i*-th mode is calculated by averaging the $\omega_{d,i}[u]$, as expressed by:

$$\overline{\omega}_{d,i} = \frac{1}{u_l}\sum_{u=0}^{u_l-1}\omega_{d,i}[u] \tag{4.14}$$

From the damped natural frequency and the fitting slope $\delta_i$, the damping coefficient is estimated by [16]:

$$\zeta_i = \frac{\delta_i/\overline{\omega}_{d,i}}{\sqrt{\left(1+\left(\delta_i/\overline{\omega}_{d,i}\right)^2\right)}} \tag{4.15}$$

These steps are briefly discussed in this subsection. More information about the STFR practical tips can be found in Appendix G.

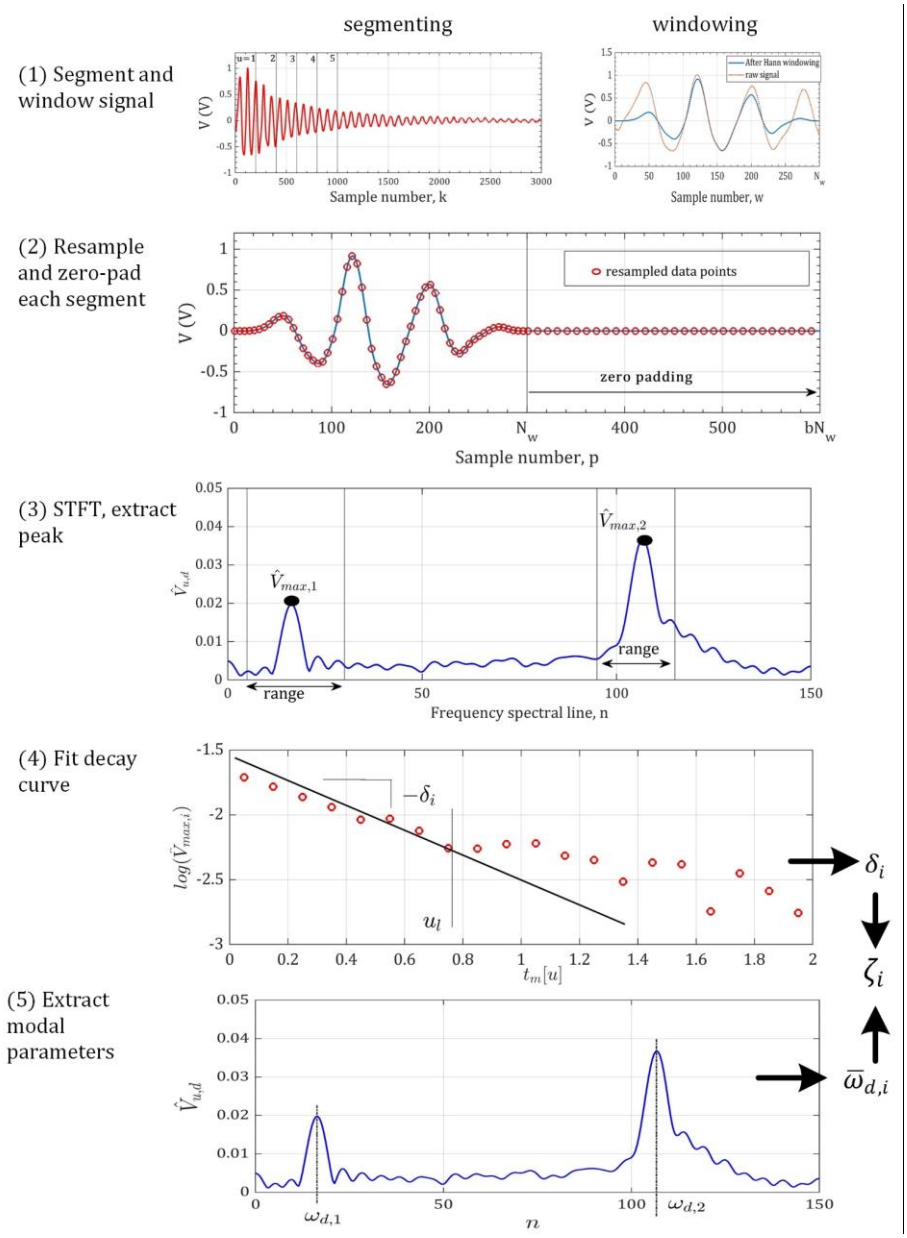


Fig. 4-22. Step-by-step guide for the modified STFR [16].

## 4.4. VISCOUS AND STRUCTURAL DAMPING CONTRIBUTIONS

As the damping mechanisms discussed, the sources of damping can be different in the PVEHs. This subsection tries to quantify the contribution of the viscous and structural damping in PVEHs with different configurations. First, using the "modified STFR" for damping coefficient determination, a technique to separate the viscous and structural contributions is introduced. Effect of the bonding layer added tip mass and additive adhesive tape on the damping coefficient would also be presented. The methods and the results of this subsection are derived from Ref. [16].

### 4.4.1. TECHNIQUE FOR SEPARATING THE VISCOUS AND STRUCTURAL CONTRIBUTIONS

According to the experimental tests [183], a proper damping model has two components: structural and viscous. The structural damping part has a negligible dependency on the vibration amplitude [146], [184]; therefore, the damping coefficient is considered to be a combination of the structural and viscous parts, as given by [16]:

$$\zeta_m = \zeta_{\text{struc}} + \alpha\zeta_a \tag{4.16}$$

If $\alpha$ and $\zeta_{\text{struc}}$ are experimentally determined, the damping model is quantified, and the structural and viscous damping parts are differentiated. The piezoelectric harvester is subjected to shock-based excitation with a series of increasing excitation amplitudes to achieve this. Then, by fitting a line to the experimental damping coefficients and extrapolating back to the zero amplitude point, the structural part $\zeta_{\text{struc}}$ Moreover, the slope $\alpha$ can be determined.

(a) (b)

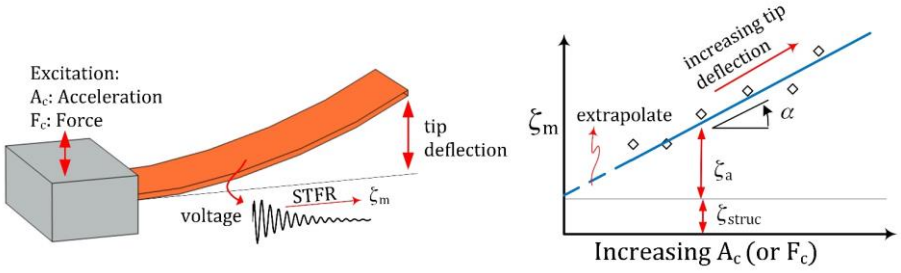


Fig. 4-23. (a) The piezoelectric beam under the shock-based impulse with the decaying voltage response and (b) the line fitting and extrapolating back for obtaining the structural $\zeta_{\text{struc}}$ and the slope $\alpha$ [16].

### 4.4.2. EXPERIMENTAL SETUP

Seven piezoelectric samples are tested for the damping determination. All the samples have one MFC 8528-P2 type serving as the piezoelectric layer. Then, different configurations are considered, with and without substrate shim, different bonding layers, and with and without tip mass. Tests are categorized into three groups, as described in Table 4-6. There are various factors that the damping coefficient for them should be determined; therefore, each sample is tested for a specific objective. Fig. 4-24 shows the objectives for carrying out tests on these seven samples.

| Group No. | Sample No. | Piezoelectric layer | Substrate shim | Bonding layer | | Tip mass (g) |
|---|---|---|---|---|---|---|
| | | | | Material | Thickness (μm) | |
| I | 1 | MFC $t_{MFC}$=300μm | - | - | - | 0 and 4.2g |
| | 2 | | $t_s$=120μm aluminum | Epoxy rapid 332 | $t_c$=260 | 0 and 4.2g |
| II | 3 | MFC $t_{MFC}$=300μm | $t_s$=100μm brass | Epoxy 3430 | $t_c$=300 | 0 and 9.2g |
| | 4 | | $t_s$=100μm brass+ Tesa® adhesive tape | Epoxy 3430 | $t_c$=300 | 0 and 9.2g |
| III | 5 | MFC $t_{MFC}$=300μm | $t_s$=100μm copper | 3M Company double-sided tape | $t_c$=100 | - |
| | 6 | | $t_s$=100μm copper | 3M Company double-sided tape | $t_c$=300 | - |
| | 7 | | $t_s$=100μm copper | Tesa® adhesive tape | $t_c$=1200 | - |

Table 4-6. The seven tested piezoelectric beams for the damping determination tests [16].

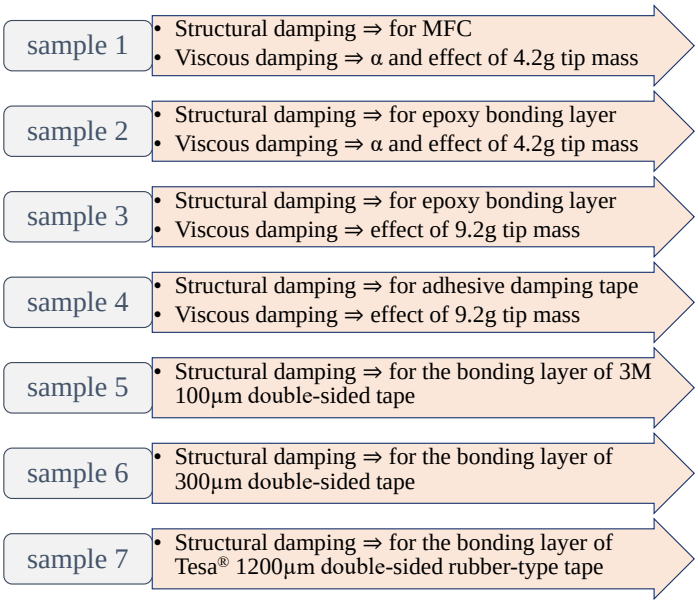


Fig. 4-24. The objectives for performing experimental tests on each sample [16].

The boundary condition for the piezoelectric samples is clamped-free. Fig. 4-25 (a) shows a typical energy harvester with a tip mass. The tip mass is made of steel and is attached to the top of the harvester by double-sided tape, as shown in Fig. 4-25 (b). Adding an adhesive tape for exploring the structural damping effect is shown in Fig. 4-25 (c). Besides, Fig. 4-25 (d) to (f) illustrate the piezoelectric samples with different bonding layers.

(a)

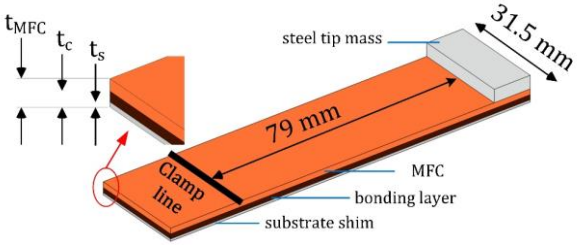


(b) (c)

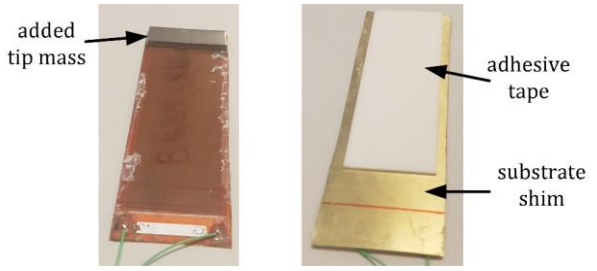


(d) (e) (f)

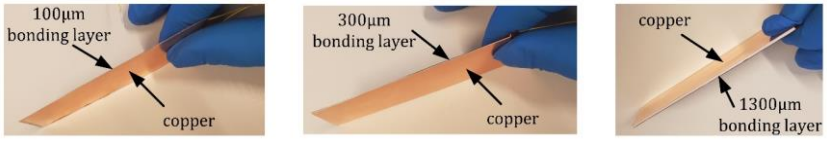


Fig. 4-25. (a) The dimensions for a typical sample with an added tip mass, (b) the tip mass connection, (c) adding an adhesive tape to the bottom of the substrate shim, (d)-(f) the piezoelectric samples with different bonding layers [16].

The experimental setup and the devices employed for measuring the acceleration and the piezoelectric responses are shown in Fig. 4-26. The cantilevered piezoelectric sample connected to the shaker is shown in Fig. 4-26 (a) and (b). The data acquisition systems for measuring the acceleration, force, and piezoelectric voltage response are also shown in Fig. 4-26 (c).

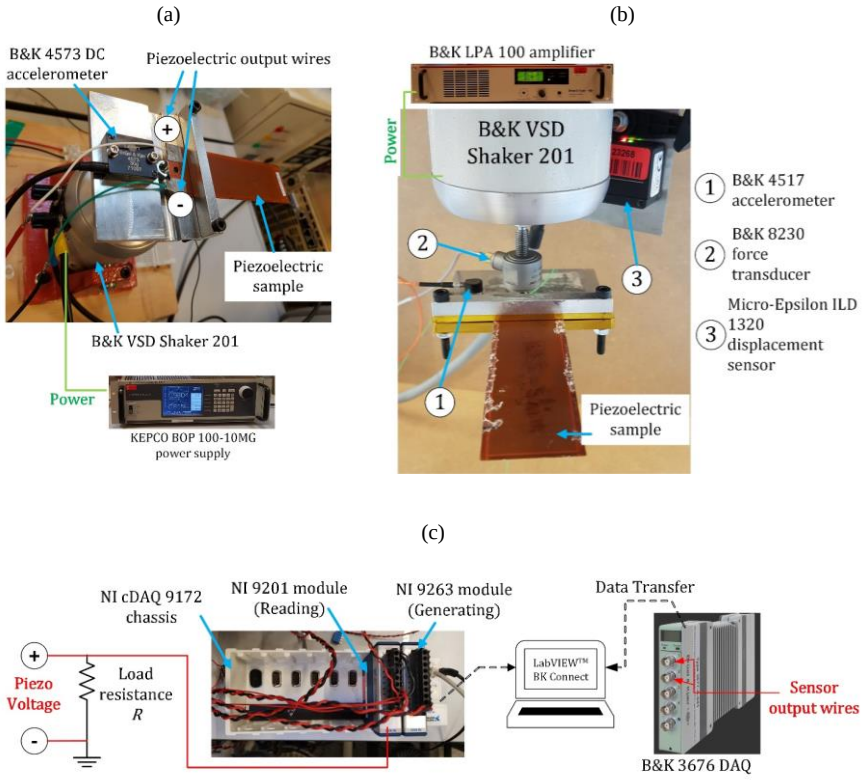


Fig. 4-26. The cantilevered piezoelectric sample in connection with the shaker for (a) Group I tests, (b) Group II tests, and (c) the data acquisition systems [16].

### 4.4.3. ADDED TIP MASS EFFECT ON THE DAMPING

In samples 1 and 2, a tip mass of 4.2g is added to the beam tip. The damping coefficient for samples 1 and 2, extracted by the modified STFR, is shown in Fig. 4-27 (a) and (b), respectively. Overall, it can be concluded that due to the presence of tip mass, the damping coefficient increases, or in other words, the voltage response decays faster.

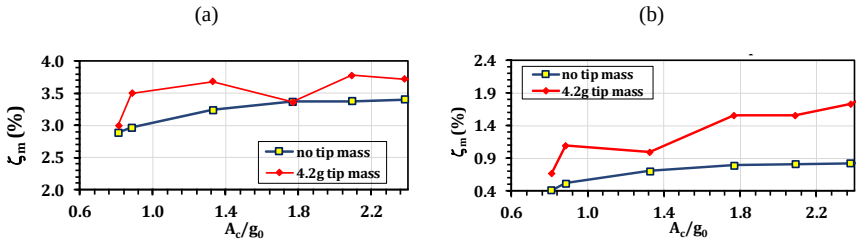


Fig. 4-27. The variation of damping coefficient due to the 4.2g added tip mass for (a) sample 1 (No-Shim sample) and (b) sample 2 (Aluminum substrate shim) [16].

In total, samples 1 to 4 have been tested with and without tip mass. Table 4-7 shows how the natural frequency and the damping coefficient vary because of the added tip mass. In all the samples, adding tip mass reduces the natural frequency significantly. Besides, the damping coefficient overall increases by adding tip mass; the decaying voltage response vanishes faster. The variation in the natural frequency is identical between the samples; nevertheless, the damping coefficient variations are not in the same range because the tip mass changes the beam tip deflection according to the beam stiffness.

In the first sample, where no substrate shim is present, the harvester is the most flexible case so that the tip mass increases the beam tip deflection significantly, and therefore, the damping coefficient increases more substantially than in other cases. In sample 2, with the thickest substrate shim (120µm aluminum shim), the beam is the stiffest sample, and therefore the damping increase is less than the other samples. Samples 3 and 4, with 100µm brass shim, have an increase of around 40% to 70%.

| tip mass (g) | 0 | | 4.20 | | 9.20 | | Variation (%) | |
|---|---|---|---|---|---|---|---|---|
| Sample No. | $\omega_n$ (Hz) | $\zeta_m$ (%) | $\omega_n$ (Hz) | $\zeta_m$ (%) | $\omega_n$ (Hz) | $\zeta_m$ (%) | $\omega_n$ | $\zeta_m$ |
| 1 | 16.20 | 0.78 | 8.20 | 1.59 | - | - | -49.38 | 103.85 |
| 2 | 21.30 | 3.34 | 10.80 | 3.59 | - | - | -49.30 | 7.49 |
| 3 | 23.42 | 2.31 | - | - | 9.84 | 3.31 | -57.97 | 43.73 |
| 4 | 23.14 | 3.79 | - | - | 10.14 | 6.52 | -56.2 | 72.13 |

Table 4-7. The variation of natural frequency and damping due to the tip mass [16].

### 4.4.4. A MEASUREMENT OF THE STRUCTURAL DAMPING

As a measurement of the structural damping, an adhesive strip with 60×20×1.2 $mm^3$ dimensions, Tesa® rubber-type adhesive tape, is attached to the harvester with 100µm brass and the MFC. These samples are sample 3 (No adhesive tape) and sample 4 (With adhesive tape).

An adhesive tape is added because the damping increase due to the extra adhesive tape can be related to the structural damping because this adhesive tape will not change the beam's stiffness properties. Therefore, any variation in the damping coefficient can be related to the adhesive tape's structural damping.

Fig. 4-28 (a) shows the voltage-time responses made on piezoelectric samples 3 (no adhesive tape) and 4 (with adhesive tape) with and without a tip mass. In both no-tip-mass and tip mass cases, adding adhesive tape reduces the peak voltage generation and leads to faster voltage depredation. Therefore, the effect of adhesive tape can be substantial concerning power generation. Fig. 4-28 (b) compares the samples' peak voltage without and with the adhesive tape. As can be seen from Fig. 4-28 (b), the peak voltage is reduced because of adding the extra adhesive tape to the substrate.

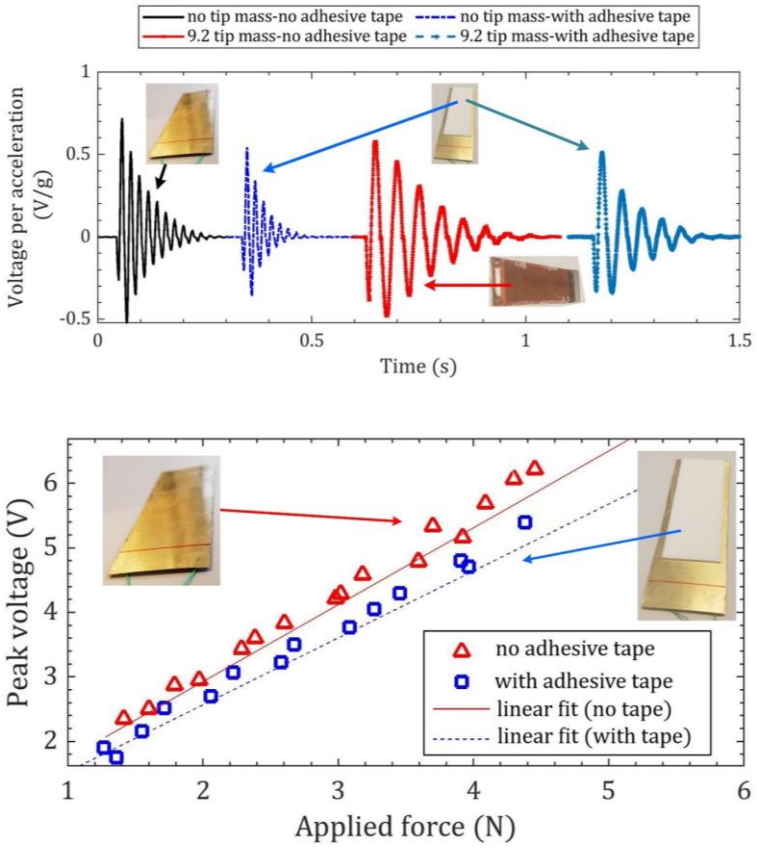


Fig. 4-28. (a) Comparing the voltage responses with the adhesive tape attachment and (b) the peak voltage comparison between the samples with no adhesive and with adhesive tape [16].

For further investigating the effect of the adhesive tape, the modal parameters from the modified STFR method are compared in Fig. 4-29. Fig. 4-29 (a) shows that the adhesive tape does not change the natural frequency, meaning that the beam stiffness properties remain relatively unchanged. However, from Fig. 4-29 (b), the damping coefficient is increased by adding the adhesive tape. This increase in the damping is sole because of the structural damping of the adhesive tape. Therefore, it can conclude that the structural damping contribution is not negligible.

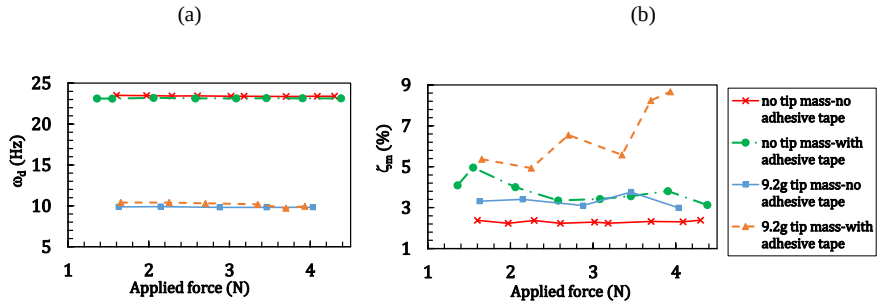


Fig. 4-29. (a) The natural frequency and (b) damping coefficient variations due to adhesive tape [16].

## 4.4.5. THE EFFECT OF BONDING LAYER ON THE DAMPING

The shock-based excitation tests three samples with different bonding layers, and the damping coefficient is extracted by the STFR method. Fig. 4-30 shows the details about the contact layers in these three samples.

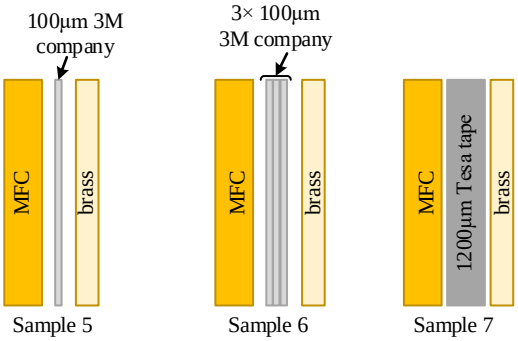


Fig. 4-30. The detail of the different bonding layers for samples 5, 6, and 7.

Fig. 4-31 compares the damping coefficient between the samples with different bonding layers. The apparent differences can be seen among the damping coefficients for these samples. The smallest damping ratio is for sample 5 with a 100µm-tape bonding layer. The bonding layer for sample 6 is made of three attached layers of the

100µm-tape. Therefore, the adhesion force between these layers is strong, and therefore, the damping coefficient for sample 6 is the highest value. The damping coefficient for sample 7 lies between these two samples' damping coefficient. Table 4-8 summarizes the damping coefficient obtained from samples with the different bonding layers.

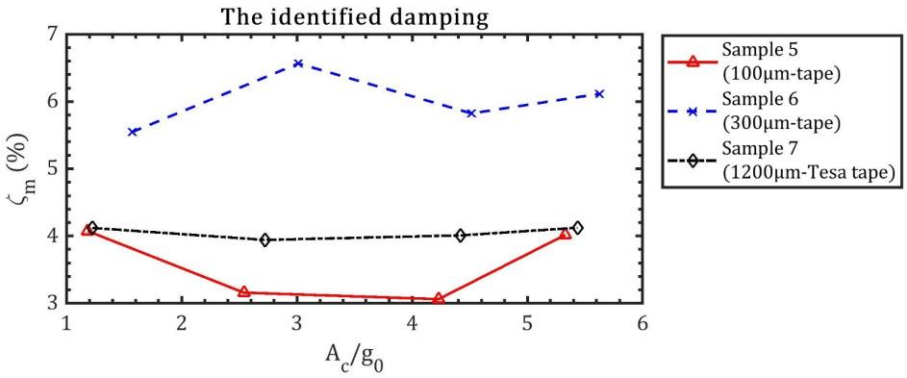


Fig. 4-31. The identified damping for three samples with different bonding layers [16].

| Sample No. | Bonding layer | $\zeta_m$ (%) | Variation |
|---|---|---|---|
| Sample 5 | 100µm tape | 3.6 | - |
| Sample 6 | 300µm tape | 6.0 | 68% |
| Sample 7 | 1200µm Tesa® tape | 4.1 | 13% |

Table 4-8. The variation of the damping coefficient for the samples with different bonding layers [16].

The structural damping coefficient can be estimated for the different bonding layers by separating the structural and air damping mechanisms. Fig. 4-32 shows the estimated structural damping for four bonding layers. Generally, the double-sided tapes have a lower damping ratio compared to the epoxy viscoelastic bonding-layer. Besides, the thinner double-sided tape (3M Company tape) has less damping coefficient, showing that it is better to use less flexible materials for the bonding layer from a damping point of view.

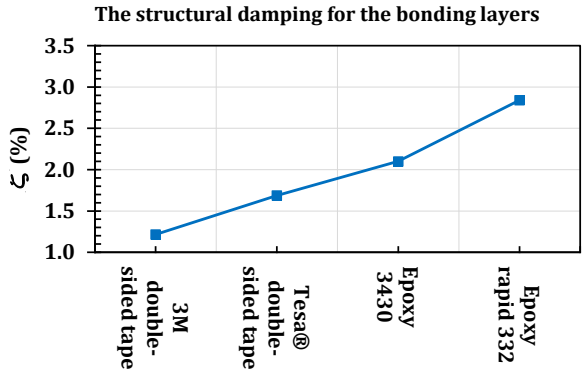


Fig. 4-32. The identified structural damping for four different bonding layers [16].

### 4.4.6. THE CONTRIBUTION OF VISCOUS AND STRUCTURAL DAMPING

According to the damping coefficient results, the damping has a constant part and an amplitude-dependent part. The amplitude-dependent part changes with the excitation amplitude because the tip deflection will change the fluid-structure forces. Therefore, the amplitude-dependent part is called viscous air damping. The resistance air force causes the viscous air damping against the beam, and as the air resistance force has a functionality of the velocity, the air damping is influenced by the velocity [146]. On the other hand, the structural damping shows no dependency on the excitation frequency [185]. Hence, these two damping mechanisms should be differently accounted for in the vibration equation, as given by [186]

$$\ddot{x}(t)+2\zeta_m\omega_n\dot{x}(t)+\omega_n^2(1+j\eta)x-\alpha_{mass}\omega_n^2 d_{31}V_p(t)=-\ddot{x}_B(t)\,. \tag{4.17}$$

In Eq. (4.17), $\zeta_m$, the viscous air damping, depends on the velocity, while η, the structural damping coefficients, depends on the displacement. The total mechanical damping is the combination of $\zeta_a$ and η, but these coefficients' contribution in the total damping should be investigated. As can be seen from Fig. 4-33, different assumptions about the viscous and air damping contributions greatly influence the peak power output. If only the viscous air-damping model is employed, the power generation is underestimated considerably. If the total damping is assumed structural damping, the peak power output will be overestimated. Thus, an appropriate model for the viscous and structural damping mechanisms is needed.

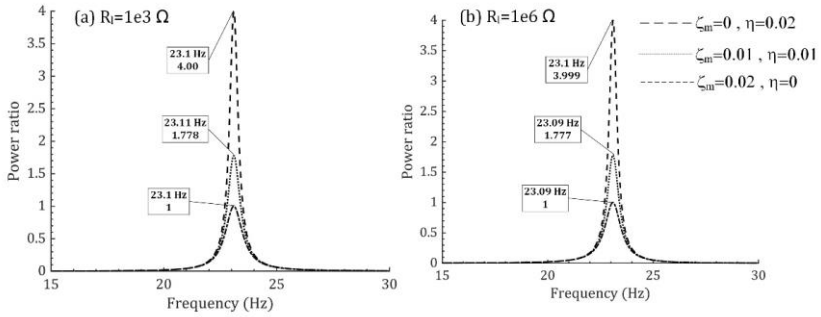


Fig. 4-33. The effect of different viscous and structural damping contributions on the power output [186].

The viscous air damping's influence becomes more extensive by increasing the excitation amplitude, as shown in Fig. 4-34. The contribution of the viscous and structural damping depends on the bonding layer as well. Therefore, as can be seen from Fig. 4-34, for the sample with the substrate shim and bonding layer, the viscous air damping is accountable for less than 20% of the total damping, showing that the structural damping contribution is higher than 80%, and is more significant due to the epoxy bonding layer. Nevertheless, if the 100µm 3M double-sided tape is used as the bonding layer, the structural damping contribution is 34% [16], which is remarkably lower than the samples with epoxy contact layers.

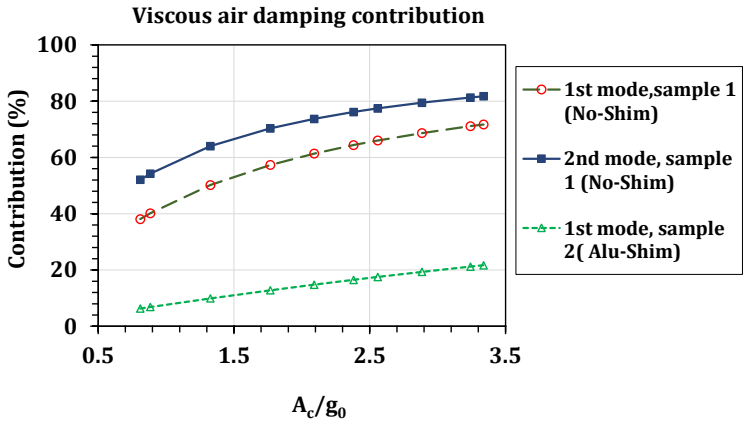


Fig. 4-34. The contribution of the viscous air damping as a function of the excitation amplitude [16].

# CHAPTER 5. DIFFERENT PEH DESIGNS AND APPLICATIONS

This section discusses the applications, different designs, and optimization processes for the piezoelectric vibration energy harvester (PVEH) toward a better performance harvester.

First, a series of piezoelectric beams are attached to a practical vibration source (DC motor), and the power output from these beams is measured.

Next, an energy-harvesting box is designed based on resonant matching for a moving car as a practical vibration source.

Afterward, as an application of piezoelectric energy harvesting, the feasibility and functionality of an autonomous condition monitoring for a water pump are investigated by a resonant-matched bimorph harvester.

Later on, it has been observed that the narrowband power can be an issue for practical piezoelectric energy harvesters. Therefore, some initiative designs in the geometrical configuration and the material layup are proposed to enhance the power density generation

## 5.1. ENERGY HARVESTING FROM A PRACTICAL VIBRATION SOURCE (DC MOTOR)

This subsection's results are derived from Ref. [177] (See Appendix J).

As a practical source of vibration, a DC motor is selected as a kinetic energy source, and it has been tried to estimate the amount of power that a piezoelectric energy harvester can produce. The DC motor is a V88.57 type motor from DRIVE SYSTEMS, with 1.7kW power (maximum supply voltage 24V and maximum current 85A) and a maximum 1500 Rpm. The motor's output shaft is connected to an intermediate bearing connected to a coupling and brake system. While the motor rotates in the ideal condition, the bearing vibration amplitude is the lowest value. However, an energy-harvesting box is attached to the main bearing to estimate the power generation in an ideal condition. The setup for this DC motor test is shown in Fig. 5-1 (a). The energy-harvesting box is designed in a way that can accommodate multiple piezoelectric harvesters. Fig. 5-1 (b) shows one configuration of a energy harvesting box consisting of two piezoelectric beams: the MFC unimorph (with 8528-P2 MFC from the Smart Materials) and the other is the PZT bimorph (T215-A4-503Y). A B&K accelerometer measures the acceleration in the R- and Z-directions.

Fig. 5-2 (a) and (b) show the measured acceleration in the R and Z directions, respectively. The R-direction acceleration level is 35% larger than the Z-direction. Therefore, both R and Z-direction accelerations can be employed for power generation.

(a)

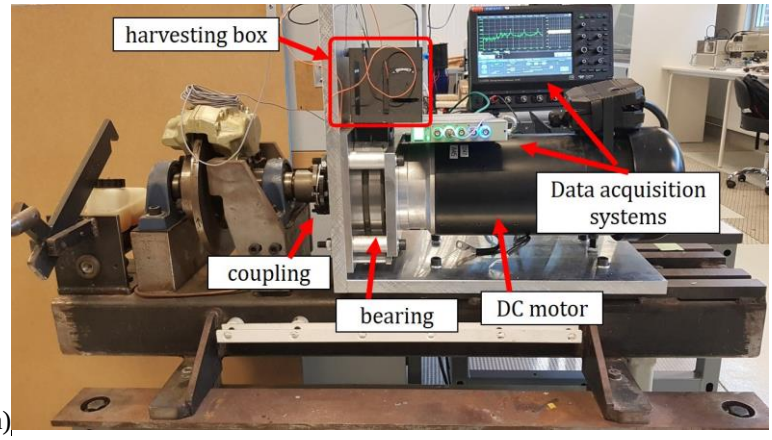


(b)

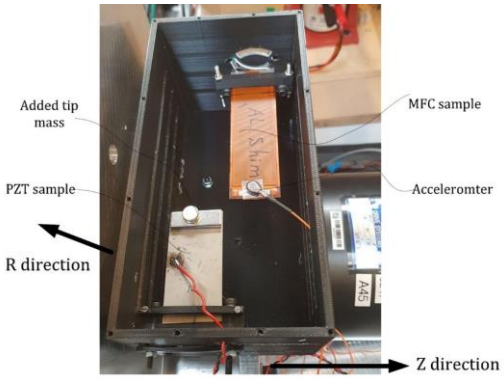


Fig. 5-1. (a) The DC motor experimental setup, and (b) the energy harvesting box with two piezoelectric beams with tip mass [177].

(a) (b)

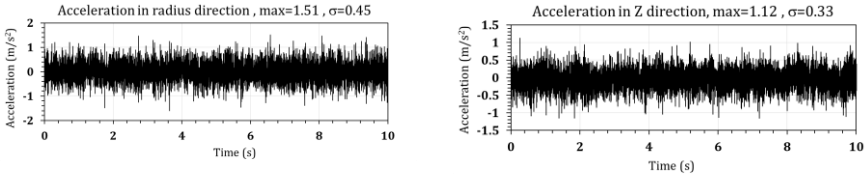


Fig. 5-2. The measured acceleration from the DC motor in 24V supply [24.65Hz or 1480 Rpm rotation speed], (a) radius, and (b) Z directions [177].

Three configurations are testes, MFC unimorph without tip mass, PZT bimorph without tip mass, and PZT bimorph with 13.8-g tip mass. When the motor starts, the piezoelectric harvesters start generating power. However, the initial power generation is not the same as the steady-state condition. Therefore, the voltage output values will be reported for the steady-state condition.

Fig. 5-3 illustrates the output open-circuit voltage from the DC motor working at an ideal condition. The PZT bimorph generates 0.5 V, which is approximately double the MFC sample voltage output according to Fig. 5-3 (a). This higher voltage generation is expected because the PZT sample has two piezo-layers while the MFC sample has one MFC layer. Adding the tip mass to the PZT bimorph enhances the voltage generation in both transient and steady-state parts. The steady-state voltage is around 1.1 V in the open-circuit condition, which is 120% higher than the no-tip-mass configuration. The orientation of tip mass is also explored, and it has been demonstrated that the width-wise tip mass attachment generates higher power, see Fig. 5-3.

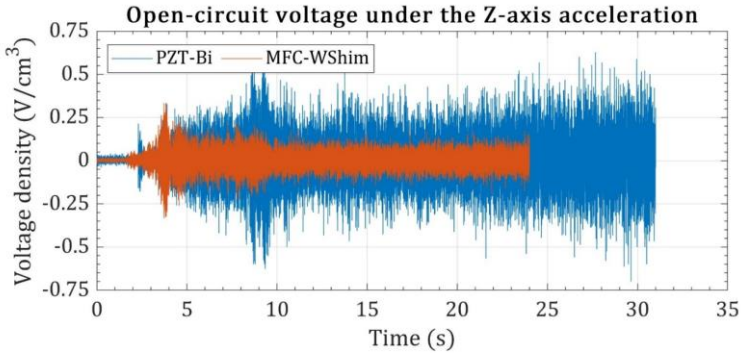


(a)

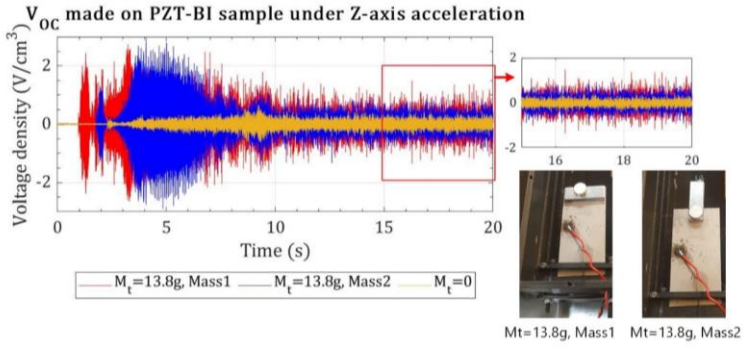


(b)

Fig. 5-3. The open-circuit voltage from the DC motor in ideal condition for (a) MFC unimorph and PZT bimorph without tip mass and (b) PZT bimorph with 13.8g tip mass [177].

Next, artificially, a 1.5% shaft misalignment is created to assess the piezoelectric power generation in the shaft misalignment condition. A PZT bimorph (Quickpack Q220-H4BR-2513YB) with 8.6g tip mass is served as the energy harvester in the shaft misalignment condition. Fig. 5-4 (a) shows the method for creating the shaft misalignment, and Fig. 5-4 (b) shows the PZT harvester.

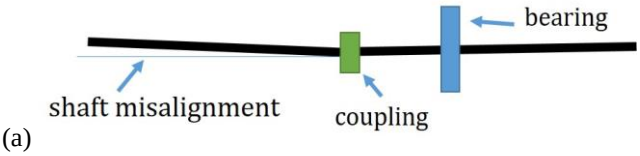


(a)

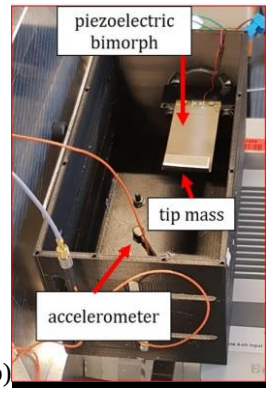


(b)

Fig. 5-4. (a) 1.5% Shaft misalignment applied to the DC motor setup and (b) PZT sample (Quickpack Q220-H4BR-2513YB) with the accelerometer [177].

Fig. 5-5 shows the DC motor measured acceleration with shaft misalignment fault working with different supply voltage values. When the DC motor's supply voltage increases, the rotation speed also increases, which consequently increases the level of the DC motor's vibration, as can be seen from Fig. 5-5. By comparing acceleration signals in ideal and misalignment conditions in Fig. 5-2 and Fig. 5-5, it can be clearly seen that the bearing acceleration is considerably increased due to the shaft misalignment. Thus, the output voltage in the shaft misalignment condition is expected to be higher.

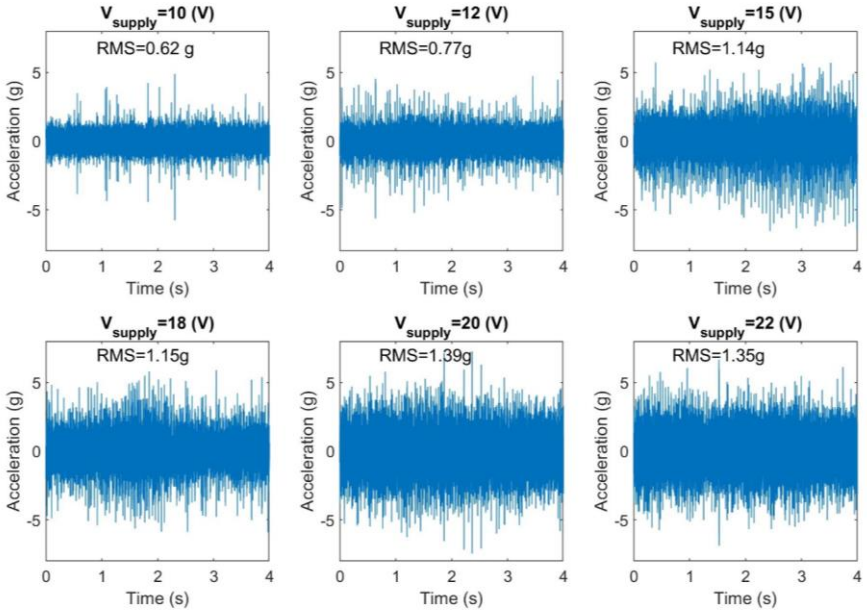


Fig. 5-5. The R-direction acceleration from the DC motor in shaft-misalignment condition with different supply voltage [177].

The output voltage made on the PZT bimorph from the shaft misaligned DC motor is measured under different DC motor supply voltage. The FRF of the voltage signal is calculated to extract the motor's rotational speed at each supply voltage. The voltage responses, time, and FRF signals, made from the piezoelectric harvester are plotted in Fig. 5-6.

The piezoelectric voltage generation under the motor excitation in shaft misalignment condition is considerably higher than in the ideal working condition. This considerable difference implies that the voltage output from piezoelectric harvesters can be treated as an indicator for damage detection in high-speed rotatory machines.

The acceleration increases by the supply voltage, and therefore the voltage generation increases, see Fig. 5-6. However, the voltage generation growth is much more significant than the acceleration increase; by increasing the motor's supply voltage, the motor rotational frequency increases, and hence the base excitation frequency increases. This frequency increase in the base excitation acts like an influential positive factor in the voltage generation. Therefore, it can be concluded that by increasing the motor supply voltage, the motor's rotational speed becomes closer to the harvester's natural frequency.

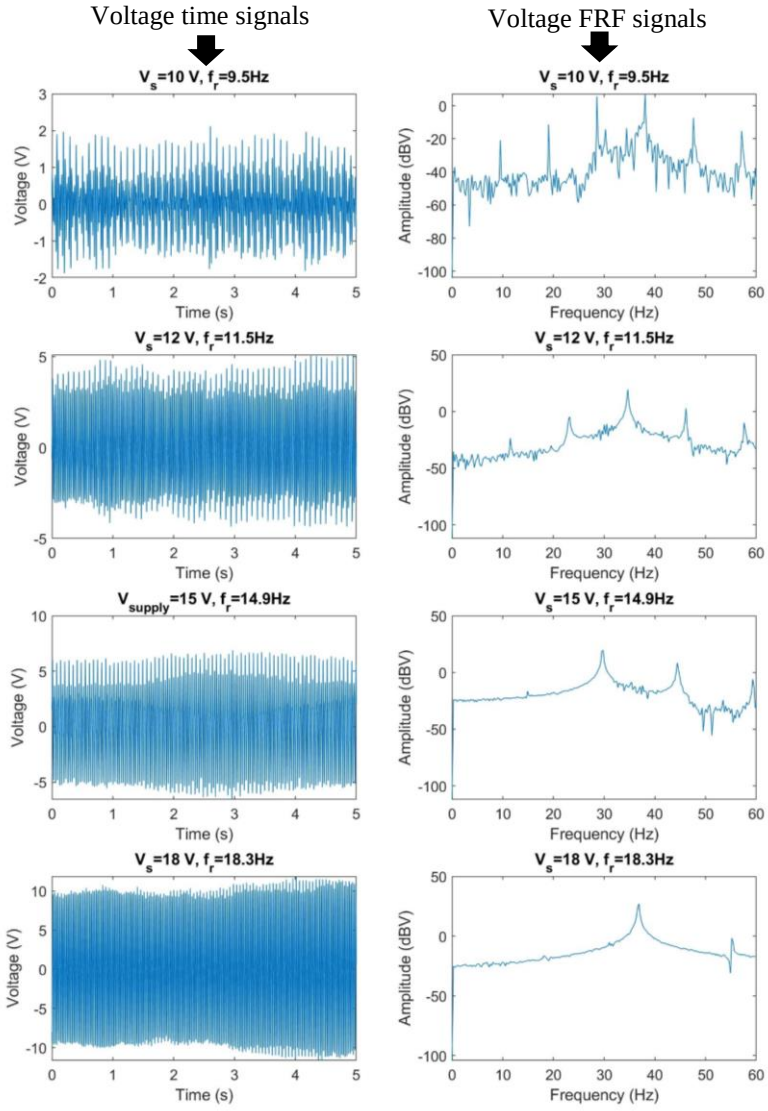


Fig. 5-6. The PZT sample open-circuit voltage responses, time and FRF, from the shaft-misaligned DC motor in different rotational speeds [177].

The power normalized to the square input acceleration is plotted in Fig. 5-7 against the rotation speed to investigate further the relationship between rotation speed and power generation. The motor's rotation speeds are 9.5 Hz, 11.5 Hz, 14.9 Hz, 18.3 Hz, 20.75 Hz, and 22.95 Hz. For both 56-kΩ and 110-kΩ electrical loads, the power generation is maximum at the 18.3-Hz rotation frequency, showing that the PZT sample natural frequency is matched to the 18.3-Hz rotation speed.

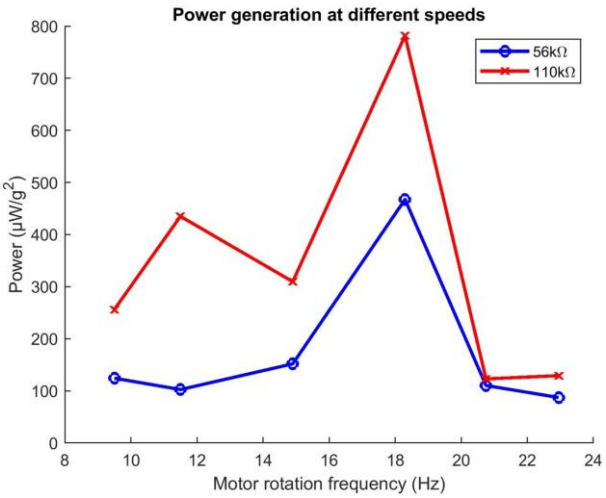


Fig. 5-7. Power normalized to square input acceleration for different rotation speeds [177].

As observed in Fig. 5-7, the power generation with $f_r$=18.3 Hz excitation leads to higher power generation. However, if the excitation frequency is slightly decreased to $f_r$=17.8 Hz, the power generation drastically enhances. The 0.5-Hz difference in the excitation frequency increases the power by 90%, demonstrating the high sensitivity of power to the excitation frequency (or DC motor's rotation frequency). It can also conclude that the 17.8-Hz is closer to the resonant frequency than the 18.3Hz. Observing the beating phenomenon in the 17.8-Hz base excitation can also demonstrate that the rotation speed of 17.8-Hz approaches the harvester's natural frequency; however, it is not precisely the harvester's natural frequency.

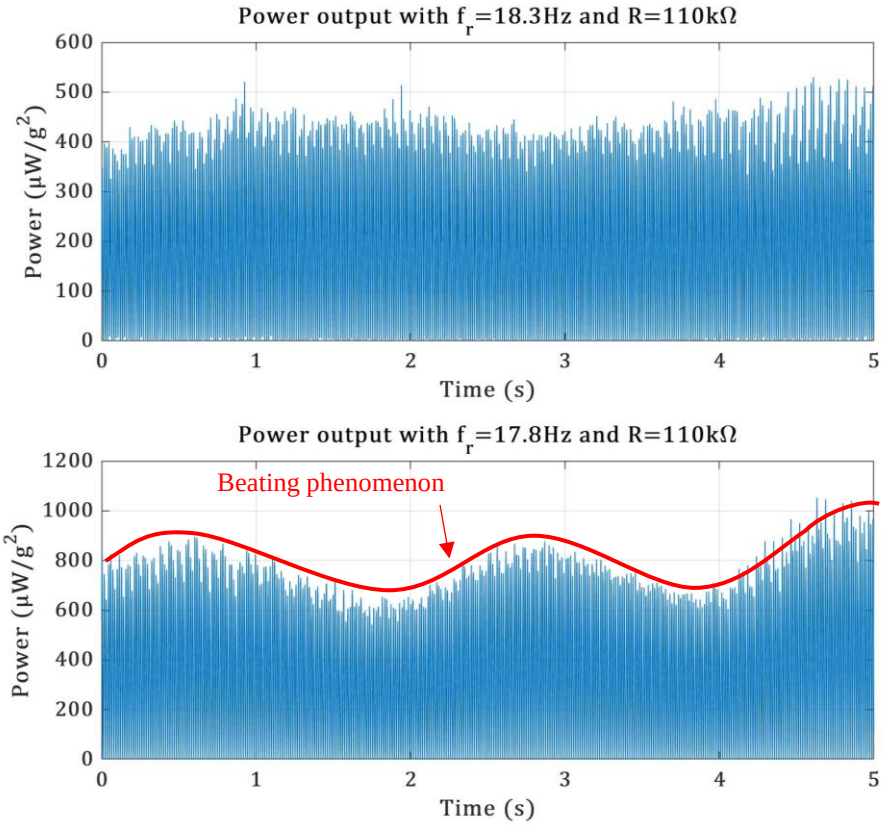


Fig. 5-8. The demonstration of the power generation's high sensitivity to the excitation frequency in the DC motor (R=110kΩ) [177].

In a simple vibrating system, DC motor in this study, the electrical load also has a considerable effect on the power generation. By increasing the electrical load, the voltage increases; however, the current flow decreases. Thus, there is an optimum point for power generation. In this study, the optimum load is 110kΩ. The voltage and power with 110-kΩ load are 8 V and 520 μW/g$^2$, sufficient to be fed into a wide range of commercial power management systems. The power density is 5200 μW/cm$^3$ per 1g$^2$ acceleration for the DC motor vibration (with 18V motor supply power).

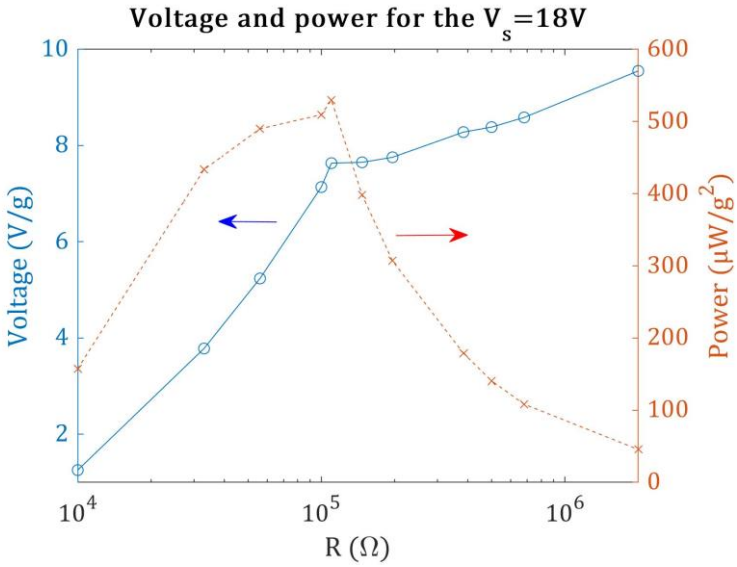


Fig. 5-9. Finding the optimum electrical load for the best power generation [177].

## 5.2. FREQUENCY MATCHING DESIGN FOR CAR VIBRATION

As observed in subsection 5.1, power output highly depends on the excitation frequency. Therefore, one way to deal with this high sensitivity is to use the frequency matching design. In this design, the energy harvester's resonant frequency is designed to be as close as possible to the vibration source's dominant frequency. This subsection presents a resonant-based harvester design for energy harvesting from a moving car. This subsection's results are derived from Ref. [187] (See Appendix I).

The acceleration measured from a Grande Punto diesel car moving in an urban road is shown in Fig. 5-10. The car vibration data is retrieved from the Real Vibration database [170]. Fig. 5-10 (b) also shows the FFT signals from the car vibration data. From Fig. 5-10, neither the acceleration levels nor the dominant frequencies in the x, y, and z-direction are the same. Therefore, for each direction, one piezoelectric harvester is considered. The dominant frequencies for the x, y, and z directions are 19.3Hz, 31.2Hz, and 12.1Hz.

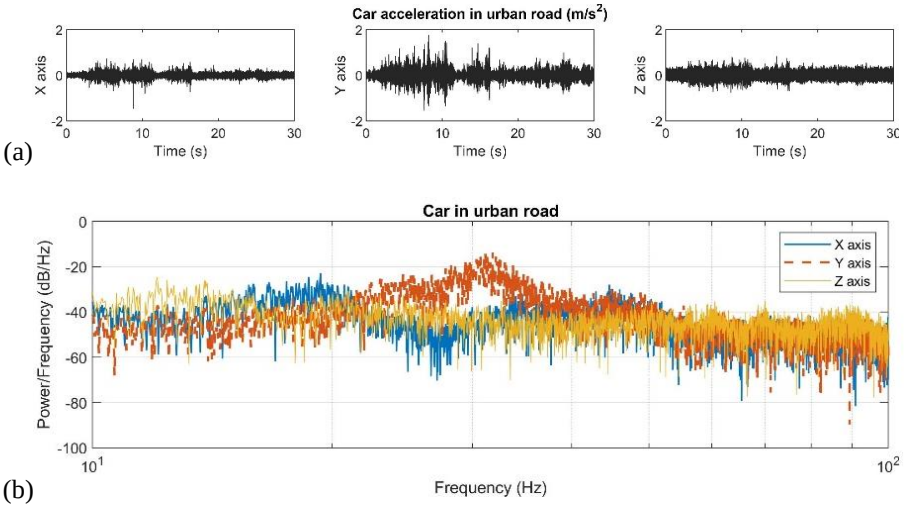


Fig. 5-10. Car vibration data for a car on the urban road from Real Vibration dataset [170] (a) time signals and (b) FFT signals in x, y, and z axes [187].

Fig. 5-11 shows the energy-harvesting box layout with three harvesters. $PH_x$, $PH_y$, and $PH_z$ are excited from the acceleration in the x, y, and z directions, respectively. With this configuration, the vibration in the width and length directions will have negligible effects because the excitation frequencies are on a low-frequency scale.

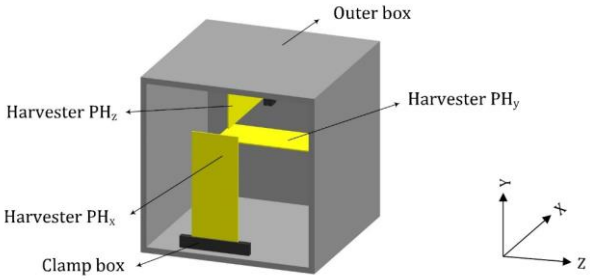


Fig. 5-11. The energy harvesting box with three harvesting beams; each beam is excited with the acceleration in one direction [187].

For each piezoelectric beam, the material properties from a PZT bimorph are employed, but the harvester length is considered the tuning parameter for the resonant frequency matching. Table 5-1 shows the material properties, thicknesses, and beam width for this PZT bimorph.

| Properties | Values |
|---|---|
| Piezoelectric stiffness at the constant field, $c\_11^E$, GPa | 66.7 |
| Piezoelectric density, $\rho_p$, kg/m$^3$ | 7870 |
| Electromechanical coupling coefficient, $e_{31}$, C/m$^2$ | -35.5 |
| Piezoelectric layer thickness (each), t, mm | 0.19 |
| Piezoelectric permittivity constant, $\bar{\varepsilon}_{33}$, F/m | $3800\times\varepsilon_0$ |
| Substrate Young's modulus, $Y_s$, GPa | 100 |
| Substrate thickness, h, mm | 0.13 |
| Substrate density, kg/m$^3$ | 8300 |
| Piezoelectric beam length, L, mm | 57.2 |

Table 5-1. Material properties of bimorph piezoelectric energy harvester (QP220-H4BR-2513YB)) [187].

This bimorph harvester's power generation performance is estimated using the FE method and employing the viscous-structural damping model. Fig. 5-12 (a) and (b) show the bimorph model and the FE model verification experimental setup. The experimental power output is plotted in Fig. 5-12 (c) against the FE model results for two damping models, namely pure viscous damping and combined viscous-structural damping models. The contribution of structural damping is considered 40% based on the results developed by Ref. [16]. The pure viscous damping model underestimates the resonant power while the FE output results agree with the experimental data. Thus, it can be concluded that the combined viscous-structural damping model has better accuracy for the power estimation.

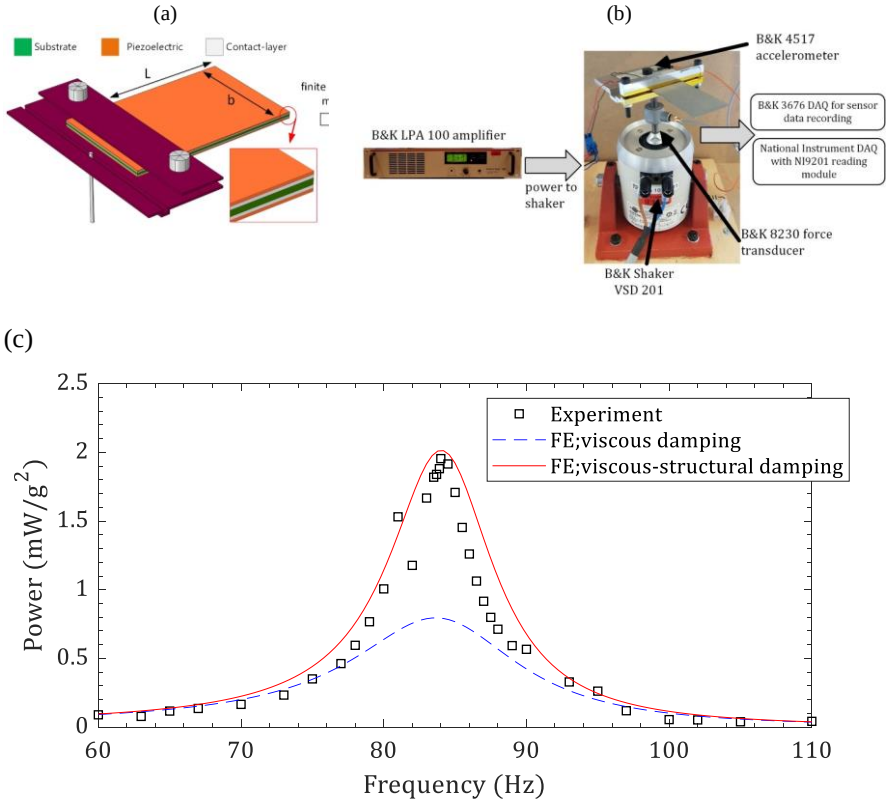


Fig. 5-12. (a) The FE method for modeling the Quick Pack piezo-bimorph, (b) the experimental setup for FE verification, and (c) correlation between experimental data and FE model with viscous and viscous-structural damping models [187].

Now, the validated FE model is used for the analysis and frequency matching design. For the frequency matching design, the objective function is defined as the difference between the car vibration's dominant frequency and the harvester's natural frequency. Fig. 5-13 shows that the harvester length can change the natural frequency considerably; therefore, the beam length is considered the tuning parameter. For the $PH_x$, $PH_y$, and $PH_z$ harvesters, the objective functions are $(\hat{\omega}_{1,PH_x} - 19.3)^2$, $(\hat{\omega}_{1,PH_y} - 31.2)^2$ and $(\hat{\omega}_{1,PH_z} - 12.1)^2$, respectively. Fig. 5-14 shows the optimization history for the $PH_x$, $PH_y$, and $PH_z$ harvesters. The beam length for the $PH_x$, $PH_y$, and $PH_z$ harvesters are 111.3 mm, 87.6 mm, and 140.6 mm.

Furthermore, the power output is plotted in Fig. 5-15 for these optimal length values against the electrical load to determine the optimum electrical load.

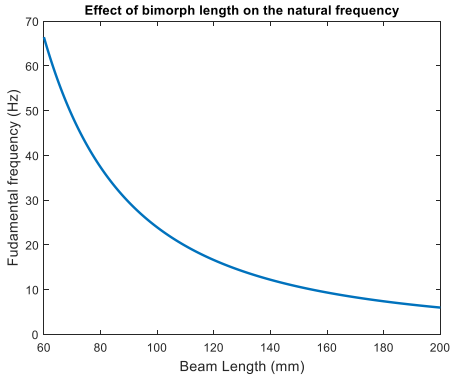


Fig. 5-13. The effect of harvester's length on the fundamental resonant frequency [187].

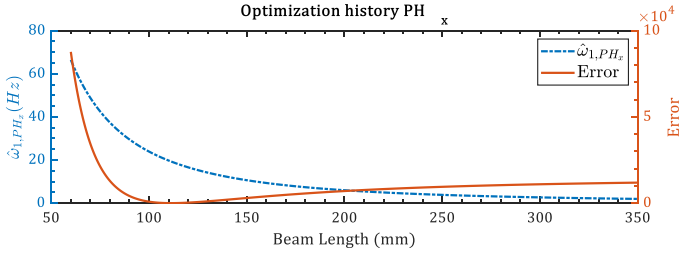


(a)

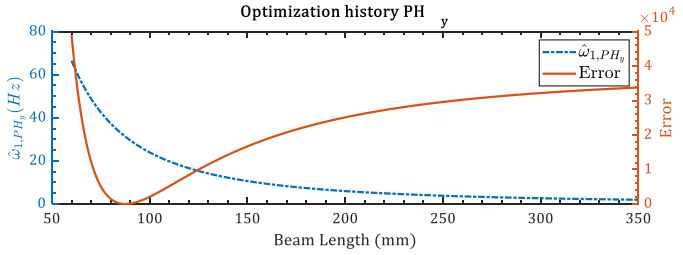


(b)

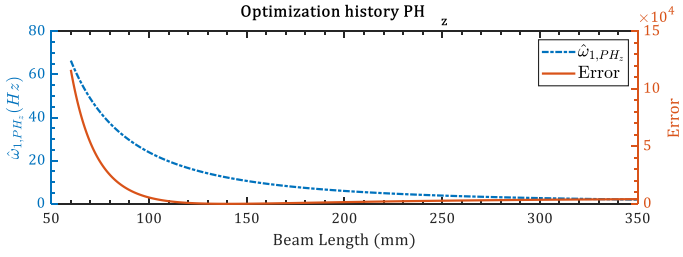


(c)

Fig. 5-14. Optimization history as a function of the beam length for (a) $PH_x$, (b) $PH_y$, and (c) $PH_z$ [187].

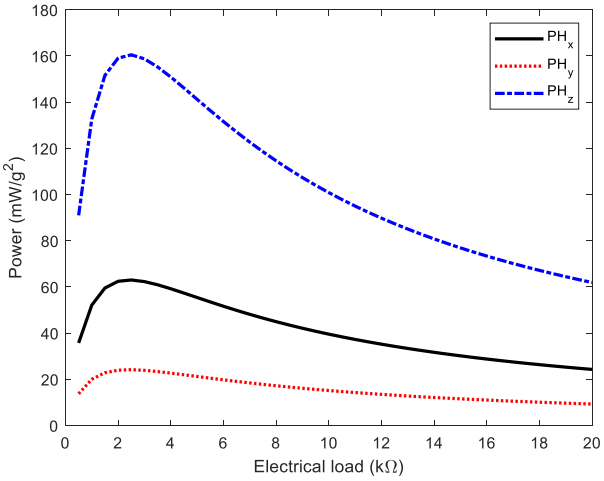


Fig. 5-15. Finding the optimum electrical load for the $PH_x$, $PH_y$, and $PH_z$ harvesters [187].

The acceleration level over the 0-100 Hz frequency span for the moving car is illustrated in Fig. 5-16 (a). The acceleration in the y-direction is more than five times larger than the acceleration in x and z directions. Hence, the voltage output will be considerably higher in the y-direction, as can be seen from Fig. 5-16 (b). The peak voltage output from the $PH_y$ is 0.05V, six times larger than the $PH_x$ and $PH_z$ harvester. The peak power for the $PH_y$ is 0.55μW, which is considerably higher than 0.03μW for the other harvesters. Thus, these results imply that designing an energy harvester in the direction with the highest acceleration level is much better than having multi-directional harvesting beams.

The power generation in the frequency span of 30-35 Hz is substantial for the $PH_y$ harvester. By summing the power generation over the frequency span, the total power output is 407 μW for the $PH_y$ harvester and 7.34 μW and 9.35 μW for the $PH_x$ and $PH_z$ harvesters, respectively.

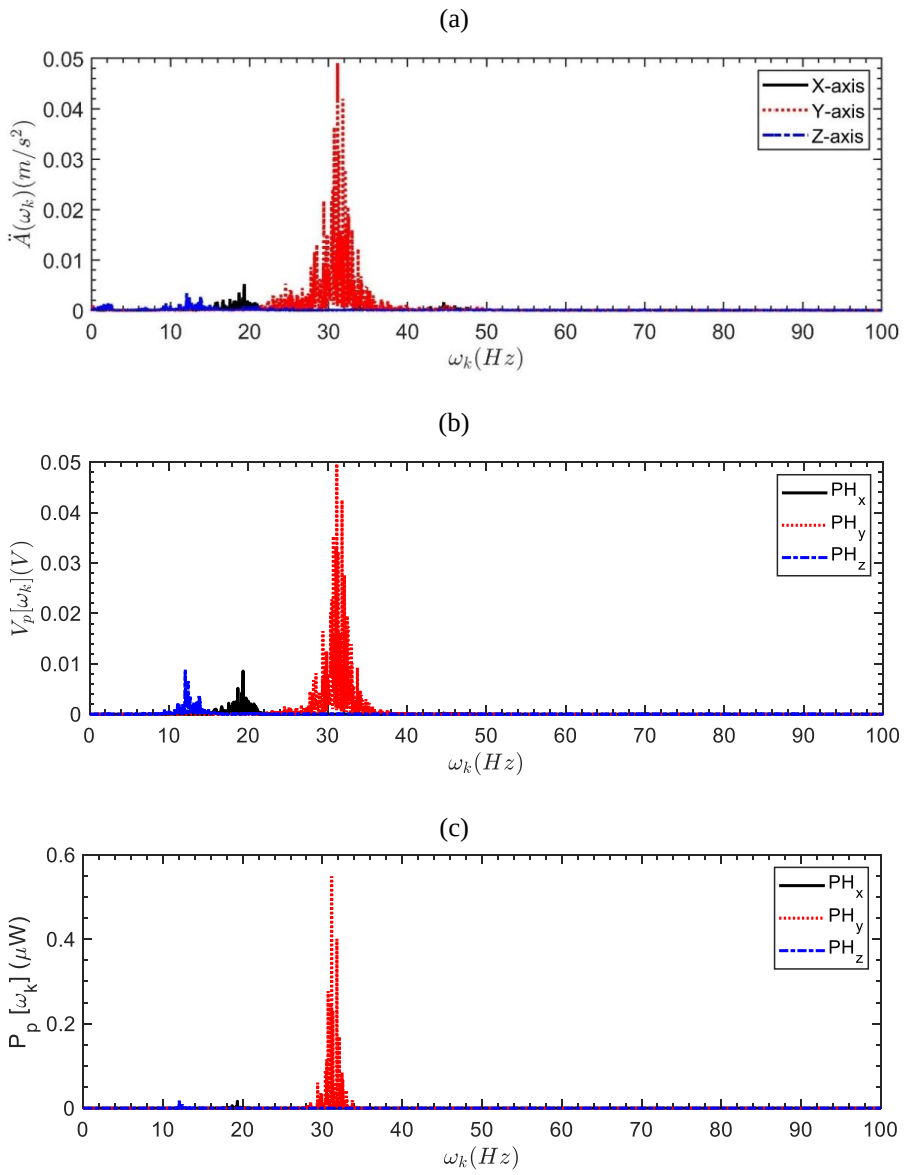


Fig. 5-16. (a) The acceleration level for the moving car in different directions, (b) the voltage, and (c) power output with $R_{opt}$ electrical load in different directions [187].

## 5.3. TOWARD REMOTE AUTONOMOUS CONDITION MONITORING: WATER PUMP CASE STUDY

In subsection 5.1, it has been demonstrated that the shaft misalignment will considerably increase the voltage generation. This conclusion then becomes the central idea for applying the piezoelectric energy harvesting; remote condition monitoring for the high-speed rotating machinery. This subsection's results are derived from Ref. [4] (See Appendix D).

The idea for remote condition monitoring is that an RF transmitter, which is being powered by a piezoelectric harvester, sends a pulse signal to an RF receiver, and by investigating the time elapse between pulses, one can assess the machine state. Because piezoelectric power generation depends on the vibration level and frequency, if any fault changes the vibration amplitude or shifts the dominant frequencies, the pulses' elapsed time will alter. Fig. 5-17 shows the protocol for this approach for remote condition monitoring. Ref. [4] suggest the PIC16F676 microcontroller, which consumes 17μW (8.5μA at 2.0V). The RF transmitter consumes 23.1mW (7mA at 3.3V) during the transmission data and 330nW (100nA at 3.3V) in standby mode.

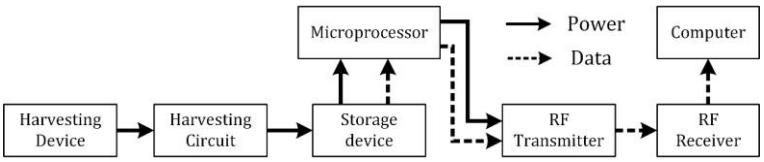


Fig. 5-17. The protocol for remote condition monitoring using the piezoelectric energy harvester [4].

When the water pump works normally, the piezoelectric harvester, designed based on the normal working condition, charges the energy storage. After the energy reaches a specific value, the microprocessor will be activated. After this point, the microprocessor permits one RF signal transmission when the capacitor voltage reaches a designed value. Sending RF signal will discharge the capacitor; nevertheless, the piezoelectric harvester charges the capacitor repeatedly. Fig. 5-18 (a) is the condition monitoring performance under normal conditions. If a defect increases the acceleration level, then the charging process is faster, while the RF power consumption is the same. Thus, sending the RF pulses will be faster. By analyzing the elapsed time between the RF pulses, water pump condition monitoring can be obtained. If the effect of each specific defect on the acceleration signal in terms of vibration amplitude and frequency domain signals can be determined, the defect type can also be determined [4]. More details about the pulse condition monitoring approach can be found in Ref. [4].

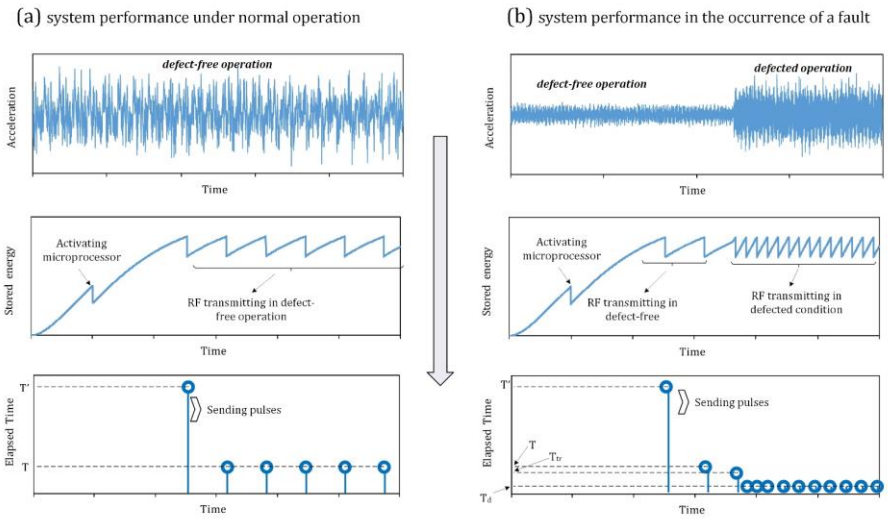


Fig. 5-18. The pulse system performance at (a) defect-free and (b) defected condition [4].

Fig. 5-19 (a) shows the conceptual design for the energy-harvesting unit and the RF transmitter. The energy harvesting unit is directly attached to the bearing's external box as the bearing is sensitive to damages (the Ref. [188]). The energy-harvesting beam is a bimorph (T226-A4-503X from Piezo Systems) with tip mass in the clamped-free boundary condition. The harvesting beam will undergo base excitation from the bearing acceleration. The harvester output wires are connected to an electrical load and then to a rectifier-conditioner-storage circuit. Fig. 5-19 (b) shows the energy harvesting unit. To create the AC output to an always-positive output and scale-up the output voltage, a five-stage Multistage Dickson Charge Pump (MDCP) is used, as shown in Fig. 5-19 (c).

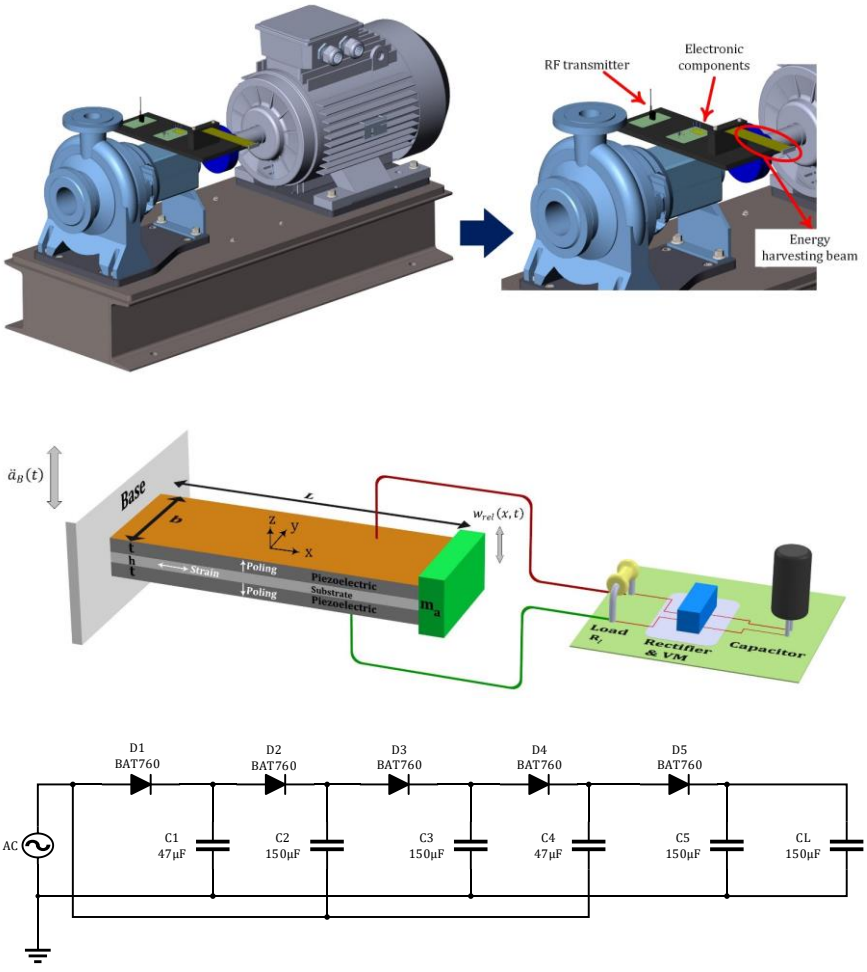


Fig. 5-19. (a) The conceptual design for the water pump remote condition monitoring, (b) the piezoelectric beam with the harvesting circuit, and (c) the five-stage Multistage Dickson Charge Pump (MDCP) [4].

The acceleration data is measured from an actual water pump during working, as shown in Fig. 5-20 (a). The acceleration data is recorded at three conditions: defect-free, shaft misalignment, and shaft looseness, as shown in Fig. 5-20 (b). Fig. 5-20 (b) shows that the shaft looseness and misalignment faults increase the vibration level; nevertheless, the shift in the dominant frequencies does not occur, see Fig. 5-20 (c).

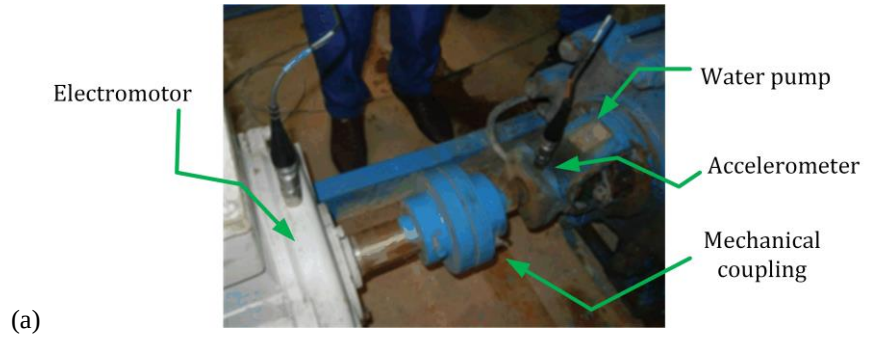


(a)

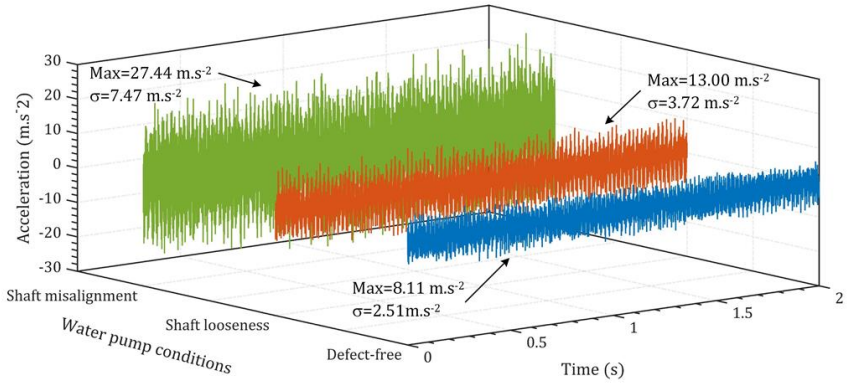


(b)

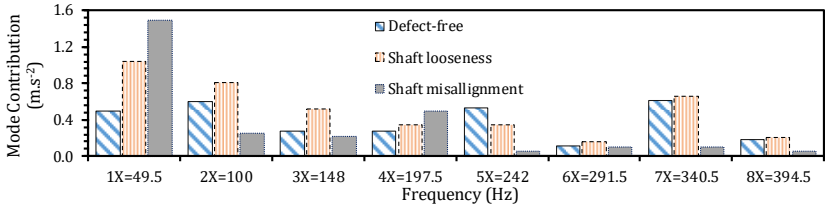


(c)

Fig. 5-20. (a) Measuring the acceleration from the water pump bearing, (b) the measured acceleration at defect-free, shaft looseness and shaft misalignment conditions, (c) the contribution of the FFT peaks [4].

The piezoelectric beam is designed so that the piezo-beam natural frequency matches 49.5Hz, the 1X rotation speed of the water pump. The frequency tuning is accomplished by tunning the tip mass, so the piezoelectric geometry is unchanged. Fig. 5-21 (a) shows the tip mass tuning process. An 8-gr tip mass, shown in Fig. 5-21 (b), is found to match the natural frequency to 49.5Hz. Therefore, the designed energy harvester is a bimorph (T226-A4-503X from Piezo Systems) with an 8-gr tip mass. The voltage frequency responses for different load resistances are shown in Fig. 5-21 (c). The power output versus the electrical load is shown in Fig. 5-21 (d). As discussed

in subsection 2.3.4, the resonant frequency will change by the resistance connection, and because the uncoupled harvester's resonant frequency is matched to the 49.5Hz, the harvester's coupled resonant frequency will be slightly higher than 49.5Hz. In the electrical load range of 50kΩ, the coupled resonant frequency is 50.1Hz.

Consequently, the power output for 49.5Hz excitation is less than the power for 50.1Hz excitation. Similarly, the optimum load for the 49.5Hz and the 50.1Hz excitations is slightly different. Nevertheless, the optimum load for the 49.5Hz shall be selected because the measured excitation source (water pump) has the 49.5Hz dominant frequency.

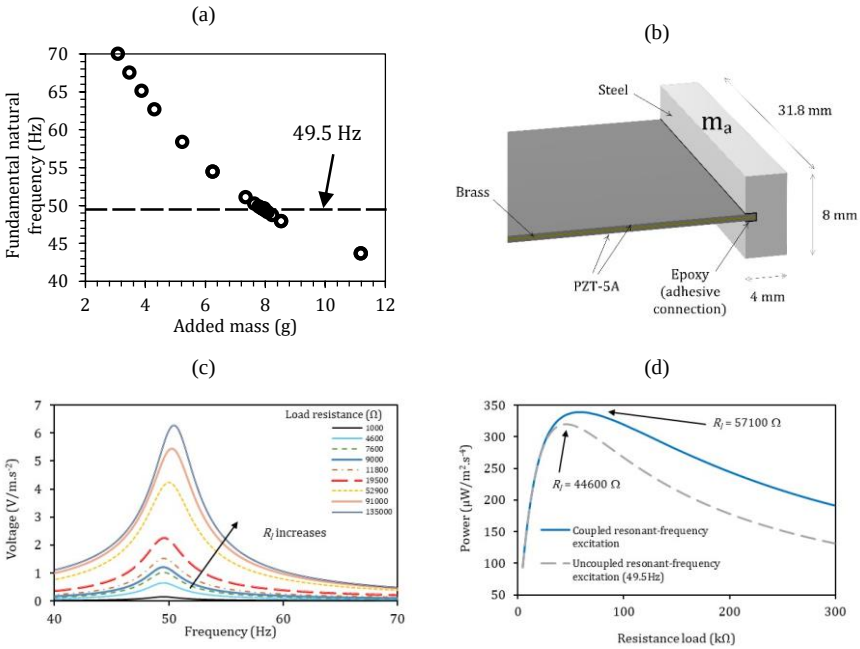


Fig. 5-21. (a) Resonant matching using tuning tip mass, (b) the tip mass for the matched resonant, (c) the voltage frequency response over different loads, and (d) power versus the electrical load [4].

Because the water pump acceleration is different at different conditions, the voltage and power output from the piezoelectric beam would be different as Fig. 5-22 (a) shows the direct voltage and power from the piezo-beam per cm$^3$ for different working conditions. The capacitor voltage under different working conditions would be higher than the original piezo-beam voltage output by considering the five-stage VM circuit. Fig. 5-22 (b) shows the capacitor voltage, which is charged by the piezo-beam and the five-stage MDCP circuit, in the absence of the RF transmission. It can be seen that the defect-free condition leads to the lowest voltage output.

The capacitor's voltage from the starting point is shown in Fig. 5-22 (c) when all the energy harvesting and power management circuit elements are active. After the initial point, the voltage reaches a level that the microprocessor is activated. Afterward, an RF signal is transmitted when the capacitor voltage reaches 8V (pre-defined by the designer). Again, as the water pump is working, the capacitor will be re-charged until the subsequent RF transmission. However, the charging process at different working conditions is not the same as the vibration level is different at different working conditions. Therefore, the time elapsed between the RF pulses becomes shorter when a shaft looseness or shaft misalignment occurs in the water pump. The elapsed time between the RF pulses transmissions under different working conditions are shown in Fig. 5-22 (d) and (e).

Thus, this concept can be used for assessing the condition of a machine. By defining a state parameter according to the elapsed time, the machine state is monitored continuously. Fig. 5-23 illustrates the performance of this remote condition monitoring for the water pump's acceleration signals. A transition period is added between the defect-free and shaft-misalignment condition to resemble real damage. In the first 8 seconds, where the machine is working at defect-free condition, the elapsed time is constant, so the state parameter is 1. While the abnormal condition starts, the elapsed time becomes shorter so that the state parameter deviates from 1, showing that a fault occurs in the system.

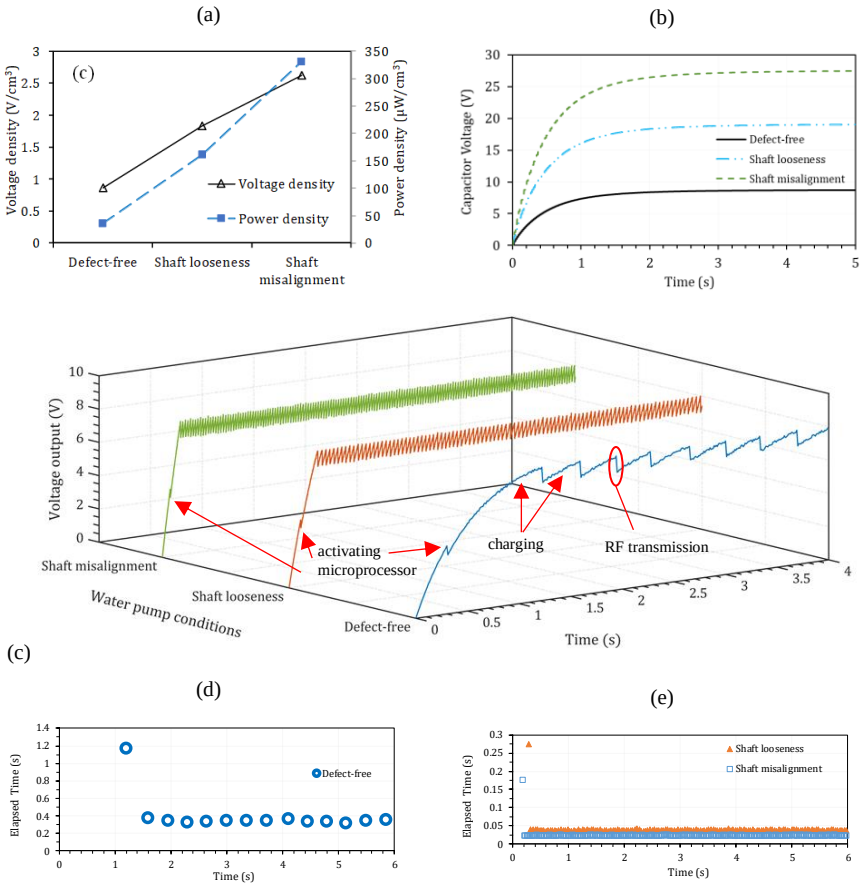


Fig. 5-22. The harvesting unit and the RF system performance at different water pump conditions. (a) voltage and power without adding the power management circuit, (b) the capacitor's voltage without sending RF pulses by considering the VM circuit, (c) the capacitor's voltage with sending RF pulses and by considering the VM circuit, (d) the elapsed time between the RF pulses at defect-free condition, and (e) the elapsed time between the RF pulses at defected conditions [4].

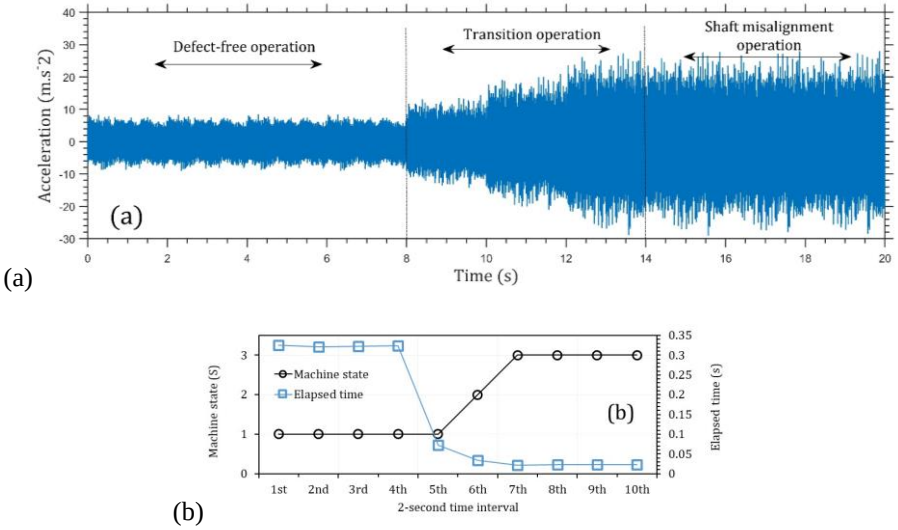


Fig. 5-23. (a) The acceleration signal from a defect-free condition to a shaft-misalignment condition, and (b) the elapsed time between the pulses and the machine state [4].

## 5.4. ENERGY HARVESTERS WITH VARIABLE THICKNESS PIEZO LAYER AND COMPOSITE SUBSTRATE

This section's results are derived from Ref. [163] (See Appendix E). The analysis of this proposed energy harvester is carried out based on the FEM, presented in subsection 2.4.

Toward enhancing the power generation, a non-uniform energy harvester with variable-thickness piezoelectric sheets and the composite substrate is proposed. In this design, the piezoelectric sheets partially cover the substrate layer so that the beam becomes less stiff and has a low natural frequency. The substrate shim is a composite lamina with E-glass fibers so that by changing the fiber orientation, the harvester performance can be improved. Besides, variable thicknesses of piezoelectric sheets are considered for the analysis. Fig. 5-24 shows the understudy piezoelectric energy harvester. The dimensions and material properties for this example are given in Table 5-2.

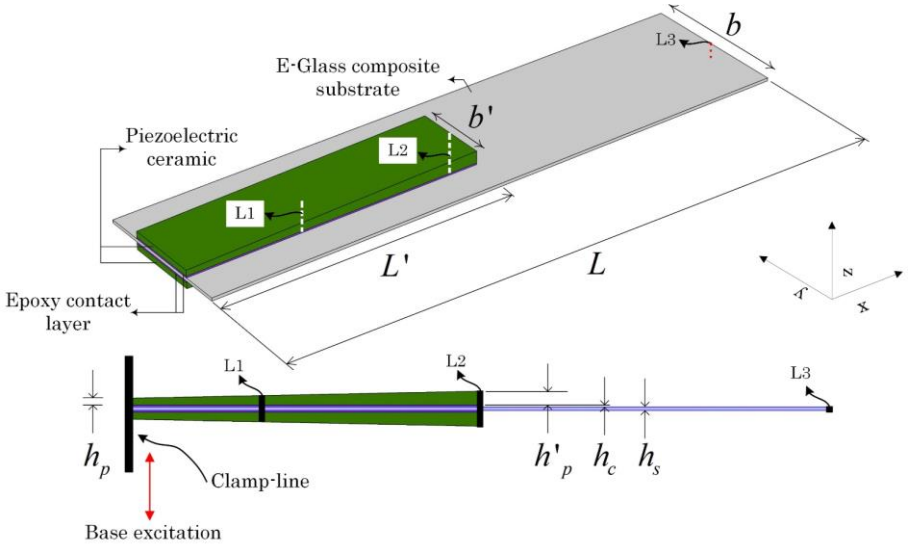


Fig. 5-24. A non-uniform piezoelectric harvester with variable thickness piezo-layers [163].

| Description | Piezoelectric (PZT-5A) | Substrate (E-Glass composite) | Contact layer (Epoxy adhesive) |
|---|---|---|---|
| Length (mm) | 100 | 200 | 100 |
| Width (mm) | 25 | 50 | 25 |
| Added tip mass (kg) | 0.01 | | |
| Thickness (mm) | $h_p = 0.3$ (each layer)<br>$h'_p$ is variable | $h_s = 0.2$ | $h_c = 0.02$ |
| Density (kg/m³) | 7800 | 1759 | 2750 |
| Structural constants<br>$Q_{11}$ (GPa)<br>$Q_{22}$ (GPa)<br>$Q_{12}$ (GPa)<br>$Q_{44}$ (GPa)<br>$G_{55}$ (GPa)<br>$G_{66}$ (GPa) | <br>66.0<br>66.0<br>20.46<br>22.8<br>22.8<br>22.8 | $\theta$=10° (standard configuration)<br>56.4<br>18.0<br>3.6<br>9.0<br>9.0<br>9.0 | <br><br><br>$E = 1.05$ (GPa)<br>$\nu = 0.3$ |

Table 5-2. The material properties and the dimensions for the non-uniform variable-thickness harvester [163].

Using a variable thickness will increase the power generation, as shown in Fig. 5-25. Besides, the natural frequency will slightly change, about 1.5Hz, when $h_p < h'_p <$

$2.5h'_p$. The natural frequency change can be positive or negative depending on the thickness increase ratio. Overall, the variable piezoelectric thickness enhances the power output, which is a positive effect.

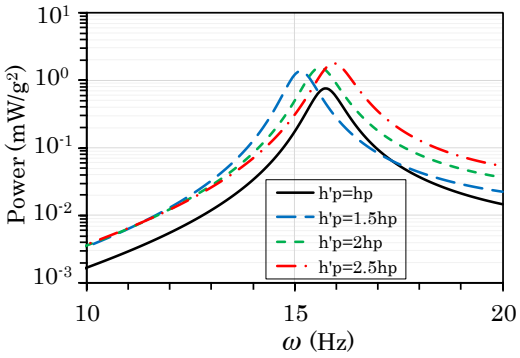


Fig. 5-25. The effect of variable thickness on the harvester power output [163].

Changing the fiber orientation in the substrate composite lamina will initially increase the power output and decrease the power, as can be seen from Fig. 5-26. The harvester's natural frequency reduces from 16 Hz to 13 Hz with θ=40°. The natural frequency variation by tuning the fiber orientation can be used as an approach for frequency matching design, positively affecting the power output.

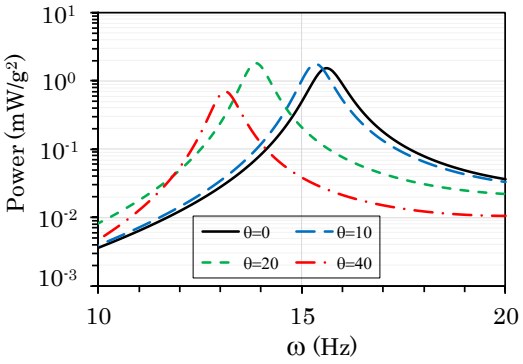


Fig. 5-26. The effect of changing the fiber orientation in the composite substrate on the harvester power output [163].

As a measure to find the optimal power generation condition, Fig. 5-27 illustrates the power versus the fiber orientation and the thickness increase ratio. As shown in the zoomed-in view, the maximum power output is obtained with θ=20° and $h'_p$=2.75$h'_p$. The power output is 104.7mW/g$^2$ at the optimal condition, which is 50% higher than

the standard design power output. Nevertheless, by the variable thickness design, the harvesting device volume is increased by 33.7%.

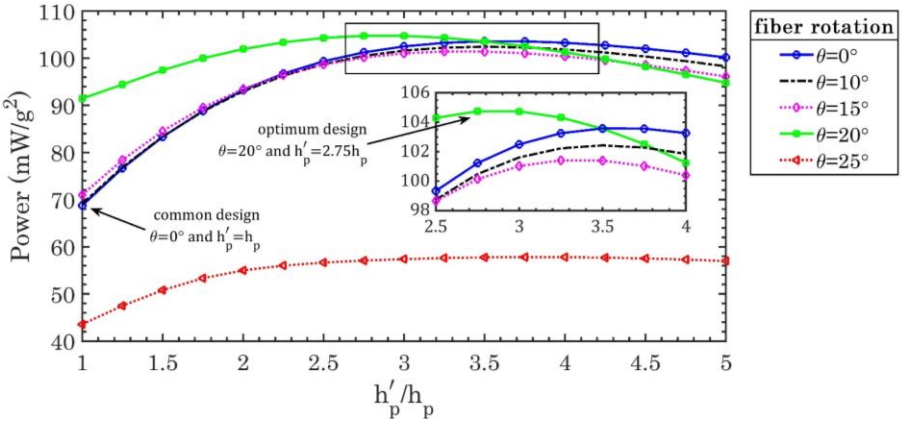


Fig. 5-27. Power sensitivity (with optimum load connection) to the thickness variability and fiber orientation [163].

## 5.5. A BROADBAND PERFORMANCE IMPROVED COMPOSITE ENERGY HARVESTER WITH CAR VIBRATION CASE STUDY

A conceptual design for a broadband energy harvester with higher power generation performance will be proposed and investigated in this subsection. Afterward, the power generation using this proposed harvester will be simulated under the car vibration input by the FEM modeling in subsection 2.4 and 2.5. These subsection results are derived from Ref. [164] (SeeAppendix F).

In a common clamped-free boundary condition, the stresses near the clamped line are considerably higher. Fig. 5-28 shows the von Mises stress for a clamped-free piezoelectric beam. Thus, in the piezoelectric cantilever beam, the high-stress regions generate considerably higher power than the other regions. Therefore, a large portion of the piezoelectric sheet does not contribute to power generation.

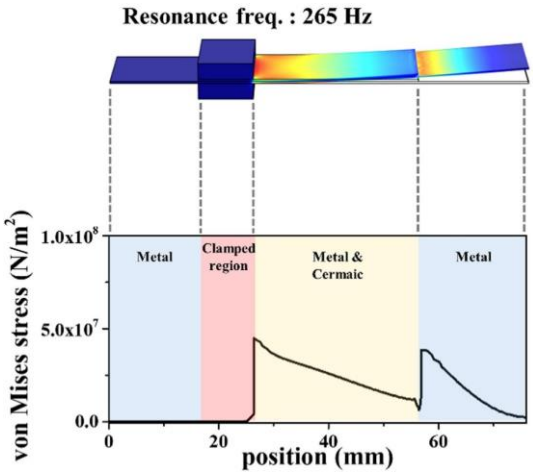


Fig. 5-28. The von Mises stress along the beam length for a piezoelectric harvester vibrating with its resonant frequency [189], the stress near the clamped region is high, so the power generation around the clamped regions is considerably larger than other regions.

An energy harvesting beam has been proposed in Ref. [164] with a composite substrate and two composite MFCs, see Fig. 5-29 (a). The substrate and the piezo-MFC, fiber rotations of $\theta_s$ and $\theta_p$ are considered, and the power generation variation is studied. As can be seen from, the piezoelectric fiber orientation $\theta_p$ will substantially increase the power output and with more influence than the substrate fiber orientation $\theta_s$. This piezoelectric fiber orientation will also reduce the harvester's natural frequency. These two conclusions can be seen in Fig. 5-29 (b) and (c).

The piezoelectric fiber orientation improves the stress (or strain) contour, increasing the power output [164]. When $\theta_p$=0˚, there are uniform displacement, strain and electrical displacement contours, as can be seen from Fig. 5-30 (a)-(d). On the other hand, when $\theta_p$=35˚, there are non-uniform contours for the displacement and strain contours. While the displacement field is due to pure bending motion for $\theta_p$=0˚, the beam deformation is a mix bending-torsion motion for $\theta_p$=35˚.

In addition to the uniform contour distortion, the beam stiffness in the x-direction will be reduced by rotating the piezo-fibers because their Young's modulus in the length direction is greater than the width direction, leading to more significant displacement and strain values.

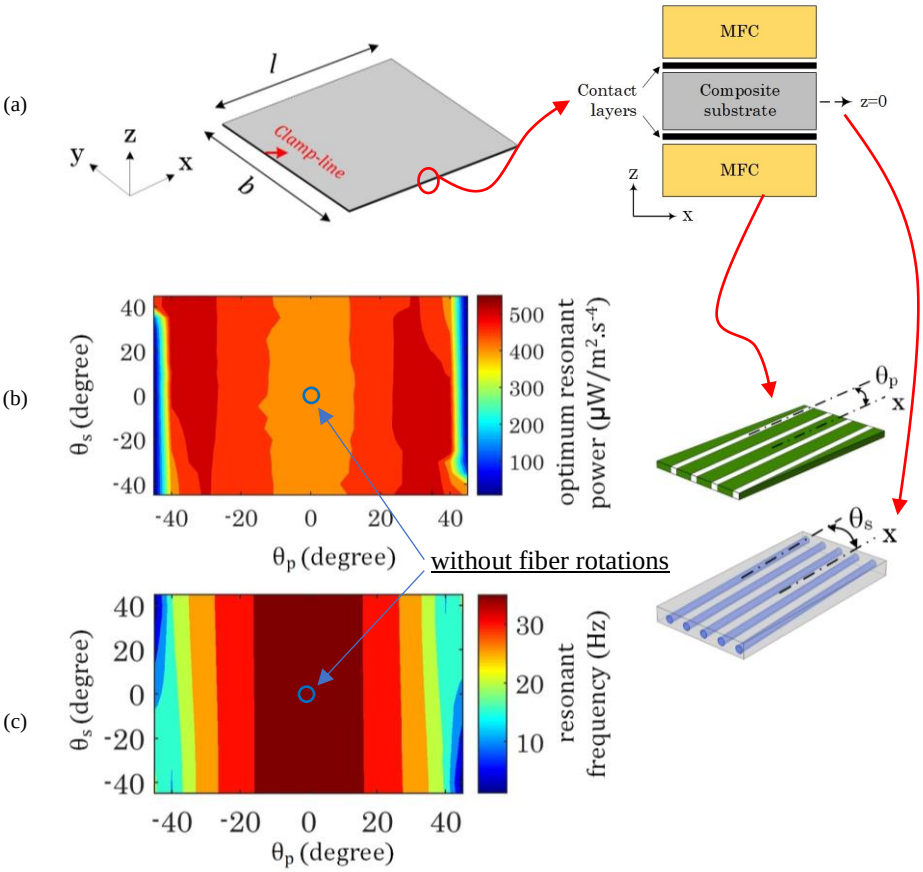


Fig. 5-29. (a) The composite energy harvester, (b) power output, and (c) natural frequency variations by changing the piezoelectric and substrate fiber orientation [164].

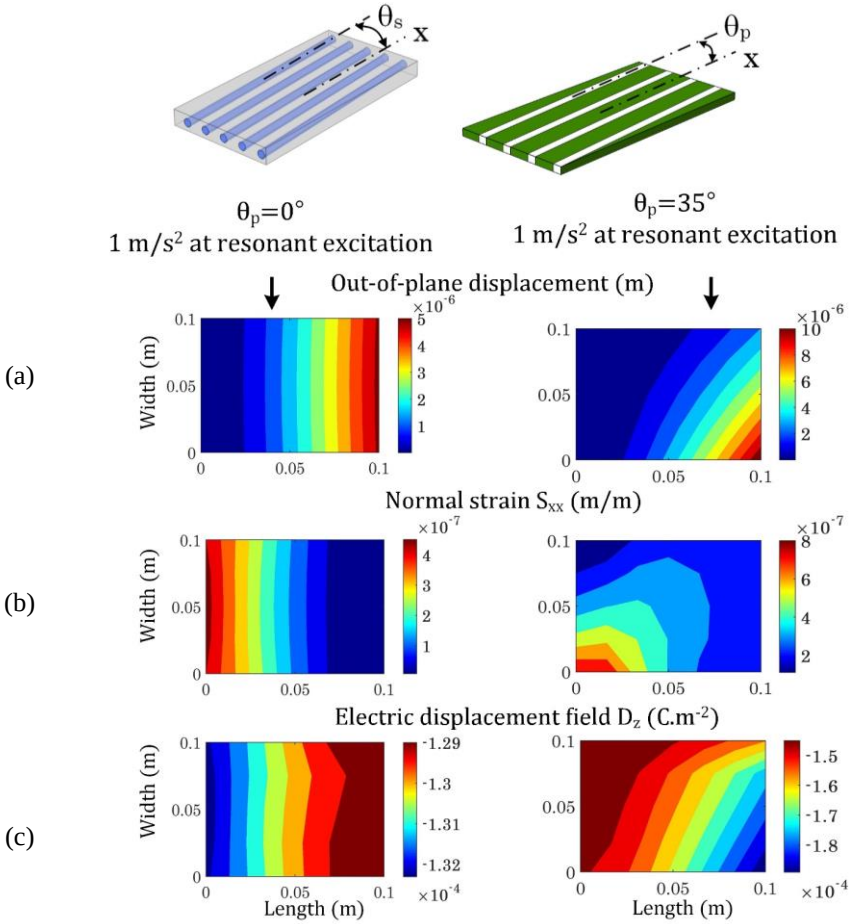


Fig. 5-30. (a) Beam deformation, (b) normal strain, and (c) electrical displacement for 0º and 35º piezoelectric fiber orientation [164].

It is known that the trapezoid configurations, Fig. 5-31 (a), can lead to better power generation, as can be seen from Fig. 5-31 (b). The trapezoid configurations can have another important feature; they can vary the natural frequency substantially. The power and power density of trapezoid (extended and tapered) configurations are compared with the reference beam model in Fig. 5-31 (a) and (b). The extended configuration generates higher power output, see Fig. 5-31 (b); however, its volume is larger than the reference configuration. On the other hand, the tapered beam power density is larger than the reference configuration because of its smaller volume. The tapered beam has a greater natural frequency, while the extended beam's natural frequency is smaller than the reference configuration.

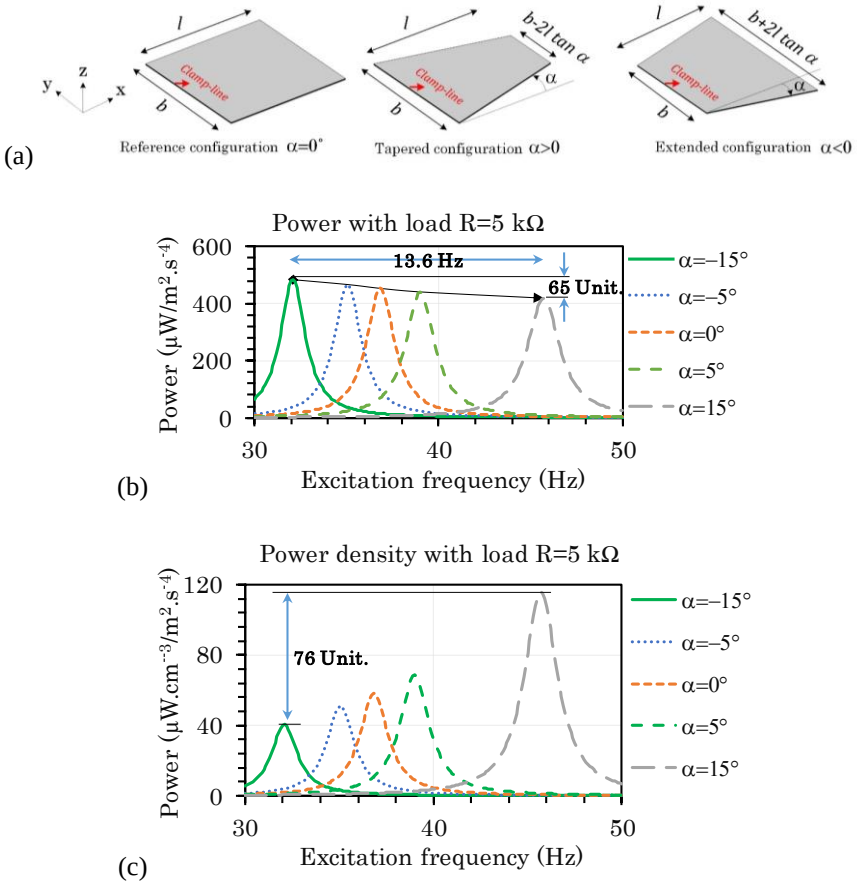


Fig. 5-31. (a) The reference, extended, and tapered configurations, (b) power output for trapezoid configurations, and (c) power density trapezoid configurations [164].

Increasing the piezoelectric fiber orientation enhances the power output up to an optimum value, which afterward, the power drops sharply. The same trend can be seen for the power density. The natural frequency also decreases until the optimum fiber orientation. The optimum range for the piezoelectric fiber orientation, shown in Fig. 5-32, has a peak power generation performance with a reduced natural frequency that is merit for low-power energy harvesting applications.

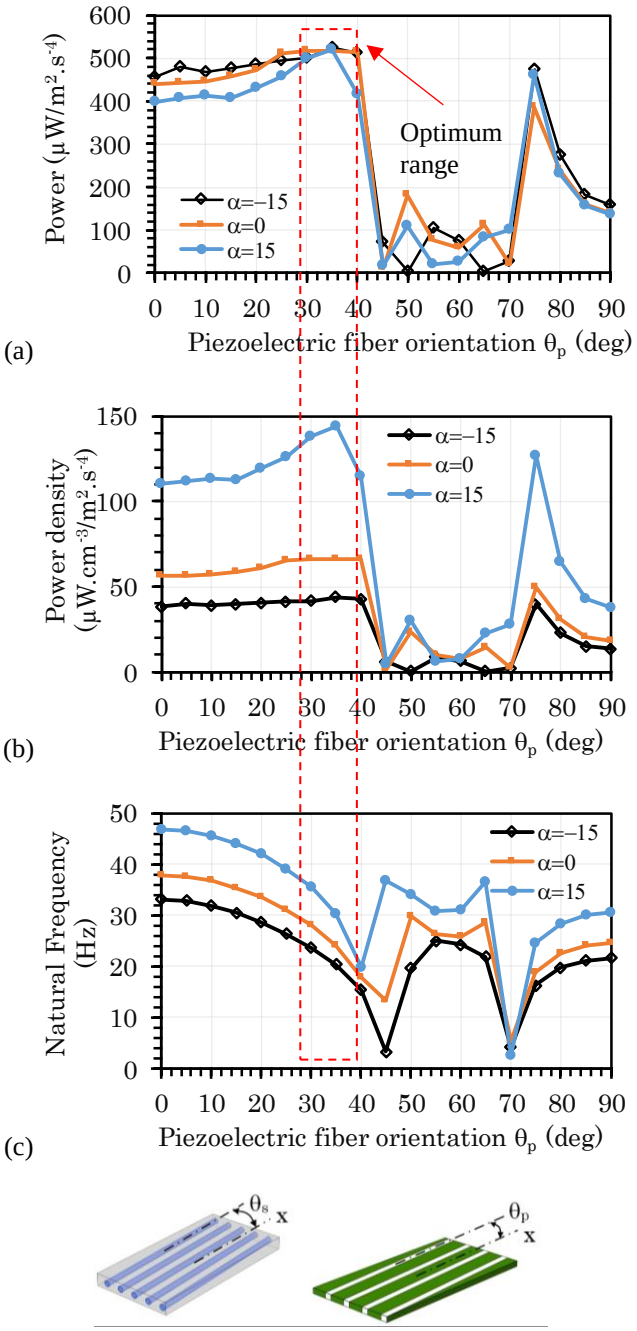


Fig. 5-32. The sensitivity analysis to the fiber orientation and beam tapered angle, (a) power output, (b) power density, and (c) natural frequency [164].

By introducing two optimizing parameter, one material, and one geometry, a design performance envelope are obtained. Table 5-3 presents the variation study for these parameters. The natural frequency can be varied from -45% to 24% of the reference's natural frequency, giving a wide design range for the resonant matching design approach. The power output and power density can be enhanced by a proper selection of these two optimizing parameters.

| Parameter | Natural frequency | | Power | | Power density | |
|---|---|---|---|---|---|---|
| | Value (Hz) | Variation (%) | Value ($\mu W/m^2.s^{-4}$) | Variation* (%) | Value ($\mu W.cm^{-3}/m^2.s^{-4}$) | Variation (%) |
| #$\alpha$=0, $\theta_p$=0 | 37.81 | - | 440.03 | - | 56.41 | - |
| $\alpha$=-15, $\theta_p$=0 | 33.11 | -12.43 | 457.50 | 3.97 | 38.19 | -32.31 |
| $\alpha$=15, $\theta_p$=0 | 46.73 | 23.59 | 399.22 | -9.27 | 110.28 | 95.49 |
| $\alpha$=0, $\theta_p=\theta_{opt}$ | 24.06 | -36.37 | 518.24 | 17.77 | 66.44 | 17.77 |
| $\alpha$=-15, $\theta_p=\theta_{opt}$ | 20.40 | -46.05 | 524.64 | 19.23 | 43.79 | -22.37 |
| $\alpha$=15, $\theta_p=\theta_{opt}$ | 30.31 | -19.84 | 521.31 | 18.47 | 144.01 | 155.27 |

Table 5-3. The variation study for the fiber orientation parameter and taper angle [164].

As the case study, the car vibration data is taken from Chapter 2, and an energy harvester with multiple beams is proposed for this case study. The time-domain and FFT of the car vibration are shown below. The acceleration between 26Hz to 35Hz is always higher than 0.011g ($g=9.81m/s^2$). Therefore, the car acceleration is considerable in a 9Hz range, while the power frequency response of a piezoelectric is extremely narrowband, approximately 1-2 Hz. Thus, for obtaining the best power generation from the car vibration, a multiple-beam energy harvester will be analyzed. The multiple-beam harvester for covering the 9 Hz range can be designed in two ways: a standard way by having multiple beams with different beam length values and using the taper angle as a tuning parameter considering the optimum fiber orientation. Fig. 5-33 (a) and (b) demonstrate the proposed and the standard designs.

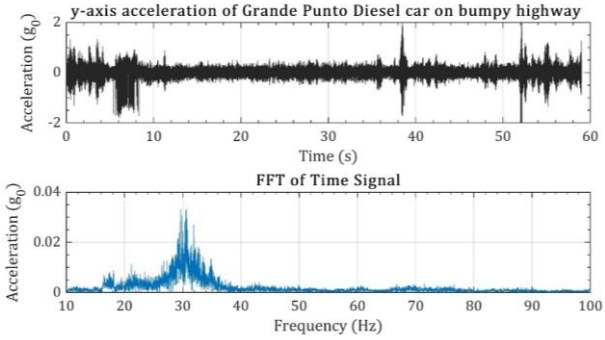


Fig. 2-11. Time domain and FFT of the car acceleration data for a Grande Punto car on a bumpy highway [170].

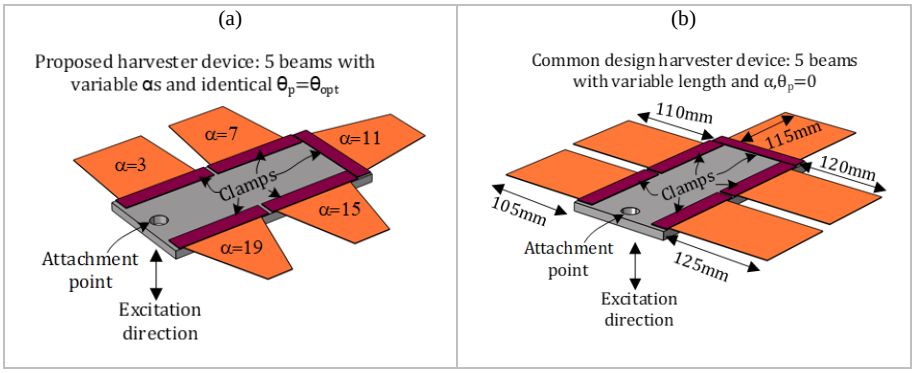


Fig. 5-33. Multiple-beam energy harvester for broadband energy harvesting, (a) the proposed design by the taper angle as the tuning parameter, and (b) standard design by the beam length as the tuning parameter [17].

Fig. 5-34 (a) shows that the proposed harvester's power frequency response has a larger amplitude than the standard design. The proposed harvester power response has fewer fluctuations with a smoother trend in addition to the larger amplitude. By multiplying the power frequency response to the FFT acceleration square, the generated power by the car vibration can be determined. The power generated by the proposed and the standard designs is shown in Fig. 5-34 (b). Fig. 5-34 (b) shows that the proposed generated power is considerably higher than the standard design. The generated peak power is 120 µW for the proposed design with a 23.7 $cm^3$ volume, comparing with the 50 µW peak power with a 44.9 $cm^3$ volume for the standard design.

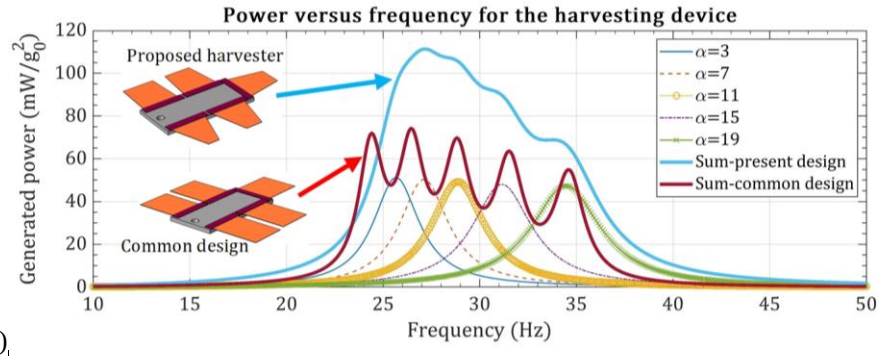


(a)

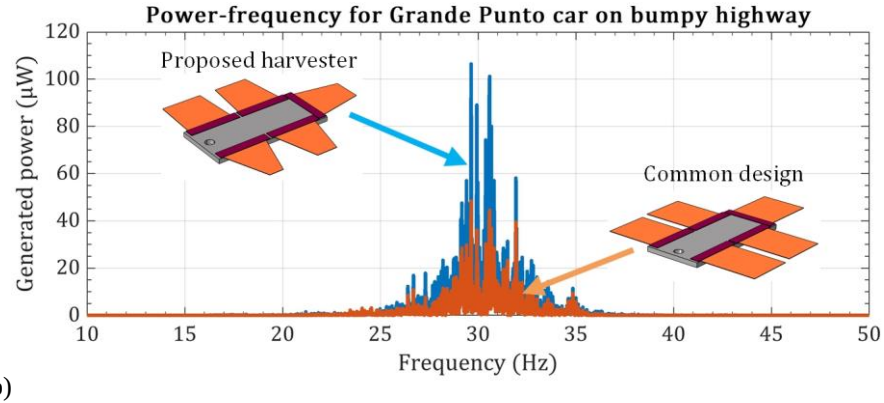


(b)

Fig. 5-34. (a) Power frequency response, and (b) power output for the proposed and common designs [17].

# CHAPTER 6. CONCLUDING REMARKS

## 6.1. REMARKS ON THE MODELING TECHNIQUES

Chapter 2 presents the modeling approaches for analyzing the piezoelectric energy harvesters. Three kinds of models have been presented: the SDOF model, analytical beam model, and the FE method. These modeling techniques will be used to analyze, optimize, and design the energy harvesters for different applications in the following chapters.

The SDOF method replaces a piezoelectric beam with a single mass-spring-damper system with an electromechanically coupled term due to the piezoelectricity. The SDOF method does not accurately estimate the natural frequency, leading to inaccurate power output estimations. The Equivalent Beam Method (EBM) is introduced to estimate the natural frequencies in the unimorph and bimorph configurations with a tip mass. The EBM improves the $1^{st}$ mode natural frequency accuracy; nevertheless, the higher modes' inaccuracies exist. Besides, the optimum load obtained by the SDOF method is not accurate.

The analytical beam model is suitable for single or double piezoelectric beams, with contact thickness layers and rectangular configurations. The beam model has good accuracy in the first resonant frequency in the constant cross-section and rectangular shape. However, the natural frequency estimation accuracy drops for the higher modes, yet with considerably better performance than the SDOF method. The beam model has good agreement with the FE method over the optimum load selection, while it slightly overestimates the power. However, for the load range around the optimum load, the power overestimation is smaller than the extremely large or small loads.

The FE model developed and presented covers a wide range of analysis for piezoelectric energy harvesters, including the non-uniform, variable thickness, non-rectangular, multi-layered, and composite designs. The FE method considers high-order shear elements suitable for thick-layer and bulk configurations. The FE model is also modified to accommodate Micro-Fiber Composite (MFC) piezo-layers modeling in a multi-layered manner. The FE model is validated for various cases, namely the bimorph without tip mass, bimorph with a tip mass, unimorph with the MFC, and trapezoid bimorph beams.

The modeling techniques for the PEHs are derived in the linear framework. However, it is shown that by increasing the amplitude of the base excitation, the resonant frequency shifts backward. This resonant frequency shift can be around 3%. By increasing the base excitation amplitude, the beam tip deflection also increases, and, eventually, due to the large deflections, the beam's natural frequency becomes smaller.

## 6.2. REMARKS ON PARAMETER INVESTIGATIONS

In Chapter 3, some of the characteristics of piezoelectric energy harvesters are investigated to understand the harvesters' behavior better.

The substrate shim will positively increase the output power for piezo-beams because it will distance the beam's neutral axis from the center of the piezoelectric layer, and therefore, the piezoelectric layer generates higher power under the bending. Besides, the substrate layer affects the natural frequency.

As a general rule, added tip mass increases the beam deflection, and therefore the output power will be increased. Tip mass also shifts the natural frequency to the left substantially. The tip mass inertia will make the voltage damped out slower under shock excitations and lasts longer. If the beam is less stiff, the tip mass increases the output voltage more considerably than for a stiff beam.

The contact layer is an inevitable part of a piezoelectric beam, as the piezoelectric layers are joined to a substructure. For the commercially manufactures samples, this contact layer can have a negligible thickness; nevertheless, for the samples built by hand, controlling the contact layer thickens is difficult. The laboratory samples may have influential contact layer thickness. The contact layer can change the natural frequency and the power generation performance of the energy harvester.

## 6.3. REMARKS ON DAMPING MECHANISMS

In Chapter 4, damping in the piezoelectric energy harvesters was studied. Two methods were presented for the damping coefficient determination, namely the HTVR and modified STFR. Numerical and experimental results were presented about each method. Both methods are derived for the piezoelectric beams, and only the voltage responses are required, without the need for extra sensor installation and structural response measuring. Therefore, these methods can be used for in-situ damping measurement using only the piezoelectric beams' voltage recording.

Moreover, by testing different piezoelectric harvesters, it has been tried to quantify the damping coefficient at different configurations, with and without substrate shim, with and without the tip mass and different bonding layers. The contribution of the viscous and structural damping mechanisms was also presented.

## 6.4. REMARKS ON APPLICATIONS FOR THE PIEZOELECTRIC ENERGY HARVESTERS

The focus of Chapter 5 is the applications of piezoelectric energy harvesting. The vibration from the moving car, water pump, and DC motor is assumed to excite the piezoelectric beams.

In the DC-motor tests, the power generation depends on the motor rotation speed; even a 0.5-Hz difference in the rotation speed considerably changes the power output. In the actual application, experiments show an optimum load leading to the maximum power generation. It has been also demonstrated that the shaft misalignment in the DC motor would vary the piezoelectric voltage generation considerably.

For a moving car with vibration in three-axes, an energy-harvesting box consisting of three harvesting beams is analyzed for power generation. Resonant frequency matching was carried out by tuning the beam length values. It has been demonstrated that the energy generation from one axis is considerably higher than the other two axes.

Using the conclusion from the DC-motor tests, remote condition monitoring is developed, and its performance is studied for a water pump acceleration. The method is based on the RF pulse transmission, and the machine condition is investigated by analyzing the elapsed time between the RF pulses. It has been shown that the piezoelectric energy harvester can provide power for a microprocessor and an RF transmitter for sending limited-time pulses.

One geometry parameter and one material parameter are introduced that can improve the power generation by piezoelectric beams. The material factor, the piezoelectric fiber orientation in a composite harvester, will increase the strain contours over the beam surface to increase the power generation. The geometry parameter, tapered or extended angle, leads to trapezoid configurations that will improve the power generation. The geometry parameter can also be used as a tuning factor for frequency matching. Using these two parameters, an energy-harvesting system with multiple beams is proposed for broadband energy harvesting from a car vibration.

Three tuning parameters have been investigated for the resonant matching method, namely beam length, added mass, and tapered angle. The beam length is the least practical among these tuning parameters because the natural frequency is sensitive to the beam length, so the tuned beam length cannot be manufacturing accurately. Tuning added mass is the most practical method; however, one should be careful because it may increase the viscous air damping and reduce the harvester's fatigue life. The taper angle is the best from a power generation perspective; however, manufacturing trapezoid configuration can be challenging.

## 6.5. FUTURE WORKS

The thesis structure has been categorized into modeling, sensitivity analysis, and applications. According to these categories, the direction of further research in the PEH can be suggested as follows:

- On the modeling techniques.

- Developing nonlinear finite element model.
- Estimate the power under random vibrations.
- Estimate the power by solving the equations time-dependent, especially for non-harmonic excitations.

- On the sensitivity analysis
  - Further investigation of the added mass effect on the output power with changing the added mass's location and dimensions.
  - Employing different shim materials with a particular focus on the flexible substrates.
  - Further investigation of the contact layer effect by employing controlled thickness layers and exploring new bonding processes like UV adhesives.
  - Further investigation of the viscous air damping by testing the harvester performance in different air pressures and under different air temperatures.
  - Further investigation of the tip-mass effect on the damping with a focus on harmonic excitations.

- On the application
  - Experimental testing on the composite piezoelectric harvesters with variable fiber directions.
  - Focusing on the optimum electrical load for calculating the optimum load quickly and time-dependent for practical applications.
  - Exploring the long-term performance of piezoelectric harvesters.
  - Exploring the power variation due to the packaging and under variable surrounding conditions.
  - Further exploration for broadband energy harvesting so that the power output is less dependent on the excitation frequency.

# LITERATURE LIST

Bibliography

[1] A. Toprak and O. Tigli, “Piezoelectric energy harvesting: State-of-the-art and challenges,” *Appl. Phys. Rev.*, vol. 1, no. 3, p. 031104, 2014, doi: 10.1063/1.4896166.

[2] H. Toshiyoshi, S. Ju, H. Honma, C. H. Ji, and H. Fujita, “MEMS vibrational energy harvesters,” *Sci. Technol. Adv. Mater.*, vol. 20, no. 1, pp. 124–143, 2019, doi: 10.1080/14686996.2019.1569828.

[3] H. Li, C. Tian, and Z. D. Deng, “Energy harvesting from low frequency applications using piezoelectric materials,” 2014.

[4] M. Khazaee, A. Rezaniakolaie, A. Moosavian, and L. Rosendahl, “A novel method for autonomous remote condition monitoring of rotating machines using piezoelectric energy harvesting approach,” *Sensors Actuators A Phys.*, vol. 295, pp. 37–50, 2019, doi: 10.1016/j.sna.2019.05.016.

[5] A. Erturk and D. J. Inman, *Piezoelectric Energy Harvesting*, 1st ed. Wiley, 2011.

[6] S. R. Anton and H. A. Sodano, “A review of power harvesting using piezoelectric materials (2003–2006),” *Smart Mater. Struct.*, vol. 16, no. 3, pp. R1–R21, 2007, doi: 10.1088/0964-1726/16/3/R01.

[7] H. Li, C. Tian, and Z. D. Deng, “Energy harvesting from low frequency applications using piezoelectric materials,” *Appl. Phys. Rev.*, vol. 1, no. 4, p. 041301, 2014, doi: 10.1063/1.4900845.

[8] N. Elvin and A. Erturk, *Advances in energy harvesting technologies*. Springer Science & Business Media, 2013.

[9] N. Sezer and M. Koç, “A comprehensive review on the state-of-the-art of piezoelectric energy harvesting,” *Nano Energy*, vol. 80, no. October 2020, p. 105567, 2021, doi: 10.1016/j.nanoen.2020.105567.

[10] H. Liu, J. Zhong, C. Lee, S. W. Lee, and L. Lin, “A comprehensive review on piezoelectric energy harvesting technology: Materials, mechanisms, and applications,” *Appl. Phys. Rev.*, vol. 5, no. 4, 2018, doi: 10.1063/1.5074184.

[11] C. R. Bowen, V. Y. Topolov, and H. A. Kim, *Modern piezoelectric energy-harvesting materials*, 1st ed., vol. 238. Springer, 2016.

[12] M. Płaczek and G. Kokot, “Modelling and laboratory tests of the temperature influence on the efficiency of the energy harvesting system based on MFC piezoelectric transducers,” *Sensors (Switzerland)*, vol. 19, no. 7, 2019, doi: 10.3390/s19071558.

[13] Kentaro Nakamura, *Ultrasonic transducers Materials and design for sensors, actuators and medical applications*. Woodhead Publishing L, 2012.

[14] Z. Yang and J. Zu, “Comparison of PZN-PT, PMN-PT single crystals and PZT ceramic for vibration energy harvesting,” *Energy Convers. Manag.*, vol. 122, pp. 321–329, 2016.

[15] C. Covaci and A. Gontean, “Piezoelectric energy harvesting solutions: A review,” *Sensors (Switzerland)*, vol. 20, no. 12, pp. 1–37, 2020, doi: 10.3390/s20123512.

[16] M. Khazaee, J. E. Huber, L. Rosendahl, and A. Rezania, “On the determination of viscous and structural damping coefficients for piezoelectric energy harvesters using only time-domain voltage measurements,” *Appl. Energy*, vol. 285, p. 116427, 2021.

[17] M. Khazaee, A. Rezaniakolaei, and L. Rosendahl, “An experimental study on macro Piezoceramic fiber composites for energy harvesting,” *Mater. Sci. Forum*, vol. 951, pp. 3–8, 2019, doi: https://doi.org/10.4028/www.scientific.net/MSF.951.3.

[18] M. F. Daqaq, R. Masana, A. Erturk, and D. Dane Quinn, “On the Role of Nonlinearities in Vibratory Energy Harvesting: A Critical Review and Discussion,” *Appl. Mech. Rev.*, vol. 66, no. 4, p. 040801, 2014, doi: 10.1115/1.4026278.

[19] R. Caliò *et al.*, “Piezoelectric Energy Harvesting Solutions,” *Sensors*, vol. 14, no. 3, pp. 4755–4790, 2014, doi: 10.3390/s140304755.

[20] C. Wong, Z. Dahari, A. Abd, and M. A. Miskam, “Harvesting Raindrop Energy with Piezoelectrics : a Review,” *J. Electron. Mater.*, vol. 44, no. 1, pp. 29–32, 2015, doi: 10.1007/s11664-014-3443-4.

[21] F. K. Shaikh and S. Zeadally, “Energy harvesting in wireless sensor networks: A comprehensive review,” *Renew. Sustain. Energy Rev.*, vol. 55, pp. 1041–1054, 2016, doi: 10.1016/j.rser.2015.11.010.

[22] C. Wei and X. Jing, “A comprehensive review on vibration energy harvesting: Modelling and realization,” *Renew. Sustain. Energy Rev.*, vol. 74, no. January,

pp. 1–18, 2017, doi: 10.1016/j.rser.2017.01.073.

[23] H. Elahi, M. Eugeni, and P. Gaudenzi, “A review on mechanisms for piezoelectric-based energy harvesters,” *Energies*, vol. 11, no. 7, 2018, doi: 10.3390/en11071850.

[24] M. Safaei, H. A. Sodano, and S. R. Anton, “A review of energy harvesting using piezoelectric materials: State-of-the-art a decade later (2008-2018),” *Smart Mater. Struct.*, vol. 28, no. 11, 2019, doi: 10.1088/1361-665X/ab36e4.

[25] H. A. Sodano, D. J. Inman, and G. Park, “A review of power harvesting from vibration using piezoelectric materials,” *Shock Vib. Dig.*, vol. 36, no. 3, pp. 197–205, 2004, doi: 10.1177/0583102404043275.

[26] S. R. Anton and H. A. Sodano, “A review of power harvesting using piezoelectric materials (2003-2006),” *Smart Mater. Struct.*, vol. 16, no. 3, 2007, doi: 10.1088/0964-1726/16/3/R01.

[27] S. Priya, “Advances in energy harvesting using low profile piezoelectric transducers,” *J. Electroceramics*, vol. 19, no. 1, pp. 165–182, 2007, doi: 10.1007/s10832-007-9043-4.

[28] K. A. Cook-Chennault, N. Thambi, and A. M. Sastry, “Powering MEMS portable devices - A review of non-regenerative and regenerative power supply systems with special emphasis on piezoelectric energy harvesting systems,” *Smart Mater. Struct.*, vol. 17, no. 4, 2008, doi: 10.1088/0964-1726/17/4/043001.

[29] H. S. Kim, J. H. Kim, and J. Kim, “A review of piezoelectric energy harvesting based on vibration,” *Int. J. Precis. Eng. Manuf.*, vol. 12, no. 6, pp. 1129–1141, 2011, doi: 10.1007/s12541-011-0151-3.

[30] S. D. Kwon, “A T-shaped piezoelectric cantilever for fluid energy harvesting,” *Appl. Phys. Lett.*, vol. 97, no. 16, pp. 1–4, 2010, doi: 10.1063/1.3503609.

[31] S. Anton and D. Inman, “Vibration energy harvesting for unmanned aerial vehicles,” *... Mater. ...*, vol. 6928, pp. 1–10, 2008, doi: 10.1117/12.774990.

[32] M. Akbar and J. L. Curiel-Sosa, “Piezoelectric energy harvester composite under dynamic bending with implementation to aircraft wingbox structure,” *Compos. Struct.*, vol. 153, pp. 193–203, 2016, doi: 10.1016/j.compstruct.2016.06.010.

[33] Y. Shi, S. R. Hallett, and M. Zhu, "Energy harvesting behaviour for aircraft composites structures using macro-fibre composite: Part I – Integration and experiment," *Composite Structures*, vol. 160. pp. 1279–1286, 2017, doi: 10.1016/j.compstruct.2016.11.037.

[34] D. Lim, S. C. Mantell, P. J. Seiler, and R. Yang, "Wind Turbine Blades as a Strain Energy Source for Energy Harvesting," in *51st AIAA Aerospace Sciences Meeting including the New Horizons Forum and Aerospace Exposition*, 2013, no. January, pp. 1–8.

[35] D.-W. Lim, S. C. Mantell, and P. J. Seiler, "Wireless monitoring algorithm for wind turbine blades using Piezo-electric energy harvesters," *Wind Energy*, vol. 20, no. 3, pp. 551–565, 2017, doi: 10.1002/we.

[36] M. A. Ilyas and J. Swingler, "Piezoelectric energy harvesting from raindrop impacts," *Energy*, vol. 90, pp. 796–806, 2015, doi: 10.1016/j.energy.2015.07.114.

[37] X. D. Xie, Q. Wang, and N. Wu, "Energy harvesting from transverse ocean waves by a piezoelectric plate," *Int. J. Eng. Sci.*, vol. 81, pp. 41–48, 2014, doi: 10.1016/j.ijengsci.2014.04.003.

[38] V. K. Wong, J. H. Ho, and A. B. Chai, "Performance of a piezoelectric energy harvester in actual rain," *Energy*, vol. 124, pp. 364–371, 2017, doi: 10.1016/j.energy.2017.02.015.

[39] M. Wischke, M. Masur, M. Kröner, and P. Woias, "Vibration harvesting in traffic tunnels to power wireless sensor nodes," *Smart Mater. Struct.*, vol. 20, no. 8, 2011, doi: 10.1088/0964-1726/20/8/085014.

[40] S. Cafiso, M. Cuomo, A. Di Graziano, and C. Vecchio, "Experimental Analysis for Piezoelectric Transducers Applications into Roads Pavements," *Adv. Mater. Res.*, vol. 684, no. 11, pp. 253–257, 2013, doi: 10.4028/www.scientific.net/AMR.684.253.

[41] H. Roshani, S. Dessouky, A. Montoya, and A. T. Papagiannakis, "Energy harvesting from asphalt pavement roadways vehicle-induced stresses: A feasibility study," *Appl. Energy*, vol. 182, pp. 210–218, 2016, doi: 10.1016/j.apenergy.2016.08.116.

[42] J. Lee and B. Choi, "Development of a piezoelectric energy harvesting system for implementing wireless sensors on the tires," *Energy Convers. Manag.*, vol. 78, pp. 32–38, 2014, doi: 10.1016/j.enconman.2013.09.054.

[43] X. D. Xie and Q. Wang, "Energy harvesting from a vehicle suspension system," *Energy*, vol. 86, pp. 382–395, 2015, doi: 10.1016/j.energy.2015.04.009.

[44] D. Mauryaab, P. Kumara, S. Khaleghian, and R. Sriramdas, "Energy harvesting and strain sensing in smart tire for next generation autonomous behicles," *Appl. Energy*, vol. 232, pp. 312–322, 2018, doi: .1037//0033-2909.I26.1.78.

[45] C. H. Yang *et al.*, "Feasibility study of impact-based piezoelectric road energy harvester for wireless sensor networks in smart highways," *Sensors Actuators, A Phys.*, vol. 261, pp. 317–324, 2017, doi: 10.1016/j.sna.2017.04.025.

[46] M. Peigney and D. Siegert, "Piezoelectric energy harvesting from traffic-induced bridge vibrations," *Smart Mater. Struct.*, vol. 22, no. 9, p. 095019, 2013, doi: 10.1088/0964-1726/22/9/095019.

[47] F. Duarte, F. Casimiro, D. Correia, R. Mendes, and A. Ferreira, "A new pavement energy harvest system," *Proc. 2013 Int. Renew. Sustain. Energy Conf. IRSEC 2013*, pp. 408–413, 2013, doi: 10.1109/IRSEC.2013.6529704.

[48] S. J. Hwang *et al.*, "Designing and manufacturing a piezoelectric tile for harvesting energy from footsteps," *Curr. Appl. Phys.*, vol. 15, no. 6, pp. 669–674, 2015, doi: 10.1016/j.cap.2015.02.009.

[49] X. Li and V. Strezov, "Modelling piezoelectric energy harvesting potential in an educational building," *Energy Convers. Manag.*, vol. 85, pp. 435–442, 2014, doi: 10.1016/j.enconman.2014.05.096.

[50] Z. Zhang, H. Xiang, and Z. Shi, "Mechanism exploration of piezoelectric energy harvesting from vibration in beams subjected to moving harmonic loads," *Compos. Struct.*, vol. 179, pp. 368–376, 2017, doi: 10.1016/j.compstruct.2017.07.013.

[51] J. Wang, Z. Shi, H. Xiang, and G. Song, "Modeling on energy harvesting from a railway system using piezoelectric transducers," *Smart Mater. Struct.*, vol. 24, no. 10, p. 105017, 2015, doi: 10.1088/0964-1726/24/10/105017.

[52] Y. Amini, M. Heshmati, P. Fatehi, and S. E. Habibi, "Piezoelectric energy harvesting from vibrations of a beam subjected to multi-moving loads," *Appl. Math. Model.*, vol. 49, pp. 1–16, 2017, doi: 10.1016/j.apm.2017.04.043.

[53] Eziwarman, G. L. Forbes, and I. M. Howard, "Experimental power harvesting from a pipe using a macro fiber composite (MFC)," *Adv. Intell. Soft Comput.*,

vol. 144 AISC, no. VOL. 1, pp. 443–449, 2012, doi: 10.1007/978-3-642-28314-7_59.

[54] Z. Zhanga, C. Nib, and X. Zhangc, "Experiment Research on Power Generation Performance of Double Piezoelectric Vibration Energy Harvester," *IOP Conf. Ser. Mater. Sci. Eng.*, vol. 269, no. 1, 2017, doi: 10.1088/1757-899X/269/1/012094.

[55] M. Guan and W. H. Liao, "Design and analysis of a piezoelectric energy harvester for rotational motion system," *Energy Convers. Manag.*, vol. 111, pp. 239–244, 2016, doi: 10.1016/j.enconman.2015.12.061.

[56] A. Garg and S. K. Dwivedy, "Piezoelectric energy harvester under parametric excitation: A theoretical and experimental investigation," *J. Intell. Mater. Syst. Struct.*, vol. 31, no. 4, pp. 612–631, 2020, doi: 10.1177/1045389X19891523.

[57] H. Fu and E. M. Yeatman, "Rotational energy harvesting using bi-stability and frequency up-conversion for low-power sensing applications: Theoretical modelling and experimental validation," *Mechanical Systems and Signal Processing*, vol. 125. pp. 229–244, 2019, doi: 10.1016/j.ymssp.2018.04.043.

[58] X. Wei and J. Liu, "Power sources and electrical recharging strategies for implantable medical devices," *Front. Energy Power Eng. China*, vol. 2, no. 1, pp. 1–13, 2008, doi: 10.1007/s11708-008-0016-3.

[59] R. J. M. Vullers and R. Van Schaijk, "Energy Harvesting for Autonomous Wireless Sensor Ntworks," *IEEE Solid-State Circuits Mag. Spring*, pp. 29–38, 2010.

[60] C. Dagdeviren, Z. Li, and Z. L. Wang, "Energy Harvesting from the Animal-Human Body for Self-Powered Electronics," *Annu. Rev. Biomed. Eng.*, vol. 19, pp. 85–108, 2017, doi: 10.1146/annurev-bioeng-071516-044517.

[61] S. Roundy and S. Trolier-Mckinstry, "Materials and approaches for on-body energy harvesting," *MRS Bull.*, vol. 43, no. 3, pp. 206–213, 2018, doi: 10.1557/mrs.2018.33.

[62] K. Words and I. The, "Human powered piezoelectric batteries to supply power to wearable electronic," *Int. J. Soc. Mater. Eng. Resour.*, vol. 10, no. 1, pp. 34–40, 2002.

[63] F. Invernizzi, S. Dulio, M. Patrini, G. Guizzetti, and P. Mustarelli, "Energy harvesting from human motion: materials and techniques," *Chem. Soc. Rev.*,

vol. 45, no. 20, pp. 5455–5473, 2016, doi: 10.1039/C5CS00812C.

[64] S. R. Platt, S. Farritor, K. Garvin, and H. Haider, "The use of piezoelectric ceramics for electric power generation within orthopedic implants," *IEEE/ASME Trans. Mechatronics*, vol. 10, no. 4, pp. 455–461, 2005, doi: 10.1109/TMECH.2005.852482.

[65] S. R. P. S. R. Platt, S. F. S. Farritor, and H. H. H. Haider, "On low-frequency electric power generation with PZT ceramics," *IEEE/ASME Trans. Mechatronics*, vol. 10, no. 2, pp. 240–252, 2005, doi: 10.1109/TMECH.2005.844704.

[66] K. Fan, B. Yu, Y. Zhu, Z. Liu, and L. Wang, "Scavenging energy from the motion of human lower limbs via a piezoelectric energy harvester," *Int. J. Mod. Phys. B*, vol. 31, p. 1741011, 2017, doi: 10.1142/S0217979217410119.

[67] W. Wang, J. Cao, C. R. Bowen, S. Zhou, and J. Lin, "Optimum resistance analysis and experimental verification of nonlinear piezoelectric energy harvesting from human motions," *Energy*, vol. 118, pp. 221–230, 2017, doi: 10.1016/j.energy.2016.12.035.

[68] A. Delnavaz and J. Voix, "Flexible piezoelectric energy harvesting from jaw movements," *Smart Mater. Struct.*, vol. 23, no. 10, p. 105020, 2014, doi: 10.1088/0964-1726/23/10/105020.

[69] H. Zhang *et al.*, "A flexible and implantable piezoelectric generator harvesting energy from the pulsation of ascending aorta: In vitro and in vivo studies," *Nano Energy*, vol. 12, pp. 296–304, 2015, doi: 10.1016/j.nanoen.2014.12.038.

[70] C. Dagdeviren *et al.*, "Conformal piezoelectric energy harvesting and storage from motions of the heart, lung, and diaphragm," *Proc. Natl. Acad. Sci.*, vol. 111, no. 5, pp. 1927–1932, 2014, doi: 10.1073/pnas.1317233111.

[71] G. T. Hwang *et al.*, "Self-powered cardiac pacemaker enabled by flexible single crystalline PMN-PT piezoelectric energy harvester," *Adv. Mater.*, vol. 26, no. 28, pp. 4880–4887, 2014, doi: 10.1002/adma.201400562.

[72] A. American and N. Standard, "An American National Standard: IEEE Standard on Piezoelectricity," *IEEE Trans. Sonics Ultrason.*, vol. 31, no. 2, pp. 8–10, 1984, doi: 10.1109/T-SU.1984.31464.

[73] S. P. Joshi, "Non-linear constitutive relations for piezoceramic materials," *Smart Mater. Struct.*, vol. 1, no. 1, pp. 80–83, 1992.

[74] Q. M. Wang and L. Eric Gross, "Constitutive equations of symmetrical triple layer piezoelectric benders," *IEEE Trans. Ultrason. Ferroelectr. Freq. Control*, vol. 46, no. 6, pp. 1343–1351, 1999, doi: 10.1109/58.808857.

[75] C. H. Nguyen, U. Hanke, and E. Halvorsen, "The Constitutive Equations of Piezoelectric Layered Beams with Interdigitated Electrodes," *IEEE Trans. Ultrason. Ferroelectr. Freq. Control*, vol. 3010, no. c, pp. 1–15, 2018, doi: 10.1109/TUFFC.2018.2844183.

[76] C. B. Williams and R. B. Yates, "Analysis of a micro-electric generator for microsystems," *Sensors Actuators, A Phys.*, vol. 52, no. 1–3, pp. 8–11, 1996, doi: 10.1016/0924-4247(96)80118-X.

[77] N. E. DuToit, B. L. Wardle, and S. G. Kim, "Design considerations for MEMS-scale piezoelectric mechanical vibration energy harvesters," *Integr. Ferroelectr.*, vol. 71, pp. 121–160, 2005, doi: 10.1080/10584580590964574.

[78] A. Erturk and D. J. Inman, "On mechanical modeling of cantilevered piezoelectric vibration energy harvesters," *J. Intell. Mater. Syst. Struct.*, vol. 19, no. 11, pp. 1311–1325, 2008, doi: 10.1177/1045389X07085639.

[79] Y. C. Shu and I. C. Lien, "Analysis of power output for piezoelectric energy harvesting systems," *Smart Mater. Struct.*, vol. 15, no. 6, pp. 1499–1512, 2006, doi: 10.1088/0964-1726/15/6/001.

[80] L. Luschi, G. Iannaccone, and F. Pieri, "A critical review of reduced one-dimensional beam models of piezoelectric composite beams," *J. Intell. Mater. Syst. Struct.*, vol. 30, no. 8, pp. 1148–1162, 2019, doi: 10.1177/1045389X19828529.

[81] X. Li, W. Y. Shin, I. A. Aksay, and W. H. Shin, "Electromechanical behavior of PZT-brass unimorphs," *J. Am. Ceram. Soc.*, vol. 82, no. 7, pp. 1733–1740, 1999, doi: 10.1111/j.1151-2916.1999.tb01993.x.

[82] N. E. DuToit and B. L. Wardle, "Experimental verification of models for microfabricated piezoelectric vibration energy harvesters," *AIAA J.*, vol. 45, no. 5, pp. 1126–1137, 2007, doi: 10.2514/1.25047.

[83] A. Erturk and D. J. Inman, "Issues in mathematical modeling of piezoelectric energy harvesters," *Smart Mater. Struct.*, vol. 17, no. 6, 2008, doi: 10.1088/0964-1726/17/6/065016.

[84] A. Erturk and D. J. Inman, "A Distributed Parameter Electromechanical Model for Cantilevered Piezoelectric Energy Harvesters," *J. Vib. Acoust.*, vol.

130, no. 4, p. 041002, 2008, doi: 10.1115/1.2890402.

[85] A. Erturk and D. J. Inman, "An experimentally validated bimorph cantilever model for piezoelectric energy harvesting from base excitations," *Smart Mater. Struct.*, vol. 18, no. 2, p. 025009, 2009, doi: 10.1088/0964-1726/18/2/025009.

[86] Y. Liao and H. A. Sodano, "Model of a single mode energy harvester and properties for optimal power generation," *Smart Mater. Struct.*, vol. 17, no. 6, 2008, doi: 10.1088/0964-1726/17/6/065026.

[87] S. Banerjee and S. Roy, "A dimensionally reduced order piezoelectric energy harvester model," *Energy*, vol. 148, pp. 112–122, 2018, doi: 10.1016/j.energy.2018.01.116.

[88] J. Ajitsaria, S. Y. Choe, D. Shen, and D. J. Kim, "Modeling and analysis of a bimorph piezoelectric cantilever beam for voltage generation," *Smart Mater. Struct.*, vol. 16, no. 2, pp. 447–454, 2007, doi: 10.1088/0964-1726/16/2/024.

[89] M. Kim, M. Hoegen, J. Dugundji, and B. L. Wardle, "Modeling and experimental verification of proof mass effects on vibration energy harvester performance," *Smart Mater. Struct.*, vol. 19, no. 4, p. 045023, 2010, doi: 10.1088/0964-1726/19/4/045023.

[90] M. F. Lumentut and I. M. Howard, "Analytical and experimental comparisons of electromechanical vibration response of a piezoelectric bimorph beam for power harvesting," *Mech. Syst. Signal Process.*, vol. 36, no. 1, pp. 66–86, 2013, doi: 10.1016/j.ymssp.2011.07.010.

[91] J. E. Kim, H. Kim, H. Yoon, Y. Y. Kim, and B. D. Youn, "An energy conversion model for cantilevered piezoelectric vibration energy harvesters using only measurable parameters," *Int. J. Precis. Eng. Manuf. - Green Technol.*, vol. 2, no. 1, pp. 51–57, 2015, doi: 10.1007/s40684-015-0007-x.

[92] A. G. A. Muthalif and N. H. D. Nordin, "Optimal piezoelectric beam shape for single and broadband vibration energy harvesting: Modeling, simulation and experimental results," *Mech. Syst. Signal Process.*, vol. 54, pp. 417–426, 2015, doi: 10.1016/j.ymssp.2014.07.014.

[93] X. D. Xie, A. Carpinteri, and Q. Wang, "A theoretical model for a piezoelectric energy harvester with a tapered shape," *Eng. Struct.*, vol. 144, pp. 19–25, 2017, doi: 10.1016/j.engstruct.2017.04.050.

[94] A. S. Kherbeet, H. Salleh, B. H. Salman, and M. Salim, "Vibration-based

piezoelectric micropower generator for power plant wireless monitoring application," *Sustain. Energy Technol. Assessments*, vol. 11, pp. 42–52, 2015, doi: 10.1016/j.seta.2015.05.004.

[95] S. Banerjee and S. Roy, "A Timoshenko like model for piezoelectric energy harvester with shear mode," *Compos. Struct.*, vol. 204, no. December 2017, pp. 677–688, 2018, doi: 10.1016/j.compstruct.2018.07.117.

[96] A. Paknejad, G. Rahimi, A. Farrokhabadi, and M. M. Khatibi, "Analytical solution of piezoelectric energy harvester patch for various thin multilayer composite beams," *Compos. Struct.*, vol. 154, pp. 694–706, 2016, doi: 10.1016/j.compstruct.2016.06.074.

[97] K. F. Wang and B. L. Wang, "An analytical model for nanoscale unimorph piezoelectric energy harvesters with flexoelectric effect," *Compos. Struct.*, vol. 153, pp. 253–261, 2016, doi: 10.1016/j.compstruct.2016.05.104.

[98] M. Mallouli and M. Chouchane, "Piezoelectric energy harvesting using macro fiber composite patches," *Proc. Inst. Mech. Eng. Part C J. Mech. Eng. Sci.*, vol. 234, no. 21, pp. 4331–4349, 2020, doi: 10.1177/0954406220920321.

[99] M. Zhou and H. Zhao, "Revisit to the theoretical analysis of a classical piezoelectric vibration energy harvester," *Arch. Appl. Mech.*, vol. 90, no. 11, pp. 2379–2395, 2020, doi: 10.1007/s00419-020-01727-x.

[100] Z.-Q. Lu, J. Chen, H. Ding, and L.-Q. Chen, "Two-span piezoelectric beam energy harvesting," *Int. J. Mech. Sci.*, vol. 175, 2020.

[101] J. A. Hossack and G. Hayward, "Finite-Element Analysis of 1-3 Composite Transducers," *IEEE Trans. Ultrason. Ferroelectr. Freq. Control*, vol. 38, no. 6, pp. 618–629, 1991, doi: 10.1109/58.108860.

[102] K. Y. Lam, X. Q. Peng, G. R. Liu, and J. N. Reddy, "A finite-element model for piezoelectric composite laminates," *Smart Mater. Struct.*, vol. 6, no. 5, pp. 583–591, 1997, doi: 10.1088/0964-1726/6/5/009.

[103] J. N. Reddy, "On laminated composite plates with integrated sensors and actuators," *Eng. Struct.*, vol. 21, no. 7, pp. 568–593, 1999, doi: 10.1016/S0141-0296(97)00212-5.

[104] M. S. Azzouz, J. S. Bevana, J. J. Rob, and C. Mei, "Finite element modeling of MFC / AFC actuators," *Smart Struct. Mater. 2001 Model. Signal Process. Control Smart Struct.*, vol. 4326, no. September 2001, pp. 376–387, 2001, doi: 10.1106/AGN1-XVKP-DGDB-XMF4.

[105] M. Yaman, "Finite element vibration analysis of a partially covered cantilever beam with concentrated tip mass," *Mater. Des.*, vol. 27, no. 3, pp. 243–250, 2006, doi: 10.1016/j.matdes.2004.10.009.

[106] R. Moradi-Dastjerdi, A. Radhi, and K. Behdinan, "Damped dynamic behavior of an advanced piezoelectric sandwich plate," *Compos. Struct.*, vol. 243, no. March, 2020, doi: 10.1016/j.compstruct.2020.112243.

[107] M. Lezgy-Nazargah, P. Vidal, and O. Polit, "An efficient finite element model for static and dynamic analyses of functionally graded piezoelectric beams," *Compos. Struct.*, vol. 104, pp. 71–84, 2013, doi: 10.1016/j.compstruct.2013.04.010.

[108] C. De Marqui Junior, A. Erturk, and D. J. Inman, "An electromechanical finite element model for piezoelectric energy harvester plates," *J. Sound Vib.*, vol. 327, no. 1–2, pp. 9–25, 2009, doi: 10.1016/j.jsv.2009.05.015.

[109] D. Ballhause, M. D'Ottavio, B. Kröplin, and E. Carrera, "A unified formulation to assess multilayered theories for piezoelectric plates," *Comput. Struct.*, vol. 83, no. 15–16, pp. 1217–1235, 2005, doi: 10.1016/j.compstruc.2004.09.015.

[110] A. Milazzo, "Unified formulation for a family of advanced finite elements for smart multilayered plates," *Mech. Adv. Mater. Struct.*, vol. 23, no. 9, pp. 971–980, 2016, doi: 10.1080/15376494.2015.1121523.

[111] S. Priya, D. Viehland, A. V. Carazo, J. Ryu, and K. Uchino, "High-power resonant measurements of piezoelectric materials: Importance of elastic nonlinearities," *J. Appl. Phys.*, vol. 90, no. 3, pp. 1469–1479, 2001, doi: 10.1063/1.1381046.

[112] A. Abdelkefi, A. H. Nayfeh, and M. R. Hajj, "Effects of nonlinear piezoelectric coupling on energy harvesters under direct excitation," *Nonlinear Dyn.*, vol. 67, no. 2, pp. 1221–1232, 2012, doi: 10.1007/s11071-011-0064-9.

[113] A. Abdelkefi, A. H. Nayfeh, and M. R. Hajj, "Global nonlinear distributed-parameter model of parametrically excited piezoelectric energy harvesters," *Nonlinear Dyn.*, vol. 67, no. 2, pp. 1147–1160, 2012, doi: 10.1007/s11071-011-0059-6.

[114] K. Mam, M. Peigney, and D. Siegert, "Finite strain effects in piezoelectric energy harvesters under direct and parametric excitations," *J. Sound Vib.*, vol. 389, pp. 411–437, 2017, doi: 10.1016/j.jsv.2016.11.022.

[115] P. Firoozy, siamak e Khadem, and s mehrdad Pourkiaee, “Power enhancement of broadband piezoelectric energy harvesting using a proof mass and nonlinearities in curvature and inertia,” *Int. J. Mech. Sci.*, vol. 133, pp. 227–239, 2017, doi: .1037//0033-2909.I26.1.78.

[116] E. S. Leland and P. K. Wright, “Resonance tuning of piezoelectric vibration energy scavenging generators using compressive axial preload,” *Smart Mater. Struct.*, vol. 15, no. 5, pp. 1413–1420, 2006, doi: 10.1088/0964-1726/15/5/030.

[117] Y. H. Shin *et al.*, “Automatic resonance tuning mechanism for ultra-wide bandwidth mechanical energy harvesting,” *Nano Energy*, vol. 77, no. April, p. 104986, 2020, doi: 10.1016/j.nanoen.2020.104986.

[118] X. Wang *et al.*, “A frequency and bandwidth tunable piezoelectric vibration energy harvester using multiple nonlinear techniques,” *Appl. Energy*, vol. 190, pp. 368–375, 2017, doi: 10.1016/j.apenergy.2016.12.168.

[119] S. Bouhedma, Y. Zheng, F. Lange, and D. Hohlfeld, “Magnetic frequency tuning of a multimodal vibration energy harvester,” *Sensors (Switzerland)*, vol. 19, no. 5, 2019, doi: 10.3390/s19051149.

[120] J. Le Scornec, B. Guiffard, R. Seveno, and V. Le Cam, “Frequency tunable, flexible and low cost piezoelectric micro-generator for energy harvesting,” *Sensors Actuators, A Phys.*, vol. 312, p. 112148, 2020, doi: 10.1016/j.sna.2020.112148.

[121] L. Tang and Y. Yang, “A nonlinear piezoelectric energy harvester with magnetic oscillator,” *Appl. Phys. Lett.*, vol. 101, no. 9, 2012, doi: 10.1063/1.4748794.

[122] A. Lei and E. V Thomsen, “Wideband Piezomagnetoelastic Vibration Energy Harvesting,” *J. Phys. Conf. Ser.*, vol. 557, p. 012121, 2014, doi: 10.1088/1742-6596/557/1/012121.

[123] H. Abdelmoula, S. Zimmerman, and A. Abdelkefi, “Accurate modeling, comparative analysis, and performance enhancement of broadband piezoelectric energy harvesters with single and dual magnetic forces,” *Int. J. Non. Linear. Mech.*, vol. 95, no. January, pp. 355–363, 2017, doi: 10.1016/j.ijnonlinmec.2017.07.008.

[124] Shengxi Zou, J. Cao, D. J. Inman, J. Lin, S. Liu, and Z. Wang, “Broadband tristable energy harvester_ Modeling and experiment verification.pdf,” *Appl. Energy*, vol. 133, pp. 33–39, 2014.

[125] H. Fu and E. M. Yeatman, “Rotation energy harvesting using bi stablility and frequnecy up conversion for low power sensing applicati,” *Mech. Syst. Signal Process.*, vol. 125, pp. 229–244, 2019.

[126] C. Wang, Q. Zhang, and W. Wang, “Low-frequency wideband vibration energy harvesting by using frequency up-conversion and quin-stable nonlinearity,” *J. Sound Vib.*, vol. 399, pp. 169–181, 2017, doi: 10.1016/j.jsv.2017.02.048.

[127] H. Liu, C. Lee, T. Kobayashi, C. J. Tay, and C. Quan, “Investigation of a MEMS piezoelectric energy harvester system with a frequency-widened-bandwidth mechanism introduced by mechanical stoppers,” *Smart Mater. Struct.*, vol. 21, no. 3, 2012, doi: 10.1088/0964-1726/21/3/035005.

[128] M. S. M. Soliman, E. M. Abdel-Rahman, E. F. El-Saadany, and R. R. Mansour, “A wideband vibration-based energy harvester,” *J. Micromechanics Microengineering*, vol. 18, no. 11, 2008, doi: 10.1088/0960-1317/18/11/115021.

[129] L. C. Julin Blystad and E. Halvorsen, “A piezoelectric energy harvester with a mechanical end stop on one side,” *Microsyst. Technol.*, vol. 17, no. 4, pp. 505–511, 2011, doi: 10.1007/s00542-010-1163-0.

[130] M. A. Halim and J. Y. Park, “Theoretical modeling and analysis of mechanical impact driven and frequency up-converted piezoelectric energy harvester for low-frequency and wide-bandwidth operation,” *Sensors Actuators, A Phys.*, vol. 208, pp. 56–65, 2014, doi: 10.1016/j.sna.2013.12.033.

[131] S. Liu, Q. Cheng, D. Zhao, and L. Feng, “Theoretical modeling and analysis of two-degree-of-freedom piezoelectric energy harvester with stopper,” *Sensors Actuators, A Phys.*, vol. 245, pp. 97–105, 2016, doi: 10.1016/j.sna.2016.04.060.

[132] H. Hu, L. Tang, R. Das, and P. Marzocca, “A two-degree-of-freedom piezoelectric energy harvester with stoppers for achieving enhanced performance,” *Int. J. Mech. Sci.*, vol. 149, pp. 500–5007, 2018.

[133] X. Li, D. Upadrashta, K. Yu, and Y. Yang, “Analytical modeling and validation of multi-mode piezoelectric energy harvester,” *Mech. Syst. Signal Process.*, vol. 124, pp. 613–631, 2019, doi: 10.1016/j.ymssp.2019.02.003.

[134] M. R. Larkin and Y. Tadesse, “Characterization of a rotary hybrid multimodal energy harvester,” *Act. Passiv. Smart Struct. Integr. Syst. 2014*, vol. 9057, no.

April 2014, p. 90570U, 2014, doi: 10.1117/12.2045271.

[135] S. Qi, R. Shuttleworth, S. O. Oyadiji, and J. Wright, "Design of a multiresonant beam for broadband piezoelectric energy harvesting," *Smart Mater. Struct.*, vol. 19, no. 9, 2010, doi: 10.1088/0964-1726/19/9/094009.

[136] S. M. Shahruz, "Design of mechanical band-pass filters with large frequency bands for energy scavenging," *Mechatronics*, vol. 16, no. 9, pp. 523–531, 2006, doi: 10.1016/j.mechatronics.2006.04.003.

[137] A. Abedini and F. Wang, "Energy harvesting of a frequency up-conversion piezoelectric harvester with controlled impact," *Eur. Phys. J. Spec. Top.*, vol. 228, no. 6, pp. 1459–1474, 2019, doi: 10.1140/epjst/e2019-800211-8.

[138] L. Gu and C. Livermore, "Impact-driven, frequency up-converting coupled vibration energy harvesting device for low frequency operation," *Smart Mater. Struct.*, vol. 20, no. 4, 2011, doi: 10.1088/0964-1726/20/4/045004.

[139] L. Zhao and Y. Yang, "An impact-based broadband aeroelastic energy harvester for concurrent wind and base vibration energy harvesting," *Applied Energy*, vol. 212. pp. 233–243, 2018, doi: 10.1016/j.apenergy.2017.12.042.

[140] M. Su, W. Xu, and Y. Zhang, "Theoretical analysis of piezoelectric energy harvesting system with impact under random excitation," *Int. J. Non. Linear. Mech.*, vol. 119, no. June 2019, 2020, doi: 10.1016/j.ijnonlinmec.2019.103322.

[141] E. Jacquelin, S. Adhikari, and M. I. Friswell, "A piezoelectric device for impact energy harvesting," *Smart Mater. Struct.*, vol. 20, no. 10, p. 105008, 2011, doi: 10.1088/0964-1726/20/10/105008.

[142] M. W. Shafer, M. Bryant, and E. Garcia, "Designing maximum power output into piezoelectric energy harvesters," *Smart Mater. Struct.*, vol. 21, no. 8, 2012, doi: 10.1088/0964-1726/21/10/109601.

[143] J. Dayou, J. Kim, J. Im, L. Zhai, A. T. C. How, and W. Y. H. Liew, "The effects of width reduction on the damping of a cantilever beam and its application in increasing the harvesting power of piezoelectric energy harvester," *Smart Mater. Struct.*, vol. 24, no. 4, p. 045006, 2015, doi: 10.1088/0964-1726/24/4/045006.

[144] D. Shen, H. C. Wikle, S. Y. Choe, and D. J. Kim, "Piezoelectric energy harvesting device in a viscous fluid for high amplitude vibration application," *Appl. Phys. Express*, vol. 1, no. 9, pp. 0980021–0980023, 2008, doi:

10.1143/APEX.1.098002.

[145] R. Elfrink *et al.*, "Vacuum-packaged piezoelectric vibration energy harvesters: Damping contributions and autonomy for a wireless sensor system," *J. Micromechanics Microengineering*, vol. 20, no. 10, 2010, doi: 10.1088/0960-1317/20/10/104001.

[146] W. E. Baker, W. E. Woolam, and D. Young, "Air and internal damping of thin cantilever beams," *Int. J. Mech. Sci.*, vol. 9, pp. 743–766, 1967.

[147] S. H. Crandall, "The role of damping in vibration theory," *J. Sound Vib.*, vol. 11, no. 1, pp. 3–18, 1970, doi: 10.1016/S0022-460X(70)80105-5.

[148] G. M. Sessler, "Piezoelectricity in polyvinylidenefleoride," *J. Acoust. Soc. Am.*, vol. 70, no. 6, pp. 1596–1608, 1981.

[149] R. Fragoudakis, J. A. Gallagher, and V. Kim, "Direct a computational analysis of the energy harvested by GFRP and NFRP laminated beams under cyclic loading," *Procedia Eng.*, vol. 200, pp. 221–228, 2017, doi: 10.1016/j.proeng.2017.07.032.

[150] S. Crossley and S. Kar-Narayan, "Energy harvesting performance of piezoelectric ceramic and polymer nanowires," *Nanotechnology*, vol. 26, no. 34, p. 344001, 2015, doi: 10.1088/0957-4484/26/34/344001.

[151] Y. Sun, Jianguo Chen, X. Li, Y. Lu, S. Zhang, and Z. Cheng, "Flexible piezoelectric energy harvester/sensor with high voltage output over wide temperature range," *Nano Energy*, vol. 61, pp. 337–345, 2019.

[152] S. Bodkhe, G. Turcot, F. P. Gosselin, and D. Therriault, "One-Step Solvent Evaporation-Assisted 3D Printing of Piezoelectric PVDF Nanocomposite Structures," *ACS Appl. Mater. Interfaces*, vol. 9, no. 24, pp. 20833–20842, 2017, doi: 10.1021/acsami.7b04095.

[153] S. Bairagi, S. Ghosh, and S. W. Ali, "A fully sustainable, self-poled, bio-waste based piezoelectric nanogenerator: electricity generation from pomelo fruit membrane," *Sci. Rep.*, vol. 10, no. 1, pp. 1–13, 2020, doi: 10.1038/s41598-020-68751-3.

[154] X. Lin, H. Chen, Y. Ma, J. G. Fisher, S. Huang, and D. Zhang, "Investigation of temperature sensitivity of actuation performance for piezoelectric fi ber composites," *Ceram. Int.*, vol. 43, no. 13, pp. 10590–10594, 2017, doi: 10.1016/j.ceramint.2017.04.172.

[155] Z. Butt and R. A. Pasha, "Effect of temperature and loading on output voltage of lead zirconate titanate ( PZT-5A ) piezoelectric energy harvester," in *IOP Conference Series: Materials Science and Engineering 146*, 2016, p. 012016, doi: 10.1088/1757-899X/146/1/012016.

[156] R.Salazar, M. Serrano, and A.Abdelkefi, "Fatigue in piezoelectric ceramic vibrational energy harvesting A review," *Appl. Energy*, vol. 270, p. 115161, 2020.

[157] P. Pillatsch, B. L. Xiao, N. Shashoua, H. M. Gramling, E. M. Yeatman, and P. K. Wright, "Degradation of bimorph piezoelectric bending beams in energy harvesting applications," *Smart Mater. Struct.*, vol. 26, no. 3, 2017, doi: 10.1088/1361-665X/aa5a5d.

[158] M. Peddigari *et al.*, "A comparison study of fatigue behavior of hard and soft piezoelectric single crystal macro-fiber composites for vibration energy harvesting," *Sensors (Switzerland)*, vol. 19, no. 9, pp. 1–11, 2019, doi: 10.3390/s19092196.

[159] D. Upadrashta and Y. Yang, "Experimental investigation of performance reliability of macro fiber composite for piezoelectric energy harvesting applications," *Sensors Actuators, A Phys.*, vol. 244, pp. 223–232, 2016, doi: 10.1016/j.sna.2016.04.043.

[160] J. Hirst, J. Wang, M. R. A. Nabawy, and A. Cioncolini, "Long-term power degradation testing of piezoelectric vibration energy harvesters for low-frequency applications," *Eng. Res. Express*, vol. 2, no. 3, 2020, doi: 10.1088/2631-8695/abaf09.

[161] M. Khazaee, A. Rezania, and L. Rosendahl, "Effect of damage and support damping mechanisms on unimorph piezoelectric energy harvester," *J. Vib. Control*, no. May, p. 107754631985516, 2019, doi: 10.1177/1077546319855162.

[162] M. Khazaee, A. Rezania, and L. Rosendahl, "An experimental study to determine damping of piezoelectric harvesters using transient analysis of unified electromechanical voltage equation," *Energy Convers. Manag.*, vol. 227, no. July 2020, p. 113567, 2021, doi: 10.1016/j.enconman.2020.113567.

[163] M. Khazaee, A. Rezaniakolaei, and L. Rosendahl, "A comprehensive electromechanically coupled model for non-uniform piezoelectric energy harvesting composite laminates," *Mech. Syst. Signal Process.*, vol. 145, no. November-December, p. 106927, 2020.

[164] M. Khazaee, A. Rezaniakolaei, and L. Rosendahl, “A broadband Macro-Fiber-Composite piezoelectric energy harvester for higher energy conversion from practical wideband vibrations,” *Nano Energy*, vol. 76, no. October 2020, p. 104978, 2020.

[165] A. Erturk and D. J. Inman, “An experimentally validated bimorph cantilever model for piezoelectric energy harvesting from base excitations,” *Smart Mater. Struct.*, vol. 18, no. 2, p. 025009, 2009, doi: 10.1088/0964-1726/18/2/025009.

[166] J. He and Z.-F. Fu, *Modal analysis*, 1st ed. Butterworth-Heinemann, 2001.

[167] J. W. Yi, W. Y. Shih, and W. H. Shih, “Effect of length, width, and mode on the mass detection sensitivity of piezoelectric unimorph cantilevers,” *J. Appl. Phys.*, vol. 91, no. 3, pp. 1680–1686, 2002, doi: 10.1063/1.1427403.

[168] S. Timoshenko, *Vibration problems in engineering*, 2nd ed. D. Van Nostrand Company, Inc., 1937.

[169] D. Young and R. P. Felgar, “Tables of characteristic functions representing normal modes of vibration of a beam,” *University of Texas Engineering Research series*, vol. 44. pp. 1–31, 1949, [Online]. Available: http://scholar.google.com/scholar?hl=en&btnG=Search&q=intitle:Tables+of+characteristic+functions+representing+normal+modes+of+vibration+of+a+beam#0.

[170] I. Neri, F. Travasso, R. Mincigrucci, H. Vocca, F. Orfei, and L. Gammaitoni, “A real vibration database for kinetic energy harvesting application,” *J. Intell. Mater. Syst. Struct.*, vol. 23, no. 18, pp. 2095–2101, 2012, doi: 10.1177/1045389X12444488.

[171] D.J.Ewins, *Modal Testing : Theory , Practice and Application*, Second. RSP, 2000.

[172] R. M. Jones, *Mechanics of composite materials*, 2nd ed. Philadelphia: Taylor & Francis, 2010.

[173] A. Deraemaeker, H. Nasser, A. Benjeddou, and A. Preumont, “Mixing rules for the piezoelectric properties of macro fiber composites,” *J. Intell. Mater. Syst. Struct.*, vol. 20, no. 12, pp. 1475–1482, 2009, doi: 10.1177/1045389X09335615.

[174] “Smart Material Inc.,” *April*, 2020. .

[175] R. B. Williams and D. J. Inman, “Nonlinear Mechanical and Actuation Characterization of Piezoceramic Fiber Composites,” Virginia Polytechnic, 2004.

[176] M. Khazaee, A. Rezaniakolaei, and L. Rosendahl, “On the effect of driving amplitude, frequency and frequency-amplitude interaction on piezoelectric generated power for MFC unimorph,” *Proc. 26th Int. Congr. Sound Vib. ICSV 2019*, pp. 1–7, 2019.

[177] M. Khazaee, A. Rezania, and L. Rosendahl, “Power generation from a DC motor at defect-free and misaligned shaft conditions by piezoelectric energy harvester attached to the shaft bearing,” *To be Submitt.*

[178] Y. Hong, L. Sui, M. Zhang, and G. Shi, “Theoretical analysis and experimental study of the effect of the neutral plane of a composite piezoelectric cantilever,” *Energy Convers. Manag.*, vol. 171, no. June, pp. 1020–1029, 2018, doi: 10.1016/j.enconman.2018.06.045.

[179] S. Roundy, P. K. Wright, and J. M. Rabaey, *Energy scavenging for wireless sensor networks*, 1st ed. Springer Science, 2004.

[180] G. A. Papagiannopoulos and G. D. Hatzigeorgiou, “On the use of the half-power bandwidth method to estimate damping in building structures,” *Soil Dyn. Earthq. Eng.*, vol. 31, no. 7, pp. 1075–1079, 2011, doi: 10.1016/j.soildyn.2011.02.007.

[181] M. Khazaee, A. S. Nobari, and M. H. F. Aliabadi, “Experimental Investigation of Delamination Effects on Modal Damping of a CFRP Laminate, Using a Statistical Rationalization Approach,” in *Computational and Experimental Methods in Structures*, vol. 10, 2018, pp. 75–103.

[182] O. P. Hentschel, L. P. Von Scheidt, J. Wallaschek, and M. Denk, “Introduction and evaluation of a damping determination method based on the Short-Term fourier transform and Resampling (STFR),” *J. Theor. Appl. Mech.*, vol. 53, no. 2, pp. 439–452, 2015, doi: 10.15632/jtam-pl.53.2.395.

[183] H. T. Banks and D. J. Inman, “On damping mechanisms in beams,” *J. Appl. Mech. Trans. ASME*, vol. 58, no. 3, pp. 716–723, 1991, doi: 10.1115/1.2897253.

[184] W. E. Woolam, “Drag coefficients for flat square plates oscillating normal to their planes in air,” Langley Research Center, 1972.

[185] B. J. Lazan, “Material and structural damping for vibration control,” *SAE*

*Tech. Pap.*, vol. 68, no. 1960, pp. 537–547, 1960, doi: 10.4271/600055.

[186] M. Khazaee, A. Rezaniakolaei, and L. Rosendahl, "A proof for looking differently into damping modeling in piezoelectric energy harvesting systems," in *Proceedings of the 26th International Congress on Sound and Vibration, ICSV 2019*, 2019, pp. 1–8.

[187] M. Khazaee, A. Rezania, and L. Rosendahl, "An optimum practical piezoelectric energy-harvesting device for energy scavenging from car vibration," in *To be submitted*.

[188] A. Moosavian, M. Khazaee, H. Ahmadi, M. Khazaee, and G. Najafi, "Fault diagnosis and classification of water pump using adaptive neuro-fuzzy inference system based on vibration signals," *Struct. Heal. Monit.*, vol. 14, no. 5, pp. 402–410, 2015, doi: 10.1177/1475921715591873.

[189] S.-W. Kim *et al.*, "Determination of the appropriate piezoelectric materials for various types of piezoelectric energy harvesters with high output power," *Nano Energy*, vol. 57, pp. 581–591, 2019.

# APPENDICES

# Appendix A. Paper 1: Reference [161]

## Effect of damage and support damping mechanisms on unimorph piezoelectric energy harvester

M. Khazaee, A. Rezaniakolaei, L. Rosendahl

This paper has been published in

*Journal of Vibration and Control*, vol. 25, no. 7, pp. 2409-2422, 2019

Article

Journal of Vibration and Control
2019, Vol. 25(18) 2409–2422

DOI: 10.1177/1077546319855162
journals.sagepub.com/home/jvc
SAGE

# Effect of damage and support damping mechanisms on unimorph piezoelectric energy harvester

**Majid Khazaee, Alireza Rezania and Lasse Rosendahl**

**Abstract**

Damping plays a critical role in power generation by piezoelectric energy harvesting, and yet there is a lack of sensitivity studies on different sources of damping. In this paper, two damping sources in unimorph piezoelectric energy harvesters, namely support loss and damage damping mechanisms, are experimentally investigated. Variations of the power generation are evaluated with respect to the sources of damping. Accordingly, the power generation model is developed according to the experimental results in this work and using a single degree of freedom analytical model. This study focuses on the debonding effect, as an internal damping source, and support loss, as a critical source of external energy dissipation. The results show that the debonding reduces the output power dramatically at resonance and, particularly, at anti-resonance frequencies. Moreover, investigation of the support loss shows that the material of clamp as well as installation torque have an impact on the support loss and, consequently, affect the output power.

**Keywords**

Piezoelectric energy harvesting, unimorph, damping effect, debonding effect, support loss

## 1. Introduction

With the recent developments in electronics, for example, the decrease in power consumption (Khaligh et al., 2010), low power energy harvesting from thermal and kinetic sources of energy is being widely considered as an essential tool to introduce self-powered devices for elaborating system abilities in terms of life time and accessibility of remote systems (Ahmed et al., 2017). Furthermore, energy harvesting systems can be manufactured using additive manufacturing techniques (Mortazavinatanzi et al., 2018) for flexible ink-based nonflat surfaces (Qing et al., 2018; PiezeTech Arkema Group, n.d.). Among the energy harvesting mechanisms, piezoelectric energy harvesters (PEHs) have drawn much attention due to structure simplicity and ease of integration into the host structure (Khazaee et al., 2019). Piezoelectric materials can be grouped into three types: ceramic; polymer; and composite (Ahmed et al., 2017). Macro-fiber composite (MFC) with ceramic fibers is a composite material with excellent electromechanical properties of ceramics as well as polymeric flexibility (Khazaee et al., 2019), that makes it an ideal material for long-endurance kinetic energy harvesting.

Unimorph geometry is one of the most widely used configuration for PEHs (Li et al., 2014), in which one piezoelectric layer is bonded into a nonpiezoelectric substrate shim with clamped-free boundary condition. A number of researchers used MFC materials for PEH in unimorph configuration (Sodano et al., 2006; Erturk et al., 2008; Shan et al., 2015; Khazaee et al., 2019). Shan et al. (2015) used a bonded beam from MFC and polyvinyl chloride layers in the clamp-free boundary condition. The beam was subjected to water vertexes induced from an upstream cylinder for PEH and obtained a maximum output power of 1.32 μW. Moreover, by an experimental study. Sodano et al. (2006) compared the maximum instantaneous power of three types of materials in unimorph geometry, including the MFC material, over 12 bending modes and obtained 11.714 μW at third bending mode.

Department of Energy Technology, Aalborg University, Denmark

Received: 24 December 2018; accepted: 11 May 2019

**Corresponding author:**
Alireza Rezania, Department of Energy Technology, Aalborg University, Pontoppidanstræde 111, Aalborg East 9220, Denmark.
Email: alr@et.aau.dk

Obtaining maximum power from vibration sources is the main research subject within PEHs. Reddy et al. (2016) introduced a cavity inside the substrate beam in order to enhance harvested power from PEHs. In the context of power estimation, it is a well-known fact that damping has a critical role on the output power by PEHs (Roundy et al., 2003). Four factors contribute into energy dissipation of unimorph PEHs, namely energy dissipation from air resistance force, squeeze force, internal energy dissipation, and support loss (Hosaka et al., 1995).

Internal energy dissipation in composite structures is a parameter influenced by five factors, namely matrix or fiber viscoelasticity, interphase, damage, viscoplastic, and thermoelastic (Chandra et al., 1999; Bhattacharjee and Nanda, 2018). In almost all numerical and experimental studies on PEHs, a perfect bonding has been assumed, while adhesion loss or debonding due to the aging or improper manufacturing process is a major concern about adhesive joints (Pazand and Nobari, 2017). Saravanos and Hopkins (1996) showed that delamination cracks between layers of a composite beam increases modal damping of the beam. Although debonding can have a substantial effect on damping (Khazaee et al., 2018) and consequently will change the PEH power dramatically, there is currently no investigation on the effect of this damage on the output power.

Support loss, also called clamping loss, is the energy dissipated from a vibrating structure through its support. As the structure undergoes flexural vibration, it excites its support both by shear and moment forces causing elastic wave propagating into the support, which consequently leads to energy absorption by the support (Hao et al., 2003). Chen et al. (2017) looked at the support loss in micro-electromechanical systems and introduced it as the inverse of quality factor, which can be obtained through elastic wave propagation through the support. Although all the cantilever clamps are created by screw joints, the studies by Hao et al. (2003) and Chen et al. (2017) did not consider the effect of joint characteristics on the support loss. If the joints are used to provide clamps, then friction regions due to the bolted joints may cause slipping, which is a source of damping (Goyder, 2018). An important source of energy dissipation in bolted joints is joint tightness. High clamping pressure produces greater penetration forces (Ibrahim and Pettit, 2005). Since unimorph geometry is built by clamping the piezoelectric harvester with the screw, any source of energy dissipation in the clamps, including joint tightness, should be considered for investigation of power generation by a piezoelectric layer.

Within the energy harvesting research area, which is highly dependent on the different aspects of vibrational characteristics of the device, there is a lack of studies investigating the dependency of the power to vibrational features within the system such as damage and support damping mechanisms. Thus, in this paper a series of experimental studies are carried out to investigate the effect of debonding, as one of the regular defects in adhesive layers, and support loss on output power of a composite beam with MFC piezoelectric layer. In addition, using a single degree of freedom method, change of the power with respect to debonding and support loss is modeled as the damping variation within the system.

## 2. A modeling technique for unimorph harvester

There are various techniques for modeling of PEHs ranging from simple one degree of freedom (1D) to two-dimensional multi degree of freedom methods. While 1D methods require fewer parameters to model the system, other methods require more parameters to be defined and are computationally time consuming. Moreover, as proposed by Erturk and Inman (2008), a 1D method that considers electro-mechanical coupling can be a suitable method for assessment behavior of piezoelectric harvesters. 1D methods were previously used for studying PEHs (Roundy et al., 2003; DuToit et al., 2005; DuToit and Wardle, 2007). In this study, the experimental data and analytical model are correlated to obtain the damping coefficient in many case studies in order to keep the model as simple as possible but still accurate. Hence, a 1D model with electro-mechanical coupling is created in a suitable form for the investigation by elaborating the damping coefficient in this model. In the result section, the accuracy of the model is presented to predict the experimental data. Figure 1 presents the schematic of the model, which comprises a piezoelectric mass with internal resistance of $R_p$, and a proof mass simply connected to a load resistor, $R_l$. This model is valid for the case in which there is no substrate shim. In order to comprise the effect of the substrate, a coefficient, $\alpha_m$, which is the proportion of piezoelectric mass to device mass, is added. Therefore, the equations of motion for a piezoelectric harvester with the substrate and piezoelectric layer can be shown as (DuToit et al., 2005)

$$\ddot{x}(t) + 2\zeta_m\omega_n\dot{x}(t) + \omega_n^2 x(t) - \alpha_m\omega_n^2 d_{31} V_p(t) = -\ddot{x}_B(t) \quad (1)$$

$$R_{eq}C_p\dot{V}_p(t) + V_p(t) + m_{eff}R_{eq}d_{31}\omega_n^2\dot{x}(t) = 0 \quad (2)$$

where $\ddot{x}_B$ [m/s$^2$] is the base excitation acceleration, $x$ [m] is the relative displacement of harvester tip in respect to the base, $\omega_n$ [1/rad] is the undamped natural frequency of harvester defined as $\sqrt{k/m_b}$, $\zeta_m$ is the

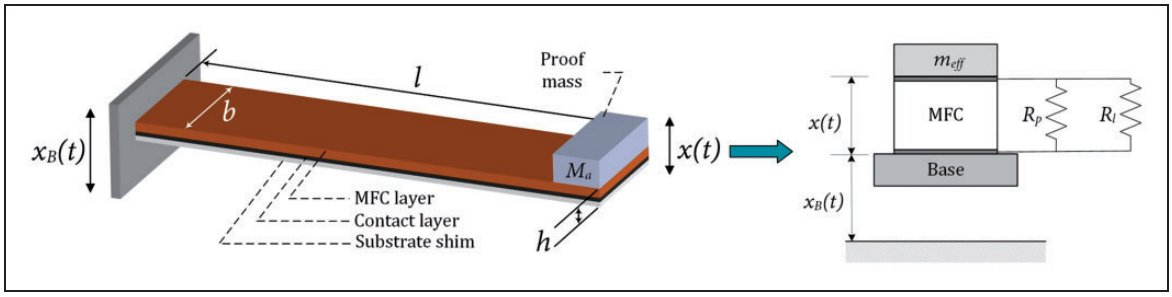


**Figure 1.** Single degree of freedom electromechanical model (DuToit et al., 2005).

mechanical viscous damping ratio, $V_p$ [V] is the output voltage, and $m_{eff} = M_a + m_p/3$ [kg] (DuToit et al., 2005) is the effective mass of piezoelectric layer contributed to shunt damping effect. The overhead dot indicates the time derivative. In addition, $d_{31}$ [C/N] is the piezoelectric coupling coefficient in 3−1 mode, $R_{eq}$ [Ω] is the equivalent electric resistance, $C_p$ is the capacitance of the piezoelectric coupling. The capacitance is defined in terms of dielectric constant $K$, the permittivity of free space ($\varepsilon_0 = 8.9$ nF/m), piezoelectric area $A_p$ [m$^2$] and thickness $t_p$ [m] with $C_p = K\,\varepsilon_0\,A_p/t_p$.

If the base excitation is assumed to be harmonic, $\ddot{x}_B(t) = \bar{X}_B e^{j\omega t}$, then the displacement and voltage will be a harmonic function with the same frequency but with different phase, for example, $V_p(t) = \overline{V}_p e^{j\omega t+\varphi}$ and $x(t) = \bar{X} e^{j\omega t+\varphi}$. By defining magnitude of power to be $\bar{P}_{out} = \left(\overline{V_p}\right)^2/R_{eq}$, it can be expressed as (DuToit et al., 2005)

$$\left|\frac{\bar{P}_{out}}{\bar{X}_B}\right| = \frac{(1/\omega_n) m_{eff} r\, k_e^2 \left(R_{eq}/R_l\right)_{31} \Omega^2}{\sqrt{\left[\left(1-(1+2r\zeta_m)\Omega^2\right)^2 + \left((2\zeta_m\Omega) + \left(r\Omega - r\Omega^3\right) + \alpha_m r k_e^2 \Omega\right)^2\right]}} \quad (3)$$

where $r = R_{eq}\omega_n C_p$ is dimensionless resistance term, $\Omega = \omega/\omega_n$ is dimensionless frequency, and $k_e$ is the electromechanical coupling factor defined with $k_e^2 = k_{31}^2/\left(1-k_{31}^2\right)$. As can be seen in equation (3), as well as physical properties of the piezoelectric harvester, the output voltage depends on load resistance and excitation frequency for a given excitation magnitude. The output power from the piezoelectric harvester is maximum at an optimum load resistance called optimum load, $R_{opt}$. Moreover, plotting the maximum power at short-circuit and open-circuit conditions versus the frequency shows that two frequencies, called short-circuit, $\omega_{sc}$, and open-circuit resonant frequencies, $\omega_{oc}$, respectively, are assigned to the maximum power. According to these values, one can calculate the electromechanical coupling factor,$k_e$, of the piezoelectric harvester with $k_e^2 = \sqrt{(\omega_{oc}/\omega_{sc})^2 - 1}$.

The presented model is a simple 1D model. However, because the output power obtained by this method is expressed in terms of coefficients obtained experimentally, see equation (3), the model presents accurate data compared to the experimental data, as shown in DuToit and Wardle (2007). For instance, $\omega_n$ can be obtained through experimental tests. By evaluating $\omega_{oc}$ and $\omega_{sc}$ through measurements of the power over a wide frequency range, $k_e$ can be calculated. However, the damping coefficient needs to be investigated. The analytical model is assigned a single coefficient, for example, $\zeta_m$, for considering energy dissipation in the energy harvesting system in the cantilever configuration. This study aims to capture the effects of two sources of damping mechanisms, for example, damage damping and support loss, which have different natures. Thus, to make the damping model closer to the actual one, all sources of energy dissipation in the system are identified, and all the other damping mechanisms are evaluated analytically while the damage and support loss damping are extracted according to the measurements.

The energy dissipation consists of internal energy dissipation, fluid-structural viscous damping and support loss due to the cantilever boundary condition. For the case of the debonded sample, a damaged damping term is considered. The sources of energy dissipation are shown in Figure 2. Thus, $\zeta_m$ can be expressed by equation (4)

$$\zeta_m = \zeta_{Structural} + \zeta_{Fluid\text{-}Structure} + \zeta_{Support} + \zeta_{Damage} \quad (4)$$

The fluid-structural damping, $\zeta_{Fluid\text{-}Structure}$, is due to airflow force by vibration of beam in free air and squeeze force by airstream from the near fixed boundary wall. Internal energy dissipation, $\zeta_{Structural}$, is the energy dissipated inside the material, which is an energy dissipation source inside the beam. Calculation of the fluid-structural damping terms are straightforward as analytical formulas were reported, such as in Hosaka et al. (1995). These authors estimated the resistance force against beam transverse vibration induced

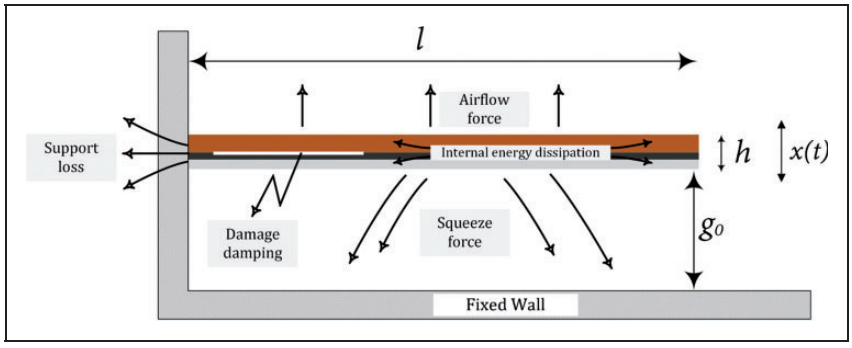


**Figure 2.** Different sources of energy dissipation considered in this study.

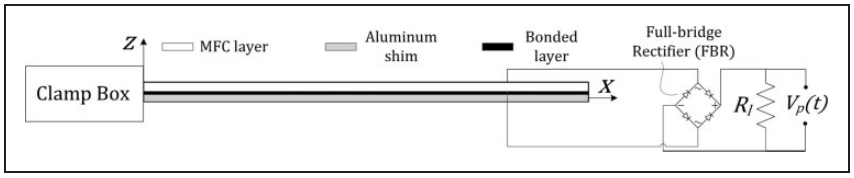


**Figure 3.** Piezoelectric energy harvester configuration.

from the surrounded fluid. On the other hand, damage ($\zeta_{Damage}$) and support loss ($\zeta_{Support}$) mechanisms are difficult to deal with and are often measured with experimental data. In the current research, fluid-structural and internal energy dissipation mechanisms are calculated according to analytical expressions in equation (5) (Hosaka et al., 1995), and the support loss and damage damping mechanisms are evaluated based on experimental data

$$\zeta_{Fluid\text{-}Structure} = \frac{\mu b^2}{2\rho_b g_0^3 h\omega_n} + \frac{\frac{3}{4}\pi b^2\sqrt{2\rho_{air}\mu\omega_n}}{2\rho_b hbl\omega_n} \qquad \zeta_{Structural} = \eta/2 \tag{5}$$

where $\mu$ and $\rho_{air}$ are dynamic viscosity and density of air. In addition, $g_0$ is distance between the fixed wall and beam outer surface as shown in Figure 2 and $\eta$ is the structural damping coefficient. In this study a value of $0.5 \times 10^{-6}$ is considered for $\eta$ (Blom et al., 1992).

Due to the presence of damping in the equation for output power, equation (3), damping will have a significant effect on the output power in a unimorph energy harvester. This work aims to investigate the effect of changing the damping coefficient, $\zeta_m$, through debonding and the support tightness, on the output power while four damping mechanisms are considered (see equation (4)). In Section 4, the support loss damping is evaluated from the defect-free state, which can be used for the debonded state to evaluate the actual damage damping.

## 3. Experimental procedure

The effects of the debonding and support loss on the output power were investigated through experiments. The experiments were carried out with piezoelectric samples in unimorph geometry. The piezoelectric samples were clamped with a clamp box on one end. Then, they were excited with a magnetic vibration shaker by sinusoidal input signal, where their response in terms of output voltage and current were recorded. Figure 3 shows the configuration of the PEHs throughout the study.

The piezoelectric layer is an MFC with elastic modulus of 30.336 GPa and 15.857 GPa in x- and y-directions, respectively, and Poisson's ratios of 0.31 in xy and 0.16 in yx and shear modulus of 5.515 GPa. Thickness of the MFC is 0.30 mm while the thickness of the lead zirconate titanate fibers are 190 μm with a density of active area of 5.44 g/cm$^3$. The electromechanical properties of the piezoelectric layer are $d_{33} = 460$ pC/N, and $d_{31} = -210$ pC/N. The center shim is made of aluminum with thickness of 0.12 mm, elastic modulus of 68.9 GPa, and density of 2.7 g/cm$^3$. The piezoelectric layer is bonded to the center shim with epoxy rapid 332 adhesive with density of 1.16 g/cm$^3$. For investigation of the debonding effects in Section 4, thickness of the bond layer in perfect and poorly cured bond conditions are 400 and 189 $\mu$m, respectively. In Section 5, where effect of the support loss damping is investigated, the bond layer thickness is equal to 245 μm.

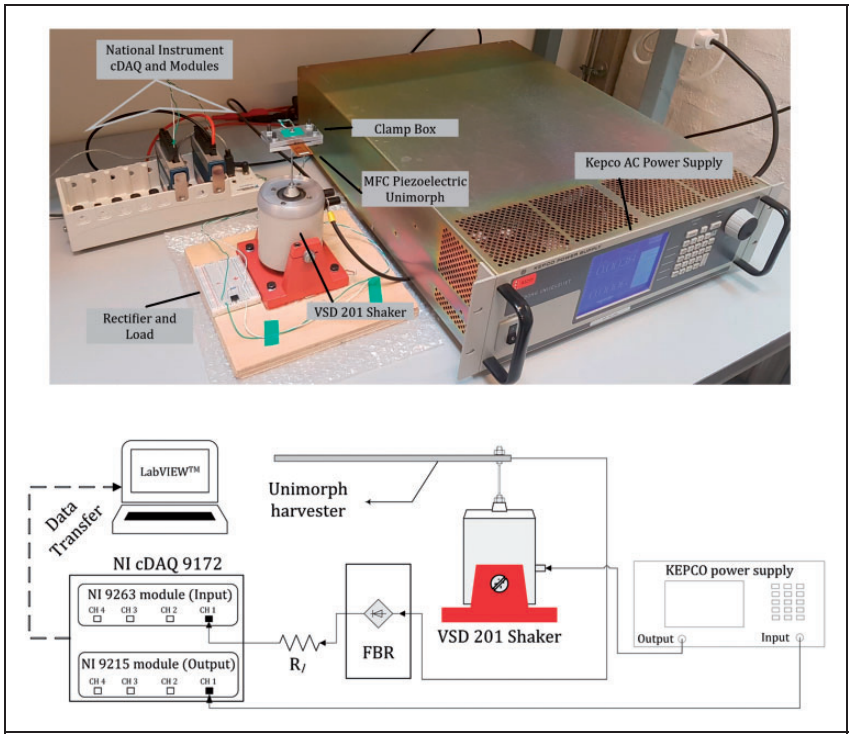


**Figure 4.** Setup for measuring voltage output.

The aforementioned unimorph energy harvester is excited with a VSD 201 Shaker while its input voltage and electrical power are measured. Signal generation and data recording were carried out with National Instrument modules. For signal generation, NI 9263 module, a 4-channel ± 10 V 16-Bit Analog Voltage Output, which is adjusted by LabVIEW™ 2013 is connected to a Kepco AC power generation and the output from Kepco power supply is wired to the shaker. A NI 9215 module with 4-channel ± 10 V 16-Bit Analog Voltage Input is used for recording the voltage output of the piezoelectric harvester. A National Instrument Compact data acquisition system (cDAQ) type 9172 is used as the medium between the modules and experimental components, for example, the shaker and piezoelectric samples. Figure 4 shows the experimental setup.

## 4. Debonding effects

During the model derivation for the PEH from vibration, mostly cantilever configuration is considered with the perfect bonding between piezoelectric and metal substrate. In practice, the perfect bonding assumption may be degraded over time during operation or during the manufacturing process in the first stage (Pazand and Nobari, 2017). In particular, as the loading condition is dynamic and the harvester mostly vibrates close to its fundamental natural frequency, it is likely to observe debonding between the substrate and the piezoelectric layer. The debonding might have two influences on the output power. An obvious effect is that it prevents the vibration of a part of the energy harvester, so it will reduce the active area for power generation. Moreover, the debonding may increase the damping ratio of the device, which results in less power generation. This increment in the damping depends on the vibration mode (Khazaee et al., 2018). In this section, an experimental verification of the debonding effect on the output power is presented.

Two samples are tested with the same length and width, each consisting of a 0.3 mm thickness MFC piezoelectric layer. The samples are bonded to an aluminum substrate with 0.12 mm thickness by epoxy rapid 332 adhesive. Figure 5 shows the pristine and debonded samples with capacitance of $C_p = 177.07\,nF/m$ for an active length of 85 mm. The piezoelectric harvester is connected to a 31500-Ω resistance load. The unimorph is excited over a frequency range of 5 to 100 Hz with 1 Hz frequency step with the same excitation amplitude. Three replications are used to show the repeatability of tests.

As can be interpreted from Figure 5, thickness of the adhesive layer for one sample was considered 211 μm less than the other sample to make it vulnerable to debonding due to inappropriate debonding thickness. Then, the sample was excited by the shaker on its natural frequency until a debonding area is initiated and developed. It is worth mentioning that after initiation of the debonding, the propagation was quick.

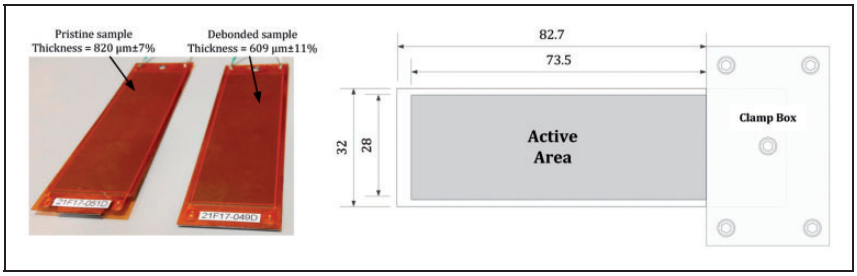


**Figure 5.** Macro-fiber composite pristine and debonded dimensions and unimorph configuration with clamp box screws.

The samples were scanned using Acoustic Microscope KSI V8 from the aluminum substrate and from MFC layer down to the other front side to find out the layers within them in which debonding occurred. Figure 6 shows the Acoustic Microscope KSI V8 for scanning the samples from the aluminum side.

Figure 7 shows the scanned pictures of the samples in depth with ultrasonic waves. Areas with different colors in Figure 7 represent the regions with different densities. In order to recognize debonding regions, similar regions with different colors should be observed at different depth levels. It has been observed that, the debonding was initiated between aluminum shim and adhesive layer, as the color scattering in the surface can be seen from Figure 7 (b)–(c). Since the dark color regions exist at different depths, from Figure 7 (a)–(e), this area is the likelihood-debonding region. This region is marked with a white box in Figure 6. In addition, there are two regions with distinctive colors in Figure 7 (e)–(f) on the pristine sample, which based on thickness measurements is found to be the result of higher density of adhesive in these regions.

Figure 8 shows the frequency spectrum of root mean square (RMS) of the power generation for three replications. Firstly, the results obtained from the duplications are identical, showing that the experiments are repeatable. As it can be seen from the frequency spectrum, there are two peaks for the output power at frequencies of 30 Hz and 49 Hz. The first peak frequency is related to the device fundamental bending natural frequency, while the second peak is a result of the anti-resonance frequency of the device. Anti-resonance frequency is the result of electromechanical coupling. At this frequency, the voltage and current are considerably different from resonance frequency even though the power is similar (DuToit et al., 2005).

The debonding reduces the active area in the device, which is an important factor in the power generation, and it increases the internal structural. Figure 9 shows the output power from the pristine and debonded samples as a function of frequency. Table 1 shows the variation of peak frequencies and output power between pristine and debonded samples. The debonding reduces

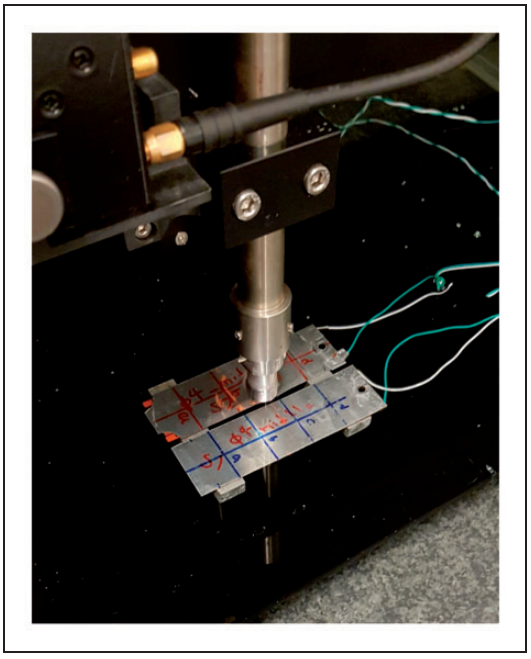

**Figure 6.** Pristine and debonded samples scanned with Acoustic Microscope KSI V8.

the device stiffness and, hence, decreases the resonance and anti-resonance frequencies by 23% and 18%, respectively. Reductions in the peak frequencies are in the same order, showing the stiffness reduction of the beam. Moreover, the presence of the debonding area causes a dramatic reduction in the output power at resonance and anti-resonance frequencies. There are two reasons for reduction of the power generation due to the debonding: reduction of the active area; and increment in the damage damping. To measure the real debonding area, the debonded sample is exploited and the debonding region is marked, as shown in Figure 10. The debonding area is measured to be 15% of the active area. If a uniform generation of power is assigned to the whole area, 15% active area reduction will reduce output power by 15%. Hence, the rest of the power reduction is due to increment of the damage damping. In addition, it can be noted from Figure 9

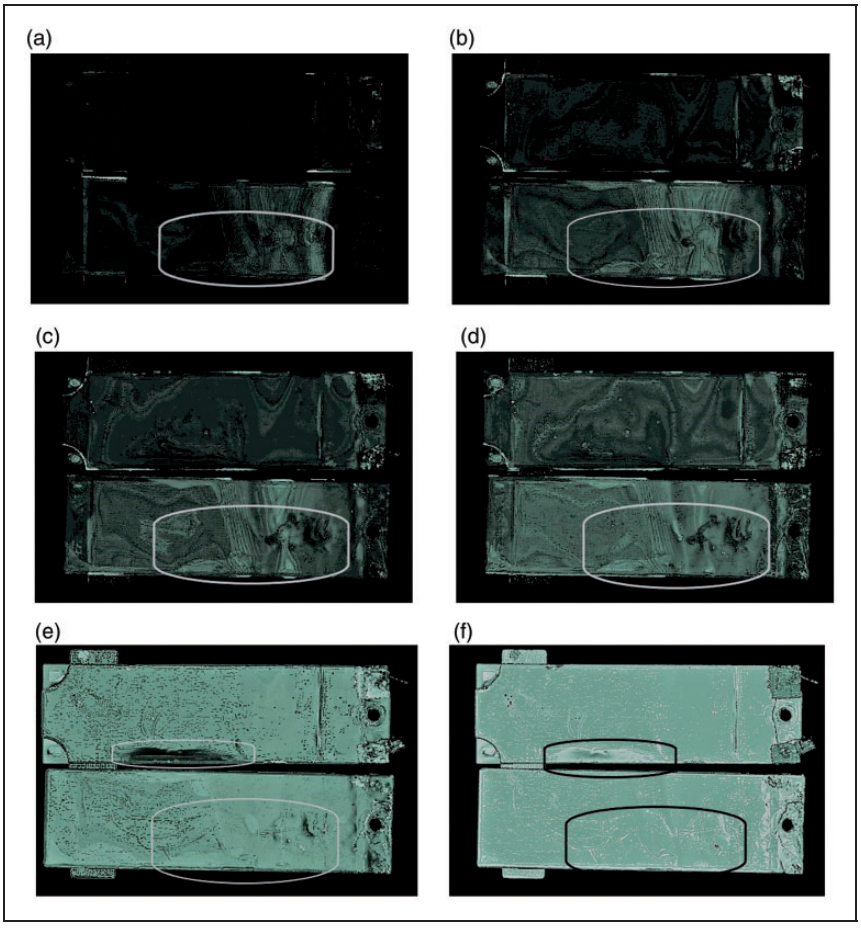


**Figure 7.** Pristine (top sample) and debonded (bottom sample) samples scanned with ultrasonic waves through depth from the aluminum shim side (a)–(f).

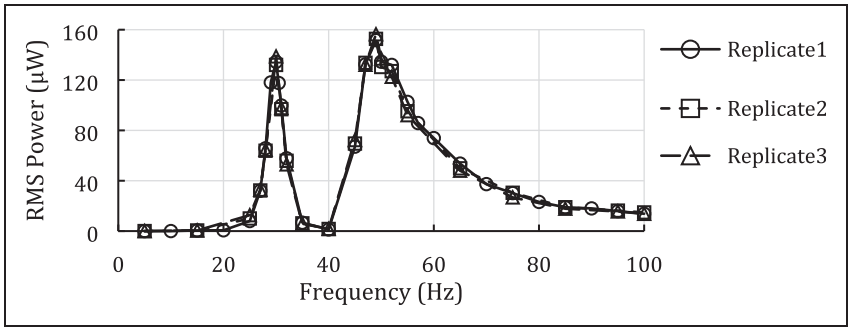


**Figure 8.** Frequency spectrum of power for three replications on macro-fiber composite sample.

that degradation of the output power is two times at the anti-resonance compared to at the power reduction at the resonance frequency, proving that the power at anti-resonance is much more sensitive to the debonding effect.

By applying the model presented by equation (3) and by updating the $\zeta_m$ through an error-minimization process, the analytical output power is correlated with respect to the experimental output power. This process is then repeated for the case in which the debonding occurs by reduction of the active area. Figure 11 shows the comparison of the resonance power between the undamaged and bonded states based on the analytical and experimental results, and variation of the mechanical damping obtained after the model updating process. Figure 11 (a) shows that the power is

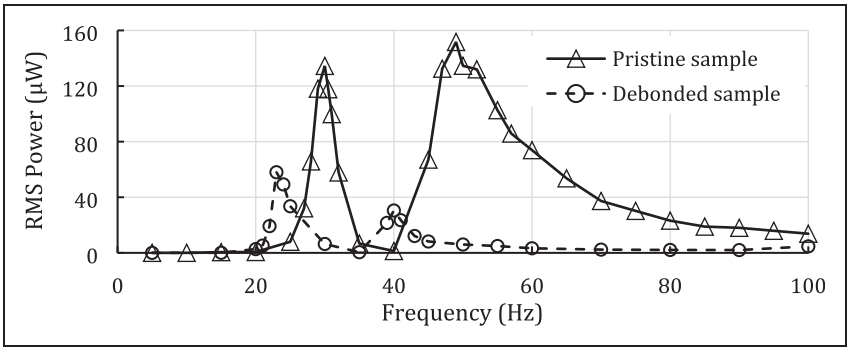


**Figure 9.** Comparison between power for pristine and debonded samples over different frequencies.

**Table 1.** Comparison between pristine and debonded samples.

| Parameter | Pristine | Debonded | Variation (%) |
|---|---|---|---|
| Resonance frequency (Hz) | 30 | 23 | −23.3 |
| Anti-resonance frequency (Hz) | 49 | 40 | −18.4 |
| Root mean square (RMS) of power at resonance | 132.0 | 77.9 | −41.0 |
| RMS of power at anti-resonance | 152.7 | 30.5 | −80.0 |

successfully correlated at resonance by updating damping in the presented model. The presented model with the correlation factor has better accuracy at resonant frequency compared to the other frequencies. However, as maximum available power is of interest in energy harvesting applications and this maximum power is obtained at resonance, the presented model can be used for maximum power correlation. Moreover, Figure 11 (a) shows that correlation for the pristine sample is more accurate than for the debonded sample. This is due to the nonlinearity that is introduced into system due to debonding. As shown in Figure 11 (b), correlated mechanical damping for the debonding sample shows that the debonding caused to increase the $\zeta_m$ from 0.0483 to 0.0765. $\zeta_m$ comprises the support loss, fluid-structural and internal friction damping mechanisms for defect-free state and damage damping for the case of debonded state. Fluid-structural damping is the same for both cases and is evaluated using equation (5). Since during the tests the boundary conditions remained unchanged, the support loss is identical for both pristine and debonded states. However, the thickness of samples was slightly different for pristine and debonded samples, and the viscous damping coefficient was calculated for each


**Figure 10.** Debonded area within adhesive and aluminum layer.

condition. The damage damping was calculated by subtracting the calculated fluid-structural damping and the structural damping and, moreover, the experimentally obtained support loss damping from the correlated mechanical damping.

Table 2 summarizes the obtained results from this section. As was shown, the debonding area reduces 15% of the active area responsible for the power generation. This reduction decreased the RMS resonant power density 20.53% from 60.83 to 48.34 $\mu W/cm^3$. The support loss, which is obtained by subtracting the fluid-structure and structural damping from the correlated damping coefficient, has a great contribution in the total damping proving that the support loss damping is an important part of the energy dissipation in the system. Hence, the next section is dedicated to this support loss. The damage damping in the debonded sample is responsible for 27% of the total damping mechanisms, showing that the debonding can strongly affect the damping coefficient.

The nature of the damping variation due to delamination in the composite materials has been investigated by Khazaee et al. (2018). The variation in damping depends on the vibrating mode, which causes penetration motion or slip motion between layers near the delamination (Khazaee et al., 2018). Fundamental mode shape of the unimorph harvester is shown in Figure 12. In this mode, if a debonding region is present, layers on top and bottom of the debonding area

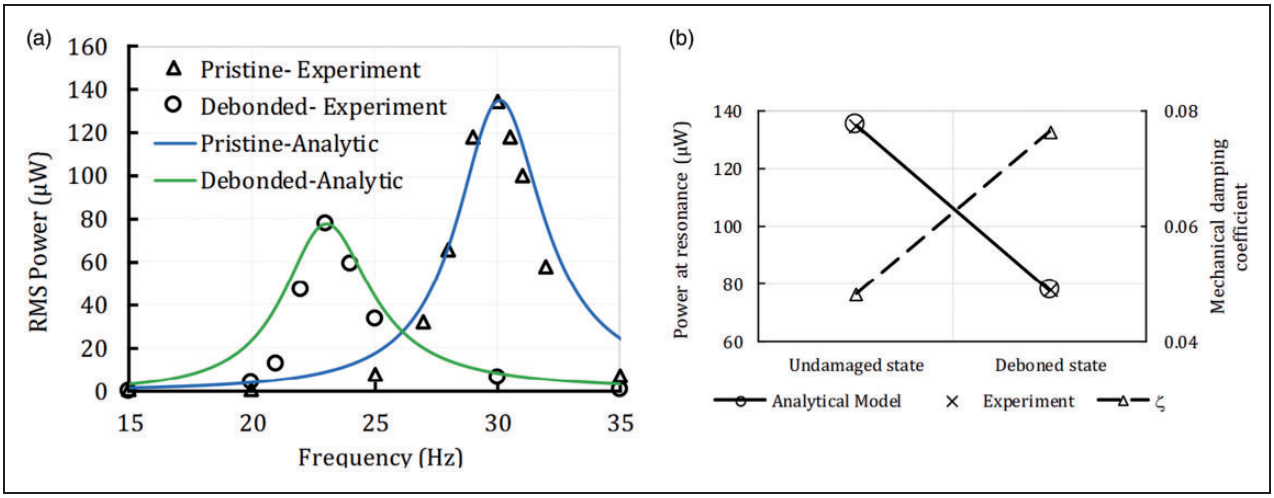


**Figure 11.** (a) correlated data versus experimental data; and (b) comparison between maximum power at resonance and damping increase due to debonding.

**Table 2.** Variation of output power, mechanical damping and structural damping due to improper bonding.

| Parameter | Undamaged sample | Debonded sample |
|---|---|---|
| Active area ($cm^2$) | 20.58 | 17.49 |
| Root mean square resonant power density ($\mu W/cm^3$) | 60.83 | 48.34 |
| $\zeta_m$ (correlated value) | 4.83E-02 | 7.65E-02 |
| $\zeta_{Fluid\text{-}Structure}$ (equation (5)) | 7.90E-04 | 1.24E-03 |
| $\zeta_{Structural}$ (equation (5)) | 5.00E-07 | 5.00E-07 |
| $\zeta_{Support}$ $(=\zeta_m-\zeta_{Fluid\text{-}Structure}-\zeta_{Structural})$ | 4.75E-02 | 4.75E-02 |
| $\zeta_{Damage}$ $(=\zeta_m-\zeta_{Fluid\text{-}Structure}-\zeta_{Structural}-\zeta_{Support})$ | – | 2.78E-02 |

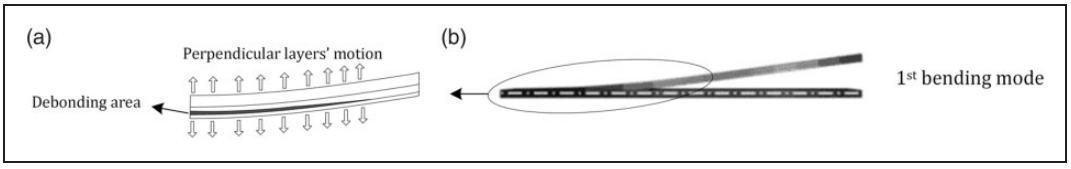


**Figure 12.** Mechanical damping increases due to debonding in the first bending mode.

have a penetration motion in a perpendicular direction which causes an extra energy dissipation mechanism inside the harvesting material.

## 5. Support loss damping

Unimorph or bimorph is among the most applicable configurations of PEHs, where one end is clamped and the other end is free. To create the clamp, often a part of the energy harvester is clamped within a clamp box in which screws are tightened to provide a nonmoving area. Due to this clamp, an extra loss is introduced into the system, called support loss (Hosaka et al., 1995). In this section, output powers from a unimorph PEH under a clamp-free boundary condition with different clamp box configuration are compared to each other in order to study the effect of the clamp characteristics on the output power.

Figure 12 (a) shows the sample for testing the support loss effect on the output power. The thickness of the MFC piezoelectric, adhesive and substrate layers are 300, 245, and 120 μm, respectively. The clamp box consists of two $60 \times 30$ mm blocks with four screws placed symmetrically in the corners with 6 mm center-

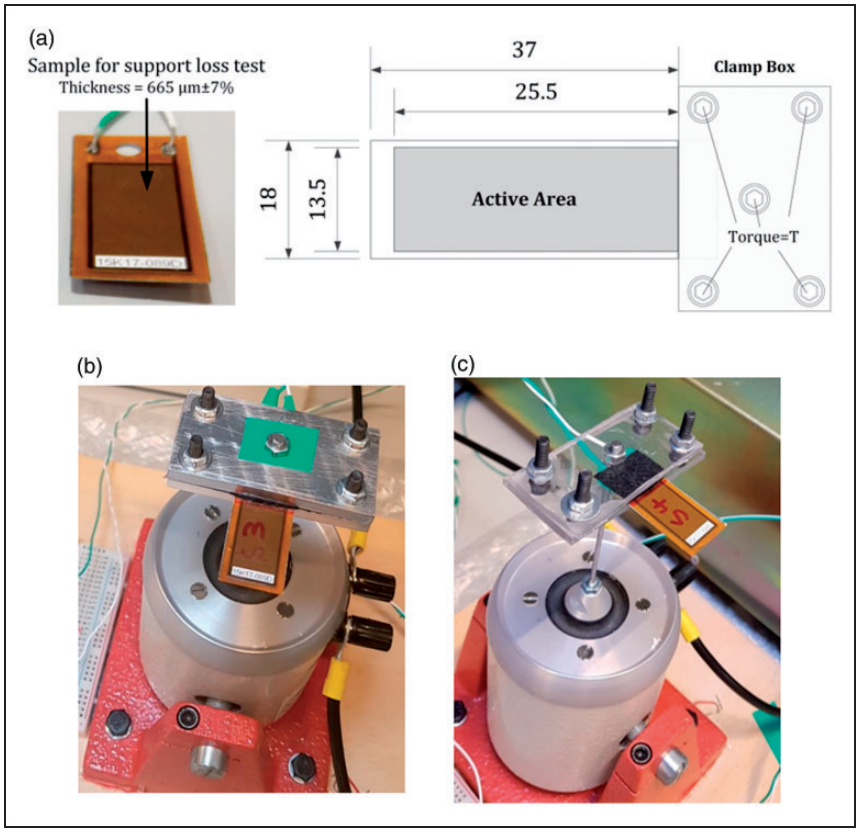


**Figure 13.** (a) macro-fiber composite (MFC) harvester dimensions and unimorph configuration with clamp box screws; (b) aluminum; and (c) plastic clamp boxes clamping the MFC harvester.

to-edge distance and one center hole for the shaker attachment. To observe the effect of the support loss, two types of materials were used for clamp box made by plastic and aluminum, as shown in Figure 13. The weight of clamp box set with screws for aluminum and plastic types are 59.09 g and 25.86 g, respectively. Moreover, the screws of the clamp box were tightened with different torques, and for each set of torques the power was measured over a frequency range close to its natural frequency.

Figure 14 shows the output power density in μW/g over a frequency range including the resonant frequency of the PEH, where $g = 9.81\,m/s^2$, from the MFC sample with the aluminum and plastic clamp boxes at different levels of tightening torques. The vertical axis shows the output power normalized to input base acceleration in terms of RMS, when the MFC sample was excited by a harmonic excitation with the maximum force of 17.8 N. For each case of excitation with the specific frequency, the output voltage and current were measured with 31500 Ω resistance load and then the power was calculated by product of the voltage and current. Tightening torque, N.m., was the torque used for fastening the four screws of the clamp box as well as the shaker attachment screw, as shown in Figure 13 (a). A sample of the measured voltage, current, and output power is shown in Figure 15 for a plastic clamp box with tightening torque 0.5 N.m and excitation frequency of 220 Hz. The immediate conclusion to be drawn from Figure 14 is that, the output power spectrums represent different values for different clamp box materials and tightening torques. Therefore, the clamping characteristics play an important role in the energy harvesting by cantilevered piezoelectric beams. The resonant frequency, as displayed in Figure 16, for plastic clamp lies between 212.1 Hz and 220.4 Hz with an average value of 215.8 Hz that is higher than the resonant frequency for the aluminum clamp with an average of 199.5 Hz lying in the interval 198.4, 202.1 Hz. It can be seen that the tightening torque on the clamp box changes the output power of the energy harvester as well as slightly altering the resonant frequency of the piezoelectric harvester. The output RMS power at resonance is 0.39 μW/g for T = 0.5 N.m, while it is 0.26 μW/g for T = 0.8 N.m when an aluminum clamp box is used. Therefore, the output power reduces 33% due to the tightening torque. This power reduction for the plastic clamp box is 14%, showing a lower dependency of the power to the tightening torque. In addition, the

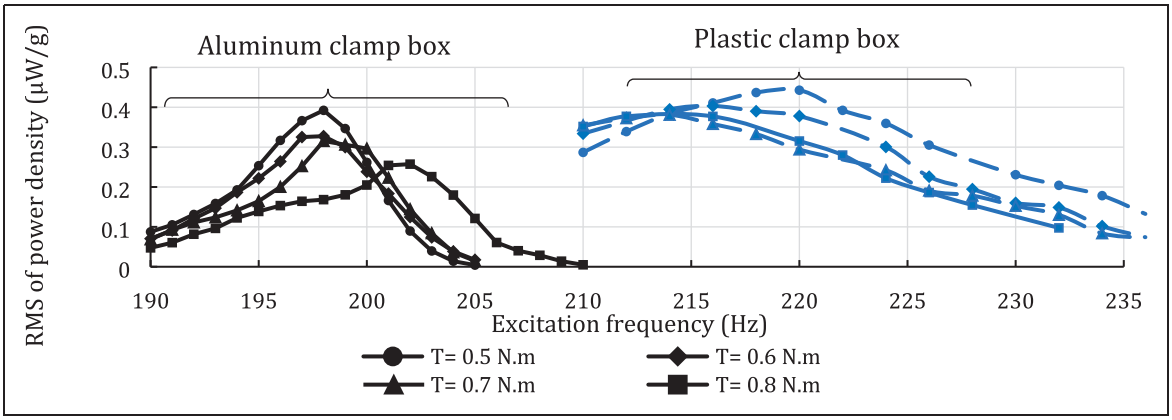


**Figure 14.** Power frequency spectrum for sample 3 over changing torque T of aluminum clamp boxes.

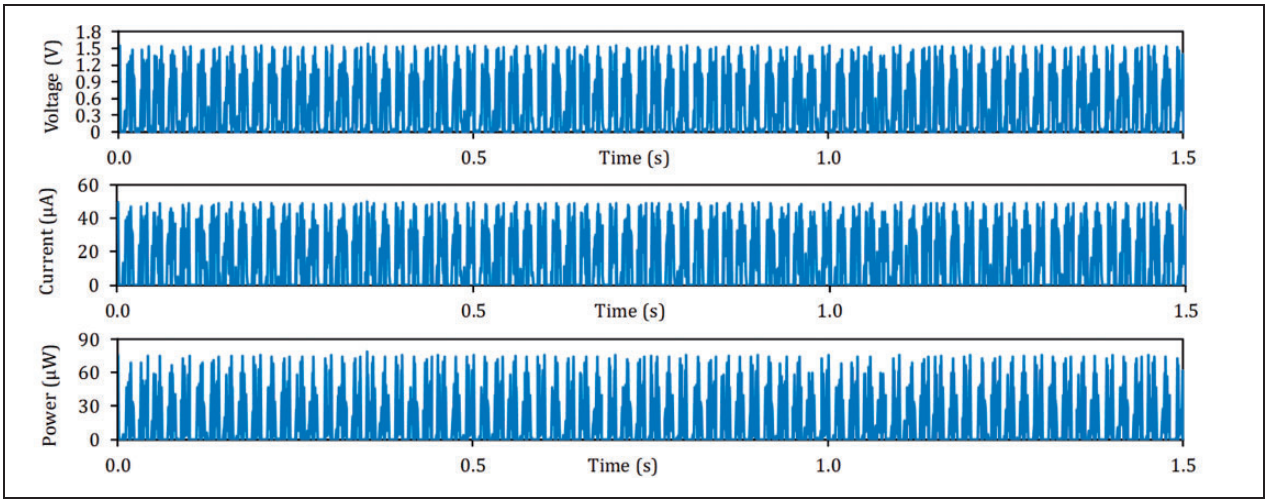


**Figure 15.** Voltage, current and power from piezoelectric harvester with plastic clamp with T = 0.5 N.m at 220 Hz excitation.

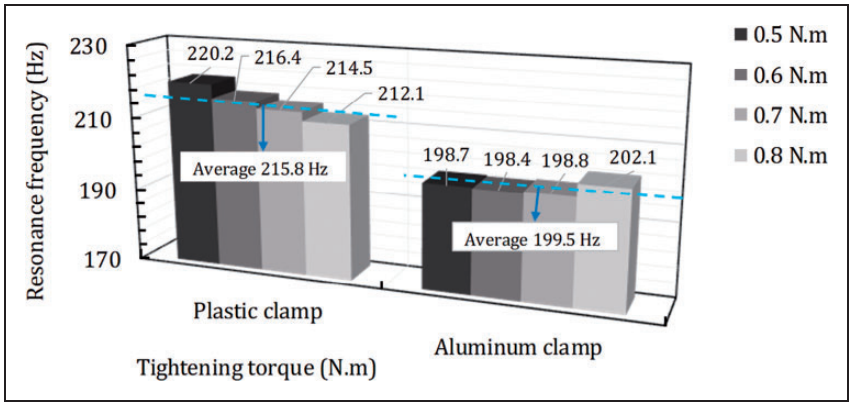


**Figure 16.** Resonant frequency of piezoelectric harvester for different tightening torques on plastic and aluminum clamps.

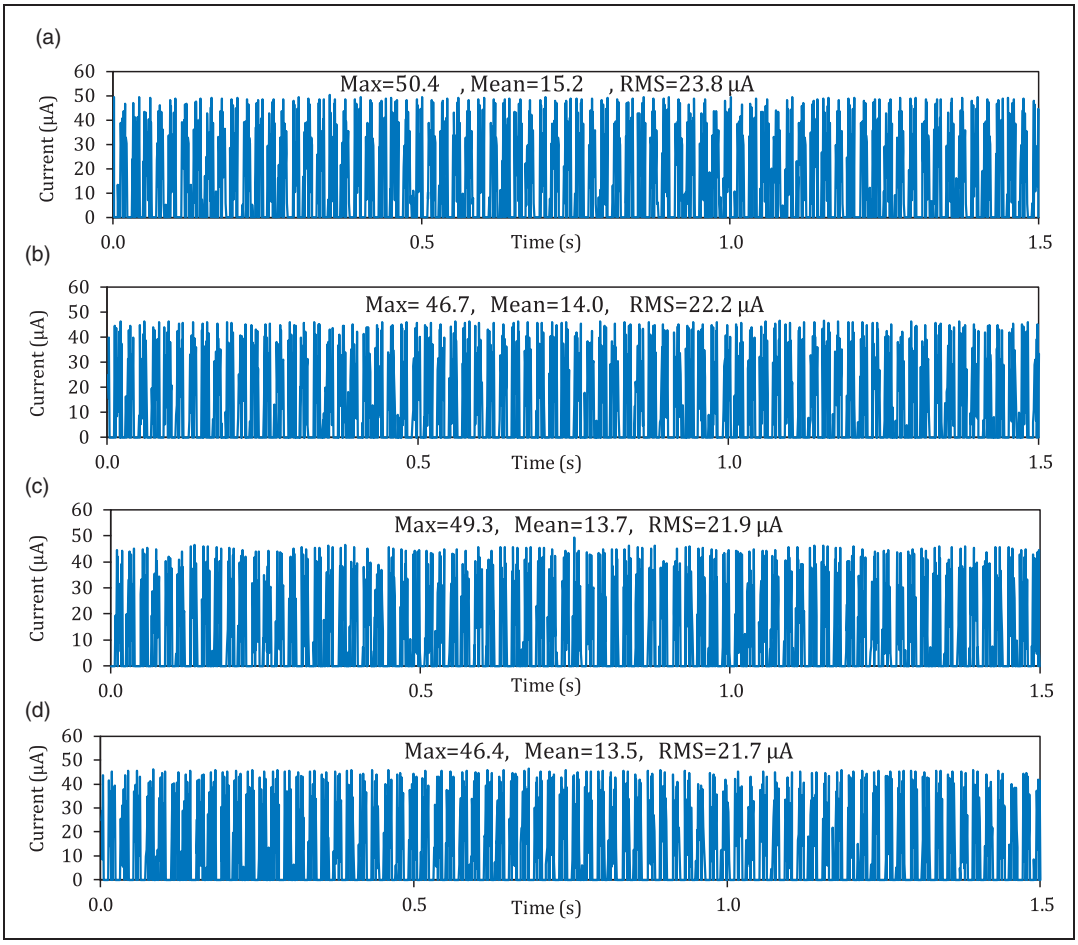


**Figure 17.** Comparison between current measurements at resonant frequency excitation for plastic clamp at tightening torque: (a) 0.5 N.m; (b) 0.6 N.m; and (c) 0.7 N.m and 0.8 N.m.

resonant frequency varies maximum 3.7% in the case of the plastic clamp while this variation is maximum 1.7% with the aluminum clamp.

Output current signals over a 1.5 seconds period from the piezoelectric harvester with plastic clamp vibrating at its resonant frequency for different tightening torques are displayed in Figure 17. The RMS of the output currents for tightening torques of 0.5, 0.6, 0.7, and 0.8 N.m are 23.8, 22.2, 21.9, and 21.7 $\mu$A, respectively. Therefore, increasing the tightening torque on the cantilever clamp box reduces the output current. Increasing tightening torque from 0.5 to 0.6 N.m reduced the current by 6.7 % while this drop is 1.4% for 0.6 to 0.7 N.m, and 0.9 % for 0.7 to 0.8 N.m tightening torque. Figure 18 shows the power at the resonance at different levels of tightening torque for the aluminum and plastic clamp boxes. Since the plastic clips have a degree of flexibility, to prove that the trend is reciprocal, the tests were performed from the lowest torque, T = 0.5 N.m, to the highest torque, T = 0.8 N.m and vice versa. The results show that the harvester with

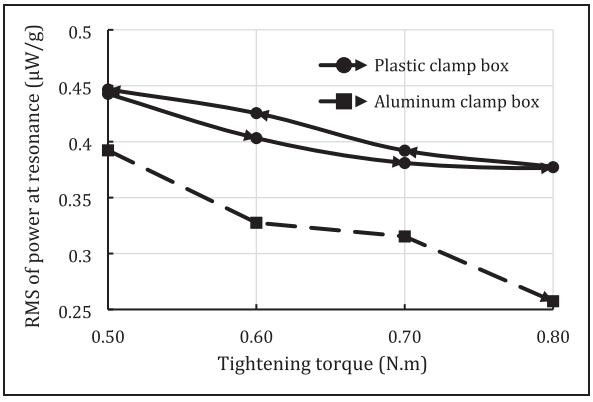


**Figure 18.** Variation of power versus torque applied on clamp screws for different clamp box.

the aluminum clamp box produced lower power. On the other hand, by increasing the tightening torque of the screws of the clamp box, RMS of the maximum power decreases, for both the aluminum

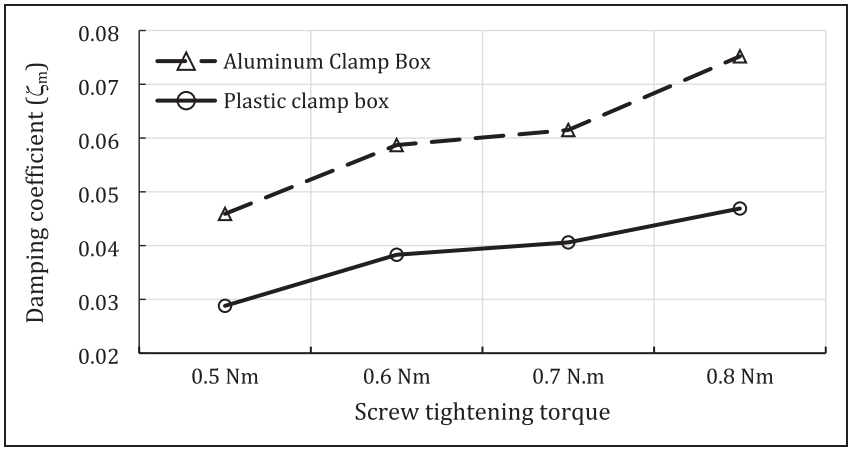


**Figure 19.** Variations of identified damping variations versus clamp pressure for aluminum and plastic clamps.

and plastic clamps. Figure 18 implies that the plastic clips, which are more flexible than the aluminum, can provide higher output power and lower support loss compared to that with the aluminum clamp.

Similar to the previous section, using the developed model for the unimorph harvester, and with the minimization of the error between the maximum resonance powers, the mechanical damping ratios are identified for different clamp boxes at different tightening levels. These identified damping ratios are shown in Figure 19. Overall, the aluminum clamp introduces higher energy dissipation, which in turn causes to reduce the damped natural frequency in Figure 14. Therefore, in comparison with the aluminum clamp box with higher support damping, the lower resonance frequency of the harvester with the plastic clamp box is due to lower support damping. However, with increasing the clamp pressure by higher tightening torque, the support loss increases for both clamp boxes, independent of clamp material.

## 6. Conclusions

This study presented an experimental investigation of the effect of damage and support losses damping mechanisms on the output power of PEHs in unimorph geometry. The results show that by using a simple, but practical, single degree of freedom model, the power variation can be modeled with the mechanical damping variation. The debonding, as an internal source of damping inside the harvester, is investigated in this study. It is concluded that the debonding increases the damping and reduces the output power dramatically. Moreover, the support loss, as an external damping source, has an effect on the output power in such a way that the clamp material as well as clamp pressure will change the output power.

### Declaration of Conflicting Interests

The author(s) declared no potential conflicts of interest with respect to the research, authorship, and/or publication of this article.

### Funding

The author(s) received no financial support for the research, authorship, and/or publication of this article.

### ORCID iD

Alireza Rezania https://orcid.org/0000-0003-4582-2342

### References

Ahmed R, Mir F and Banerjee S (2017) A review on energy harvesting approaches for renewable energies from ambient vibrations and acoustic waves using piezoelectricity. *Smart Materials and Structures* 26(8): 085031. DOI: 10.1088/1361-665X/aa7bfb.

Bhattacharjee A and Nanda BK (2018) Damping study of composites using wavelet analysis. *Journal of Vibration and Control* 24(21): 5141–5151.

Blom FR, Bouwstra S, Elwenspoek M, et al. (1992) Dependence of the quality factor of micromachined silicon beam resonators on pressure and geometry. *Journal of Vacuum Science & Technology B: Microelectronics and Nanometer Structures* 10(1): 19–26.

Chandra R, Singh SP and Gupta K (1999) Damping studies in fiber reinforced composites – A review. *Composite Structures* 46(1): 41–51.

Chen SY, Liu JZ and Guo FL (2017) Evaluation of support loss in micro-beam resonators: A revisit. *Journal of Sound and Vibration* 411: 148–164.

DuToit NE and Wardle BL (2007) Experimental verification of models for microfabricated piezoelectric vibration energy harvesters. *AIAA Journal* 45(5): 1126–1137.

DuToit NE, Wardle BL and Kim SG (2005) Design considerations for MEMS-scale piezoelectric mechanical vibration energy harvesters. *Integrated Ferroelectrics* 71(1): 121–160.

Erturk A and Inman DJ (2008) Issues in mathematical modeling of piezoelectric energy harvesters. *Smart Materials and Structures* 17(6): 065016. DOI: 10.1088/0964-1726/17/6/065016.

Erturk A, Bilgen O, Fontenille M, et al. (2008) Piezoelectric energy harvesting from macro-fiber composites with an application to morphing wing aircrafts. In: *Proceedings of the 19th International Conference of Adaptive Structures and Technologies*, Ascona, Switzerland, 6–9 October 2008. Available at: http://library.eawag-empa.ch/icast_proceedings_2008_open_access/ICAST2008030.pdf (accessed March 2019).

Goyder HGD (2018) Damping due to joints in built-up structures. In: Brake MRW (ed.) *The Mechanics of Jointed Structures: Recent Research and Open Challenges for Developing Predictive Models for Structural Dynamics*. Cham: Springer International Publishing, pp.135–147.

Hao Z, Erbil A and Ayazi F (2003) An analytical model for support loss in micromachined beam resonators with in-plane flexural vibrations. *Sensors and Actuators, A: Physical* 109(1–2): 156–164.

Hosaka H, Itao K and Kuroda S (1995) Damping characteristics of beam-shaped micro-oscillators. *Sensors and Actuators A: Physical* 49(1–2): 87–95.

Ibrahim RA and Pettit CL (2005) Uncertainties and dynamic problems of bolted joints and other fasteners. *Journal of Sound and Vibration* 279(3–5): 857–936.

Khaligh A, Zeng P and Zheng C (2010) Kinetic energy harvesting using piezoelectric and electromagnetic technologies – State of the art. *IEEE Transactions on Industrial Electronics* 57(3): 850–860.

Khazaee M, Nobari AS and Aliabadi MHF (2018) Experimental investigation of delamination effects on modal damping of a CFRP laminate, using a statistical rationalization approach. In: Nobari AS and Aliabadi MHF (eds) *Vibration-Based Techniques for Damage Detection and Localization in Engineering Structures. Computational and Experimental Methods in Structures*, Volume 10. London: World Scientific Publishing Europe, pp.75–103.

Khazaee M, Rezaniakolaei A and Rosendahl L (2019) An experimental study on macro piezoceramic fiber composites for energy harvesting. *Materials Science Forum* 951: 3–8.

Li H, Tian C and Deng ZD (2014) Energy harvesting from low frequency applications using piezoelectric materials. *Applied Physics Reviews* 1(4): 1–20.

Mortazavinatanzi S, Rezaniakolaei A and Rosendahl L (2018) Printing and folding: A solution for high-throughput processing of organic thin-film thermoelectric devices. *Sensors (Basel)* 18(4): 989. DOI: 10.3390/s18040989.

Pazand K and Nobari AS (2017) Investigation of damage effect on the effective dynamic mechanical properties of an adhesive in linear and nonlinear response regimes. *Journal of Vibration and Control* 23(14): 2209–2220.

PiezeTech Arkema Group (n.d.) Products. Available at: https://www.piezotech.eu/en/ (accessed March 2019).

Qing S, Rezania A, Rosendahl LA, et al. (2018) Characteristics and parametric analysis of a novel flexible ink-based thermoelectric generator for human body sensor. *Energy Conversion and Management* 156: 655–665.

Reddy AR, Umapathy M, Ezhilarasi D, et al. (2016) Improved energy harvesting from vibration by introducing cavity in a cantilever beam. *Journal of Vibration and Control* 22(13): 3057–3066.

Roundy S, Wright PK and Rabaey J (2003) A study of low level vibrations as a power source for wireless sensor nodes. *Computer Communications* 26(11): 1131–1144.

Saravanos DA and Hopkins DA (1996) Effect of delamination on the damped dynamic characteristics of composite laminates. analysis and experiments. *Journal of Sound and Vibration* 192(5): 977–993.

Shan X, Song R, Liu B, et al. (2015) Novel energy harvesting: A macro fiber composite piezoelectric energy harvester in the water vortex. *Ceramics International* 41(Supplement 1): S763–S767.

Sodano HA, Lloyd J and Inman DJ (2006) An experimental comparison between several active composite actuators for power generation. *Smart Materials and Structures* 15(5): 1211–1216.

# Appendix B. Paper 2: Reference [186]

## A proof for looking differently into damping modeling in piezoelectric energy harvesting systems

M. Khazaee, A. Rezaniakolaei, L. Rosendahl

This paper has been presented in

*In 26th International Congress on Sound and Vibration.* The International Institute of Acoustics and Vibration (IIAV), July 2019, Montreal, Canada.

26th INTERNATIONAL CONGRESS ON SOUND AND VIBRATION
7-11 July 2019, Montreal

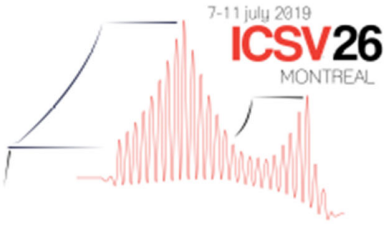


# A PROORF FOR LOOKING DIFFERENTLY INTO DAMPING MODELING IN PIEZOELECTRIC ENERGY HARVESTING SYSTEMS

Majid Khazaee, Alireza Rezaniakolaei and Lasse Rosendahl
*Department of Energy Technology, Aalborg University, 9220 Aalborg East, Denmark.*
*e-mail: alr@et.aau.dk*

Modelling of piezoelectric energy harvesting systems from vibration point of view is of interest of many researchers and plays an important role in the estimation of power output for these systems. This paper deals with the dilemma of damping modelling in piezoelectric harvesters as in most of modelling techniques only the viscous damping is considered. A discussion is firstly presented about the effect of damping modelling on the power output. Then a modelling approach for different damping mechanisms is presented by which energy dissipation in the piezoelectric harvester can accurately be modelled. Finally, based on this damping model, an analytical model is derived for power output estimation of piezoelectric energy harvesters.

Keywords: Damping Mechanisms, Piezoelectric, Energy Harvesting, Structural Damping, Viscous Damping.

## 1. Introduction

Modelling of piezoelectric energy harvesting systems from vibration point of view is of interest of many researchers and plays an important role in the estimation of output energy for these systems. There are a vast number of studies focused on vibrational modelling of piezoelectric bimorph (or unimorph) harvesters. All of these studies mentioned the effect of damping on the power output of the harvester. The less mechanical damping leads to the higher power output [1]. In the spite of great impact of damping on power output, as far as the authors are aware of, there is no deep study about different damping mechanisms in piezoelectric energy harvesters.

For energy harvesting applications, mostly researchers used viscous damping model in their approach for single-degree-of-freedom models, and for multi-degree-of-freedom modelling, they extended the concept of viscous damping and used Rayleigh proportional damping. Based on the literature [1]–[3], damping modelling techniques used for energy harvesting applications are viscous damping, which is proportional to the velocity. DuToit et al. [3] used a formulation for damping ratios from a previous study by Hosaka et al. [4], which internal friction, air-damping, squeeze force, and support loss had been reported as energy dissipation mechanisms of a cantilever beam. In DuToit formulation just the viscous damping is modelled, which is proportional to the velocity of vibrating mass. In the Finite Element formulation presented by Junior et al. [2], proportional Rayleigh damping matrix was considered.

Except one study that recently compared the structural and viscous damping [5], there is no research that taken the structural damping into account as a separate term in the vibrational equations of motion for the harvester. Just in the recent short paper by Cooley et al. [5], the role of structural damping in the modelling of piezoelectric energy harvesting has been mentioned. In the experimental work by Sodano et al. [6], they investigated the power output from PZT and MFC materials bonded to an aluminium shim with double sided tape. They mentioned the role of tape damping into decreasing power output, but no correction factor or modelling has been presented to consider damping. Crandall [7] mentioned the acoustic radiation and internal damping mechanisms as for damping in vibration of a beam. Crandall [7] stated that internal damping is a frequency-dependent factor and is a function of the material, So, it is not correct to consider a general constant value for friction damping, as considered by Hosaka model [4]. Also, Crandall [7] mentioned the dependency of air damping to frequency.

In this research, the role of damping mechanisms in output energy from piezoelectric energy harvesting are studied as not previous studies addressed this issue. Afterwards, a model for damping in piezoelectric harvesters will be presented that considers viscous and structural damping mechanisms. Moreover, a more comprehensive discussion about different mechanisms in structural damping is presented as in the previous studies this has not been studied. Section 2 gives a current 1-D modelling approach for piezoelectric harvesters. In section 3, the drawbacks of this methods are reviewed and a new model considering different damping mechanisms are presented. Section 4 presents a numerical error to emphasis on the effect of damping mechanisms for output power from the harvester.

## 2. Current 1-D Modelling

**Error! Reference source not found.** presents the schematic of 1-D model [3], which comprises of a piezoelectric mass with internal resistance $R_p$ with a proof mass simply connected to a load resistor $R_l$. In this model, the entire structure is electromechanically coupled, unlike unimorph beams in which a part of the harvester is metal substrate.

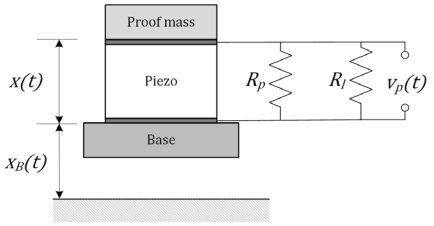


Figure 1: 1-D electromechanical model [3]

The coupled equations for the system shown in Fig. 1 can be derived from equations in [3] as

$$\ddot{x}(t) + 2\xi_m \omega_n \dot{x}(t) + \omega_n^2 x - \omega_n^2 d_{31} V_p(t) = -\ddot{x}_B(t), \tag{1}$$

$$R_{eq} C_p \dot{V}_p(t) + V_p(t) + m_{eff} R_{eq} d_{31} \omega_n^2 \dot{x}(t) = 0, \tag{2}$$

where $\ddot{x}_B$ is the base excitation acceleration, $x$ is the relative displacement of harvester tip respect to the base, $V_p$ is the output voltage, $\omega_n$ is the undamped natural frequency of harvester, $\zeta_m$ is the mechanical damping ratio, $d_{31}$ is the piezoelectric coupling coefficient in 3-1 mode, $R_{eq}$ is the equivalent electric resistance, $C_p$ is the capacitance of the piezoelectric, and $m_{eff}$ is the effective mass of piezoelectric layer. The overhead dot indicates the time derivative. The capacitance is defined in terms of dielectric constant $K$, the permittivity of free space ($\varepsilon_0 = 8.9\,nF/m$), piezoelectric area $A_p$ and thickness $t_p$ with $C_p = K\,\varepsilon_0 A_p / t_p$. In general, if only viscous damping is considered for energy dissipation from the system, energy dissipation can be modelled as

$$[C]\{\dot{x}\}, \tag{3}$$

where $\{\dot{x}\}$ is the velocity vector.

In the concept of finite element, proportional damping matrix is a linear combination of mass and stiffness matrices with constant coefficients. If *[M]* and *[K]* are global mass and stiffness matrices of a multi-degree-of-freedom vibrating system, then proportional damping matrix considered for modelling in cantilever piezoelectric energy harvesting system will be presented as

$$[C] = \alpha[M] + \beta[K], \tag{4}$$

where $\alpha$ and $\beta$ are Rayleigh damping coefficients [2]. This damping matrix will act as a viscous damper as it is proportional to velocity. Rayleigh damping coefficients should be determined with experimental vibration tests. In the study by De Marqui Junior et al. [2], no discussion about these coefficients has been presented, just these figures presented as the known variables.

## 3. Proposed model

In the study by DuToit et al. [3], the piezoelectric layer has just been considered, without any substrate layer or contact layer, so the Hosaka damping model may be applicable for their case study. However, as in most piezoelectric energy harvesting, a piezoelectric layer is attached at a substrate surface to form a unimorph or similarly bimorph. In these configurations, damping model presented in Eq. (3) will not be useful anymore, as the viscoelastic damping from the contact layer should be considered. In addition, in the Eq. (1), the vibrating system is only the piezoelectric material. However, in most piezoelectric harvesters, the piezoelectric layer is attached onto a substrate surface. Thus, the model by Eq. (1) and Eq. (2) cannot be used for these cases as there is a proportion of the device which does not contribute to the power generation. So, a model is needed to distinguish the portion of mass, which contributes to vibrating motion, and the portion for power generation.

By adding the effect of substrate using a mass coefficient and a general form of damping, the equations of motion for a piezoelectric harvester with substrate and piezoelectric layer can be shown as

$$m_b\ddot{x}(t) + f_d + kx - \alpha_{mass} k d_{31} V_p(t) = -f_B(t) \tag{5}$$

$$R_{eq} C_p \dot{V}_p(t) + V_p(t) + m_{eff} R_{eq} d_{31} \omega_n^2 \dot{x}(t) = 0 \tag{6}$$

, where $\alpha_{mass} = m_p / m_b$ is the compensation factor, $m_b$ is the device mass, $m_p$ is the piezoelectric element mass, $f_d$ is the energy dissipation, and $f_B$ is the base excitation force. The energy dissipation can be related to air resistance against beam vibration, $f_{d\text{-}air}$ , and internal structural damping, $f_{d\text{-}str}$. Air-damping force can be estimated based on viscous damping model, as it has been done by [7] and [4]. However, the internal damping is much more complex for piezoelectric harvesters, as the beam is a composite beam with materials exhibiting elastic and viscoelastic behaviours at the same time. In the following, the tools for appropriate energy dissipation for a piezoelectric harvester will be presented.

When a cantilever oscillator vibrates in the air, there is an air-resistance force, which cause to dissipate energy from the dynamic system. This energy dissipation is proportional to velocity and hence, as it can be modelled as a dashpot, it is emerged as a viscous damping term. Hosaka et al. [4] investigated the energy dissipation of a macro oscillator in the air with the assumption that beam length is much larger than the other dimensions and also width is much larger than thickness. By these assumptions, $f_{d\text{-}air}$ can be expressed as

$$f_{d-air} = \frac{\left(3\pi\mu w + \frac{3}{4}\pi w^2 \left(2\rho_a \mu\omega\right)^{1/2}\right) m_b}{\rho_b w^2 h} \dot{x} = 2\zeta_m \omega_n m_b \dot{x}, \tag{7}$$

where $\mu$ is the air dynamic viscosity, $w$ is the beam width, $h$ is the overall beam thickness, $\zeta_m$ is the viscous damping coefficient, $\rho_b$ and $\rho_a$ are the density for beam and air, respectively.

For internal energy dissipation, the energy dissipation is often introduced as the complex term of stiffness and is defined as [8]

$$f_{d-str} = jk\eta m_b x\,, \tag{8}$$

where $\eta$ is the structural damping coefficient. Here, the aim is to extract an expression for $\eta$.

Overall composite materials represent a higher energy dissipation due to the viscoelasticity of the polymeric matrix [9]. Chandra et al. [10] mentioned four main factors for energy dissipation in composites, which are viscoelasticity, interphase, viscoplastic, and thermoelastic. Viscoelastic nature of matrix or fiber creates viscoelastic damping. The region adjacent to the fibres along the length will create interphase damping. In the case of applying high vibration or stress a degree of non-linear damping due to the present of high stress is evident, which is called viscoplastic damping. Thermoelastic damping is due to the heat flow from compression stress zone to the tensile stress zone. Thermoelastic damping depends to the amplitude and frequency of applied load, sample thickness and number of cycles and is more important for metal composites [10]. A piezoelectric energy harvester consisted of one or two orthotropic piezoelectric layers, an isotropic substrate layer, and an adhesive viscoelastic layer. Due to the nature of the harvester, viscoelastic and interphase damping mechanisms are evident in the model. In addition, due to cyclic loading and the presence of metal in the harvester, thermoelastic damping should be taken into the account. So, the internal structural damping coefficient can be shown as

$$\eta = \eta_{visc} + \eta_{phas} + \eta_{thermo}\,, \tag{9}$$

where $\eta_{visc}$, $\eta_{phas}$ and $\eta_{thermo}$ are difficult coefficients, which it is not easy to evaluate an analytical expression for them. So, it is recommended to simulate $\eta$ as

$$\eta = \bar{\eta} + \hat{\eta}, \tag{10}$$

where $\bar{\eta}$ is the structural coefficient count as energy dissipation for the material and $\hat{\eta}$ is the damping due to the interphase and thermoelastic mechanisms. Here, in this modelling method, $\bar{\eta}$ is estimated for the materials and then $\hat{\eta}$ is tuned in such a way that the experimental data match the output from the analytical method. It is worth mentioning that tuning $\hat{\eta}$ should be regarded as an iteration process.

Internal energy dissipation for homogenous metal materials was proved that does not depend to the stress level but to the frequency , although some small dependency observed for glass/epoxy composites [11]. If the stress-dependency of structural damping is ignored, it can be shown that internal energy dissipation is identical to the theoretical loss factor due to transverse heat flow [7]. Hence, the internal structural coefficient can be estimated as [7]

$$\bar{\eta} = \frac{\alpha^2 E T}{c_v} \frac{\omega/\omega_0}{1+\left(\omega/\omega_0\right)^2} \tag{11}$$

where $\alpha$ is thermal expansion coefficient, $T$ is temperature, $E$ is modulus of material, $c_v$ is specific heat, and $\omega$ is vibrating frequency, and $\omega_0$ is the material relaxation frequency, which is given as

$$\omega_0 = \frac{\pi}{2}\frac{\bar{k}}{c_v h^2}, \tag{12}$$

where $\bar{k}$ is material conductivity.

To sum up, the equations of motion shown by equations (5) and (6) can now be given by

$$\ddot{x}(t) + 2\zeta_m \omega_n \dot{x}(t) + \omega_n^2 (1 + j\eta) x - \alpha_{mass}\omega_n^2 d_{31} V_p(t) = -\ddot{x}_B(t), \tag{13}$$

$$R_{eq}C_p\dot{V}_p(t)+V_p(t)+m_{eff}R_{eq}d_{31}\omega_n^2\dot{x}(t)=0, \tag{14}$$

where $\omega_n$ is defined as $\sqrt{k/m_b}$.

If a harmonic excitation is assumed, $\ddot{x}_B(t)=\bar{X}_B e^{j\omega t}$, then the displacement and voltage will be a harmonic function with the same frequency but with complex magnitude, e.g. $V_p(t)=\bar{V}_p e^{j\omega t}$ and $x(t)=\bar{X}e^{j\omega t}$. By substituting these expression into equations (13) and (14),

$$\left[\left(\left(\omega_n^2-\omega^2\right)+j\left(2\zeta_m\omega_n\omega+\eta\omega_n^2\right)\right)\bar{X}-\alpha_{mass}\omega_n^2 d_{31}\bar{V}_p\right]e^{j\omega t}=-\bar{X}_B e^{j\omega t} \tag{15}$$

$$\left(\left(1+jR_{eq}C_p\omega\right)\bar{V}_p+jm_{eff}R_{eq}d_{31}\omega_n^2\omega\bar{X}\right)e^{j\omega t}=0 \tag{16}$$

Then, by defining the dimensionless frequency and load with $\Omega=\omega/\omega_n$ and $r=R_{eq}C_P\omega_n$, the steady state solutions for output voltage as a function of input frequency can expressed as:

$$\left|\frac{\bar{V}_p}{\bar{X}_B}\right|=\frac{m_{eff}\,R_{eq}\,d_{31}\,\omega_n\,\Omega}{\sqrt{\left[\left(\left(1-\Omega^2\right)-r\Omega\left(2\zeta_m\Omega+\eta\right)\right)^2+\left(\left(2\zeta_m\Omega+\eta\right)+r\Omega\left(1-r\Omega^3\right)+\left(\alpha_{mass}m_{eff}R_{eq}d_{31}^2\omega_n^3\Omega\right)\right)^2\right]}} \tag{17}$$

Using the calculated voltage from Eq.(17), the magnitude of output power from piezoelectric harvester can be calculated with $P_p=\left|\bar{V}_p\right|^2/R_l$. By defining a new electromechanical coupling coefficient $k_e^2$ [3], power can be estimated from Eq. (18).

$$\left|\frac{P_p}{\left(\bar{X}_B\right)^2}\right|=\frac{m_{eff}\,r\,k_e^{\,2}\,\Omega^2}{\omega_n\left[\left(\left(1-\Omega^2\right)-r\Omega\left(2\zeta_m\Omega+\eta\right)\right)^2+\left(\left(2\zeta_m\Omega+\eta\right)+r\Omega\left(1-\Omega^2\right)+\left(\alpha_{mass}\,r\,k_e^{\,2}\Omega\right)\right)^2\right]} \tag{18}$$

As it can be seen from Eq.(18), the energy dissipation term is $2\zeta_m\Omega+\eta$, which has two parts, one is constant at all frequencies and the other changes with Ω.

## 4. Numerical example

Now, to clear the role of damping mechanisms, a numerical example is presented. This numerical example is the analysis of a bimorph piezoelectric energy harvester with dimension 120×30 mm. Piezo-electric layer is a PZT-5A Piezoceramic with elastic modulus of 66.0 GPa, Poisson's ratio of 0.33 and density of 7.75 g/cm$^3$ with the thickness of 0.27 mm. The electromechanical coupling properties of the piezoelectric layer are as follows: $d_{33}$=374 pC/N, $d_{31}$=-171 pC/N, and $C_p$=177.07 nF/m. Centre shim is made of brass with thickness of 0.14 mm, elastic modulus of 105 GPa, Poisson's ratio 0.3 and density of 9.0 g/cm$^3$. In order to estimate the natural frequency for this harvester, COMSOL Multiphysics software under license number 12073023 was used. As it was shown in Fig. 2, the piezoelectric beam is meshed with Tetrahedral elements and the natural frequency of the harvester was obtained $\omega_n$=23.1 Hz.

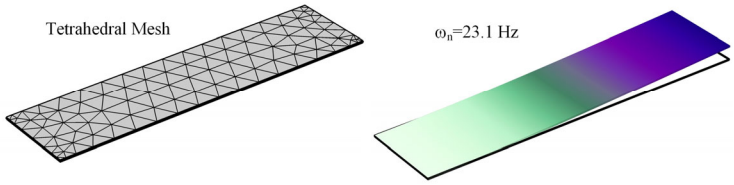


Figure 2: Finite Element analysis of bimorph for natural frequency

Now based on the presented method in Eq. (18), output power from piezoelectric harvester is compared for different cases. Three different systems in terms of energy dissipation were considered which are denoted with lightly, medium and highly damped system according to their damping coefficient. In lightly, medium and highly damped system $\zeta_m+\eta$ are 0.02, 0.04 and 0.1, respectively. Moreover, load resistances were considered to be 1e3 or 1e6 **Ω** for all these three cases. At each case, three combination of damping mechanisms were considered, namely structural damping only, viscous damping only or half combination of both damping mechanisms. Power ration for lightly, medium and highly damped systems are shown in Fig. 3, Fig. 4 and Fig. 5, respectively. It is worth mentioning that power ratio is the power normalized with the case of viscous damping only. As it can be seen from Fig. 3, the output power in the case of structural damping only is 4 times and in the case of combined damping mechanisms are 1.8 times higher than the viscous only case, independent of the load resistance. These figures are approximately the same for medium and highly damped systems in Fig. 4 and Fig. 5. There is only a slight shift in the resonant frequency due to increasing damping, as can be seen by comparing Fig. 3 and Fig. 5.

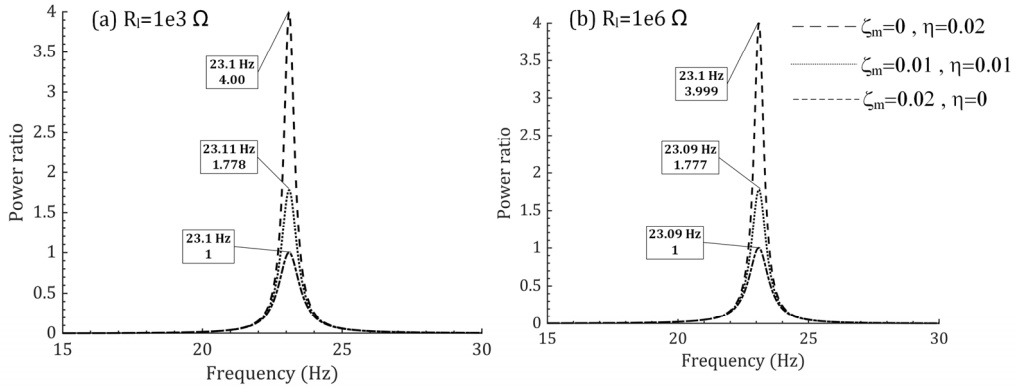


Figure 3: Effect of different damping mechanisms on power for lightly damped system

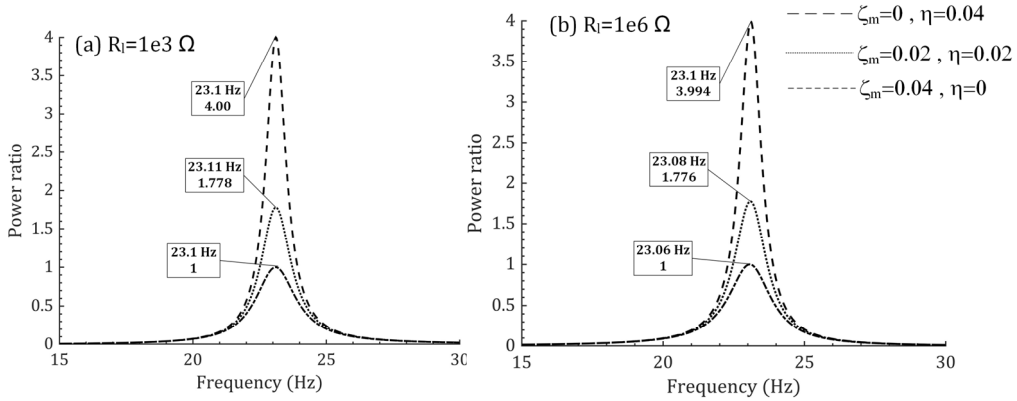


Figure 4: Effect of different damping mechanisms on power for medium damped system

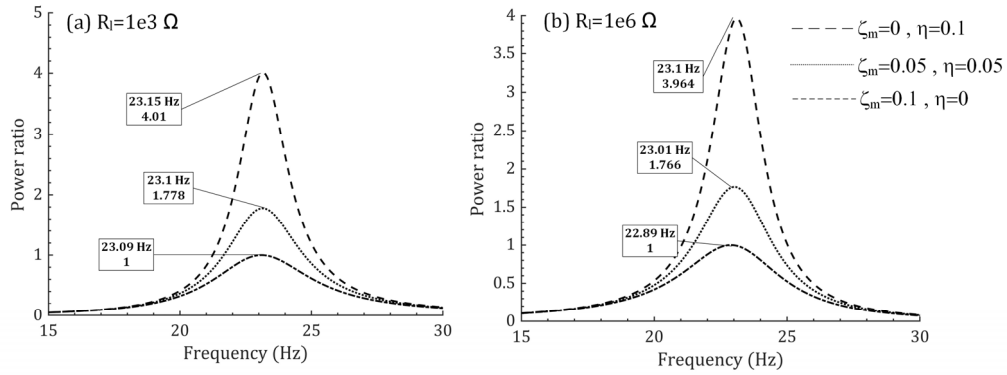


Figure 5: Effect of different damping mechanisms on power for highly damped system

The variation of power respect to damping mechanisms emphasis that it is important to select the correct form of damping mechanisms unless the viscous only damping model will underestimate output energy by piezoelectric energy harvester. DoToit et al. [12], presented a model for predicting output power from piezoelectric only by considering viscous damping and their experimental verification showed that output power in the resonant was underestimated with this model. Fig. 6 shows the output power from their piezoelectric harvester using analytical model and experimental data. It is obvious that their model could not predict output power close to resonance. This can be due to inappropriate consideration of only viscous damping mechanisms.

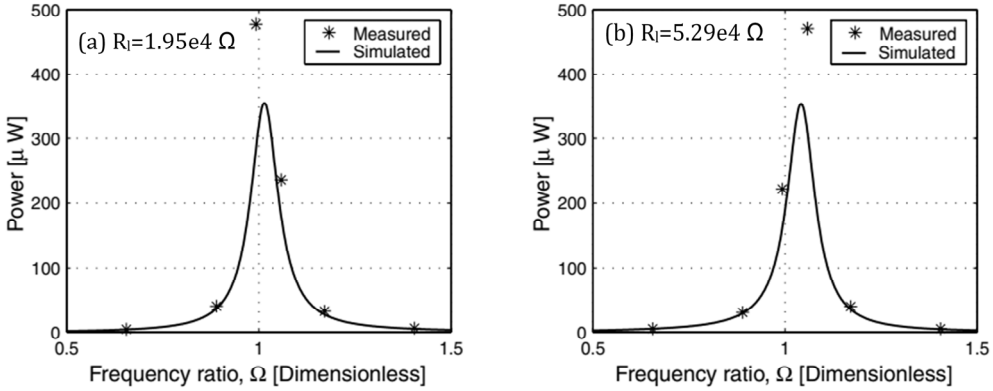


Figure 6: A comparison between experiment and analytical model with only viscous damping modelling $\zeta_m$=0.0178 [12]

## 5. Conclusion

This paper dealt with the problem of proper damping modelling in piezoelectric energy harvesters. After reviewing current popular damping modelling approach, viscous only damping mechanism, a damping model was presented that considers both viscous and structural damping mechanisms. Viscous damping was related to the energy dissipation from the system by air resistance while structural damping comprises of energy dissipation through elastic waves inside material, interphase and thermoplastic mechanisms. An analytical estimation for structural damping also was presented. A numerical example was presented that showed the role of different damping mechanisms in output power from piezoelectric harvester. It was shown that if only viscous damping is taken into the account, then output power at resonance will be underestimated considerably.

## REFERENCES


[1] S. Roundy, P. K. Wright, and J. Rabaey, “A study of low level vibrations as a power source for wireless sensor nodes,” *Comput. Commun.*, vol. 26, no. 11, pp. 1131–1144, 2003.

[2] C. De Marqui Junior, A. Erturk, and D. J. Inman, “An electromechanical finite element model for piezoelectric energy harvester plates,” *J. Sound Vib.*, vol. 327, no. 1–2, pp. 9–25, 2009.

[3] N. E. DuToit, B. L. Wardle, and S. G. Kim, “Design considerations for MEMS-scale piezoelectric mechanical vibration energy harvesters,” *Integr. Ferroelectr.*, vol. 71, pp. 121–160, 2005.

[4] H. Hosaka, K. Itao, and S. Kuroda, “Damping characteristics of beam-shaped micro-oscillators,” *“Sensors and Actuators, A: Physical,”* vol. 49, no. 1–2. pp. 87–95, 1995.

[5] C. G. Cooley, T. Q. Tran, and T. Chai, “Comparison of viscous and structural damping models for piezoelectric vibration energy harvesters,” *Mech. Syst. Signal Process.*, vol. 110, pp. 130–138, 2018.

[6] H. A. Sodano *et al.*, “Use of piezoelectric energy harvesting devices for charging batteries,” in *SPIE Vol. 5050*, 2003, pp. 101–108.

[7] S. H. Crandall, “The role of damping in vibration theory,” *J. Sound Vib.*, vol. 11, no. 1, pp. 3–18, 1970.

[8] W. W. Soroka, “Note on the Relations Between Viscous and Structural Damping Coefficients,” *J. Aeronaut. Sci.*, vol. 16, no. 7, pp. 409–410, 1949.

[9] A. Treviso, B. Van Genechten, D. Mundo, and M. Tournour, “Damping in composite materials: Properties and models,” *Compos. Part B Eng.*, vol. 78, pp. 144–152, 2015.

[10] R. Chandra, S. P. Singh, and K. Gupta, “Damping studies in fiber-reinforced composites - a review,” *Compos. Struct.*, vol. 46, no. 1, pp. 41–51, 1999.

[11] E. F. Crawley, G. L. Sarver, and D. G. Mohr, “STRUCTURAL DAMPING FOR FLEXIBLE SPACE STRUCTURES,” vol. 10, no. 5, pp. 381–393, 1983.

[12] N. E. DuToit and B. L. Wardle, “Experimental Verification of Models for Microfabricated Piezoelectric Vibration Energy Harvesters,” *AIAA J.*, vol. 45, no. 5, pp. 1126–1137, 2007.

# Appendix C. Paper 3: Reference [176]

## On the effect of driving amplitude, frequency and frequency-amplitude interaction on piezoelectric generated power for MFC unimorph

M. Khazaee, A. Rezaniakolaei, L. Rosendahl

This paper has been presented in

*In 26th International Congress on Sound and Vibration.* The International Institute of Acoustics and Vibration (IIAV), July 2019, Montreal, Canada.

26th INTERNATIONAL CONGRESS ON SOUND AND VIBRATION
7-11 July 2019, Montreal

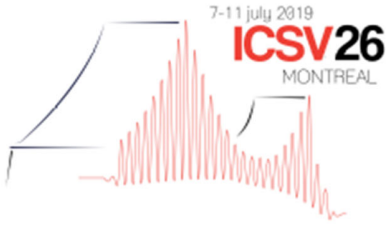


# ON THE EFFECT OF DRIVING AMPLITUDE, FREQUENCY AND FREQUENCY-AMPLITUDE INTERACTION ON PIEZOELECTRIC GENERATED POWER FOR MFC UNIMORPH

Majid Khazaee, Alireza Rezaniakolaei and Lasse Rosendahl
*Department of Energy Technology, Aalborg University, 9220 Aalborg East, Denmark.*
*e-mail: alr@et.aau.dk*

In this paper, an experimental study on effects of frequency, amplitude and frequency-amplitude interaction of base excitation on vibration piezoelectric energy harvesters is presented. To do so, a unimorph piezoelectric harvester made from macro fiber composite (MFC) piezoelectric layer is tested. A two-factor factorial design with two replications is considered, in which frequency and amplitude of driving vibration are the treatment factors. For changing treatment factors, an appropriate frequency range is considered to include the device fundamental frequency and three excitation levels are considered. In order to investigate the effects of treatment factors on the power output, a linear model is considered. Results show that increasing amplitude of excitation vibration causes a stiffness softening behavior of the piezoelectric oscillatory beam leading to reduction in the harvester natural frequency. In addition, from the frequency-amplitude interaction analysis, output power is much more sensitive to vibration amplitude for driving frequencies near the harvester natural frequency compared to frequencies far away from the harvester natural frequency.

Keywords: Piezoelectric Harvester, Driving Frequency, Vibration Amplitude, Nonlinear Behaviour, Frequency-Amplitude Interaction

## 1. Introduction

In order to enhance system performance in terms of life time and accessibility for remote systems [1], piezoelectric energy harvesting (PEH) has become an important part of energy harvesting techniques because of its simplicity, easy integration [2] and availability of vibration in any environment [3]. In PEH, frequency and amplitude of vibration source have great effects on output power. Consequently, researchers focused on the study of influential parameters on the output power from PEH [4], [5].

Excitation frequency is the most critical parameter in PEH, as frequency matching to the natural frequency of harvester is essential in order to obtain suitable amount of power in practice. Therefore, two types of harvesters exist, namely linear and nonlinear generators [3]. In linear generators, there are two optimum frequencies for operating a piezoelectric harvester, namely fundamental natural frequency of the device and the anti-resonance frequency [6], depending on electrical and mechanical properties of the device. Roundy et al. [5] investigated the dependency of power output versus driving frequency, added mass, and piezoelectric coupling coefficient based on simulations. In the previous studies, only a one-factor analysis has been carried out that only considered one parameter in each study.

Amplitude of vibration is another important factor affecting generated power. Wei and Jing [7] and Roundy et al. [8] using a general linear and inertial-based generator, Erturk and Inmarn [9] using a beam-type model, and De Marqui Junior et al. [10] using a two-dimensional finite element model showed that for harmonic base excitation, the power is dependent to the square of external vibration magnitude. On the other hand, in the nonlinear framework, natural frequency of the harvester as a dynamical system can experience a minor change due to high amplitude vibration [11] or due to other parameters such as pre-load [4]. Evensen [11] showed that by increasing the vibration excitation on a beam, a degree of nonlinearity in fundamental frequency will emerge. This nonlinear effect is much more prominent for the boundary conditions those that are more flexible [11]. In the spite of the nonlinear effect of vibration amplitude on the beam resonance frequency and the fact that piezoelectric harvesters are mostly clamped-free flexible beams, there is no previous studies presented this effect on piezoelectric power output.

PEH is a research area, which has close connection to harvester vibration characteristics and yet there are many vibrational phenomenon that should be addressed. To investigate the interactions of driving frequency and amplitude on piezoelectric generated power, a two-factor factorial design is considered for the experimental test, in which frequency and amplitude of driving vibration are two treatment factors. Then with two replications, a set of runs with different treatment factor levels is carried out. Using an experimental model for the designed tests, main effects of frequency and amplitude as well as frequency-amplitude interaction are investigated.

## 2. Experimental Setup

Excitation frequency and magnitude can cause important changes in the power generated by piezoelectric materials. To track these changes at different frequencies, a set of experiments are designed to investigate the effect of excitation frequency and amplitude of excitation on piezoelectric harvester.

Unimorph geometry as one the commonest configuration of piezoelectric harvesters was used in this study. Piezoelectric sample comprises of a Macro Fiber Piezoceramic-Composite (MFC M2814 P2) from Smart Materials Corporation [12] bonded to an aluminium substrate with epoxy rapid 332 adhesive with the density of 1.16 g/cm3. Centre shim is a 0.12-mm thickness aluminium shim with elastic modulus of 68.9 GPa and density of 2.7 g/cm3. Piezoelectric harvester was clamped at one end with a clamp box as shown in Figure 1 and then was connected to a VSD 201 shaker for base excitation. VSD 201 shaker is fed by a Kepco AC power generation. National Instruments modules NI 9263 and NI 9215 were connected to a National Instrument Compact data acquisition system (cDAQ) type 9172 for performing signal generation and data recording, respectively. LabVIEWTM 2013 was used as the graphical interface between computer and experimental equipment. Figure 1 shows the experimental setup.

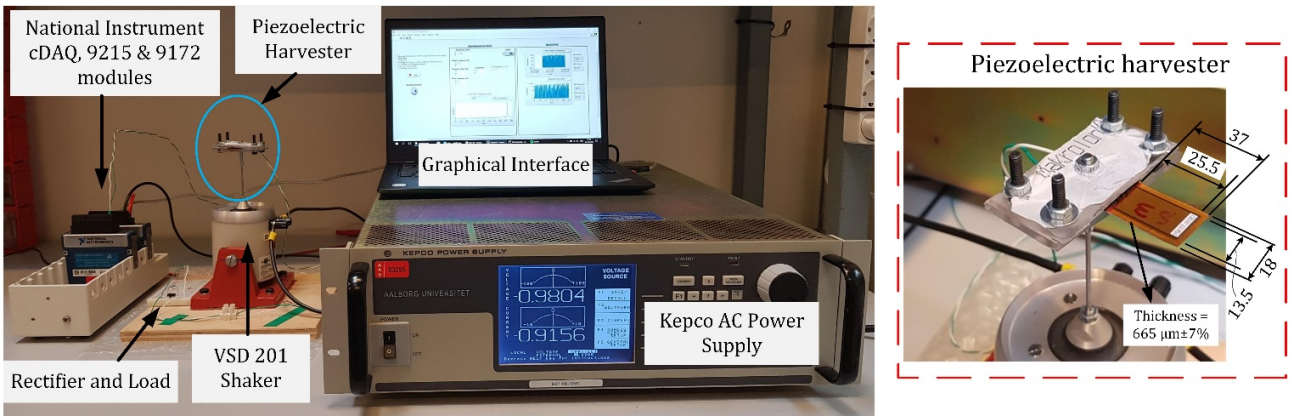


Figure 1: Experimental Setup and piezoelectric harvester

It is aimed to investigate the dependency of harvested power to excitation magnitude over a range of frequencies containing device natural frequency. Since there are frequency and amplitude of excitation as input factors, a two-factor factorial design should be used. The response is the RMS of output power when the piezoelectric harvester is connected to a 31500-Ω resistance load. Frequency factor is named Factor A and is a continuous parameter rather than a factor with discontinuous levels, hence a random sampling technique will be used. Factor B is the levels of excitation and is a level-based factor. Two replications are considered for the test as well as 40 frequencies with three amplitude levels of 0.1, 0.2, and 0.25 V for shaker input. Therefore, in total, 240 runs will be tested.

## 3. Results and Discussion

In this section, outcomes of this paper will be presented. It is categorized into three subsections. The first part presents the primarily assessment of experimental data. The next two subsections deal with the investigation of the trend in changing output power with respect to the magnitude and frequency of excitation.

### 3.1 Primarily Experimental Data

Figure 2 shows the RMS of generated power at different frequencies and with different levels of amplitude excitation, e.g. 0.1, 0.2 and 0.25 V. Power responses for two replications in Fig. 2 show that the experimental runs are met with each other. A well-known fact also is proven here; output power is maximum at the resonance frequency for all three excitation amplitudes. However, by comparing power responses for three different amplitudes, it can be observed that resonance frequency was decreased by increasing excitation amplitude. This behaviour shows that another factor will play a role in piezoelectric power generation.

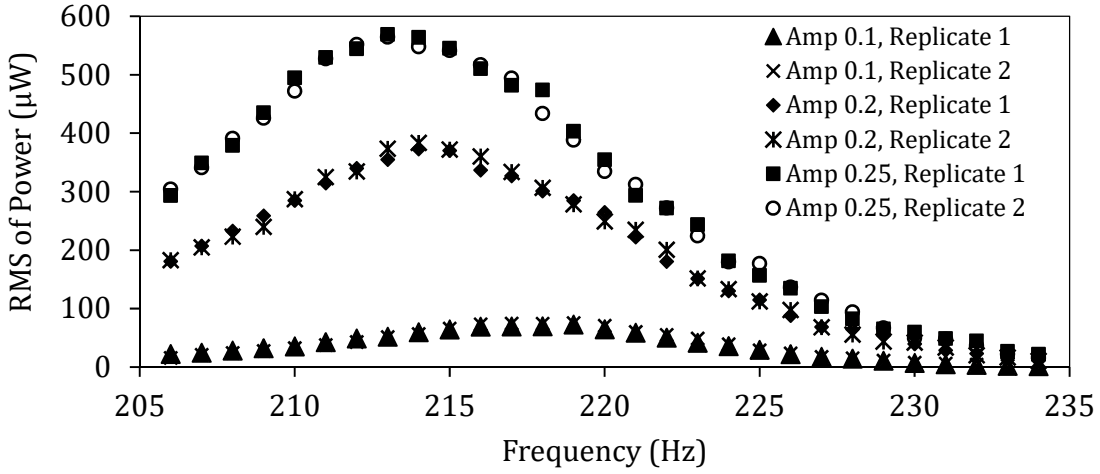


Figure 2: RMS of power obtained from experiments at different amplitude levels versus frequency

### 3.2 Nonlinear Behaviour of Unimorph

From vibration theory for a viscous damped single degree of freedom system, oscillatory frequency will be $\omega_d = \omega_n\sqrt{1-\zeta_m^2}$ [13], where $\omega_n = \sqrt{k/m}$ is the undamped natural frequency and $\zeta_m$ is the viscous damping coefficient. The reduction in oscillatory frequency in Fig. 2 can be due to reducing $\omega_n$ or increasing $\zeta_m$. Using the relation between damped and undamped natural frequencies, one can concluded that $\zeta_m$ should increase from 0.01 to 19.1% in order to cause a decrease in $\omega_d$ from 219 Hz at 0.1 V to 214 Hz at 0.2 V provided that $\omega_n$ remain constant. This increase in mechanical damping ratios is not realistic, and hence a reduction in $\omega_n$ is necessary to occur during increase in excitation amplitude for

causing a decrease in $\omega_d$. As the harvester mass remained unchanged during tests, it can be concluded that stiffness of the piezoelectric harvester decreased when it is subjected to higher excitation amplitudes.

If the test with excitation amplitude of 0.1 V is considered as standard and denoted with 0, one can compare the fundamental natural frequency, $\omega_n$, and resonant power output, $P_{max}$ with respect to the standard state, as shown in Fig. 3. From Fig. 3, it is observed that as excitation magnitude increases, the fundamental frequency of the device nonlinearly decreases, while maximum power increases. The power increase due to vibration amplitude will be thoroughly investigated in the next section. Here, the main focus is the change of piezoelectric resonance frequency due to excitation magnitude. Since piezoelectric resonance frequency decreases with excitation magnitude increase, a softening stiffness behaviour is present in piezoelectric unimorph harvester.

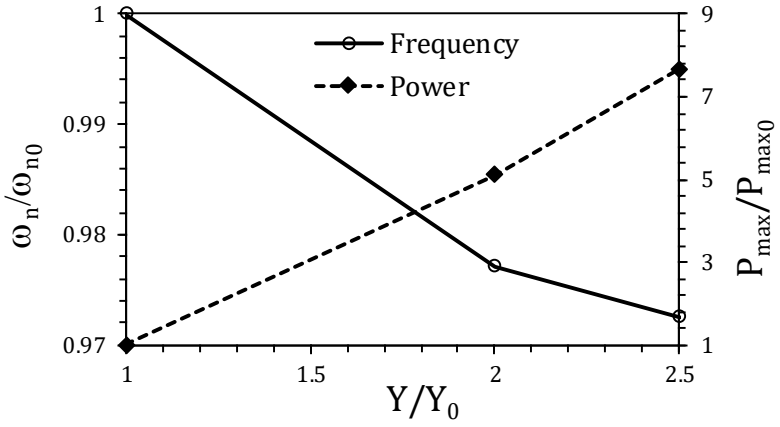


Figure 3: The effect of excitation amplitude on oscillatory frequency and resonant power

### 3.3 Sensitivity of Interaction Analyses

In this section, it is aimed to perform an appropriate sensitivity investigation on excitation magnitude and frequency. Hence, a statistical model is needed to describe the experimental data for the sensitivity analysis. To do so, a well-known linear model for two-factor factorial design will be used for data treatment. Based on two-factor factorial design, the linear model for these experiments can be expressed as [14],

$$y_{ijk} = \overbrace{\mu + \alpha_i + \beta_j + (\alpha\beta)_{ij}}^{\boldsymbol{\mu_{ij}}} + \epsilon_{ijk}, \qquad i = 1, \dots, 40,\ j = 1,2, J = 3,\ k = 1,2 \tag{1}$$

where $i$ associated to frequency level, $j$ to amplitude level and $k$ is the replicates. In Eq. (1), $y_{ijk}$ is the RMS of output power, $\mu$ is the grand mean of RMS power, $\alpha_i$ is the effect of frequency, $\beta_j$ is the effect of excitation amplitude, $(\alpha\beta)_{ij}$ is the interaction effect of frequency-amplitude and $\epsilon_{ijk}$ is the experimental error. It is assumed that the experimental errors are independent and normally distributed with zero mean and standard deviation of $\sigma^2$, e.g. $\epsilon_{ijk} \sim N(0, \sigma^2)$. This assumption later on will be evaluated.

The model in matrix form can be represented as [14],

$$[\boldsymbol{Y}] = [\boldsymbol{X}][\boldsymbol{\Psi}] + [\boldsymbol{\epsilon}] = \left[\boldsymbol{1} \parallel \boldsymbol{X_\alpha} \parallel \boldsymbol{X_\beta}\right] \begin{bmatrix} \boldsymbol{\mu} \\ \boldsymbol{\Psi_\alpha} \\ \boldsymbol{\Psi_\beta} \\ \boldsymbol{\Psi_{\alpha\beta}} \end{bmatrix} + [\boldsymbol{\epsilon}] \tag{2}$$

where $[Y]$ is the $12 \times 1$ response matrix, $[X]$ is the $12 \times 12$ coefficient matrix, $[\Psi]$ is the $12 \times 1$ matrix containing grand mean, main effect, and interactions, and $[\epsilon]$ is the $12 \times 1$ error matrix. In order to solve Eq. (2) for $[\Psi]$, one can easily state that $[X]'[X]$ should not be singular. As $[X]'[X]$ is singular, a

method should be used in which $\mu_{ij}$ cell mean is made the standard and consequently $[\Psi]$ will be changed to $[\hat{\Psi}]$, by dropping the first level of factors in the main effect [14]. By this transformation, treatment effect and the error sum of squares (ssE) can be expressed with equations (3) and (4).

$$[\hat{\boldsymbol{\Psi}}] = ([\boldsymbol{X}]'[\boldsymbol{X}])^{-1}[\boldsymbol{X}]'[\boldsymbol{Y}] \quad (3)$$

$$\boldsymbol{ssE} = [\boldsymbol{Y}]'[\boldsymbol{Y}] - [\hat{\boldsymbol{\Psi}}]'[\boldsymbol{X}]'[\boldsymbol{Y}] \quad (4)$$

As it was mentioned, it is assumed that the residuals are independent and normally distributed. Figure 4 (a) shows the experimental residuals versus frequency. It can be seen that residuals scattered randomly for different frequencies, emphasizing residuals' independency. Moreover, as it can be seen from normal Q-Q plot in Fig. 4 (b), experimental data are located close to the fitted line, showing that the residuals can be considered normally distributed figures.

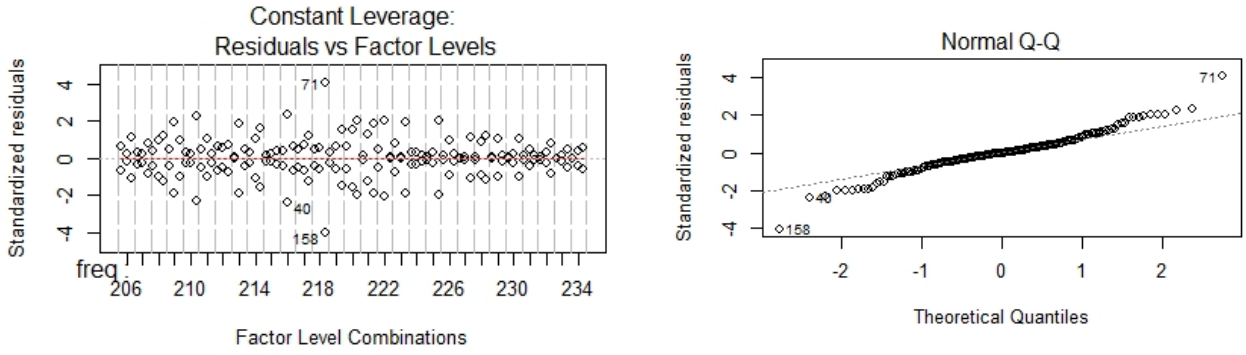


(a) (b)

Figure 4: (a) Experimental residuals versus frequency and (b) Norm Q-Q plot

Figure 5 shows residuals of experimental units at different treatment levels. For first experimental unit, frequency, Fig. 5 (a) shows a randomly distributed residuals over frequency range. However, for the second experimental unit, residuals increase with the increase in excitation amplitude. This shows that generated power by piezoelectric harvester is not a linear factor of excitation amplitude. This conclusion is already known from literature, such as Roundy et al. [8].

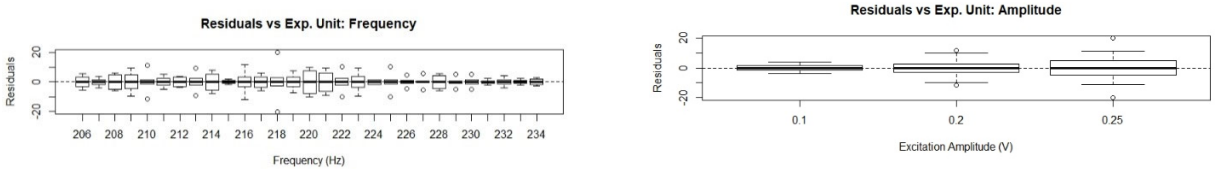


(a) (b)

Figure 5: Distribution of residuals at different levels of experimental units

Figure 6 shows the main effects, α and β, in the model presented by Eq. (1), with respect to the marginal average of the other factor. As it can be seen from Fig 6 (a), generated power is maximized at a specific frequency, which is equal to resonant frequency of the harvester with that excitation amplitude. In addition, Fig. 6 (b) shows that increasing the excitation level will lead to dramatic increase in the output power. This conclusion with the analysis of residuals in Fig. 5 (b) proved that the increase in the power with respect to excitation amplitude is exponential rather than linear.

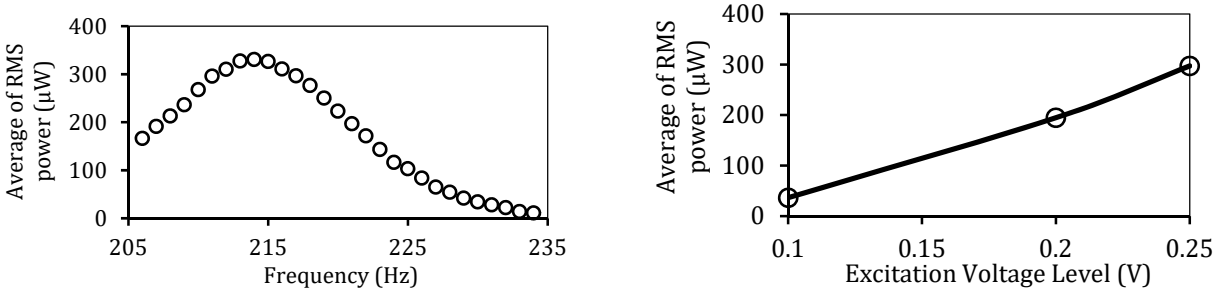


(a) (b)

Figure 6. Main effects of treatment factors (a) frequency ($\alpha_i$) and (b) excitation amplitude ($\beta_j$) effects

Figure 7 shows the interaction effects of frequency-amplitude on generated power. Each curve represents output power over different excitation levels with the same excitation frequency. As it was shown in Fig. 6 (a), power is maximum at 214 Hz. In order to observe interaction effects at different frequencies. A set of frequencies ranging from far away from natural frequency, for instance 206, 210, and 222 Hz, to the natural frequency is considered. Figure 7 shows that frequency-amplitude interaction is much more prominent at frequencies close to the natural frequency. For instance, curves assigned to frequencies 213 and 214 Hz having the highest dependency to excitation amplitude while the interaction effect will be lesser for frequencies far away from natural frequency.

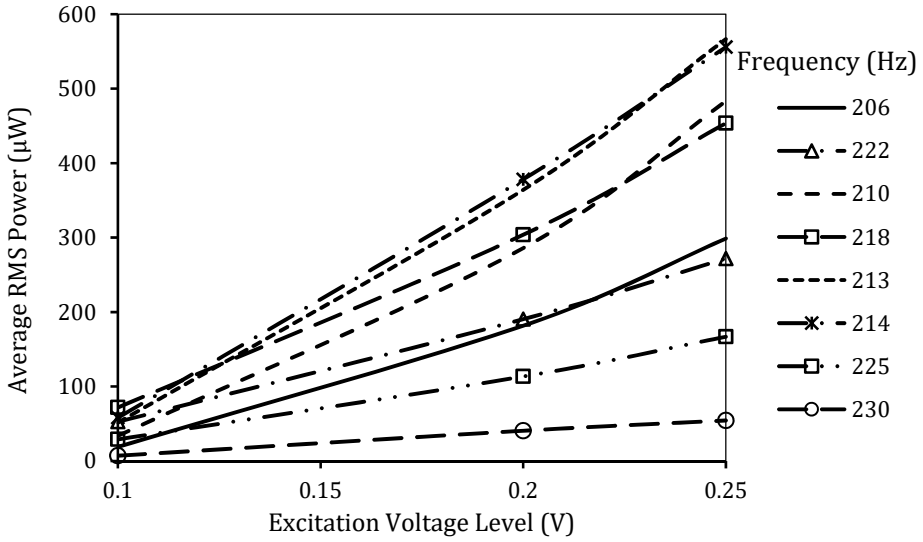


Figure 7: Frequency-amplitude interaction ($\alpha\beta_{ij}$) on average of RMS power

## 4. Conclusion

This paper dealt with an experimental investigation of driving amplitude, frequency and frequency-amplitude interaction on piezoelectric output power from a MFC piezoelectric harvester in unimorph geometry. Varying excitation frequency showed that the output power is maximum while the device is vibrating at its natural frequency. On the other hand, increasing amplitude of vibration will lead to the exponential increase of power output. By considering frequency-amplitude interaction, two main conclusions were made. Firstly, piezoelectric harvester in unimorph geometry represented a nonlinear stiffness softening behaviour in such a way that resonance frequency will decrease as excitation amplitude

increases. Furthermore, the sensitivity of output power to driving amplitude is different for different driving frequencies in such a way that output power is much more sensitive to the driving amplitude at frequencies near resonance frequency.

## REFERENCES


[1] R. Ahmed, F. Mir, and S. Banerjee, "A review on energy harvesting approaches for renewable energies from ambient vibrations and acoustic waves using piezoelectricity," *Smart Mater. Struct.*, vol. 26, no. 8, p. 085031, 2017.

[2] M. Khazaee, A. Rezaniakolaei, and L. Rosendahl, "An experimental study on macro Piezoceramic fiber composites for energy harvesting," *Mater. Sci. Forum*, vol., no., p. , 2019.

[3] R. Usharani, G. Uma, M. Umapathy, and S.-B. Choi, "A Novel Piezoelectric Energy Harvester Using a Multi-Stepped Beam with Rectangular Cavities," *Appl. Sci.*, vol. 8, no. 11, p. 2091, 2018.

[4] E. S. Leland and P. K. Wright, "Resonance tuning of piezoelectric vibration energy scavenging generators using compressive axial preload," *Smart Mater. Struct.*, vol. 15, no. 5, pp. 1413–1420, 2006.

[5] S. Roundy *et al.*, "Improving power output for vibration-based energy scavengers," *IEEE Pervasive Comput.*, vol. 4, no. 1, pp. 28–36, 2005.

[6] N. E. DuToit, B. L. Wardle, and S. G. Kim, "Design considerations for MEMS-scale piezoelectric mechanical vibration energy harvesters," *Integr. Ferroelectr.*, vol. 71, pp. 121–160, 2005.

[7] C. Wei and X. Jing, "A comprehensive review on vibration energy harvesting: Modelling and realization," *Renew. Sustain. Energy Rev.*, vol. 74, no. January, pp. 1–18, 2017.

[8] S. Roundy, P. K. Wright, and J. Rabaey, "A study of low level vibrations as a power source for wireless sensor nodes," *Comput. Commun.*, vol. 26, no. 11, pp. 1131–1144, 2003.

[9] A. Erturk and D. J. Inman, "An experimentally validated bimorph cantilever model for piezoelectric energy harvesting from base excitations," *Smart Mater. Struct.*, vol. 18, no. 2, p. 025009, 2009.

[10] C. De Marqui Junior, A. Erturk, and D. J. Inman, "An electromechanical finite element model for piezoelectric energy harvester plates," *J. Sound Vib.*, vol. 327, no. 1–2, pp. 9–25, 2009.

[11] D. A. Evensen, "Nonlinear vibrations of beams with various boundary conditions.," *AIAA J.*, vol. 6, no. 2, pp. 370–372, 1968.

[12] S. Material, "https://www.smart-material.com." .

[13] D.J.Ewins, *Modal Testing : Theory , Practice and Application*, Second. RSP, 2000.

[14] J. Lawson, *Design and Analysis of Experiments with R*. 2014.

# Appendix D. Paper 4: Reference [4]

## A novel method for autonomous remote condition monitoring of rotating machines using piezoelectric energy harvesting approach

M. Khazaee, A. Rezaniakolaei, A. Moosavian, L. Rosendahl

This paper has been published in

*Sensors and Actuators A: Physical.* vol. 295, pp. 37-50, 2019

Sensors and Actuators A 295 (2019) 37–50

Contents lists available at ScienceDirect

Sensors and Actuators A: Physical

journal homepage: www.elsevier.com/locate/sna

# A novel method for autonomous remote condition monitoring of rotating machines using piezoelectric energy harvesting approach

Majid Khazaee[a], Alireza Rezaniakolaie[a,*], Ashkan Moosavian[b], Lasse Rosendahl[a]

[a] Department of Energy Technology, Aalborg University, Pontopisanstraede 111, DK 9220, Aalborg, Denmark
[b] Department of Mechanical Engineering of Agricultural Machinery, Tarbiat Modares University, Jalal AleAhmad, Nasr, Tehran, Iran

ARTICLE INFO

*Article history:*
Received 14 March 2019
Received in revised form 8 May 2019
Accepted 11 May 2019
Available online 18 May 2019

*Keywords:*
Condition monitoring
Autonomous system
Piezoelectirc harvesting
Power management
Fault diagnosis
Water pump

ABSTRACT

This paper presents a novel autonomous method for condition monitoring of rotating machines during operation based on radio frequency (RF) pulse transmission using energy harvesting from operational vibration. An energy harvesting unit is designed to generate and rectify the energy harvested from the machine vibration using Voltage Multiplier (VM) circuit and to store the energy into a capacitor. Then, this energy harvesting unit runs a smart system consisting of a microcontroller and the RF transmitter designed to send a pulse at specific capacitor voltage. A pulse-based condition monitoring approach is introduced which monitors the state of the machine during the operation. In order to estimate power output of the piezoelectric harvester for a realistic vibration signal, the Fourier Transform concept for signal decomposition is incorporated into the well-known electromechanical distributed parameter model. Using experimental data, performance of this autonomous condition monitoring system is tested for a water pump at different conditions. To do so, acceleration data from a centrifugal water pump are acquired with an accelerometer, which then decomposed into a series of harmonics using Fast Fourier Transform. Then using analytical distribute model, a bimorph energy harvester with two Piezoceramic layers is optimized to generate maximum power from the water pump vibration. Consequently, the condition monitoring of the water pump is performed using the presented pulse-based approach. Results of this study show that, the fault diagnosis can be performed autonomously by applying the pulse-based method presented in this work, and by using the piezoelectric harvesting device as an energy source.


## 1. Introduction

Online condition monitoring (CM) of machines during operation is a key approach for reducing unscheduled downtime and maintenance cost during useful life. CM of rotary machines is one of the most successful and established method using so-called pattern recognition in time or spectra responses [1]. There are vast number of studies for CM using different measurement sensors, which record one response of system during operation, and applying different analyses on the recorded data, such as Fourier or Wavelet transforms. Regarding the connection type for sensors, contact and contactless sensors have been widely practiced for CM of rotating machines. For instance, accelerometer installed on bearing housing [2], accelerometer installed on machine outer case and current sensors on input wires [3], accelerometer installed on bearing housing for shaft [4] and accelerometer on outer case of a water pump [5] were employed for condition monitoring applications. In recent years, to overcome difficulties related to direct instrumentation of rotating components, some researchers applied non-contact sensors for condition monitoring of rotating machines using K-Band Doppler radar [6], laser sensors [7] and vision-based non-projection fringe pattern [8]. Although using contactless sensors helped the direct instrumentation complexities, these methods still suffer from wiring, instrumentation complexities and battery-related problems.

All the aforementioned approaches used conventional measurement methods which require wiring for sensors to transfer data to a control room. For an industrial plant that includes many rotating machines, the cost of wiring and regular inspection of wires and their connections will be considerable. To eliminate problems in conventional methods, e.g. wiring difficulties, setup implementation and immobility [9], an outline for machine condition monitoring was presented using wireless sensor networks (WSNs) [10]. Although WSNs improved common CM approaches, those that are powered with batteries suffer from short lifetime due to the battery lifespan [11]. In an attempt toward self-powered CM

* Corresponding author.
*E-mail address:* alr@et.aau.dk (A. Rezaniakolaie).

https://doi.org/10.1016/j.sna.2019.05.016
0924-4247/

methods, energy harvesting (EH) has emerged as a source of energy for powering batteries in CM applications [11].The energy harvesting has seen a worldwide growing attention in academic and industry during recently [12]. There are various methods to convert often-lost mechanical energy into electrical energy for motor or generator applications, including electromagnetic induction, electrostatic induction and the piezoelectric effect [13]. In the recent years, the number of studies considering energy harvesting for structural health monitoring is rapidly increasing [11]. Energy harvesting by piezoelectric materials provides higher energy density, and can be simply integrated into a system [13,14].

Recently, smart materials as sensors for system operational condition and structural health monitoring were employed. In some cases, these smart materials also acted as transducers that generate voltage according to the sensed vibration. This concept was used for bridge condition monitoring under forced vibration by adopting piezoelectric energy harvester [15]. In cases, it has been demonstrated that these sensors can provide enough energy for themselves and, hence, can be regarded as self-powered sensors without the need for wiring [16,17]. Moreover, in some studies, it was shown that a wireless connection can be powered by these self-powered sensors for transferring data or sending a pulse [18,19]. In the research by Lim et al. [20], piezoelectric patches were installed on wind turbine blades to demonstrate that the patches can provide power for wireless connection from blade strain energy. In the existence of a structural imperfection or a fault in the system, introduced vibration on these smart materials will be different and, hence, this concept can be used for condition monitoring or structural health monitoring. In another study, Lim et al. [21] showed that, by analyzing the time of sending discrete signals between three blades, blade state can be monitored. Patange et al. [22] installed piezoelectric patches onto composite beams in defect-free and delaminated conditions to study output power from these patches under low-frequency vibration excitation. They showed that delaminated beams will generate less energy compared to defect-free ones by demonstrating that the energy harvesting can be employed for health monitoring. However, they did not assess whether this energy output could be enough for running a self-powered system or how to manipulate output power differences in order to perform health monitoring.

Most of state-of-the-art about fault detection and condition monitoring using smart materials presented only the feasibility of such systems and have not adequately focused on power management and system performance for self-powered condition monitoring. On the other hand, studies that focused on electrical power management for these self-powered systems have not presented appropriate condition monitoring approaches. In addition, in the self-powered condition monitoring systems, the design of vibration energy harvester and related optimization process, as a significant step, has not been addressed. Moreover, most of previous studies about self-powered CM were carried out for structural imperfections such as crack and delamination while there are, apart from the structural faults, some other faults that can occur in an operating machine. One study reported the use of harvested energy from an electromotor for transferring acceleration data through wireless connection [23]. In the presented study, all three essential sections for a vibration-based self-power condition monitoring, namely, the design of energy harvester, power management and condition monitoring approach, are addressed. To the best knowledge of the authors, such a study containing all these areas has not been presented. The presented study uses a new established method based on pulse timing for fault detection of a complex rotating system in conjunction with cantilever piezoelectric beam for generating electrical power, which is easy to integrate in the system. By applying the presented energy harvester and pulse timing method for CM, power and data-transfer wires are no longer necessary. This system can be integrated into an industrial production plant with many rotating machines in a cost effective manner. This study will contribute to the elimination of the need for expensive accelerometers, data acquisition unit with high sampling rate, sensor and equipment, which are typically being used for condition monitoring of high-speed rotary machines.

A robust self-power system is proposed for remote condition monitoring in which elapsed times between RF transmissions are investigated. In this study, experimental data from a real operating water pump is used as self-vibration machine. Then, the vibration signals are considered as base excitation for a piezoelectric harvester beam. Afterwards, using a well-known analytical model based on distributed Euler beam theory, output power from a bimorph with an added tip mass is optimized for maximum power generation from the experimental vibration data. Lastly, a method for remote condition monitoring is established that is relied on pulse-sending times. In this framework, section 2 is dedicated to propose the condition monitoring approach in system level, the conceptual design of energy harvesting unit and pulse-based condition monitoring method. The piezoelectric harvester contributes to energy harvesting from piezoelectric direct effect. In section 3, the energy harvester model is developed to estimate the output voltage analytically from operational vibration using the Fourier Transform of real vibration signals. Section 4 is dedicated to the experimental test study with a primarily signal processing step for the experimental signals. Finally, results of the applying the proposed condition monitoring on the presented case study is presented in section 5.

## 2. Autonomous remote condition monitoring

The main objective of this study is to design an autonomous condition monitoring system capable of remote health monitoring for rotating machines during the operation. Therefore, at first, components of the system are selected based on requirements that should be met to achieve online condition monitoring. Then, these components are evaluated regarding power consumption which is followed by an assessment that shows the required energy for the condition monitoring can be provided by the energy harvesting device and, therefore, the system is autonomous. This studs introduces a novel method based on pulse transmission from RF technology for remote condition monitoring. The method relies on comparing the elapsed time between pulses from a continuous operation machine generating vibration during operation. Since vibration is an unavoidable phenomena in operational machines, the focus for energy harvesting in this study is piezoelectric technology as the vibration of machines often contains high frequency harmonics. This section is dedicated to demonstrate such a system in terms of system design, power consumption, energy harvesting unit and pulse condition monitoring approach.

### 2.1. System design and power consumption

According to the functionality of this novel CM approach, the system should comprise a harvesting unit to generate, rectify and store energy, a low-power microprocessor to control the signal emitting, and RF transmitting unit for sending a binary signal when microprocessor allows. The storage system should always maintain the energy for running microprocessor as well as providing the energy for RF transmitter when it is enabled. Microprocessor can be programmed to power RF circuits when the voltage in the storage reaches to a specific value. This signal transmitting will repeatedly continue after the harvested energy reaches to the defined value each time. If the level of acceleration changes, the harvested energy will be directly influenced and, consequently, the time of RF transmitting is altered. Furthermore, a Failure Index is introduced in

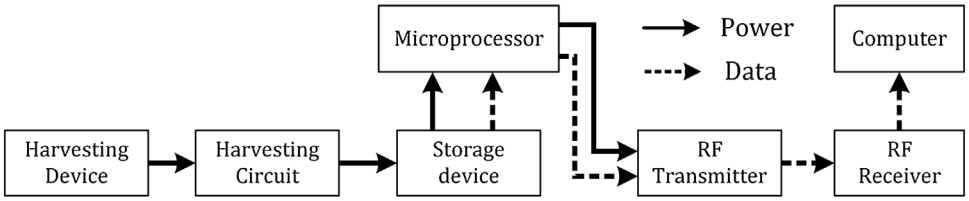


**Fig. 1.** The protocol for remote condition monitorings.

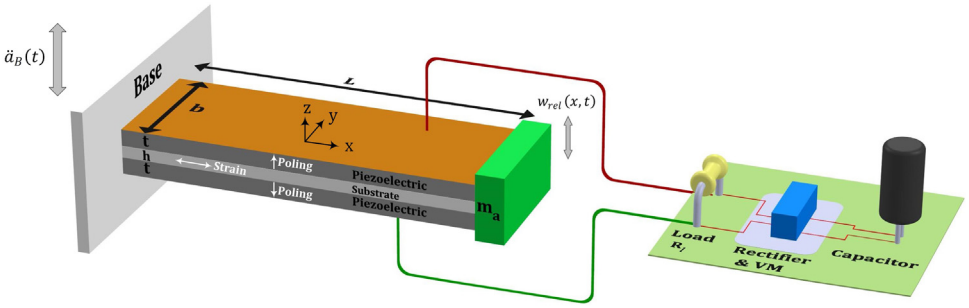


**Fig. 2.** Energy harvesting unit comprises of piezoelectric bimorph, resistance load, harvesting circuit and capacitor.

this work, which is defined based on the elapsed time between signal transmissions in operation compared to values recorded in defect-free condition. The component in this system are shown in Fig. 1.

The units in the protocol Fig. 1, which consume energy, are microprocessor and RF transmitter. Among these, the RF transmitter only consumes energy when it is activated by the microprocessor for signal transmitting. On the other hand, the microprocessor needs a permanent energy supply through running. For this reason and to fulfill requirements for this CM method, the microprocessor should have low-power consumption, operate in low voltage, be capable to perform simple calculations and have at least one comparator.

Microchip Technology Inc. [24] is a leading provider of low-power and high-speed flash technology microprocessors, which are appropriate selections for microprocessors in the wireless system design [19,25]. PIC16F676 as an 8-bit microcontroller is selected for this system because of its low-power consumption, operating at low voltage and very low standby current of 1 nA. It also has 1 comparator and 128 bytes of memory, which makes it suitable for programming with one checking condition. According to [26], this microcontroller consumes 8.5 μA at typical 2.0 V during operating at 32 kHz.

The RF module transmits the data from the Microprocessor when needed. The RF module stands in standby mode for the rest of cycle. The RF module in this work, RTFQ1P [27], is a 9.6 Kbps data transmitter with transmitting range up to 250 m with low-power consumption operating with 3.0 V supply voltage in the standby mode. This RF transmitter consumes 7 mA at 3.3 V voltage supply during the transmission of date and requires a maximum current of 100 nA in the standby mode [27].

### 2.2. Energy harvesting unit

In this study, the piezoelectric based energy harvesting unit is responsible for providing continuous energy to run the microprocessor and RF transmitter request. The harvesting unit consists of an energy harvester, a harvesting circuit and storage system as shown in Fig. 1. The piezoelectric energy harvester is considered as the source of energy production from the machine vibration. The harvester is designed to generate adequate energy to power the remote condition monitoring system. This device should accommodate two critical goals. At first, it should have capability to generate enough electrical energy for continuous operation of the remote condition monitoring system described in subsection 2.1. Secondly, this device should be designed to be sensitive to occurrence of faults. In many practical cases, the output voltage from the piezoelectric harvester is less than the input voltage required for running the electronic components. In addition, the generated voltage is an A.C. signal while the end-users require D.C. Thus, it is essential to provide a circuit for voltage enhancement as well as converting the A.C. to D.C. In this work, therefore, the energy harvesting circuit provides power supply suitable for the end-users. The capacity of the capacitor in the energy harvesting unit plays an important role in the health monitoring. The energy capacity should be large enough to provide energy in order to guarantee the system operation. On the other hand, since the microprocessor can activate or deactivate the RF transmitter based on voltage level of the capacitor, the capacitor should be small enough to experience a sensible voltage drop due to a short RF transmission. Fig. 2 shows these components in the energy harvesting unit.

There are different types of piezoelectric harvesters and harvester's configuration generally depends to the nature of available load and its frequency. A typical piezoelectric energy harvester as shown in Fig. 2 is made of a bimorph harvester. This bimorph structure is made of a thin substructure shim (usually a metal helping for charge transferring) which is bracketed with two piezoelectric layers. Among piezoelectric harvesters, cantilever configuration is the most widely used option, especially for vibration energy harvesting from mechanical systems [13]. In addition, in some cases an added mass $m_a$ is attached to the end of bimorph for frequency matching. This typical configuration is popular since, in a reasonably small volume, it delivers higher power density [13]. Piezoelectric ceramics have the best piezoelectric characteristics in comparison with the composites and polymers [28]. Among piezoelectric ceramics, PZT is an important material because of its high Curie temperature and excellent energy harvesting potential. It is a well-known fact that piezoelectric harvester generates the maximum voltage when it is excited by an external force with frequency close to its natural frequencies [14]. Generated power from bimorph piezoelectric harvester at resonance is higher than other frequencies even anti-resonance frequency [29]. Hence, in order to scavenge the

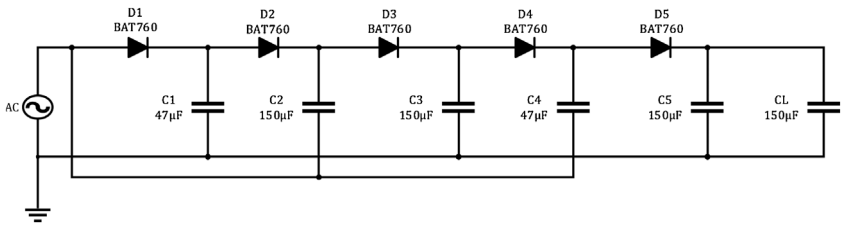


**Fig. 3.** Optimum 5 stage MDCP circuit for use with the designed piezoelectric harvester.

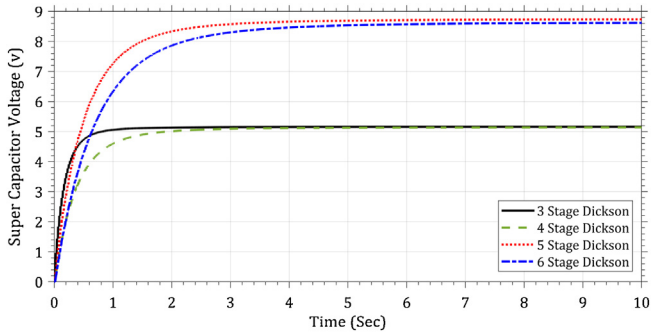


**Fig. 4.** Storing capacitor voltage outputs for an input magnitude of 1.85 V at 49.5 Hz.

maximum energy from piezoelectric bimorph, a configuration containing PZT material as the piezoelectric layers should be designed to be excited at its fundamental natural frequency.

One solution for the energy harvesting circuit to increase the voltage and to convert AC to DC is so-called voltage multiplier (VM) or charge pump circuit [30], where a capacitor is charged in one-half of the A.C. input and then discharged into the next circuit section during the second half cycle. Within the framework of VM, Multistage Villard Voltage Multiplier (MVVM) and Multistage Dickson Charge Pump (MDCP) can be used in order to increase the power [31] as have been done by Torah et al. [26] and Galchev et al. [32]. In this study, a MDCP circuit is applied in order to amplify the generated voltage. The MDCP circuit consists of diodes and capacitors, where the stage of MDCP determines the number of diodes and capacitors. In order to obtain the optimum staged of the MDCP, a number of different circuits were compared using MATLAB® Simulink. Siemens BAT760 diodes with a forward bias voltage of ~100 mV and current of 0.1 mA were used due to the low forward voltage drop and reverse leak current. For the energy storage, a capacitor with 150 μF was considered in the simulations and the voltage of the capacitor is compromised at different MDCPs in order to obtain the optimum VM circuit. Fig. 3 shows a 5 stage MDCP circuit with BAT760 diodes and the optimum values for the capacitors. The storing output voltage of the capacitors for different MDCP stage circuits and input of 1.85 V at 49.5 Hz are shown in Fig. 4. As can be seen, the 5 stage MDCP delivers the highest voltage output with fast charging time. Therefore, the configuration shown in Fig. 3 is selected as the best design for amplifying the output voltage from the piezoelectric harvester and it is used for the further steps in this study as of the optimized VM configuration.

### 2.3. Pulse condition monitoring

The presented method relies on the pulse timing method by the RF transmitter for remote condition monitoring. As discussed, the RF transmitter will be enabled by microprocessor to transmit a signal whenever the level of energy in the storage device reaches to the defined value. If the machine is working under normal conditions, no major changes in energy capacitor charging and, consequently, in the RF transmitting processes are expected. Therefore, the pulse timing lies within a band. However, if any fault occurs during machine operation, the immediate change in the acceleration affects the energy storage charging and, consequently, the pulse timing.

Fig. 5 shows the process of condition monitoring based on the pulse timing method. In Fig. 5 (a), the system performance during the normal operation is shown. On top, a typical acceleration of the system is shown. Then, the stored energy is plotted and finally, in the bottom, elapsed time of the pulses are shown versus time. It is worth mentioning that plots do not contain specific values since these figures are presented for showing the concept of this approach rather than focusing on one specific application. When the stored energy reaches to the limit for microprocessor, the microprocessor will be activated through a voltage-level switch to the circuit. Thus, the energy drops in the stored energy curve. This process is before sending any pulses and is only for the start phase. From this moment the microprocessor is active and tunes the RF transmitting. After the energy in the storage device reaches to an peak value, the microprocessor allows RF transmitter to send the first pulse at time $T'$. Sending pulses will continue each time after the elapsed time, $T$, in the regular operation. In Fig. 5(b), the performance of the system is shown when the fault occurs. The first and second pulses are transmitted after $T'$ and $T$ elapsed times, respectively, just similar to the normal operation. After a specific time, it is assumed that a fault occurred in the machine causing increment in the acceleration and, consequently, the charging process will be faster. Therefore, the elapsed time reduces from normal $T$ to a value of $T_d$ where $T_d < T$. It can be seen that if the fault occurred during one of the charging phases, the elapsed time is not equal to $T$ nor $T_d$ as the capacitor has not been charged in none of healthy and damage conditions. This charging phase is called transient interval and its elapsed time is denoted with $T_{tr}$, where $T_d < T_{tr} < T$. This transition phase is an indicator that machine state is being changed. It is worthy to note fast charging of capacitor at abnormal condition.

One important assessment in this method is the statistical analysis of elapsed time as obviously the elapsed time of the pulses undergoes minor differences due to the nature of experimental errors. The elapsed time between the pulses can be modeled as:

$$T_{ij} = \mu + \tau_i + \varepsilon_{ij}\, i = 1, \ldots, N_{cnd},\ j = 1, \ldots,\ N_{exp} \tag{1}$$

where $\mu$ is the average of elapsed times in defect-free condition, $\tau_i$ is the effect of machine condition on the elapsed time, $\varepsilon_{ij}$ are the experimental errors, $N_{cnd}$ is the number of conditions considered and $N_{exp}$ is the maximum number of elapsed time figures obtained experimentally for different conditions of the machine. The experimental errors are independent and normally distributed due to randomness of experiments, e.g. $\varepsilon_{ij} \sim N\left(0, \sigma_i^2\right)$, where $\sigma_i$ is the standard deviation of errors. It is worth mentioning that $i = 1$ is the defect-free condition while $i > 1$ corresponds to faulty conditions. Based on these definitions, $\tau_1 = 0$ while $\tau_{i>1} \neq 0$.

Now, the pulse condition monitoring can be performed as follows:

Step 1: A set of data from the machine at different working conditions including defect-free state is formed and then one should

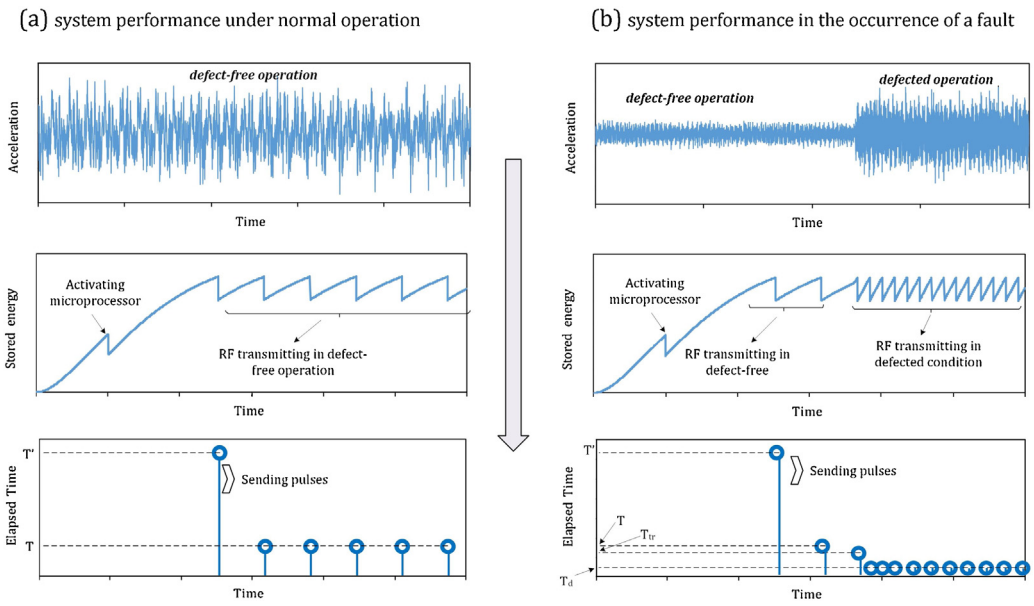


**Fig. 5.** Condition monitoring based on pulse timing method.

be able to compute the statistical features in Eq. (1), e.g. $\mu$, $\tau_i$ and $\sigma_i$.

Step 2: After each pulse transmission, the elapsed time, called $\hat{T}$, between the current pulse and previous pulse should be computed.

Step 3: Fault Index (FI) is defined as:

$$FI = \left(\hat{T}/\mu - 1\right)^2 \tag{2}$$

FI is in the range of 0–1, where 0 means the machine is in defect-free condition while 1 means that the machine works abnormally. In addition, a considerable change in the FI identifies a change in the machine state. This FI has a confident limit (CL) of:

$$CL = 1 - \mathcal{D}_k/\mu + \tau_k \tag{3}$$

where $\mathcal{D}_k$ is the distance between elapsed time $\hat{T}$ and the average of elapsed time in $k$-th machine condition. In addition, $k$ is the class in which $\mathcal{D}_k = \left|\hat{T} - (\mu + \tau_k)\right|$ is minimum. By this definition, CL is the certainty of FI, which demonstrates assurance of the identified machine condition. The higher CL is, the more reliable the machine condition monitored.

Step 4: In order to detect type of the fault, a state parameter can be defined as $\mathcal{S}$:

$$\Gamma_{\mathcal{S}} = min\left\{\left(\frac{\hat{T}}{\mu + \tau_{\mathcal{S}}} - 1\right)^2\right\} \tag{4}$$

If $\mathcal{S}$ is equal to 1, the state of machine is normal, otherwise $\mathcal{S}$ is the class of defined fault.

In order to show the performance of this CM method, a situation is considered in which the state of a machine changes from "1" to "2" and then to "3". State "2" has lower elapsed transmission time while elapsed transmission time of "3" is higher than "1". Fig. 6(a) shows the considered elapsed time between the transmissions over time. Based on these values, the FI and machine state $\mathcal{S}$ are calculated using Eqs. (2) and (4), respectively and graphically shown in Fig. 6(b). As shown, the FI is close to 0 until the elapsed time is within the range of "1" state. After the system state changed to "2", $\mathcal{S}$ jumped to 2 and FI is no longer close to 0. Finally, in the second change of system state to "3", $\mathcal{S}$ remains at 3 and a change in the FI scatter can be observed. Although this is a numerical example of the pulse system performance, it shows that in the both cases whether the elapsed time is lower or higher than the standard elapsed time, this method can predict state of the machine and the FI value can be an accurate indicator of the state.

## 3. Modeling of piezoelectric energy harvesting device

This work will model the piezoelectric bimorph harvester with electromechanical distributed parameter model in which the bimorph harvester is considered as a uniform beam with Euler-Bernoulli beam assumptions according to the study by Erturk and Inman [33]. A perfect bonding between substructure and piezoelectric layers are considered. Moreover, it is assumed that the piezoelectric layers are covered with negligible thickness continuous electrode layers and are connected in series. In this study, it is assumed that the base displacement induced from the machine operation is only defined by translation and not rotation as the vibration is in translation form. However, if rotation plays an important role in base excitation, its effect can be added to the equations but here only translational base excitation is considered.

As shown in Fig. 2, the base acceleration expressed with $\ddot{a}_B(t)$ causes a relative transverse deflection of the beam to its base at location $x$ and time $t$ shown with $w_{rel}(x, t)$. it is of interest to define $w_{rel}(x, t)$ with modal expansion such as:

$$w_{rel}(x, t) = \sum_{i=1}^{\infty} \phi_i(x)\,\eta_i(t) \tag{5}$$

where $\phi_i(x)$ is the beam mode shapes of the $i$-th vibration mode and $\eta_i(t)$ is the mechanical response in modal coordinates. For the clamped-free boundary conditions, beam mode shapes is given by Eq. (6) [34]:

$$\phi_i(x) = \chi_i\left[cosh\lambda_i x - cos\lambda_i x + \alpha_i\left(sinh\lambda_i x - sin\lambda_i x\right)\right] \tag{6}$$

where $\alpha_i$ is a constant given by Eq. (7) and $\chi_i$ is a constant for satisfying mass normalization of the mode shapes, e.g. $\int_0^l m^* \phi_i^2(x)\,dx + m_a \phi_i^2(L) = 1$.

$$\alpha_i = \frac{\sin\lambda_i - \sinh\lambda_i + \lambda_i \frac{m_a}{m^* L}\left[\cos\lambda_i - \cosh\lambda_i\right]}{\cos\lambda_i + \cosh\lambda_i - \lambda_i \frac{m_a}{m^* L}\left[\sin\lambda_i - \sinh\lambda_i\right]} \tag{7}$$

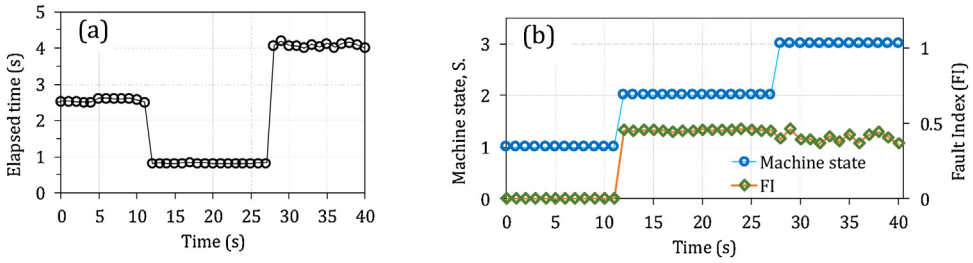


**Fig. 6.** An example for pulse condition monitoring, (a) Elapsed transmission time and (b) FI and machine state.

With the modal expansion defined and applying the modal orthogonality conditions, the electromechanical coupling equations can be expressed with:

$$\ddot{\eta}_i(t) + 2\zeta_i\hat{\omega}_i\dot{\eta}_i(t) + \omega_i^2\eta_i(t) + \mathrm{Y}_i V_P(t) = f_i(t)$$

$$C_P\dot{V}_P(t) + \left(1/R_l\right)V_P(t) = \sum_{j=1}^{\infty}\Lambda_i\dot{\eta}_i(t) \tag{8}$$

where $\hat{\omega}_i$ is the undamped natural frequency of the beam in short circuit condition expressed with Eq. (9), $\zeta_i$ is the mechanical damping ratio, $f_i(t)$ is the modal mechanical force given by Eq. (10), $C_P$ is the internal capacitance given by Eq. (11) as a function of relative permittivity $\bar{\varepsilon}_{33}$ and piezoelectric layer geometry, $\mathrm{Y}_i$ is the modal electromechanical term defined by Eq. (12) and $\Lambda_i$ is the modal electrical coupling term expressed in Eq. (13):

$$\hat{\omega}_i = (\lambda_i l)^2\sqrt{YI/m^* L^4} \tag{9}$$

$$f_i(t) = -m^* a_B(t)\left[\int_0^L \phi_i(x)\,dx + m_a\phi_i(L)\right] \tag{10}$$

$$C_P = \bar{\varepsilon}_{33}bL/t \tag{11}$$

$$\mathrm{Y}_i = \frac{\bar{e}_{31}b}{2t}\left[h^2/4 - \left(t + h/2\right)^2\right]\cdot\left.\frac{d\phi_i(x)}{dx}\right|_{x=L} \tag{12}$$

$$\Lambda_i = -\frac{\bar{e}_{31}(t+h)b}{2}\cdot\left.\frac{d\phi_i(x)}{dx}\right|_{x=L} \tag{13}$$

In Eq. (9) $\lambda_i$ is the characteristic number shown obtained from solving Eq. (14), $\bar{e}_{31}$ is piezoelectric constant in 31 mode and $\bar{\varepsilon}_{33}$ is the permittivity constant. Also, $m^*$ is the unit mass per length and $EI$ is the bending stiffness given by Eq. (15) [33].

$$1 + \cos\lambda_i\cosh\lambda_i + \lambda_i\frac{m_a}{m^* L}(\cos\lambda_i\sinh\lambda_i - \sin\lambda_i\cosh\lambda_i) = 0 \tag{14}$$

$$YI = 2b/3\left[Y_s h^3/8 + \bar{c}_{11}^E\left(\left(t + h/2\right)^3 - h^3/8\right)\right] \tag{15}$$

where $Y_s$ is the Young's modulus of substrate layer and $\bar{c}_{11}^E$ is the stiffness of piezoelectric material at constant electrical field.

If $\ddot{a}_B$ is presented with a series of harmonic functions using the Fourier Transform, Eq. (20), then by defining the sampled frequency with $\omega_k = \frac{2\pi k}{N}$, the force term becomes $f_i(t) = \sum_{k=0}^{N-1}F_i(\omega_k)e^{+\mathrm{j}\omega_k t}$, where $F_i(\omega_k)$ is expressed as follows:

$$F_i(\omega_k) = -m^*\left(\frac{1}{N}\left|\ddot{A}(\omega_k)\right|\right)\left[\int_0^L \phi_i(x)\,dx + m_a\phi_i(L)\right] \tag{16}$$

By this harmonic representation of base excitation and superimpose characteristic for linear systems, the resulting complex voltage amplitude is also a series of harmonic functions shown as:

$$V_P(t) = \sum_{k=0}^{N-1}\overline{V}_P(\omega_k)e^{+j\omega_k t} \tag{17}$$

where $\overline{V}_P(\omega)$ is the magnitude of output voltage corresponding to each frequency. By substituting Eqs. (16) and (17), the steady state voltage response can be shown as:

$$V_P(t) = \sum_{k=0}^{N-1}\frac{\sum_{i=1}^{\infty}\frac{j\omega_k\Lambda_i F_i(\omega_k)}{\hat{\omega}_i^2 - \omega_k^2 + j2\zeta_i\omega_k\hat{\omega}_i}}{\frac{1}{R_l} + j\omega_k\frac{C_P}{2} + \sum_{i=1}^{\infty}\frac{j\omega_k\Lambda_i Y_i}{\hat{\omega}_i^2 - \omega_k^2 + j2\zeta_i\omega_k\hat{\omega}_i}}e^{+j\omega_k t} \tag{18}$$

Using the calculated voltage from Eq. (18), the magnitude of output power from piezoelectric harvester can be calculated as $P_p = \left|V_p\right|^2/R_l$.

## 4. Experimental procedure and primarily signal processing

For the tests, a centrifugal pump with five vanes connected to an electromotor was equipped with an accelerometer type VMI-102, as shown in Fig. 7. Vibration signals in time-domain were directly measured from the water pump working under different conditions at a constant rotation speed of 2970 rpm. The accelerometer has a sensitivity of 100 mV/g and a resonant frequency of 30 kHz, was mounted vertically on the water pump body.

The accelerometer was connected to the signal conditioning unit (X-Viber FFT analyzer), where the signal goes through a charge amplifier. The software SpectraPro-4, which accompanies with the signal conditioning unit, was used for recording the signals directly in the computer. The vibration signal for each pump condition was acquired with an 8192-Hz sampling frequency at a duration of 100 s. Each vibration signal was segmented into 50 smaller vibration signals called data samples. Therefore, each data sample included a 2-s vibration signal with 16,384 data points. Each data sample was then transferred into frequency-domain by FFT method.

Acceleration data in time domain from water pump in healthy, shaft misalignment and shaft looseness conditions are shown in Fig. 8. A rough look into these signals reveals that the amplitude of the acceleration is different when water pump is working in faulty conditions. Shaft looseness and misalignment enhanced the acceleration sensed by the sensor, from a maximum of 8.11 $\mathrm{ms}^{-2}$ in defect-free condition to 13.00 $\mathrm{ms}^{-2}$ and 27.44 $\mathrm{ms}^{-2}$, respectively. It can also note that not only the maximum acceleration was increased by the faults, the dispersion of the data increased from $\sigma = 2.51\ m.s^{-2}$ in defect-free condition to $\sigma = 7.47\ m.s^{-2}$ for shaft misalignment and $\sigma = 3.72\ m.s^{-2}$ for shaft looseness conditions too.

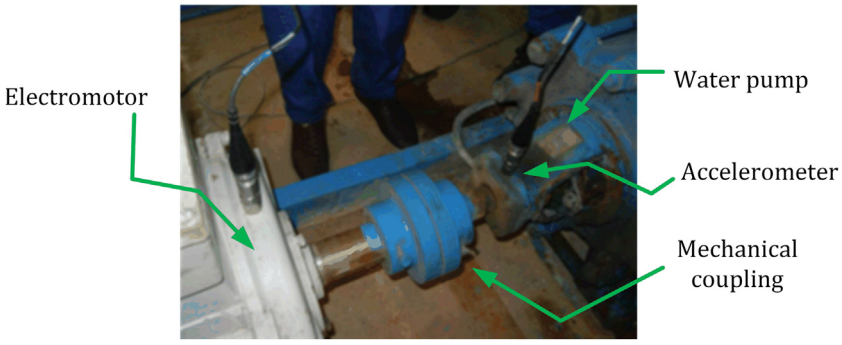


**Fig. 7.** The water pump connected to the accelerometer.

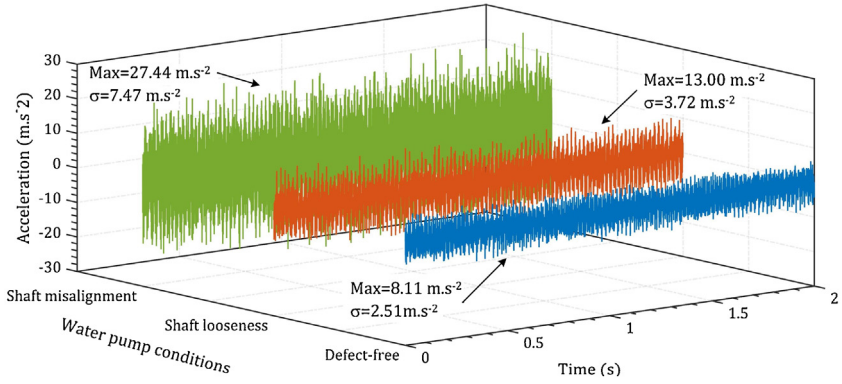


**Fig. 8.** Time signals of the water pump in defect-free, shaft looseness and shaft misalignment conditions.

In this work, a primary signal processing using the Fourier Transform is performed for two reasons. Firstly, frequency matching between fundamental frequency of the harvester and vibration source is essential for designing the harvester. Second, in order to demonstrate which frequency from the vibration source is more sensitive to the faults, amplitude of the Fourier Transform coefficients at dominant frequencies was compared. Since each acceleration signal is a finite sequence of the data, Discrete Fourier Transform (DFT) was applied. If $\ddot{a}(t)$ is the acceleration data which is defined at $N$ time sequences, DFT $\ddot{\mathrm{A}}(\omega)$ and inverse of DFT $\ddot{a}(k)$ are defined by Eqs. (19) and (20), respectively [35]:

$$\ddot{\mathrm{A}}(\omega) = \sum_{k=0}^{N-1} \ddot{a}(k) e^{-j\frac{2\pi}{N}\omega k} \tag{19}$$

$$\ddot{a}(k) = \frac{1}{N} \sum_{\omega=0}^{N-1} \ddot{\mathrm{A}}(\omega) e^{+j\frac{2\pi}{N}\omega k} \tag{20}$$

Note that $\ddot{\mathrm{A}}(\omega)$ is complex while $\ddot{a}(k)$ is real. From the inverse DFT and Euler formula for complex numbers, the contribution of $\ddot{a}(k)$ from $\ddot{\mathrm{A}}(\omega)$ is expressed as:

$$\ddot{a}_{\omega}(k) = \frac{1}{N} \left|\ddot{\mathrm{A}}(\omega)\right| e^{+j\frac{2\pi}{N}\omega_k} = \frac{1}{N} \left|\ddot{\mathrm{A}}(\omega)\right| sin\left(\frac{2\pi}{N}\omega k + \frac{\pi}{2} + Arg\left\{\ddot{\mathrm{A}}(\omega)\right\}\right) \tag{21}$$

Fast Fourier Transform (FFT) is a fast numerical method to apply DFT on signals [35]. FFT of acceleration signals from the water pump at different working conditions are extracted by MATLAB® and are shown in Fig. 9. To carefully consider frequencies of interest and for better view, a detailed view of FFT signals in 0–500 Hz range is plotted in dB scale. Working under normal condition, the water pump response has dominant frequencies of 49.5 Hz, 100.0 Hz, 148.0 Hz, 197.5 Hz, etc. These frequencies are the 1X, 2X, 3X, and 4X frequencies of the water pump. When water pump is working under faulty conditions, either shaft looseness or misalignment faults, dominant frequencies experience no change in 1X and a minor change in 2 × .

By applying Eq. (21) on the FFT signals, contribution of the eight dominant frequencies in the pump acceleration signals at different working conditions is shown in Fig. 10. Unlike the resonant frequencies which slightly changed, the contribution of the frequencies in the acceleration signals varied considerably for different conditions. The contribution of 1X frequency 49.5 Hz in the shaft misalignment and looseness conditions are 1.04 and 1.49 $m.s^{-2}$, respectively, which are considerably higher than 0.49 $m.s^{-2}$ for the defect-free condition. However, the mode contribution is not always higher in defected conditions. For instance, contribution of 2X frequency in shaft misalignment is less than the value for the defect-free and shaft looseness conditions.

## 5. Condition monitoring results and discussion

For presenting the condition monitoring results for the water pump based on the designed system in section 2, the acceleration data from the experiments, presented in section 4, is used as the base excitation for piezoelectric beam. The piezoelectric beam is connected to the outer case of the water pump with a solid plate, so the piezoelectric beam will be excited from the clamped end with acceleration signal measured experimentally. Fig. 11 shows a schematic of energy harvester attached to the water pump. Afterwards, output power are estimated analytically by using the distributed beam model with the measured base excitation signal at different pump conditions. Lastly, the state of the water pump is monitored by applying the pulse-timing based method. Piezoelectric beam optimization is performed with COMSOL®. All other numerical simulations, including the output power estima-

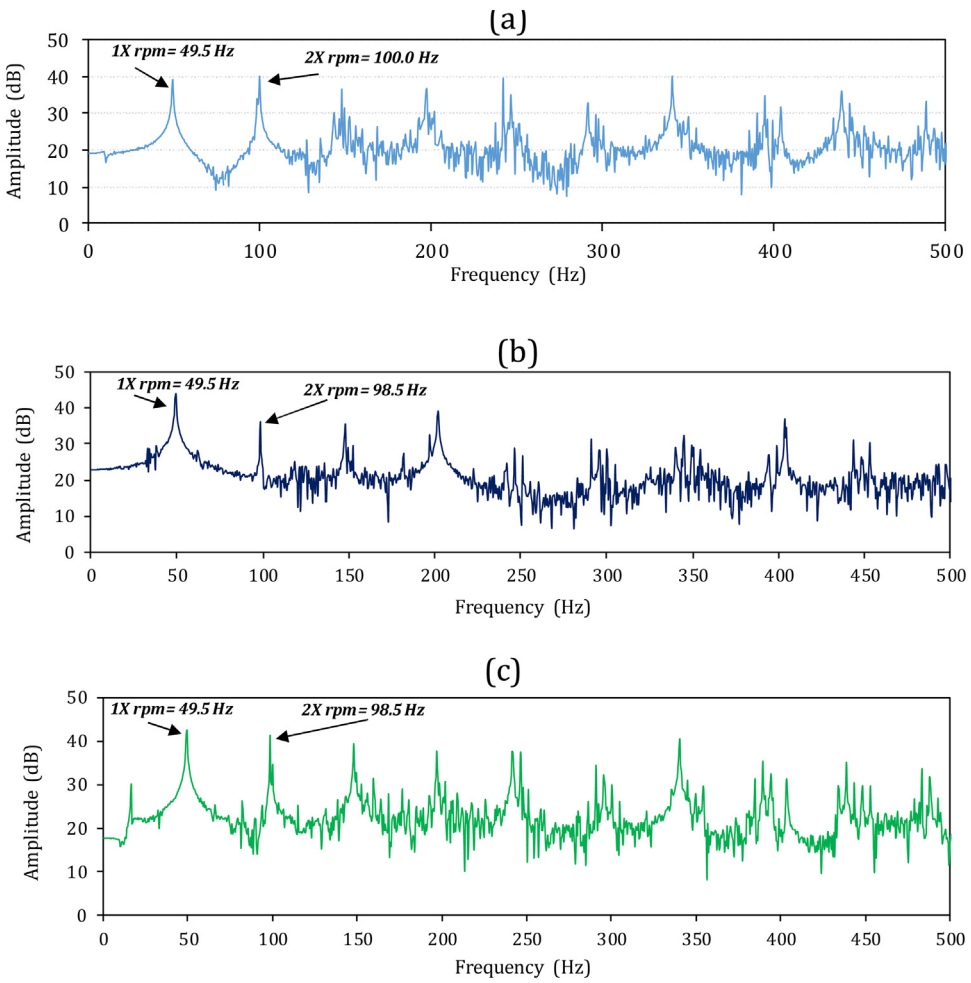


**Fig. 9.** Fast Fourier Transform (FFT) of time signals from water pump at different conditions with focus on 0–500 Hz range (a) defect-free, (b) shaft misalignment, and (c) shaft looseness conditions.

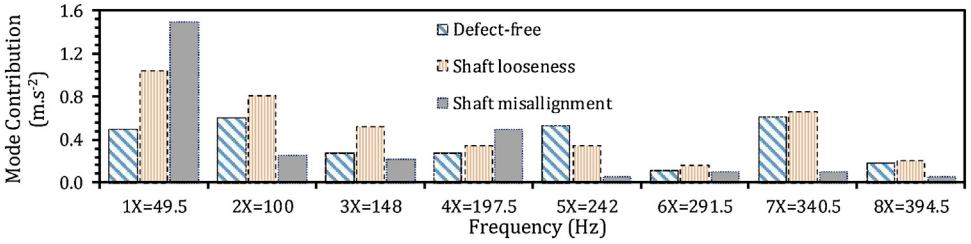


**Fig. 10.** Contribution of the eight dominant frequencies of the water pump acceleration at different working conditions.

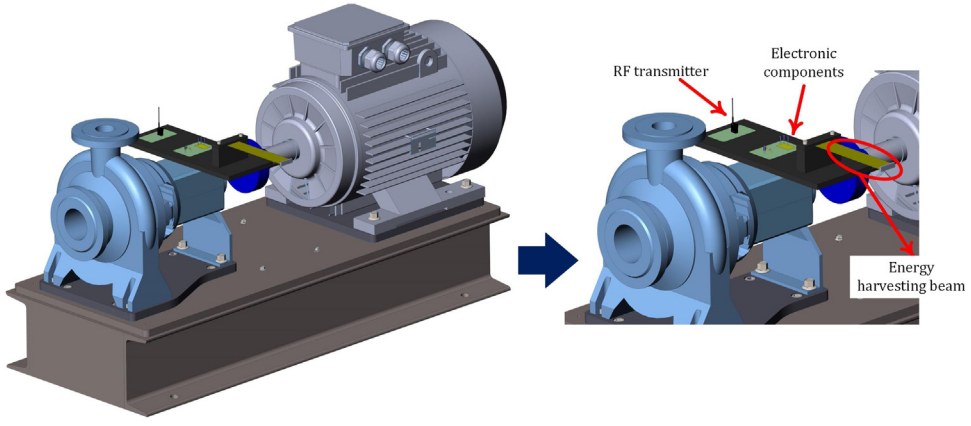


**Fig. 11.** A schematic of possible assembling of the proposed system into outer case of the water pump.

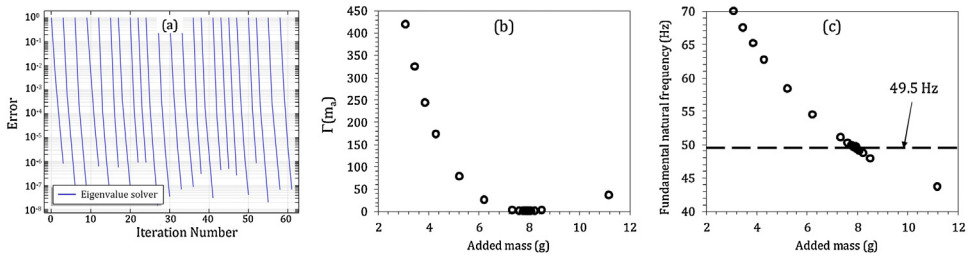


**Fig. 12.** (a) Convergence history of optimization, (b) objective function (c) the effect of added mass on the harvester fundamental natural frequency.

**Table 1**
Material properties of bimorph piezoelectric energy harvester (T226-A4-503X).

| Properties | Values |
|---|---|
| Piezoelectric stiffness at constant field, $c_{11}^E$, GPa | 66.0 |
| Piezoelectric density, $\rho_p$, kg/m$^3$ | 7750 |
| Electromechanical coupling coefficient, $e_{31}$, C/m$^2$ | −14 |
| Piezoelectric layer thickness (each), $t$, mm | 0.26 |
| Piezoelectric permittivity constant, $\bar{\varepsilon}_{33}$, F/m | $1800\times\varepsilon_0$ |
| Substrate Young's modulus, $Y_s$, GPa | 105 |
| Substrate thickness, $h$, mm | 0.14 |
| Substrate density, kg/m$^3$ | 9000 |
| Device length (active length as clamped), $L$, mm | 55 |
| Device width, $b$, mm | 31.8 |

tion, voltage multiplier simulation and pulse-timing method are carried out with MATLAB®.

Piezoelectric bimorph generates the maximum power when vibrates at its resonance. Since the power generation has a square factor of magnitude of the excitation acceleration [36], it is preferable that this frequency has a high mode contribution. Furthermore, in order to satisfy the criteria for condition monitoring, the contribution of this frequency should vary noticeably with respect to water pump condition. Thus, optimal design of the piezoelectric harvester has a fundamental frequency close to one of the dominant frequencies in the water pump acceleration signals. By considering these guidelines and analyzing Fig. 10, the 1X frequency is selected as the fundamental frequency of the piezoelectric harvester since the contribution of the frequency 49.5 Hz is high at every working condition and is, moreover, sensitive to the pump working conditions.

Maximum power from piezoelectric harvester is obtained when optimum load resistance is connected and the harvester natural frequency matches to excitation frequency. In this research, with the bimorph topology shown in Fig. 2 and PZT-5A as selected piezoelectric material, the optimization process for frequency matching was proceeded. Afterwards, using analytical modeling approach in section 3, optimum load resistance was selected. Piezoelectric harvesters are available in different geometries and therefore the optimization can be performed for any combination of these geometric parameters, such as length or thickness. In order to narrow down optimization factors, a commercial piezoelectric harvester with low natural frequency from Piezo Systems Inc. (T226-A4-503X) was selected and then by tuning the added mass, frequency matching was performed to match the fundamental natural frequency of the harvester to 49.5 Hz from the water pump acceleration. This piezoelectric sample have been previously used for energy harvesting by [33,37]. The bimorph sample consists of two oppositely polled PZT-5A layers embracing a brass substrate, representing series connection between the piezoelectric elements. Geometric and material properties of this samples is presented in Table 1.

To optimize the energy harvester, an objective function is defined as the square of difference between the fundamental natural frequency of the harvester, which is a function of added mass,

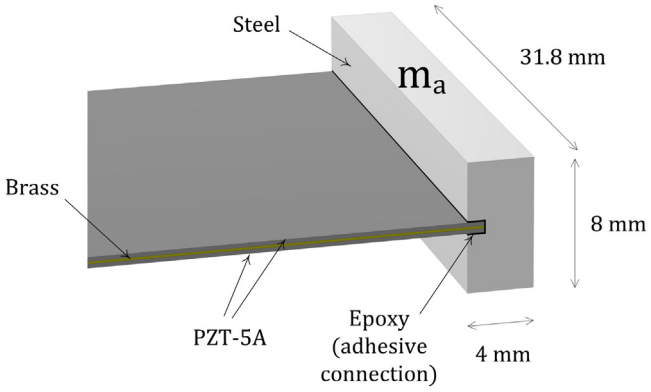


**Fig. 13.** Detail view of harvester beam with dimensions of the added mass and its connection to the piezoelectric sheet.

and frequency of 49.5 Hz as the excitation frequency from the water pump. The objective function shown by Eq. (22) is employed to find the value of $m_a$ by minimizing the objective function.

$$\Gamma(m_a) = \left(\hat{\omega}_1(m_a) - 49.5\right)^2 \tag{22}$$

Fig. 12(a)–(c) show the error versus iteration number, objective function and the variation of the harvester first natural frequency with respect to the added mass, respectively. Objective function in Fig. 12(b) shows that, with an added mass of $7.3 \leq m_a \leq 8.5$ g, the objective function is less than 2.5, which is equal to 3% error. As can be seen from Fig. 12(c), with an added mass of 8 g, the fundamental natural frequency of the harvester matches to 49.5 Hz. For structural steel with the density of 7850 kg/m$^3$ for the added mass, 8 g will be equal to a solid block with $4 \times 31.8 \times 8$ mm dimensions. Hence, the volume of the energy harvester, including the piezoelectric sheets, substrate layer and tip added mass, are 2.15 cm$^3$. The added mass block can be connected to the piezoelectric sheet with an adhesive connection by an epoxy. For stronger connection, it is recommend to cut a groove in the added mass in order to insert the sheet and fill the gap with the epoxy. Fig. 13 shows added mass features, e.g. material and dimensions, and its connection to the piezoelectric sheet.

An analytical modal analysis was performed for this designed bimorph configuration with 8 g added mass and the results are shown in Fig. 14. It can be seen that the first natural frequency of the beam is 49.5 Hz. Moreover Fig. 14 shows that, the other natural frequencies do not match with the operational working frequencies of the water pump. Hence, the contribution of other working frequencies, e.g. 2X, 4X, is negligible. Therefore, in Eq. (18), $\omega_k = 49.5\,Hz$.

The next step in the design of piezoelectric harvester is selection of load resistance $R_l$ in order to obtain the maximum power. The output voltage and power, considering a unit excitation magnitude of 1 $m/s^2$ using Eq. (18), are plotted in Fig. 15(a) and (b), respectively, for different resistance loads. As shown, by increasing $R_l$, the voltage continuously increases while the output power decreases when the applied load resistance is higher than the opti-

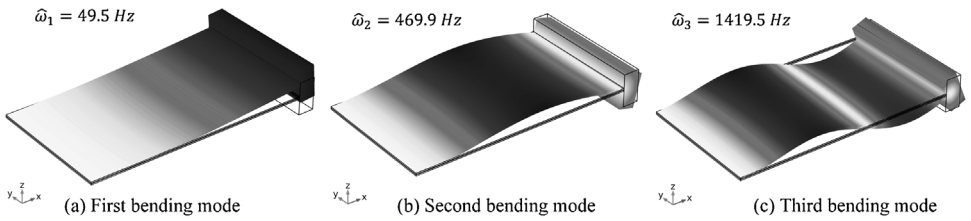


**Fig. 14.** The first three bending modes for the optimum bimorph harvester.

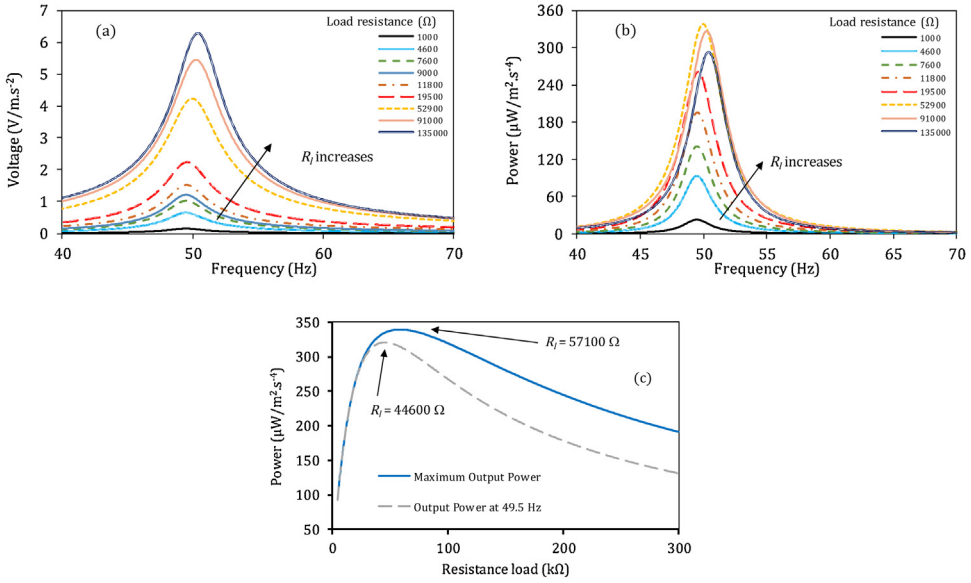


**Fig. 15.** (a) Voltage and (b) power for different resistance loads versus frequency (c) power for resistance loads at resonance.

mal resistance. In addition, resonance frequency is slightly changed by increasing the load resistance due to the back piezoelectric effects. To find the optimum $R_l$, output power curves at resonance and at 49.5 Hz are shown versus the load resistance in Fig. 15(c). Since the resonant frequency experiences a small change due to increment of the load resistance, the power plots separate after a specific load resistance. The resonant output power is higher than the power at 49.5 Hz, but power at 49.5 Hz is of interest because of the dominant frequency of the water pump vibration. The maximum power is 320 μW/m$^2$.s$^{-4}$ at 49.5 Hz at load resistance $(R_l)_{opt}$ equals to 44.6 kΩ.

If the designed harvester is attached on the accelerometer location, as shown in Fig. 11, the measured vibration shown in Fig. 8 can be applied as the base excitation for the harvester. Acceleration in theory is a summation of indefinite number of harmonic functions. In practice, the acceleration signal can be decomposed into a series of defined harmonic functions, as shown in section 4, where the FFT is employed for decomposing the signal into harmonic functions. However, since piezoelectric energy harvesters generate the maximum power at its resonant frequency and the designed harvester has a natural frequency of 49.5 Hz, the significant harmonic in the water pump acceleration is the main dominant frequency, e.g. 1X = 49.5 Hz. According to Fig. 10, the magnitudes of 1X harmonic in the water pump acceleration are 0.49, 1.04 and 1.49 m.s$^{-2}$ in defect-free, looseness conditions and shaft misalignment, respectively. Using these figures as the input acceleration, one can calculate output voltage and power for the optimum load resistance. Fig. 16(a) and (b) show the output voltage and power from one bimorph harvester over a frequency range. As stated, the important figure for the output voltage and power is that of frequency 49.5 Hz, which is plotted for different water pump conditions. The output peak-to-peak voltages from the water pump acceleration at the optimum load are 1.85, 3.93 and 5.63 V at defect-free, shaft looseness and shaft misalignment conditions, respectively. The corresponding powers are 76.84, 343.12 and 710.45 μW, respectively. If the power density per device volume is divided into square of the input acceleration, power density per square acceleration is 30.8 mW/cm$^3$. g$^2$ in all operating conditions. The results does not depend to the input acceleration and is only a function of geometries of the piezoelectric harvester and its material. The voltage and power densities per device volume for different working conditions are shown in Fig. 16(c). The power density values are equal to 35.7, 160.99 and 330.4 μW/cm$^3$ for defect-free, shaft looseness and misalignment, respectively. Therefore, the power density is increased by 350% and 824% due to presence of the shaft looseness and shaft misalignment, respectively. This high variation of the power density proves that the storage capacitor will be charged faster in the faulty working condition.

Using the optimum VM configuration with 150 μF capacitor, the stored energy in the capacitor from the water pump vibration was calculated. Since the pump acceleration is different at different working conditions, the generated voltage and, hence, the stored energy in the super capacitor are not similar. Fig. 17 shows voltage in the storage capacitor for various water pump conditions. As expected, the voltage is distinctively higher in both shaft misalignment and looseness than the voltage in defect-free condition. Moreover, the capacitor voltage is significantly higher for the shaft misalignment compared to the looseness condition.

The performance of this designed system is moreover investigated for condition monitoring application. It is worthy to note the microprocessor consumes 28.05 μW (8.5 μA and 3.3 V). By considering the capacitor constant, e.g. 150 μF, a voltage drop occurs in

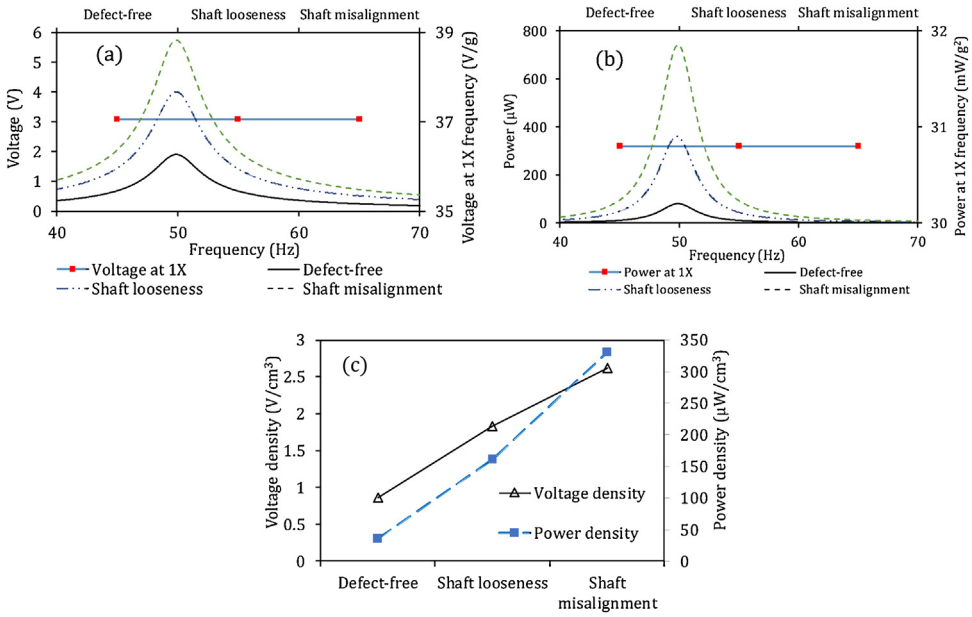


**Fig. 16.** (a) Voltage, (b) power from water pump acceleration versus frequency and (c) voltage and power densities from the water pump acceleration at 49.5 Hz.

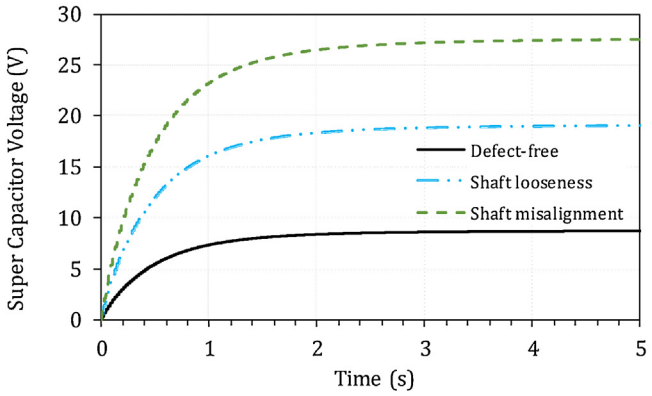


**Fig. 17.** Voltage outputs in the capacitor from the piezoelectric harvester at different pump conditions.

the capacitor during operation of the microprocessor. Hence, a voltage level switch is considered that enables the microprocessor after 4.0 V to ensure the continuous operation of the microcontroller. As advantage of this level switch, Torah et al. [26] noticed the cold start problem during experiments, where PIC microcontroller drew significant power as the voltage reached to a specific value. This level switch addresses the cold start problem. After the microprocessor starts operating, the microprocessor enables the RF transmitter for a period of time when the voltage reaches to a specific figure. During the transmission, the RF transmitter consumes 7 mA current. For this simulation, the PIC microcontroller enables the RF transmitter when the storage capacitor reaches to 7 V for a duration of 0.02 s. By considering the voltage equation across the capacitor with C = 150 μF, the voltage drop during the transmission time is calculated as 0.93 V. After the transmission period, the storage capacitor is charged by the piezoelectric harvester. Nevertheless, the charging time to reach 8 V depends on the voltage generation by the piezoelectric, which is different for different pump working conditions. The storage capacitor voltage during the full operation from the initial conditions are shown in Fig. 18. In this work, to include unknown errors during the operation, 2% random error is added to the capacitor voltage. As shown, due to less pump acceleration during the defect-free condition, the charging process is slower than the other conditions; so that the first RF transmission occurred at 1.18 s. On the other hand, the water pump acceleration is higher for the defected conditions. Therefore, the first transmission time and the time intervals between the transmissions are significantly lower compared to the defect-free condition.

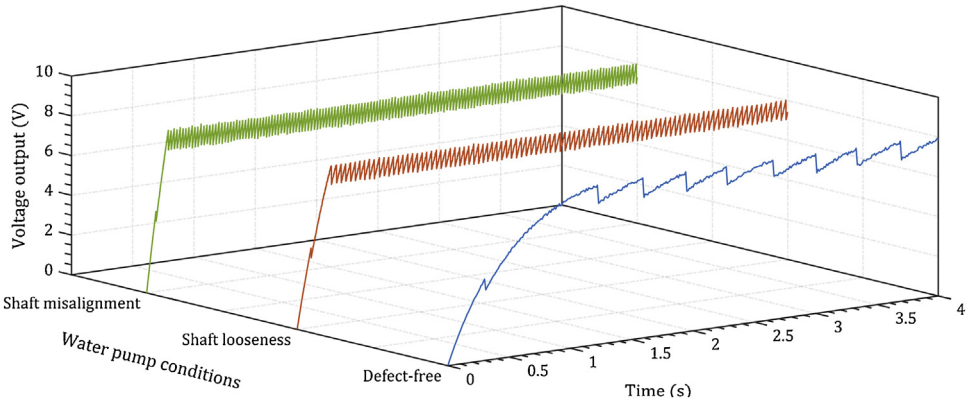


**Fig. 18.** Voltage output from storing capacitor during full operation for different water pump conditions.

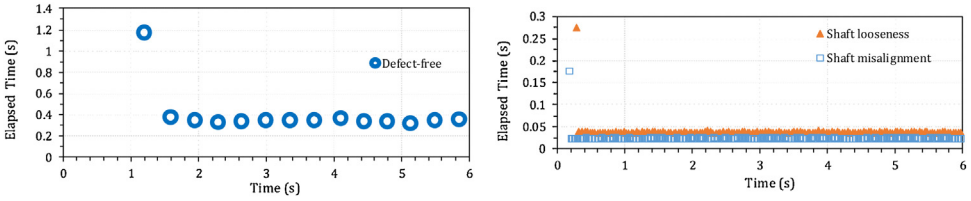


**Fig. 19.** The elapsed time between the RF transmissions for (a) defect-free and (b) defected conditions.

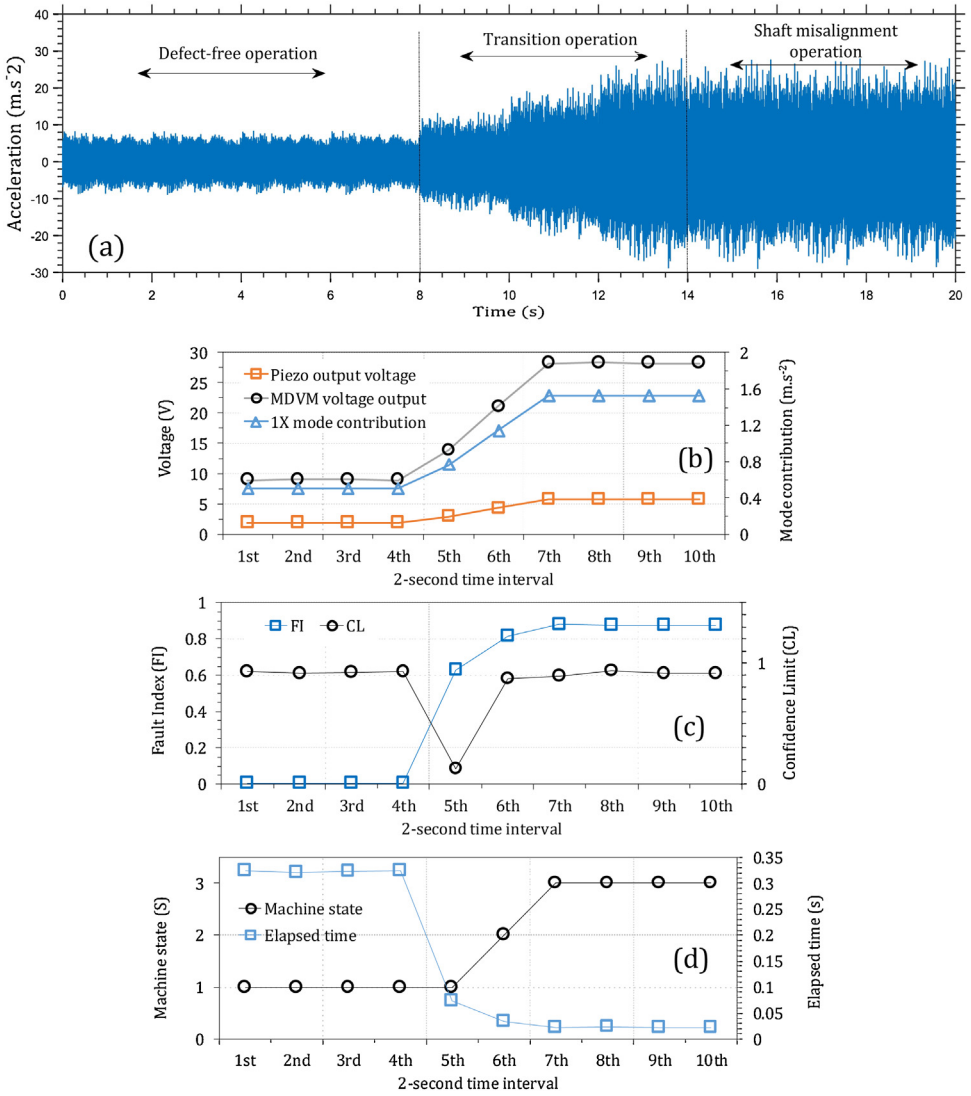


**Fig. 20.** The process of condition monitoring for a simulated case from reconstructed signals of the water pump. (a) Time signals, (b) 1X mode contribution from FFT and voltage output from harvesting unit, (c) FI and CL and (d) Water pump state and elapsed times between transmissions.

The elapsed times between the RF transmissions are shown in Fig. 19 for different water pump conditions. While the first transmission for the defect-free occurs at 1.18 s, it happens after 277 and 177 ms for shaft looseness and misalignment conditions, respectively. More important than the first transmission is the time between the transmissions as it is directly proportional to the charging process which is linked to the water pump acceleration. The elapsed time values between the transmissions are 350, 39 and 25 ms for the defect-free, shaft looseness and shaft misalignment conditions, respectively. Therefore, if the water pump condition changes from the defect-free to one of these faults, the elapsed time between the transmissions decreases immediately.

To analysis the elapsed time data from Fig. 19, the parameters in Eq. (1) are obtained as $\mu = 0.350$, $\tau_0 = 0$, $\tau_1 = -0.311$, $\tau_2 = -0.326$, $\sigma_1 = 1.63E-2$, $\sigma_2 = 1.39E-3$ and $\sigma_3 = 9.98E-4$. Since a statistical model for the elapsed time for the different operating conditions was obtained, the state of water pump was conditioned by calculating the FI and $\mathcal{S}$ using Eqs. (2) and (4).

In order to demonstrate possibility of the procedure, one case is considered in which the state of the water pump changes from the defect-free to the shaft misalignment in a duration of 20 s. Fig. 19(a) shows the reconstructed time signals. Here a 5% random noise is added to the data in order to test the performance of the system in case of noisy environment. For 2-second interval, the FFT is applied on the signals and the contribution of 1X = 49.5 Hz in the signal is

extracted. This mode contribution is within the range of 0.50 $m/s^{-2}$ in the defect-free condition to 1.53 $m/s^{-2}$ in the shaft misalignment condition. The 1X contribution is fed into the bimorph piezoelectric model, Eq. (18), with the calculated optimum load resistance of $(R_l)_{opt}$ = 44,600 Ω. Range of the piezoelectric voltage output is from 1.9 V in the defect-free to 5.8 V in the shaft-misalignment conditions. Moreover, the voltage generation from the bimorph is considered as the input for the optimum MDCP circuit and the voltage outputs are obtained using simulation. The final voltage in the storage capacitor ranges from 9.0 V to 28.3 V for the defect-free and shaft misalignment conditions, respectively. Fig. 19(b) shows the 1X mode contribution, piezoelectric voltage and MDVM voltage output over ten 2-second period intervals. According to the immediate capacitor voltage, the elapsed time between the transmissions are calculated upon which the FI, CL and machine state $\mathcal{S}$ are obtained through Eqs. (2) to (4), respectively. Fig. 19(c) shows the FI of the water pump and the CL for this index over 20 s period. As shown for a duration of 8 s, from 1st to 4th 2-second intervals, the FI lies closely on 0 value. However, once the machine condition changes to the transition operation and the acceleration increases, the FI tends to rise from 0. The FI further increases until reaches to a symptom value for the shaft misalignment condition. The CL, which is an accuracy indicator for the condition monitoring process, is always close to 1 except for transition period which is dramatically less than the other values. Consequently, the machine state $\mathcal{S}$ is shown in Fig. 19(d) with elapsed time over this 20 s time period. It can be seen that, the state of the water pump is correctly identified as "3" state through the faulty operation, which corresponds to the shaft misalignment. However, during the transition period, the system identified "2" for the machine state which is not correct. By considering the CL values for transition period, one can avoid from incorrect conditions of the machine (Fig. 20).

## 6. Conclusions

In this study, a self-powered condition monitoring system is designed to perform operational condition monitoring based on the RF transmission pulses. After design of the system, an energy harvesting unit is proposed to provide sufficient energy and voltage level for this system. This energy harvesting unit comprises a piezoelectric bimorph harvester and Voltage Multiplier circuit. For this study, input acceleration, which is a signal consisting of harmonics from a frequency range, is decomposed into a series of harmonic function using FFT. A distributed parameter model of piezoelectric harvester was used to estimate the output voltage. For the machine condition monitoring, a pulse-based approach has been proposed relying on the analysis of elapsed times between the RF transmission pulses. The performance of this system has been demonstrated for condition monitoring of a water pump. The designed system has been applied on experimental vibration signals captured from the water pump and shown that the water pump condition can be monitored during the operation. This system can be applied on larger network of machines for autonomous condition monitoring.

## References


[1] S.W. Doebling, C.R. Farrar, M.B. Prime, A summary review of vibration-based damage identification methods, Shock Vib. Dig. 30 (2) (1998) 91–105.
[2] O. Janssens, et al., Convolutional neural network based fault detection for rotating machinery, J. Sound Vib. 377 (2016) 331–345.
[3] C. Ruiz-Cárcel, V.H. Jaramillo, D. Mba, J.R. Ottewill, Y. Cao, Combination of process and vibration data for improved condition monitoring of industrial systems working under variable operating conditions, Mech. Syst. Signal Process. 66–67 (2016) 699–714.
[4] A. Ragab, S. Yacout, M.S. Ouali, H. Osman, Prognostics of multiple failure modes in rotating machinery using a pattern-based classifier and cumulative incidence functions, J. Intell. Manuf. 30 (no. 1) (2019) 255–274.
[5] A. Moosavian, M. Khazaee, H. Ahmadi, M. Khazaee, G. Najafi, Fault diagnosis and classification of water pump using adaptive neuro-fuzzy inference system based on vibration signals, Struct. Heal. Monit. 14 (no. 5) (2015) 402–410.
[6] Y.T. Im, S.G. Doo, J.S. Hwang, Condition monitoring of cooling tower fan using K-band Doppler radar, Microw. Opt. Technol. Lett. 61 (no. 1) (2019) 158–162.
[7] A. Simm, Q. Wang, S. Huang, W. Zhao, Laser based measurement for the monitoring of shaft misalignment, Meas. J. Int. Meas. Confed. 87 (2016) 104–116.
[8] J. Zhong, et al., Vision-based system for simultaneous monitoring of shaft rotational speed and axial vibration using non-projection composite rfinge pattern, Mech. Syst. Signal Process. 120 (2019) 765–776.
[9] J. Huang, G. Chen, L. Shu, H. Lin, K. Liu, Designing wireless vibration monitoring system for petrochemical units fault diagnosis, Proc. - 2015 IEEE 12th Int. Conf. Ubiquitous Intell. Comput. 20 (2016) 582–588.
[10] J. Neuzil, O. Kreibich, R. Smid, A distributed fault detection system based on IWSN for machine condition monitoring, IEEE Trans. Ind. Inf. 10 (no. 2) (2014) 1118–1123.
[11] S. Cao, J. Li, A survey on ambient energy sources and harvesting methods for structural health monitoring applications, Adv. Mech. Eng. 9 (4) (2017), p. 168781401769621.
[12] C. De Marqui, A. Erturk, Electroaeroelastic analysis of airfoil-based wind energy harvesting using piezoelectric transduction and electromagnetic induction, J. Intell. Mater. Syst. Struct. 24 (no. 7) (2013) 846–854.
[13] H. Li, C. Tian, Z.D. Deng, Energy harvesting from low frequency applications using piezoelectric materials, Appl. Phys. Rev. 1 (4) (2014) 0–20.
[14] M. Khazaee, A. Rezaniakolaei, L. Rosendahl, An experimental study on macro Piezoceramic fiber composites for energy harvesting, Mater. Sci. Forum 951 (2019) 3–8.
[15] P. Cahill, B. Hazra, R. Karoumi, A. Mathewson, V. Pakrashi, Vibration energy harvesting based monitoring of an operational bridge undegoing forced vibration and train passage, Mech. Syst. Signal Process. 106 (2018) 265–283.
[16] C. Maruccio, G. Quaranta, L. De Lorenzis, G. Monti, Energy harvesting from electrospun piezoelectric nanofibers for structural health monitoring of a cable-stayed bridge, Smart Mater. Struct., vol. 25 (8) (2016), p. 085040.
[17] X. Zhao, et al., Self-powered triboelectric nano vibration accelerometer based wireless sensor system for railway state health monitoring, Nano Energy 34 (February) (2017) 549–555.
[18] D. Lim, S.C. Mantell, P.J. Seiler, Wireless structural health monitoring of wind turbine blades using an energy harvester as a sensor, in: 32nd ASME Wind Energy Symp., 2010, pp. 1–10.
[19] T.H. Owen, S. Kestermann, R. Torah, S.P. Beeby, Self powered wireless sensors for condition monitoring applications, Sens. Rev. 29 (no. 1) (2009) 38–43.
[20] D. Lim, S.C. Mantell, P.J. Seiler, R. Yang, Wind turbine blades as a strain energy source for energy harvesting, in: 51st AIAA Aerospace Sciences Meeting Including the New Horizons Forum and Aerospace Exposition, 2013, pp. 1–8, no. January.
[21] D.-W. Lim, S.C. Mantell, P.J. Seiler, Wireless monitoring algorithm for wind turbine blades using Piezo-electric energy harvesters, Wind Energy 20 (3) (2017) 551–565.
[22] S.S.R. Patange, S. Raja, M.P. Vijayakumar, V.R. Ranganath, Study on low frequency energy harvesting system in laminated aluminum beam structures with delamination, J. Mech. Sci. Technol. 32 (no. 5) (2018) 1985–1993.
[23] W.W. Clark, J.R. Romeiko, D. a Charnegie, G. Kusic, C. Mo, A case study in energy harvesting for powering a wireless measurement system, in: Struct. Heal. Monit. 2007 Quantif. Validation, Implementation, 12, September 2007, 2007, pp. 1765–1772.
[24] "https://www.microchip.com," Date Accessed March 2019.
[25] O.O. Esu, S.D. Lloyd, J.A. Flint, S.J. Watson, Feasibility of a fully autonomous wireless monitoring system for a wind turbine blade, Renew. Energy 97 (2016) 89–96.
[26] R.N. Torah, M.J. Tudor, K. Patel, I.N. Garcia, S.P. Beeby, Autonomous low power microsystem powered by vibration energy harvesting, Proc. IEEE Sens. (2007) 264–267.
[27] Https://www.rfsolutions.co.uk/, "RTFQ1P.".
[28] H.A. Sodano, D.J. Inman, G. Park, Comparison of piezoelectric energy harvesting devices for recharging batteries, J. Intell. Mater. Syst. Struct. 16 (10) (2005) 799–807.
[29] M. Kim, J. Dugundji, B.L. Wardle, Efficiency of piezoelectric mechanical vibration energy harvesting, Smart Mater. Struct. 24 (5) (2015), p. 055006.
[30] F. Pan, T. Samaddar, Charge Pump Circuit Design, McGraw-Hill Professional, 2006.
[31] F.K. Shaikh, S. Zeadally, Energy harvesting in wireless sensor networks: a comprehensive review, Renew. Sustain. Energy Rev. 55 (2016) 1041–1054.
[32] T.V. Galchev, J. McCullagh, R.L. Peterson, K. Najafi, Harvesting traffic-induced vibrations for structural health monitoring of bridges, J. Micromech. Microeng. 21 (10) (2011), p. 104005.
[33] A. Erturk, D.J. Inman, An experimentally validated bimorph cantilever model for piezoelectric energy harvesting from base excitations, Smart Mater. Struct. 18 (2) (2009), p. 025009.
[34] D. Young, R.P. Felgar, Tables of characteristic functions representing normal modes of vibration of a beam, Univ. Texas Eng. Res. Ser. 44 (1949) 1–31.
[35] J.W. Cooley, P.W. Lewis, P.D. Welch, The fast Fourier transform and its applications, IEEE Trans. Educ. 12 (1) (1969) 27–34.
[36] S. Roundy, P.K. Wright, J. Rabaey, A study of low level vibrations as a power source for wireless sensor nodes, Comput. Commun. 26 (no. 11) (2003) 1131–1144.

[37] N.E. DuToit, B.L. Wardle, Experimental verification of models for microfabricated piezoelectric vibration energy harvesters, AIAA J. 45 (no. 5) (2007) 1126–1137.

## Biographies

**Majid Khazaee** received his Bachelor and Master of Technology from Amirkabir University of Technology (Tehran Polytechnic) in 2013 and 2016. He is currently pursuing PhD in Energy Technology at Aalborg University, Aalborg, Denmark and is working on piezoelectric energy harvesters for autonomous sensors and actuators. He worked as senior project engineer in AS industrial group, during 2016–2017 on production line installation. His current research interests include low-power vibration harvesting piezoelectric harvester design, industrial vibration, autonomous condition monitoring and dynamical modeling of systems.

**Alireza Rezaniakolaei** was born in Babol, Iran, on August 04, 1983. He is an Associates Professor of energy technologies. He is head of Low Power Energy Harvesting & i-Solutions Research Programme at Department of Energy Technology, Aalborg University, Denmark with 10 years experiences in this field. His current research interests include fluid mechanics, thermal engineering and energy harvesting technologies, micro heat-transfer surfaces and integration of these technologies with renewable systems, actuators and sensor applications.

**Ashkan Moosavian** was born in 1988 in Tehran/Iran, received his B.Sc. and M.Sc. degrees in Agricultural Machinery Engineering from the Tehran University, Iran, in 2010 and 2012. He received PhD from Trbiat Modares University in Tehran/Iran. He is now senior test engineer in Irankhodro Powertrain Company (IPCO). His research fields include Application of Support Vector Machine and Neural Network in Mechanical Systems, Artificial Intelligence, Condition Monitoring, Fault Diagnosis, Application of Mechatronic in Agricultural Engineering.

**Lasse A. Rosendahl** was born in Ribe, Denmark, on October 13, 1967. He received the M.Sc.M.E. and Ph.D.M.E. Degrees from Aalborg University, Aalborg, Denmark. From 1998–1999, he was with the Department of Energy Technology (ET), Aalborg University, as an Assistant Professor, where he was an Associate Professor from 2000 to 2007, and has been a Professor since 2007. He is leader of Biomass Research Programme at ET. His current research interests include fluid mechanics, thermal energy technology, liquid biofuels and novel energy technologies, including modeling, simulation, and design with focus on optimized efficiency.

# Appendix E. Paper 5: Reference [163]

## A comprehensive electromechanically coupled model for non-uniform piezoelectric energy harvesting composite laminates

M. Khazaee, L. Rosendahl, A. Rezaniakolaei.

This paper has been published in

*Mechanical Systems and Signal Processing.* vol. 145, pp. 106927, 2020

Mechanical Systems and Signal Processing 145 (2020) 106927

Contents lists available at ScienceDirect

Mechanical Systems and Signal Processing

journal homepage: www.elsevier.com/locate/ymssp

# A comprehensive electromechanically coupled model for non-uniform piezoelectric energy harvesting composite laminates

Majid Khazaee, Lasse Rosendahl, Alireza Rezania *

*Department of Energy Technology, Aalborg University, Pontoppidanstræde 111, 9220 Aalborg East, Denmark*

ARTICLE INFO

*Article history:*
Received 25 November 2019
Received in revised form 7 April 2020
Accepted 22 April 2020

*Keywords:*
Finite element method
High-order element
Piezoelectric elements
Energy harvester design
Shear stress

ABSTRACT

Achieving high power densities through initiative designs of piezoelectric harvester in various geometries is a key point in vibration energy harvesting. State-of-the-art analytical and finite element models (FEMs) ignore structural damping, inter-laminar continuity, shear stresses, and contact layer effect between the substrate and piezoelectric layers and in addition cannot predict the performance of many recently introduced piezoelectric harvester configurations, such as non-uniform, thick piezoelectric patches, and variable thickness beams. This paper presents a comprehensive finite element formulation to calculate power generation by piezoelectric harvesters in a broader range of design cases. The presented high-order shear FEM not only is suitable for thick composite-based harvesters but also accommodates the drawbacks of the previous methods. The coupled finite element approach is verified versus experimental and analytical results. The model developed in this work is employed to analyze a non-uniform energy harvester with an E-glass fiber composite substrate layer sandwiched between piezoelectric layers with variable thickness. The numerical results show that, the advance formulation is capable of analyzing various piezoelectric harvesters including various influential parameters such as contact layer and damping dissipation. The results, furthermore, indicate that variable piezoelectric-layer thickness and an optimum fiber direction in composite substrate lamina can enhance performance of the piezoelectric harvester.



## 1. Introduction

Vibration-based piezoelectric energy harvesting (VPEH) has been extensively employed as a mean to feed electrical power to small electronic devices from available kinetic energy due to its high energy density, easy integration into the system and the availability of unwanted vibration in many operational systems [1]. In many systems with low-power sensors, piezoelectric energy harvester (PEH) has been integrated into system to harvest energy from the system kinetic energy in order to provide self-power sensors [2,3] or wireless sensor networks [4,5]. The clamped-free cantilever beam configuration, also known as the 3–1 mode PEH, is the most widely used boundary condition in VPEH with benefits including relatively low natural frequency, large deformations and simplicity of design and integration [2]. In this configuration, the clamped end is fixed to a vibration source and consequently vibration acts as a base excitation, causing transverse motion of the cantilever that applies a significant normal strain to the piezoelectric element [6] in the length direction, i.e. 1-direction. The piezoelectric layer in this configuration is poled through its thickness, i.e. 3-direction. Regarding the PEH material, Lead Zirconate

* Corresponding author.
*E-mail address:* alr@et.aau.dk (A. Rezania).

https://doi.org/10.1016/j.ymssp.2020.106927
0888-3270/

**Nomenclature**

*Abbreviation*

| | |
|---|---|
| CUF | Carrera's unified formulation |
| PEH | piezoelectric energy harvester |
| FEM | finite element method |
| VPEH | Vibration-based piezoelectric energy harvesting |
| KE | kinetic energy, $J$ |
| PE | potential energy, $J$ |
| DoF | degrees-of-freedom |
| CLPT | classical laminate plate theory |
| FSDT | first shear-order deformation theory |
| TSDT | third shear-order deformation theory |

*Greek script*

| | |
|---|---|
| $\beta$, $\Gamma$ | dimensionless damping coefficients |
| $\gamma$ | shear strains |
| $\Delta$ | $z$-displacement at nodes in one element |
| $\epsilon_0$ | permittivity constant in free-space, $F/m$ |
| $\epsilon$ | permittivity constant, $F/m$ |
| $\varepsilon$ | normal strains |
| $\mathcal{E}$ | electric field, $N/C$ |
| $\zeta_n$ | modal viscous damping coefficient |
| $\eta_n$ | modal structural damping coefficient |
| $\theta$ | rotation angle of fibers, *rad* |
| $\lambda$ | multiplier for material's lay-up |
| $\Lambda$ | Hermite interpolation function |
| $\mu$ | density, $kg/m^3$ |
| $\nu$ | Poisson's ratio |
| $\kappa_1$ | mass correlation factor |
| $\Pi$ | element area, $m$ |
| $\sigma$ | normal stress |
| $\tau$ | shear stress |
| $\mathcal{T}$ | applied acceleration DoFs |
| $\Phi$ | electrical potential |
| $\phi_x$ | rotation of $x$-axis after deformation |
| $\phi_y$ | rotation of $y$-axis after deformation |
| $\chi$ | nodal mechanical degrees of freedom |
| $\psi$ | Lagrange interpolation function |
| $\omega$ | driving excitation frequency, *rad* |
| $\omega_n$ | natural frequency, *rad* |
| $\Omega$ | frequency ratio |
| $\Xi$ | nodal value of$\mathcal{W}_1$ |

*Latin script*

| | |
|---|---|
| $A, B$ | integration auxiliary matrices |
| $\ddot{a}_B$ | input base excitation acceleration, $m/s^2$ |
| $b$ | harvester active width, $m$ |
| $\mathcal{C}_1$ | high-order deformation coefficient |
| $C$ | viscous damping matrix |
| $D$ | electrical displacement, $C/m^2$ |
| $E$ | Elastic moduli, $N/m^2$ |
| $e$ | Piezoelectric coefficient, $C/m^2$ |
| $f$ | frequency, *rad* |
| $\boldsymbol{f}$ | applied external load, $N$ |
| $G$ | shear moduli, $N/m^2$ |
| $g$ | 9.81 $m/s^2$ |
| $\langle$ | frequency response function, $m/N$ |
| $h$ | layer thickness, $m$ |
| $H$ | structural damping matrix, $N/m$ |
| $I$ | Moment of inertia |

| | |
|---|---|
| $K_{qq}$ | general structural related stiffness matrix |
| $K_{q\phi}$ | general piezoelectric related stiffness matrix |
| $K_{\phi\phi}$ | general dielectric related stiffness scalar |
| $L$ | harvester active length, $m$ |
| $m_{eff}$ | effective mass of the harvester, $kg$ |
| $M$ | general mass matrix |
| $M_t$ | added tip mass, $kg$ |
| $N, P, X, Z$ | interpolation function auxiliaries |
| $P$ | instantaneous generated power, $W$ |
| $q$ | extracted electric charge, $C$ |
| $Q$ | plane stress-reduces stiffness |
| $\boldsymbol{r}$ | displacement field vector |
| $R$ | electrical load, $\Omega$ |
| $\boldsymbol{S}$ | strain vector |
| t | time, $s$ |
| $\boldsymbol{T}$ | stress vector |
| $\mathcal{V}$ | volume, $m^3$ |
| $V_p$ | total voltage of one piezoelectric layer, $V$ |
| v | voltage difference, $V$ |
| $w$ | $z$ axis displacement of mid-plane, $m$ |
| $\mathcal{W}_1$ | $z$ axis displacement through thickness, $m$ |
| $W$ | energy, $J$ |
| $X$ | nodal value of$\phi_x$ |
| $Y$ | nodal value of$\phi_y$ |

*Subscript*

| | |
|---|---|
| c | Contact layer |
| eff | effective |
| e | electrical |
| E | external |
| p | piezoelectric layer |
| r | resonant |
| s | Substrate layer |
| $\wr$ | layer type |

*Superscript*

| | |
|---|---|
| e | related to element |
| oc | open-circuit |
| sc | short-circuit |
| t | matrix transpose |

*Coordinates*

| | |
|---|---|
| $(1, 2, 3)$ | principal coordinate (1 along fibers) |
| $(x, y, z)$ | physical coordinate ($x$ along harvester's length) |

Titanate (or PZT ceramic) has high piezoelectric coefficient compared to polymer and composite piezoelectric materials [7]. Morimoto et al. [8] obtained the normalized power density of 0.0345 $\mu W/g^2mm^3Hz$ from a 4.88-$mm^3$ PEH fabricated from epitaxial PZT films. Hu et al [10] obtained a high power density of 0.166 $\mu W/g^2mm^3Hz$ from a non-uniform PEH made of thinned bulk PZT and proof mass. This high power density was due to the high average strain distribution [10]. Recently, Muthalif and Nordin [9] designed a triangle piezoelectric beams with PZT-5H material that generates 2.9 V at resonant excitation, which is 30% higher than a rectangular piezoelectric beam. According to these studies, non-conventional designs, such as non-uniform and non-rectangular beams, generate higher output power relatively.

In order to model the coupling between mechanical and electrical physics in PEHs, various methods have been developed to estimate electrical voltage from a piezoelectric beam. The analytical distributed models such as [12,13], provide closed-form solutions for unimorph and bimorph piezoelectric energy harvesters, where configurations of the harvester are considered as rectangular beam with constant thickness under clamp-free boundary condition. Adding more than two piezoelectric layers requires the calculation of the neutral axis, the bending stiffness and the mode-shape coefficients. Consequently, the equation derivation should be modified. In addition, for each boundary condition, the equation derivation needs to be repeated due to the mode shapes change. The beam models are derived for the special case of rectangular constant cross-

section with constant thickness. Therefore, many initiative designs, such as non-rectangular geometries [9], which can harvest more power compared to the rectangular configuration, cannot be studied by the models presented in [12,13].

Even though analytical modeling techniques can reach an impressive accuracy, the investigation of practically designed piezoelectric structures requires developing of FEMs [14]. FEM provides a great capacity to model different harvester configurations [15] by breaking the calculation domain into small domains. Each of these can be analyzed numerically with one-dimensional beam [16] and two-dimensional plate/shell [17] elements. FEMs for smart structures can be broadly break into two categories: (1) classical and (2) advanced theories [18]. In the classical theories, the out-of-plane deformation through the thickness is constant and is equal to that of the mid-surface. While in the advanced theories, all the displacement field components are considered variable through the thickness. In order to study potential of smart structure applications, Reddy [19] introduced classical laminate plate theory (CLPT) and shear deformation theories (FSDT and TSDT) as the classical methods for multi-layered composites with embedded piezoelectric patches. The CLPT is not useful for multilayered composite laminates where exhibits higher transverse normal and transverse shear stresses. Although the shear deformation theories compensate these stresses, these theories do not satisfy the Cauchy theorem, where the out-of-plane stresses should be continuous [20] due to discontinuity of the mechanical properties through the thickness. In order to satisfy the interlaminar continuity (IC), Robaldo et al. [14] presented advanced theories for piezoelectric adaptive plates in multilayered composites. To model piezoelectric harvesters with FEM, mostly the CLPT theory in the classic framework has been applied [21,22] even though the PEHs were multilayered beams and the IC was not satisfied in the classical methods. In addition, if piezoelectric layers are embedded into structures such as aircraft wing structure or wind turbine blade, in which the thickness is not necessarily small, using the CLPT, as considered in Marqui Junior's model [21], is not appropriate. Therefore, for the accurate modeling of the PEH for various applications, there is a need for developing a FE model that considers the higher transverse normal and transverse shear stresses as well as satisfying the IC.

In addition, almost in all studies evaluating PEH, the damping mechanism was considered to be viscous damping as in Marqui Junior's model [21], while Cooley et al. [23] showed that using inappropriate damping model will lead to incorrect estimation of harvested power. Furthermore, in approaches presented for modeling of piezoelectric energy harvesters, the effect of contact layer between the substrate layer and piezoelectric sheets was ignored. Nevertheless, in practice, in order to fabricate a piezoelectric harvester, it is necessary to use an adhesive layer for attaching piezoelectric material to the substrate layer. According to Palosaari et al. [24], the thickness of passive layer has an influence on both tip displacement and the harvester power and therefore the effect of contact layer also should be accommodated.

To overcome the critical issues in the analytical distributed models and FE models, and in order to analyze a wider range of problems in piezoelectric harvesters, a comprehensive finite element formulation is proposed in the current study. The TSDT and advanced plate theory, suitable for multilayered composite structures and thick plates, are employed for the presented FEM formulation. Energy dissipation model in this method is a combination of viscous and structural damping mechanisms. The proposed method is verified by analytical results presented in [11,25] and experimental data from [13] for bimorph piezoelectric beams under the base excitation at different electrical conditions and excitation frequencies. Moreover, the electrical and mechanical analyses are carried out for an energy-harvesting beam with non-uniform and non-constant piezoelectric sheets covering the E-glass orthotropic laminae. Furthermore, effects of variation of the piezoelectric thickness and the fiber rotation in substrate layer on deformation of the beam and level of power generation are investigated. Although the presented method employs high-order shear deformation theory, using a creative representation of finite element matrices, global finite element matrices are expressed with separately function matrices easier for computer manipulation. By using this model, performance of a wide range of piezoelectric beams, from simple standard configurations such as unimorph and bimorph to non-uniform beams with variable piezoelectric thickness and thick piezoelectric patches, can be investigated.

## 2. Finite element modeling of piezoelectric energy harvester

A typical piezoelectric harvester consists of a piezoelectric sheet and a substrate layer, which are joined together with a contact layer. Conventional 3–1 mode PEH is clamped at one end and is free at the other end. The vibration acts on the harvester as base excitation and the free end experiences large-deflection vibration. Fig. 1 shows a typical 3–1 mode piezoelectric energy harvester that generates electrical voltage from base excitation. The output wires from positive and negative poles are connected to an electrical load of $R$ for generating electrical power. In this section, a comprehensive finite element model for modeling various types of materials for the substrate and piezoelectric layers and different geometrical configurations is presented. The key features of this method can be summarized as follow:

- Both substrate and piezoelectric materials are defined as orthotropic materials with different rotations of principal directions.
- The effect of contact layer with its damping effects is accommodated.
- High order deformation theory is used for displacement approximation, which is a proper approach for thick composite plates that considers Shear stresses are considered. The energy harvesting beams are considered non-uniform, where the piezoelectric sheet partially covers the substrate.
- Thickness of the piezoelectric sheet is variable.

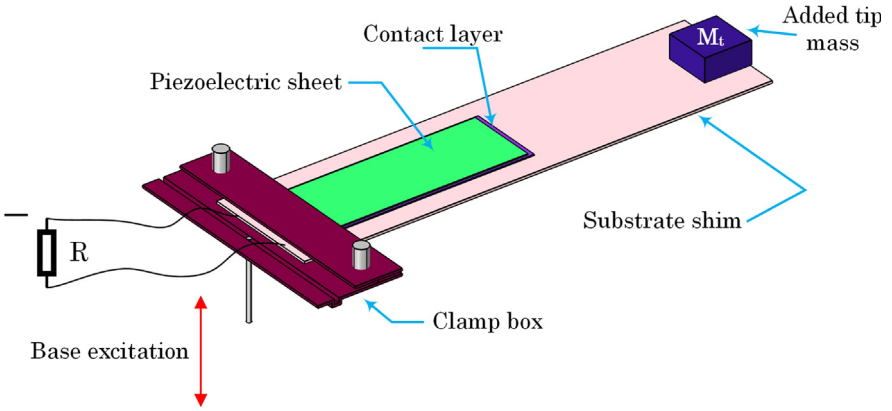


**Fig. 1.** A typical 3–1 mode piezoelectric energy harvester comprises piezoelectric sheet, contact layer, substrate shim and added tip mass with base excitation.

- The damping mechanisms include viscous and structural mechanisms, which are frequency dependent and independent, respectively.
- Added tip mass attached to the harvester is considered in the model.

In the following subsections, the developed finite model will be presented in details. First, due to different material domains, constitutive equations for the piezoelectric, the substrate and contact layers are shown with presenting the equations for principal direction rotation. These constitutive equations will relate the mechanical strain to mechanical stress and electrical voltage. In next step strain tensors are defined based on physical displacements with third-order shear deformation element in Section 2.2; so that the stress vector and voltage are related to the displacement fields. In this study, the physical displacements are approximated according to the finite element method in which the main domain is discretized into a number of small domains and displacements are approximated using a spatial approximation for each discretized domain. Section 2.3 presents the spatial approximation and the relationships between the displacement vector, as well as strain tensor, and discretized degrees of freedom. Section 2.4 extracts the mechanical and electromechanical finite element matrices for each discretized domain using extended Hamilton's principle and considering the previous spatial approximation. Finally, assembling the element matrices in form of global finite element matrices are presented for steady state solution for the harmonic applied load in Sections and 2.6, respectively.

### 2.1. Constitutive relations

According to Fig. 1 showing the studied energy harvester, there are three different domains, where each one has its own constitutive equations. These three domains are the piezoelectric, substructure and contact layer. It is assumed that both of the piezoelectric and substrate layers are orthotropic materials meaning that, there are two orthogonal planes of the materials property symmetry. On the other hand, the contact layer is considered as an isotropic material. The piezoelectric domain has electromechanically coupled constitutive relations, while the substructure and contact layer domains are only mechanical relations. Since principal directions may not coincide with coordinate directions in orthotropic materials, a rotation in principal directions is taken into the account for the piezoelectric and substrate domains.

The linear constitutive equations for an orthotropic material in two dimensions considering piezoelectric effect are:

$$\begin{Bmatrix} \sigma_1 \\ \sigma_2 \\ \tau_{23} \\ \tau_{31} \\ \tau_{12} \end{Bmatrix}_p = \begin{bmatrix} Q_{11} & Q_{12} & 0 & 0 & 0 \\ Q_{12} & Q_{22} & 0 & 0 & 0 \\ 0 & 0 & Q_{44} & 0 & 0 \\ 0 & 0 & 0 & Q_{55} & 0 \\ 0 & 0 & 0 & 0 & Q_{66} \end{bmatrix}_p \begin{Bmatrix} \varepsilon_1 \\ \varepsilon_2 \\ \gamma_{23} \\ \gamma_{31} \\ \gamma_{12} \end{Bmatrix}_p - \begin{bmatrix} 0 & 0 & e_{31} \\ 0 & 0 & e_{32} \\ 0 & e_{24} & 0 \\ e_{15} & 0 & 0 \\ 0 & 0 & 0 \end{bmatrix} \begin{Bmatrix} \mathcal{E}_1 \\ \mathcal{E}_2 \\ \mathcal{E}_3 \end{Bmatrix} \tag{1}$$

The plane stress stiffnesses can be related to engineering constants as:

$$Q_{11} = \frac{E_1}{1 - \nu_{12}\nu_{21}},\ Q_{12} = \frac{\nu_{12}E_2}{1 - \nu_{12}\nu_{21}},\ Q_{22} = \frac{E_2}{1 - \nu_{12}\nu_{21}},\ Q_{44} = G_{23},\ Q_{55} = G_{31},\ Q_{66} = G_{12} \tag{2}$$

For the substrate layer, constitutive equations are the same as Eq. (1) without the piezoelectric effect, e.g. $e_{ij} = 0$.

In addition, the constitutive equation for the contact layer as an isotropic material is as follows:

$$\begin{Bmatrix}\sigma_1\\ \sigma_2\\ \tau_{23}\\ \tau_{31}\\ \tau_{12}\end{Bmatrix}=\begin{bmatrix}Q_{11} & Q_{12} & 0 & 0 & 0\\ Q_{12} & Q_{11} & 0 & 0 & 0\\ 0 & 0 & (Q_{11}-Q_{12})/2 & 0 & 0\\ 0 & 0 & 0 & (Q_{11}-Q_{12})/2 & 0\\ 0 & 0 & 0 & 0 & (Q_{11}-Q_{12})/2\end{bmatrix}_c\begin{Bmatrix}\varepsilon_1\\ \varepsilon_2\\ \gamma_{23}\\ \gamma_{31}\\ \gamma_{12}\end{Bmatrix} \tag{3}$$

Piezoelectric property is a two-way coupling between electrical polarization and mechanical strains. Hence, the effect of strains on the electrical displacement vector can be shown as [19]:

$$\begin{Bmatrix}D_1\\ D_2\\ D_3\end{Bmatrix}=\begin{bmatrix}0 & 0 & 0 & e_{15} & 0\\ 0 & 0 & e_{24} & 0 & 0\\ e_{31} & e_{32} & 0 & 0 & 0\end{bmatrix}\begin{Bmatrix}\varepsilon_1\\ \varepsilon_2\\ \gamma_{23}\\ \gamma_{31}\\ \gamma_{12}\end{Bmatrix}+\begin{bmatrix}\epsilon_{11} & 0 & 0\\ 0 & \epsilon_{22} & 0\\ 0 & 0 & \epsilon_{33}\end{bmatrix}\begin{Bmatrix}\mathcal{E}_1\\ \mathcal{E}_2\\ \mathcal{E}_3\end{Bmatrix} \tag{4}$$

As stated, a general case is considered in which the principal directions do not coincide with the coordinate directions. This case is shown in Fig. 2, where rotations of piezoelectric and substrate layers are not the same. In such case, in order to calculate the stresses in coordinate system, the transformation of material properties should be considered.

In a general case, constitutive equations considering a transformation of principal coordinates to geometry coordinates for the piezoelectric sheets, the substrate layers and contact layer can be shown as:

$$\begin{aligned}&\boldsymbol{T}_p=\left[\overline{\boldsymbol{Q}}\right]_p\boldsymbol{S}-[\overline{\boldsymbol{e}}]\mathcal{E} && \text{Piezoelectric sheets}\\ &\boldsymbol{T}_s=\left[\overline{\boldsymbol{Q}}\right]_s\boldsymbol{S} && \text{Substrate layer}\\ &\boldsymbol{T}_c=[\boldsymbol{Q}]_c\boldsymbol{S} && \text{Contact layers}\end{aligned} \tag{5}$$

In Eq. (5), over-bar indicates that the parameter is presented in physical coordinate. So, $\left[\overline{Q}\right]$ and $[\overline{e}]$ are stiffness and piezoelectric matrices after the transformation. It is worth mentioning that, the transformation is not necessary for contact layer since it is an isotropic material. In Eq. (5), $\boldsymbol{T}$, $\boldsymbol{S}$ and $\mathcal{E}$ are stress, strain and electrical field vectors. These terms are tensors in three dimensions and Eq. (6) shows components of these parameters:

$$\boldsymbol{T}=\begin{Bmatrix}\sigma_{xx}\\ \sigma_{yy}\\ \sigma_{yz}\\ \sigma_{xz}\\ \sigma_{xy}\end{Bmatrix},\boldsymbol{S}=\begin{Bmatrix}\varepsilon_{xx}\\ \varepsilon_{yy}\\ \gamma_{yz}\\ \gamma_{xz}\\ \gamma_{xy}\end{Bmatrix},\mathcal{E}=\begin{Bmatrix}\mathcal{E}_x\\ \mathcal{E}_y\\ \mathcal{E}_z\end{Bmatrix}$$

$$\left[\overline{\boldsymbol{Q}}\right]=\begin{bmatrix}\overline{Q}_{11} & \overline{Q}_{12} & 0 & 0 & \overline{Q}_{16}\\ \overline{Q}_{12} & \overline{Q}_{22} & 0 & 0 & \overline{Q}_{26}\\ 0 & 0 & \overline{Q}_{44} & \overline{Q}_{45} & 0\\ 0 & 0 & \overline{Q}_{45} & \overline{Q}_{55} & 0\\ \overline{Q}_{16} & \overline{Q}_{26} & 0 & 0 & \overline{Q}_{66}\end{bmatrix},[\overline{\boldsymbol{e}}]=\begin{bmatrix}0 & 0 & \overline{e}_{31}\\ 0 & 0 & \overline{e}_{32}\\ 0 & 0 & \overline{e}_{36}\\ \overline{e}_{14} & \overline{e}_{24} & 0\\ \overline{e}_{15} & \overline{e}_{25} & 0\end{bmatrix} \tag{6}$$

The relationship between components of the stiffness and the piezoelectric matrices in geometrical coordinates and principal coordinates under $\theta$ rotation is shown in Eq. (A.1) and (A.2) in Appendix A.

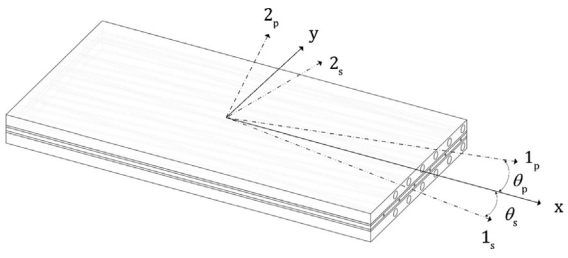


**Fig. 2.** Piezoelectric and substrate layers with $+\theta_p$ and $-\theta_s$ rotations, respectively.

Similarly, the electrical displacement vector can be expressed in the geometric coordinates as follows:

$$\boldsymbol{D} = \begin{Bmatrix} D_x \\ D_y \\ D_z \end{Bmatrix} = \begin{bmatrix} 0 & 0 & \bar{e}_{14} & \bar{e}_{15} & 0 \\ 0 & 0 & \bar{e}_{24} & \bar{e}_{25} & 0 \\ \bar{e}_{31} & \bar{e}_{32} & 0 & 0 & \bar{e}_{36} \end{bmatrix} \begin{Bmatrix} \varepsilon_{xx} \\ \varepsilon_{yy} \\ \gamma_{yz} \\ \gamma_{xz} \\ \gamma_{xy} \end{Bmatrix} + \begin{bmatrix} \bar{\epsilon}_{11} & \bar{\epsilon}_{12} & 0 \\ \bar{\epsilon}_{12} & \bar{\epsilon}_{22} & 0 \\ 0 & 0 & \bar{\epsilon}_{33} \end{bmatrix} \begin{Bmatrix} \mathcal{E}_x \\ \mathcal{E}_y \\ \mathcal{E}_z \end{Bmatrix} = [\bar{\boldsymbol{e}}]^t \boldsymbol{S} + [\bar{\epsilon}^s]\mathcal{E} \tag{7}$$

where $[\bar{\epsilon}^s]$ is the permittivity matrix in physical coordinates and its components are related to the permittivity matrix in principal coordinates with Eq. (A.3) in Appendix A.

In 3–1 mode energy harvesting applications, poling direction is along z-axis, so only the z part of the electric field component is non-zero. Therefore, when the voltage between two electrode pairs is denoted by $v$, the vector of the electric field becomes:

$$\mathcal{E} = \begin{Bmatrix} 0 \\ 0 \\ -v/h_p \end{Bmatrix} = \{A_e\}_{3\times 1} v \tag{8}$$

### 2.2. Displacement fields and strains

In Section 2.1, the mechanical stress and electrical displacement vectors were related to the strain vectors. However, strains should be related to displacement fields since the fields are replaced with a series approximation in the FE approach. The relationships between the displacement fields and the strains depend on to the theory of the considered plates. In the classical plate theories the out-of-plane displacement is assumed constant in $z$-direction, while in the unified formulation, such as CUF, the out-of-plane displacement is dependent to the $z$– direction. In the classical theories, there are various approaches for estimation of the displacement field in $x$ and $y$ directions. For instance, in CLPT, which is based on the Kirchhoff plate theory, it is assumed that the lines perpendicular to the mid-surface rotate in such a way that they remain perpendicular after the deformation. In FSDT, the perpendicular lines to the mid-surface are not no longer perpendicular after the deformation, but they still remains as line. In the third shear-order deformation theory TSDT, the perpendicular lines to the mid-surface will not be perpendicular nor remain lines after the deformation [26]. These theories are shown in Fig. 3 (a).

In the current formulation, a general case based on the CUF suggestions [27] with the TSDT is employed as shown in Fig. 3 (a). In this formulation, $w = w(x,y,t)$, $\mathcal{W}_1 = \mathcal{W}_1(x,y,t)$, $\phi_x = \phi_x(x,y,t)$ and $\phi_y = \phi_y(x,y,t)$ are four independent functions for representing the displacement fields.

Based on the geometry coordinates in Fig. 3, the displacement field vector, $\boldsymbol{r}$, can be expressed as [28]:

$$\boldsymbol{r} = \begin{Bmatrix} r_x(x,y,z,t) \\ r_y(x,y,z,t) \\ r_z(x,y,z,t) \end{Bmatrix} = \begin{Bmatrix} 0 \\ 0 \\ w \end{Bmatrix} + z \begin{Bmatrix} \frac{5}{4}\phi_x + \frac{1}{4}w_{,x} \\ \frac{5}{4}\phi_y + \frac{1}{4}w_{,y} \\ \mathcal{W}_1 \end{Bmatrix} - \mathcal{C}_1 z^3 \begin{Bmatrix} \frac{5}{4}\phi_x + \frac{5}{4}w_{,x} \\ \frac{5}{4}\phi_y + \frac{5}{4}w_{,y} \\ 0 \end{Bmatrix} \tag{9}$$

where $\mathcal{C}_1 = 4/\left(3h^2\right)$ and $h$ is the thickness of plate, including all the layers, and $z$ is the distance to the mid-surface. Subscript "," represents the partial differential. Classical plate theories (CLPT, FSDT, and TSDT) consider $\mathcal{W}_1 = 0$ while in CUFs $\mathcal{W}_1 \neq 0$. It

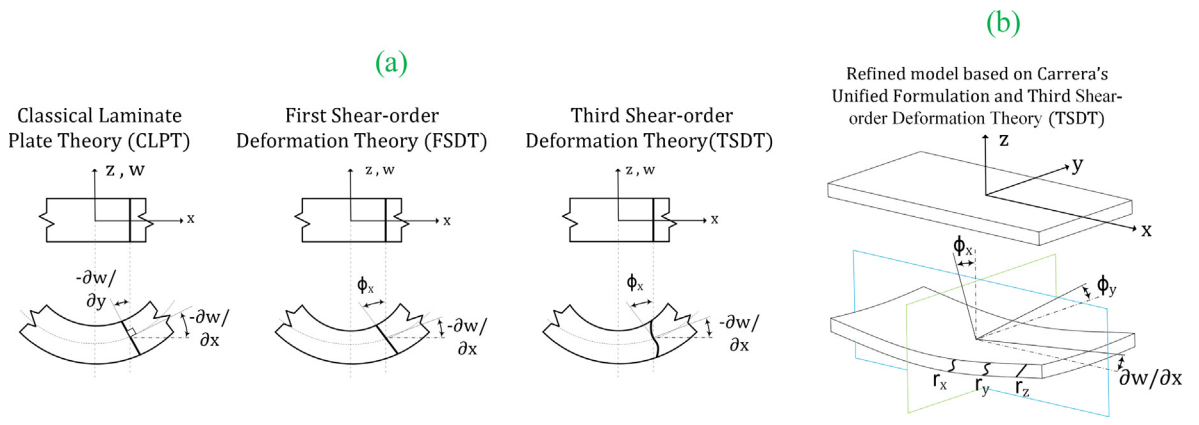


**Fig. 3.** (a) Cross-sectional views of different classical theories for presenting the plate deformation and (b) the plate deformation theory considered in this study.

is worth mentioning that, in this formulation if $\mathcal{C}_1 \neq 0$, each displacement component is a polynomial of third degree, while in the CLPT and FSDT it is a straight line. Eq. (9) can be used for FSDT by setting $\mathcal{C}_1$ to 0. In addition, Eq. (9) can be used for the CLPT by setting $\mathcal{C}_1 = 0$, $\phi_x = -w_{,x}$ and $\phi_y = -w_{,y}$.

The strain vector can be related to the displacement field vector through:

$$\boldsymbol{S} = \begin{Bmatrix} \varepsilon_{xx} \\ \varepsilon_{yy} \\ \gamma_{yz} \\ \gamma_{xz} \\ \gamma_{xy} \end{Bmatrix} = \begin{Bmatrix} r_{x,x} \\ r_{y,y} \\ r_{y,z} + r_{z,y} \\ r_{x,z} + r_{z,x} \\ r_{x,y} + r_{y,x} \end{Bmatrix}. \tag{10}$$

By substituting the displacement vector from Eq. (9) into Eq. (10) and knowing that the derivative of $\phi_x$, $\phi_y$ and $w$ are zero with respect to $z$, the strain vector can be related to the deformation by Eq. (11):

$$\boldsymbol{S} = \begin{Bmatrix} 0 \\ 0 \\ \frac{5}{4}\phi_y + \frac{5}{4}w_{,y} \\ \frac{5}{4}\phi_x + \frac{5}{4}w_{,x} \\ 0 \end{Bmatrix} + z\begin{Bmatrix} \frac{5}{4}\phi_{x,x} + \frac{1}{4}w_{,xx} \\ \frac{5}{4}\phi_{y,y} + \frac{1}{4}w_{,yy} \\ \mathcal{W}_{1,y} \\ \mathcal{W}_{1,x} \\ \frac{5}{4}\phi_{x,y} + \frac{5}{4}\phi_{y,x} + \frac{1}{2}w_{,xy} \end{Bmatrix} - 3\mathcal{C}_1 z^2 \begin{Bmatrix} 0 \\ 0 \\ \frac{5}{4}\phi_y + \frac{5}{4}w_{,y} \\ \frac{5}{4}\phi_x + \frac{5}{4}w_{,x} \\ 0 \end{Bmatrix} - \mathcal{C}_1 z^3 \begin{Bmatrix} \frac{5}{4}\phi_{x,x} + \frac{5}{4}w_{,xx} \\ \frac{5}{4}\phi_{y,y} + \frac{5}{4}w_{,yy} \\ 0 \\ 0 \\ \frac{5}{4}\phi_{x,y} + \frac{5}{4}\phi_{y,x} + \frac{5}{2}w_{,xy} \end{Bmatrix} \tag{11}$$

Consequently, the stress vector can be related to the physical displacement field by using Eq. (5) and the relationship between the strains and physical displacements in Eq. (11).

### 2.3. Discretization and spatial approximation

This subsection deals with spatial approximation for the displacement fields, so that by expressing these physical displacements, the stress vectors can be approximated with a series of estimations. As it can be observed from Eqs. (9) and (11), the strain vector contains the first derivative of $\phi_x$, $\phi_y$ and $\mathcal{W}_1$ and the second derivatives of out of plane displacement with respect to $x$ and $y$. Hence, $\phi_x$, $\phi_y$ and $\mathcal{W}_1$ are approximated using the Lagrange interpolations functions, and $w$ by the Hermite interpolation functions. Fig. 4 shows a rectangular element having $(w, w_{,x}, w_{,y}, \mathcal{W}_1, \phi_x, \phi_y)$ degrees of freedom (DoFs) for each node and one electrical DoF, $v_e$, for the element. The vector of degrees of freedom for each element is defined by Eq. (12).

$$DoF_e = \left\{ w^1\ w^1_{,x}\ w^1_{,y}\ \mathcal{W}^1_1\ \phi^1_x\ \phi^1_y\ w^2\ w^2_{,x}\ w^2_{,y}\ \mathcal{W}^2_1\ \phi^2_x\ \phi^2_y\ w^3\ w^3_{,x}\ w^3_{,y}\ \mathcal{W}^3_1\ \phi^3_x\ \phi^3_y\ w^4\ w^4_{,x}\ w^4_{,y}\ \mathcal{W}^4_1\ \phi^4_x\ \phi^4_y \right\}^t \tag{12}$$

It is assumed that $\phi_x$, $\phi_y$, $\mathcal{W}_1$ and $w$ have the following approximations:

$$\begin{aligned} \phi_x(x,y,t) &\approx \textstyle\sum_{i=1}^{4} X_i^e(t)\psi_i(x,y) \\ \phi_y(x,y,t) &\approx \textstyle\sum_{i=1}^{4} Y_i^e(t)\psi_i(x,y) \\ w(x,y,t) &\approx \textstyle\sum_{i=1}^{12} \Delta_i^e(t)\Lambda_i(x,y) \\ \mathcal{W}_1(x,y,t) &\approx \textstyle\sum_{i=1}^{4} \Xi_i^e(t)\psi_i(x,y) \end{aligned} \tag{13}$$

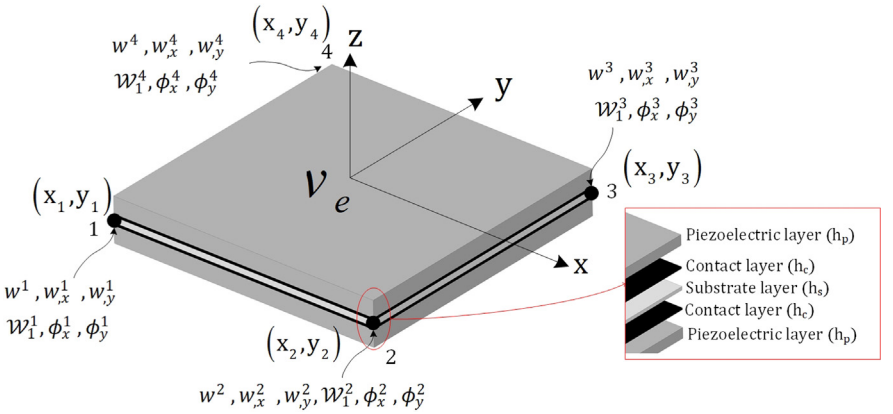


**Fig. 4.** A rectangular plate element with 24 mechanical DoFs and 1 electrical DoF.

where subscript $i$ in Eq. (13) addresses the $i$-th node in a typical element. These interpolation functions can be expressed with Eq. (14) [29].

$$[\psi]=[\psi_1\cdots\psi_4]=\{1\ x\ y\ xy\}\begin{bmatrix}1&x_1&y_1&x_1y_1\\1&x_2&y_2&x_2y_2\\1&x_3&y_3&x_3y_3\\1&x_4&y_4&x_4y_4\end{bmatrix}^{-1}=\{N\}[X]^{-1}[\Lambda]=[\Lambda_1\cdots\Lambda_{12}]=\{P\}[Z]^{-1}$$
$$=\begin{Bmatrix}1\ x\ y\ x^2\ xy\ y^2\ x^3\\x^2y\ xy^2\ y^3\ x^3y\ xy^3\end{Bmatrix}\left[\begin{bmatrix}\{P\}\\\{P\}_{,x}\\\{P\}_{,y}\end{bmatrix}_{(x_1,y_1)}\begin{bmatrix}\{P\}\\\{P\}_{,x}\\\{P\}_{,y}\end{bmatrix}_{(x_2,y_2)}\begin{bmatrix}\{P\}\\\{P\}_{,x}\\\{P\}_{,y}\end{bmatrix}_{(x_3,y_3)}\begin{bmatrix}\{P\}\\\{P\}_{,x}\\\{P\}_{,y}\end{bmatrix}_{(x_4,y_4)}\right]^{-T} \tag{14}$$

wherein superscript $-T$ means the transpose of the inverse matrix.

Substituting the spatial approximation from Eq. (13) into Eqs. (9) and (11), the displacement field vector is expressed by the following matrix representations:

$$\boldsymbol{r}(x,y,z,t)=\begin{Bmatrix}\frac{5}{4}(z-\mathcal{C}_1z^3)\sum_{i=1}^{4}X_i^e(t)\psi_i+(\frac{1}{4}z-\frac{5}{4}\mathcal{C}_1z^3)\sum_{i=1}^{12}\Delta_i^e(t)\Lambda_{i,x}\\\frac{5}{4}(z-\mathcal{C}_1z^3)\sum_{i=1}^{4}Y_i^e(t)\psi_i+(\frac{1}{4}z-\frac{5}{4}\mathcal{C}_1z^3)\sum_{i=1}^{12}\Delta_i^e(t)\Lambda_{i,y}\\z\sum_{i=1}^{4}\Xi_i^e(t)\psi_i(x,y)+\sum_{i=1}^{12}\Delta_i^e(t)\Lambda_i\end{Bmatrix}=[A_m(z)]_{3\times6}[B_m(x,y)]_{6\times24}\{\chi^e(t)\}_{24\times1} \tag{15}$$

The element DoF vector ($\chi^e$) and auxiliary matrices $[A_m]$ and $[B_m]$ are given by:

$$\{\chi^e(t)\}=\{X_1^e\ \cdots\ X_4^e\ \ Y_1^e\ \cdots\ Y_4^e\ \Xi_1^e\cdots\Xi_4^e\ \Delta_1^e\ \cdots\ \Delta_{12}^e\}^t[A_m(z)]$$
$$=\begin{bmatrix}\frac{5}{4}(z-\mathcal{C}_1z^3)&0&0&0&(\frac{1}{4}z-\frac{5}{4}\mathcal{C}_1z^3)&0\\0&\frac{5}{4}(z-\mathcal{C}_1z^3)&0&0&0&(\frac{1}{4}z-\frac{5}{4}\mathcal{C}_1z^3)\\0&0&z&1&0&0\end{bmatrix}[B_m(x,y)]$$
$$=\begin{bmatrix}[\psi]&[0]&[0]&[0]\\[0]&[\psi]&[0]&[0]\\[0]&[0]&[\psi]&[0]\\[0]&[0]&[0]&[\Lambda]\\[0]&[0]&[0]&[\Lambda]_{,x}\\\underbrace{[0]}_{1\times4}&\underbrace{[0]}_{1\times4}&\underbrace{[0]}_{1\times4}&\underbrace{[\Lambda]_{,y}}_{1\times12}\end{bmatrix}=\begin{bmatrix}\{N\}[X]^{-1}&[0]&[0]&[0]\\[0]&\{N\}[X]^{-1}&[0]&[0]\\[0]&[0]&\{N\}[X]^{-1}&[0]\\[0]&[0]&[0]&\{P\}[Z]^{-1}\\[0]&[0]&[0]&\{P\}_{,x}[Z]^{-1}\\[0]&[0]&[0]&\{P\}_{,y}[Z]^{-1}\end{bmatrix} \tag{16}$$

Similar to the displacement field vector, the strain vector can be expressed with:

$$\boldsymbol{S}(x,y,z,t)=\begin{Bmatrix}\frac{5}{4}(z-\mathcal{C}_1z^3)\sum_{i=1}^{4}X_i^e(t)\psi_{i,x}+(\frac{1}{4}z-\frac{5}{4}\mathcal{C}_1z^3)\sum_{i=1}^{12}\Delta_i^e(t)\Lambda_{i,xx}\\\frac{5}{4}(z-\mathcal{C}_1z^3)\sum_{i=1}^{4}Y_i^e(t)\psi_{i,y}+(\frac{1}{4}z-\frac{5}{4}\mathcal{C}_1z^3)\sum_{i=1}^{12}\Delta_i^e(t)\Lambda_{i,yy}\\z\sum_{i=1}^{4}\Xi_i^e(t)\psi_{i,y}+\frac{5}{4}(1-3\mathcal{C}_1z^2)\left(\sum_{i=1}^{4}Y_i^e(t)\psi_i+\sum_{i=1}^{12}\Delta_i^e(t)\Lambda_{i,y}\right)\\z\sum_{i=1}^{4}\Xi_i^e(t)\psi_{i,x}+\frac{5}{4}(1-3\mathcal{C}_1z^2)\left(\sum_{i=1}^{4}X_i^e(t)\psi_i+\sum_{i=1}^{12}\Delta_i^e(t)\Lambda_{i,x}\right)\\\frac{5}{4}(z-\mathcal{C}_1z^3)\sum_{i=1}^{4}X_i^e(t)\psi_{i,y}+\frac{5}{4}(z-\mathcal{C}_1z^3)\sum_{i=1}^{4}Y_i^e(t)\psi_{i,x}+2(\frac{1}{4}-\frac{5}{4}\mathcal{C}_1z^3)\sum_{i=1}^{12}\Delta_i^e(t)\Lambda_{i,xy}\end{Bmatrix}$$
$$=[A_k(z)]_{5\times13}[B_k(x,y)]_{13\times24}\{\chi^e(t)\}_{24\times1} \tag{17}$$

where the auxiliary matrices are given by:

$$[A_k(z)]=\begin{bmatrix}0&0&\frac{5}{4}(z-\mathcal{C}_1z^3)&0&0&0\\0&0&0&0&0&\frac{5}{4}(z-\mathcal{C}_1z^3)\\0&\frac{5}{4}(1-3\mathcal{C}_1z^2)&0&0&0&0\\\frac{5}{4}(1-3\mathcal{C}_1z^2)&0&0&0&0&0\\0&0&0&\frac{5}{4}(z-\mathcal{C}_1z^3)&\frac{5}{4}(z-\mathcal{C}_1z^3)&0\end{bmatrix}$$

$$\begin{bmatrix}0&0&0&0&0&(\frac{1}{4}z-\frac{5}{4}\mathcal{C}_1z^3)&0\\0&0&0&0&0&0&(\frac{1}{4}z-\frac{5}{4}\mathcal{C}_1z^3)\\0&z&0&1+\frac{5}{4}(1-3\mathcal{C}_1z^2)&0&0&0\\z&0&1+\frac{5}{4}(1-3\mathcal{C}_1z^2)&0&0&0&0\\0&0&0&0&2(\frac{1}{4}-\frac{5}{4}\mathcal{C}_1z^3)&0&0\end{bmatrix} \tag{18}$$

$$[B_k(x,y)] = \begin{bmatrix} [\psi] & [0] & [0] & [0] \\ [0] & [\psi] & [0] & [0] \\ [\psi]_{,x} & [0] & [0] & [0] \\ [0] & [\psi]_{,x} & [0] & [0] \\ [\psi]_{,y} & [0] & [0] & [0] \\ [0] & [\psi]_{,y} & [0] & [0] \\ [0] & [0] & [\psi]_{,x} & [0] \\ [0] & [0] & [\psi]_{,y} & [0] \\ [0] & [0] & [0] & [\Lambda]_{,x} \\ [0] & [0] & [0] & [\Lambda]_{,y} \\ [0] & [0] & [0] & [\Lambda]_{,xy} \\ [0] & [0] & [0] & [\Lambda]_{,xx} \\ \underbrace{[0]}_{1\times4} & \underbrace{[0]}_{1\times4} & \underbrace{[0]}_{1\times4} & \underbrace{[\Lambda]_{,y}}_{1\times12} \end{bmatrix} = \begin{bmatrix} \{N\}[X]^{-1} & [0] & [0] & [0] \\ [0] & \{N\}[X]^{-1} & [0] & [0] \\ \{N\}_{,x}[X]^{-1} & [0] & [0] & [0] \\ [0] & \{N\}_{,x}[X]^{-1} & [0] & [0] \\ \{N\}_{,y}[X]^{-1} & [0] & [0] & [0] \\ [0] & \{N\}_{,y}[X]^{-1} & [0] & [0] \\ [0] & [0] & \{N\}_{,x}[X]^{-1} & [0] \\ [0] & [0] & \{N\}_{,y}[X]^{-1} & [0] \\ [0] & [0] & [0] & \{P\}_{,x}[Z]^{-1} \\ [0] & [0] & [0] & \{P\}_{,y}[Z]^{-1} \\ [0] & [0] & [0] & \{P\}_{,xy}[Z]^{-1} \\ [0] & [0] & [0] & \{P\}_{,xx}[Z]^{-1} \\ [0] & [0] & [0] & \{P\}_{,yy}[Z]^{-1} \end{bmatrix} \tag{19}$$

It is worth to note that, the displacement field and strain vectors are expressed with separately functioned matrices. In the other words, Eqs. (15) and (17) help to decompose the displacement field and strain vectors as a product of the three matrices for easier numerical integration in the next subsection. In addition, this type of matrix representation is a tool for easy handling of various shell and plate elements, including the classical (CLPT, FSDT and TSDT) and the advanced models, with one generic matrix formulation.

### 2.4. Finite element formulation for discretized domains

The Hamilton's principle is a key tool in analytical mechanics in order to derive equations of motions for a dynamical system. Generalized Hamilton's principle states that for a holonomic system between time 0 and $t_0$, the definite integral

$$I = \int_0^{t_0} [(KE - PE + W_e) + W_E]dt \tag{20}$$

is stationary with respect to all arbitrary path variations, e.g. $\delta I = 0$. In Eq. (18), $W_e$ is the electrical energy caused by transferring electrical charge and $W_E$ is the external work done by both mechanical forces and electrical charges. The terms in the integrant in Eq. (20) are defined with Eq. (21).

$$\begin{aligned} KE &= \int_{V_s} \tfrac{1}{2}\dot{\boldsymbol{r}}^{\boldsymbol{t}}\mu_s\dot{\boldsymbol{r}}dV_s + \int_{V_c} \tfrac{1}{2}\dot{\boldsymbol{r}}^{\boldsymbol{t}}\mu_c\dot{\boldsymbol{r}}dV_c + \int_{V_p} \tfrac{1}{2}\dot{\boldsymbol{r}}^{\boldsymbol{t}}\mu_p\dot{\boldsymbol{r}}dV_p \\ PE &= \int_{V_s} \tfrac{1}{2}\boldsymbol{S}^{\boldsymbol{t}}\boldsymbol{T}_{\boldsymbol{s}}dV_s + \int_{V_c} \tfrac{1}{2}\boldsymbol{S}^{\boldsymbol{t}}\boldsymbol{T}_{\boldsymbol{c}}dV_c + \int_{V_p} \tfrac{1}{2}\boldsymbol{S}^{\boldsymbol{t}}\boldsymbol{T}_{\boldsymbol{p}}dV_p \\ W_e &= \int_{V_p} \tfrac{1}{2}\mathcal{E}^{\boldsymbol{t}}\boldsymbol{D}dV_p \\ W_E &= \delta\boldsymbol{r}_E\boldsymbol{f}_E + \delta\Phi_e q_e \end{aligned} \tag{21}$$

$\boldsymbol{f}_E$ is the external load applied on the element at $\boldsymbol{r}_E$ location and $q_e$ is the charge that is extracted from the element by conductive electrode on that element. By substituting these energy terms into Eq. (20) and applying the constitutive equations presented in Eqs. (5) and (8) on Eqs. (15) and (8), $\delta I = 0$ will be as:

$$\begin{aligned} \delta I = \int_0^{t_0} \Bigg[ \delta\{\chi\}^t \Bigg[ &\int_{V_s} [B_m]^t[A_m]^t\mu_s[A_m][B_m]\{\ddot{\chi}^e\}d\mathcal{V}_s + \int_{V_c} [B_m]^t[A_m]^t\mu_c[A_m][B_m]\{\ddot{\chi}^e\}d\mathcal{V}_c + \int_{V_p} [B_m]^t[A_m]^t\mu_p[A_m][B_m]\{\ddot{\chi}^e\}d\mathcal{V}_p \\ &+ \int_{V_s} [B_k]^t[A_k]^t\left[\overline{\boldsymbol{Q}}\right]_s[A_k][B_k]\{\chi^e\}d\mathcal{V}_s + \int_{V_c} [B_k]^t[A_k]^t[\boldsymbol{Q}]_c[A_k][B_k]\{\chi^e\}d\mathcal{V}_c + \int_{V_s} [B_k]^t[A_k]^t\left[\overline{\boldsymbol{Q}}\right]_p[A_k][B_k]\{\chi^e\}d\mathcal{V}_p \\ &- \int_{V_s} [B_k]^t[A_k]^t[\overline{\boldsymbol{e}}][A_e]v_e d\mathcal{V}_p - \boldsymbol{f}_E \Bigg] + \delta\{\Phi\}\left[\int_{V_p} [A_e]^t[\overline{\boldsymbol{e}}]^t[A_k][B_k]\{\chi^e\}d\mathcal{V}_p + \int_{V_p} [A_e]^t[\overline{\epsilon}^s][A_e]v_e d\mathcal{V}_p + \boldsymbol{q}_e\right]\Bigg]dt = 0 \end{aligned} \tag{22}$$

by letting $\delta\{\chi\}^t = 0$ and $\delta\{\Phi\} = 0$, the electro-mechanical coupling equations for one element can be extracted as:

$$[m^e]\{\ddot{\chi}^e\} + \left[k^e_{qq}\right]\{\chi^e\} - \left\{k^e_{q\phi}\right\}v_e = \boldsymbol{f}_E\left[k^e_{q\phi}\right]^t\{\chi^e\} + q_e + k^e_{\phi\phi}v_e = 0 \tag{23}$$

$\boldsymbol{f}_E$ and $q_e$ are the external mechanical load vector and extracted charge, respectively. The element considered in Fig. 4 comprises all the piezoelectric, contact and substrate layers. However, in real applications, the harvester beam may have the non-uniform configuration in which the piezoelectric layer only covers a fraction of the substrate layer as shown in Fig. 5. Therefore, to accommodate these types of harvesters, $\lambda_\circ$ multipliers are defined for each element showing whether the piezoelectric, contact and substrate layers present in the element. $\circ$ denotes material type and can be $s$ (substrate layer), $c$ (contact layer) or $p$ (piezoelectric layer). The value of 1 represents existence of the material while 0 is for the material absence. For instance, in bottom of Fig. 5, in the zone that both of the piezoelectric and substrate layers exist, $(\lambda_p, \lambda_c, \lambda_s) = (1,1,1)$ while in the rest of the beam $(\lambda_p, \lambda_c, \lambda_s) = (0,0,1)$.

Considering the multipliers, the mass, mechanical stiffness, electro-mechanical coupling and the electric stiffness can be defined as Eq. (24).

$$\begin{aligned}
&[m^e] = \textstyle\sum_{\circ=s,c,p} \lambda_\circ \int_{V_Q} [B_m]^t [A_m]^t \mu_\circ [A_m][B_m] dV_\circ \\
&\left[k^e_{qq}\right] = \textstyle\sum_{\circ=s,c,p} \lambda_\circ \int_{V_Q} [B_k]^t [A_k]^t \left[\overline{\boldsymbol{Q}}\right]_\circ [A_k][B_k] dV_\circ \\
&\left\{k^e_{q\phi}\right\} = \lambda_p \int_{V_p} [B_k]^t [A_k]^t [\overline{\boldsymbol{e}}][A_e] dV_p \\
&k^e_{\phi\phi} = \lambda_p \int_{V_p} \{A_e\}^t [\overline{\varepsilon^s}]\{A_e\} dV_p
\end{aligned} \tag{24}$$

For calculating the finite element matrices in Eq. (24), numerical integration over the element volume is carried out. For a bimorph piezoelectric harvester with the thicknesses shown in Fig. 4, the volumes of different zones can be expressed as follow:

$$\begin{aligned}
(d\mathcal{V}_p)_{lower} &= \int_{\frac{-h_s}{2}-h_c-h_p}^{\frac{-h_s}{2}-h_c} dz \int_{A_p} dxdy \\
(d\mathcal{V}_c)_{lower} &= \int_{-h_s/2-h_c}^{-h_s/2} dz \int_{A_c} dxdy \\
d\mathcal{V}_s &= \int_{-h_s/2}^{+h_s/2} dz \int_{A_S} dxdy \\
(d\mathcal{V}_c)_{upper} &= \int_{h_s/2}^{h_s/2+h_c} dz \int_{A_c} dxdy \\
(d\mathcal{V}_p)_{upper} &= \int_{h_s/2+h_c}^{h_s/2+h_c+h_p} dz \int_{A_p} dxdy
\end{aligned} \tag{25}$$

As it can be seen from Eq. (24), for calculating the finite element matrices, integration over the element volume is needed. The analytical integration for these expressions is time consuming. Hence, an alternative approach using the Gauss quadrature integration is proposed here. However, there are two issues to be addressed. The Gauss quadrature is valid for square domains from $-1$ to +1, while, as Fig. 6 the quadrilateral elements are not essentially squares in range of $-1$ to +1. To overcome these issues, the quadrilateral element is divided into three subdomains and a transformation is introduced to map the

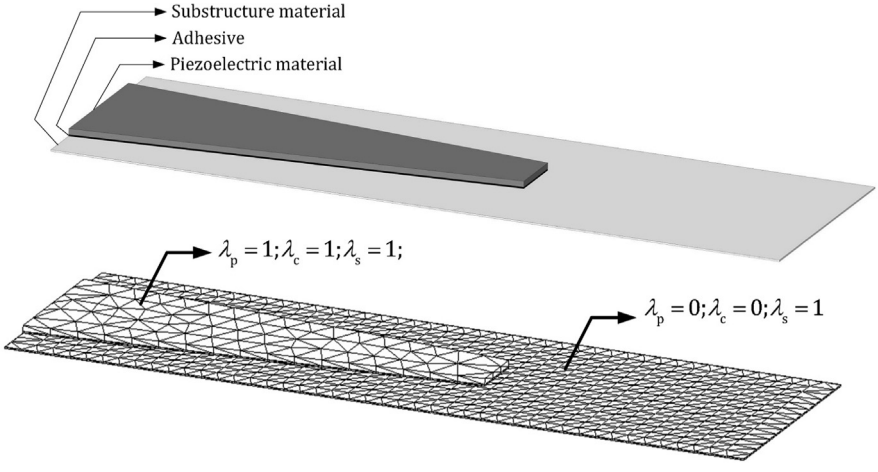


**Fig. 5.** An example of non-uniform harvester beam with fractioned piezoelectric layer.

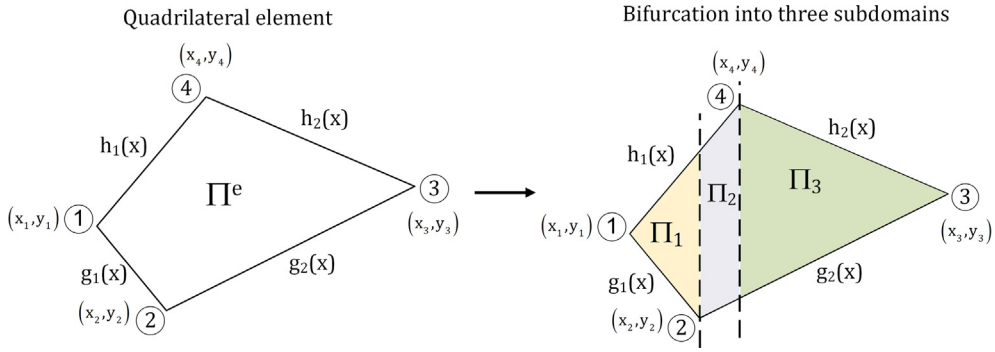


**Fig. 6.** Bifurcation of quadrilateral element $\Pi^e$ into three subdomains $\Pi^1$, $\Pi^2$ and.$\Pi^3$

physical domain into a square [−1, +1] domain. Fig. 6 shows the bifurcation of a quadrilateral element into two triangle and one trapezoid subdomains. For instance, if $\not(x,y,z)$ is the integrant function over the quadrilateral element volume, the integration can be divided into three integrals as shown in Eq. (26)

$$II = \int_{\prod^e} \not(x,y,z)d\mathcal{V} = \int_{\prod_1} \not(x,y,z)d\mathcal{V} + \int_{\prod_2} \not(x,y,z)d\mathcal{V} + \int_{\prod_3} \not(x,y,z)d\mathcal{V} = I_1 + I_2 + I_3 \tag{26}$$

In Eq. (24), each of $I_1$, $I_2$ and $I_3$ can be numerically calculated by applying the Gaussian quadrature rule thrice. More information about details of performing this numerical integration can be found in Appendix B.

### 2.5. Forming general finite element matrices

The general matrices for the harvester can be derived by assembling the element matrices and scalars in Eq. (24). In the assembling element matrices, one should carefully consider the order of degrees of freedom in element matrix so that the general matrices are formed in the correct form. For making the numerical integration in the element matrices about x, y, and z attainable in reasonably fast executing time, by using an initiative order of the element degrees of freedom, the numerical integrations were separated to z and x and y domains, as seen in Eq. (19). This initiative order of degrees of freedom is different from what introduced in Eq. (12). Hence, it is necessary to rearrange the degrees of freedom in the element for assembling into the general matrices.

Some mechanical and electrical considerations should be made in this vibrating system prior to the matrix assembling. The first concern is about the damping mechanisms in the piezoelectric harvester. In a study by De Marqui Junior et al. [21], a proportional viscous damping was considered for harvester energy dissipation mechanisms. However, it was shown by Cooley et al. [23] and Khazaee et al. [30] that depending on types of the damping mechanisms, e.g. viscous or structural, the output power from the piezoelectric cantilever harvester is different. To accommodate both of the damping mechanisms in our model, a proportional damping for viscous and structural mechanisms is considered and denoted as $[C]$ and $[H]$, respectively. Secondly, piezoelectric harvesters commonly include a uniform electrode, which covered the piezoelectric layer. Therefore, the voltage, denoted as $V_p$ for piezoelectric layer, is identical in the all elements. Lastly, in order to link the charged extracted from the piezoelectric layer to the piezoelectric voltage, a time derivative of electric equation in Eq. (24) is performed. Since the total charge on the piezoelectric layer is denoted as $Q$ and the connected load resistance is $R$, then $\dot{Q} = V_p/\mathrm{R}$. Hence, the general form of the finite element model can be expressed with Eq. (27).

$$[M]\{\ddot{\chi}\} + [C]\{\dot{\chi}\} + ([K_{qq}] + j[H])\{\chi\} - \left[K_{q\phi}\right]V_p = \{\boldsymbol{f}_E\}\left[K_{q\phi}\right]^t\{\dot{\chi}\} + V_p/\mathrm{R} + K_{\phi\phi}\dot{V}_p = 0 \tag{27}$$

where $\left[K_{q\phi}\right] = [K_{q\phi}]\{diag(I_{N_e})\}$ ($I_{N_e}$ is the $N_e \times N_e$ identity matrix), where $N_e$ is total number of the elements. It is worth mentioning that now $\{\boldsymbol{f}_E\}$ is now the external mechanical load vector for the hole domain. Since the piezoelectric layers is covert with a conductive layer, $K_{\phi\phi} = \left(\sum_{i=1}^{N_e} k^e_{\phi\phi}\right)$.

This FEM can easily accommodate the added mass by updating the global mass matrix at the degrees of freedom associated with the added mass node. Mass ($M_t$) and moments of inertia of the added mass ($I_{xx}$, $I_{yy}$) are added to the mass matrix elements. This operation can be repeated if more than one added tip mass is present. Note that, stiffness matrix is remained unchanged if the added mass is solid enough compared to the energy harvester. If the added mass is located at the $i$-th node, then the following matrix at the mentioned DoFs is added to the global mass matrix.

$$\begin{array}{c} \overbrace{\phantom{xxxxxx}}^{DoFs} \\ \begin{matrix} 6i-5 \\ 6i-4 \\ 6i-3 \\ 6i-2 \\ 6i-1 \\ 6i \end{matrix} \end{array} \begin{bmatrix} M_t & 0 & 0 & 0 & 0 & 0 \\ 0 & 0 & 0 & 0 & 0 & 0 \\ 0 & 0 & 0 & 0 & 0 & 0 \\ 0 & 0 & 0 & 0 & 0 & 0 \\ 0 & 0 & 0 & 0 & I_{xx} & 0 \\ 0 & 0 & 0 & 0 & 0 & I_{yy} \end{bmatrix} \tag{28}$$

It is shown that, different mechanism will lead to considerably different output power [23]. Therefore, in this study, the energy dissipation is broken into the structural and viscous damping mechanisms. The structural and viscous damping energies are modeled as proportional damping with $[H] = \Gamma[K_{qq}]$ and $[C] = \beta_1[M] + \beta_2[K_{qq}]$, respectively. The relationships between these constants and the viscous damping ratios and a constant structural damping ratio can be defined with [31]:

$$\zeta_n = \frac{\beta_1}{2\omega_n} + \frac{\beta_2\omega_n}{2}, \eta_n = \gamma \tag{29}$$

Eq. (29) relates the Rayleigh damping coefficients to the modal damping ratios. Nonetheless, in many applications, it is desirable to extract the Rayleigh coefficients from the experimentally obtained damping ratios. To do so, by substituting damping ratios $\zeta_1$ at $f_1$ and $\zeta_2$ at $f_2$ in Eq. (29), after some basic calculations the Rayleigh coefficients can be shown to be obtained with Eq. (30).

$$\beta_1 = 4\pi f_1 f_2 \frac{\zeta_1 f_2 - \zeta_2 f_1}{f_2^2 - f_1^2}, \beta_2 = \frac{1}{\pi}\frac{\zeta_2 f_2 - \zeta_1 f_1}{f_2^2 - f_1^2} \tag{30}$$

In Eq. (27), the output voltage from all the elements reduces to only one output voltage because of the common electrical electrode on the piezoelectric layers. However, a modification on the electromechanical coupling factors and on the electric stiffness should be performed when there are two piezoelectric layers. The piezoelectric layers can be connected in parallel for larger current or in series for higher voltage. In the case of parallel connection, effective electric capacitance is equal to the summation of that for both piezoelectric layers ($K_{\phi\phi_{eff}} = K_{\phi\phi_{lower}} + K_{\phi\phi_{upper}}$) and, similarly, $[K_{q\phi}]_{eff} = [K_{q\phi}]_{lower} + [K_{q\phi}]_{upper}$. On the other hand, for the series connection, the effective capacitance is half of one layer and the electromechanical coupling matrix equals to that of one piezoelectric layer, e.g. $K_{\phi\phi_{eff}} = K_{\phi\phi_{lower}}/2$ and $[K_{q\phi}]_{eff} = [K_{q\phi}]_{lower}$ [21].

### 2.6. Steady state solution

In order to estimate the output power from the piezoelectric harvester, the electro-mechanically coupled finite element equations are solved for the output voltage and accordingly power.

A harmonic motion is considered as base excitation $\{F_E\} = \left\{\widehat{F}_E\right\}e^{j\omega t}$. Therefore, the displacement field and output voltage in steady state can be shown as harmonic functions showing with $\{\chi\} = \{\widehat{\chi}\}e^{j\omega t}$ and $V_p = \widehat{V}_p e^{j\omega t}$, where $\{\widehat{\chi}\}$ and $\widehat{V}_p$ are complex values representing the magnitude of the mechanical displacement and electrical voltage, respectively, and the over hat demonstrates the magnitude of the parameter in the steady state condition under the harmonic excitation at driving frequency of $\omega$. Substituting these expressions into Eq. (27) relates the mechanical and the voltage response with respect to the input force, as expressed in Eq. (31).

$$\left(-\omega^2[M] + j\omega(\beta_1[M] + \beta_2[K_{qq}]) + (1 + j\gamma)[K_{qq}]\right)\{\widehat{\chi}\} - \left[K_{q\phi}\right]\widehat{V}_p = \left\{\widehat{F}_e\right\}j\omega\left[K_{q\phi}\right]^t\{\widehat{\chi}\} + (1/R + j\omega K_{\phi\phi})\widehat{V}_p = 0 \tag{31}$$

After some basic mathematical simplifications in Eq. (31), the relationships between the mechanical force to the displacement and electrical voltage can be shown as:

$$\{\widehat{\chi}\} = [\mathcal{H}(\omega)]\left\{\widehat{F}_e\right\}\widehat{V}_p = j\omega(1/R + j\omega K_{\phi\phi})^{-1}\left[K_{q\phi}\right]^t[\mathcal{H}(\omega)]\left\{\widehat{F}_e\right\} \tag{32}$$

The electromechanically coupled frequency response function between the displacement and mechanical force vectors from Eq. (31) is defined as:

$$[\mathcal{H}(\omega)] = \left((-\omega^2 + j\omega\beta_1)[M] + (1 + j(\gamma + \omega\beta_2))[K_{qq}] + j\omega(1/R + j\omega K_{\phi\phi})^{-1}\left[K_{q\phi}\right]\left[K_{q\phi}\right]^t\right)^{-1} \tag{33}$$

In Eq. (29), $\left\{\widehat{F}_e\right\}$ can be replaced with a single load acting at one node in the finite element mesh according to the input acceleration and the effective mass of the energy harvester as $\left\{\widehat{F}_e\right\} = m_{eff}\ddot{a}_B\{\mathcal{T}\}$, where $\{\mathcal{T}\}$ is the vector representing degree of freedom at which the acceleration is applied. $m_{eff}$ is the effective mass of the beam mass and the proof mass (if is present).

The $m_{eff}$ can be calculated with the beam mass, proof mass and a correlation factor of $\mu_1$ [32,33]. It is worth mentioning that $\{\mathcal{T}\}$ has only non-zero element equal to 1 at the degree of freedom at which the input acceleration are exerting. By this definition, the generated instantaneous power can be calculated as:

$$\frac{P(t)}{(\ddot{a}_B)^2}=\frac{m_{eff}^2}{R}\left(\frac{j\omega\left(1/R+j\omega K_{\phi\phi}\right)^{-1}\left[K_{q\phi}\right]^t}{\left((-\omega^2+j\omega\beta_1)[M]+(1+j(\gamma+\omega\beta_2))\left[K_{qq}\right]+j\omega\left(1/R+j\omega K_{\phi\phi}\right)^{-1}\left[K_{q\phi}\right]\left[K_{q\phi}\right]^t\right)}\{\mathcal{T}\}\right)^2 e^{j\omega t} \tag{34}$$

Once the solution for all the mechanical degrees of freedom is derived from Eq. (32), one can extract the stress tensors and electrical displacements for the discretized domain. To do so, with knowing $\{\widehat{\chi}\}$ at the driving frequency, $\omega$, from Eq. (32), the degrees of freedom, e.g. $\{\widehat{\chi}^e\}$, can be extracted for each element. Then, at any point in the domain, the mechanical displacements and strain tensors are obtained using Eqs. (35) and (36), respectively.

$$\widehat{\boldsymbol{r}}(x,y,z)=\left\{\widehat{r}_x\widehat{r}_y\widehat{r}_z\right\}^t=[A_m(z)][B_m(x,y)]\left\{\widehat{\chi}^e\right\} \tag{35}$$

$$\widehat{\boldsymbol{S}}(x,y,z)=\left\{\widehat{\varepsilon}_{xx}\widehat{\varepsilon}_{yy}\widehat{\gamma}_{yz}\widehat{\gamma}_{xz}\widehat{\gamma}_{xy}\right\}^t=[A_k(z)][B_k(x,y)]\left\{\widehat{\chi}^e\right\} \tag{36}$$

Finally, from the generated voltage generation and mechanical strain tensors, the electrical displacements and stress tensors are evaluated from the constitutive equations:

$$\begin{aligned}\widehat{\boldsymbol{D}}=\left\{\widehat{D}_x\widehat{D}_y\widehat{D}_z\right\}^t&=[\overline{\boldsymbol{e}}]^t\widehat{\boldsymbol{S}}(x,y,z)+[\overline{\varepsilon}^s]\{00-1/h_p\}\widehat{V}_p\widehat{\boldsymbol{T}}_p=\left[\overline{\boldsymbol{Q}}\right]_p\widehat{\boldsymbol{S}}(x,y,z)-[\overline{\boldsymbol{e}}]\{00-1/h_p\}\widehat{V}_p,\widehat{\boldsymbol{T}}_s\\&=\left[\overline{\boldsymbol{Q}}\right]_s\widehat{\boldsymbol{S}}(x,y,z),\widehat{\boldsymbol{T}}_c=[\boldsymbol{Q}]_c\widehat{\boldsymbol{S}}(x,y,z)\end{aligned} \tag{37}$$

If the piezoelectric sheet thickness is not constant, in Eq. (37), $h_p$ is the thickness of the piezoelectric layer at the node where the parameters are calculated.

## 3. Validation and comparison with state-of-art model and experimental data

This section deals with validation of the present finite element (FE) model and the computational procedure versus the analytical and experimental results. In the first example, the resonant frequencies of the bimorph, without added tip mass and in open-circuit and short-circuit conditions, are compared with the state-of-the-art analytical results. In the second example, for a bimorph with added tip mass, the fundamental natural frequency, the generated voltage, and the beam-tip velocity are compared with the experimental results. In addition, the FE results are compared with the analytical beam distributed model, and evaluation discussions are made between the present FE and distributed beam models.

### 3.1. Validation versus analytical results from a bimorph without tip mass

In this subsection, the results of studies from the Erturk and Inman [25] (Chapter 3) and Akbar and Curiel-Sosa [11] studies are compared with the results of the developed finite element model in this study. The analytical results by Erturk and Inman's [25] example has been used as a benchmark for validating models for bimorph piezoelectric harvesters under base excitation. For instance, Akbar and Curiel-Sosa [11] used this example for validating their analytical model and FEM results for both structural responses and energy harvesting evaluation. Here, first, the structural response is evaluated. Secondly, the short-circuit and open-circuit resonant frequencies, $f_r^{sc}$ and $f_r^{oc}$, respectively, are compared with [25].

The benchmark is a bimorph piezoelectric energy harvester without added tip mass subjected to the base excitation without consideration of the contact layer. The example includes isotropic model for the substrate and orthotropic model for the piezoelectric layer. The piezoelectric layer is made from PZT-5A with the given material properties in Table 1. Table 2 shows the dimensions and material properties in the validation example.

Table 3 shows the comparison between the undamped natural frequencies. The results show that, all the bending natural frequencies are in a good agreement with<3.5% error. Nevertheless, for higher bending modes, the error between the beam analytical model and this high-order shear deformation FEM model increases. This implies that, the shear stresses, that have

**Table 1**
Material properties for piezoceramic PZT-5A.

| | | | |
|---|---|---|---|
| Density (kg/m$^3$) | 7800 | | |
| $Q_{11}^E, Q_{22}^E$(GPa) | 66.0 | $Q_{12}^E, Q_{21}^E$ (GPa) | 20.46 |
| $Q_{44}^E, Q_{55}^E, Q_{66}^E$ (GPa) | 22.8 | $e_{12}, e_{32}$(C/m$^2$) | −15.9 |
| $e_{33}$(C/m$^2$) | 15.9 | Permittivity (F/m) | $1.593\times10^{-8}$ |

**Table 2**
The properties of the bimorph piezoelectric harvester [25].

| Description | Piezoelectric sheet | Aluminum substrate |
|---|---|---|
| Length (mm) | $L = 30$ | |
| Width (mm) | $b = 5$ | |
| Thickness (mm) | $h_p = 0.15$(each layer) | $h_s = 0.05$ |
| Density (kg/m$^3$) | See Table 1 | $\mu_s = 2700$ |
| Elastic modulus (GPa) | | $(E_1)_s = 62.3$ |
| Poisson's ration | | 0.33 |

**Table 3**
Comparison between undamped natural frequencies for the configuration in Table 2.

| Vibration mode | Natural frequency (Hz) | | | |
|---|---|---|---|---|
| | Erturk-Inman [25] | Akbar-Curiel-Sosa [11] | | Present FE |
| | | Beam analytical | Finite element | TSDT approx. |
| 1st bending | 185.1 | 185.1 | 187 | 185.9 |
| 2nd bending | 1159.8 | 1160.1 | 1162.3 | 1174.4 |
| 3rd bending | 3247.6 | 3248.3 | 3238.5 | 3356.4 |

not been considered in both of the studies by Erturk and Inman [25] and Akbar and Curiel-Sosa [11], become more significant for higher bending modes. Even though the first mode natural frequency, obtained from the FE model, is almost identical with that of the beam model, the second and third natural frequencies are higher than the analytical model. Therefore, the results show that, considering the shear stresses makes the beam stiffer.

Due to the electromechanically coupled effects of the piezoelectric materials, the resonant frequency in the tip displacement and power frequency functions slightly depends on the electrical load connected to the piezoelectric harvester. In particular, two special cases are of interest for reporting the results, namely, open-circuit and short-circuit frequencies, as their proportion is a function of the piezoelectric constants [32]. Table 4 shows the comparison between the open-circuit and short-circuit frequencies from the present FEM model and the results from [25]. As expected from [32], the open-circuit resonant frequency is higher than the short-circuit frequency in both of the methods. As can be seen from the fraction of $\frac{f_r^{oc}}{f_r^{sc}}$, results of the both methods are in a good agreement for modeling the effect of the electrical load on resonant frequency.

### 3.2. Validation versus experimental data of a bimorph with tip mass

For a bimorph energy harvester with proof mass, the results from the presented FEM are compared with experimental results in other studies. The experimental results are derived from a study by Erturk and Inman [13], where they conducted experimental tests on a bimorph harvester with PZT-5A piezoceramic and a 0.012-kg proof mass under the harmonic base excitation. Geometric properties are exactly copied from Erturk and Inman [13] as shown in Table 5.

Table 6 shows the fundamental frequencies without and with proof mass. The 0.012-kg proof mass, which is equal to 140% of the harvester beam mass, causes a 62% reduction in the fundamental frequency, namely from 119.8 Hz to 45.7 Hz. In addition, Table 6 compares fundamental frequency in short-circuit condition for the bimorph harvester. Results of current FEM are in good agreement with the experimental data with an error 0.2%.

Table 7 shows the comparison of natural frequencies obtained from different FE models in this case study. The FE results are presented in two sub-categories, namely classic and Carrera's unified formulation (CUF). In the classical methods, three plate theories (CLPT, FSDT, and TSDT) are analyzed while for the CUF approach only the TSDT is analyzed. As can be seen, the classic CLPT results are less accurate compared to the other models especially in torsional modes and higher bending modes, where the difference between them becomes considerable. There is a good agreement between the results from the FSDT and

**Table 4**
Comparison between short-circuit and open-circuit frequencies for configuration in Table 2.

| Mode | 1st bending (Hz) | | 2nd bending (Hz) | | 3rd bending (Hz) | |
|---|---|---|---|---|---|---|
| Method | $f_r^{sc}$ | $f_r^{oc}$ | $f_r^{sc}$ | $f_r^{oc}$ | $f_r^{sc}$ | $f_r^{oc}$ |
| Erturk-Inman [25] | 185.1 | 191.1 | 1159.7 | 1171.6 | 3245.3 | 3254.1 |
| Present finite element- TSDT approx. | 185.7 | 191.3 | 1174.4 | 1186.4 | 3356.4 | 3368.0 |
| $\frac{f_r^{oc}}{f_r^{sc}} \cong$ | 1.03 | | 1.01 | | 1.004 | |

**Table 5**
Geometric properties of bimorph with added mass.

| | | | |
|---|---|---|---|
| Length of the beam (mm) | 50.8 | Width of the beam (mm) | 31.8 |
| PZT thickness- each layer (mm) | 0.26 | Tip mass, (kg) | 0.012 |
| Substrate density (kg/m$^3$) | 9000 | Young's modulus (GPa) | 105 |
| Substrate thickness (mm) | 0.14 | | |

**Table 6**
Fundamental frequency comparison for the bimorph with added tip mass given in Table 5.

| | no proof mass | with proof mass | |
|---|---|---|---|
| | Present FE | Present FEM | Experiment [13] |
| Fundamental frequency (Hz) | 119.8 | 45.69 | 45.6 |

**Table 7**
Comparison of natural frequencies between various FE approaches for the bimorph with added tip mass given in Table 5.

| Mode number and type | Classical methods | | | CUF |
|---|---|---|---|---|
| | CLPT | FSDT | TSDT | TSDT |
| 1st bending (Hz) | 45.00778 | 45.70266 | 45.68668 | 45.68741 |
| 1st torsion (Hz) | 318.84079 | 424.20583 | 423.59242 | 423.98667 |
| 2nd bending (Hz) | 500.12100 | 521.55566 | 521.23325 | 521.48227 |
| 2nd torsion (Hz) | 1138.69341 | 1458.35721 | 1454.94244 | 1457.17431 |
| 3rd bending (Hz) | 1286.33597 | 1486.86323 | 1483.32038 | 1484.45300 |
| 4th bending (Hz) | 2183.62439 | 2335.92377 | 2332.04895 | 2333.48623 |
| 3rd torsion (Hz) | 2444.33313 | 3052.32948 | 3041.00076 | 3047.85320 |
| 5th bending (Hz) | 2490.30352 | 3211.72280 | 3190.17430 | 3194.82131 |

TSDT classical models for all the bending and torsional modes. Moreover, there is remarkable consistency between the natural frequencies obtained from the CUF and classic models in this example.

Fig. 7 compares the output voltage and the beam-tip velocity as a function of the excitation frequency for three different resistive loads, namely 1 kΩ, 6.7 kΩ, and 100 kΩ. These values are normalized to the unit base acceleration of $g$, as reported by [13]. As can be seen from Fig. 7 (a), the voltage estimated from the present FEM is in a good agreement with the experiments at all the resistive loads. In compliance with the experimental data, the shift in the frequency of the voltage peak for higher resistive loads can be also observed in the FEM. The present FEM also estimated the beam-tip velocity with reasonably good accuracy. The FEM has better resonance simulation of the beam-tip compared to the FEM by Akbar and Curiel-Sosa [11]. In their FEM [11], the accuracy of the resonant tip-displacement from the FEM was not satisfactory. Nonetheless, the disparity between the simulated and experimental data in the tip velocity, Fig. 7 (b), are greater compared to the values for the voltage generation. In the study by Erturk and Inman [13], the experimental and simulated correlation of the tip-velocity was also weaker than that of for the voltage data. One reason for this difference can be due to experimental errors. Based on the comparison results, the consistency between the FEM and experimental results are better for smaller resistive loads (<100 kΩ). This can be due to the nonlinear piezoelectric properties, which can be more significant at higher voltages. Priya et al. [34] previously reported the electromechanical nonlinearities for PZTs.

As a comparison of the power generation, the power output over a wide range of resistive loads from the present FEM (classic and CUF models with TSDT approximations) are compared with the analytical beam distributed model by Erturk and Inman [13], as shown in Fig. 8. The power generation is due to the resonant harmonic excitation. The FE classic and CUF models results are the same for this example. The overall behavior of the output power are identical between the FE

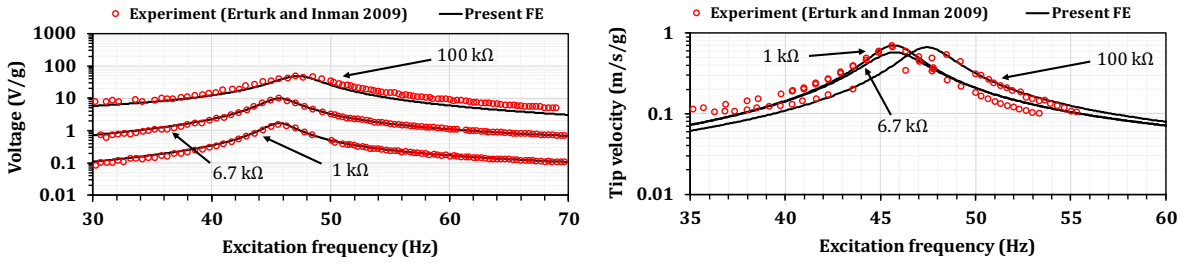


**Fig. 7.** Comparison of (a) output voltage and (b) tip velocity between experimental data and the present FEM.

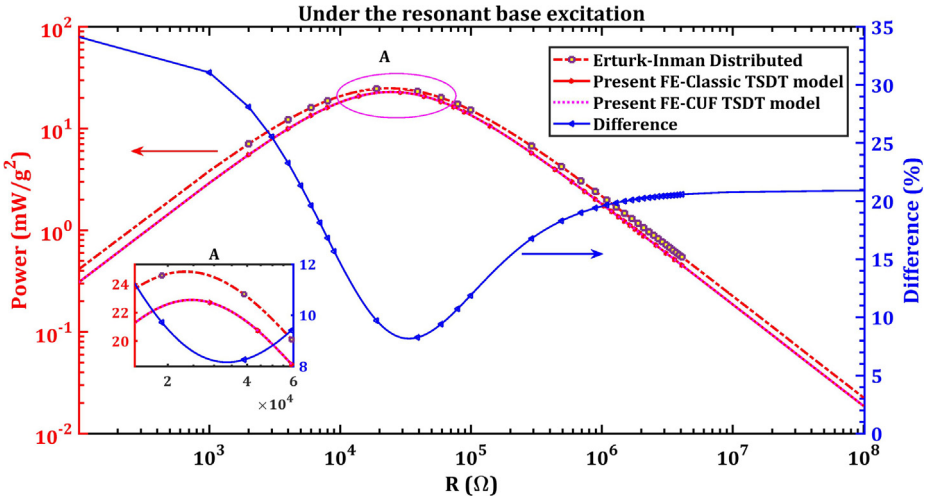


**Fig. 8.** Out power comparison between the present FEMs (Classic and CUF methods based on TSDT approximation) and the Erturk and Inman distributed model [13] versus resistive load.

and beam models. Both models point to an optimum electrical load associated with the maximum power output, but this optimum value is slightly different in the results based on these models. The optimum load from the present FEM is 25 kΩ while it 23 kΩ for the distributed model. The power output around the optimum load has more consistency between the models compared to the small or great resistive loads. As shown in the zoomed-in view in Fig. 8, the minimum difference is 8%, and it occurs around the optimum resistive load. The difference of the output power between the models becomes significantly greater in small loads (<100 Ω) and great loads (>100 MΩ) with the respective differences of 34% and 21%, respectively. This indicates that, the beam-distributed model cannot accurately model the electromechanical coupling in all range of electric loads.

As a further comparison, the voltage outputs with load of R = 25 kΩ are shown in Fig. 9 over a range of frequency ratios. The frequency ratio is the excitation frequency divided by the natural frequency of the beam, e.g. $\Omega = \omega/\omega_n$, where $\omega_n$ is the harvester natural frequency. With this definition, $\Omega = 1$ means that the energy harvester is subjected to a harmonic load with the driving frequency equal to the beam natural frequency. It can be seen that, the voltage outputs obtained from the models are in a good agreement around $\Omega = 1$. On the other hand, for the off-resonance excitations, the beam-distributed model overestimates the voltage generation.

## 4. Application of the present method for non-uniform variable thickness piezoelectric beam

In this section, a numerical case study is presented to show ability of the presented model for estimation of the output power in a bimorph piezoelectric harvester beam that previous method cannot be employed on this configuration. The piezoelectric beam in this numeric example is a non-uniform bimorph piezoelectric beam with non-constant thickness of the piezoelectric sheets. A composite substrate shim with rotated fibers is assumed to join the two piezoelectric sheets. Moreover, the energy harvester includes a contact layer between the substrate shim and the piezoelectric sheets. First, the role of optimum load on the output power is investigated in subsection 0 and the effect of the external input acceleration

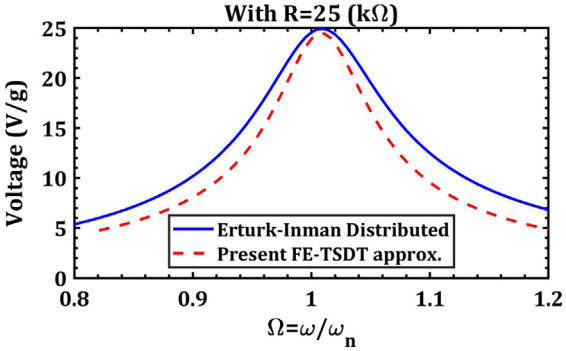


**Fig. 9.** Comparison of the output voltage obtained from the present FEM and the Erturk and Inman distributed model [13] versus frequency ratio.

on the optimum load is shown. In addition, the power generation with optimum load resistance over five bending modes is calculated by considering the support loss, fluid-structure and the structural damping mechanisms. Deformations in different driving frequencies for the harvester are reported in Section 4.3. Finally, Section 4.4 reports effects of the thickness variation of the piezoelectric sheet and the fiber rotation in the substrate layer on the output electrical power by a parametric study.

### 4.1. Harvester description and characterization

Fig. 10 shows the bimorph energy harvester with non-uniform piezoelectric sheets. Unlike the previous studies, which used metal substrates, the substrate layer in this study is an E-Glass composite material. This type of material provides an opportunity to change the natural frequency of the beam and the tip displacement by rotating the fiber direction in the substrate shim. The substrate layer is considered to have the E-Glass fiber with epoxy matrix and a volume fraction of 60%. Fiber direction is $\theta = 10^{\circ}$ for all cases except those that are mentioned separately. In addition, the thickness of the piezoelectric sheet is not constant along the length and increases with a slight slope. Table 8 shows geometrical dimensions and material properties of the piezoelectric beam in Fig. 10. Lines L1 to L3 are lines in the middle of the beam width at different $x$ through the thickness from the top layer to the bottom layer. These lines demonstrate the displacements through the thickness.

For modeling the damping mechanisms in this energy harvester with clamp-free boundary condition, two types of mechanisms are assumed. First, the fluid-structure damping mechanism, which is frequency dependent, is modeled with the viscous FEM damping matrix $[C]$. Secondly, the structural and support loss mechanisms, that are frequency independent, are modelled with the structural FEM matrix $[H]$. By using the damping ratios from previous study of the authors [35], and Eqs. (29) and (30), the coefficients of the damping matrices are calculated as $\beta_1 = 0.42$, $\beta_2 = 6.48 \times 10^{-7}$ and $\Gamma = 0.0475$.

Two mesh densities, one with course elements and one with finer elements, are considered in this study, as shown in Fig. 11. In mesh I, the piezoelectric sheet is divided into two divisions in width-wise, while in mesh II it is divided into four divisions. In both meshes, there are two regions with different materials. The yellow region is the region where the piezoelectric layers and adhesive contacts are present, $(\lambda_p, \lambda_c, \lambda_s) = (1, 1, 1)$, while in the purple region only the substrate material exists, $(\lambda_p, \lambda_c, \lambda_s) = (0, 0, 1)$.

### 4.2. Generated power spectrums

As it can be seen from Fig. 12, there is a considerable different between output power for resonant and off-resonance input excitations for all the electrical loads. For each frequency ratio, an optimum electrical load resistance leads to a maximum power. This load is slightly dependent to the excitation frequency. For instance, $R_{opt}$ is 83.1, 78.6 and 74.6 kΩ for frequency ratios of 0.9, 1 and 1.1, with corresponding output power of 7.1, 7.7 and 96.1 mW/$g^2$, respectively. The optimum load for under-resonant excitations ($\Omega < 1$) is greater that of for the resonant excitation ($\Omega = 1$). In addition, the optimum load for over-resonant excitations is smaller than the resonant excitation. The curves for $\Omega = 0.9$ and 1.1 are almost identical, which is due to symmetry of the structural response around the natural frequency. Nonetheless, this symmetry is deteriorated for excitation cases of $\Omega = 0.8$ and 1.2. The output power with $\Omega = 1.1$ and 1.2 is slightly greater than that for their symmetric frequency ratios, i.e. $\Omega = 0.9$ and $\Omega = 0.8$.

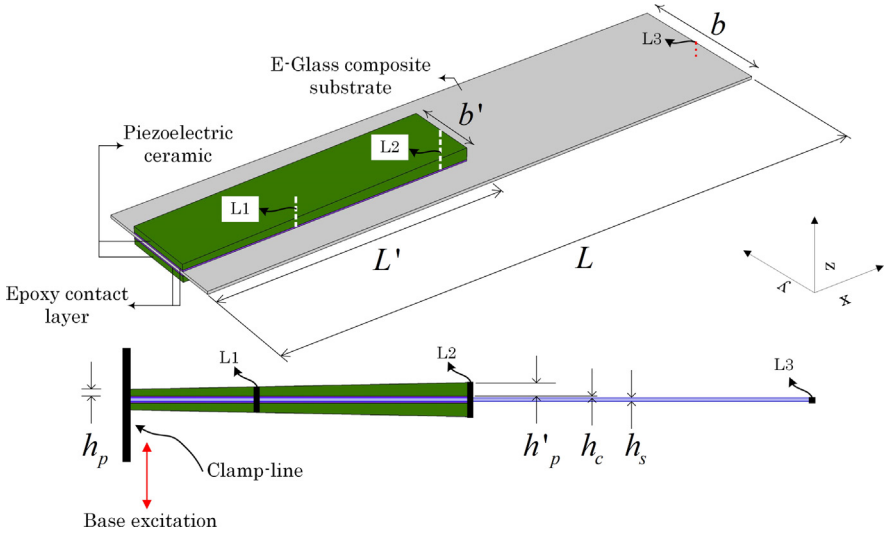


**Fig. 10.** A non-uniform energy harvester with two piezoelectric ceramic sheets attached on E-glass composite substrate with epoxy contact layer.

**Table 8**
Dimensions and material properties for the piezoelectric harvester shown in Fig. 10.

| Description | Piezoelectric (PZT-5A) | Substrate (E-Glass composite) | Contact layer (Epoxy adhesive) |
|---|---|---|---|
| Length (mm) | 100 | 200 | 100 |
| Width (mm) | 25 | 50 | 25 |
| Added tip mass (kg) | 0.01 | | |
| Thickness (mm) | $h_p = 0.3$(each layer)<br>$h'_p = 0.6$ (each layer) | $h_s = 0.2$ | $h_c = 0.02$ |
| Density (kg/m$^3$) | See Table 1 | $\mu_s = 1759$ | $\mu_c = 2750$ |
| Structural constants | | $\theta = 10°$ | $E = 1.05$(GPa) |
| - $Q_{11}$ (GPa) | | 56.4 | $\nu = 0.3$ |
| - $Q_{22}$ (GPa) | | 18.0 | |
| - $Q_{12}$ (GPa) | | 3.6 | |
| - $Q_{44}$ (GPa) | | 9.0 | |
| - $G_{55}$ (GPa) | | 9.0 | |
| - $G_{66}$ (GPa) | | 9.0 | |

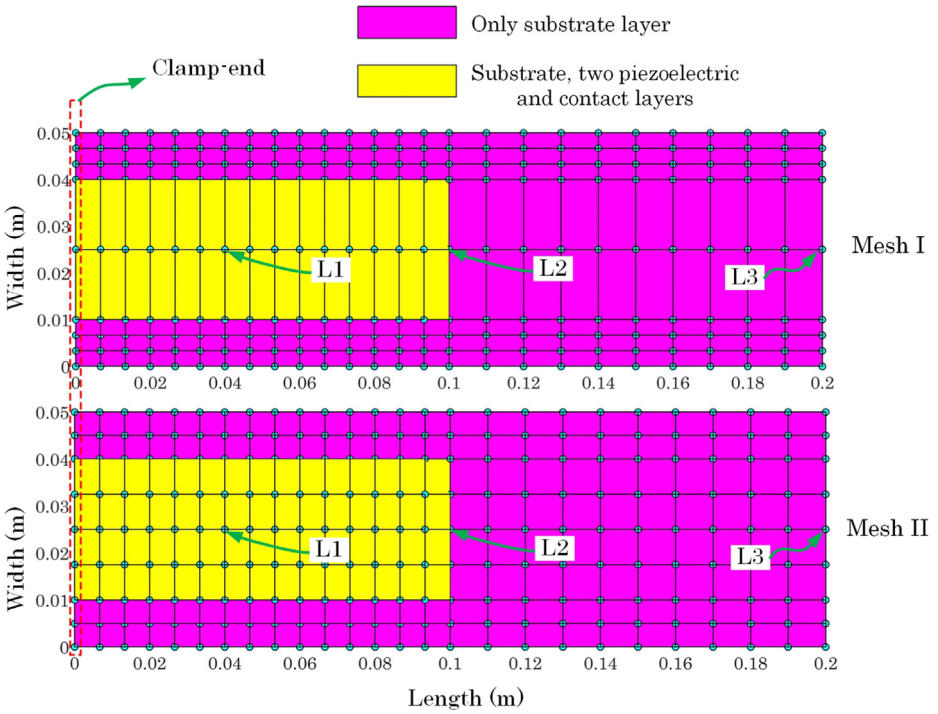


**Fig. 11.** Mesh for the numerical example with material distribution.

If one selects a non-optimum load resistance, for instance $R = 10$ kΩ, the output power at $\Omega = 1$ will be 25.7 mW/g$^2$, which is only 26.8% of the maximum available power. The results shown in Fig. 10 emphasize importance of selection of optimum load resistance to enhance the output power. Since the optimum load resistance becomes different for different frequencies and, on the other hand, the applied electrical load has an effect on the resonant frequency, as presented in Table 4, selecting the precise optimum load resistance is an iterative process that needs more consideration than a simple analysis. Furthermore, as shown by Khazaee et al. [30], amplitude of base excitation affects resonant frequency of the generated power, and therefore will influence optimum electrical load. Nevertheless, in the context of the presented paper, no further action on optimum load is carried out because it is not in the scope.

Output power for electrical loads of 100Ω, 10MΩ and $R_{opt}$ conditions in a range of 0–300 Hz are shown in Fig. 13. In addition, the output power in optimum load connection is calculated from both meshes II and I. The output powers in $R_{opt}$ condition are almost coincide for the both meshes at all frequencies with an intangible error < 2% at the bending peaks. As high-order elements are employed in the present method, results with course elements (mesh I) have also reasonable accuracy. Nonetheless, there is a small difference in the frequency range 50–70 Hz, which is the result of identifying a non-strong mode around 57 Hz that is a mixed bending and torsion mode, as shown in Fig. 14. Since this mode has a negligible effect on the energy harvesting by the piezoelectric beams, the effect of this mode can be ignored. Therefore, mesh I is selected over mesh II because it has less elements and consequently less computation time while it has reasonable accuracy.

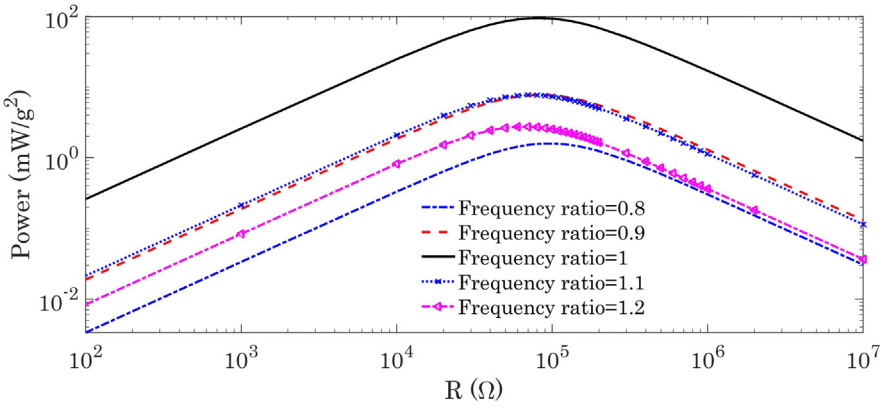


**Fig. 12.** Output power from the piezoelectric beam in Fig. 10 versus electrical load for different frequency ratios (Ω = 0.8, 0.9, 1.0, 1.1 and 1.2).

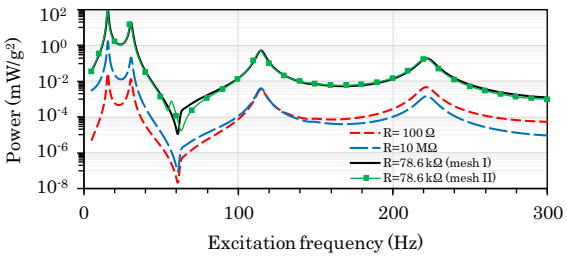


**Fig. 13.** Output power from the piezoelectric beam in Fig. 10 over 0–300 Hz input acceleration frequency for 100Ω, 10$M\Omega$, and $R_{opt}$ load resistance conditions.

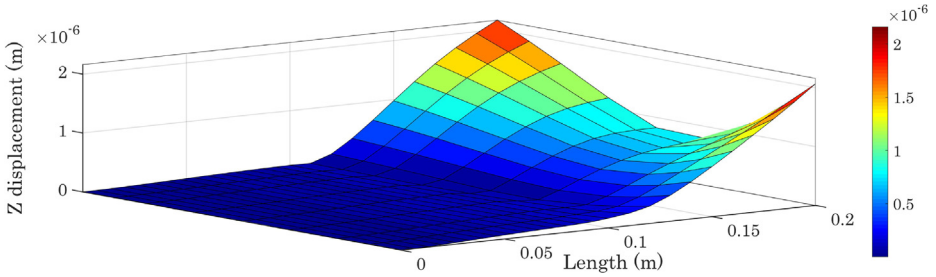


**Fig. 14.** The non-strong mode at 57 (Hz) frequency for mesh II.

There are four bending modes in this frequency range, which power has local maximums at these frequencies. As can be seen, the output power for the optimum load condition is considerably higher in all the resonant frequencies. At the optimum load condition, the resonant frequencies are 15.4, 30.5, 114.5 and 221 Hz. According to Eq. (29), the modal viscous damping coefficient is higher by increasing the frequency and, therefore, the power for higher bending modes become lower than the power for the first bending mode.

### *4.3. Evaluation of displacements*

Fig. 15 shows the displacement in z-direction at frequencies around the first bending mode as well as the second and third bending modes. Because the piezoelectric sheets, with considerable thickness compared to the substrate layer, exist until x = 0.1 m, there is small deflection before x = 0.1 m at the all frequencies. Fig. 15 (a) emphasizes on the fact that, the beam deflection and, therefore, the output power is remarkably higher at the resonant frequency compared to other frequencies even close to the resonance. For instance, if the excitation frequency changes 0.9 Hz from the resonance, the tip beam displacement reduces 25%, reducing the output power significantly. Fig. 15 (b) shows the displacements in z-direction for three bending modes under steady state solution. Since, the displacements in the second and third modes are smaller than the first mode; these two modes are magnified by a factor of five in the figure. The displacement for these

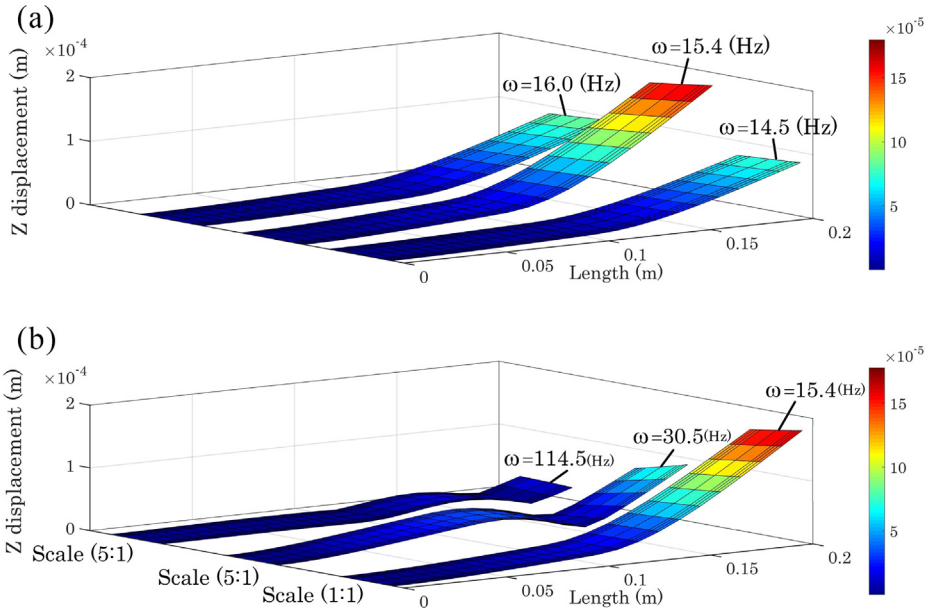


**Fig. 15.** Displacement in z-direction for mid-surface at (a) around first bending mode and (b) first to third bending modes.

three modes matches to the standard mode shapes of the clamp-free beam. Consequently, the results prove that the identified modes are the bending modes.

The curves in Fig. 16 show in-plane displacements, e.g. $r_x$ and $r_y$, at three locations, lines L1 to L3, through thickness for different bending modes. It is worth mentioning that, L1 and L2 are at x = 0.04 m and 0.1 m and the piezoelectric layers are present at these lines, while L3 is at x = 0.2 m where the substrate layer is only present. In addition, the beam thickness at these lines are not the same as can be seen in Fig. 10. Maximum thicknesses at lines L1 to L3 are 5.4E-4, 7.2E-4 and 1E-4 (m), respectively. The positive displacement in *x* direction shows that, the point is in extension while the negative displacement shows compression. When the beam has thin thickness, at L3 for example, in-plane displacements through the thickness are very close to linear. While for lines L1 and L2, where the beam is thicker because of the piezoelectric sheets, the in-plane displacements are cubic polynomials. Moreover, as the beam at L2 is thicker than the beam at L1, the displacement for L2 has larger curvature than the L1. Therefore, if the beam befits thicker, then the non-linear deformation through thickness becomes more important and should be considered in design of piezoelectric system. The in-plane displacement at L3 is overall larger than the other lines (L1 and L2), which is due to the flexibility of the thin substrate layer with a length of 0.2 m. Fig. 16 (b) shows comparison the in-plane displacements at line L2 for three bending modes. As can be seen, the dis-

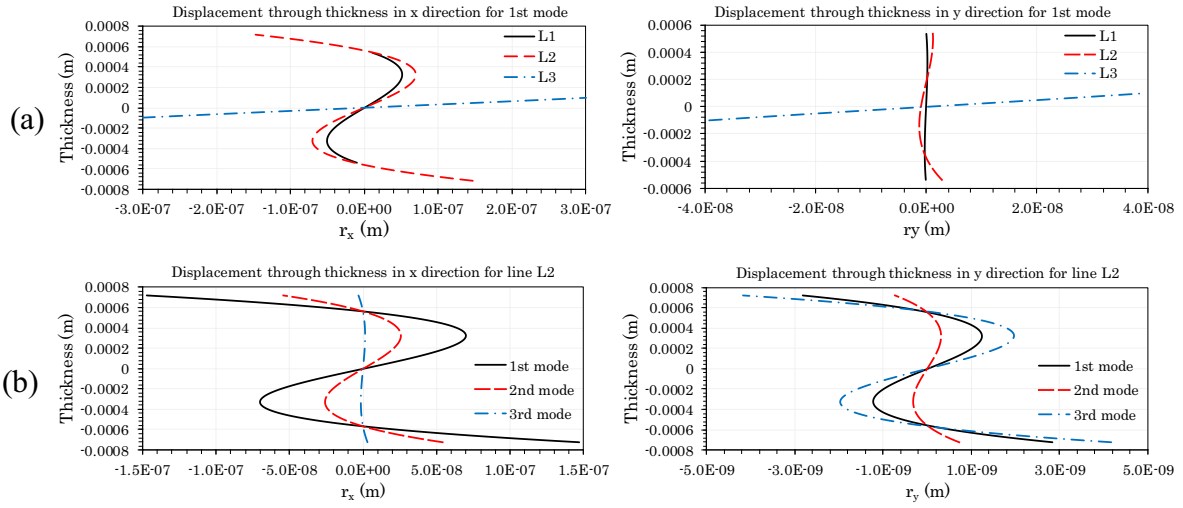


**Fig. 16.** Displacement through thickness in x- and y-directions for different lines and bending modes, (a) for first mode and lines L1 to L3 and (b) Line L2 for three bending modes.

placements in the first mode is larger than the displacement in the second mode, and it is larger in the second mode compared to the third mode. This statement can be also concluded from Fig. 15 (b).

### 4.4. The sensitivity of power to piezoelectric variable thickness and substrate fiber rotation

In order to observe the effect of non-constant thickness in the piezoelectric sheet, the tip displacement and output power are plotted in Fig. 17 in frequency range of 10–20 Hz under $R = 10$ kΩ load resistance and fiber rotation $\theta = 0$. The solid line represents the constant thickness while dashed lines are for non-constant thicknesses. The thickness variation makes a shift in the resonant frequency, which can be in positive or negative direction, depending on the slope of the thickness increment along the length. Furthermore, the output power becomes greater with increment of the slope of the piezoelectric thickness. Increasing the piezoelectric thickness causes an increase in the tip displacement as well as in the power generation. For instance, the power generation by the non-constant thickness of the piezoelectric layer with $h'_p = 2.5h_p$ is 1.74 mW/g$^2$ that is considerably higher than the power generation in the piezoelectric layers (0.76 mW/g$^2$) with a constant thickness. Therefore, the output power enhances by 130% only by increasing volume of the harvesting device by 31% when the tip displacement increases from 4.5 mm to 5.9 mm

By rotating the fiber direction from the physical direction in a composite substrate shim, it is possible to alter the stiffness matrix of the substrate beam without changing its overall geometry. This modification leads to a change in the natural frequency and the beam deflection. Moreover, it changes the stress distribution in the piezoelectric sheets and, therefore, the output power will be different. Fig. 18 shows the tip displacement and output power at four fiber angles, $\theta$= 0°, 10°, 20°, and 40°.As shown, the resonant frequency constantly plunges by increasing the fiber rotation. Nevertheless, the tip displacement and output power increase up to $\theta$ = 20° and then dramatically decreased as $\theta$ increases. This variation indicates that, changing the fiber rotation is a trade-off for maximizing the power. A fiber rotation from $\theta$ = 0° to $\theta$ = 20° causes the power to increase from 1.56 to 1.79 mW/g$^2$, showing 15% increment in the power generation without adding more energy harvesting material.

### 4.5. Practical comments on the PEH design for power optimization

The natural frequency and beam deformation are the most important vibrational parameters in the PEH. According to numerous studies [1,2,32,36] PEHs generate the maximum voltage output when deformed with a driving frequency close

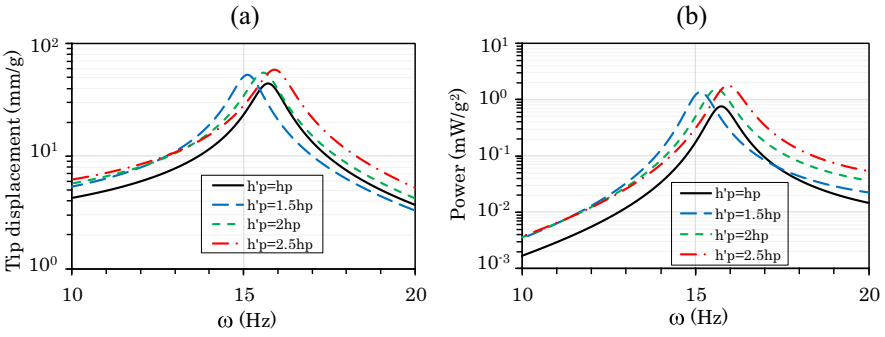


**Fig. 17.** The effect of piezoelectric sheet thickness on (a) tip displacement and (b) output power with $R = 10$ (kΩ) and fiber rotation $\theta = 0$. $h'_p = h_p$ is constant thickness and $h'_p > h_p$ is non-constant thickness.

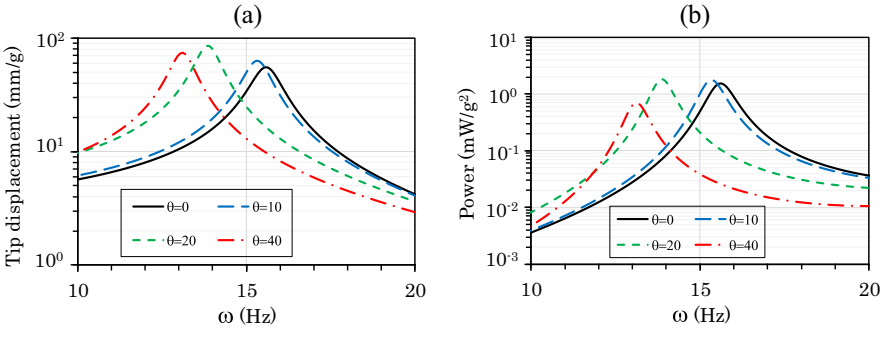


**Fig. 18.** The effect of fiber rotation in substrate composite shim on (a) tip displacement and (b) output power with $R = 10$ (kΩ) and $h'_p = 2h_p$.

to their fundamental frequency. In many practical cases, an added mass can be used to control the fundamental frequency [3,37], enabling the structural deformation to be considerably amplified at the working frequency [38]. Therefore, in practice, the fundamental frequency, matching and enhancing the output power, are important in the design of PEHs. This section gives practical remarks about these two parameters.

The contact-layer thickness is a factor, which can cause variations in the output power and the natural frequencies because it changes stiffness of the PEH, the mass and the damping properties. The damping effect of the contact layer is not in the scope of the current study, where it is assumed unchanged. Neglecting the contact-layer damping effect, the contact layer increases the harvester effective-mass slightly and, therefore, increases the inertial load acting at the harvester base. On the other hand, the beam-tip deflection becomes smaller as the contact-layer adds stiffness to the beam's stiffness. These two consequences have contradictory effect on the output power. Fig. 19 shows variation of the PEH power spectrum for contact-layer thicknesses of 0, 10, 20, 40 and 50 μm. By increasing the bonding-layer thickness, the resonant frequency increases as the beam becomes stiffer. The peak resonant power is reduced by increasing the bonding-layer thickness. This shows that, the bonding-layer thickness overall reduces the beam-tip deflection and the output power.

For the illustration of the power optimization, the output power from the harvester is plotted in Fig. 20 versus $h_p^{'}/h_p$s for different fiber rotation ($\theta$) angles. The output power increases with respect to $\theta$ until $\theta$ =20° and after this point, it sharply reduces. At this optimum $\theta$ point, the substrate modulus of elasticity in $x$-axis becomes minimum and, therefore, the beam-tip displacement becomes maximum allowing the maximum power generation. By increasing $h_p^{'}/h_p$, the output power is increased until a certain point, where it smoothly reduced eventually. The maximum output power is 104.7 mW/g$^2$ and is generated with $\theta$ =20° and $h_p^{'} = 2.75h_p$. This power is more than 50% higher than the power by the PEH in common design, i.e. $\theta$ =0° and $h_p^{'} = h_p$.

The added tip mass reduces the natural frequencies and increases the beam-tip displacement, as shown in Fig. 21. Therefore, if the kinetic energy source is low frequency vibration, the added tip mass can be used for matching to the vibration source frequency. In addition to frequency reduction, the added tip mass increases the output power due to the higher tip displacement.

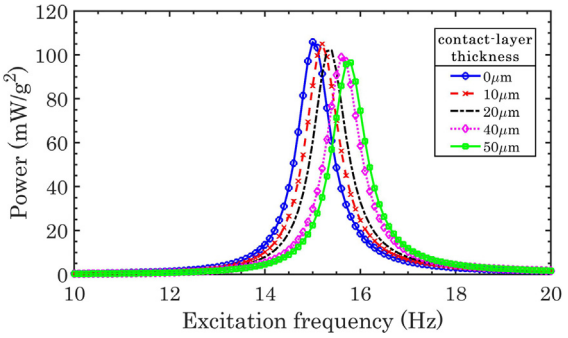


**Fig. 19.** Contact-layer thickness effect on the output power with $R = R_{opt}$ (kΩ) and $h'_p = 2h_p$.

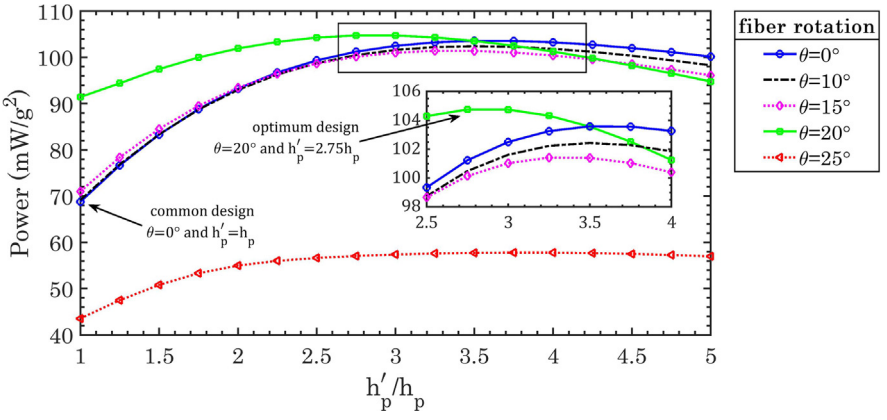


**Fig. 20.** Power analysis with $R = R_{opt}$ as a function of $h'_p/h_p$ and $\theta$.

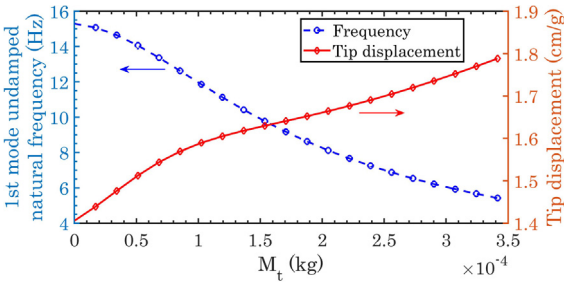


**Fig. 21.** Natural frequency reduction and beam-tip displacement increase with added tip mass.

## 5. Concluding remarks

In this study, a comprehensive finite element formulation is proposed within the framework of piezoelectric energy harvesting for accurate structural and energy harvesting modeling of piezoelectric beams. The present approach is derived from third-shear-deformation theory and considers the Carrera's Unified Formulation for displacement fields. The method also considers the contact layer thickness in the harvester beams, non-uniformity in the piezoelectric sheet, non-constant thickness of the piezoelectric sheet and principal coordinate rotation. The proposed method is evaluated with some state-of-the-art methods in various conditions in structural analysis and energy harvesting parameters. By considering these features, the present method can be used for the design of high performance piezoelectric harvesters in different applications. With presenting the numerical results of a case study, effect of the variation in the piezoelectric sheet thickness and the rotation of principal coordinates in the substrate layer is demonstrated. The results show that increasing the piezoelectric thickness along the beam length enhances the piezoelectric output power. In addition, by changing the fiber direction in the substrate layer, the energy harvester beam becomes less stiff leading to a lower natural frequency and higher output power.

### CRediT authorship contribution statement

**Majid Khazaee:** Conceptualization, Methodology, Writing - original draft, Software, Data curation, Visualization, Software. **Lasse Rosendahl:** Methodology, Supervision. **Alireza Rezania:** Conceptualization, Methodology, Investigation, Validation, Writing - review & editing, Supervision.

### Appendixes A. Transformation

In this study, a rotation between physical coordinates and principal coordinates was considered for orthotropic materials in the piezoelectric harvester. Due to this rotation, the material properties in physical coordinates will be different from the principal coordinates and, therefore, it is necessary to perform a transformation from physical to the principal coordinates.

Eq. (A.1) shows the structural stiffnesses in the physical coordinates for a rotation of $\theta$ for both of the piezoelectric and substrate materials.

$$\begin{aligned}
\overline{Q}_{11} &= Q_{11}\cos^4\theta + 2(Q_{12}+2Q_{66})\sin^2\theta\cos^2\theta + Q_{22}\sin^4\theta\overline{Q}_{12} \\
&= (Q_{11}+Q_{22}-4Q_{66})\sin^2\theta\cos^2\theta + Q_{12}\left(\sin^4\theta+\cos^4\theta\right)\overline{Q}_{22} \\
&= Q_{11}\sin^4\theta + 2(Q_{12}+2Q_{66})\sin^2\theta\cos^2\theta + Q_{22}\cos^4\theta\overline{Q}_{16} \\
&= (Q_{11}-Q_{12}-2Q_{66})\sin\theta\cos^3\theta + \begin{pmatrix} Q_{11}-Q_{12}+ \\ 2Q_{66} \end{pmatrix}\sin^3\theta\cos\theta\overline{Q}_{26} \\
&= (Q_{11}-Q_{12}-2Q_{66})\sin^3\theta\cos\theta + (Q_{11}-Q_{12}+2Q_{66})\sin\theta\cos^3\theta\overline{Q}_{66} \\
&= (Q_{11}+Q_{22}-2Q_{12}-2Q_{66})\sin^2\theta\cos^2\theta + Q_{66}\left(\sin^4\theta+\cos^4\theta\right)\overline{Q}_{44} \\
&= Q_{44}\cos^2\theta + Q_{55}\sin^2\theta\overline{Q}_{45} = (Q_{55}-Q_{44})\cos\theta\sin\theta\overline{Q}_{55} = Q_{55}\cos^2\theta + Q_{44}\sin^2\theta
\end{aligned} \tag{A.1}$$

The electromechanically coupled coefficients of the piezoelectric for a rotation of $\theta$ are shown in Eq. (A.2). In addition, Eq. (A.3) can calculate the permittivity coefficients in the physical coordinates.

**Table B1**
Gaussian points and weights for $N_G = 5$.

| Index | Gaussian point | Weight |
|---|---|---|
| 1 | 5.65222820508010E-03 | 2.10469457918546E-02 |
| 2 | 7.34303717426523E-02 | 1.30705540744447E-01 |
| 3 | 2.84957404462558E-01 | 2.89702301671314E-01 |
| 4 | 6.19482264084778E-01 | 3.50220370120399E-01 |
| 5 | 9.15758083004698E-01 | 2.08324841671986E-01 |

$$\begin{aligned}
\bar{e}_{31} &= e_{31}\cos^2\theta + e_{32}\sin^2\theta \\
\bar{e}_{32} &= e_{31}\sin^2\theta + e_{32}\cos^2\theta \\
\bar{e}_{36} &= (e_{31} - e_{32})\sin\theta\cos\theta \\
\bar{e}_{14} &= (e_{15} - e_{24})\sin\theta\cos\theta \\
\bar{e}_{24} &= e_{24}\cos^2\theta + e_{15}\sin^2\theta \\
\bar{e}_{15} &= e_{15}\cos^2\theta + e_{24}\sin^2\theta \\
\bar{e}_{25} &= (e_{15} - e_{24})\sin\theta\cos\theta
\end{aligned} \tag{A.2}$$

$$\begin{aligned}
\bar{\epsilon}_{11} &= \epsilon_{11}\cos^2\theta + \epsilon_{22}\sin^2\theta \\
\bar{\epsilon}_{22} &= \epsilon_{11}\sin^2\theta + \epsilon_{22}\cos^2\theta \\
\bar{\epsilon}_{12} &= (\epsilon_{11} - \epsilon_{22})\sin\theta\cos\theta \\
\bar{\epsilon}_{33} &= \epsilon_{33}
\end{aligned} \tag{A.3}$$

## Appendix B. Gauss quadrature integration

For evaluating the finite element matrices in Eq. (24) over a volume with trapezoid cross-sectional area, the Generalized Gaussian Quadrature (GGQ) is proposed in this study. First, the domain is broken into smaller volumes with triangle cross-sectional shapes, as illustrated in Eq. (26). Then the GGQ is applied for each smaller volumes with formulation in this appendix derived from Ref. [39]. Thus, in this appendix the volume integral of $I_1 = \int_{\Omega_1} \mathscr{f}(x,y,z)dv$ is evaluated numerically over subdomain $\Omega_1$ with boundaries shown in Eq. (B.1).

$$I_1 = \int_a^b \int_{g_1(x)}^{g_2(x)} \int_{h_1(x,y)}^{h_2(x,y)} \mathscr{f}(x,y,z)dzdydx \tag{B.1}$$

In order to apply the GGQ on the subdomain $\Omega_1$ in $xyz$ space, this subdomain should be transferred into a zero-one cube $\mathcal{Q}_1$ in $\mathscr{p}\mathscr{q}\mathscr{r}$ space by transformation shown in Eq. (B.3).

$$\begin{aligned}
\Omega_1 &= \{(x,y,z)|a \le x \le b, g_1(x) \le y \le g_2(x), h_1(x,y) \le z \le h_2(x,y)\}\mathcal{Q}_1 \\
&= \{(\mathscr{p},\mathscr{q},\mathscr{r})|0 \le \mathscr{p} \le 1, 0 \le \mathscr{q} \le 1, 0 \le \mathscr{r} \le 1\}
\end{aligned} \tag{B.2}$$

$$x_{\mathcal{P}} = (b-a)\mathscr{p} + a y_{\mathscr{q}} = [g_2(x_p) - g_1(x_p)]\mathscr{q} + g_1(x_p) z_{\mathscr{r}} = \left[h_2\left(x_p, y_{\mathscr{q}}\right) - h_1\left(x_p, y_{\mathscr{q}}\right)\right]\mathscr{r} + h_1\left(x_p, y_{\mathscr{q}}\right) \tag{B.3}$$

With these domain transformations, $I_1$ can be numerically evaluated with the GGQ with $N_G$ Gaussian points and following approximation:

$$I_1 = \int_{\Omega_1} \mathscr{f}(x,y,z)dv \approx \sum_{i=1}^{N_G}\sum_{j=1}^{N_G}\sum_{k=1}^{N_G} \omega_1^i \omega_2^j \omega_3^k |J| \mathscr{f}\left(x_{\mathcal{P}_i}, y_{\mathscr{q}_j}, z_{\mathscr{r}_k}\right) \tag{B.4}$$

where $|J|$ is the Jacobi of the transformation, $x_{\mathcal{P}_i}$, $y_{\mathscr{q}_j}$ and $z_{\mathscr{r}_k}$ are the Gaussian point in (0,1) and $\omega_1^i$, $\omega_2^j$ and $\omega_3^k$ are their corresponding weights. There are variety of the Gaussian points and weights with $N_G = 5, 10, 20$, etc. In this study, the Gaussian points and weightsshown in Table B.1. were used. In addition, the transformation Jacobi can be extracted with Eq. (B.4).

$$|J| = (b-a)[g_2(x_{\mathcal{P}_i}) - g_1(x_{\mathcal{P}_i})]\left[h_2\left(x_{\mathcal{P}_i}, y_{\mathscr{q}_j}\right) - h_1\left(x_{\mathcal{P}_i}, y_{\mathscr{q}_j}\right)\right] \tag{B.5}$$

## References

[1] M. Khazaee, A. Rezaniakolaei, L. Rosendahl, An experimental study on macro Piezoceramic fiber composites for energy harvesting, Mater. Sci. Forum. 951 (2019) 3–8, https://doi.org/10.4028/www.scientific.net/MSF.951.3.
[2] H. Li, C. Tian, Z.D. Deng, Energy harvesting from low frequency applications using piezoelectric materials, Appl. Phys. Rev. 1 (2014), https://doi.org/10.1063/1.4900845 041301.

[3] M. Khazaee, A. Rezaniakolaie, A. Moosavian, L. Rosendahl, A novel method for autonomous remote condition monitoring of rotating machines using piezoelectric energy harvesting approach, Sensors Actuators A Phys. 295 (2019) 37–50, https://doi.org/10.1016/j.sna.2019.05.016.
[4] F.K. Shaikh, S. Zeadally, Energy harvesting in wireless sensor networks: A comprehensive review, Renew. Sustain. Energy Rev. 55 (2016) 1041–1054, https://doi.org/10.1016/j.rser.2015.11.010.
[5] A. Toprak, O. Tigli, Piezoelectric energy harvesting: State-of-the-art and challenges, Appl. Phys. Rev. 1 (2014), https://doi.org/10.1063/1.4896166 031104.
[6] M.G. Kang, W.S. Jung, C.Y. Kang, S.J. Yoon, Recent progress on PZT based piezoelectric energy harvesting technologies, Actuators 5 (2016), https://doi.org/10.3390/act5010005.
[7] H.A. Sodano, D.J. Inman, G. Park, Comparison of Piezoelectric Energy Harvesting Devices for Recharging Batteries, J. Intell. Mater. Syst. Struct. 16 (2005) 799–807, https://doi.org/10.1177/1045389X05056681.
[8] K. Morimoto, I. Kanno, K. Wasa, H. Kotera, High-efficiency piezoelectric energy harvesters of c-axis-oriented epitaxial PZT films transferred onto stainless steel cantilevers, Sensors Actuators, A Phys. 163 (2010) 428–432, https://doi.org/10.1016/j.sna.2010.06.028.
[9] A.G.A. Muthalif, N.H.D. Nordin, Optimal piezoelectric beam shape for single and broadband vibration energy harvesting: Modeling, simulation and experimental results, Mech. Syst. Signal Process. 54 (2015) 417–426, https://doi.org/10.1016/j.ymssp.2014.07.014.
[10] Y. Hu, Z. Yi, X. Dong, F. Mou, Y. Tian, Q. Yang, B. Yang, J. Liu, High power density energy harvester with non uniform cantilever structure due to high average strain distribution, Energy. 294–304 (2019).
[11] M. Akbar, J.L. Curiel-Sosa, Piezoelectric energy harvester composite under dynamic bending with implementation to aircraft wingbox structure, Compos. Struct. 153 (2016) 193–203, https://doi.org/10.1016/j.compstruct.2016.06.010.
[12] A. Erturk, D.J. Inman, A distributed parameter electromechanical model for cantilevered piezoelectric energy harvesters, J. Vib. Acoust. 130 (2008), https://doi.org/10.1115/1.2890402 041002.
[13] A. Erturk, D.J. Inman, An experimentally validated bimorph cantilever model for piezoelectric energy harvesting from base excitations, Smart Mater. Struct. 18 (2009), https://doi.org/10.1088/0964-1726/18/2/025009 025009.
[14] A. Robaldo, E. Carrera, A. Benjeddou, A unified formulation for finite element analysis of piezoelectric adaptive plates, Comput. Struct. 84 (2006) 1494–1505, https://doi.org/10.1016/j.compstruc.2006.01.029.
[15] G. De Giuseppe, A. Centuri, A. Malvasi, An improved PZT cantilever SPICE model for practical energy harvesting circuits simulations and measurements, Measurement. 98 (2018) 374–383.
[16] Y. Amini, P. Fatehi, M. Heshmati, H. Parandvar, Time domain and frequency domain analysis of functionally graded piezoelectric harvesters subjected to random vibration, Compos. Struct. 136 (2016) 384–393.
[17] I. Fattahi, H.R. Mirdamadi, Novel composite finite element model for piezoelectric energy harvesters based on 3D beam kinematics, Compos. Struct. 179 (2017) 161–171.
[18] E. Carrera, S. Brischetto, P. Nali, Plates and shells for smart structures: classical and advanced theories for modeling and analysis, 1st ed., John Wiley & Sons, Ltd, 2011. https://doi.org/10.1002/9781119950004.
[19] J.N. Reddy, On laminated composite plates with integrated sensors and actuators, Eng. Struct. 21 (1999) 568–593, https://doi.org/10.1016/S0141-0296(97)00212-5.
[20] D. Ballhause, M. D'Ottavio, B. Kröplin, E. Carrera, A unified formulation to assess multilayered theories for piezoelectric plates, Comput. Struct. 83 (2005) 1217–1235, https://doi.org/10.1016/j.compstruc.2004.09.015.
[21] C. De Marqui Junior, A. Erturk, D.J. Inman, An electromechanical finite element model for piezoelectric energy harvester plates, J. Sound Vib. 327 (2009) 9–25, https://doi.org/10.1016/j.jsv.2009.05.015.
[22] G.L.C.M. de Abreu, J.F. Ribeiro, V. Steffen, Finite element modeling of a plate with localized piezoelectric sensors and actuators, J. Braz. Soc. Mech. Sci. Eng XXVI (2004) 117–128, https://doi.org/10.1590/S1678-58782004000200002.
[23] C.G. Cooley, T.Q. Tran, T. Chai, Comparison of viscous and structural damping models for piezoelectric vibration energy harvesters, Mech. Syst. Signal Process. 110 (2018) 130–138, https://doi.org/10.1016/j.ymssp.2018.03.017.
[24] J. Palosaari, M. Leinonen, J. Juuti, H. Jantunen, The effects of substrate layer thickness on piezoelectric vibration energy harvesting with a bimorph type cantilever, Mech. Syst. Signal Process. 106 (2018) 114–118, https://doi.org/10.1016/j.ymssp.2017.12.029.
[25] A. Erturk, D.J. Inman, Piezoelectric Energy Harvesting, 1st ed., Wiley, 2011.
[26] M. D'Ottavio, O. Polit, Classical, first order, and advanced theories, 2017. https://doi.org/10.1016/B978-0-08-100410-4.00003-X.
[27] E. Carrera, An assessment of mixed and classical theories for the thermal stress analysis of orthotropic multilayered plates, J. Therm. Stress. 23 (2000) 797–831, https://doi.org/10.1080/014957300750040096.
[28] G. Shi, A new simple third-order shear deformation theory of plates, Int. J. Solids Struct. 44 (2007) 4399–4417, https://doi.org/10.1016/j.ijsolstr.2006.11.031.
[29] J.N. Reddy, An introduction to the finite element method, 2nd ed., McGraw-Hill Professional, New York, 1993.
[30] M. Khazaee, A. Rezaniakolaei, L. Rosendahl, On the effect of driving amplitude, frequency and frequency-amplitude interaction on piezoelectric generated power for MFC unimorph, Proc. 26th Int. Congr. Sound Vib. ICSV (2019, 2019,) 1–7.
[31] J. He, Z.-F. Fu, Modal analysis, 1st ed., Butterworth-Heinemann, 2001.
[32] N.E. DuToit, B.L. Wardle, S.G. Kim, Design considerations for MEMS-scale piezoelectric mechanical vibration energy harvesters, Integr. Ferroelectr. 71 (2005) 121–160, https://doi.org/10.1080/10584580590964574.
[33] A. Erturk, D.J. Inman, Issues in mathematical modeling of piezoelectric energy harvesters, Smart Mater. Struct. 17 (2008), https://doi.org/10.1088/0964-1726/17/6/065016.
[34] S. Priya, D. Viehland, A.V. Carazo, J. Ryu, K. Uchino, High-power resonant measurements of piezoelectric materials: Importance of elastic nonlinearities, J. Appl. Phys. 90 (2001) 1469–1479, https://doi.org/10.1063/1.1381046.
[35] M. Khazaee, A. Rezania, L. Rosendahl, Effect of damage and support damping mechanisms on unimorph piezoelectric energy harvester, J. Vib. Control. 107754631985516 (2019), https://doi.org/10.1177/1077546319855162.
[36] R. Ahmed, F. Mir, S. Banerjee, A review on energy harvesting approaches for renewable energies from ambient vibrations and acoustic waves using piezoelectricity, Smart Mater. Struct. 26 (2017), https://doi.org/10.1088/1361-665X/aa7bfb 085031.
[37] J.W. Yi, W.Y. Shih, W.H. Shih, Effect of length, width, and mode on the mass detection sensitivity of piezoelectric unimorph cantilevers, J. Appl. Phys. 91 (2002) 1680–1686, https://doi.org/10.1063/1.1427403.
[38] M. Kim, M. Hoegen, J. Dugundji, B.L. Wardle, Modeling and experimental verification of proof mass effects on vibration energy harvester performance, Smart Mater. Struct. 19 (2010), https://doi.org/10.1088/0964-1726/19/4/045023 045023.
[39] S. Jayan, K.V. Nagaraja, A General and Effective Numerical Integration Method to Evaluate Triple Integrals Using Generalized Gaussian Quadrature, Procedia Eng. 127 (2015) 1041–1047, https://doi.org/10.1016/j.proeng.2015.11.457.

# Appendix F. Paper 6: Reference [164]

## A broadband macro-fiber-composite piezoelectric energy harvester for higher energy conversion from practical wideband vibrations

M. Khazaee, A. Rezaniakolaei, L. Rosendahl.

This paper has been published in

*Nano Energy*. vol. 76, pp. 104978, 2020

Nano Energy 76 (2020) 104978

Contents lists available at ScienceDirect

Nano Energy

journal homepage: http://www.elsevier.com/locate/nanoen

# A broadband macro-fiber-composite piezoelectric energy harvester for higher energy conversion from practical wideband vibrations

Majid Khazaee, Alireza Rezaniakolaie *, Lasse Rosendahl

*Department of Energy Technology, Aalborg University, Pontopidanstraede 111, 9220, Aalborg, Denmark*

ARTICLE INFO

*Keywords:*
Piezoelectric
Energy harvesting
Broadband
Macro-fiber-composite

ABSTRACT

This paper presents an initiative concept in geometry and material lay-up toward energy conversion enhancement of piezoelectric energy harvesters from wideband excitation signals. The energy harvester demonstrated in this work has Macro-fiber-composite (MFC) as active layers and composite laminate as the center shim. This concept utilizes variable cross-sectional area and rotating fiber orientation in the MFC active layer. The simulation of the energy harvester is carried out using finite element (FE) method with high-order shear elements. Results of the FE mode is validated with experimental data and numerical results from COMSOL®. Effects of changing the cross-section, rotation of fibers in the substrate and the active piezoelectric layers on output power and natural frequency of the harvester are analyzed. The results point out the optimum piezoelectric fiber orientation, at which power and power density are, respectively, 20% and 60% higher compared to zero-fiber angle. In addition, taper angle, as a key parameter in shifting the harvester natural frequency, can be used for broadband energy harvesters. By a combination of the taper angle and optimum fiber orientation, a broadband energy harvester was optimally designed for a moving car. Power generation by the designed harvester is 84% greater than a common multi-beam design at a 47%-reduced volume resulting a 160% power density improvement.

## 1. Introduction

Low-power piezoelectric energy harvesting from wasted kinetic energy sources has drawn much attention during the past years [1]. There are several studies focusing on the design and fabrication of piezoelectric energy harvesters (PEHs). To design PEHs, frequency and frequency bandwidth are of great importance parameters because PEHs have the best performance in their resonant frequencies in linear framework and base harmonic excitation [2]. From an energy harvesting perspective, the harvester performance is assessed with power density (the ratio of power generation over volume of the PEH). In order to achieve high power density and maximizing the volumetric power generation, mechanical damping should be minimized [3] to limit the frequency spectrum to a narrow bandwidth, i.e. typically few hertz [4]. On the other hand, as practical vibrational systems have a broadband frequency spectrum, the narrowband piezoelectric harvester wastes a large fraction of the available kinetic energy deteriorating the energy conversion performance. As a result, for maximizing the overall performance of PEHs, enhancing power generation over a wide frequency range is of great significance. These improvements lead to higher conversion efficiency for PEHs.

For achieving better PEH performance, previous studied had focused mostly on only one design aspect including geometrical optimization [5], nonlinear boundary condition [6], coupling piezoelectricity with magnetic force [7,8], and material improvements [9]. Muthalif and Nordin [5] demonstrated an improved power performance of trapezoid and triangle harvesting beams. They also reported the greater natural frequency of a trapezoid beam in comparison with the same-length rectangular beam. Attaching beam-tip iron pieces and magnets around the beam-tip was used for broadband power generation from harmonic base excitation [7] and from impact driven forces [8]. Coupling the electromagnetic force with triboelectric nano generator was investigated by Yang et al. [10,11] for obtaining a hybrid low-frequency energy harvester. Applying nonlinear boundary condition was investigated by Hu et al. [6], where they introduced nonlinear stiffness by placing stoppers in a two degree-of-freedom system. Their harvester design generated higher power in a larger bandwidth. The impact-based nonlinear boundary condition was also used for broadband energy

* Corresponding author.
*E-mail addresses:* mad@et.aau.dk (M. Khazaee), alr@et.aau.dk (A. Rezaniakolaie).

https://doi.org/10.1016/j.nanoen.2020.104978
Received 24 March 2020; Received in revised form 4 May 2020; Accepted 16 May 2020
Available online 17 June 2020

harvesting by Bhatia et al. [12]. The use of multi beams was investigated by researchers for obtaining the appropriate frequency response function in the frequency range of interest. Ramalingam et al. [13] used a two-beam design with an inner cavity for the illustration of wideband power output. Moreover, Qi et al. [14] employed a multi beam concept from Shahruz [15] in order to fabricate a multi resonant structure for hosting the piezoceramic fiber composite. They showed that, the output power is improved and its bandwidth has increased using this concept.

In the clamped-free cantilever beam configuration, the most widely used boundary condition in energy harvesting [2], the normal strain is maximum in the clamped-end region and becomes zero in the free-end [16]. Thus, the regions around the clamped-line are accountable for most of the power generation leaving the major volume of the harvester ineffective. This becomes more significant if the available PEH volume is limited because the major PEH volume does not contribute to the power generation. In addition, developing flexible piezoelectric modules is of great interest for extending applications of energy harvesting toward flexible electronics [17]. One concept for changing strain contours over the harvester surface is to tailor the beam stiffness in desirable direction. Macro-fiber composites (MFCs) has the unique capacity that fiber orientation can be varied for changing the beam stiffness in different directions. MFCs were invented for delivering high-electromechanical coupling effects in PEH as well as offering great module flexibility (see Fig. 1 (a)). The MFC is a multi-layered composite having an active layer of piezoceramic with micro-scale rectangular cross-section fibers (see Fig. 1 (b)) [18]. The MFC has a moderate power density, approximately 10.37 $\mu W/cm^3 g_0^2$ where $g_0 = 9.81\ m/s^2$ [19], which is greater than that of Polyvinylidene Fluoride (PVDF) with 4 $\mu W/cm^3.g_0^2$ [20], still lower than the power density obtained from Lead Zirconate Titanate (or PZT ceramic) [20]. Using different fiber orientations, a bi-stable lamina energy harvester was fabricated by Lee and Inman [21] with two Macro-Fiber Composites (MFCs) in 0° and 90° fiber orientations.

Increasing voltage generation over the whole harvester surface is an unmet goal that can lead to substantial increment in the power generation by nano generators. Moreover, although previous studied multi-beam harvesters increase the power bandwidth, the power spectrum still has sharp peaks at resonances due to the high sensitivity of power to the beam length. Thus, having a wideband power output is still needed to be investigated because of the wide frequency-band in practical vibration signals. For modeling of energy harvesters with the MFC, there are few works focusing on finite element (FE) modeling of MFCs [22,23]. Nonetheless, there is a need for a layer-wised FE method (FEM) capable of modeling energy harvesters with MFC in various geometries and lay-ups.

This study aims to improve the power conversion efficiency of piezoelectric nano generators by developing broadband strain-engineered piezoelectric composite harvesting beams. Using a combination of geometric and material modifications for a flexible composite MFC, a broadband PEH with improved power-density is developed. Strain contours over the beam area is modified toward better power generation using an innovative material modification in the MFC layer, which has not been studied yet. In addition, by combining the concept of trapezoid harvesting beam with the material modification, the model for improved broadband power generation is proposed. To analyze these modifications for a composite MFC harvesting beam, the shell formulation by Khazaee et al. [24] is modified for precise layer-wised modeling of MFC harvesters in this study, as described in section 2. The presented structural FE model can be used for investigation of structural-electrical behavior of piezoelectric beams in micro to macro scales. Section 3 is dedicated to derivation of the MFC material properties and damping coefficients for a PEH with the MFC. Next, the sensitivity results of the power generation to the cross-section area and the fiber orientations are presented in section 4. The proposed harvester design is used for designing a wideband energy harvester with improved power density.

## 2. Problem statement and FEM formulation

A bimorph beam with the active length of $l$ and the base width of $b$ serves as the PEH in this study. The piezoelectric sample is clamped at one-end using a clamp box. The clamped-end is fixed to the vibration source causing transverse motion of the cantilever. The beam width is non-constant, as shown in Fig. 2, and increases (or decreases) with a positive (or negative) slope angle α. The electrical output wires are connected to a purely resistive electrical load ($R$). Two piezoelectric layers with thickness of $h_p$ are in ideal contact with the $h_s$-thickness substrate shim. The contact layers has thickness of $h_c$. In practice, each piezoelectric layer comes with two-side electrodes to collect the charge generation. Therefore, there is no necessity for the substrate shim of being metal. Thus, the substrate shim is assumed made of orthotropic composite laminae. The electrodes from the two piezoelectric layers are wired in series and, therefore, the piezoelectric layers are poled in the opposite direction, as shown in Fig. 2. A linear FE formulation based on the third-order shear deformation theory is derived for analyzing the bimorph. In the FE model, unknown parameters in the beam vibration equations are estimated using a spatial approximation for each parameter. To make the approximation errors smaller, the differential equations are solved for small-discretized domains. Thus, the harvester area is discretized into several small elements and electromechanically coupled equations are developed for each element. As shown in Fig. 2, each element has four nodes with five degrees-of-freedom per node, namely $w$, $\partial w/\partial x$, $\partial w/\partial y$, $\varphi_x$, and $\varphi_y$ and one voltage value $V_e$ for the element, where $w$ is $z$-axis displacement of mid-plane, $\varphi_x$ is the rotation of $x$-axis after deformation and $\varphi_y$ is the rotation of $y$-axis after deformation.

The general FE equations can be derived from the extended Hamilton's principle in absence of electromagnetic forces, as follows [24]:

$$\begin{aligned} &[M]\{\ddot{\chi}\} + [C]\{\dot{\chi}\} + \left(\left[K_{qq}\right] + j[H]\right)\{\chi\} - \left[\tilde{K}_{q\varphi}\right]V_p = \{F_e\} \\ &\left[\tilde{K}_{q\varphi}\right]^t\{\dot{\chi}\} + V_p \ /\mathrm{R} + K_{\varphi\varphi}\dot{V}_p = 0 \end{aligned} \tag{1}$$

where $\{\chi\}$ is the vector of total mechanical degree of freedom, $V_p$ is the

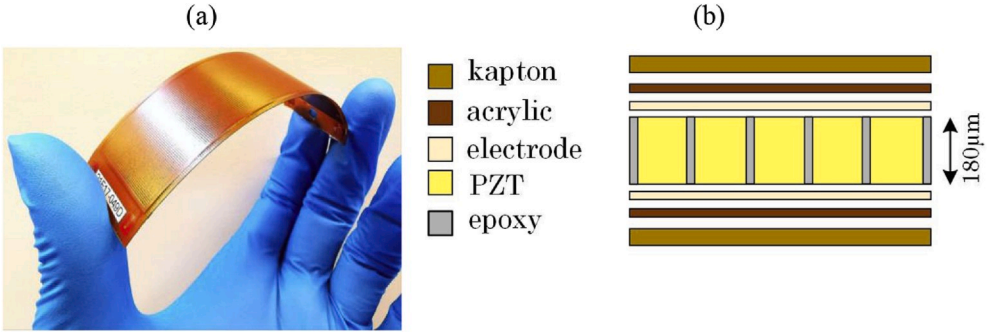


**Fig. 1.** (a) The flexibility of the MFC and (b) PZT micro-scale fibers in the MFC.

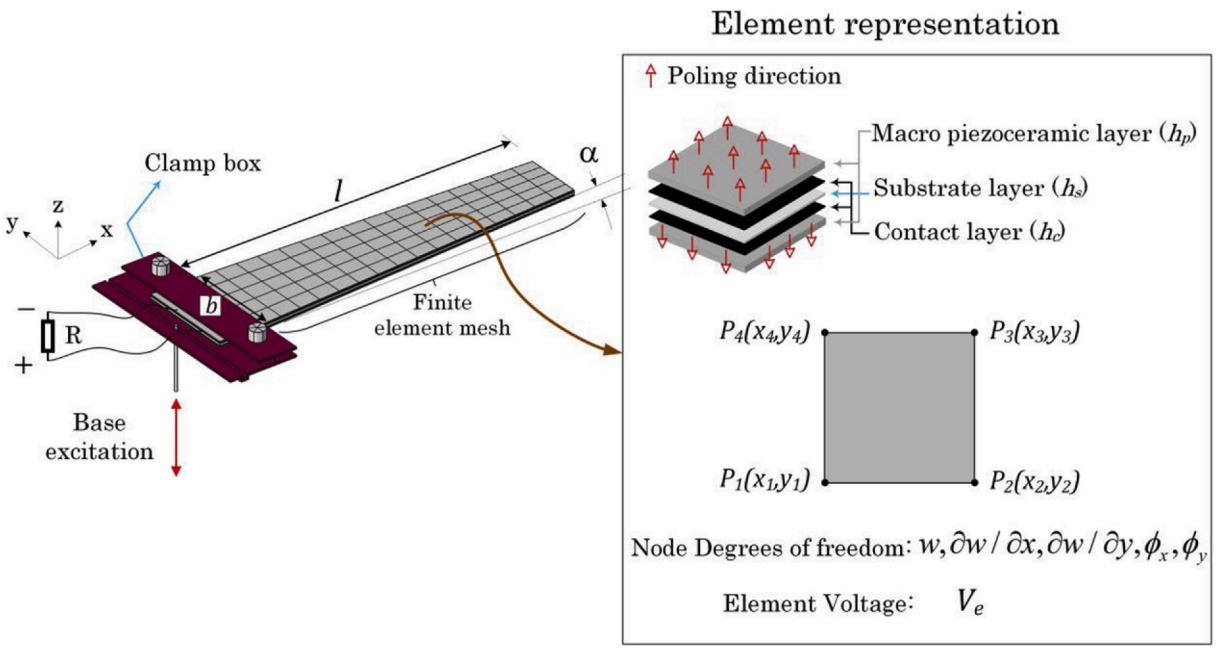


**Fig. 2.** Schematic of piezoelectric bimorph with piezoelectric layers connected to a composite substrate with contact layers and FE discretization.

generated voltage, $\{F_e\}$ is the external mechanical load vector, $[\tilde{K}_{q\varphi}] = [K_{q\varphi}]\{diag(I_{N_e})\}$ and $I_{N_e}$ is the identity matrix ($N_e$ is total number of elements). In addition, $[M]$, $[C]$, $[H]$, $[K_{qq}]$, $[K_{q\varphi}]$ and $K_{\varphi\varphi}$ are FE parameters called as the general mass, viscous damping, structural damping, mechanical stiffness, electromechanical coupling matrices and electric capacitance. Structural and viscous damping mechanisms are modeled as proportional damping with $[H] = \gamma[K_{qq}]$ and $[C] = \beta_1[M] + \beta_2[K_{qq}]$, respectively, where $\gamma$, $\beta_1$ and $\beta_2$ are real positive dimensionless constants. These FE parameters and matrices are presented in Refs. [24] by applying the concept of Shi's high-order shear element [25] on electromechanically coupled equations of piezoelectric materials. Mass matrix $[M] \in \mathbb{R}^{5N_e \times 5N_e}$, mechanical stiffness matrix $[K_{qq}] \in \mathbb{R}^{5N_e \times 5N_e}$, electromechanical coupling matrix $[K_{q\varphi}] \in \mathbb{R}^{5N_e \times N_e}$ and capacitance $K_{\varphi\varphi} \in \mathbb{R}$ are obtained from density properties, material structural stiffness properties, piezoelectric coupling coefficients and permittivity of piezoelectric material, respectively. More details about derivation of these matrices can be found in Refs. [24].

Fig. 3 (a) shows the layered bimorph energy harvester with two active MFCs. Different layers in the MFC are also shown in Fig. 3 (b). In order to investigate the harvester performance at different fiber orientations in substrate and active layers, as shown in Fig. 3 (c) and (d), the substrate and PZT fibers are not aligned with physical coordinates $(x,y)$,

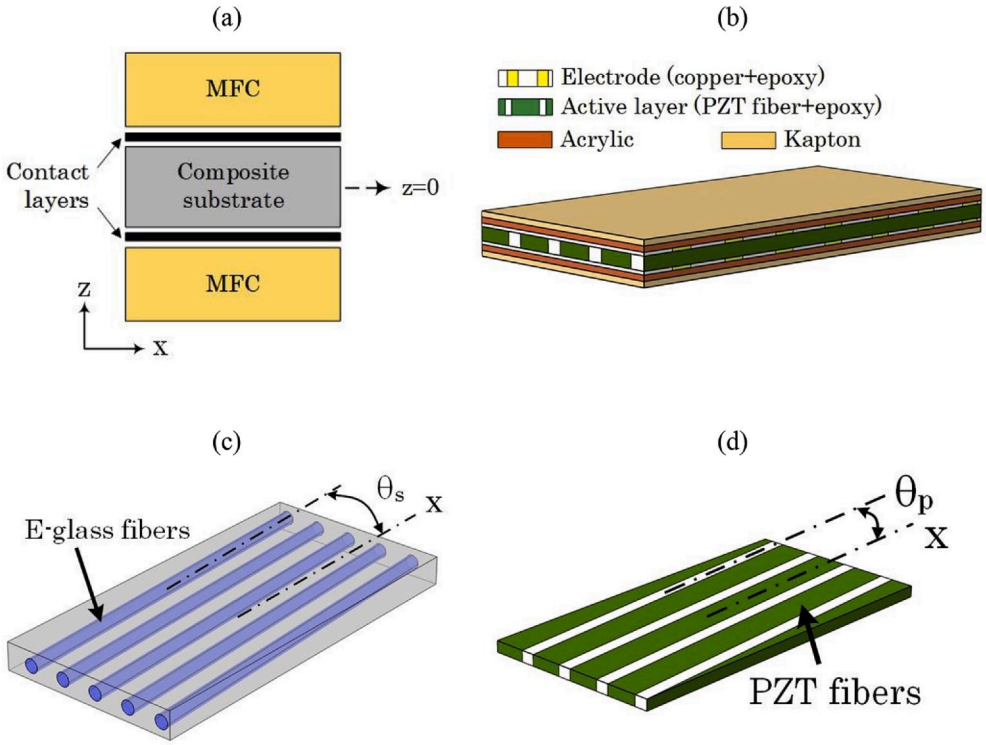


**Fig. 3.** (a) Layered bimorph energy harvester, (b) the MFC sub-plies, (c) rotation of substrate shim principal coordinates, and (d) rotation of PZT fibers.

having a rotation of $\theta_s$ and $\theta_p$, respectively. These rotations change the material properties in these layers and, consequently, alter the natural frequency and output power. The active layer in MFC has rectangular PZT fibers aligned and fixed with epoxy matrix. It is worthy to note that, PZTs are not isotropic materials and have different material properties in different directions [26].

Khazaee et al. [24] developed FE matrices, where the active layers are made of a single piezoelectric material, which is different from the MFC. A MFC layer, as shown in Fig. 3, consists of an active layer sandwiched between the electrode layers, which are then protected from electrolyte and environmental conditions with an acrylic and a Kapton layer on both sides. The electrode and active layers are also composite layers made of copper and PZT fiber with epoxy, respectively. Material properties of the composite layers in the PEH are obtained using rules of mixture as suggested in Refs. [27]. Let's use superscripts *'f'* and *'m'* referring the material properties of the fibers and matrix, respectively. Then, the material properties for the composite laminae in principal coordinates of $(1,2)$, when fiber volume fraction is $\mathscr{V}_f$, can be shown as follows [28]:

$$
\begin{aligned}
E_1 &= \mathscr{V}_f E_1^f + (1-\mathscr{V}_f)E^m \\
\frac{1}{E_2} &= \frac{\mathscr{V}_f}{E_2^f} + \frac{1-\mathscr{V}_f}{E^m} \\
v_{12} &= \mathscr{V}_f v_{12}^f + (1-\mathscr{V}_f)v_{12}^m \\
\frac{1}{G_{12}} &= \frac{\mathscr{V}_f}{G_{12}^f} + \frac{1-\mathscr{V}_f}{G^m} \\
G_{13} &= \mathscr{V}_f G_{13}^f + (1-\mathscr{V}_f)G^m \\
\frac{1}{G_{23}} &= \frac{\mathscr{V}_f}{G_{23}^f} + \frac{1-\mathscr{V}_f}{G^m}
\end{aligned}
\tag{2}
$$

Furthermore, considering the active layer with volume of $\mathscr{V}_f$, the piezoelectric properties can be calculated from Eq. (3) [27]:

$$
\begin{aligned}
d_{31} &= \frac{1}{E_1}\mathscr{V}_f d_{31}^p E_1^p \\
d_{32} &= -d_{31}^p v_{12} + \mathscr{V}_f d_{31}^p E_1^p (1+v_{12}^p) \\
\varepsilon_{33} &= \mathscr{V}_f \varepsilon_{33}^p
\end{aligned}
\tag{3}
$$

Eq. (2) and Eq. (3) present the material properties in the principal coordinates. Nonetheless, these material properties need to be transformed to the physical coordinates. Note that the copper fibers in the electrode layer have a rotation of 90. Let's assume $[Q_{ij}]$ and $[\overline{Q}_{ij}]$ as the structural stiffness in principal coordinates and physical coordinates, respectively, with a rotation of $\theta$. The relationships between these parameters is shown in Eq. (4) [29]:

$$
\begin{aligned}
\overline{Q}_{11} &= Q_{11}\cos^4\theta + 2(Q_{12}+2Q_{66})\sin^2\theta\cos^2\theta + Q_{22}\sin^4\theta \\
\overline{Q}_{12} &= (Q_{11}+Q_{22}-4Q_{66})\sin^2\theta\cos^2\theta + Q_{12}(\sin^4\theta+\cos^4\theta) \\
\overline{Q}_{22} &= Q_{11}\sin^4\theta + 2(Q_{12}+2Q_{66})\sin^2\theta\cos^2\theta + Q_{22}\cos^4\theta \\
\overline{Q}_{16} &= (Q_{11}-Q_{12}-2Q_{66})\sin\theta\cos^3\theta + (Q_{11}-Q_{12}+2Q_{66})\sin^3\theta\cos\theta \\
\overline{Q}_{26} &= (Q_{11}-Q_{12}-2Q_{66})\sin^3\theta\cos\theta + (Q_{11}-Q_{12}+2Q_{66})\sin\theta\cos^3\theta \\
\overline{Q}_{66} &= (Q_{11}+Q_{22}-2Q_{12}-2Q_{66})\sin^2\theta\cos^2\theta + Q_{66}(\sin^4\theta+\cos^4\theta) \\
\overline{Q}_{44} &= Q_{44}\cos^2\theta + Q_{55}\sin^2\theta \\
\overline{Q}_{45} &= (Q_{55}-Q_{44})\cos\theta\sin\theta \\
\overline{Q}_{55} &= Q_{55}\cos^2\theta + Q_{44}\sin^2\theta
\end{aligned}
\tag{4}
$$

Similarly, due to a $\theta$ rotation, the piezoelectric material properties are expressed as follows [29]:

$$
\begin{aligned}
\overline{e}_{31} &= e_{31}\cos^2\theta + e_{32}\sin^2\theta \\
\overline{e}_{32} &= e_{31}\sin^2\theta + e_{32}\cos^2\theta \\
\overline{e}_{36} &= (e_{31}-e_{32})\sin\theta\cos\theta \\
\overline{e}_{14} &= (e_{15}-e_{24})\sin\theta\cos\theta \\
\overline{e}_{24} &= e_{24}\cos^2\theta + e_{15}\sin^2\theta \\
\overline{e}_{15} &= e_{15}\cos^2\theta + e_{24}\sin^2\theta \\
\overline{e}_{25} &= (e_{15}-e_{24})\sin\theta\cos\theta \\
\overline{\varepsilon}_{11} &= \varepsilon_{11}\cos^2\theta + \varepsilon_{22}\sin^2\theta \\
\overline{\varepsilon}_{22} &= \varepsilon_{11}\sin^2\theta + \varepsilon_{22}\cos^2\theta \\
\overline{\varepsilon}_{12} &= (\varepsilon_{11}-\varepsilon_{22})\sin\theta\cos\theta \\
\overline{\varepsilon}_{33} &= \varepsilon_{33}
\end{aligned}
\tag{5}
$$

By combination of the mixing rules presented in Eq. (2) and Eq. (3), and the equations for the principal coordinate rotation, we are able to extract the FE matrices from the material properties. By having the FE matrices and assuming a harmonic input acceleration of $\ddot{a}_B = |\ddot{a}_B|e^{j\omega t}$ acting on $\{\mathscr{T}\}$ mechanical degree of freedom, the normalized power generation to the square of acceleration magnitude is derived as:

$$
\frac{P(t)}{(|\ddot{a}_B|)^2} = \frac{m_{eff}^2}{R}\left(\frac{j\omega\left({}^1\!/_R + j\omega K_{\varphi\varphi}\right)^{-1}\left[\tilde{K}_{q\varphi}\right]^t}{\left((-\omega^2+j\omega\beta_1)[M] + (1+j(\gamma+\omega\beta_2))[K_{qq}] + j\omega\left({}^1\!/_R + j\omega K_{\varphi\varphi}\right)^{-1}\left[\tilde{K}_{q\varphi}\right]\left[\tilde{K}_{q\varphi}\right]^t\right)}\{\mathscr{T}\}\right)^2 e^{j\omega t}
\tag{6}
$$

where $m_{eff}$ is the effective mass of the PEH. $\frac{P(t)}{(|\ddot{a}_B|)^2}$ is the normalized power to the square of input acceleration, with unit of $\frac{W}{m^2.s^{-4}}$, and has no dependency to the magnitude of the input acceleration. In the result section of this paper, normalized power is demonstrated.

For the accurate power calculation, see Eq. (6), three coefficients $\beta_1$, $\beta_2$, and $\gamma$ in the damping matrices $[C]$ and $[H]$ are estimated. Damping properties of an unknown system are often identified with the aid of FEM and experimental tests using model updating methods [30]. In model updating methods, a residual function is minimized by updating certain model coefficients. In this study, as the most important result for the PEH is the output power, the residual function is the difference of output power between the experimental test and the FE model. By expressing the updating parameters with $\widehat{\theta} = \{\beta_1, \beta_2, \gamma\} \in \mathbb{R}^3$, the residual function, $\varepsilon(\widehat{\theta})$, is defined as:

$$
\varepsilon(\widehat{\theta}) = (P^{meas} - P(\widehat{\theta}))
\tag{7}
$$

where $P^{meas}$ is the measured power and $P(\widehat{\theta})$ is the power calculated from the FE model. Moreover, if the updating parameters are restricted by upper and lower bands as $\mathscr{L} < \widehat{\theta} < \mathscr{U}$, the model updating problem leads to a constrained least square problem given by $\min_{\widehat{\theta}\in\mathbb{R}^3,\ \mathscr{L}<\widehat{\theta}<\mathscr{U}} |\varepsilon(\widehat{\theta})|^2$. This nonlinear least square problem has no closed-

**Table 1**
Characteristics for sub-plies in a MFC from Smart Material Inc [33].

| Properties | Active layer | Electrode layer | Acrylic layer | Kapton layer |
|---|---|---|---|---|
| Fiber volume fraction $\mathscr{V}_f$ [27] | 0.86 | 0.24 | – | – |
| Layer thickness ($\mu m$) [31] | 177.8 | 17.78 | 12.7 | 25.4 |
| Fiber material | PZT-5A | Copper | – | – |
| Matrix material | Epoxy | Epoxy | – | – |

from solution and should be solved iteratively.

## 3. Characterization of MFC layer and modeling of an PEH with MFC layer

The MFC is a multi-layered composite comprising various materials. In the MFC, characterization of the geometrical dimensions and the material properties for each layer is essential to achieve a close-to-reality FE model. For the MFC characterization, the material properties are derived from the previous studies on the MFCs and then mixing rules are employed for obtaining final properties in the composite sub-plies. Moreover, comparison results between the present FE model and experimental data for the MFC harvester are reported. Additionally, the damping coefficients are extracted from the FE model-updating scheme. The damping coefficients are used for the analyses in section 4.

Table 1 shows the characteristics of the MFC sub-plies. The thicknesses for these sub-plies, presented in Table 1, are derived from Ref. [31], while the fiber volume fractions are that estimations reported by Deraemaeker et al. [27]. Five different materials are used in the MFC sub-plies, namely PZT fibers, epoxy, copper, acrylic and Kapton. Solid properties of these materials are given by Williams [31]. In order to obtain realistic piezoelectric coupling properties, the constant $d_{31}$ is derived from the experimental study on low-voltage ranges by Prasath and Arockiarajan [32], where they experimentally studied the relation between the strain and electrical field. Table 2 summarizes material properties derived from the aforementioned studies.

Using the properties mentioned in Tables 1 and 2, the results of the presented FE formulation are compared with the experimental data from Khazaee et al. [34]. The piezoelectric sample used by them is a unimorph PEH comprising a 120-μm-thickness aluminum substrate with an M-2814-P2 MFC from Smart Material Inc. having the top surface area of $37 \times 18$ mm$^2$ in connection to an electrical load resistance of 31.5 kΩ. Fig. 4 shows the experimental setup used in Ref. [34]. More details about the experimental setup can be found in Refs. [34]. The fundamental natural frequency was 197.5 Hz according to the experimental results. From the present FE simulation, the fundamental natural frequency is 205.7 Hz showing an error of ≈4%. Therefore, there is a good agreement between the present FE model and the experiment since many associated

**Table 2**
Material properties for materials used in a MFC layer from Smart Material Inc.

| Properties | PZT fibers | Epoxy | Copper | Acrylic | Kapton |
|---|---|---|---|---|---|
| Young's modulus ($GPa$) [31] | $E_1 = 53$<br>$E_2 = 61$ | 3.378 | 117.2 | 2.7 | 2.5 |
| Shear modulus ($GPa$) [31] | $G_{12} = 12$<br>$G_{23} = 22.6$<br>$G_{13} = 22.6$ | 1.33 | 44.7 | 1.0 | 0.93 |
| Poisson's ratio [31] | $\nu_{12} = 0.384$<br>$\nu_{23} = 0.35$ | 0.27 | 0.31 | 0.35 | 0.34 |
| Density ($g/cm^3$) [31] | 7.75 | 1.4 | 8.96 | 1.185 | 1.42 |
| Coupling charge constants ($pC/N$) [32] | $d_{31} = -167.28$<br>$d_{32} = -167.28$ | – | – | – | – |
| Dielectric constants ($nF/m$) [27] | $1850\varepsilon_0$ | – | – | – | – |

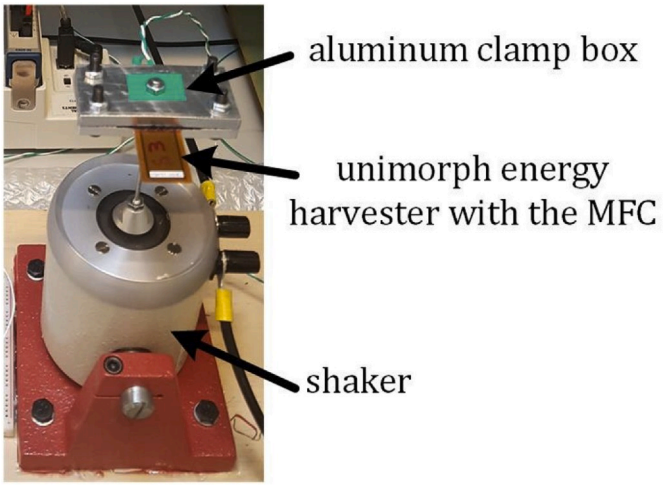


**Fig. 4.** Experimental setup for the unimorph PEH [34].

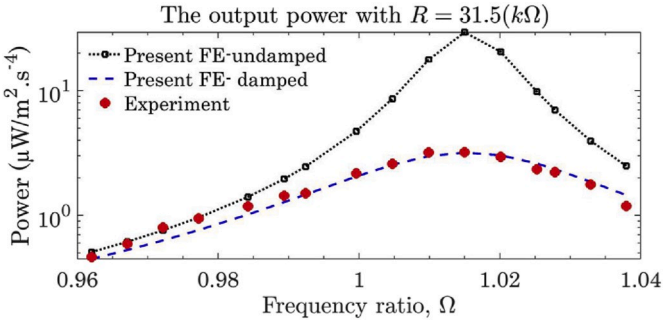


**Fig. 5.** Comparison between the experimental data [34] and the present finite element (FE) method in undamped and structural-viscous damped models.

parameters in the MFC have been obtained from the mixing rules.

Fig. 5 shows the electrical power measured experimentally from the unimorph MFC as a function of frequency ratio (Ω). The frequency ratio is the fraction of excitation frequency to the fundamental natural frequency of the harvester. The output power from the present FE approach is presented in undamped and damped models. Due to electromechanical coupling effects, the maximum power point is occurs slightly after the fundamental frequency, at Ω≈1.016. The FE maximum power point in either damping models are in good agreement with the experimental result. The proportional damping coefficients from the model updating are $\beta_1 = 4.886$, $\beta_2 = 1.243 \times 10^{-5}$ and $\gamma = 0.824 \times 10^{-2}$. Comparing the power generation from the FE model with the experimental data in Fig. 5 shows that, the none-damped model is extremely overestimated the resonant output power. On the other hand, in the damped model, the output power presents a good agreement with the experiments. In the next numerical analysis in section 4, these damping coefficients are used as the model inputs.

## 4. Results and discussion

In this section, performance of a typical PEH is investigated at different configurations using the FE model verified experimentally. From the FE model presented in Figs. 2 and 3, a sensitivity analysis is carried out focusing on variation of three parameters, namely the angle of changing cross-section area ($\alpha$), piezoelectric fiber direction ($\theta_p$) and composite substrate fiber direction ($\theta_s$). First, the variations of the output power and resonant frequencies are analyzed by changing the $\alpha$ angle in the tapered and extended configurations. In this analysis, the FE natural frequencies at different $\alpha$ values are compared with the results

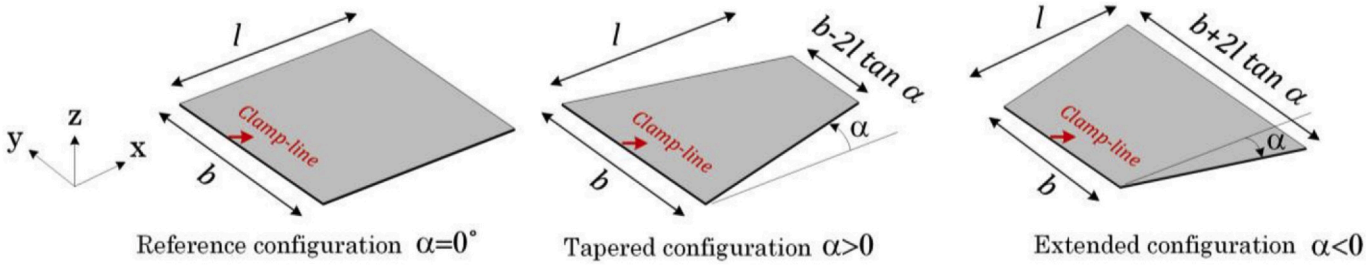


**Fig. 6.** Geometries of the under study piezoelectric harvester in reference, tapered and extended cross-section configurations.

**Table 3**
Material properties of the substrate shim and contact layers.

| Properties | E-glass fibers | Contact layer |
|---|---|---|
| Young's modulus (*GPa*) | $E = 30$ | 1.05 |
| Shear modulus (*GPa*) | $G = 30$ | 0.40 |
| Poisson's ratio | $\nu = 0.32$ | 0.3 |
| Density ($g/cm^3$) | 2.540 | 1.4 |

from COMSOL Multiphysics® software. Secondly, the effects of variations of $\theta_p$ and $\theta_s$ on the resonant frequency and power are reported followed by presenting contours of the strain and electrical displacement field. These investigations are finally employed to design an optimum PEH with two MFC layers for a diesel car moving on a bumpy highway.

### 4.1. Effect of cross-sectional angle on output power and natural frequency

Three beam configurations are studied in this paper, as shown in Fig. 6, which are constant cross-sectional (reference configuration), tapered and extended configurations. The analyzed PEH has two MFC layers with the material properties presented in Tables 1 and 2. The composite substrate is unidirectional laminae made of E-glass fibers with epoxy matrix and 60% volume fraction. Two contact layers are assumed for joining the MFCs and the substrate layer. Table 3 shows material properties of the substrate and contact layers. A reference lay-up is regarded at which the tapered angle is zero but the fiber rotations in the substrate and active layer are non-zero. The layered properties for the reference configuration are presented in Table 4.

Fig. 7 compares the natural frequencies from the present FE method with that of the modelling software at the reference lay-up but at different tapered angles ($\alpha$). Fig. 7 (a) presents the first three natural frequencies versus the element numbers when $\alpha = -5^\circ$. According to the mode shapes, as shown in Fig. 7 (b), only the first identified mode is the bending mode, while the other two modes are torsional modes, which are not of interest in the present study because of negligible piezoelectric couplings at these displacements. While the first natural frequency does not differ considerably by increasing the element numbers, the second and third natural frequencies can be inaccurately estimated with low number of elements. Similarly, for the numerical results, while the first natural frequency demonstrates weak dependency to the element number, the second and third natural frequencies have strong dependency to the element number. The present FE results using a high element number are in good agreement with the numerical results. Computation time plotted in Fig. 7 (a) soars exponentially by increasing the element number. Therefore, selection of the element number is a trade-off between the accuracy and computational time. In most applications of piezoelectric energy harvesting, the first bending mode is of interest for the PEH design. A total number of 24 elements has good accuracy for the natural frequency estimation at low computation time. This domain discretization, six divisions in length and four divisions in width, is selected as the optimal mesh in this study. The first natural frequency at different α angles, obtained by the 24-element FE model, agrees well with that of obtained by COMSOL®, as shown in Fig. 7 (c).

**Table 4**
Layered characteristic assumed for reference configuration.

| Properties | Active layer | Substrate layer | Electrode layer | Contact layer |
|---|---|---|---|---|
| Tapered angle $\alpha$ (*deg*) | 0 | | | |
| Length (*mm*) | 100 | | | |
| Width (*mm*) | 100 | | | |
| Fiber direction $\theta$ (*deg*) | $\theta_p = 10$ | $\theta_s = 30$ | 90 | – |
| Layer thickness ($\mu m$) | 177.8 | 150.0 | 17.78 | 50.0 |
| Fiber material | PZT-5A | E-glass $\mathcal{V}_f = 60\%$ | Copper | – |
| Matrix material | Epoxy | Epoxy | Epoxy | – |

Fig. 8 illustrates the resonant tip displacement and resonant power over electrical resistive load by varying $\alpha$ for the reference lay-up properties and $\theta_p = \theta_s = 0^\circ$. The PEH device volumes corresponding to the taper angles $\alpha = -15^\circ$, $0^\circ$, and $15^\circ$ are 119.8, 78.0, and 36.2 $cm^3$, respectively. Fig. 8 (a) shows that, the extended beam has higher tip deflection and, hence, higher axial strain. Eventually, higher power output is achieved as can be seen in Fig. 8 (b). By comparing the resonant power in Fig. 8 (b), it is furthermore found that, changing $\alpha$ has a small effect on the optimum electrical load resistance. Comparing the power outputs at $\alpha = -15^\circ$ and $\alpha = 0^\circ$ cases furthermore shows that, the resonant power is increased by 6% in the case with $\alpha = -15^\circ$. The volumetric power in optimum electrical resistance load for $\alpha = -15^\circ$, $0^\circ$, and $15^\circ$ are respectively 3.87, 5.56, and 11.41 $\mu W/m^2\ s^{-4}\ cm^3$. In the tapered configuration with $\alpha = 15^\circ$, the power density is enhanced by 105% compared with $\alpha = 0^\circ$.

The output power and the normalized power to the PEH volume are plotted in Fig. 9 for different $\alpha$s with 5 kΩ electrical load. The extended configuration has smaller resonant frequency and generates higher electrical power. Both of these variations are desirable for the PEH performance. The natural frequency and resonant power for the PEH with $\alpha = -15^\circ$ are respectively 13.6 Hz lower and 65-$\mu W/m^2.s^{-4}$ higher in comparison with the case with $\alpha = 15^\circ$ showing a large reduction in the resonant frequency and increment in the power generation. However, if high power density is of interest, the tapered geometry with $\alpha = 15^\circ$ generates 76 $\mu W.\ cm^{-3}/m^2.s^{-4}$ more power than the extended case $\alpha = -15^\circ$, which is a drastic increment in the power density (see Fig. 9 (b)). The results of Fig. 9 indicate that, the extended configuration is desirable for higher power output while the tapered configuration delivers higher power density even though the magnitude of the power is lower than the standard configuration.

Apart from the power enhancement, the angle $\alpha$ can also be a tuning factor for matching the excitation dominant frequency to the PEH natural frequency. In many practical energy-harvesting applications, the PEH must be adapted to the changes of the input vibration characteristics to provide the maximum possible power output. For instance, a car hood at 700 rpm has a highest peak power at 35.6 Hz with acceleration magnitude about 0.0744 $m/s^2$ [35]. In this scenario, two different approaches for the power optimization are considered. The first approach

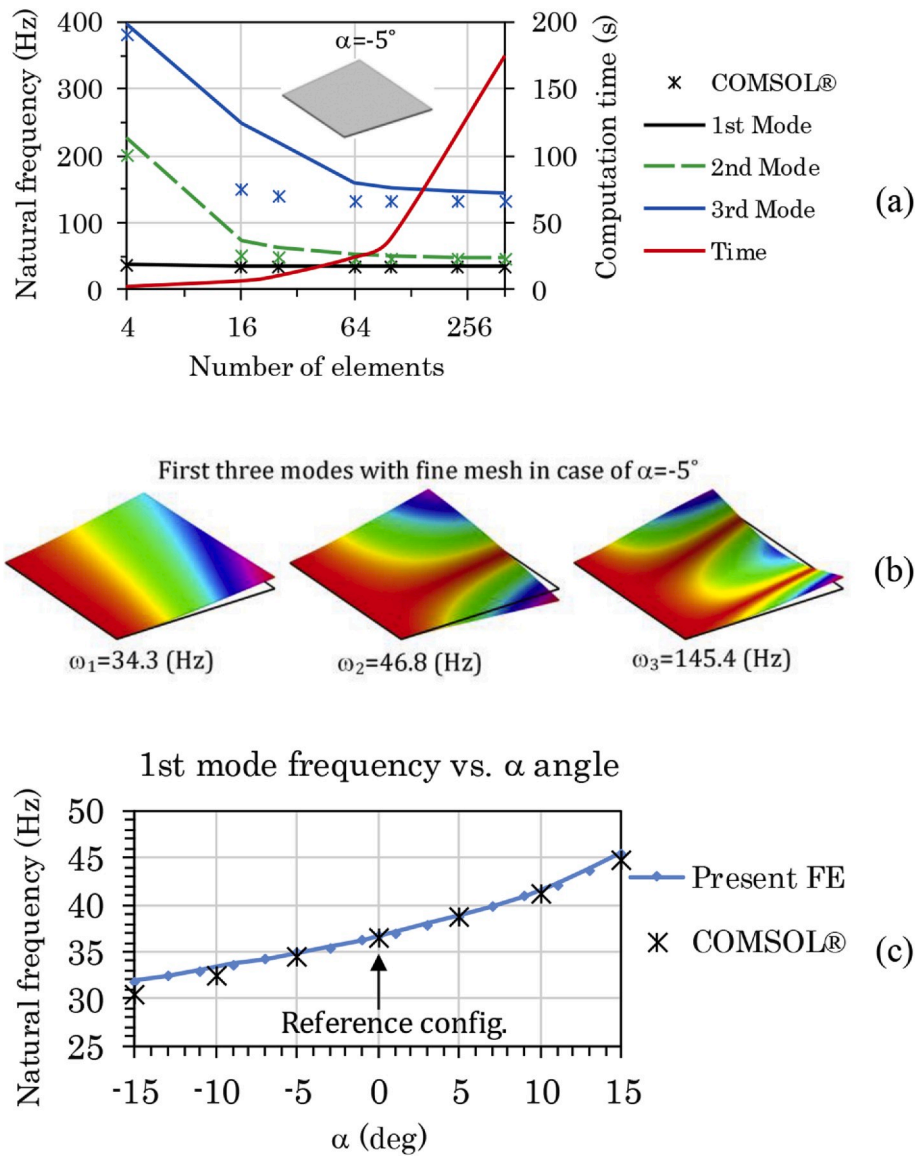


**Fig. 7.** (a) Comparison results between the present FE and COMSOL® software at standard configuration, (b) the first three bending modes at $\alpha = -5^{\circ}$ in different element numbers, (c) the first natural frequency variation versus $\alpha$ with 24 elements.

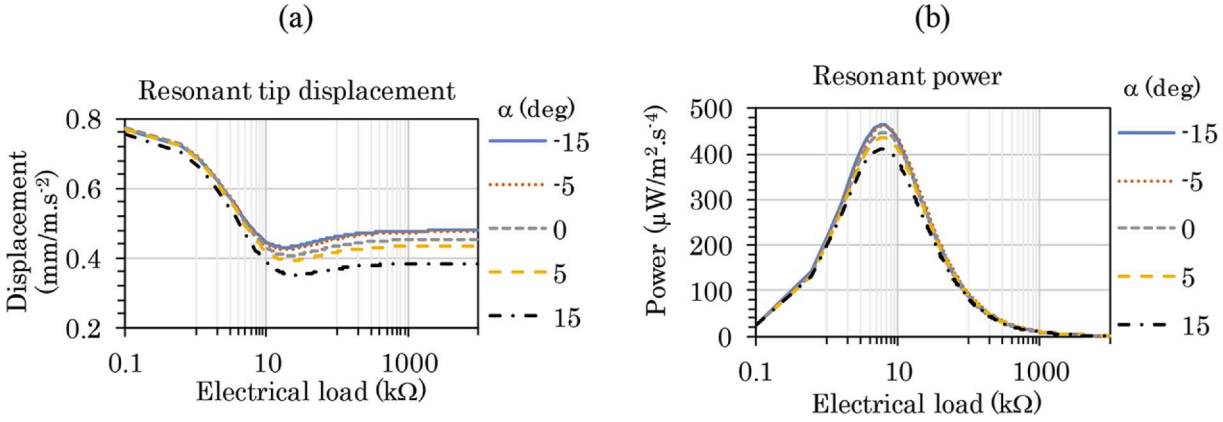


**Fig. 8.** The effect of beam trapezoid angle versus the electrical load on the (a) tip deflection, (b) power output in the first bending mode.

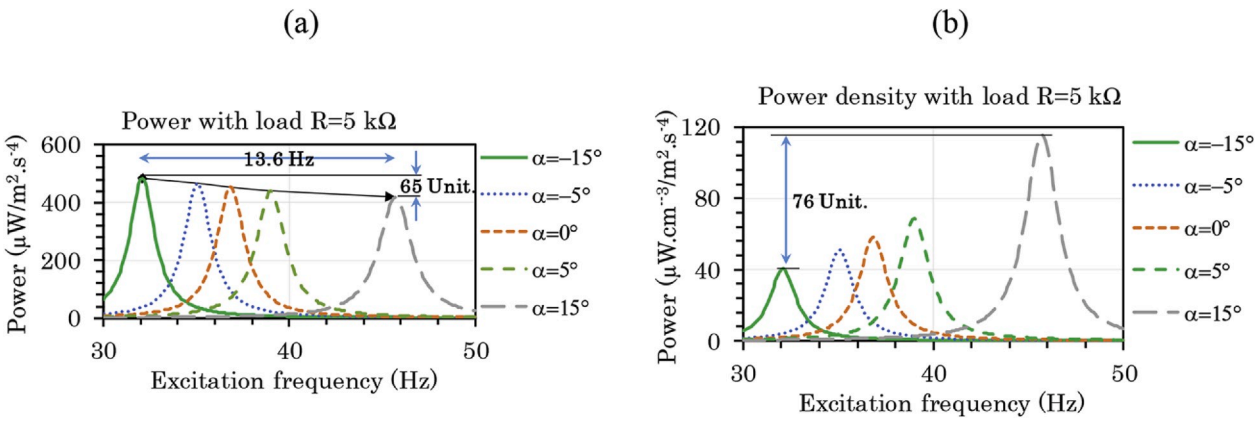


**Fig. 9.** (a) Power and (b) power density versus excitation frequency for different taper angles.

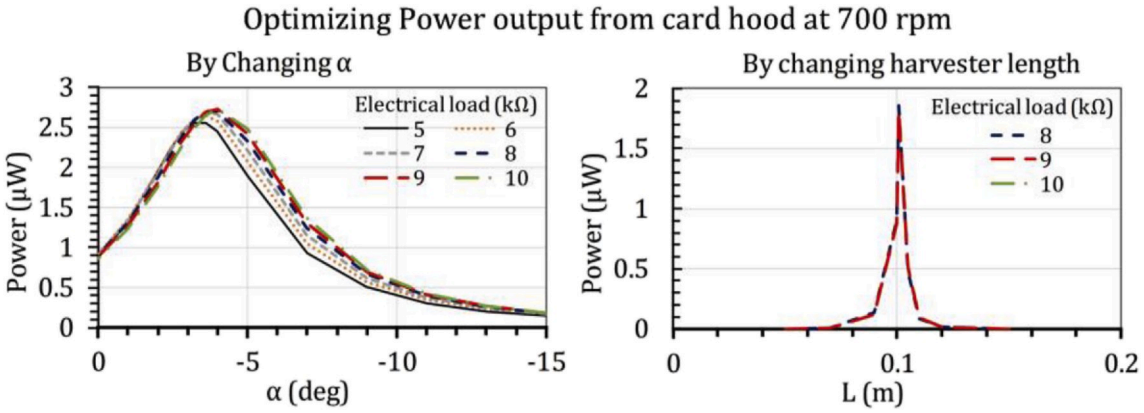


**Fig. 10.** Power generation from a car hood working at 700 rpm versus (a) extended angle and (b) PEH length.

is to change $\alpha$, while in the second approach, the PEH length is tuned. Fig. 10 shows the results for these two optimization approaches. The maximum power outputs in these two approaches are respectively 2.73 μW for $\alpha = 4^\circ$ and 1.87 μW for L = 0.101 m at 10 kΩ electrical load. The power output in the $\alpha$-tuning approach is 45% greater than the power in the L-tuning approach.

### 4.2. Variation of fiber rotation in active and substrate layers

Contours shown in Fig. 11 present the PEH optimum resonant power and natural frequency with respect to the fiber orientations in the substrate and piezoelectric layers for $\alpha = 0^\circ$ and $-15^\circ$. Overall, the natural frequency and the resonant power of $\alpha = -15^\circ$ case are respectively lower and higher than that of the case with $\alpha = 0^\circ$. In Fig. 11, the contours show that, $\theta_p$ has greater impact on the natural frequency than $\theta_s$ due to the smaller thickness of the substrate layer. As can be seen from the contours in Fig. 11 (a) and (b), the PEH optimal performance can be obtained by only optimizing $\theta_p$ and setting $\theta_s$ constant. For instance, in $\alpha = 0^\circ$ configuration, changing $\theta_p$ from 0° to 40°, while $\theta_s = 0^\circ$, increases the power generation from 440 to 514.6 $\mu W/m^2.s^{-4}$, and decreases the natural frequency from 37.8 to 17.7 Hz. A similar trend can be also seen for $\alpha = -15^\circ$. Based on the aforementioned argument, only optimization of the $\theta_p$ can derive the practical optimal design. Therefore, further investigation of $\theta_s$ is not proceeded in this study.

Fig. 12 shows the resonant power, the power density and the resonant frequency versus $\theta_p$. There is a symmetric line at $\theta_p = 90^\circ$ and, therefore, the same behavior can be seen between 90° and 180°. Starting from $\theta_p = 0^\circ$ to 90°, the power generation increases until the optimal fiber direction, $\theta_{opt} = 35^\circ$. The second significant local maxima occurs at $\theta_p = 75^\circ$. The maximum power output at $\theta_{opt}$ is identical for the $\alpha_{-15^\circ}$, $\alpha_{0^\circ}$ and $\alpha_{15^\circ}$ cases. If the PEH volume is a significant design parameter, then the power density, Fig. 12 (b), will be of interest. The case with $\alpha_{15^\circ}$ offers highest power density. The optimal power density for $\alpha_{15^\circ}$ is 117% higher than the $\alpha_{0^\circ}$ case. The natural frequency of the PEH is another important parameter. The resonant frequency, as shown in Fig. 12 (c), reduces until $\theta_p = 45^\circ$ and then increases, however one should be careful about the dramatic power drop after $\theta_p = 40^\circ$. The PEH with $\alpha_{-15^\circ}$ has the lowest natural frequency. For instance, at $\theta_{opt}$, the natural frequency for the cases with $\alpha_{-15^\circ}$ and $\alpha_{15^\circ}$ are 17% lower and 25% higher, respectively, compared to the case with $\alpha_{0^\circ}$. To sum up, an optimal region for the resonant power can be defined as $\theta_p \in [30^\circ, 40^\circ]$, where $\alpha$ is viewed as a tuning factor for the natural frequency matching.

In order to observe the influence of the piezoelectric fiber orientation on the performance of a PEH, out-of-place displacement $r_z$, normal strain $S_{xx}$ and electrical displacement $D_z$ at the mid-plane of the active piezoelectric layer are shown in Fig. 13. The base excitation for the results in Fig. 13 is 1 $m/s^2$ at the fundamental natural frequency of each configuration. Therefore, as the natural frequencies for $\theta_p = 0^\circ$ and 35° are respectively 37.8 Hz and 24.1 Hz, the magnitude of the base excitation displacement reach 17.7 μm and 43.6 μm, respectively. In overall, uniform and symmetric contours are resulted from $\theta_p = 0^\circ$ fiber orientation, while the contours are distorted with circular patterns for $\theta_p = 35^\circ$. This implies that, while the first mode in $\theta_p = 0^\circ$ is a pure bending mode, it is a mix bending-torsion mode in $\theta_p = 35^\circ$ case because of the non-uniform bending stiffness due to the fiber orientation. This bending-torsion mode at $\theta_p = 35^\circ$ causes non-uniform circular patterns in the normal strain and electrical displacement field in the piezoelectric layer.

Improving the normal strain contour on the PEH surface area im-

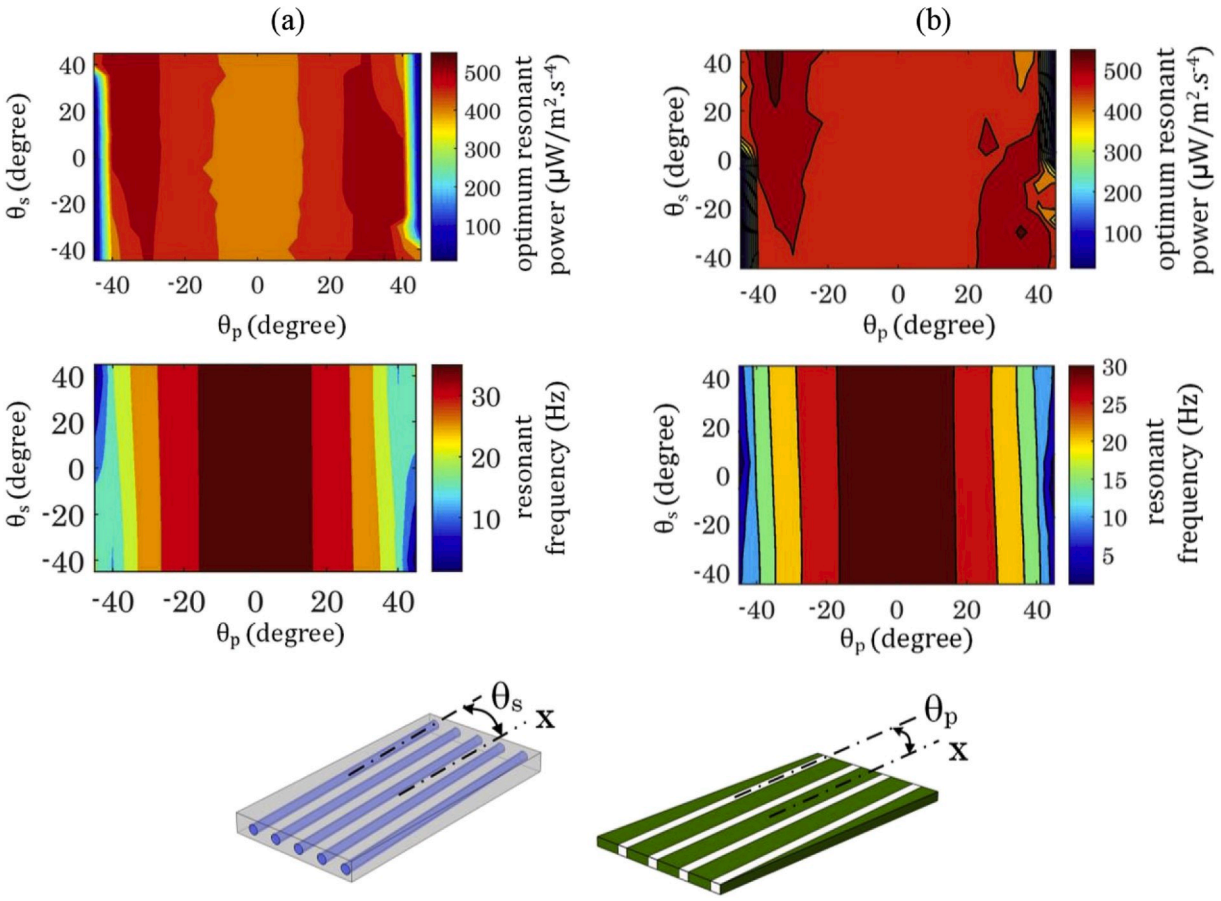


**Fig. 11.** Contours for optimum resonant power with $R = 6$ kΩ and fundamental natural frequency for (a) $\alpha = 0^\circ$ and (b) $\alpha = -15^\circ$.

proves the PEH power generation. This can be achieved by reducing the PEH stiffness in $x$-direction, which is equivalent to increment in $\theta_p$. By looking into the strain and electrical displacement contours for $\theta_p = 35^\circ$, the improvements of these parameters can be clearly seen in comparison with the $\theta_p = 0^\circ$ case. For instance, the maximum value of $S_{xx}$ in $\theta_p = 0^\circ$ and $\alpha = 0^\circ$ case is $4.5 \times 10^{-7}$ m/m while it is $8.0 \times 10^{-7}$ m/m in the case with $\theta_p = 35^\circ$ and $\alpha = 0^\circ$. Moreover, the magnitude of $D_z$ at the optimum fiber orientation is greater than that of the $\theta_p = 0^\circ$ case. The $D_z$ in $\theta_p = 0^\circ$ is approximately $-1.3 \times 10^{-4}$ C m$^{-2}$ while this figure lies in [-1.45,-1.85] $\times 10^{-4}$ C m$^{-2}$ in $\theta_p = 35^\circ$. Due to the greater $D_z$ at $\theta_{opt}$, the power generation is greater than zero-fiber angle. This fact is valid for all the studied cases, $\alpha_{-15^\circ}$, $\alpha_{0^\circ}$, and $\alpha_{15^\circ}$, as was shown in Fig. 12.

For the case with $\theta_p = 0^\circ$, $S_{xx}$ and $D_z$ has the greatest value near the clamped-line. These figures gradually reduce toward the beam free-end. Therefore, in this fiber orientation, a large portion of the piezoelectric layer has low contribution in the power generation. Nonetheless, these patterns distort for the $\theta_p = 35^\circ$ case, so that the regions close to the free-end generate more power than the regions close to the clamped-line. To quantify the power generation contributions of different surface regions, the beam is divided into seven equal regions, and then the average $D_z$ over each partition area is calculated. Fig. 14 presents the average $D_z$ values over the partition areas for different $\alpha$s and $\theta_p$s. In the common PEHs with zero-fiber-orientation MFCs, the regions near the clamped-end generate more power compared to the free-end region. Nevertheless, in the optimal piezoelectric fiber orientation where $\theta_p = 35^\circ$, the regions near the free-end have greater $D_z$ value. In the other words, the role of unproductive surface regions near the free-end becomes more prominent by changing the strain contours in the piezoelectric layer. Consequently, the voltage potential in the whole PEH area is higher compared to the uniform strain contours.

The electrical displacement field ($D_z$) in the poling direction for two cases, i.e. $\alpha_{-15^\circ}$ and $\alpha_{15^\circ}$, at $\theta_{opt}$ are shown in Fig. 15 when the external electrical load is 6 kΩ. The $D_z$ magnitude for $\alpha_{-15^\circ}$ is approximately 10% higher than the $\alpha_{15^\circ}$ case. This also can be interpreted from Fig. 14, which illustrates the greater average $D_z$ in the all beam area for $\alpha_{-15^\circ}$. However, one can observes resemble patterns by comparing the patterns in Fig. 15 for both $\alpha_{-15^\circ}$ and $\alpha_{15^\circ}$ cases, which are completely different from the uniform contours for the $\theta_p = 0^\circ$. In a 3-1 mode piezoelectric harvester, the voltage generation is proportional to the normal strain. In the case $\theta_p = \theta_{opt}$, the structural stiffness matrix differs from that of the case $\theta_p = 0^\circ$ and, therefore, the strains are not identical between these cases. It causes different patterns of the electric displacement field between the cases where $\theta_p = \theta_{opt}$ and $\theta_p = 0^\circ$.

## 5. Summary and discussion on the proposed design in practical cases

In subsections 4.1 and 4.2, the variations of the output power and natural frequency were investigated with respect to the variations in the beam cross-section area and piezoelectric fiber orientation. It was shown that, changing the cross-section area causes a considerable shift in the natural frequency. In addition, setting the piezoelectric fiber orientation in the MFC to an optimum angle enhances the electrical displacement field over the surface so that the power generation increases considerably. Table 5 presents summary of the results obtained through the sensitivity studies in sections 4.1 and 4.2. For cases that $\alpha < 0$, both of the natural frequency and power density decrease while the power generation increases. These variations have opposite pattern for $\alpha > 0$. The power density can be increased by 95% only with changing $\alpha$ from 0° to 15°. The power density can be further increased by a factor of

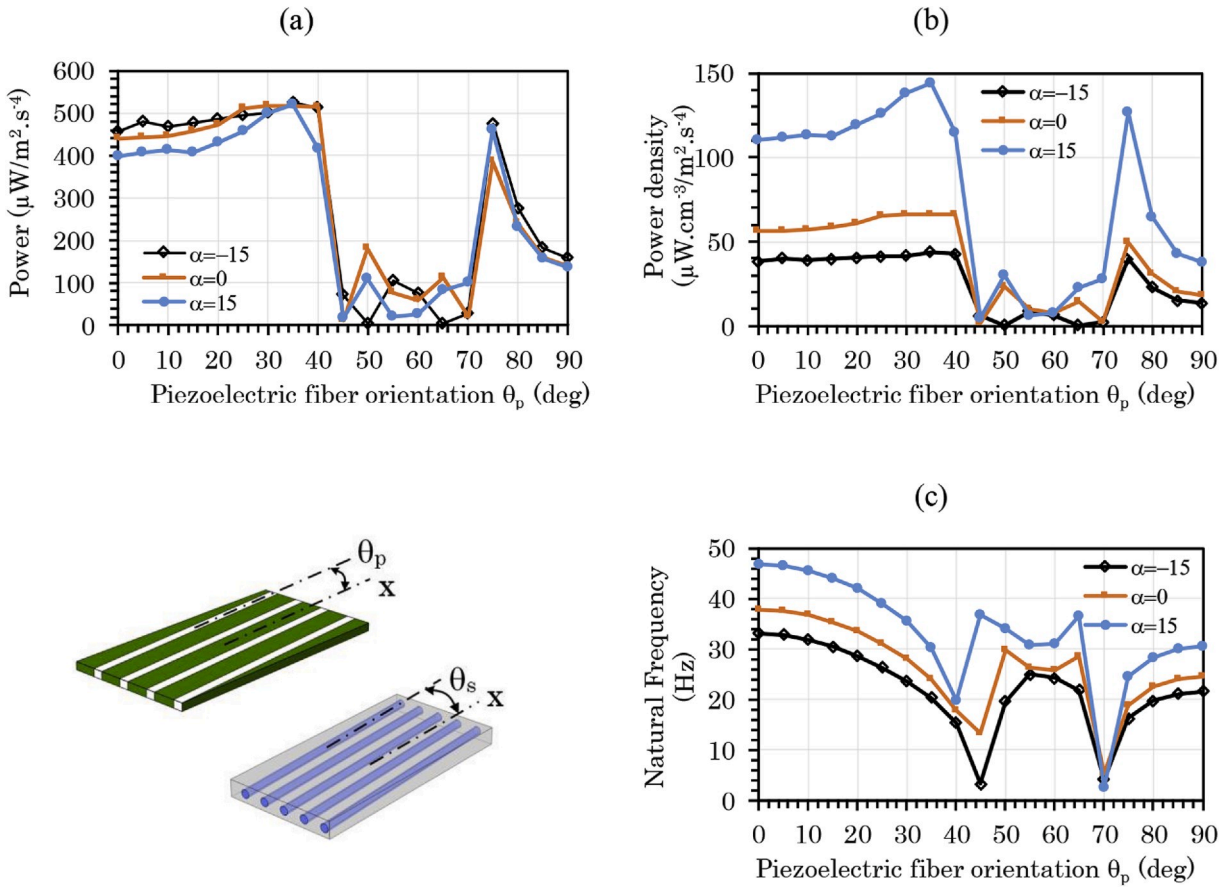


**Fig. 12.** (a) Resonant power, (b) power density and (c) fundamental natural frequency versus piezoelectric fiber orientation.

155% with setting $\theta_p = \theta_{opt}$ offering a remarkable change in the power density. In addition, changing the taper angle from −15° to 15° results a variation in the natural frequency from −12.4% to +23%. By setting $\theta_p = \theta_{opt}$, the natural frequency can be further reduced by 46%. Moreover, if the PEH volume is not a critical design parameter and only the power generation is of interest, a design case with $\alpha$ = -15° and $\theta_p = \theta_{opt}$ gives a 19% increment in the power generation. Overall, the optimum design is the configuration with $\alpha$ = 15° and $\theta_p = \theta_{opt}$, which has the greatest power density and an 18%-increased output power. In this optimum design, the output voltage and current are respectively 1.77 V/m.s$^{-2}$ and 294.8 μA/m.s$^{-2}$ resulting an output power of 521.31 μW/m$^2$.s$^{-4}$.

The studied parameters, fiber orientation and tapered/extended angles, provide a great suppleness in the PEH design so that a wide range of operation conditions can be covered with an identical design. Although the investigated example is in cm-scale, the optimum PEH design, with considerably greater power density, can also be used for small-scale energy harvesting. In particular, using fiber orientation to create the desirable strain contour is highly beneficial for small-scale PEH designs as it increases the power density noticeable by employing whole the harvester surface for power generation. In addition, the reasonably good flexibility of the MFC extends the applications of the current design toward small-scale flexible electronics.

To show the application of the proposed PEH design in practice, an energy-harvesting device is designed for a practical wideband vibration source. In practice, the vibrational sources may have variable vibration emissions in terms of frequency spectrum or acceleration magnitude, depending on the operational condition. In addition, frequency of a vibration signal from a practical vibration source does not only point out to a specific frequency, but normally the signal has high acceleration amplitudes over a frequency range. To clear this point, experimental vibration signals from a moving car, as a practical vibration source, was considered in this study. The experimental vibration data is retrieved from the real vibration data base [36]. The car under the study was Grande Punto diesel equipped with an accelerometer and a data acquisition system. The acceleration data was recorded for 60 s in three directions with the sample rate of 20 kHz. The time signal and Fourier transform, obtained using Fast Fourier Transform (FFT), are shown in Fig. 16 in $g_0 = 9.81$ m/s$^2$ unit. The root mean square of the time signal is equal to $0.21g_0$ and the acceleration has a peak of $0.033g_0$ at 29.64 Hz. The frequency spectrum of the acceleration shows that, the acceleration is always higher than $0.011g_0$ in a frequency sweep of 9 Hz, between 26 and 35 Hz. Using a single energy harvester with the matched natural frequency for the vibration of 29.64 Hz, will waste the vibrational energy available in the other frequencies. One solution for tackling this issue is to broaden the frequency bandwidth of the PEH. Using multi-resonant beam [14], placing a stopper along beam length [37] and tapered beam with cavity [13] can be named as some solutions for broadband power generation. In this study, it is considered that, a number of harvester beams with different $\alpha$ but the same $\theta_p$ are mounted on a base plate, so that each energy harvester covers a frequency range but, overall, all of these PEHs cover a broad bandwidth together.

According to the FFT of time signals of the car vibration, the frequency range of interest chosen to be [25,35] Hz, where the magnitude of the acceleration is high compared to the other frequencies. To cover this frequency range, we considered five harvester beams with $\theta_p = \theta_{opt}$ and different $\alpha$s, i.e. $\alpha$ = 3°, 7°, 11°, 15°, and 19°, while keeping the material properties as used through this study. Fig. 17 (a) shows a schematic of the proposed energy harvester. To show the superiority of the proposed method over the common multi-beam harvesters, a common harvester, as shown in Fig. 17 (b), with variable beam lengths, i.e. L = 105, 110, 115, 120, and 125 mm, is furthermore investigated. In the proposed design, the power output has a broader bandwidth due to

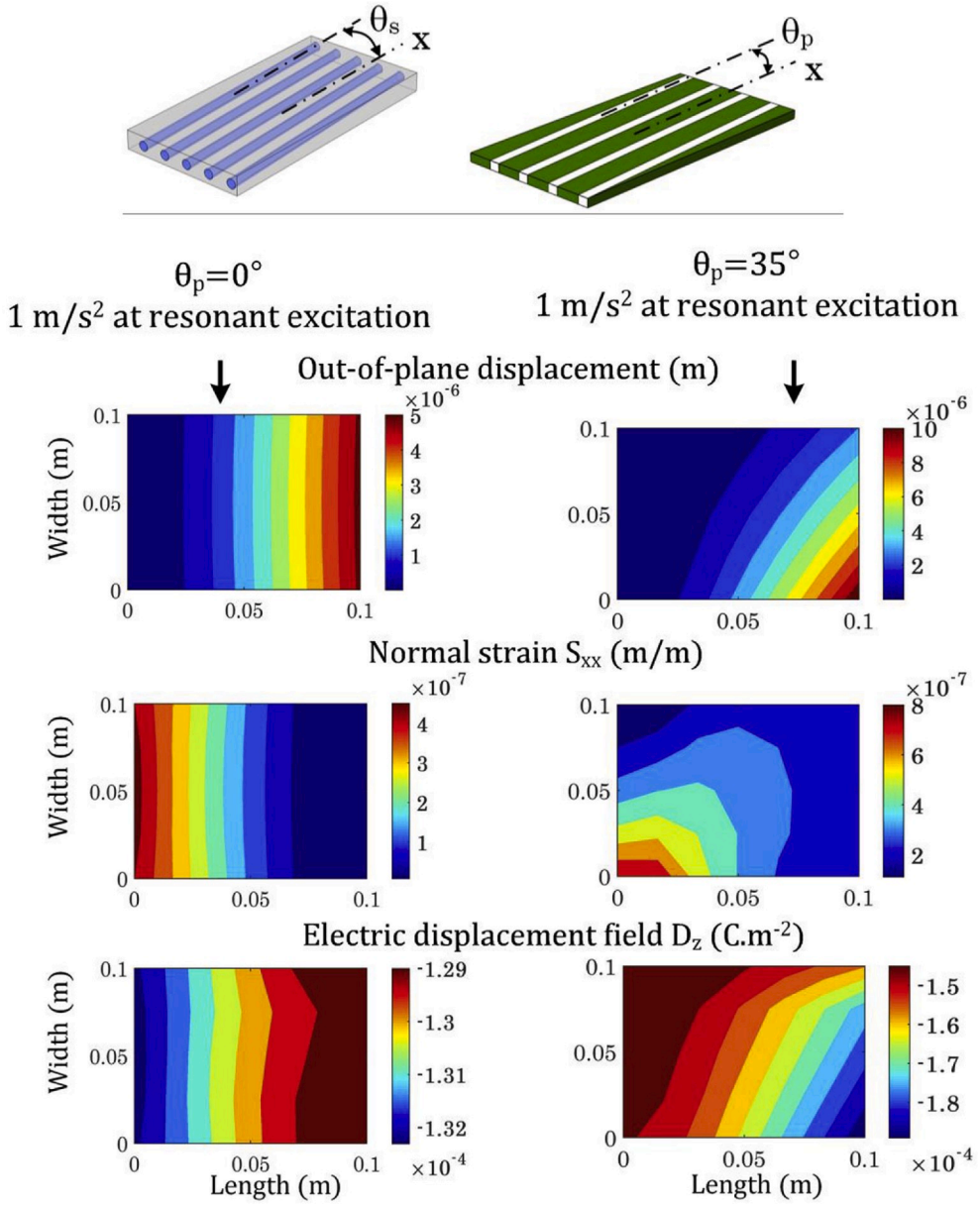


**Fig. 13.** Out-of-plane displacement ($r_z$), normal strain ($S_{xx}$), and electric displacement field in poling direction ($D_z$) with $R = 6$ kΩ versus fiber orientation ($\theta_p$=0° and $\theta_{opt}$) for $\alpha = 0°$.

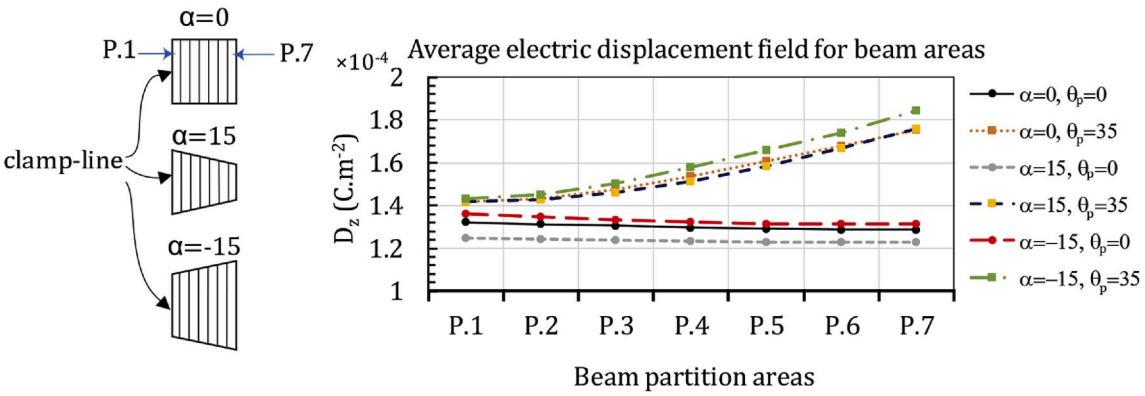


**Fig. 14.** Average electric displacement field ($D_z$) with $R = 6$ kΩ for different $\alpha$ and $\theta_p$ over the seven partition areas of the beam.

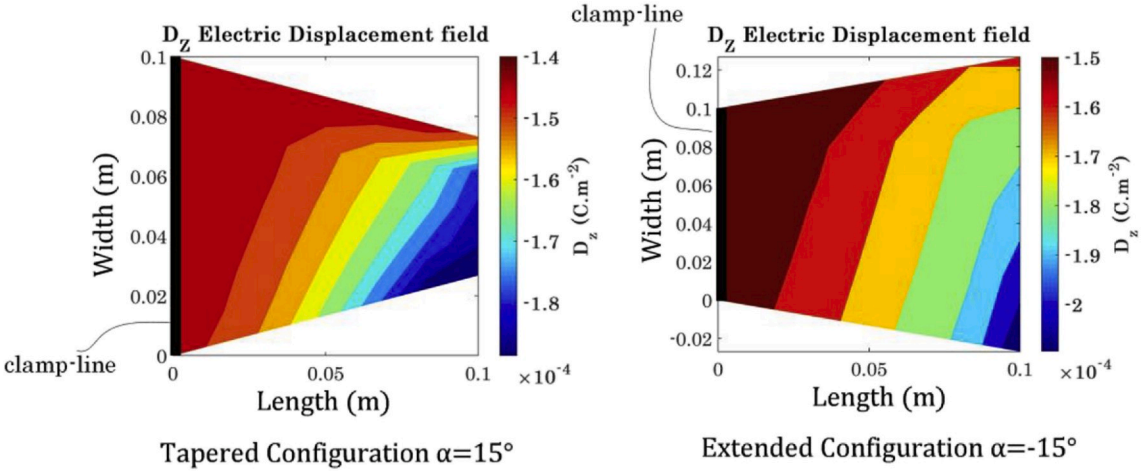


**Fig. 15.** Electrical displacement field in poling direction for mid-surface of the active layer with $R = 6$ kΩ for $\theta_{opt}$ piezoelectric fiber orientation at $\alpha = -15°$ and 15°.

**Table 5**
Summary of the sensitivity results of $\alpha$ and $\theta_p$ on the natural frequency, power generation and power density when $R = 6$ kΩ.

| Parameter | Natural frequency | | Power | | Power density[b] | |
|---|---|---|---|---|---|---|
| | Value (Hz) | Variation[a] (%) | Value (μW/m$^2$.s$^{-4}$) | Variation[a] (%) | Value (μW.cm$^{-3}$/m$^2$.s$^{-4}$) | Variation[a] (%) |
| $\alpha = 0, \theta_p = 0$ | 37.81 | – | 440.03 | – | 56.41 | – |
| $\alpha = -15, \theta_p = 0$ | 33.11 | −12.43 | 457.50 | 3.97 | 38.19 | −32.31 |
| $\alpha = +15, \theta_p = 0$ | 46.73 | 23.59 | 399.22 | −9.27 | 110.28 | 95.49 |
| $\alpha = 0, \theta_p = \theta_{opt}$ | 24.06 | −36.37 | 518.24 | 17.77 | 66.44 | 17.77 |
| $\alpha = -15, \theta_p = \theta_{opt}$ | 20.40 | −46.05 | 524.64 | 19.23 | 43.79 | −22.37 |
| $\alpha = +15, \theta_p = \theta_{opt}$ | 30.31 | −19.84 | 521.31 | 18.47 | 144.01 | 155.27 |

[a] Variation is compared to the $\alpha = \theta_p = 0$ design case.
[b] Power density is calculated based on the PEH device volume.

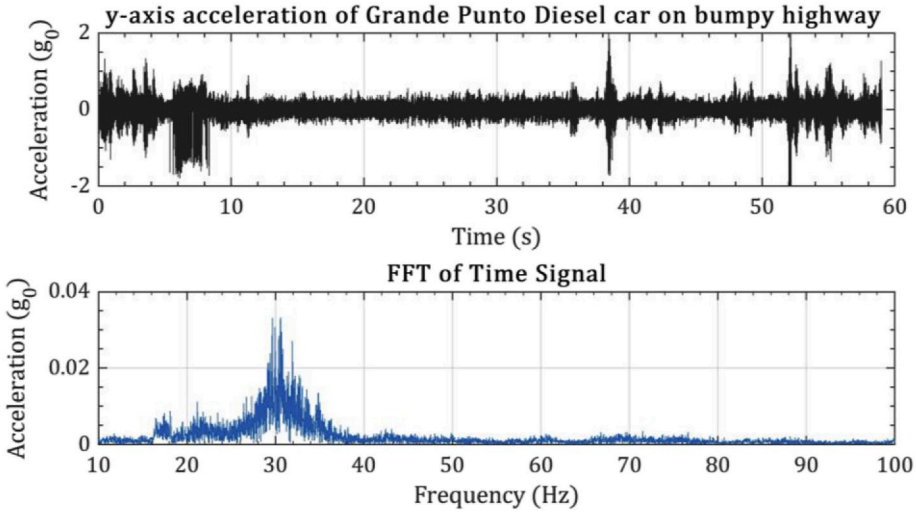


**Fig. 16.** Time signal and Fourier transform of y-axis acceleration signal from Grande Punto diesel car moving on bumpy highway configurations [36].

different $\alpha$s while in the common design the power output is broadband due to the different lengths. The power generation curves with R = 10 kΩ over frequency of 10–50 Hz are shown in Fig. 17 (a) for the both designs. The power output for the present design has a maximum value of 111.3 mW/$g_0^2$. Due to setting the fiber orientation to $\theta_{opt}$, this value is approximately 50% higher than the maximum power with the common design. This power improvement can be seen over the whole frequency range. In addition, due to the very narrow power bandwidth from each beam in the common design, the power curve in the common design has a fluctuation pattern. In contrast, in the present design power has a smaller amplitude fluctuating pattern.

According to Khazaee et al. [38], when the frequency spectrum of a practical signal is present, the power-frequency curve can be estimated by considering each point in the frequency domain as a single harmonic

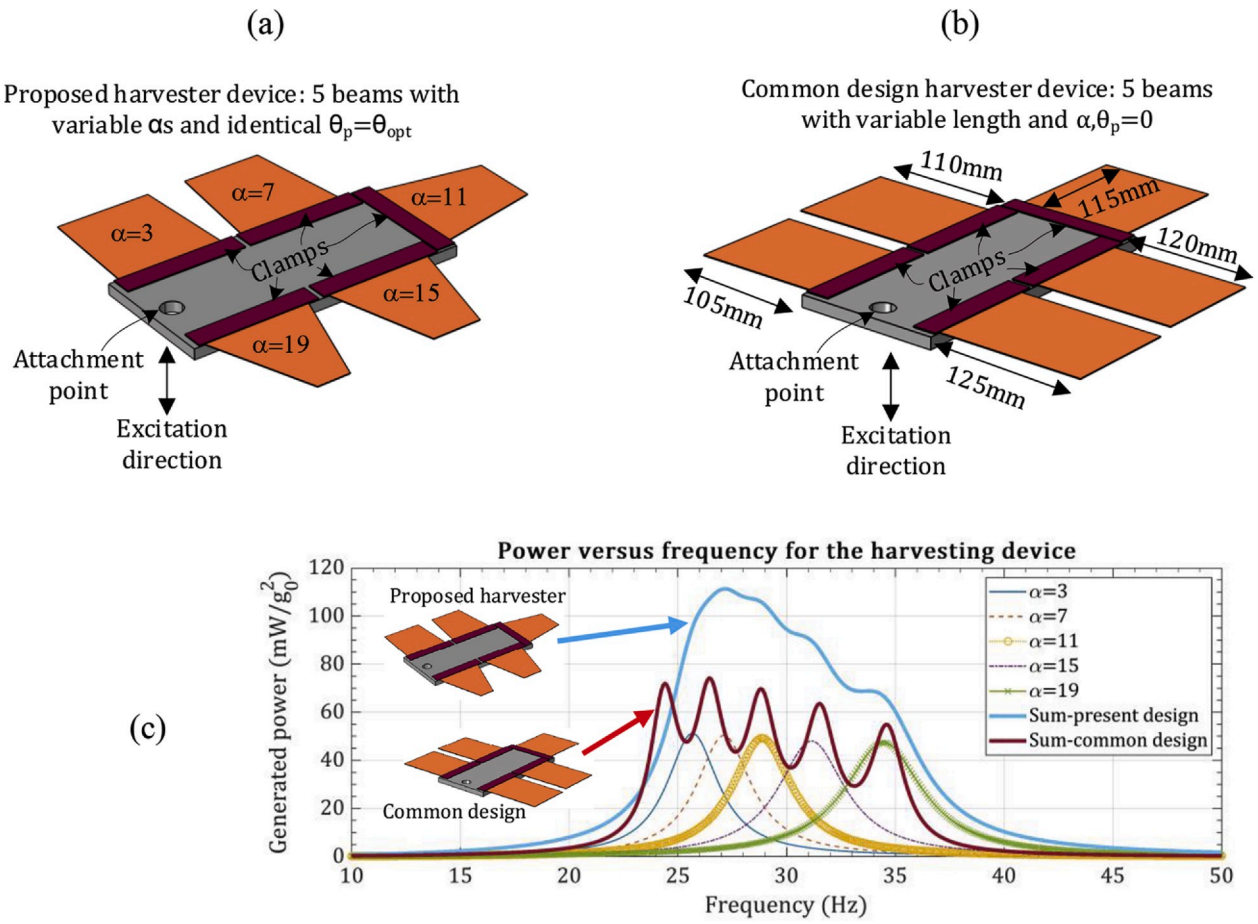


**Fig. 17.** (a) Proposed harvester design, (b) a common multi beam with variable lengths, and (c) power generation for the PEH devices as a summation of all five beams.

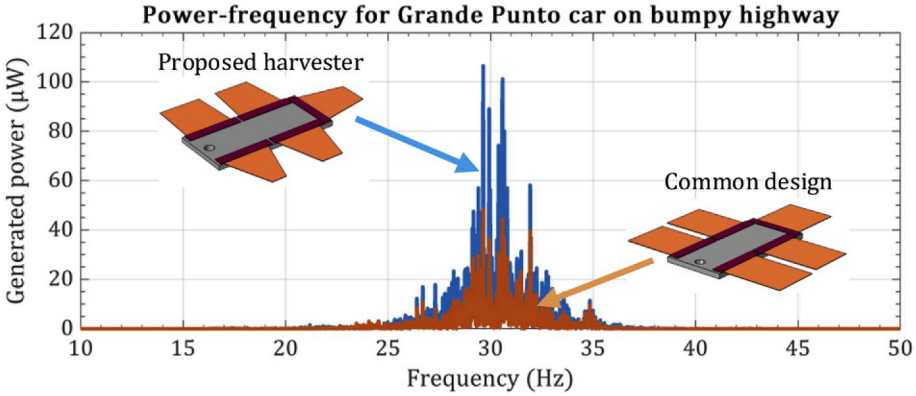


**Fig. 18.** Demonstration of power generation with car excitation for two harvesting devices proposed in Fig. 17 over 10–50 Hz frequency range.

excitation. Finally, in a linear time invariant system, the total power generation is the summation of the power generation for each frequency. By multiplying the power spectrums for the present and common designs to the square magnitude of the car acceleration signal, shown in Fig. 16 (c), one can estimate the power output from the PEH devices. Fig. 18 presents the power output with R = 10 kΩ in the considered range of frequency, where the acceleration amplitude is greater than the other frequencies. The power output for the proposed PEH is considerably higher, compared with the commonly designed PEH. After implementing the series summation of the power output at the all frequencies, the total power is obtained 5.26 and 2.85 mW for the proposed and common designs, respectively, showing a vivid increase of 84.6% in the total power generation. If only the harvesting beams are considered to calculate the volume of the device, the proposed energy-harvesting device has a volume of 23.7 $cm^3$, while the common design PEH has volume of 44.9 $cm^3$. Consequently, the power density in the proposed device is 222.1 $\mu W/cm^3$ that is 160% higher than the power density in the common design.

## 6. Conclusion

In this paper, an initiative configuration for PEH with MFCs, as the

active layers, was proposed for achieving higher energy harvesting performance. Three controlling parameters were introduced in the PEH design, namely taper or extended cross-section angles, piezoelectric fiber rotation and substrate fiber rotation. The results showed that, the taper or extended angle has a great impact on the natural frequency of the PEH and, at the same time, the taper angle causes a significant increment in the power density. Rotation of the substrate fiber has small impact, compared to rotation of the piezoelectric fiber because of the small substrate thickness compared to the piezoelectric layer. On the other hand, by changing the PZT fiber orientation in the MFC, the power generation increased dramatically due to the modification in the strain contours over the beam area. Finally, by using the proposed design method, a broadband energy harvester consisting of five harvesting beams was optimized for power generation from a moving car. The results showed that, the power output is 85% higher in 47% reduced volume, compared to the common design with five rectangular beams. The results of this study provide a guideline for geometry optimization of flexible PEH modules with MFCs for maximizing the energy harvesting performance.

## Declaration of competing interest

The authors declare that they have no known competing financial interests or personal relationships that could have appeared to influence the work reported in this paper.

## CRediT authorship contribution statement

**Majid Khazaee:** Conceptualization, Data curation, Formal analysis, Investigation, Methodology, Software, Writing - original draft, Validation. **Alireza Rezaniakolaie:** Conceptualization, Methodology, Investigation, Validation, Writing - review & editing, Supervision. **Lasse Rosendahl:** Methodology, Supervision.

## References


[1] F. Narita, M. Fox, A review on piezoelectric, magnetostrictive, and magnetoelectric materials and device technologies for energy harvesting applications, Adv. Eng. Mater. 20 (2018) 1–22, https://doi.org/10.1002/adem.201700743.

[2] H. Li, C. Tian, Z.D. Deng, Energy harvesting from low frequency applications using piezoelectric materials, Appl. Phys. Rev. 1 (2014), 041301, https://doi.org/10.1063/1.4900845.

[3] S. Roundy, P.K. Wright, J. Rabaey, A study of low level vibrations as a power source for wireless sensor nodes, Comput. Commun. 26 (2003) 1131–1144, https://doi.org/10.1016/S0140-3664(02)00248-7.

[4] R. Caliò, U. Rongala, D. Camboni, M. Milazzo, C. Stefanini, G. de Petris, C. Oddo, Piezoelectric energy harvesting solutions, Sensors 14 (2014) 4755–4790, https://doi.org/10.3390/s140304755.

[5] A.G.A. Muthalif, N.H.D. Nordin, Optimal piezoelectric beam shape for single and broadband vibration energy harvesting: modeling, simulation and experimental results, Mech. Syst. Signal Process. 54 (2015) 417–426, https://doi.org/10.1016/j.ymssp.2014.07.014.

[6] H. Hu, L. Tang, R. Das, P. Marzocca, A two-degree-of-freedom piezoelectric energy harvester with stoppers for achieving enhanced performance, Int. J. Mech. Sci. 149 (2018) 500–5007.

[7] A. Lei, E.V. Thomsen, Wideband piezomagnetoelastic vibration energy harvesting, J. Phys. Conf. Ser. 557 (2014), 012121, https://doi.org/10.1088/1742-6596/557/1/012121.

[8] C. Wang, Q. Zhang, W. Wang, Low-frequency wideband vibration energy harvesting by using frequency up-conversion and quin-stable nonlinearity, J. Sound Vib. 399 (2017) 169–181, https://doi.org/10.1016/j.jsv.2017.02.048.

[9] Y. Sun, J. Chen, X. Li, Y. Lu, S. Zhang, Z. Cheng, Flexible piezoelectric energy harvester/sensor with high voltage output over wide temperature range, Nano Energy 61 (2019) 337–345, https://doi.org/10.1016/J.NANOEN.2019.04.055.

[10] H. Yang, M. Deng, Q. Tang, W. He, C. Hu, Y. Xi, R. Liu, Z.L. Wang, A nonencapsulative pendulum-like paper–based hybrid nanogenerator for energy harvesting, Adv. Energy Mater. 9 (2019) 1–8, https://doi.org/10.1002/aenm.201901149.

[11] H. Yang, M. Deng, Q. Zeng, X. Zhang, J. Hu, Q. Tang, H. Yang, C. Hu, Y. Xi, Z. L. Wang, Polydirectional microvibration energy collection for self-powered multifunctional systems based on hybridized nanogenerators, ACS Nano 14 (2020) 3328–3336, https://doi.org/10.1021/acsnano.9b08998.

[12] D. Bhatia, W. Kim, S. Lee, S.W. Kim, D. Choi, Tandem triboelectric nanogenerators for optimally scavenging mechanical energy with broadband vibration frequencies, Nano Energy 33 (2017) 515–521, https://doi.org/10.1016/j.nanoen.2017.01.059.

[13] U. Ramalingam, U. Gandhi, U. Mangalanathan, S.-B. Choi, A new piezoelectric energy harvester using two beams with tapered cavity for high power and wide broadband, Int. J. Mech. Sci. 142 (2018) 224–234.

[14] S. Qi, R. Shuttleworth, S.O. Oyadiji, J. Wright, Design of a multiresonant beam for broadband piezoelectric energy harvesting, Smart Mater. Struct. 19 (2010), https://doi.org/10.1088/0964-1726/19/9/094009.

[15] S.M. Shahruz, Design of mechanical band-pass filters with large frequency bands for energy scavenging, Mechatronics 16 (2006) 523–531, https://doi.org/10.1016/j.mechatronics.2006.04.003.

[16] S.-W. Kim, Tae-Gon Lee, D.-H. Kim, K.-T. Lee, I. Jung, C.-Y. Kang, S.H. Han, H.-W. Kang, S. Nah, Determination of the appropriate piezoelectric materials for various types of piezoelectric energy harvesters with high output power, Nano Energy 57 (2019) 581–591.

[17] S.S. Won, H. Seo, M. Kawahara, S. Glinsek, J. Lee, Y. Kim, C.K. Jeong, A.I. Kingon, S.-H. Kim, Flexible vibrational energy harvesting devices using strain-engineered perovskite piezoelectric thin films, Nano Energy 55 (2019) 182–192, https://doi.org/10.1016/J.NANOEN.2018.10.068.

[18] Smart Material Inc., 2020. April.

[19] M. Khazaee, A. Rezaniakolaei, L. Rosendahl, An experimental study on macro Piezoceramic fiber composites for energy harvesting, Mater. Sci. Forum 951 (2019) 3–8. https://doi.org/10.4028/www.scientific.net/MSF.951.3.

[20] D. Shen, A, Piezoelectric Energy Harvesting Devices for Low Frequency Vibration Applications, Auburn University, 2009.

[21] A.J. Lee, D.J. Inman, Electromechanical modelling of a bistable plate with Macro Fiber Composites under nonlinear vibrations, J. Sound Vib. 446 (2019) 326–342, https://doi.org/10.1016/j.jsv.2019.01.045.

[22] M.S. Azzouz, J.S. Bevana, J.J. Rob, C. Mei, Finite element modeling of MFC/AFC actuators, Smart Struct. Mater. 2001 Model. Signal Process. Control Smart Struct. 4326 (2001) 376–387, https://doi.org/10.1106/AGN1-XVKP-DGDB-XMF4.

[23] Y. Yang, L. Tang, H. Li, Vibration energy harvesting using macro-fiber composites, Smart Mater. Struct. 18 (2009), https://doi.org/10.1088/0964-1726/18/11/115025.

[24] M. Khazaee, L. Rosendahl, A. Rezaniakolaei, A comprehensive electromechanically coupled model for non-uniform piezoelectric energy harvesting composite laminates, Mech. Syst. Signal Process. 145 (2020) 106927, https://doi.org/10.1016/j.ymssp.2020.106927.

[25] G. Shi, A new simple third-order shear deformation theory of plates, Int. J. Solid Struct. 44 (2007) 4399–4417, https://doi.org/10.1016/j.ijsolstr.2006.11.031.

[26] C.R. Bowen, V.Y. Topolov, H.A. Kim, Modern Piezoelectric Energy-Harvesting Materials, first ed., Springer, 2016 https://doi.org/10.1007/978-3-319-29143-7.

[27] A. Deraemaeker, H. Nasser, A. Benjeddou, A. Preumont, Mixing rules for the piezoelectric properties of macro fiber composites, J. Intell. Mater. Syst. Struct. 20 (2009) 1475–1482, https://doi.org/10.1177/1045389X09335615.

[28] R.M. Jones, Mechanics of Composite Materials, second ed., Taylor & Francis, Philadelphia, 2010 https://doi.org/10.1016/B978-0-444-99713-5.50002-6.

[29] J.N. Reddy, On laminated composite plates with integrated sensors and actuators, Eng. Struct. 21 (1999) 568–593, https://doi.org/10.1016/S0141-0296(97)00212-5.

[30] K. Pazand, A.S. Nobari, Identification of the effect of debonding on the linear and nonlinear effective damping of an adhesive joint, J. Sound Vib. 380 (2016) 267–278.

[31] R.B. Williams, D.J. Inman, Nonlinear Mechanical and Actuation Characterization of Piezoceramic Fiber Composites, Virginia Polytechnic, 2004.

[32] S. Sreenivasa Prasath, A. Arockiarajan, Influence of bonding layer on effective electromechanical properties of macro-fiber composites (MFCs), Smart Mater. Struct. 23 (2014), https://doi.org/10.1088/0964-1726/23/9/095046.

[33] C. De Marqui Junior, A. Erturk, D.J. Inman, An electromechanical finite element model for piezoelectric energy harvester plates, J. Sound Vib. 327 (2009) 9–25, https://doi.org/10.1016/j.jsv.2009.05.015.

[34] M. Khazaee, A. Rezania, L. Rosendahl, Effect of damage and support damping mechanisms on unimorph piezoelectric energy harvester, J. Vib. Contr. (2019), https://doi.org/10.1177/1077546319855162, 107754631985516.

[35] N.E. DuToit, B.L. Wardle, S.G. Kim, Design considerations for MEMS-scale piezoelectric mechanical vibration energy harvesters, Integr. Ferroelectr. 71 (2005) 121–160, https://doi.org/10.1080/10584580590964574.

[36] I. Neri, F. Travasso, R. Mincigrucci, H. Vocca, F. Orfei, L. Gammaitoni, A real vibration database for kinetic energy harvesting application, J. Intell. Mater. Syst. Struct. 23 (2012) 2095–2101, https://doi.org/10.1177/1045389X12444488.

[37] M.S.M. Soliman, E.M. Abdel-Rahman, E.F. El-Saadany, R.R. Mansour, A wideband vibration-based energy harvester, J. Micromech. Microeng. 18 (2008), https://doi.org/10.1088/0960-1317/18/11/115021.

[38] M. Khazaee, A. Rezaniakolaie, A. Moosavian, L. Rosendahl, A novel method for autonomous remote condition monitoring of rotating machines using piezoelectric energy harvesting approach, Sensors Actuators A Phys. 295 (2019) 37–50, https://doi.org/10.1016/j.sna.2019.05.016.

**Majid Khazaee** was born in Qom, Iran in 1991. He received his Bachelor and Master degrees in Aerospace Engineering from Tehran Polytechnic in 2013 and 2016. He is currently pursuing PhD in the department of Energy Technology at Aalborg University, Aalborg, Denmark and is working on piezoelectric energy harvesters for autonomous sensors and actuators. His current research interests include finite element modeling of piezoelectric materials, low-power vibration harvesting piezoelectric harvester design, industrial vibration, autonomous condition monitoring and dynamical modeling of systems.

**Alireza Rezaniakolaei**, was born in Babol, Iran in 1983. He received the Ph.D. degree from Aalborg University, Aalborg, Denmark in 2012. Currently, he is Associates Professor of Energy Technology at Aalborg University. He is head of Low Power Energy Harvesting & i-Solutions Research Programme with more than 10 years experiences in this field. His current research interests include fluid mechanics, thermal engineering and energy harvesting technologies, micro heat-transfer surfaces and integration of these technologies with renewable systems, actuators and sensor applications.

**Lasse A. Rosendahl** was born in Ribe, Denmark, in 1967. He received the M.Sc.M.E. and Ph.D.M.E. Degrees from Aalborg University, Aalborg, Denmark. From 1998 to 1999, he was with the Department of Energy Technology, Aalborg University, as an Assistant Professor, where he was an Associate Professor from 2000 to 2007, and has been a Professor since 2007. His current research interests include fluid mechanics, thermal energy technology, liquid biofuels and novel energy technologies, including modeling, simulation, and design with focus on optimized efficiency.

# Appendix G. Paper 7: Reference [16]

## The investigation of viscous and structural damping for piezoelectric energy harvesters using only time-domain voltage measurements

M. Khazaee, John. E. Huber, L. Rosendahl, A. Rezaniakolaei.

This paper has been published in

*Applied Energy*. vol. 285, pp. 116427, 2021.

Applied Energy 285 (2021) 116427

Contents lists available at ScienceDirect

Applied Energy

journal homepage: www.elsevier.com/locate/apenergy

# The investigation of viscous and structural damping for piezoelectric energy harvesters using only time-domain voltage measurements

Majid Khazaee [a], John E. Huber [b], Lasse Rosendahl [a], Alireza Rezania [a,*]

[a] Department of Energy Technology, Aalborg University, Pontopidanstraede 111, 9220 Aalborg, Denmark
[b] Department of Engineering Science, University of Oxford, Parks Rd, Oxford OX1 3PJ, United Kingdom

## HIGHLIGHTS

- A method for determining damping coefficient from voltage measurements presented.
- Structural and viscous damping mechanisms differentiated.
- Bonding layer has a significant effect on the damping.
- Viscous air damping becomes more influential at higher beam deflection.
- Tip mass increases viscous damping effect due to increasing the tip deflection.

## ARTICLE INFO

*Keywords:*
Piezoelectric
Energy harvesting
Viscous damping
Structural damping
Bonding layer

## ABSTRACT

Knowing the nature of damping in piezoelectric energy harvesters can lead to proper damping and electromechanical models and designing highly efficient harvesters with less damping. As an attempt toward a better understanding of damping in piezoelectric energy harvesters, this paper presents experimental results for structural and viscous air damping coefficients extracted directly from voltage measurements under shock-induced tests. Free-vibration excitations are analyzed using the modified Short-Term Fourier Transform and Resampling method. Seven cases are studied, namely Macro Fiber Composite with different substrate shims, different bonding layers, and with or without a tip mass. The damping coefficients can be reliably extracted using an up-chirp driving signal and analyzing the system's decay curve, without the need for full measurement of harmonic response over a wide frequency range. The results also indicate that the damping coefficient is not independent of the base excitation amplitude and can increase up to 30%. The relative significance of viscous air damping and structural damping mechanisms is identified in each case. The dependency of viscous air damping on the base excitation amplitude is also evaluated. The experimental results highlight the significance of the bonding layer in structural damping, which can account for approximately 60% of the total damping. In the absence of a substrate shim and bonding layer, the main contribution to energy dissipation is viscous air damping. While an added tip mass increases the output power, it also escalates the viscous air damping to approximately 40% due to increased beam tip deflection.

## 1. Introduction

The recovery of wasted energy using energy harvesting technologies is now widespread due to the global energy crisis, rising power demand, and environmental pollution [1], leading to alternative ways to power electronic devices. Nowadays, microelectronic devices consume significantly less energy, thanks to rapid science and technology advances, enabling battery replacement or battery recharging [2]. This will enable electronic devices to be installed in remote areas using available natural energies, avoiding pollution, labor cost, and replacement cost [3]. The direct piezoelectric effect [4] has been widely used for vibration energy harvesting (VEH) applications [5], aiming to generate low power for small electronic components, such as autonomous sensors [6], or for large-scale power generation, such as smart pavement systems [7]. The essential vibrational parameters in piezoelectric VEH are the natural frequency, the damping ratio, and mode shapes. Piezoelectric energy

* Corresponding author.
*E-mail address:* alr@et.aau.dk (A. Rezania).

https://doi.org/10.1016/j.apenergy.2020.116427
Received 10 May 2020; Received in revised form 22 December 2020; Accepted 29 December 2020
Available online 12 January 2021

harvesters (PEHs) generate maximum voltage output when deformed with a driving frequency close to their fundamental frequency [8]. In many practical cases, an added mass can control the fundamental frequency [8,9], enabling structural deformation to be considerably amplified at the working frequency [10]. Moreover, any source of energy dissipation, such as strain rate material damping or air resistance, reduces the generated power [11], and accordingly, efforts are made to keep the damping ratio as low as possible in harvester design [12]. Finally, mode shapes determine the mechanical strain pattern in the energy harvester (strain is proportional to the applied stress [13]) and consequently influence the electrical power output.

Although damping affects the power output of PEHs [14], there appears to be no comprehensive study determining the damping systematically in a typical harvester. For instance, for modeling a multilayer piezoelectric harvester, the damping coefficients of different layers are often considered constant [7]. While studies calculate damping coefficients from measured responses, there are considerable differences in their results. For instance, DuToit and Wardle [15] reported mechanical damping of $\zeta_m = 1.78\%$ for a PZT-5A bimorph from Piezo Systems, Inc. (T226-A4-503X), while Erturk and Inman [16] reported $\zeta_m = 2.7\%$ for the same bimorph with 12 g added tip mass, and Kim et al. [17] reported $\zeta_m = 8.2\%$ for the same bimorph with the same added tip mass.

Energy dissipation sources comprise air resistance, support loss, and structural damping [18]. Typically, a cantilever PEH comprises several layers, with a piezoelectric layer bonded to other layers. The bonding layer may become a source of structural damping. In a hybrid material comprising two low damping materials, the viscoelastic contact layer's damping effect can be substantial [19]. Zhou et al. [20] investigated viscoelastic damping materials. Khazaee et al. [21] showed that the bonding layer condition could significantly affect mechanical damping. Arafa and Baz [22] investigated the piezoelectric composites' structural damping and showed that the composite internal structure would change the internal loss factor. Nevertheless, in many PEH studies, energy dissipation is assumed to be purely due to viscous damping [15], while, for instance, the damping source in a piezoelectric harvester can be due to the hysteresis behavior [23] and also internal material frictions. In piezoelectric composites, the structural lay-up can amplify the material internal damping [24]. Khazaee et al. [25] employed a simple one-degree-of-freedom model to show how different proportions of structural and viscous damping could affect resonant electrical power estimation. In particular, they showed that the use of a purely viscous damping model could lead to inaccuracy. Cooley et al. [26] pointed out the importance of viscous and structural damping models, stating that experimental tests are required to clarify viscous and structural damping roles in each configuration.

For the damping parameter determination in PEHs, the simple peak decay [27], the peak bandwidth [28], curve fitting [29], and the subspace system identification (SSI) [30] methods can be used. In the simple peak decay method, the damping parameter is estimated from the logarithmic decrement observed in the free-vibration response [31]. Due to noise in a measured time-domain signal, the decrement analysis is often accompanied by uncertainties. Moreover, the simple peak decay can only extract the fundamental vibration mode damping, not that for any higher modes. In the peak bandwidth method, the damping is extracted from the bandwidth of the frequency response function. In this method, the harvester needs to be excited in a wide range of frequencies for forming the frequency response function, which will be very time consuming because of the numerous test tries. Classical curve fitting or SSI methods, such as a circle or line fitting, require multi-sensory data obtained from various experimental tests followed by complex numerical and optimization algorithms [32].

An inaccurate assumption about the damping mechanism contributions leads to inaccurate power output estimation. Therefore, there is a need for a systematic method to identify and measure the contributions of viscous and structural damping mechanisms. Both viscous damping [33] and structural damping [34] can be significant in each specific application due to the load conditions, boundary conditions, and material lay-up. Banks and Inman [35] showed a combination model of the viscous air and the structural internal friction damping would have the best agreement with experimental results. Nonetheless, clarifying the contributions of viscous and structural damping mechanisms is still an unmet goal. Potentially, the bonding layer, as an inseparable part of piezoelectric energy harvesters, can be a source of damping; yet its damping effect has not been studied. Approaches for the damping coefficient extraction require many experimental tests, multi-sensory data, or complex numerical and optimization algorithms. Thus, deriving an objective approach applied directly on the piezoelectric voltage measurements, capable of extracting modal parameters for different vibration modes, is an unmet goal. In this study, a modified Short-Term Fourier Transform and Resampling (STFR) approach is proposed for the damping determination that can be simply applied on the voltage measurements without any pre-knowledge or model about the harvester. The modified STFR is capable of extracting modal parameters for each mode of interest from one set of data.

By testing piezoelectric harvesters at various base acceleration amplitudes and with different beam structures, the viscous air damping and the structural damping are determined. This systematic way of investigating the damping is novel. Furthermore, the present study experimentally separates the damping effects of the viscous air damping, the bonding layer's structural damping, and the structural damping of the piezoelectric composite. Different bonding layers, as an essential structural part in PEHs, and their damped responses are analyzed. Besides, the effect of added tip mass on the damping is investigated. These novel research outcomes extend the current knowledge of damping mechanisms in PEHs and enable accurate damping modeling in them. The approach presented here can be applied to different PEHs, and the identified viscous and structural damping coefficients can be used for accurate PEH modeling using a recently developed finite element model [36].

In this study, experimental investigations are carried out to find structural and viscous damping contributions to a piezoelectric harvester in conditions with and without added tip mass, with different substrate shims, and with different bonding layers. Macro Fiber Composite (MFC), a flexible piezoelectric composite, is used as the active layer. As discussed in Section 2, experimental tests are carried out using a cantilever PEH in series with a resistive load and measuring only the load voltage to track the vibration of the cantilever. Observations of the decay of free-vibrations are used for extracting the damping coefficient, as in some previous studies [37]. However, in contrast to previous energy harvesting studies, here, the modified STFR, as discussed in Section 3, is used. Section 4 presents air damping and structural damping data extracted for different configurations. The excitation acceleration effect on air-damping is also investigated for the bending modes in configurations with a substrate shim and without.

Comparison of different configurations shows that the structural damping coefficient for the bonding layer can be readily distinguished from viscous air damping, such that both may be quantified. The structural damping due to the bonding layer seems to be a substantial fraction of the total damping. It is shown that the viscous air damping depends on the harvester tip deflection and increases with tip deflection. The results also illustrate how the STFR method enables reliable extraction of damping parameters for different modes from a single decay curve.

## 2. Experimental setup and piezoelectric samples

The test rigs for all the experimental measurements are shown in Fig. 1 (a) and (b). An aluminum base plate is used to connect a B&K LDS V201 shaker to the piezoelectric sample as well as providing a site for the accelerometer. The piezoelectric sample is clamped to the base plate at one end using an aluminum clamp bar, tightened with two bolts. The amplifier is controlled with a National Instruments NI 9263 module,

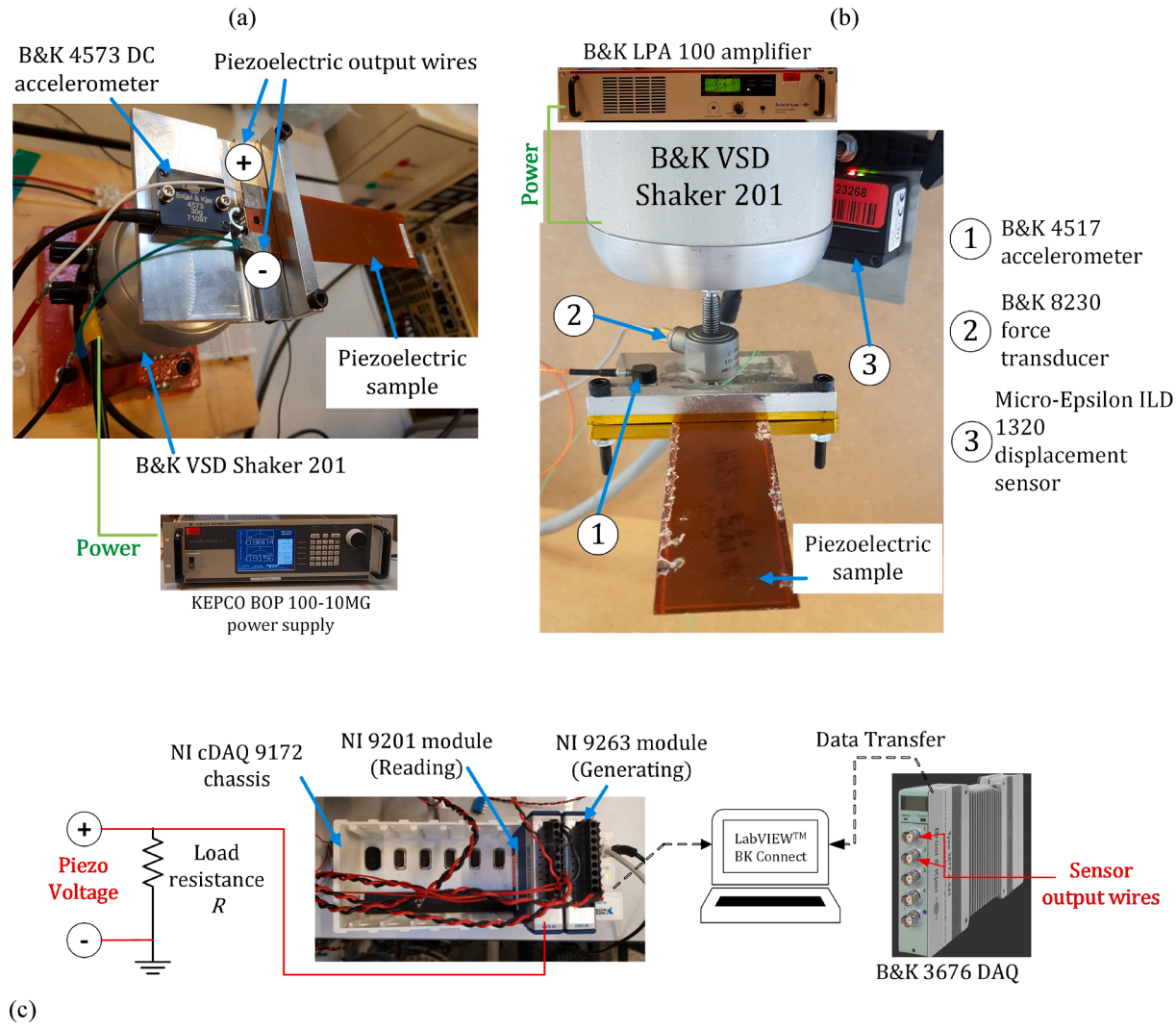


**Fig. 1.** (a) The piezoelectric sample with the cantilevered configuration attached to the shaker for Group I tests, (b) the cantilevered piezoelectric sample for Group II and III tests, and (c) data acquisition setup for recording the piezoelectric voltage, accelerometer, force transducer, and displacement laser sensor.

which generates analog voltage signals. A KEPCO BOP 100-10MG amplifier and B&K LPA 100 amplifier are used to amplify the signals and power the shaker. The accelerometer measures the applied base excitation acceleration. Output wires from each electrode of the piezoelectric harvester are connected across a purely resistive load of resistance $R$. Two Data Acquisition (DAQ) systems are employed for reading the sensor and piezoelectric voltage outputs, as shown in Fig. 1(c). The first DAQ system is an 8-channel National Instruments NI 9201 module for reading the voltage across the resistive load (which is also the voltage across the harvester) and the DC accelerometer output for a two seconds duration with a sampling rate of $F_s = 6$ kHz. Both the NI 9263 and NI 9201 modules are placed in an NI cDAQ 9172 chassis connected with a USB cable to the computer. Labview™ software is utilized for generating the desired signal and for recording data. The second DAQ system, B&K 3676 stand-alone LAN-XI DAQ, is used for recording the B&K accelerometer and the force transducer data. The BK Connect software directly controls this DAQ system.

Seven samples are tested in this study; one comprises only the MFC of 0.3 mm thickness, while the others comprise the MFC, a substrate shim, and a bonding layer. The bonding layer joins the MFC and substrate shim. The added tip mass is also considered in some configurations. Fig. 2 (a) shows the sample with the substrate shim and the tip mass. The Macro Fiber Composite (MFC) used is M-8528-P2 type, from Smart Material Inc. [38], which serves as a piezoelectric bending energy harvester. The MFC has seven sub-layers: two Kapton outer layers, two acrylic layers, two electrodes, and one central active piezoelectric layer. More information about the MFC can be found in Smart Material Inc. [38].

Six different variations of the bonding layer and the substrate shim are tested. Loctite epoxy rapid 332, Loctite epoxy 3430, 3M Company 9084 double-sided tape, and Tesa® 4964 double-sided adhesive tape are the four bonding layer materials. The 120-μm aluminum, 100-μm brass, and 100-μm copper shims serve as substrates in the harvesters. Table 1 lists the harvester materials and the thickness properties. In some harvesters, a steel tip mass is added to the beam. In Group I tests, the tip mass is cylindrical, while in the group II and III tests, the tip mass is a rectangular steel shim. Fig. 2 (b) shows the tip mass for group II and III tests. To ease comparison of results, the samples are categorized into three groups, as shown in Table 1. Group I tests are designed to separate the viscous and structural damping and isolate the bonding layer damping effect. In Group II tests, a 60-mm length Tesa® adhesive tape is attached to the substrate shim, as shown in Fig. 2 (c), and the structural damping effect of this tape is studies. In Group III tests, different bonding layer types and their damping effects are investigated. The three types of bonding layers are illustrated in Fig. 2 (d)-(f). The 3M Company's double-sided tape is a 100 μm acrylic-type adhesive with 8.0 N/cm adhesion to Stainless Steel, while the Tesa® adhesive tape is a 1200 μm natural-rubber-type adhesive. The Tesa® adhesive tape is more elastic

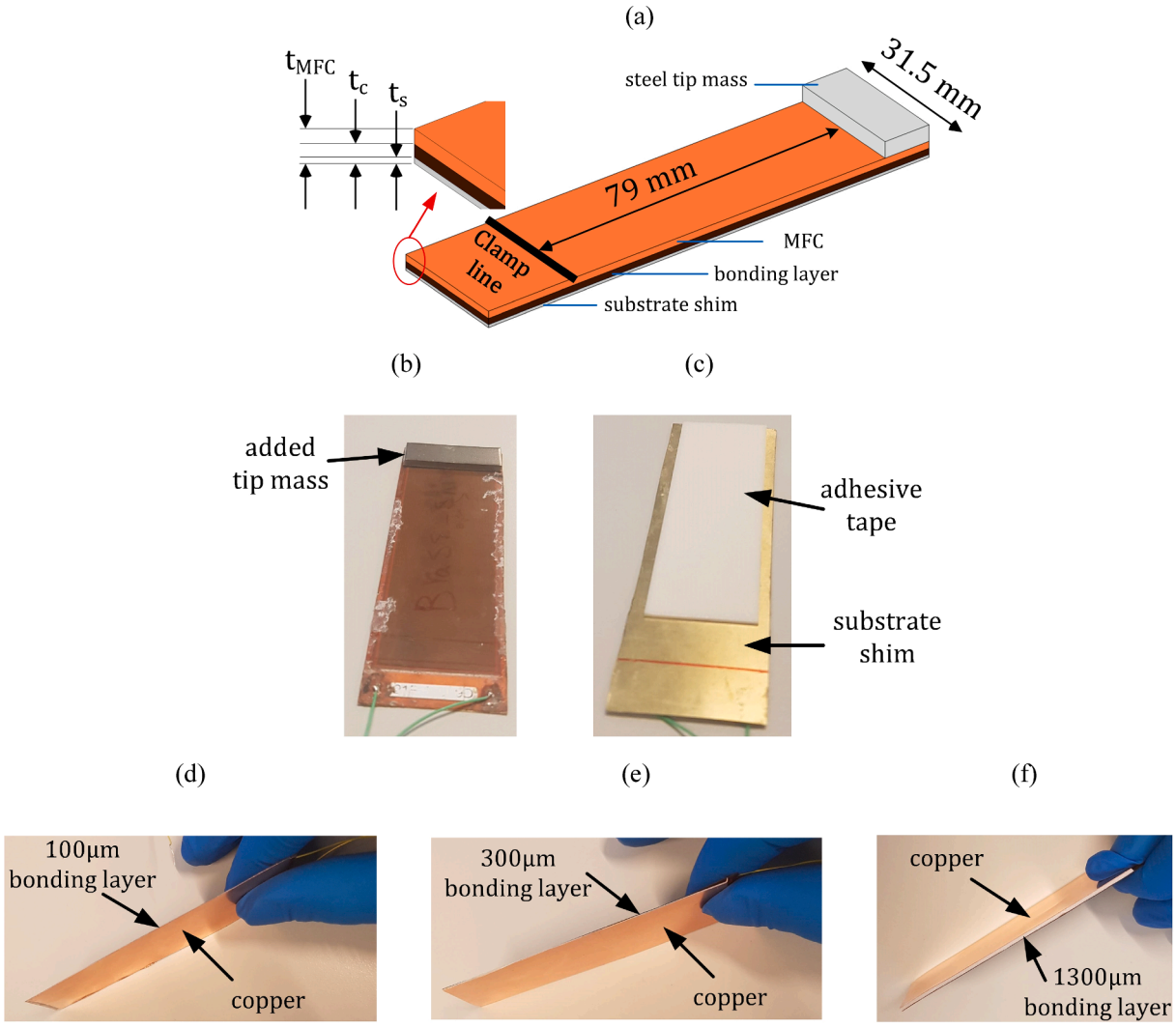


**Fig. 2.** (a) The cantilevered-piezoelectric beam with a tip mass, (b) the steel tip mass, (c) the 60-mm length adhesive (damping) tape attached to the substrate shim, (d) 100 μm double-sided tape bonding layer from the 3M Company, (e) 300 μm double-sided tape bonding layer from the 3M Company, (f) 1300 μm double-sided foam tape bonding layer from Tesa®.

**Table 1**
The tested energy harvesters' properties, dimensions, and material structure include the piezoelectric, bonding, and substrate layers.

| Group No. | Sample No. | Piezoelectric layer | Substrate shim | Bonding layer | | Tip mass (g) |
|---|---|---|---|---|---|---|
| | | | | Material | Thickness (μm) | |
| I | 1 | MFC | – | – | – | 0 and 4.2 g |
| | 2 | $t_{MFC} = 300$ μm | $t_s = 120$ μm aluminum | Epoxy rapid 332 | $t_c = 260$ | 0 and 4.2 g |
| II | 3 | MFC | $t_s = 100$ μm brass | Epoxy 3430 | $t_c = 300$ | 0 and 9.2 g |
| | 4 | $t_{MFC} = 300$ μm | $t_s = 100$ μm brass + Tesa® adhesive tape | Epoxy 3430 | $t_c = 300$ | 0 and 9.2 g |
| III | 5 | MFC | $t_s = 100$ μm copper | 3M Company double-sided tape | $t_c = 100$ | – |
| | 6 | $t_{MFC} = 300$ μm | $t_s = 100$ μm copper | 3M Company double-sided tape | $t_c = 300$ | – |
| | 7 | | $t_s = 100$ μm copper | Tesa® adhesive tape | $t_c = 1200$ | – |

than the 3M Company's tape.

For base excitation, two types of signals are used. First, a harmonic excitation with different driving frequencies is applied to extract the generated power spectrum over a frequency range. This is used at different electrical loads to identify the optimum load for maximum power extraction. Second, a linear up-chirp sweep signal is used in order to study the decay of the output voltage signal. This second signal is used to identify natural frequencies and damping parameters. The up-chirp signal $y(t)$is sinusoidal with linearly increasing frequency, given by

$$y(t) = Y_0 \sin(2\pi f(t)\, t) \tag{1}$$

where $Y_0$ is the amplitude, $t$ is the current time, and $f(t)$ is the variable frequency of chirp. For a linear up-chirp, the frequency is given by

$$f(t) = f_0 + \frac{f_1 - f_0}{T_f} t \tag{2}$$

wherein $f_0$ is the initial frequency, $f_1$ is the target frequency, and $T_f$ is

the target time. In this study, parameters are set to $T_f = 1$ s, $f_0$=1 Hz, and $f_1 = 1500$ Hz. Comparing a chirp signal to an impulse, their power spectra are similar, but the phase spectra are distinct. The chirp signal excites a range of frequencies and is locally approximately periodic. The peak acceleration, $A_c = (2\pi f_1)^2 Y_0$, will be used as a measure of the chirp acceleration amplitude. A section of the chirp signal used in this study, along with its Fast Fourier Transform (FFT) and a typical system response, is shown in Fig. 3, where the system's decaying free-vibration can be clearly seen.

## 3. Method for extracting resonant frequencies and damping coefficients

This section presents a method for calculating natural frequencies and damping coefficients using only the measured output voltage response during the free vibration stage. The method relies on analyzing the decay curve; only the system response to the chirp signal (or any impulse-like input) is needed.

A method known as Short-Term Fourier transform and Resampling (STFR) has recently been developed for natural frequency and damping extraction in free vibration tests using the time response [39]. A series of modifications are applied to the method in order to increase its accuracy for this study.

First, the STFR is developed, and the relationship between the damping and the decay of the voltage response is illustrated using a recently measured voltage response of a piezoelectric harvester [40]. Because piezoelectricity is a transducing property giving a linear relationship between mechanical strain and electric field, the measured voltage characterizes the response of the system. The natural frequencies and damping ratios can be extracted from the voltage response without requiring displacements or strains to be measured [16]. This simplifies the estimation of natural frequency and damping coefficient. Second, a Hann windowing function is introduced in the modified STFR for the segmenting of the output voltage signal; this smooths the segmented signals and improves numerical stability. Third, a linear line fit on the logarithmic decay curve is introduced and compared with the exponential fit on the original STFR; this balances the contributions of the early peaks and the later peaks in the voltage response so that they contribute equally to the estimate of damping coefficient. Finally, in the presented STFR data, some optimization processes to maintain the curve fitting with the best possible accuracy are considered. These modifications will be described in detail in subsection 3.2.

### 3.1. The damping coefficient in the decay voltage response

Now consider how the damping coefficient can be found from the voltage response. Fig. 4 shows a measured free vibration response of sample 1 (No-Shim) harvester after an up-chirp base excitation. It can be seen that the response has a maximum in the early stage and the voltage output then decays away. Because the chirp excites a wide range of frequencies, the voltage response carries superimposed characteristics from several vibration modes. A zoomed-in view of the free voltage response in Fig. 4 shows high-frequency harmonics superimposed on the fundamental. As a result, modal characteristics from the higher frequency modes can be extracted from a single decay curve. The response for a system with well-separated modes is modeled as the summation of independent responses from $N$ vibration modes [41], and here we assume the same linear superposition feature. Moreover, from the general transient response of a single degree of freedom system, the voltage response for $i$-th mode can be expressed as [40]

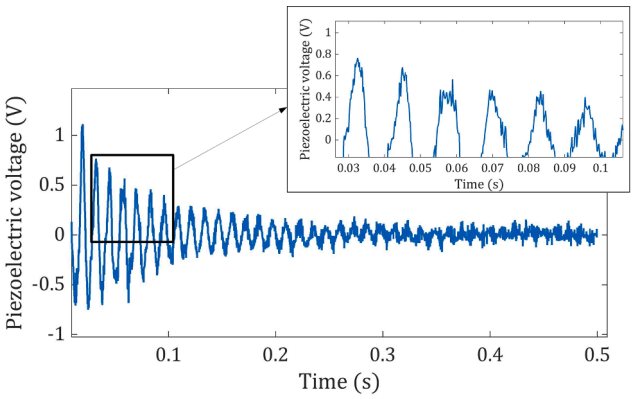


**Fig. 4.** A typical voltage response from a piezoelectric sample subjected to an up-chirp; the decay voltage response shows the effect of primary vibration mode and higher harmonics.

$$V^i[k] = A_i e^{-\zeta_i \overline{\omega}_{n,i}}(k\Delta T)\sin\left(\overline{\omega}_{d,i}(k\Delta T) + \theta_i\right) \tag{3}$$

where $\overline{\omega}_{n,i}$, $\overline{\omega}_{d,i}$ and $\zeta_i$ are the undamped natural frequency, damped natural frequency, and mechanical damping coefficient for the $i$-th mode. The damped natural frequency is given by $\overline{\omega}_{d,i} = \overline{\omega}_{n,i}\sqrt{1-\zeta_i^2}$. Furthermore, $A_i$ and $\theta_i$ are the amplitude and phase constants that depend upon the initial conditions. The goal of the method in this study is to extract modal parameters, specifically $\overline{\omega}_{ni}$ and $\zeta_i$. First, $\overline{\omega}_{d,i}$ is estimated, and then the decay curve is fitted to the functional form $A_i e^{-\zeta_i \overline{\omega}_{n,i}}(k\Delta T)$, enabling $\delta_i = \zeta_i \overline{\omega}_{n,i}$ to be evaluated. Having estimated $\delta_i$ and $\overline{\omega}_{d,i}$ for the mode under consideration, the damping coefficient can then be expressed as

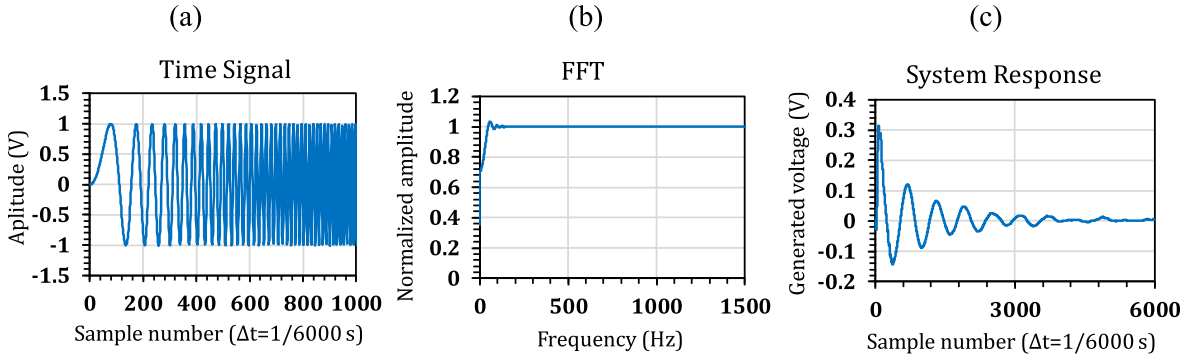


**Fig. 3.** (a) Typical examples of chirp excitation in the time domain (showing the first 1000 samples), (b) FFT of the input signal, and (c) system response, starting from the end of the chirp.

$$\zeta_i = \frac{\delta_i \Big/ \overline{\omega}_{d,i}}{\sqrt{\left(1 + \left(\delta_i \Big/ \overline{\omega}_{d,i}\right)^2\right)}} \tag{4}$$

### 3.2. Step-by-step guide for the STFR

To extract the natural frequencies, the time response signal is divided into segments, and each segment is multiplied by a Hann function to perform smoothing at the cut-off edges. Next, each smoothed signal is transformed to the frequency domain using the Fast Fourier Transform (FFT). The results give a time-dependent frequency spectrum, the Short-Term Fourier Transform (STFT) with Hann windowing. In order to extract $\delta_i$ for the $i$-th mode, the STFT is used to form a peak decay curve. This approach enables a separate curve fitting for each mode. Segmenting the signal reduces the number of data points available in each FFT operation; to maintain resolution in frequency space, each segment was first zero-padded and then resampled as described in detail below. Fig. 5 shows the five main steps of the STFR method for extracting natural frequency and damping coefficients, which are as follows:

*Step 1.* Consider the voltage signal measured with a sampling rate $F_s$,

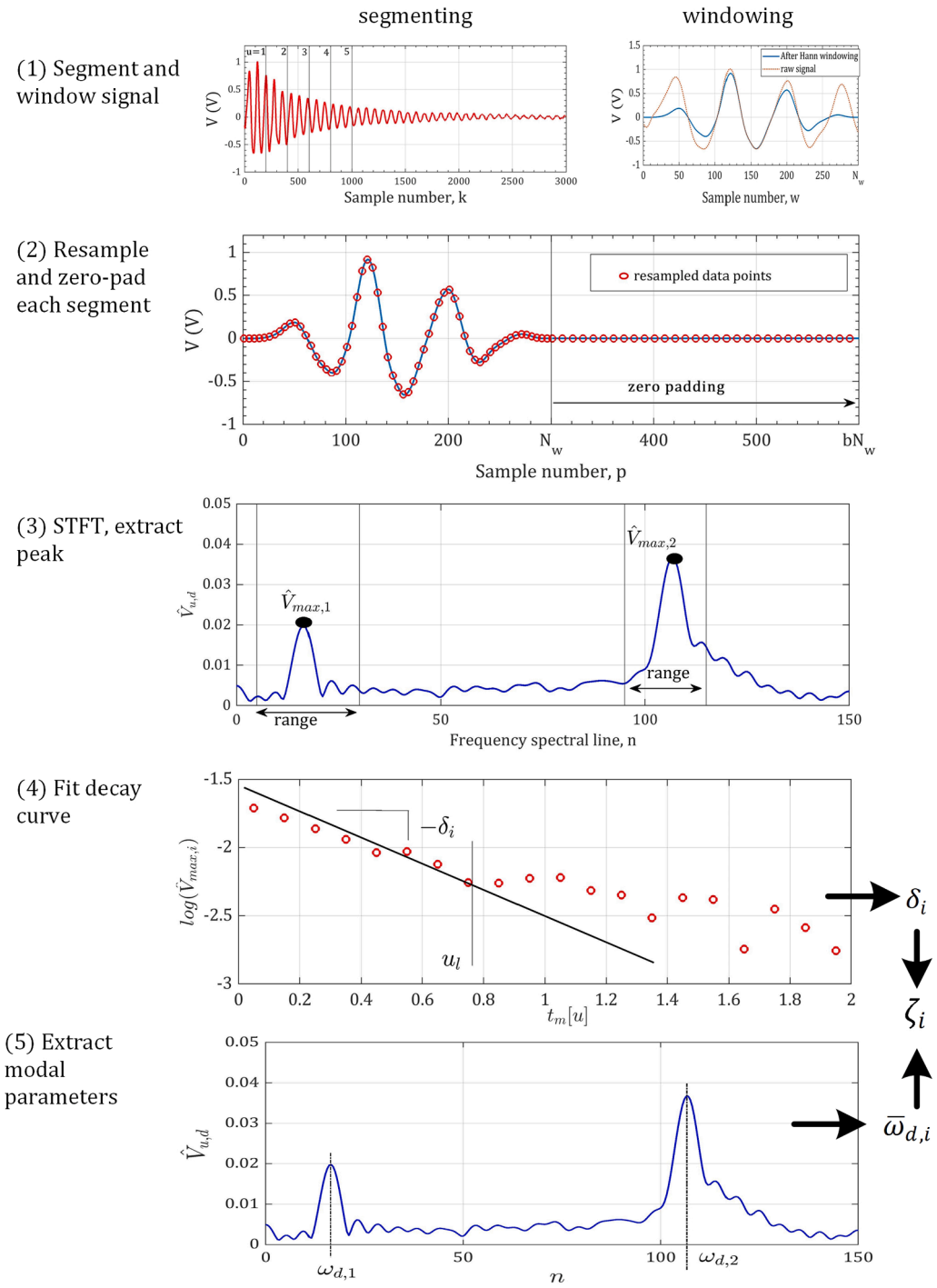


**Fig. 5.** Five main steps of the STFR process, (1) segmenting and windowing the voltage measured signal, (2) resampling and zero-padding the segmented signal, (3) Applying FFT on the segmented signal (STFT), (4) linear fit on the logarithm of the decay curve, (5) extracting the natural frequency and damping coefficient.

with $N_s$ data points, specified as a data sequence $V[k]$:

$$V[k] = V(t = k\Delta T) \text{ for } 0 \le k \le N_s - 1 \tag{5}$$

where $t$, $\Delta T = 1/F_s$, and $k$ are, respectively, the time, time-step, and the sample number.

By assuming a linear superposition characteristic for the voltage signal, all the vibration modes' effect shall be seen in the voltage signal provided that their contribution to the voltage is significant. In other words, the voltage signal is a summation of all the modes, $V[k] = \sum_{i=1}^{N} V^i[k]$.

The original measured signal $V[k]$ is divided into $U$ segments, and each divided signal is multiplied by a Hann function. The segmented signal is denoted by $V_u[w](0 \le w \le N_w - 1)$, where the number of data points in each segment is $N_w = N_s/U$. Each segment $0 \le u \le U-1$ can be expressed as

$$V_u[w] = V(t = (uN_w + w)\Delta T)\mathscr{H}(w, N_w), \quad 0 \le w \le N_w - 1 \tag{6}$$

where $w$ is an index number in each segment and $\mathscr{H}(w, N_w)$ is the symmetric Hann function with length $N_w$. In the segmented data, the average time within each segment is given by

$$t_m[u] = uN_w\Delta T + \frac{N_w}{2}\Delta T \tag{7}$$

To generate the frequency spectrum from each segment of voltage measurements, the FFT is applied to the segment, giving

$$\widehat{V}_u[n] = \sum_{w=0}^{N_w-1}(V(t = (uN_w + w))\Delta T)e^{-j2\pi\frac{nw}{N_w}} \tag{8}$$

wherein $n$ is the spectral frequency line. The FFT frequency resolution equals to $\Delta\omega_{n,U} = \frac{2\pi F_s}{N_w} = \frac{2\pi F_s U}{N_s}$. This shows that for a given total number of data points ($N_s$), by increasing the number of segments ($U$), $\Delta\omega_{n,U}$ increases, meaning that the accuracy of resonant frequency deteriorates.

*Step 2.* In order to improve the frequency resolution, the segmented signal is resampled by decimation with a factor $d$ and then is padded with zeroes by a factor of $b$. Thus, the total number of samples in the segmented signal is $N_b = bN_w$ and the sampling rate $F_s$ reduces to $F_s/d$. With this resampling and zero-padding, the frequency resolution becomes $\Delta\omega_{n,d} = \frac{2\pi F_s U}{bdN_s}$. It is also worth mentioning that the Nyquist-Shannon sampling theorem should be satisfied when the decimation factor $d$ is being set in order to avoid aliasing. In this study, for instance, $U = 40$, and $d = 10$ is employed.

Applying the FFT to the segment with resampling and zero-padding gives the spectrum

$$\widehat{V}_{u,d}[n] = \sum_{p=0}^{N_b-1}(V(t = (uN_w + w))d\Delta T)e^{-j2\pi\frac{np}{N_b}} \tag{9}$$

Because the sampled data points in the segment are changed, the FFT peak value also changes, and therefore a scaling is performed to up-scale $\widehat{V}_{u,d}[n]$ to that for the FFT without zero-padding, e.g. $\widehat{V}_u[n]$.

*Step 3.* For each mode, a range of frequency is defined within which the natural frequency is expected to lie. Then, the FFT, $\widehat{V}_{u,d}[n]$, of each resampled segment is analyzed to find the maximum value within the range, $\widehat{V}_{max,i}[u]$.

Step 4. Plotting the peak values $\widehat{V}_{max,i}[u]$ as a function of time forms a decay curve. Since the decay curve for the $i$-th mode is expected to have the exponential form $A_i e^{-\zeta_i\bar{\omega}_{n,i}}(k\Delta T)$, the peak values are represented on a logarithmic scale; there is then an approximately linear relationship between segment number $u$ and the peak value logarithm. This gives all the data points the same weight in a least-square straight line fit. From Eq. (3), for the $i$-th mode, a linear relationship between the peak values of the STFT signals over time is expected, with

$$\log\left(\widehat{V}_{\max,i}[u]\right) = \log A_i - \delta_i t_m[u] \tag{10}$$

where $-\delta_i$ is the slope of the logarithmic peak-value line obtained from the STFR process.

*Step 5.* The modal parameters $\overline{\omega}_{d,i}$ and $\zeta_i$ are extracted as follows: From each STFR segment, the damped natural frequency $\omega_{d,i}[u]$ is identified as the location of the peak value $\widehat{V}_{max,i}[u]$. The average of the $\omega_{d,i}[u]$ values is used as an estimate of the damped natural frequency for the $i$-th mode, given by

$$\overline{\omega}_{d,i} = \frac{1}{u_l}\sum_{u=0}^{u_l-1}\omega_{d,i}[u] \tag{11}$$

Finally, $\zeta_i$ is obtained from $\overline{\omega}_{d,i}$ and $\delta_i$ using Eq. (4).

In practice, steps 1 to 4 were repeated for different $U$ values in order to identify an optimum segment length. Choosing a large $U$ value produces a greater number of data points for line fitting by Eq. (10), but also reduces the number of data points per segment, $N_w$, which can result in aliasing. Typically, $U$ values of 20–40 were used. In addition, the $\widehat{V}_{\max,i}[u]$ data points eventually deviate from a linear regression at high values of $u$. This happens because the signal to noise ratio decreases as the signal decays [32]. Therefore, for calculating the damping coefficients from voltage measurements, the noise ratio is considered a data truncation factor. The data was truncated at a $u$ value, $u_l$, chosen to ensure that the error in the estimation of $\delta_i$ was less than 5% and the signal to noise ratio was greater than 5. The optimum truncation limit $u_l$ varies from test to test. In some cases, the first data point of the first segment exhibited an impact transient, which adversely affected curve fitting. In these cases, the very first data point was excluded.

### 3.3. Methodology for distinguishing the structural and viscous damping contributions

The mechanical damping, $\zeta_m$, comprises a structural part, $\zeta_{\text{struc}}$, and an air (or viscous) damping part, $\zeta_a$. This damping representation demonstrates good agreement with experimental data [35]. According to two experimental studies by Woolam [42] and Baker et al. [43], material damping shows either no dependence or slight dependence on the amplitude of vibration. Therefore, the observed amplitude-dependency of $\zeta_m$ is due to amplitude-dependent increase in air damping. Baker et al. [43] showed experimentally that air damping varies approximately linearly with beam-tip deflection. Therefore, a combined damping model is considered as:

$$\zeta_m = \zeta_{\text{struc}} + \alpha\zeta_a \tag{12}$$

The STFR method calculates the damping at each shock-induced base excitation from the voltage, as shown in Fig. 6 (a). The damping model assumes that the air damping will also change due to changing beam tip deflection. Each sample is tested over a range of excitation magnitude to distinguish the structural and air damping. As the tip deflection increases, so also the viscous air damping increases. A line fit to the experimental damping coefficient data can be extrapolated back to the zero amplitude point to determine the structural damping contribution, see Fig. 6 (b).

The process is applied to each sample for determining the structural damping effect of different materials, the amplitude-dependent part of the damping, and the investigation of the added tip mass effect on the damping. Fig. 7 presents the objectives of the experimental tests on the seven tested samples. By comparing the data from different samples, materials, and lay-ups, the relative structural and viscous damping contributions are studied.

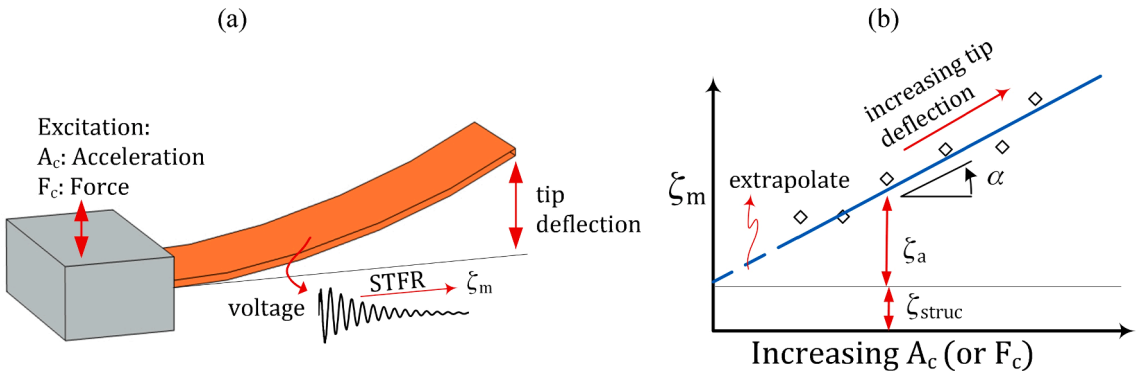


**Fig. 6.** (a) The deformed beam under a base excitation and the STFR method for extracting the damping coefficient, and (b) the process to distinguish the viscous and structural damping contributions in the total damping.

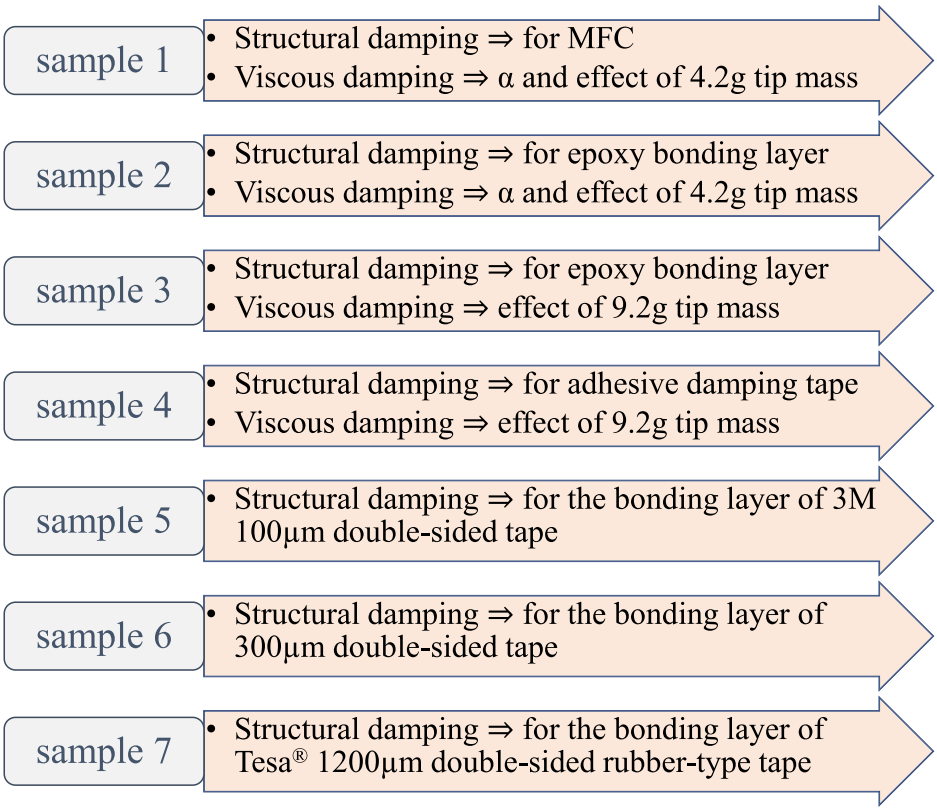


**Fig. 7.** The present study objectives for seven samples concerning the structural and viscous air damping parameters.

## 4. Experimental results

In this section, the modal parameters extracted using the STFR approach from seven sample types are reported. Results are reported in three groups; each aims to emphasize one or two particular objectives. Group I and II are designed to distinguish the structural and viscous damping and their contribution to the total damping. The effect of added tip mass is also investigated in these group tests. In Group III tests, the main objective is to explore different bonding layers.

The electromechanical equations for a piezoelectric energy harvester are coupled equations relating mechanical vibration and electrical circuit parameters. In this work, the electrical load was optimized for maximum power output. For electrical load values close to the optimum load, the power output is insensitive to the electrical load [44] in an impact harvester, and therefore, it is not critical to precisely match the optimum load. Moreover, Erturk et al. [16] showed that the resonant frequency in short-circuit differs from the resonant frequency with a matched load by less than 0.5%. Hence, it is accurate to infer the harvester's natural frequencies from the resonant frequencies extracted with the matched load present. The optimum load resistance was found to be 27 kΩ for all the harvesters used in this study.

In order to test whether the choice of load resistor affects the damping parameters, decay curves were measured with a range of resistive loads: $R = 100\ \Omega$, 27 kΩ, and 10 MΩ. A half-sine-impulse force was applied as the base excitation, and the resulting normalized voltage output is shown in Fig. 8. Comparing the voltage responses at 100 Ω (similar to short-circuit condition) and 27 kΩ shows that they are almost identical, while for the 10 MΩ case (similar to open-circuit), a deviation in both frequency and decay rate is evident. Thus the modal parameters measured with the 27 kΩ optimum load in place are expected to match the short-circuit modal parameters.

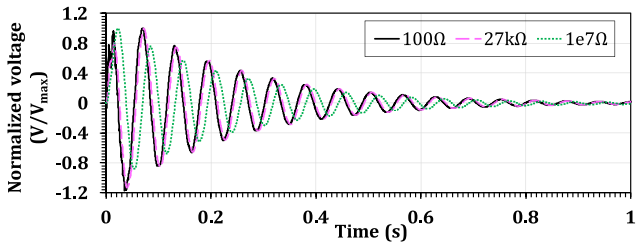


**Fig. 8.** Comparison of piezoelectric voltage outputs subjected to half-sine-impulse at different electrical loads.

### 4.1. Group I tests (the MFC without and with the aluminum substrate)

The Group I tests aim to separate viscous and structural damping roles in a cantilevered piezoelectric harvester in standard configuration and with a tip mass. Throughout this subsection, the label "No-Shim" refers to the MFC sample without substrate shim (sample 1), while "Alu-Shim" refers to the sample with a bonding layer and aluminum substrate shim (sample 2).

#### 4.1.1. Energy harvesters without tip mass

Fig. 9 shows measured voltages from harvesters with and without substrate shim for the first 0.5 s after applying chirp excitation with a maximum acceleration of 1.77 $g_0$ ($g_0 = 9.81\ ms^{-2}$). Note that the Alu-Shim case generates considerably higher voltages compared to the No-Shim case. This shows that the substrate shim can positively affect power generation from an energy harvesting perspective despite losses in the bonding layer. Another interesting outcome can be seen in the zoomed view of the signals in Fig. 9. In the No-Shim sample, high frequency (>100 Hz) voltage variations can easily be seen, unlike the Alu-Shim voltage response. This can be linked to the behavior of the bonding layer in the Alu-Shim sample, which strongly damps high frequencies in the voltage response.

As a preliminary illustration of the resonant behavior of the energy harvesters, the FFT was applied to voltage responses measured after chirp excitation with varying acceleration. Fig. 10 shows that the No-Shim sample exhibits two clearly defined resonances, while in the Alu-Shim sample, only the first mode resonance is clearly visible. The first and second resonant frequencies for the No-Shim sample are 17 Hz and 106 Hz, respectively. Meanwhile, the first resonant frequency is approximately 20 Hz for the Alu-Shim sample. Another local maximum is at approximately 38 Hz due to anti-resonance [45], similar to the observation in Khazaee et al. [46]. The natural frequencies and the corresponding modes of the harvester were estimated using the finite element method by Khazaee et al. [36]. This showed a torsional mode around 160 Hz and a bending mode around 190 Hz in the Alu-Shim case; the corresponding resonant peaks can be seen in Fig. 10 (b).

Next, the STFR approach is applied to free-vibration voltage responses in order to extract the resonant frequencies and damping ratios. Fig. 11 shows how the resonant frequency changes with respect to chirp acceleration amplitude ($A_c$) for both No-Shim and Alu-Shim samples. The first mode resonant frequency of the Alu-Shim sample is approximately 20% greater than that of the No-Shim sample. The first resonant frequency of the No-Shim sample reduces as chirp acceleration increases, perhaps due to amplitude dependence of the MFC layer stiffness. Khazaee et al. [47] have previously observed similar softening effects in an energy harvester. Nonetheless, the other natural frequencies shown in Fig. 11 are relatively independent of chirp acceleration.

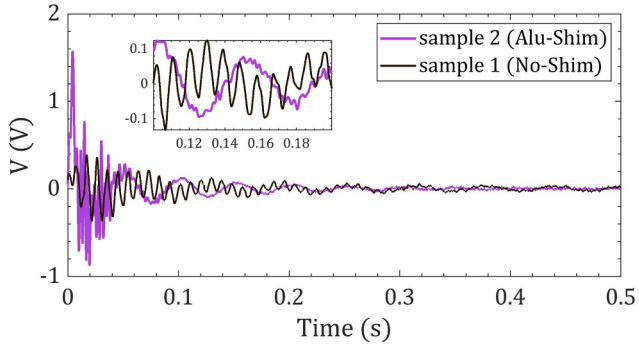


**Fig. 9.** Piezoelectric voltage outputs for sample 1 (No-Shim) and sample 2 (Alu-Shim) at 1.77 $g_0$ chirp excitation amplitude with $R = 27$ kΩ.

The curve fitting results of STFR are used to extract mechanical damping, $\zeta_m$, for the Alu-Shim and No-Shim samples. The resulting $\zeta_m$ values for two bending modes in the No-Shim sample and the first bending mode in the Alu-Shim sample are shown in Fig. 12, as a function of chirp acceleration $A_c$. By comparing the damping coefficients in Fig. 12, mechanical damping increases monotonically with amplitude in an approximately linear way. Greater $A_c$ values lead to increased beam-tip deflection, and this, according to Woolam [42], increases mechanical damping. Similarly, as shown in Fig. 12, the damping has a linear dependency on base chirp acceleration, hence on beam-tip deflection, assuming linearity.

The structural damping $\zeta_{struc}$ can also be evaluated from Fig. 12, extrapolating to $A_c = 0$. This indicates similar $\zeta_{struc}$ values for both modes in the No-Shim sample, but a much greater $\zeta_{struc}$ value for the Alu-Shim sample. Crandall [48] showed that adding a strip of viscoelastic damping tape to an aluminum plate can substantially increase the structural damping. An equivalent role is played here by the epoxy bonding layer in the Alu-Shim sample. The contribution of the aluminum shim to the structural damping is expected to be small [48].

#### 4.1.2. Effect of added tip mass

Tests were carried out with an added tip mass in the form of a 4.2 g cylindrical mass with 10 mm diameter and 4 mm height affixed to the upper surface of each harvester, with its centre 5 mm from the free end. Note that the No-Shim and Alu-Shim samples have 5.2 g and 7.2 g mass, respectively. Chirp base excitation with chirp acceleration amplitudes ranging from 0.8 $g_0$ to 2.4 $g_0$ was applied.

Fig. 13 illustrates the voltage variation due to an added tip mass for the No-Shim and Alu-Shim samples, using a 0.88 $g_0$ chirp amplitude. In both samples, the maximum voltage output is increased by adding the tip mass. The added tip mass creates a significant transient in the voltage variation, which can be easily seen for both cases in Fig. 13 (a) and (b). After approximately 0.09 s in the Alu-Shim sample, this transient vanishes but decays less rapidly in the Alu-Shim sample. A reason for this can be the greater stiffness contributed by the additional layers in the Alu-Shim sample.

Fig. 14 compares the maximum voltage measured in the Alu-Shim and No-Shim samples with and without added tip mass at various $A_c$ values. Greater chirp excitation generally causes a greater voltage. As expected from the state-of-art [49], the maximum voltage is increased by adding tip mass. Fig. 14 shows that this is so, regardless of the presence or absence of the substrate shim. Meanwhile, the fractional voltage increase is greater for the No-Shim sample. This is partly because of a greater ratio of the added tip mass to the total harvester mass for the No-Shim sample. Another aspect is that the No-Shim sample is less stiff. The average generated power is of significance from an energy harvesting perspective. The root mean square (RMS) generated power during the first 1 s after chirp excitation is shown in Fig. 15 for all the configurations tested. The RMS power for the No-Shim sample is significantly increased by adding the tip mass at all $A_c$ values. However, adding tip mass to the Alu-Shim sample did not change the RMS power significantly unless $A_c > 1.8g_0$.

As a preliminary illustration of the tip mass effect on the resonant behavior, the FFT is applied to the harvester voltage signals of Fig. 13, and the results are shown in Fig. 16. The FFT is shown in the frequency range of 0–120 Hz for clarity. While two resonances are clearly visible

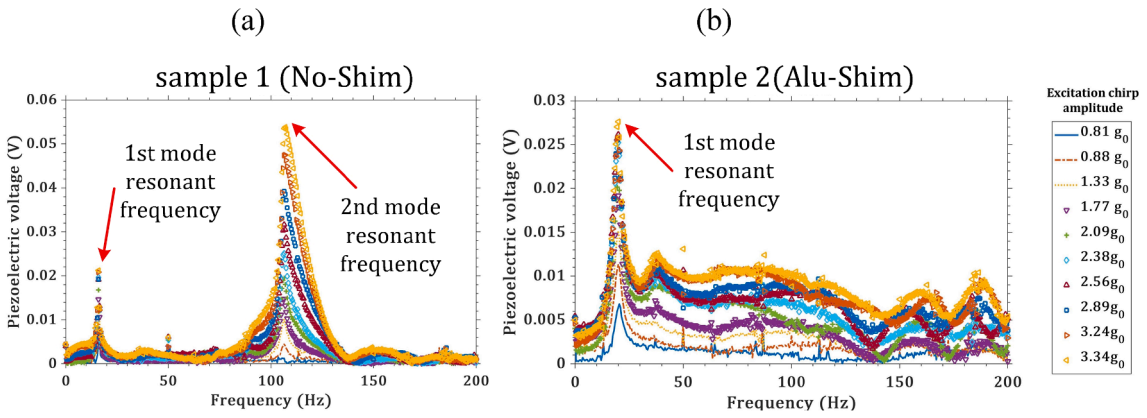


**Fig. 10.** Effect of increasing base chirp amplitude on STFT voltage responses for (a) sample 1 (No-Shim) and (b) sample 2 (Alu-Shim).

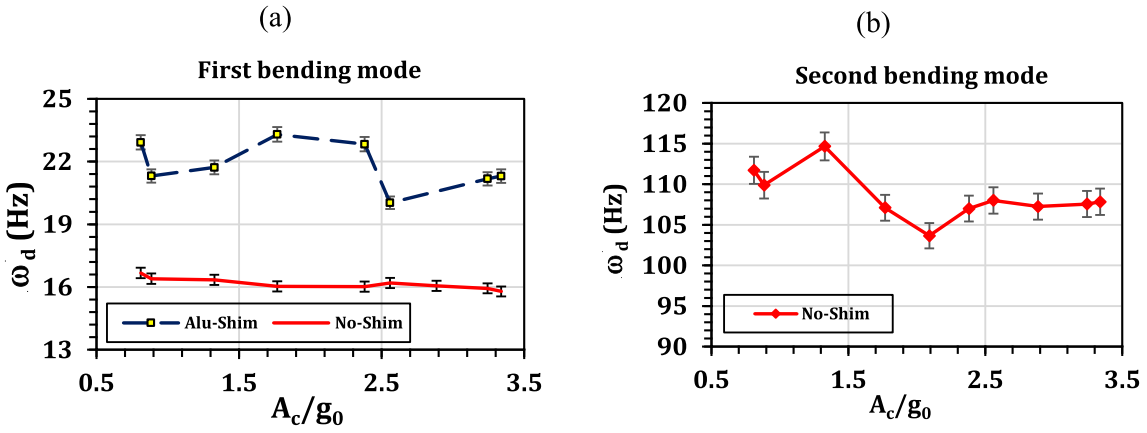


**Fig. 11.** Variation of resonant frequencies with respect to the base excitation amplitude (a) first bending mode for No-Shim and Alu-Shim samples, and (b) second bending mode for No-Shim sample.

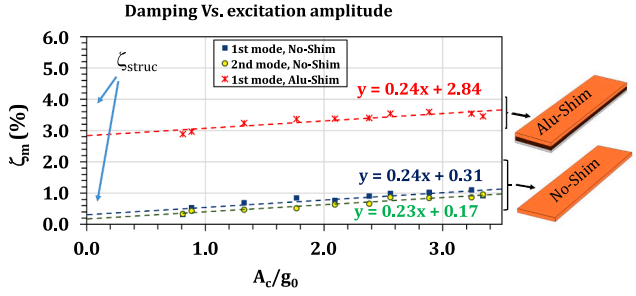


**Fig. 12.** Mechanical damping versus chirp base acceleration for the piezoelectric sample 1 (No-Shim) and sample 2 (Alu-Shim).

for the No-Shim samples, only one resonance can be seen for each Alu-Shim sample. In both sample types, adding tip mass decreases the first mode resonant frequency. However, the resonant peak value in the Alu-Shim sample remains almost constant with added tip mass while the peak value is sharply reduced for the No-Shim sample. Notice that the second-mode resonant peak increases considerably due to the tip mass for the No-Shim sample, indicating the effect of high-frequency harmonics induced by the tip mass. The appearance of these higher harmonics was also evident in the voltage-time signal of the No-Shim sample in Fig. 13 (b). In order to check the consistency of these trends across a range of excitation amplitudes, the resonant peak values are shown in Fig. 17 as a function of chirp acceleration amplitude $A_c$. This shows that the patterns of behavior observed in Fig. 16 remain valid for all the excitation amplitudes.

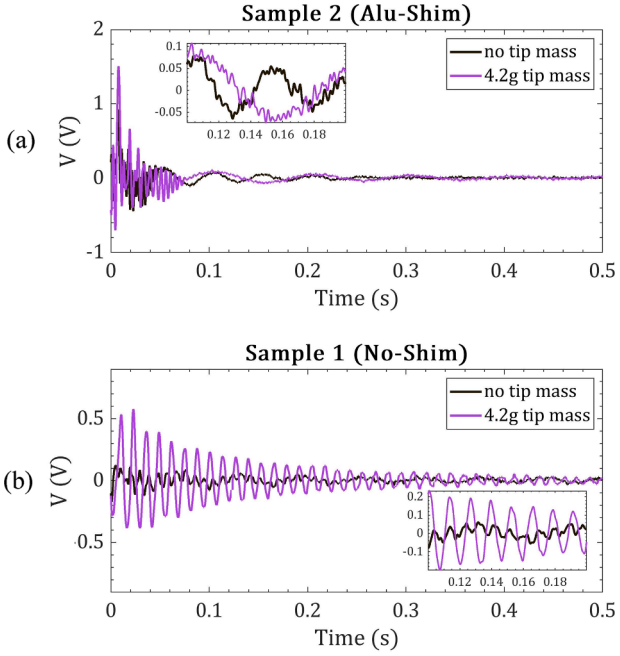


**Fig. 13.** Voltage output for samples with and without tip-mass and $A_c/g_0 = 0.88$ (a) Alu-Shim and (b) No-Shim.

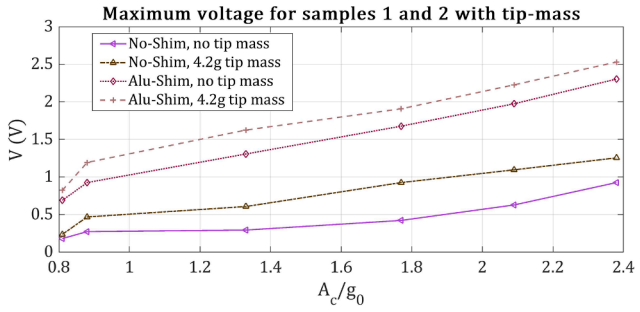


**Fig. 14.** Maximum voltage for Alu-Shim and No-Shim samples against excitation chirp amplitude.

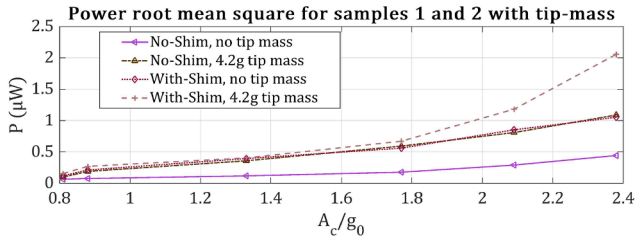


**Fig. 15.** Root mean square power for Alu-Shim and No-Shim samples against excitation chirp amplitude.

The averaged resonant frequencies, extracted using the STFR process, are shown in Table 2 for both No-Shim and Alu-Shim samples with and without tip mass when the 0.88 $g_0$ chirp amplitude was applied. For both samples, added tip mass reduces resonant frequencies, as expected. Fig. 18 shows how the damping coefficients, extracted by the STFR method, vary with chirp amplitude and added tip mass for both samples. In all cases, the damping coefficient shows an increasing trend with chirp excitation amplitude. Added tip mass increases the tip deflection, and consequently, the contribution of air damping becomes greater. This can be seen in Fig. 18, for both No-Shim and Alu-Shim samples, as an increase in the total mechanical damping, $\zeta_m$. However, this air damping increase is not the same when comparing the No-Shim and Alu-Shim samples. For an identical added tip mass, the No-Shim sample has greater deflection than the Alu-Shim sample, which has the greater stiffness. As a result, there is a more significant air damping increase in the No-Shim sample.

### 4.2. Group II tests (the brass-substrate MFC with and without adhesive tape)

Group II tests are designed to clarify the structural damping effect of adhesive layers. As in Crandall's study [48], by adding an adhesive damping tape to the beam, the adhesive tape's structural damping can be clarified. The adhesive tape is a strip of Tesa® rubber-type adhesive tape with the dimensions $60 \times 20 \times 1.2\ mm^3$. Two samples in this group are tested; sample 3, which does not have the adhesive damping tape, and sample 4, to which the adhesive damping tape is attached. The substrate for both samples is a 100 μm brass shim. The samples are also tested with an added tip mass of 9.2 g.

Fig. 19 illustrates the time signals for samples 3 and 4 with and without the 9.2 g tip mass. The 9.2 g added tip mass adversely affects the

**Table 2**
Resonant frequencies for sample 1 (No-Shim) and sample 2 (Alu-Shim) with and without tip mass.

| Description | $\overline{\omega}_d$(Hz) | | Frequency ratio |
|---|---|---|---|
| | no tip mass | 4.2 g tip mass | |
| No-Shim sample | | | |
| - first mode | 16.2 ± 0.4 | 8.2 ± 0.2 | 0.51 |
| - second mode | 108.6 ± 3.5 | 78.0 ± 3.6 | 0.72 |
| Alu-Shim sample | | | |
| - first mode | 21.3 ± 0.7 | 10.8 ± 0.5 | 0.51 |

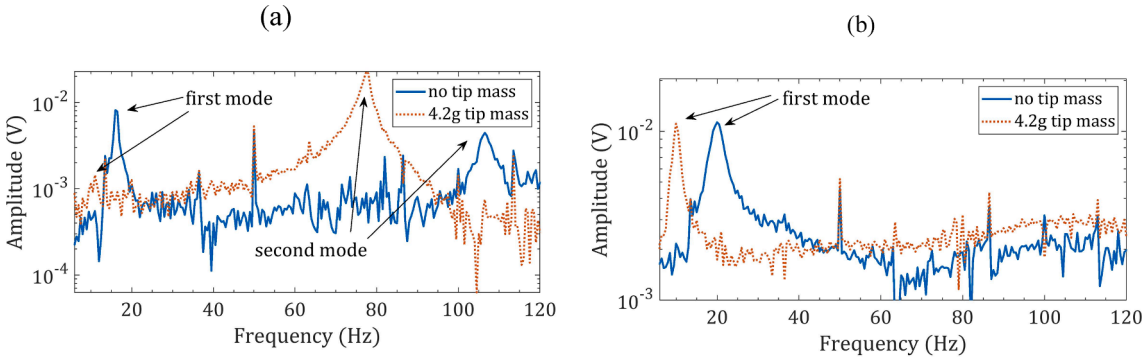


**Fig. 16.** FFT comparisons between signals with tip mass in (a) sample 1 (No-Shim) and (b) sample 2 (Alu-Shim) at 0.88 $g_0$ base chirp excitation.

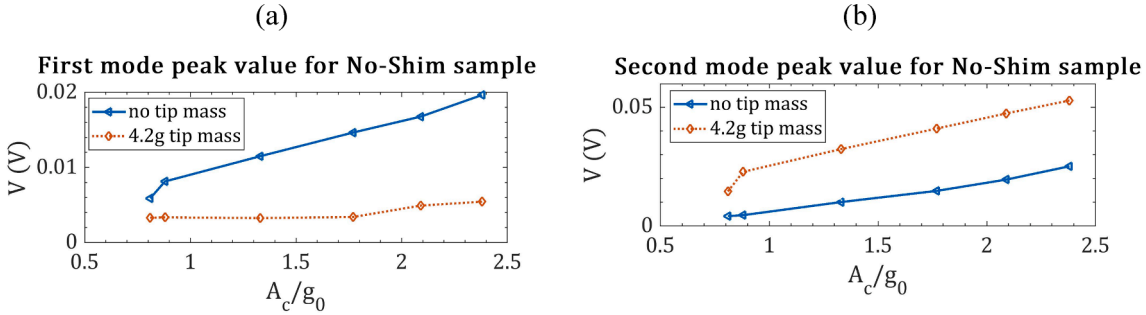


**Fig. 17.** Variation of resonant peak values for sample 1 (No-Shim) due to the added tip mass, (a) the first mode and (b) the second mode.

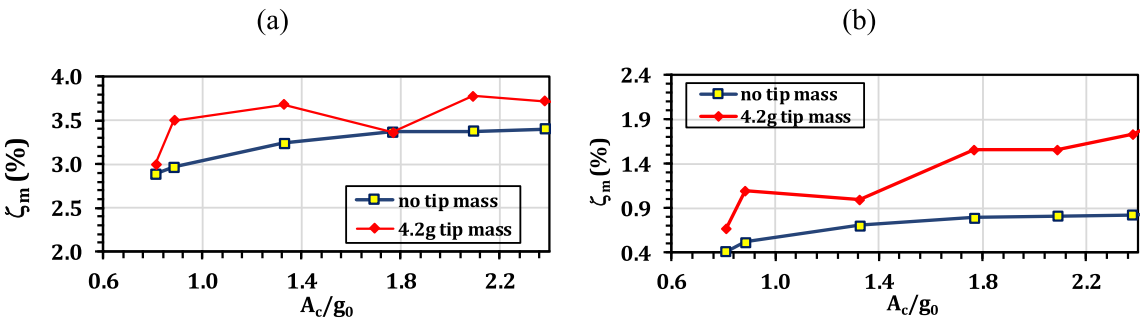


**Fig. 18.** Damping coefficient variations of first-mode due to adding 4.2 g tip mass for (a) sample 1 (No-Shim) and (b) sample 2 (Alu-Shim).

harvester voltage generation performance reducing the peak voltage magnitude. Regardless of the tip mass, when the adhesive tape is added to the substrate, the output voltage is decreased. The tests are repeated for different excitation amplitudes, and the peak voltage is shown in Fig. 20 versus the applied force. Fig. 20 shows that adding the adhesive tape reduces the peak voltage for all excitation amplitudes. Exploring the root of these voltage variations is possible by extracting the modal parameters in the different configurations because the piezoelectric layer is identical in all these configurations.

Fig. 21 (a) and (b) respectively present the natural frequencies and damping coefficients in the case with adhesive tape and a 9.2 g tip mass. As expected, the tip mass decreases the natural frequency, while the adhesive tape has a negligible effect on the natural frequency. Fig. 21 (b) shows that the adhesive tape and the tip-mass increase the damping coefficient. The adhesive tape has a more substantial effect on the damping increase than the 9.2 g added tip mass, which is a reasonable choice of the tip-mass. These damping increases are consistent with the reduction of peak voltage due to the adhesive tape and the tip mass observed in Fig. 19 and Fig. 20. The adhesive tape's structural damping can be obtained by subtracting the damping coefficient of sample 3 (no adhesive tape) from sample 4 (with adhesive tape).

### *4.3. Group III tests (the copper-substrate MFC with different bonding layers)*

Group III tests investigate the effect of the bonding layer on voltage generation and damping coefficient. Samples 5, 6, and 7 with three different bonding layers, as described in Table 1, are tested in this group. The bonding layer for samples 5 and 6 is made of the same material but with different thicknesses, while the sample 7 bonding layer has the greatest thickness, with an elastic rubber-type material.

Fig. 22 (a) and (b) respectively show the maximum and RMS voltage outputs for different bonding layers. The 1200 μm Tesa® bonding layer results in 17% lower maximum voltage and 32% lower RMS voltage than that of the 100 μm bonding layer. The RMS voltage variations are thus more significant than the maximum voltage variations. To further

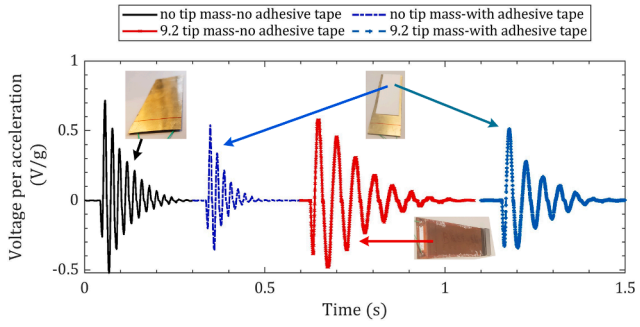


**Fig. 19.** The comparison of time signals for samples 3 (no adhesive tape) and 4 (with adhesive tape) with and without the 9.2 g tip mass.

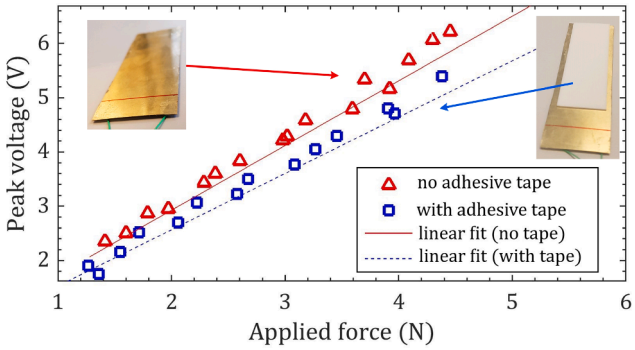


**Fig. 20.** Peak voltage for samples 3 (no adhesive tape) and 4 (with adhesive tape) versus base excitation amplitude (equivalent to applied force).

investigate this, the damping coefficients were calculated in each case.

The identified damping coefficients shown in Fig. 23 indicate that the contact layer substantially influences damping, while no significant natural frequency variations are observed. The 100 μm and 300 μm double-sided tape bonding layers have the lowest and the highest damping coefficients, while the 1300 μm rubber-type bonding layer damping between them. Fig. 23 shows that apart from the bonding layer thickness, the bonding layer damping also depends on the bonding layer material. Khazaee, Rezania, and Rosendahl [21] also demonstrated that the bonding layer state could change the damping coefficient. Therefore, the bonding layer damping is categorized as structural damping in this study, as it depends on the material dimensions and the material type. Table 3 gives the average variation of the damping coefficient due to different bonding layers. The bonding layer damping can vary up to 68% only due to adding two extra 100 μm bonding layers, while the rubber-type tape bonding layer increases the damping by 13%.

The damping coefficient rise causes the decaying voltage output to decay more rapidly, leaving a smaller RMS voltage. Therefore, the RMS voltage variations can be attributed to increased damping coefficient.

## 5. Discussions and application notes

### *5.1. The contribution of viscous and structural damping*

Experimental results show that the air damping varies as the base excitation amplitude increases. This subsection gives a detailed summary of the contributions for all the tested samples.

Fig. 24 shows the percentage contribution of viscous air damping to the total damping for the first two bending modes of sample 1 (No-Shim) and the first bending mode of sample 2 (Alu-Shim). The total damping comprises a structural component and a viscous air damping component. Thus the percentage contribution of structural damping is 100% minus that of viscous air damping. Overall, with increasing chirp acceleration amplitude ($A_c$), the beam-tip deflection increases, and the percentage contribution of air damping increases accordingly. There is a

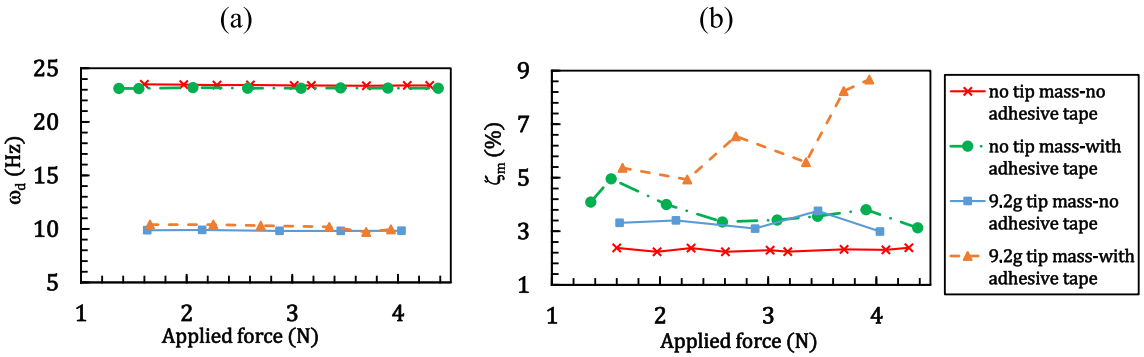


**Fig. 21.** The comparisons of (a) the natural frequency and (b) damping coefficient for samples 3 (no adhesive tape) and sample 4 (with adhesive tape) with and without a 9.2 g tip mass.

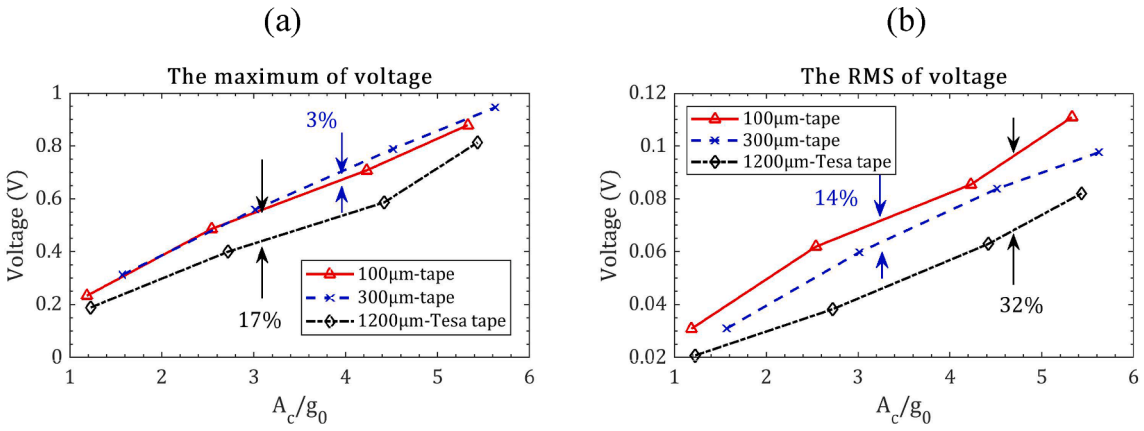


**Fig. 22.** (a) The maximum and (b) the RMS voltage for three different bonding layers (sample 5, 6, and 7) versus base excitation amplitude.

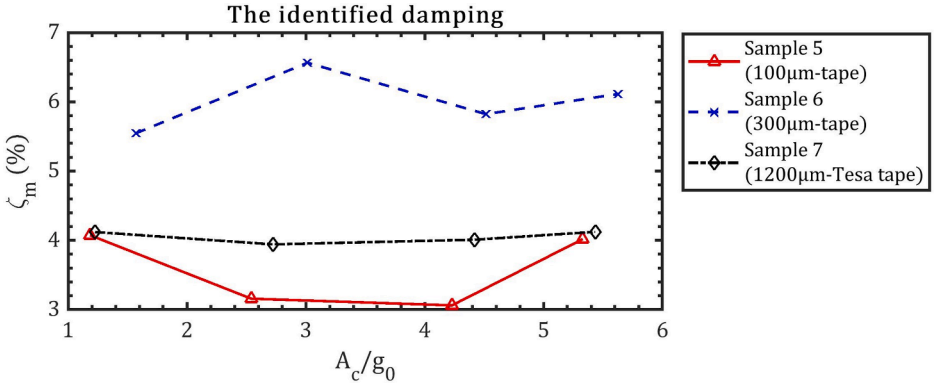


**Fig. 23.** The bonding layer's effect on the damping for the 100 μm, 300 μm, and Tesa® tape bonding layers (samples 5, 6, and 7, respectively).

corresponding reduction in the percentage contribution of structural damping. Nonetheless, even though the role of structural damping reduces with greater amplitude excitations, more than 80% of the total damping in the Alu-Shim sample is due to the structural damping. This is because of the bonding layer. By contrast, approximately 70% of the total damping in the first mode is due to air damping for the No-Shim sample. In the No-Shim sample, air damping dominates when $A_c/g_0 > 1.3$. This highlights the necessity of accounting for both structural and air damping, depending on the design of an energy harvester.

The viscous and structural damping contributions are different for different energy harvesters and depend on the bonding layer material, bonding layer thickness, and tip deflection. Table 4 presents the average of viscous and structural damping for all the test samples. Overall, the structural damping contribution is considerable compared to the viscous air damping, which can be approximately 37% to 85%, depending on the design. The MFC structural damping effect is much smaller than the bonding layer damping effect; for instance, there was only 0.3% structural damping for the MFC itself, compared with 2.8% for the epoxy bonding layer. In a typical energy harvester with a substrate shim and an epoxy bonding layer, the structural damping can contribute 75% or more of the total damping.

### 5.2. *The effect of added tip mass on the viscous damping*

As was shown in Fig. 18, the added tip mass on samples 1 and 2 increases the effective damping. The results for samples 3 and 4 in

**Table 3**
The comparison of the damping for the 100 μm, 300 μm, and Tesa® tape bonding layers (samples 5, 6, and 7).

| Sample No. | Bonding layer | $\zeta_m$ (%) | Variation |
|---|---|---|---|
| Sample 5 | 100 μm tape | 3.6 | – |
| Sample 6 | 300 μm tape | 6.0 | 68% |
| Sample 7 | 1200 μm Tesa® tape | 4.1 | 13% |

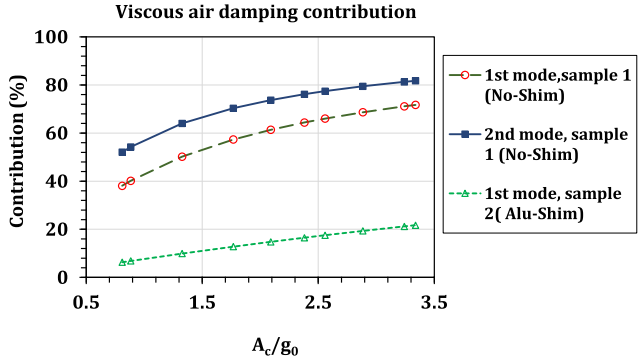


**Fig. 24.** Percentage contribution of viscous air damping in sample 1 (No-Shim) and sample 2 (Alu-Shim) versus acceleration excitation amplitudes.

Fig. 21 illustrate that added tip mass again increases the damping. Table 5 shows that when the piezoelectric harvester is more flexible (sample 1 with no substrate) the damping increase due to the tip mass is more significant than for the stiffer harvesters with substrate shim. The increased damping can be attributed to an increase in air damping due to increased vibration amplitude. Thus, in all the harvesters with a substrate, the damping increases due to the added tip mass. Consequently, the addition of a tip mass may not necessarily enhance the piezoelectric power generation performance in shock-type base excitation.

To assist understanding of the resonant behavior of the harvester with an added tip mass, a simple two-degree of freedom (2DOF) system is considered, which comprises two masses $M_1, M_2$, two springs, $k_1, k_2$, and one damper, $c_1$, as shown in Fig. 25 (a). Parameters are chosen for the standard system (System A) without tip-mass to fit the first and second mode resonant frequencies and the damping coefficients observed in the No-Shim sample. In System B, an added tip mass is appended to the free end of the 2DOF system. The damper in System B may be increased by a factor $\alpha$ to represent the observed damping increase due to air damping when a tip mass is added. In Fig. 25 (b), two bending modes in the beam and their analogs in the 2DOF system are shown. In a 3-1 mode piezoelectric harvester covered by electrodes on both sides, the generated voltage is proportional to the integral of normal strain over the length. This, in a bending beam, is proportional to the curvature integral, which implies that the generated voltage is proportional to the cantilever end rotation $\theta$. Hence $V \propto \theta$ as indicated in Fig. 25 (b). In the 2DOF analogue, the equivalent measure is the extension of spring $k_2$, given by $x_2 - x_1$.

For a given harmonic base excitation amplitude, $Y$, the transmissibility function relating the measured voltage amplitude $V$ to $Y$ is proportional to $\left|\frac{X_1}{Y} - \frac{X_2}{Y}\right|$, where

$$\begin{bmatrix} X_1/Y \\ X_2/Y \end{bmatrix} = \left( \begin{bmatrix} k_1+k_2 & -k_2 \\ -k_2 & k_2 \end{bmatrix} - \omega^2 \begin{bmatrix} m_1 & 0 \\ 0 & m_2 \end{bmatrix} + j\omega \begin{bmatrix} c_1 & 0 \\ 0 & 0 \end{bmatrix} \right)^{-1} \left( \begin{bmatrix} k_1 \\ 0 \end{bmatrix} + j\omega \begin{bmatrix} c_1 \\ 0 \end{bmatrix} \right) \tag{13}$$

Fig. 26 (a) compares $|V/Y|$ for the 4.2 g added mass with that for no tip mass (System A) for various degrees of air damping increase, $\alpha$. Note that the second-mode resonance peak value increases due to added tip mass for all $\alpha$. On the other hand, depending to the $\alpha$ value, the first-mode resonant peak value may increase or decrease when tip mass is added. Added tip mass increases the tip deflection while greater damping reduces the tip deflection. These two opposing effects balance each-other at a threshold value, $\alpha = \alpha_{thr}$. If $\alpha < \alpha_{thr}$ the effect of added tip mass increases the resonant peak, but when $\alpha > \alpha_{thr}$ the added tip mass decreases the resonant peak value. The ratio of resonant peak values of the system with tip mass to that without tip mass is shown in Fig. 26 (b), as functions of $\alpha$. The ratio of the second-mode peak values is always greater than unity while the first mode peak value crosses unity when $\alpha$ 2. The simple analogue 2DOF system has behavior similar to the experimental results given in Fig. 17. The experimental results show that the first mode peak value is not increased after adding tip mass, whereas the second-mode peak values increased by adding tip mass. It can be concluded that added tip mass, which increases beam tip deflection, also affects the viscous air damping that should be considered in designing an energy harvester.

### 5.3. The role of the bonding layer

The bonding layer in the piezoelectric energy harvesters is a thin layer that joins the piezoelectric and supporting structure. In modeling, the bonding layer is often neglected due to its low thickness. Experimental results in group II and III tests showed that the bonding layer has a small effect on the natural frequency, and therefore, from a stiffness perspective, it seems logical to neglect the bonding layer. However, the experimental tests illustrate the substantial damping and power output variations due to different bonding layers. Thus, the bonding layer can affect the piezoelectric power generation performance because of the damping change. From an energy-harvesting perspective, the less the damping, the higher the power output is. Thus, knowing the bonding layer's damping effect can lead to higher efficient energy harvesters which minimizing structural energy loss.

The measured structural damping coefficients for four different bonding layers are shown in Fig. 27, namely 3M Company double-sided tape, Tesa® double-sided tape, Epoxy 3430, and Epoxy rapid 332. Two

**Table 4**
The contribution of the viscous and structural damping for all the group tests.

| Sample No. | Piezoelectric | Substrate | Contact layer | Total damping (%) | Structural damping (%) | Viscous damping (%) | Structural damping contribution in the total damping (%) |
|---|---|---|---|---|---|---|---|
| 1 | MFC | – | – | 0.81 | 0.31 | 0.50 | 37.9 |
| 2 | | 120 μm aluminum | 260 μm Epoxy | 3.34 | 2.84 | 0.50 | 85.0 |
| 3 | | 100 μm brass | 300 μm Epoxy | 2.31 | 2.10 | 0.21 | 91.0 |
| 4 | | 100 μm brass+1 Tesa® adhesive layer | 300 μm Epoxy | 4.87 | 3.79 | 1.08 | 77.7 |
| 5 | | 100 μm copper | 100 μm 3M Company double-sided tape | 3.58 | 1.22 | 2.36 | 34.0 |
| 6 | | 100 μm copper | 300 μm 3M Company double-sided tape | 6.01 | 3.65 | 2.36 | 60.7 |
| 7 | | 100 μm copper | 1200 μm Tesa® double-sided tape | 4.05 | 1.69 | 2.36 | 41.7 |

**Table 5**
The variations of the natural frequency and the damping versus the tip mass.

| Tip mass (g) | 0 | | 4.20 | | 9.20 | | Variation (%) | |
|---|---|---|---|---|---|---|---|---|
| Sample No. | $\omega_n$ (Hz) | $\zeta_m$ (%) | $\omega_n$ (Hz) | $\zeta_m$ (%) | $\omega_n$ (Hz) | $\zeta_m$ (%) | $\omega_n$ | $\zeta_m$ |
| 1 | 16.20 | 0.78 | 8.20 | 1.59 | – | – | −49.38 | 103.85 |
| 2 | 21.30 | 3.34 | 10.80 | 3.59 | – | – | −49.30 | 7.49 |
| 3 | 23.42 | 2.31 | – | – | 9.84 | 3.31 | −57.97 | 43.73 |
| 4 | 23.14 | 3.79 | – | – | 10.14 | 6.52 | −56.2 | 72.13 |

of these bonding layers are the double-sided tapes, and two others are the cured epoxy bonding layers. The Tesa® double-sided layer is rubber-based and more elastic than the 3M Company double-sided tape. Results show that the rubber-type double-sided tape has a more significant damping effect than the 100 μm-thickness 3M Company double-sided tape. Besides, overall, the double-sided tapes have less damping effect than the epoxy bonding layers.

Crandall [48] suggested that the structural damping can be due to the transverse heat flow from the regions under compression to the tensile regions and the acoustic radiation from the vibrating beam. Therefore, if a bonding layer has a greater capacity to emit acoustic radiations or creates greater heat flow, the structural damping may be expected to be higher. The experiments also suggest that that thicker bonding layers provide greater capacity to absorb mechanical energy. Thus, the relatively thick epoxy bonding layers have the highest damping coefficient, while the thin 3M double-sided tape has the lowest damping.

### 5.4. The application notes for the design of piezoelectric harvesters

There is a wide range of vibration sources for the VEH, with different vibration levels and vibration types. The vibration sources for energy harvesting can be continuous, ranging from 0.1 g to 2 g, or shock-induced, typically >1 g, as shown in Table 6. Usually, the shock-induced and impact-based sources have greater peak amplitudes, as their acting time is small, in the order of milliseconds. This study's shock-induced vibrations range from 0.5 $g_0$ to 3.5 $g_0$, a low-to-medium range of accelerations. As in the shock-induced vibrations, the structure vibrates with its fundamental natural frequency; this shock-based beam vibration can be analogous to the resonant excitations; however, the continuous-type acceleration counterpart would be different, depending on the harvester quality factor [50]. This continuous-type acceleration range would be approximately 0.03 $g_0$ to 0.3 $g_0$ at the resonant frequency, which lies within industrial applications such as a water pump [51]. Therefore, the presented experimental results can be beneficial for a low-to-medium range of accelerations in shock-induced and continuous vibration sources.

A typical PEH contains two piezoelectric layers attached to a substrate [49] known as bimorph as it generates higher power output in almost the same volume as a one layer piezoelectric beam. In these typical PEHs, bonding layers are an essential part of the structure. Since the piezoelectric harvester is undergoing dynamic motion for energy harvesting applications, two damping energy dissipation sets occur. The kinetic motion of the structure creates air friction, and the material internal friction creates structural damping. The combined viscous and structural damping model presented here can benefit the study of all types of piezoelectric beams. The results suggest a structural damping contribution of about 40% in the 100 μm bonding layer and 60% in the

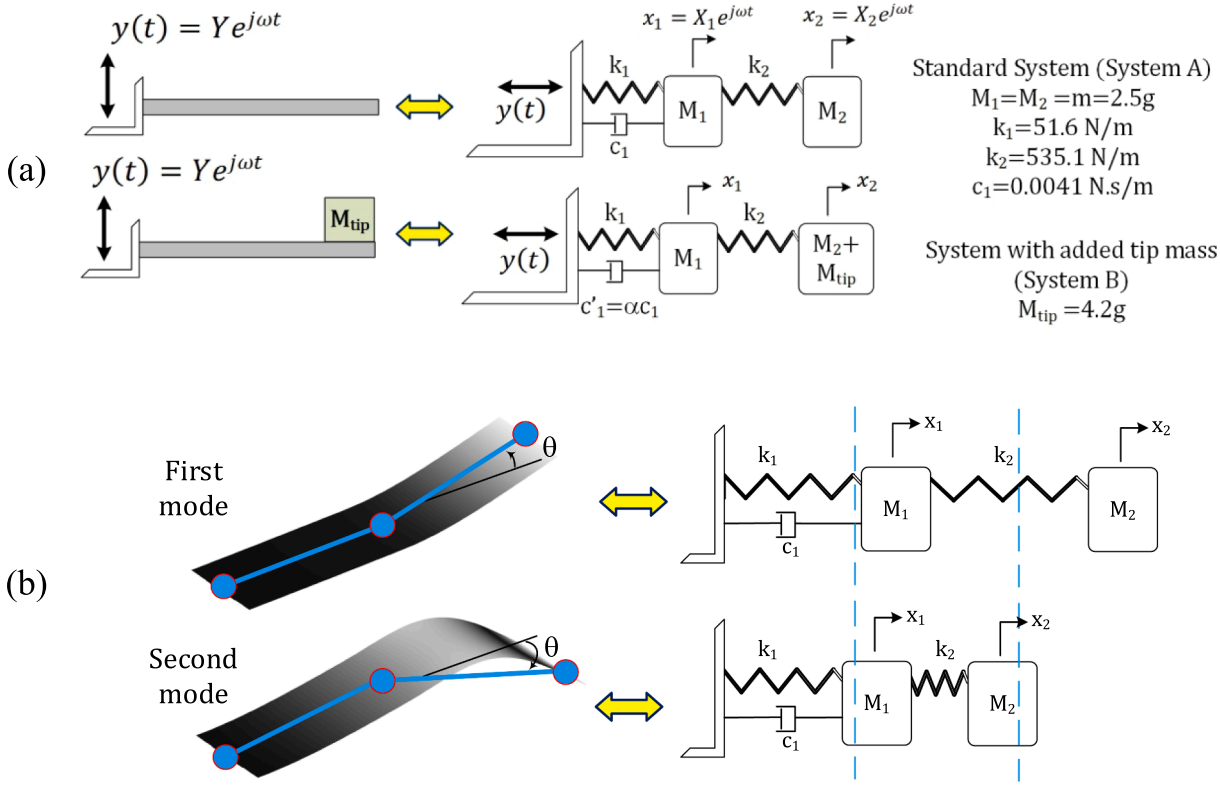


**Fig. 25.** (a) Representing the harvester transverse-vibration with an analog 2DOF system. (b) The first two bending modes of the cantilever beam and their analog modes in the 2DOF system.

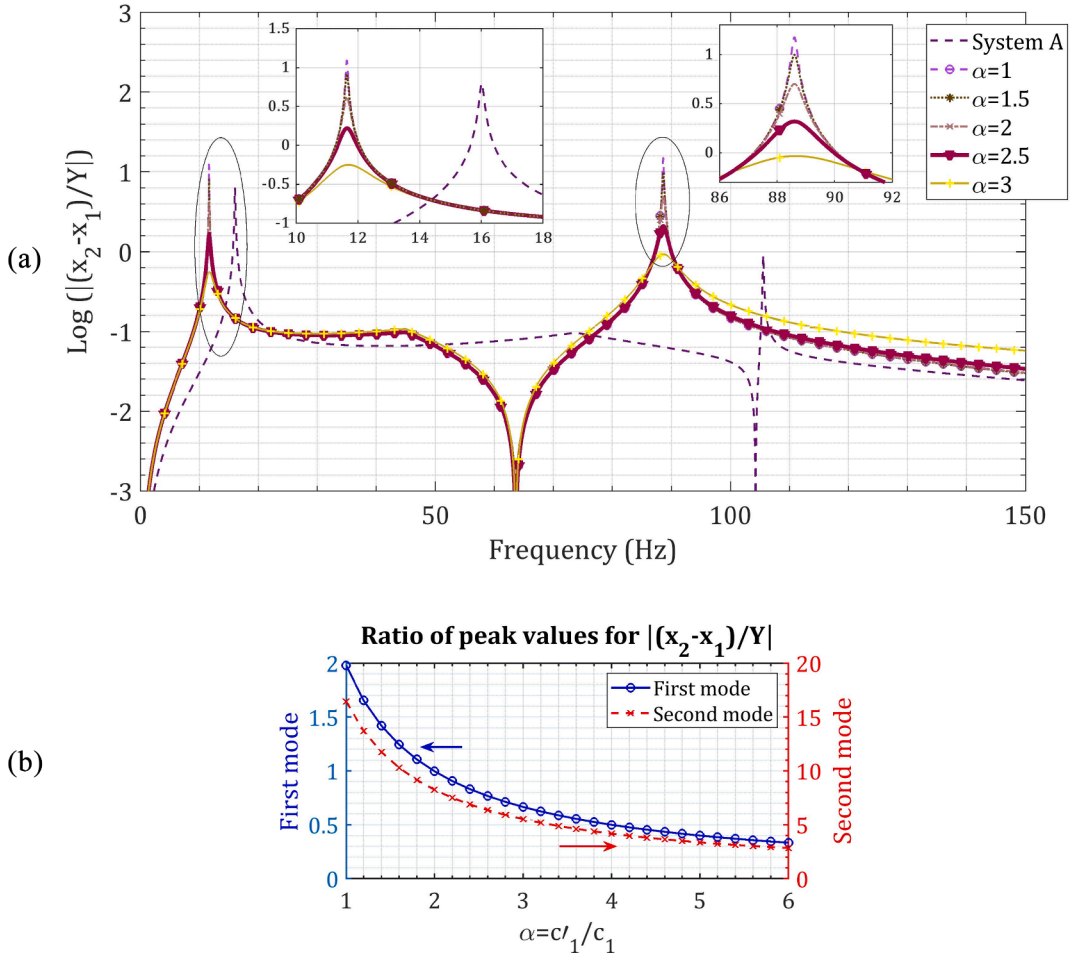


**Fig. 26.** (a) The comparison of $|(x_2 - x_1)/Y|$ between no tip mass and with tip mass (system B) with different damping constants and (b) ratios of peak values of the System B to the System A against $\alpha = c'_1/c_1$ ratio.

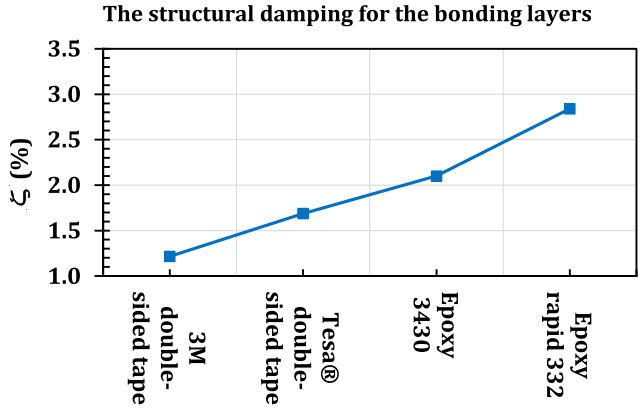


**Fig. 27.** The structural damping for the different bonding layers (3M Company double-sided tape, Tesa® double-sided tape, Epoxy 3430, and Epoxy rapid 332).

300 μm bonding layer.

The average power generation is also vital in shock-induced energy harvesters. As the average generated power is adversely affected by the damping, the damping should be minimized. Therefore, the harvester configuration should be designed for power maximization. The results suggest that the bonding layer should have a low thickness. In addition, the results highlight the importance of additional viscous damping, indirectly due to the tip mass, which can adversely affect the energy conversion efficiency. If the additional damping due to the tip mass is less than about 40% of the original damping, then the tip mass can positively affect the power generation.

**Table 6**
Different continuous and shock-induced vibration sources with potential applications for piezoelectric energy harvesting.

| Vibration source | Vibration type | Peak amplitude ($m/s^2$) [$g_0$] | Reference |
|---|---|---|---|
| Car engine compartment | Continuous | 12 [1.22 $g_0$] | [12] |
| Blender casing | Continuous | 6.4 [0.65 $g_0$] | [12] |
| Clothes dryer | Continuous | 3.5 [0.36 $g_0$] | [12] |
| Microwave oven top | Continuous | 1.11 [0.11 $g_0$] | [45] |
| Microwave oven side | Continuous | 4.21 [0.43 $g_0$] | [45] |
| Water pump | Continuous | 8.11 [0.83 $g_0$] (0.49 $m/s^2$ for 50 Hz harmonic) | [51] |
| Sheep heart | Shock induced | Peak-to-peak: 17.7 [1.8 $g_0$] | [50] |
| Car tire | Shock induced | Peak-to-peak: 1570 [160 $g_0$] | [52] |

## 6. Concluding remarks

In this paper, modal parameters are extracted using the Short-Term Fourier Transform and Resampling method for piezoelectric energy harvesters with clamped-free boundary conditions. The emphasis is on

the extraction of damping coefficients, using only the voltage response of the harvester to a shock base-excitation. The contributions of structural damping and viscous damping to the total damping are identified. This enables the damping effects of a bonding layer and shim to be interpreted, as well as providing an interpretation of the indirect effects of tip mass on damping. The method further enables the modal parameters to be separately extracted for each mode of vibration. Overall, the Short-Term Fourier Transform and Resampling method provides a promising route for assessing modal parameters, especially damping, in energy harvesters. The results demonstrate the prominent effect of a bonding layer on the structural damping but also indicate the need to include the more subtle effects of air damping when designing energy harvesters. Investigating different bonding layers shows that the bonding layer material and thickness significantly affect the structural damping. An important aspect is that the viscous air damping is not constant with respect to input excitation acceleration, becoming more influential at higher excitation (and hence higher power) levels. Adding tip mass also increases the viscous damping effect due to increasing the tip deflections. For energy harvesting applications, the voltage peak and root mean square will reduce in shock-induced excitations when the damping increases; therefore, the piezoelectric harvester performance will be reduced. The results provide essential guidance for energy harvester design.

## CRediT authorship contribution statement

**Majid Khazaee:** Conceptualization, Methodology, Writing - original draft, Software, Data curation, Visualization. **John E. Huber:** Methodology, Investigation. **Lasse Rosendahl:** Methodology, Supervision. **Alireza Rezania:** Methodology, Investigation, Supervision.

## Declaration of Competing Interest

The authors declare that they have no known competing financial interests or personal relationships that could have appeared to influence the work reported in this paper.

## References


[1] Sezer N, Koç M. A comprehensive review on the state-of-the-art of piezoelectric energy harvesting. Nano Energy 2021;80:105567. https://doi.org/10.1016/j.nanoen.2020.105567.

[2] Zou H-X, Zhao L-C, Gao Q-H, Zuo L, Liu F-R, Tan T, et al. Mechanical modulations for enhancing energy harvesting_ Principles, methods and applications _ Elsevier Enhanced Reader.pdf. Appl Energy 2019;255:113871.

[3] Sarker MR, Julai S, Sabri MFM, Said SM, Islam MM, Tahir M. Review of piezoelectric energy harvesting system and application of optimization techniques to enhance the performance of the harvesting system. Sensors Actuators, A Phys 2019;300:111634. https://doi.org/10.1016/j.sna.2019.111634.

[4] Nakamura Kentaro. Ultrasonic transducers: materials and design for sensors, actuators and medical applications. Woodhead Publishing Limited; 2012.

[5] Anton SR, Sodano HA. A review of power harvesting using piezoelectric materials (2003–2006). Smart Mater Struct 2007;16:R1–21. https://doi.org/10.1088/0964-1726/16/3/R01.

[6] Khazaee M, Rezaniakolaie A, Moosavian A, Rosendahl L. A novel method for autonomous remote condition monitoring of rotating machines using piezoelectric energy harvesting approach. Sensors Actuators A Phys 2019;295:37–50. https://doi.org/10.1016/j.sna.2019.05.016.

[7] Guo L, Lu Q. Numerical analysis of a new piezoelectric-based energy harvesting pavement system: lessons from laboratory-based and field-based simulations. Appl Energy 2019;235:963–77. https://doi.org/10.1016/j.apenergy.2018.11.037.

[8] Khazaee M, Rezaniakolaei A, Rosendahl LA. A study on interaction effects of different harmonics in translational base excitation for piezoelectric vibration energy harvesters. ECCOMAS Smart 2019;2019.

[9] Yi JW, Shih WY, Shih WH. Effect of length, width, and mode on the mass detection sensitivity of piezoelectric unimorph cantilevers. J Appl Phys 2002;91:1680–6. https://doi.org/10.1063/1.1427403.

[10] Kim M, Hoegen M, Dugundji J, Wardle BL. Modeling and experimental verification of proof mass effects on vibration energy harvester performance. Smart Mater Struct 2010;19:045023. https://doi.org/10.1088/0964-1726/19/4/045023.

[11] Lallart M, Zhou S, Yang Z, Yan L, Li K, Chen Y. Coupling mechanical and electrical nonlinearities: the effect of synchronized discharging on tristable energy harvesters. Appl Energy 2020;266. https://doi.org/10.1016/j.apenergy.2020.114516.

[12] Roundy S, Wright PK, Rabaey J. A study of low level vibrations as a power source for wireless sensor nodes. Comput Commun 2003;26:1131–44. https://doi.org/10.1016/S0140-3664(02)00248-7.

[13] Khalili M, Biten AB, Vishwakarma G, Ahmed S, Papagiannakis AT. Electromechanical characterization of a piezoelectric energy harvester. Appl Energy 2019;253. https://doi.org/10.1016/j.apenergy.2019.113585.

[14] Wang X. A study of harvested power and energy harvesting efficiency using frequency response analyses of power variables. Mech Syst Signal Process 2019;133:106277. https://doi.org/10.1016/j.ymssp.2019.106277.

[15] DuToit NE, Wardle BL. Experimental verification of models for microfabricated piezoelectric vibration energy harvesters. AIAA J 2007;45:1126–37. https://doi.org/10.2514/1.25047.

[16] Erturk A, Inman DJ. An experimentally validated bimorph cantilever model for piezoelectric energy harvesting from base excitations. Smart Mater Struct 2009;18:025009. https://doi.org/10.1088/0964-1726/18/2/025009.

[17] Kim M, Dugundji J, Wardle BL. Efficiency of piezoelectric mechanical vibration energy harvesting. Smart Mater Struct 2015;24:055006. https://doi.org/10.1088/0964-1726/24/5/055006.

[18] Hosaka H, Itao K, Kuruda S. Damping characteristics of beam-shaped micro-oscillators. Sensors Actuators, A Phys 1995;49:87–95. https://doi.org/10.1016/0924-4247(95)01003-J.

[19] Sessner V, Liebig WV, Weidenmann KA. Modal damping behavior of plane and 3D curved constrained layer damping CFRP-elastomer-metal laminates. Compos Part C Open Access 2020;2:100037. https://doi.org/10.1016/j.jcomc.2020.100037.

[20] Zhou XQ, Yu DY, Shao XY, Zhang SQ, Wang S. Research and applications of viscoelastic vibration damping materials: a review. Compos Struct 2016;136:460–80. https://doi.org/10.1016/j.compstruct.2015.10.014.

[21] Khazaee M, Rezania A, Rosendahl L. Effect of damage and support damping mechanisms on unimorph piezoelectric energy harvester. J Vib Control 2019:107754631985516. 10.1177/1077546319855162.

[22] Arafa M, Baz A. Energy dissipation characteristics of active pieozoelectric damping composites. Compos Sci Technol 2000;60:2759–68.

[23] Kwak W. Optimal design and experimental verification of piezoelectric energy harvester with fractal structure. Appl Energy 2021;282:116121.

[24] Moradi-Dastjerdi R, Radhi A, Behdinan K. Damped dynamic behavior of an advanced piezoelectric sandwich plate. Compos Struct 2020;243:112243. https://doi.org/10.1016/j.compstruct.2020.112243.

[25] Khazaee M, Rezaniakolaei A, Rosendahl L. A proof for looking differently into damping modeling in piezoelectric energy harvesting systems. Proc 26th Int Congr Sound Vib ICSV 2019;2019:1–8.

[26] Cooley CG, Tran TQ, Chai T. Comparison of viscous and structural damping models for piezoelectric vibration energy harvesters. Mech Syst Signal Process 2018;110:130–8. https://doi.org/10.1016/j.ymssp.2018.03.017.

[27] Iglesias FS, Lopez AF. Rayleigh damping parameters estimation using hammer impact tests. Mech Syst Signal Process 2020;135:106391.

[28] Ewins J. Modal Testing : Theory, Practice and Application. Second. RSP; 2000.

[29] He J, Fu Z-F. Modal analysis. 1st ed. Butterworth-Heinemann; 2001.

[30] Paknejad A, Rahimi G, Farrokhabadi A, Khatibi MM. Analytical solution of piezoelectric energy harvester patch for various thin multilayer composite beams. Compos Struct 2016;154:694–706. https://doi.org/10.1016/j.compstruct.2016.06.074.

[31] Shen D, A. Piezoelectric energy harvesting devices for low frequency vibration applications. Auburn University; 2009.

[32] Khazaee M, Nobari AS, Aliabadi MHF. Experimental investigation of delamination effects on modal damping of a CFRP laminate, using a statistical rationalization approach. Comput Exp Methods Struct 2018;10:75–103. https://doi.org/10.1142/9781786344977_0003.

[33] Shariyat M, Jahangiri M. Nonlinear impact and damping investigations of viscoporoelastic functionally graded plates with in-plane diffusion and partial supports. Compos Struct 2020;245:112345. https://doi.org/10.1016/j.compstruct.2020.112345.

[34] Vinogradov AM, Schmidt VH, Tuthill GF, Bohannan GW. Damping and electromechanical energy losses in the piezoelectric polymer PVDF. Mech Mater 2004;36:1007–16.

[35] Banks HT, Inman DJ. On damping mechanisms in beams. J Appl Mech Trans ASME 1991;58:716–23. https://doi.org/10.1115/1.2897253.

[36] Khazaee M, Rezaniakolaei A, Rosendahl L. A comprehensive electromechanically coupled model for non-uniform piezoelectric energy harvesting composite laminates. Mech Syst Signal Process 2020;145:106927.

[37] Ju S, Ji CH. Impact-based piezoelectric vibration energy harvester. Appl Energy 2018;214:139–51. https://doi.org/10.1016/j.apenergy.2018.01.076.

[38] Smart Material Inc.; April 2020.

[39] Hentschel OP, Scheidt LP Von, Wallaschek J, Denk M. Introduction and evaluation of a damping determination method based on the Short-Term fourier transform and Resampling (STFR). J Theor Appl Mech 2015;53:439–52. 10.15632/jtam-pl.53.2.395.

[40] Khazaee M, Rezania A, Rosendahl L. An experimental study to determine damping of piezoelectric harvesters using transient analysis of unified electromechanical voltage equation. Energy Convers Manag 2021;227:113567. https://doi.org/10.1016/j.enconman.2020.113567.

[41] Inman DJ. Engineering vibration. 3rd ed. New Jersey: Prentice-Hall, Inc.; 2001.

[42] Woolam WE. Drag coefficients for flat square plates oscillating normal to their planes in air. Langley Research Center; 1972.

[43] Baker WE, Woolam WE, Young D. Air and internal damping of thin cantilever beams. Int J Mech Sci 1967;9:743–66.

[44] Jacquelin E, Adhikari S, Friswell MI. A piezoelectric device for impact energy harvesting. Smart Mater Struct 2011;20:105008. https://doi.org/10.1088/0964-1726/20/10/105008.
[45] DuToit NE, Wardle BL, Kim SG. Design considerations for MEMS-scale piezoelectric mechanical vibration energy harvesters. Integr Ferroelectr 2005;71:121–60. https://doi.org/10.1080/10584580590964574.
[46] Khazaee M, Rezaniakolaei A, Rosendahl L. An experimental study on macro Piezoceramic fiber composites for energy harvesting. Mater Sci Forum 2019;951:3–8. https://doi.org/10.4028/www.scientific.net/MSF.951.3.
[47] Khazaee M, Rezaniakolaei A, Rosendahl L. On the effect of driving amplitude, frequency and frequency-amplitude interaction on piezoelectric generated power for MFC unimorph. In: Proc 26th Int Congr Sound Vib ICSV 2019 2019:1–7.
[48] Crandall SH. The role of damping in vibration theory. J Sound Vib 1970;11:3–18. https://doi.org/10.1016/S0022-460X(70)80105-5.
[49] Li H, Tian C, Deng ZD. Energy harvesting from low frequency applications using piezoelectric materials; 2014. 10.1063/1.4900845.
[50] Jackson Nathan, Olszewski Oskar Z. Cian O'Murchu and AM. shock-induced aluminum nitride piezoelectric energy harvester leadless pacemaker. Sensors Actuators, A Phys 2017;264:212–8.
[51] Moosavian A, Khazaee M, Ahmadi H, Khazaee M, Najafi G. Fault diagnosis and classification of water pump using adaptive neuro-fuzzy inference system based on vibration signals. Struct Heal Monit 2015;14:402–10. https://doi.org/10.1177/1475921715591873.
[52] Elfrink R, Matova S, De Nooijer C, Jambunathan M, Goedbloed M, Van De Molengraft J, et al. Shock induced energy harvesting with a MEMS harvester for automotive applications. Tech Dig - Int Electron Devices Meet IEDM 2011:677–80. https://doi.org/10.1109/IEDM.2011.6131639.

# Appendix H. Paper 8: Reference [162]

## An experimental study to determine damping of piezoelectric harvesters using transient analysis of unified electromechanical voltage equation

M. Khazaee, A. Rezaniakolaei, L. Rosendahl.

This paper has been published in

*Energy Conversion and Management*. vol. 227, pp. 113567, 2021.

Energy Conversion and Management 227 (2021) 113567

Contents lists available at ScienceDirect

Energy Conversion and Management

journal homepage: www.elsevier.com/locate/enconman

# An experimental study to determine damping of piezoelectric harvesters using transient analysis of unified electromechanical voltage equation

Majid Khazaee, Alireza Rezania *, Lasse Rosendahl

*Department of Energy Technology, Aalborg University, Pontopidanstræde 111, 9220 Aalborg, Denmark*

ARTICLE INFO

*Keywords:*
Transient
Piezoelectric
Energy harvesting
Resonant frequency
Damping determination

ABSTRACT

Toward the accurate electrical and mechanical modulations of the piezoelectric harvester, this paper presents a unified electromechanical-coupled voltage equation and a damping determination method. A single differential equation for the voltage is obtained that accommodates mechanical and electrical physics for which the exact transient solution is presented. In addition, the fully coupled relationship between the voltage output, the driving vibration frequency, and the resistive electrical load is clarified. A simple method is devised to determine the damping coefficient from only the voltage time-domain measurements based on the harmonic transient voltage response (HTVR). The HTVR uses the transient characteristics of the voltage measurements. The results showed that the electromechanical-coupling effect on the harvester resonant frequency is influential for the kilo Ohm scale electrical loads. This finding is contributed to the piezoelectric harvester's frequency-matched design by calculating the accurate coupled natural frequency. The results also proved the ability of the HTVR in the accurate determination of the damping coefficient without prior modeling and using only the voltage measurements made on the piezoelectric harvester. The results also demonstrate the HTVR ability for characterizing the piezoelectric harvester by accurate damping determination under any arbitrary-frequency harmonic excitation even with noisy, polluted voltage measurements.

## 1. Introduction

The direct piezoelectric effect [1] has been widely used for vibration piezoelectric energy harvesting (VPEH) applications [2,3], aiming to generate power ranging from small rain impact forces [4] to large-scale power generation such as smart pavement system [5]. Zou et al. [6] recently reported the different mechanical modulations for the kinetic energy sources to improve energy harvesting. Three of these mechanical modulations are excitation conversion, frequency-up conversion, and force/motion amplification. In these modulations, the harvester is modulated by either tuning the PEH resonant frequency, increasing the driving frequency (for frequency matching), amplifying the source amplitude, or minimizing the damping factor. In the energy-harvesting prospect, the electrical modulation is also important as the main goal is to optimize the electrical power generation. Different electrical modulations have been proposed, including purely resistive [7,8], complex impedance [8], resistive-capacitive [9], and synchronous switched extraction [10] circuits. An essential factor in these electrical modulations is the resistive load. According to the state-of-the-art [9,11,12], the optimal resistive load depends on the mechanical factors, such as the driving frequency, the natural frequency, and the damping factor. Therefore, the mechanical and electrical modulations cannot be accomplished separately as, in piezoelectric materials, mechanical and electrical physics are electromechanically coupled. Fig. 1 shows the different electrical and mechanical modulations for improving the performance of PEHs.

Two prominentand influential factors in improving energy harvesting are frequency matching [13,14] and electrical load matching [15]. Many studies have been carried out for providing a better frequency matching [16] or matching over a broader range of frequencies [17]. As a practical example, Khazaee et al. [12] matched a bimorph beam's resonant frequency to a water pump's operating frequency for designing a PEH. They showed that the PEH resonant frequency could be different from the PEH natural frequency because of the damping and electromechanical coupling factors [12]. Some studies have tried to obtain the optimum resistive load. DuToit et al. [18] obtained the optimum load in a simple circuit with only a resistive load by differentiating the analytical power equation. A similar approach for obtaining the optimum load resistance, differentiating the analytical power, has been taken in different circuits [7–10]. Kong et al. [8] showed that a purely resistive load has good efficiency around the resonant compared to complex

* Corresponding author.
*E-mail addresses:* mad@et.aau.dk (M. Khazaee), alr@et.aau.dk (A. Rezania), lar@et.aau.dk (L. Rosendahl).

https://doi.org/10.1016/j.enconman.2020.113567
Received 22 July 2020; Received in revised form 23 September 2020; Accepted 16 October 2020
Available online 9 November 2020

**Nomenclature**

*Abbreviations*

| | |
|---|---|
| FFT | Fast Fourier Transform |
| PEH | Piezoelectric energy harvester |
| VPEH | vibration piezoelectric energy harvesting |

*Latin letters*

| | |
|---|---|
| $b$ | beam width |
| $\mathscr{C}_a$ | damping coefficient, $m/s$ |
| $C_P$ | Piezoelectric capacitance, $F$ |
| $\bar{c}_{11}^{E}$ | Piezoelectric stiffness, $Pa$ |
| $\bar{e}_{31}$ | Piezoelectric coefficient, $C/m^2$ |
| $E_z$ | z-direction electric field, $N/C$ |
| g | envelope curve |
| $h$ | thickness, $m$ |
| $\mathscr{H}$ | Heaviside function |
| $I$ | Piezoelectric current, $A$ |
| $L$ | beam length |
| $m^*$ | beam mass per unit length, $kg/m$ |
| M | internal bending moment, $N.m$ |
| $M_t$ | added tip mass, $kg$ |
| N | $N$th peak value in decrement voltage response |
| $\mathscr{P}$ | Piezoelectric coupling factor |
| $R_L$ | electrical resistive load, Ω |
| t | time, $s$ |
| $T_{xx}$ | stress in x-direction, $Pa$ |
| V | voltage, $V$ |
| $v_0$, $\dot{v}_0$ | initial voltage conditions, $V$ |
| $YI$ | beam bending stiffness, $N.m^3$ |
| $Y_s$ | substrate stiffness, $Pa$ |
| w | beam transverse deformation, $m$ |
| $Y_B$ | base displacement, $m$ |
| $z$ | level from the neutral axis, $m$ |

*Greek letters*

| | |
|---|---|
| $\bar{\varepsilon}_{33}$ | permittivity constant, $F/m$ |
| $\varepsilon_{xx}$ | axial strain |
| $\phi$ | the beam mode shape |
| $\eta$ | the mechanical response in the modal coordinate |
| $\zeta$ | dimensionless damping coefficient |
| $\omega$ | driving frequency, $rad/s$ |
| $\omega_{nc}$ | coupled natural frequency, $rad/s$ |
| $\omega_{dc}$ | coupled damped natural frequency, $rad/s$ |
| $\omega_n$ | undamped natural frequency, $rad/s$ |
| Υ, Λ | Piezoelectric coupling factor in modal representation |
| $\sigma$ | base excitation inertial factor, $kg$ |
| Ω | frequency ratio |
| Γ | frequency coupling factor |
| $\theta$, $\phi$ | phase angles, $rad$ |

*subscripts*

| | |
|---|---|
| eff | effective |
| $OC$ | open-circuit |
| peak | peak voltage value |
| $s$ | substrate shim |
| steady | steady-state |
| $p$ | piezoelectric layer |
| $R$ | with resistive load |
| trans | transient state |

impedance. Liao et al. [9] showed that in the resistive-capacitive circuits, the optimum resistive load is independent of the optimum capacitance and therefore the resistance load can be optimized independently. Therefore, the role of finding the optimum resistance load in all the electrical modulations is essential. All the resistive load optimization studies point out to the fact that the optimum load depends on the driving frequency, the natural frequency, and mechanical damping factor.

Damping coefficient, which can be defined as any source of energy dissipation, affects the resonance generated power [19] and the optimum resistive load [11]. In the cantilevered configurations, the energy dissipation can be mainly due to air resistance force, squeeze force, internal energy dissipation, and support loss [20]. These energy dissipation sources are very influential and dependent to the load and boundary conditions. For instance, the tightening torque of the clamping box bolts [21] or the excitation amplitude [16] can vary the damping and, consequently the output power. The nonlinear air damping coefficient was also investigated by Dayou et al. [22]. There are approaches to extract damping coefficient from the experimental data such as the decay free-vibration [23], the frequency–response peak-based (peak picking and peak bandwidth [24]), the curve fitting [25], and the energy dissipation method [26]. In these methods, a sensor records the

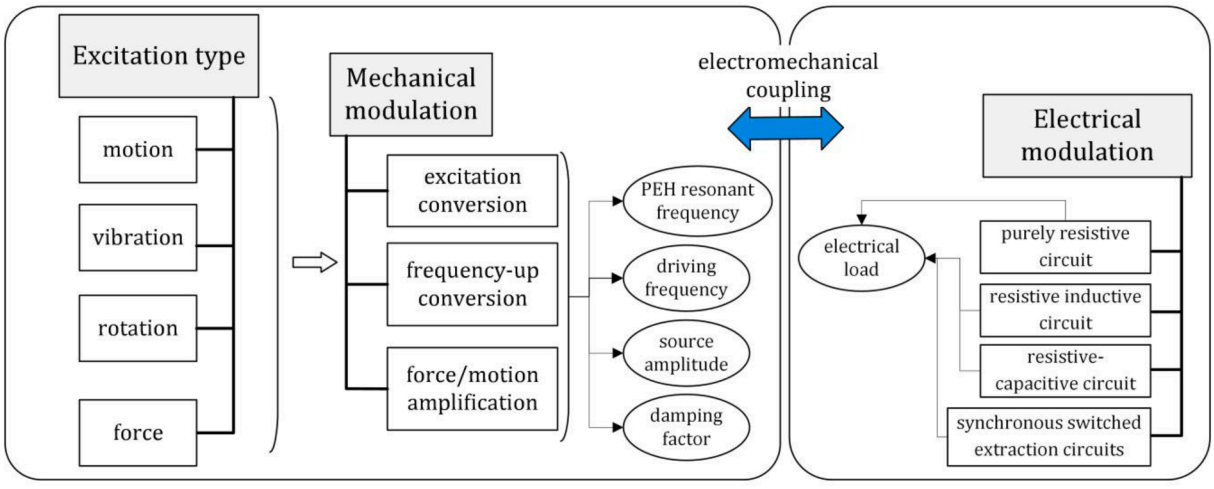


**Fig. 1.** Mechanical and electrical modulations for improving the performance of PEHs.

structure response to a controlled input force or environmental forces and by analyzing the data, the damping factor is determined. These methods are apply to all the structures, including piezoelectric harvesters. In the decay free-vibration method, the transient time domain response to an initial impact is analyzed. In the frequency–response based methods, the steady response from harmonic excitations over a range of frequencies is analyzed and the damping is extracted from the location of the peak in the frequency response function. Dayou et al. [22] applied the logarithmic decay free-vibration method and FFT on the beam's displacement measurements for obtaining the damping coefficient in piezoelectric beams. Ju and Ji [27] used a similar logarithmic free-vibration method for the damping determination of piezoelectric beams. Yang and Upadrashta [16] used the experimental velocity measurements and energy dissipation method for obtaining the damping factor in PEHs at different load conditions.

To accomplish both the electrical and mechanical modulations, understanding the exact relationship between the PEH resonant frequency and electromechanical coupling is mandatory because the optimum load and frequency matching are interdependent. Some previous studies numerically reported the PEH resonant frequency dependency to the resistive load [28,29]. However, these studies have not derived a precise relationship between the PEH natural frequency, driving frequency, and electrical load, as the mechanical and electrical physics is coupled. Consequently, simultaneous electrical and mechanical optimizations cannot be undertaken, and, instead, step-by-step optimization shall be taken, which was shown is not efficient for a practical case [12]. Moreover, state-of-the-art damping determination methods have some limitations. If the method requires an attached sensor, the sensor weight alters the vibration response and thus the identified damping will not be accurate. Moreover, the noise effect can be significant if non-contact sensors are employed for measuring the decay vibration response because the structure experiences free vibration at small beam deformations. In the logarithmic decay methods, the magnitude of the initial impact is not controllable and as the damping has nonlinearity [16], the identified damping may be different for different impact magnitudes. Therefore, the logarithmic decay method is often accompanied by uncertainties. Many measurements with adequate frequency steps are needed in the frequency-response peak-based methods, making them costly in experimental tests and data analysis. Classical curve fitting, such as the circle or line fitting, require multi-sensory data obtained from various experimental tests followed by complex numerical and optimization algorithms. Practically, it will be of great interest if the damping coefficient can be simply determined using system-specific methods [16].

In the present paper, toward a better electrical and mechanical design of PEHs, a unified voltage analytical equation will be derived that accommodates the electromechanical relationship between the driving frequency, the PEH natural frequency, and the electrical load. This unified voltage equation will facilitate simultaneous mechanical and electrical modulations. A damping determination method is derived based on only voltage measurements made on PEHs without any requirement for sensory data or pre-modeling. The damping determination method is based on the transient voltage response to the harmonic excitation and only relies on the experimental data with no need for prior knowledge of the system. Using the transient harmonic voltage response for the damping determination is novel. The current study contributes to the VPEH knowledge by providing a robust tool for evaluating the damping coefficient at any harmonic load and boundary condition and a better understanding of the PEH electromechanical coupling, which can be used for the optimal PEH design. This study also provides a simple and accurate method for the correct damping coefficient determination at any harmonic excitation, which can be used for the PEH characterization and modulations.

In the presented study, the coupled transient solution of the PEH is developed and investigated for the unimorph and bimorph piezoelectric beams. First, Section 2 reviews the mechanical and electrical equations for the unimorph and the bimorph (parallel and series connections). Section 2 is a review of the analytical modeling for the piezoelectric energy harvester and is a base for the formulation in the next sections. Section 3 deals with developing a unified electromechanically coupled equation for voltage, which also presents the relationship between the PEH resonant frequency, the resistive electrical load, and the driving vibration frequency. In Section 4, the approach for the damping determination using the transient harmonic voltage response. Verification of the presented electromechanical voltage equation and the damping determination approach is given in Section 5. Section 6 presents the results and discussions. The results emphasizes the electromechanical coupling effect of the resistive load and the driving frequency on the power generation. Numerical studies prove that the presented simple method determines the damping coefficient from the transient voltage response at any driving frequency and any resistive load, which will significantly facilitate the damping coefficient determination.

## 2. Review of mechanical and electrical coupled differential equations

In this section, a model for PEH is presented. The presented method for the PEH vibration can be used for energy harvesters in 3–1 mode with one or two piezoelectric layers, which are respectively called unimorph and bimorph harvesters. Modelling of the harvesting beam is based on the analytical distributed beam. It is considered that the piezoelectric harvester vibrates around its fundamental natural frequency, thus, the fundamental vibration mode has the main contribution in the analytical beam model. This assumption was proved to be true in many practical applications [30].

### 2.1. Mechanical vibration equation

A substrate shim is considered in both unimorph and bimorph harvesters. The PEHs is subjected to the base excitation $Y_B(t)$ causing the transverse motion of the cantilever beam. This transverse motion creates an axial strain ($\varepsilon_{xx}$) and the axial strain creates an electrical field through the thickness ($E_z$) due to the direct piezoelectric effect. A purely resistive load of $R_L$ is considered as the external electrical load. Fig. 2(a) and (b) show respectively the unimorph and bimorph harvesters in the 3–1 mode. Fig. 2(c) shows the front views and the neutral axis location of the harvesting beams.

The general equation of motions for a bending beam based on Euler-Bernoulli beam theory can be expressed as [31]:

$$\frac{\partial^2 \mathrm{M}(x,t)}{\partial \mathrm{x}^2} + \mathscr{C}_a \frac{\partial \mathrm{w}(x,t)}{\partial \mathrm{t}} + m^* \frac{\partial^2 \mathrm{w}(x,t)}{\partial \mathrm{t}^2} = -(m^* + M_t)\frac{\mathrm{d}^2 \mathrm{Y}_B(t)}{\mathrm{dt}^2} \tag{1}$$

wherein the internal bending moment, $\mathrm{M}(x,t)$, due to the axial stress for the multi-layered harvester is given by

$$\text{unimorph} \Rightarrow \mathrm{M}(x,t) = -b\left(\int_{-\mathscr{Z}_a}^{-\mathscr{Z}_b} T_{xx}^s z dz + \int_{-\mathscr{Z}_b}^{0} T_{xx}^p z dz + \int_{0}^{\mathscr{Z}_c} T_{xx}^p z dz\right) \tag{2}$$

$$\text{bimorph} \Rightarrow \mathrm{M}(x,t) = -b\left(\int_{-h_p-\frac{h_s}{2}}^{-\frac{h_s}{2}} T_{xx}^p z dz + \int_{-\frac{h_s}{2}}^{\frac{h_s}{2}} T_{xx}^s z dz + \int_{\frac{h_s}{2}}^{\frac{h_s}{2}+h_p} T_{xx}^p z dz\right)$$

wherein $\mathscr{Z}$ (the distances from the neutral axis) and $h$ (thicknesses) are shown in Fig. 2.

The base excitation $Y_B(t)$ deforms the piezoelectric beam with the deformation shape of $\mathrm{w}(x,t)$. In the linear framework of a pure bending beam, the axial strain at a certain level $z$ from the neutral axis can be obtained from the beam curvature, as given by

$$\varepsilon_{xx} = -z\frac{\partial^2 \mathrm{w}(x,t)}{\partial \mathrm{x}^2} \tag{3}$$

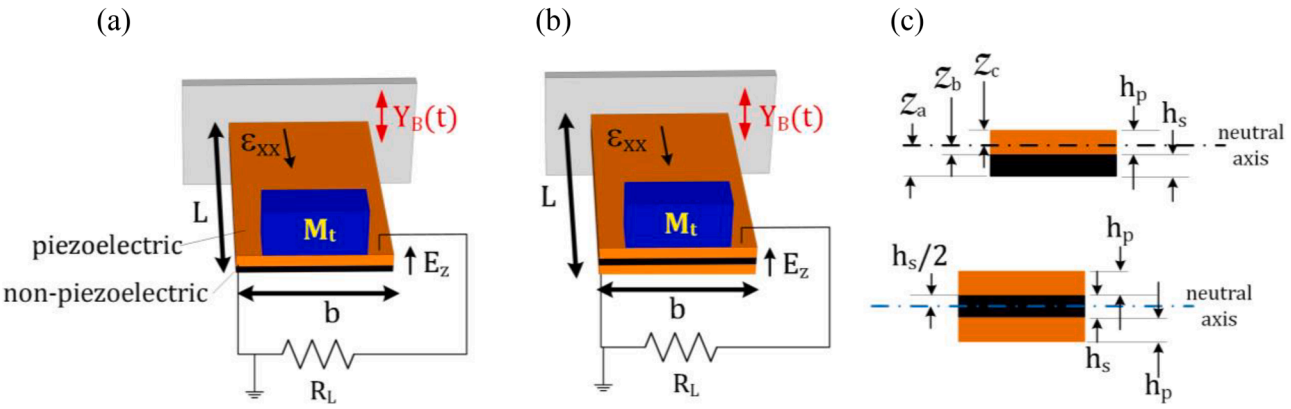


**Fig. 2.** Piezoelectric energy harvesters in connection with the electrical resistive load $R_L$ under the base excitation $Y_B$ (a) unimorph, (b) bimorph, and (c) front-views with thicknesses.

The axial strain relates to the normal stresses in the piezoelectric and substrate layers by the constitutive equations that are respectively given by [32]

$$T_{xx}^{p} = \bar{c}_{11}^{E}\varepsilon_{xx} - \bar{e}_{31}E_z \tag{4a}$$

$$T_{xx}^{s} = Y_s\varepsilon_{xx} \tag{4b}$$

By substituting Eqs. (3), (4a), and Eq. (4b) into Eq. (2), the beam bending stiffness is given by:

$$\mathrm{M}(x,t) = YI\frac{\partial^2 \mathrm{w}(x,t)}{\partial \mathrm{x}^2} + \mathscr{P}\mathrm{V_R}(t)\left(\mathscr{H}(x-x_i) - \mathscr{H}(x-x_f)\right) \tag{5}$$

wherein the Heaviside function term $\left(\mathscr{H}(x-x_i) - \mathscr{H}(x-x_f)\right)$ ensures that the piezoelectric layer starts from $x_i$ to the $x_f$. In our case studies, $x_i = 0$ and $x_f = L$.

Employing Eq. (2) for the unimorph and the bimorph, the bending stiffness $YI$ and the coupling factor $\mathscr{P}$ can be obtained. Table 1 presents $YI$ and $\mathscr{P}$ for both the unimorph and bimorph. Substituting $YI$ and $\mathscr{P}$ into the Eq. (1), the differential equations of motion can be expressed as a function of the relative beam deflection, as given by:

$$YI\frac{\partial^4 \mathrm{w}(x,t)}{\partial \mathrm{x}^4} + \mathscr{C}_a\frac{\partial \mathrm{w}(x,t)}{\partial \mathrm{t}} + m^*\frac{\partial^2 \mathrm{w}(x,t)}{\partial \mathrm{t}^2} + \mathscr{P}\mathrm{V_R}(t)\left(\frac{d\delta(x-x_i)}{dx} - \frac{d\delta(x-x_f)}{dx}\right) = -(m^* + M_t)\frac{\mathrm{d}^2 \mathrm{Y}_B(t)}{\mathrm{dt}^2} \tag{6}$$

The beam deformation is expressed with a modal approximation for solving the beam differential equation. In other words, physical coordination is transferred to modal coordination. In this study, where only the fundamental mode of the beam is of interest, the beam deflection is assumed:

$$\mathrm{w}(x,t) = \phi(x)\eta(t) \tag{7}$$

wherein $\phi(\mathrm{x})$ is given in Appendix A.

Integrating Eq. (6) from 0 to L and using the modal orthogonality characteristic [33], the following equation of beam motion is obtained:

$$\ddot{\eta}(t) + 2\zeta\omega_n\dot{\eta}(t) + \omega_n^2\eta(t) + \mathrm{YV_R}(t) = \sigma\ddot{Y}_B(t) \tag{8}$$

wherein $\omega_n$, $\sigma$, and Y are respectively given in Table 1.

### 2.2. The electrical equation for voltage output

For obtaining the electrical equation, the piezoelectric layer is replaced with a capacitance ($C_P$) and a current source denoted with $I_P(t)$ [30]. The current source is defined by Eq. (9).

$$I_P(t) = \Lambda\dot{\eta}(t) \tag{9}$$

wherein $\Lambda$ for the unimorph and bimorph harvesters is given in Table 1.

An effective electrical circuit is needed for all electrical connections to present a unified formulation for the electrical equation. Fig. 3(a)–(c) show the unimorph, the bimorph in parallel connection, and the bimorph in series connection, respectively. The equivalent capacitance and resistive load for the effective electrical circuit shown in Fig. 3(d) are reported in Table 1.

**Table 1**
Modal electromechanical parameters associated with vibration and electrical equations.

| | Unimorph | Bimorph | |
|---|---|---|---|
| $YI$ | $b/3\left[Y_s\left(\mathscr{Z}_b^3 - \mathscr{Z}_a^3\right) + \bar{c}_{11}^{E}\left(\mathscr{Z}_c^3 - \mathscr{Z}_b^3\right)\right]$. | $2b/3\left[Y_s h_s^3/8 + \bar{c}_{11}^{E}\left(\left(h_p + h_s/2\right)^3 - h_s^3/8\right)\right]$. | |
| $\mathscr{P}$ | $-\frac{\bar{e}_{31}b}{2h_p}\left[\mathscr{Z}_c^2 - \mathscr{Z}_b^2\right]$ | $\frac{\bar{e}_{31}b}{2h_p}\left[h_s^2/4 - \left(h_p + h_s/2\right)^2\right]$ | |
| $m^*$ | $b\left(h_p + h_s\right)$ | $b\left(2h_p + h_s\right)$ | |
| $\omega_n$ | $(\lambda L)^2\sqrt{\frac{YI}{m^* L^4}}$ | | |
| $\sigma$ | $m^*\int_0^L \phi(x)dx + M_t\phi(L)$ | | |
| Y | $\mathscr{P}\left(\frac{d\phi(x)}{dx}\Big\|_{x=L}\right)$ | | |
| $\Lambda$ | $-\frac{\bar{e}_{31}\left(h_p + h_s\right)b}{2}\left(\frac{d\phi(x)}{dx}\Big\|_{x=L}\right)$ | $-\frac{\bar{e}_{31}b\mathscr{Z}_c}{2}\left(\frac{d\phi(x)}{dx}\Big\|_{x=L}\right)$ | |
| $C_P$ | $\frac{\bar{e}_{33}bL}{h_p}$ | Series connection | $\frac{\bar{e}_{33}bL}{2h_p}$ |
| | | Parallel connection | $\frac{\bar{e}_{33}bL}{h_p}$ |
| $R_{\mathrm{eff}}$ | $R_L$ | Series connection | $R_L$ |
| | | Parallel connection | $2R_L$ |

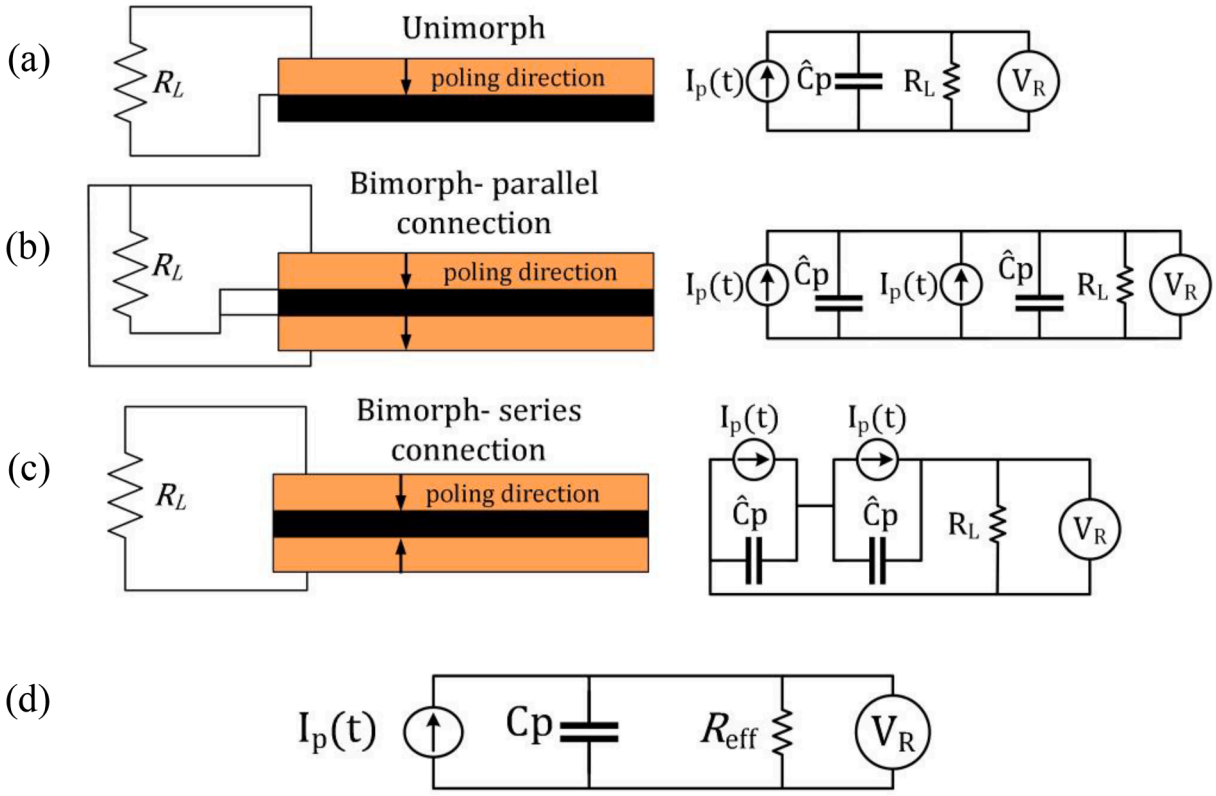


**Fig. 3.** Piezoelectric energy harvesters with their equivalent circuits, (a) Unimorph, (b) bimorph in parallel connection, (c) bimorph in series connection, and (d) the effective circuit for all the cases (a) to (c).

For the effective electrical circuit shown in Fig. 3(d), the current circuit equation is given by:

$$C_P\dot{V}_R(t) + \left(1/R_{\text{eff}}\right)\mathrm{V_R}(t) = \Lambda\dot{\eta}(t) \tag{10}$$

### 2.3. The need for a revisit to the coupled equations

The Eqs. (11) and (12), which respectively describe the mechanical vibration and electrical output voltage, are dependent on each other and therefore need to be solved simultaneously.

$$\ddot{\eta}(t) + 2\zeta\omega_n\dot{\eta}(t) + \omega_n^2\eta(t) + \mathrm{Y}\mathrm{V_R}(t) = \sigma\ddot{Y}_B(t) \tag{11}$$

$$C_P\dot{V}_R(t) + \left(1/R_{\text{eff}}\right)\mathrm{V_R}(t) - \Lambda\dot{\eta}(t) = 0 \tag{12}$$

Like a typical way of dealing with these coupled series of equations, researchers elaborate the steady-state solution under a harmonic excitation [28,34,35]. The steady-state power output per square base acceleration under a harmonic input of $Y_B(t) = \overline{Y}_B\cos(\Omega\omega_n t)$ is:

$$\frac{P_R}{\left(\ddot{Y}_B\right)^2} = \frac{R_{\text{eff}}\mathrm{C}_P\omega_n^2\Omega^2\Lambda^2\sigma^2}{\mathrm{C}_P\left[\omega_n^2\left(1-\Omega^2\left(1+2\zeta R_{\text{eff}}\mathrm{C}_P\omega_n\right)\right)^2 + \left(R_{\text{eff}}\mathrm{C}_P\omega_n(1-\Omega^2) + \Omega(2\zeta\omega_n + \Lambda\mathrm{Y})\right)^2\right]} \tag{13}$$

The steady-state response of piezoelectric harvesters provides a direct and easy expression for the voltage output; however, it will camouflage some essential voltage output signal characteristics. For instance, the damping and electrical output influences on the mechanical frequency cannot directly be interpreted from the steady response. Moreover, if the input vibration input has variations in either the amplitude or the frequency, time-dependent power variations cannot be studied by the steady-state formulation. Therefore, here, the analytical beam formulation will be elaborated toward:

- A unified equation for the voltage accommodating both electrical and mechanical characteristics. Thus, instead of dealing with two coupled differential equations, a single equation for voltage should be dealt with. This unified equation investigates power generation dependencies on the design parameters such as input frequency and electrical load.
- A straightforward transient solution of voltage to investigate time-dependent characteristics.
- An innovative approach to extract the damping coefficient only by the transient voltage measurements.

## 3. Revisit of the voltage equation

### 3.1. A unified voltage equation

To develop the unified voltage equation, two scenarios are considered: the open-circuit and the electrical-load conditions.

In open-circuit condition, where $R_L \to \infty$, inserting Eq. (12) into Eq. (11) is more straightforward than the load conditio because the term $\left(1/R_{\text{eff}}\right)\mathrm{V_R}(t)$ approaches to 0. Then, by integrating Eq. (12) over time, the

relationship between mechanical displacement and open-circuit voltage simplifies to

$$\eta(t) = \frac{C_P}{\Lambda} \mathrm{V_{OC}}(t) \tag{14}$$

Substituting Eq. (14) into Eq. (11) for open-circuit voltage, the differential equation becomes

$$\ddot{\mathrm{V}}_{\mathrm{OC}}(t) + 2\zeta\omega_n \dot{\mathrm{V}}_{\mathrm{OC}}(t) + \left(\omega_n^2 + \frac{\mathrm{Y}\Lambda}{C_P}\right)\mathrm{V_{OC}}(t) = \sigma\frac{\Lambda}{C_P}\ddot{Y}_B(t) \tag{15}$$

Eq. (15) will proceed in Section 4 for the determination of $\zeta$ from the open-circuit voltage. Eq. (15) is not only valid for the harmonic excitation but also any arbitrary base excitation.

Similarly, Eq. (12) can be simplified for the electrical-load condition, when the piezoelectric harvester is subjected to a harmonic load with the frequency $\omega$, as given by:

$$\eta(t) = \frac{\mathrm{V_R}(t)}{\Gamma(\omega)} \tag{16}$$

wherein the coefficient $\Gamma$ is

$$\Gamma(\omega) = \frac{\Lambda}{\sqrt{\left(\frac{1}{R_{\mathrm{eff}}\omega}\right)^2 + {C_P}^2}} \tag{17}$$

Consequently, the differential voltage equation across the resistor is given by

$$\ddot{\mathrm{V}}_{\mathrm{R}}(t) + 2\zeta\omega_n \dot{\mathrm{V}}_{\mathrm{R}}(t) + \left(\omega_n^2 + \mathrm{Y}\Gamma(\omega)\right)\mathrm{V}_R(t) = \sigma\Gamma\ddot{Y}_B(t) \tag{18}$$

Eq. (18) is similar to the forced vibration equation for a damped one-degree-of-freedom system. However, as can be seen from Eq. (18), the natural frequency has an extra electromechanically coupling term, i.e., $\mathrm{Y}\Gamma(\omega)$. This coupling term is frequency and electrical-load dependent. Therefore, a coupled natural frequency ($\omega_{\mathrm{nc}}$) is defined by

$$\omega_{\mathrm{nc}} = \sqrt{\omega_n^2 + \mathrm{Y}\Gamma(\omega)} \tag{19}$$

It is a well-known fact that the natural frequency of piezoelectric beams are electrical-load dependent [18], but the natural frequency-driving frequency relationship needs to be elaborated [12]. The coupled natural frequency introduced in this study accommodates both the frequency and electrical-load effects.

Having $\zeta$ from experiments, optimum resistive load for maximum power can be obtained by setting the electrical damping equal to the mechanical damping. The optimum load resistive can be given by [36]

$$R_{\mathrm{L}}^{\mathrm{opt}} = \frac{1}{\omega C_P}\frac{2\zeta}{\sqrt{4\zeta^2 + \left(\frac{\bar{e}_{31}{}^2}{\bar{c}_{11}^E \bar{\varepsilon}_{33}}\right)^2}} \tag{20}$$

### 3.2. The transient response of voltage under harmonic excitations

The unified voltage differential equation (either Eqs. (15) or (18)), is a non-homogeneous second-order differential equation that its general solution is well known. Considering a harmonic base excitation given by $\ddot{Y}_B(t) = \overline{Y}_B\omega^2\cos(\omega t)$, the solution of the Eq. (18) can be expressed with

$$V_{\mathrm{R}}(t) = V_{\mathrm{trans}} e^{-\zeta\omega_n t} sin(\omega_{\mathrm{dc}} t + \phi) + V_{\mathrm{steady}}\cos(\omega t - \theta) \tag{21}$$

The first term in Eq. (21) is related to transient behavior, while the second term points to the steady-state condition.

Both the damping factor and electromechanical coupling influence the frequency of oscillations in the transient period. $\omega_{\mathrm{dc}}$, given by Eq. (22), is the coupled-damped natural frequency of the harvester, which has the characteristics of damping and electromechanical coupling, and therefore it can mimic the harvester behavior in the damped as well as the electromechanical coupling conditions. The concept of using the coupled-damped natural frequency for piezoelectric energy harvesters is novel.

$$\omega_{\mathrm{dc}} = \omega_n\sqrt{1 - \zeta^2 + \frac{\mathrm{Y}\Gamma}{\omega_n^2}} \tag{22}$$

Parameters for the transient and steady solutions with initial conditions $\mathrm{v}_0$ and $\dot{\mathrm{v}}_0$, are respectively given by

$$V_{\mathrm{trans}} = \frac{\mathrm{v}_0 - V_{\mathrm{steady}}\cos\theta}{\sin\phi},\ \phi = \tan^{-1}\frac{\omega_{\mathrm{dc}}\left(\mathrm{v}_0 - V_{\mathrm{steady}}\cos\theta\right)}{\dot{\mathrm{v}}_0 + \zeta\omega_n\left(\mathrm{v}_0 - V_{\mathrm{steady}}\cos\theta\right) - \omega V_{\mathrm{steady}}\sin\theta} \tag{23a}$$

$$V_{\mathrm{steady}} = \frac{\sigma\Gamma\overline{Y}_B\omega^2}{\sqrt{\left(\omega_n^2 + \mathrm{Y}\Gamma - \omega^2\right)^2 + \left(2\zeta\omega_n\omega\right)^2}},\ \theta = \tan^{-1}\frac{2\zeta\omega_n\omega}{\omega_n^2 + \mathrm{Y}\Gamma - \omega^2} \tag{23b}$$

In open-circuit condition with zero initial condition, the transient and steady-state parameters can be simplified, as expressed in Eqs. (24a) and (24b).

$$V_{\mathrm{trans}} = -\kappa V_{\mathrm{steady}},\ \phi = \tan^{-1}\frac{\omega_d\cos\theta}{\zeta\omega_n\cos\theta + \omega\sin\theta} \tag{24a}$$

$$V_{\mathrm{steady}} = \frac{\sigma\frac{\Lambda}{C_P}\overline{Y}_B\omega^2}{\sqrt{\left(\omega_n^2 + \frac{\mathrm{Y}\Lambda}{C_P} - \omega^2\right)^2 + (2\zeta\omega_n\omega)^2}},\ \theta = \tan^{-1}\frac{2\zeta\omega_n\omega}{\omega_n^2 + \frac{\mathrm{Y}\Lambda}{C_P} - \omega^2} \tag{24b}$$

$$\kappa = \frac{\cos\theta}{\sin\phi}$$

Phase angles $\theta$ and $\phi$ and $\kappa$ for different frequency ratios are shown in Fig. 4. Frequency ratio is the ratio of excitation frequency to the coupled-damped natural frequency, i.e., $\Omega = \omega/\omega_{\mathrm{dc}}$. According to Fig. 4, $\kappa$ can be either $-1$ or $+1$ depending on the $\Omega$. While the transient response is in the same phase as the steady-state response for $\Omega < 1$, it is in the opposite phase for $\Omega > 1$. In zero initial condition case, Eq. (21) can be simplified to Eq. (25) for both $\Omega \leq 1$ and $\Omega > 1$ cases.

$$V_{\mathrm{R}}(t) \cong V_{\mathrm{steady}}\left(-\not{1}(\Omega)e^{-\zeta\omega_n t} sin(\omega_{\mathrm{dc}} t + \phi) + \cos(\omega t - \theta)\right) \tag{25}$$

$$\text{wherein } \not{1}(\Omega) = \begin{cases} 1 & \Omega \leq 1 \\ -1 & \Omega > 1 \end{cases}.$$

### 3.3. The approximate transient response

Approximate transient responses under different excitations are given in this section. These approximate responses are needed in the damping determination method.

#### 3.3.1. Resonance excitation

Under the resonant excitation, the following approximations can be assumed according to Fig. 4: $\theta \cong \frac{\pi}{2}$, $\phi \cong 0$ and $\kappa \cong 1$. Therefore, the open-circuit voltage for the resonant excitation is given by

$$V_{\mathrm{R}}(t) \cong V_{\mathrm{steady}}(1 - e^{-\zeta\omega_n t})\sin\omega_{\mathrm{dc}} t \tag{26}$$

Eq. (26) contains both transient and steady solutions. Initially, where $e^{-\zeta\omega_n t}$ is significant, the solution is dominated by the transient behavior, while for $t \to \infty$, transient part becomes insignificant, and the solution is the steady-state response.

Fig. 5 presents the resonant voltage outputs obtained from the exact coupled solution (Eqs. (11) and (12)) and the simplified equation (Eq. (26)). The solution is carried out with the resistive load of $R_L = 10M\Omega$. A good agreement exists between these two resonant open-circuit voltage solutions throughout the time. Therefore, the simplified resonant voltage equation is valid in the transient stage as well as the steady-state.

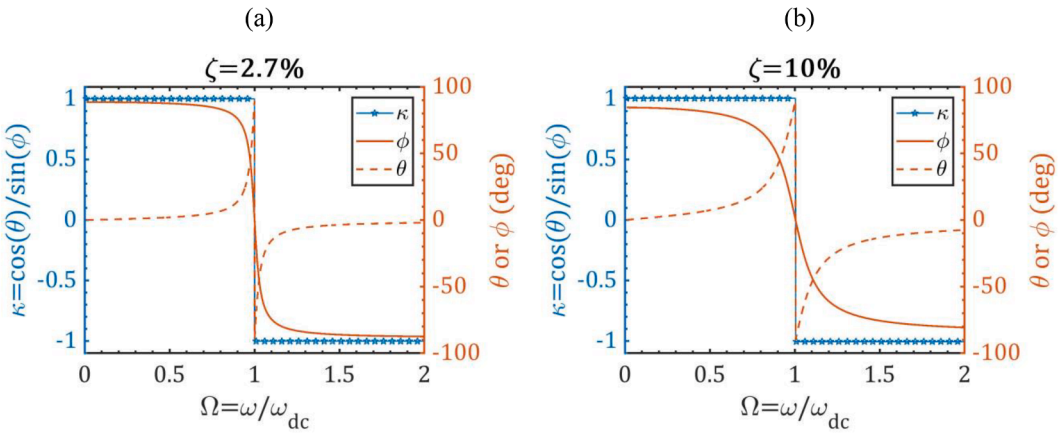


**Fig. 4.** Phase angles and $\kappa = \frac{\cos\theta}{\sin\phi}$ versus frequency ratio for (a) light damping and (b) high damping coefficients.

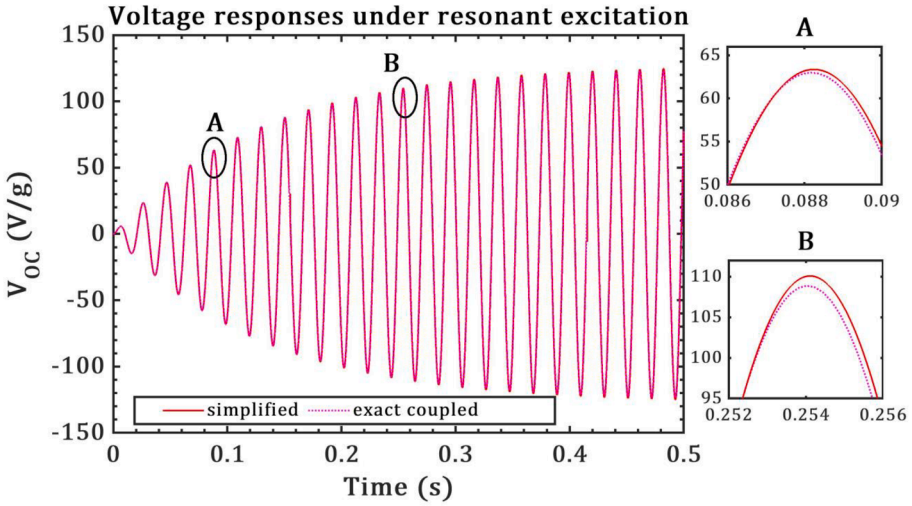


**Fig. 5.** The comparison between the exact coupled and simplified solutions at the resonant excitation.

*3.3.2. Under and near-resonant excitations*

In these cases, it is not as straightforward as the resonance case to express the general solution form with a single harmonic function Eq. (26). However, in the early response after the excitation, the transient response can be approximately derived. Assuming the phase angles to be $\theta \cong 0$, $\phi \cong \frac{\pi}{2}$ and by applying the sum to product trigonometric formula, Eq. (25) can be break into transient and steady-state solution, as given by Eq. (27).

$$V_R(t) \cong \begin{cases} V_{steady}(1+e^{-\zeta\omega_n t})sin\left(\frac{\omega_{dc}+\omega}{2}t\right)sin\left(\frac{\omega_{dc}-\omega}{2}t\right), t < \frac{1}{\tau} \\ V_{steady}\cos(\omega t-\theta), t \gg \frac{1}{\tau} \end{cases} \quad (27)$$

wherein $\tau = \zeta\omega_n$.

Fig. 6 (a)-(d) show the comparisons between the exact and the simplified (Eq. (27)) solutions at the different under-resonant excitations, i.e., $\Omega = 0.4$, 0.7, and 0.8, and near resonance, i.e., $\Omega = 0.9$. As can be seen from Fig. 6 (a)–(d), the simplified solution in Eq. (27) provides the accurate estimations of the output voltage at all the non-resonant excitations. In particular, the exact and simplified solutions demonstrate excellent consistency in voltage peaks. The accurate peak voltage estimations are of great importance for the correct damping estimation.

## 4. The harmonic transient voltage response (HTVR) method for the damping coefficient determination

This section presents the harmonic transient voltage response (HTVR) method for the damping determination from only the voltage measurements during a harmonic base excitation. This method does not need any prior knowledge about the system or pre-modeling relying on the data processing from only the transient measured voltage made on a piezoelectric harvester. The HTVR does not require sensors for measuring the structural response of the harvester, as it needs only the voltage output signal. No structural modeling in the HTVR is needed. In addition, since the system response to a harmonic excitation is employed, the measured response is a forced-vibration response, and therefore the noise to signal ratio in the voltage is smaller compared to the free-vibration decrement responses. The harmonic function with any arbitrary frequency can be used as the base excitation in the HTVR method. However, some requirements are linked with the HTVR for an accurate damping determination. Piezoelectric harvester should undergo harmonic base excitation; thus, it needs a mechanism to excite the harvester by a harmonic motion. The voltage response of the harvester should be measured from the initial (zero) condition. The HTVR uses the peak values of the transient voltage response, and therefore it requires the accurate measurements of the time-domain voltage response. Hence, the sources of environmental noise should be kept as low as possible. Additionally, a high sampling rate is required for precise peak selections in the voltage response.

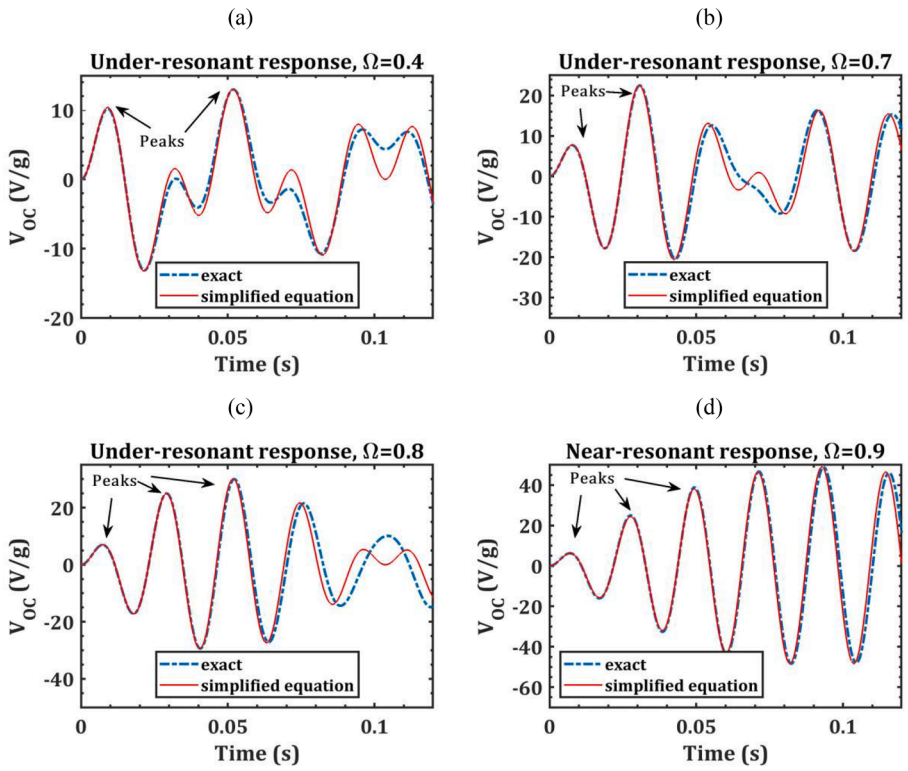


**Fig. 6.** The comparison between the exact and approximated transient solution for the under-resonant and near-resonant excitations.

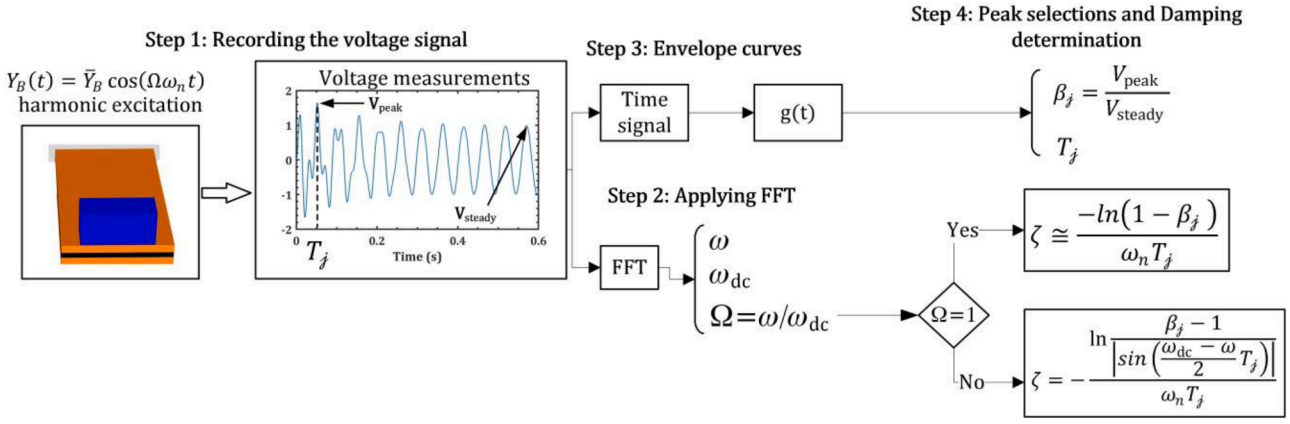


**Fig. 7.** The flowchart of the proposed method for damping using the transient voltage measurements.

Fig. 7 shows the flowchart of the HTVR damping determination approach. The method requires the recorded time-domain voltage data and Fast Fourier Transform (FFT) of the voltage data. Now, each step in Fig. 7 will be elaborated in detail.

### 4.1. Recording the voltage signal

The first step is to record the time domain voltage signal made on a piezoelectric harvester under any harmonic load. According to Eq. (25), the decaying term $e^{-\zeta\omega_n t}$ in the transient part carries the damping effect and thus theoretically the damping factor can be determined from the transient solution. Therefore, it is critical to record the voltage output from initial condition, as the transient response is of significance in this method. In general, one is free to excite the piezoelectric harvester with any harmonic load and in connection with any electrical load.

Exciting the harvester with resonant frequency gives a straightforward process for obtaining the damping coefficient. Nonetheless, for the resonant excitation case, the harvester should be excited with the exact coupled-damped natural frequency so that a pre-knowledge about the system natural frequency is needed. For removeing the need for the natural frequency pre-knowledge, the method is also developed for the harmonic excitation at an arbitrary driving frequencies (under or around resonant cases).

### 4.2. Applying FFT on the voltage signal

Applying FFT to the voltage signal reveals the dominant frequencies. As shown in Eq. (25), two harmonic functions exist in the transient voltage signal, one transient with the coupled-damped natural frequency ($\omega_{dc}$) and one steady-state with the excitation frequency ($\omega$). These two dominant frequencies are theoretically discernible in the voltage signal and can be extracted by the FFT. Fig. 8 shows the FFT results from voltage output signals in different excitation frequencies, i.e., $\Omega = 0.4$, 0.9, 1, and 1.1. $\omega_{dc}$ and $\omega$ are obvious in

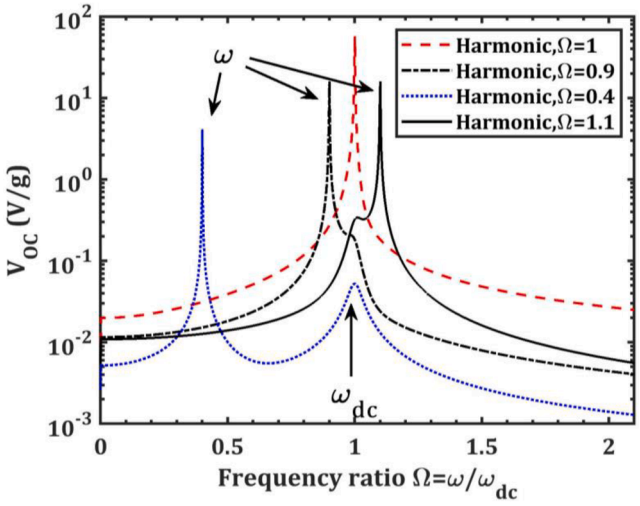


**Fig. 8.** Applying Fast Fourier Transform reveals the dominant frequencies in the voltage response.

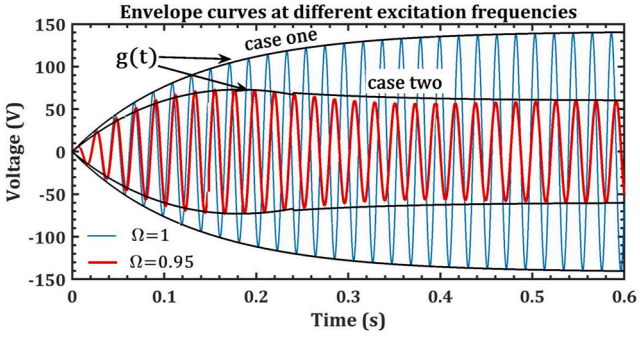


**Fig. 9.** The output voltage from harmonic excitations at different frequency ratios, $\Omega = 0.95$, and $\Omega = 1$.

the FFT signals. If only one dominant frequency exists in the FFT signal, then $\omega_{dc} = \omega$ or $\Omega = 1$.

### 4.3. Envelope curves of the voltage signal

As the peak magnitude variations are dependent onthe damping, remember the term $e^{-\zeta\omega_n t}$, the envelope curve ($g(t)$) of the transient voltage response is needed. The envelope curve does not have the same formulation for different Ωs. Therefore, the envelope curve is given for two cases, case one $\Omega = 1$ and case two $\Omega < 1$ (or $\Omega \approx 1$). Fig. 9 shows the harvester voltage outputs under two harmonic cases with their envelope curves. As can be seen, the type of envelope curves is different in these two cases. In the first case, the envelope curve is a strictly increasing function, while in the second case, the envelope curve has an overshoot and then converges to a constant value.

The envelope curve equations are derived from the approximate transient responses given in subsection 3.3.

For case one (the resonant excitation) and case two (under or near-resonant excitations) the envelope curve are respectively given by:

$$\text{Case one } (\Omega = 1): \quad g(t) = V_{steady}(1 - e^{-\zeta\omega_n t}), \quad \text{for all } t \tag{28}$$

$$\text{Case two } (\Omega < 1 \text{ or } \Omega \approx 1): \quad g(t) = V_{steady}(1 + e^{-\zeta\omega_n t})sin\left(\frac{\omega_{dc} - \omega}{2}t\right), \quad \text{for } t < \frac{1}{\tau} \tag{29}$$

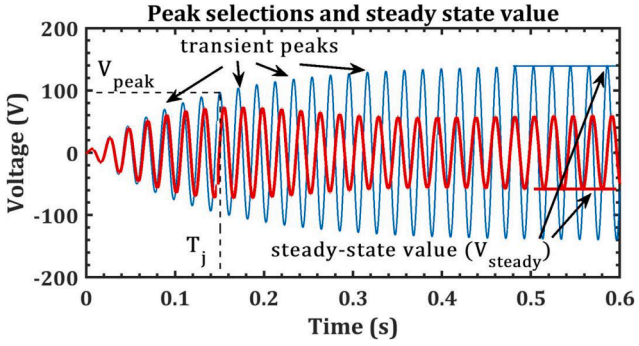


**Fig. 10.** The peak and steady-state values for two cases at different frequency ratios, $\Omega = 0.95$ and $\Omega = 1$.

### 4.4. Peak selections and damping determination

In the envelope curve equations, the exponential decaying term ($e^{-\zeta\omega_n t}$), which has a damping coefficient, is present. This exponential term has a substantial effect in the early times but vanishes at sufficiently large time. Thus, the damping coefficient will be determined by comparing the transient peaks (the exponential term is significant) to the steady-state value (exponential term vanishes).

Steady-state value is that the value of voltage peaks becomes unchanging in time. On the other hand, transient peaks are the peak values changing considerably, either ascending or descending. The relative time from the initial condition for the transient peaks is also of great significance. These parameters are shown in Fig. 10 for two voltage responses at different frequency ratios.

The ratio of the transient peak at $T_j$ to the steady-state value is defined by:

$$\beta_j = \frac{V_{peak}|_{@T_j}}{V_{steady}} \tag{30}$$

According to the envelope curves given by Eq. (28) and Eq. (29), this $\beta_j$ is related to the damping factor, as shown in Eq. (31) and Eq. (32) for cases one and two, respectively.

$$\text{Case one } (\Omega = 1): \quad \beta_j \cong (1 - e^{-\zeta\omega_n t}), \quad \text{for all } t \tag{31}$$

$$\text{Case two } (\Omega < 1 \text{ or } \Omega \approx 1): \quad \beta_j \cong (1 + e^{-\zeta\omega_n t})sin\left(\frac{\omega_{dc} - \omega}{2}t\right), \quad \text{for } t < \frac{1}{\tau} \tag{32}$$

From Eq. (31) and Eq. (32), the damping coefficient can be determined from the $\beta_j$ ratio, as for cases one and two are given by Eq. (33) and Eq. (34).

$$\text{Case one } (\Omega = 1): \quad \zeta = \frac{-ln(1 - \beta_j)}{\omega_n T_j} \tag{33}$$

$$\text{Case two } (\Omega < 1 \text{ o } r\Omega \approx 1): \quad \zeta = -\frac{\ln \frac{\beta_j - 1}{\left|sin\left(\frac{\omega_{dc} - \omega}{2}T_j\right)\right|}}{\omega_n T_j} \tag{34}$$

In Eq. (33) and Eq. (34), $\omega_n$ is needed, which can be assumed approximately equal to $\omega_{dc}$, where $\omega_{dc}$ can be directly obtained from the voltage response from the signal FFT (see Fig. 8).

## 5. Verification of the proposed models

This section verifies the presented unified voltage equation and the damping determination approach in separate subsections, respectively.

**Table 2**
Geometric and material properties of bimorph with 0.012-kg added mass.

| | | | |
|---|---|---|---|
| Length of the beam (mm) | 50.8 | Width of the beam (mm) | 31.8 |
| Tip mass, (kg) | 0.012 | Damping | 2.7% |
| Substrate shim | | | |
| density (kg/m$^3$) | 9000 | Young's modulus (GPa) | 105 |
| thickness (mm) | 0.14 | | |
| Piezoelectric layer (PZT-5A) | | | |
| Density (kg/m$^3$) | 7800 | thickness- each layer (mm) | 0.26 |
| $\bar{c}_{11}^{E}$(GPa) | 66.0 | $e_{13}$(C/m$^2$) | −15.9 |
| Permittivity (F/m) | $1.593 \times 10^{-8}$ | | |

**Table 3**
The comparisons of the undamped natural frequency, the coupled-damped natural frequency, and the steady-state voltage with 1kΩ resistive load.

| | $\omega_n$(Hz) | $\omega_{dc}$ at open-circuit (Hz) | $V_{steady}(V/g)$ with $R_L = 1k\Omega$ |
|---|---|---|---|
| Present model | 45.7 | 48.2 | 1.598 |
| Erturk and Inman experiments [30] | 45.6 | 48.4 | 1.57 |
| Difference | +0.2% | −0.4% | +1.7% |

### 5.1. Verification of the electromechanical voltage equation

As a benchmark example, a bimorph with added tip mass is considered. The bimorph harvester comprises two PZT-5A piezoelectric layers and a brass substrate shim with a 0.012-kg proof mass. First, the presented model is verified against the experimental results by Erturk and Inman [30]. As reported by Ref. [30], geometric and material properties are shown in Table 2. Second, the fully mechanical-electromechanical sensitivity analysis of coupled-damped natural frequency, voltage, and power as function of the driving frequency and resistive load is investigated. Finally, the transient response of voltage and the damping coefficient identification for this example is reported.

According to Eq. (22), the damped-electromechanical natural frequency, $\omega_{dc}$, is a function of electrical load ($R_L$) and excitation frequency ($\omega$). Table 3 compares the undamped natural frequency and the $\omega_{dc}$ at open-circuit (large $R_L$) and $R_L = 1k\Omega$ (small $R_L$) conditions with the experimental results from Erturk and Inman [30]. The good agreement between the results in both small and large $R_L$s shows that the introduced damped-electromechanical natural frequency can capture the electromechanical coupling between mechanical and electrical parameters.

The output voltage at two different electrical loads are compared in Fig. 11 with Erturk and Inman experiments [30]. The excellent consistency between the voltage results can prove the appropriate electromechanical coupling model in the presented model for the output voltage.

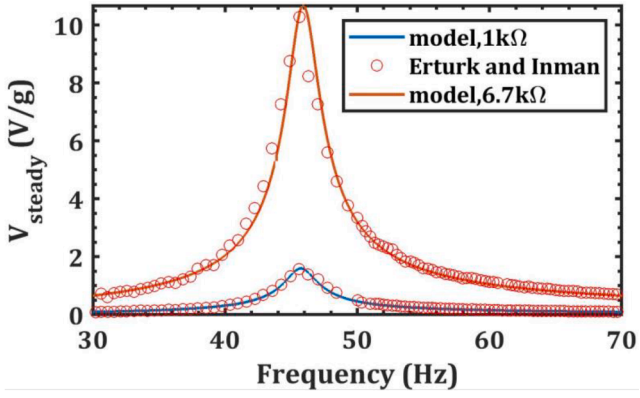


**Fig. 11.** The comparison between the presented model results with the experimental data [30]

### 5.2. Verification of the damping determination method

This section presents the experimental results from a unimorph piezoelectric harvester and applies the presented model for the transient response, damping coefficient identification, and optimum load extraction.

The test rig for experimental tests and the piezoelectric sample for the damping determination are shown in Fig. 12(a)–(c). The piezoelectric sample is a unimorph consisting of only a 0.3-mm-thickness MFC from Smart Material [37]. The unimorph is clamped at one end using an aluminum clamp bar. The dimensions of the unimorph are shown in Fig. 12(a). The clamped-free boundary condition, the unimorph-shaker connection, and the accelerometer are shown in Fig. 12(b). The piezoelectric sample is harmonically excited from the base using a vibration shaker. The transient voltage response from the piezoelectric sample is recorded. National Instrument modules 9172 and 9263 are respectively used for the harmonic signal generation and voltage response recording. Fig. 12(c) shows the setup for applying the desirable harmonic excitation and recording the piezoelectric output response and accelerometer output. Labview™ software is utilized for generating the desired signal and for recording data.

The measured voltage responses with $R_L = 27$ kΩ at $\omega_1 = 14$ Hz and $\omega_2 = 15$ Hz driving frequencies are shown in Fig. 13(a). The output voltage with $\omega_2$ excitation is greater than $\omega_1$ excitation showing that $\frac{\omega_2}{\omega_n} > \frac{\omega_1}{\omega_n}$. Because of the shape of the envelope curve (as discussed in subsection 4.3), it can be concluded that $\Omega_1 < \Omega_2 < 1$. The transient response is expected to have an overshoot voltage from the analytical transient model and then converges to a steady-state voltage. The maximum transient voltage is distinguishably greater than the steady-state voltage and therefore is easy to spot. In this experimental study, the transient stage lasts for approximately 0.5 s. Applying the FFT transform reveals the coupled-damped natural frequency ($\omega_{dc}$) to be 16 Hz, as presented in Fig. 13(b). Having $\omega_{dc}$ from Fig. 13(b) and the maximum transient peak as well as the steady-state voltage from Fig. 13 (a), damping coefficient can be extracted using Eq. (34). Table 4 presents the identified damping coefficients in both 14 Hz and 15 Hz excitations. The identified damping coefficients are similar in both cases illustrating that the damping results from the presented method are consistent.

For the optimum electrical load selection, the harmonic excitation with the first resonant frequency of the beam ($\omega_{dc} = 16$) is applied to the unimorph base, and the generated power outputs are measured with various electrical loads. The electrical circuit used in this experiment, Fig. 14(a), is a full-bridge rectifier connected to the electrical load $R_L$. The voltage and power made on the unimorph are measured at 20 different resistive loads ranging from 100Ω to 650kΩ. Two examples of measured voltages and currents at electrical load 14.7 and 27 kΩ are also shown in Fig. 14 (b). The generated voltage will increase by increasing electrical load until it reaches to open-circuit voltage while the current will decrease from the maximum current at short-circuiting to zero at the open-circuit condition. The output power can be calculated from the output voltage and current measurements. Fig. 14 (c) shows how root mean square (rms) of the generated power from the unimorph sample varies as a function of electrical load. At an electrical load of 27 kΩ, the power generation is maximum with a power rms of 18.4 μW.

Analytically, when the electrical damping becomes equal to the mechanical damping [38], power generation is maximum. For calculating this optimum load point, see Eq. (20), the mechanical damping is required. For the damping determination validation against the experimental data, the optimum analytical resistance is compared with the experimentally found optimum load, 27 kΩ. The optimum analytical load using Eq. (20) and setting the damping coefficient to the mean

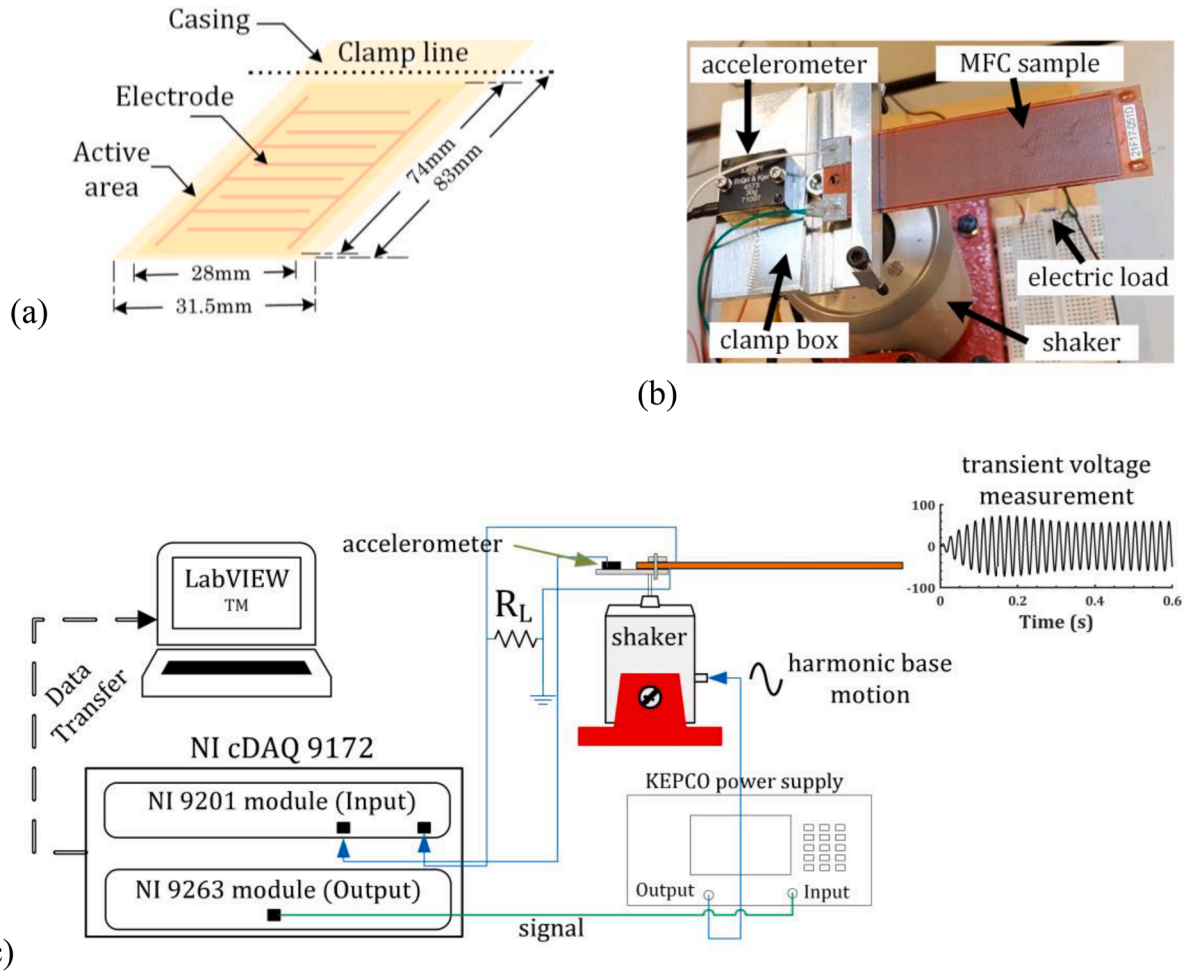


**Fig. 12.** Experimental setup and MFC dimensions, (a) the MFC dimensions, (b) the energy harvester in the clamped-free boundary condition attached to the VSD-201 shaker with the Bruel and Kjær 4573 accelerometer for measuring the applied acceleration, and (c) the experimental setup for applying base excitation and measuring the responses.

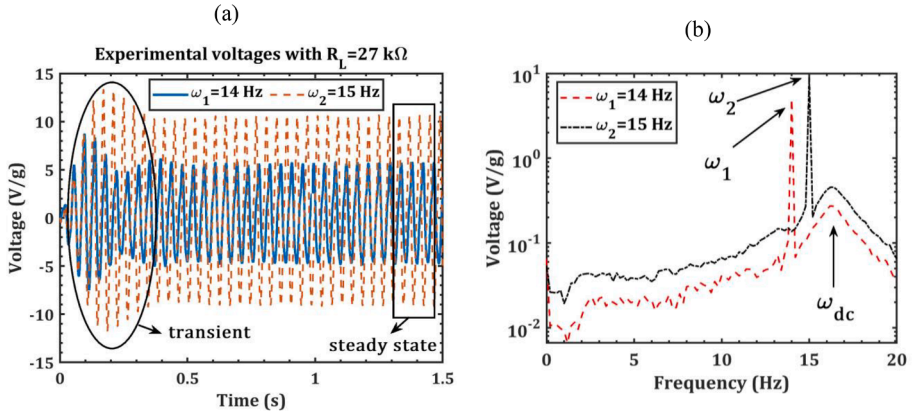


**Fig. 13.** The experimental voltage responses for the MFC under different harmonic excitations (a) time-domain signals and (b) frequency-domain signals after applying the FFT.

value of damping coefficients in Table 4 becomes 25.0 kΩ. This optimum analytical load is very close to the experimentally identified optimum load proving that the identified damping coefficient is reasonably accurate.

## 6. Results and discussions

In this section, the benchmark example used for the model verification in subsection 5.1 will be further investigated.

**Table 4**
The estimation of the damping coefficient for the experimental study.

| | $T_1$(ms) | $V(T_1)$(V/g) | $V_{steady}$(V/g) | $\frac{V(T_1)}{V_{steady}}$ | $\zeta$(%) |
|---|---|---|---|---|---|
| $\omega =$ 14Hz | 95.6 | 8.629 | 5.95 | 1.45 | 4.38 |
| $\omega =$ 15Hz | 171.0 | 13.29 | 10.1 | 1.32 | 4.82 |

### 6.1. The electromechanically coupled natural frequency

As discussed in the voltage output equation, due to electromechanical coupling, the hatvester's coupled natural frequency is a function of the resistance load and the driving frequency. Fig. 15(a) and (b) show the coupled natural frequency changes with these two factors. Greater $\frac{\omega_{nc}}{\omega_n}$ means greater electromechanical coupling effects. As can be seen from Fig. 15(a), greater electrical loads increase the ratio $\frac{\omega_{nc}}{\omega_n}$ meaning that the electromechanical coupling becomes stronger with greater electrical load. The $\frac{\omega_{nc}}{\omega_n}$ variation holds the same trend for all the different $\omega$s. In the energy harvesting applications, the optimum load lies in the range of 10kΩ-100kΩ, and the frequency is matched to the natural frequency so that $\omega \approx \omega_{nc}$. In these conditions, the coupled natural frequency can be roughly from 1.01 to 1.04 of the uncoupled natural frequency.

To further investigate the driving frequency effect on the coupled natural frequency, $\frac{\omega_{nc}}{\omega_n}$ is plotted in Fig. 15 (b) over the frequency ratio ($\Omega$) at different electrical loads. In small electrical loads, $\frac{\omega_{nc}}{\omega_n}$ is linear function of the frequency ratio, while for the greater loads becomes a nonlinear function. In addition, a greater excitation frequency causes a stronger coupling as it makes the $\frac{\omega_{nc}}{\omega_n}$ greater. In the small electrical loads (<1kΩ), $\frac{\omega_{nc}}{\omega_n}$ is always smaller than 1.003 presenting a negligible dependency on the driving frequency in the small electrical loads. However, at large electrical loads (>40kΩ), $\frac{\omega_{nc}}{\omega_n}$ becomes more important, for instance, it is approximately 1.025 around the resonant excitation. According to the plots presented in Fig. 15(a) and (b), one may use $\omega_{nc} = 1.025\omega_n$ for the frequency matching in the mechanical modulations for the electrical loads in the range of (20-60kΩ). Although this $\omega_{nc}$ frequency variation seems small, it can have substantial effect on the output power, as the output power is narrowband due to the high mechanical quality factor of the piezoelectric energy harvester.

### 6.2. Voltage and power generation

The electrical load and driving frequency change the $\omega_{dc}$ and therefore the output voltage-load curve will be different for different excitation frequencies. The output voltage under the harmonic excitations with short-circuit (45.7 Hz) and open-circuit (48.2 Hz) resonant frequencies are shown in Fig. 16. Even though these two driving

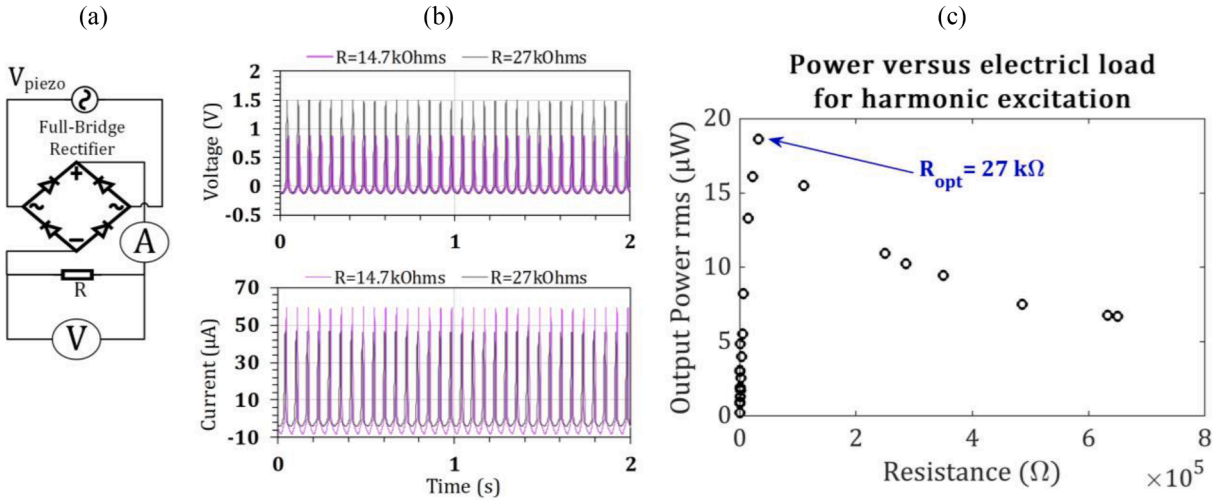


**Fig. 14.** Experimental extraction of the optimum load resistance using harmonic base excitation with different electrical resistive loads, (a) the electrical circuit for maximum-power load determination, (b) two examples of the voltage and current measurements, and (c) the output power versus resistive load.

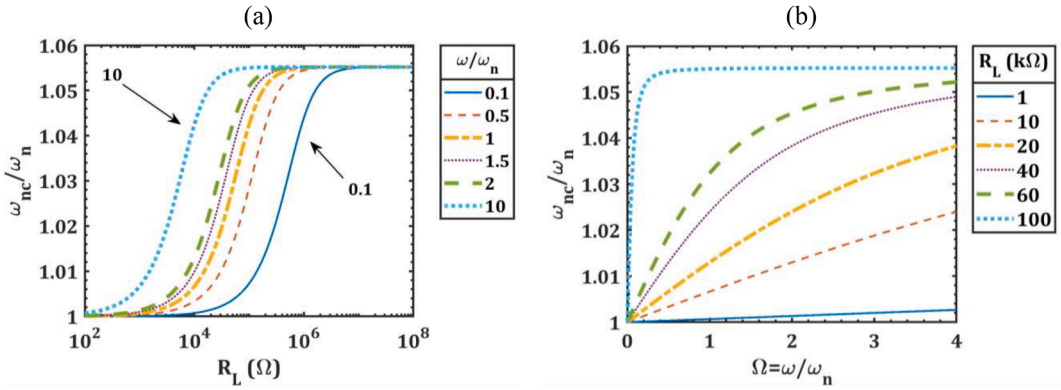


**Fig. 15.** The ratio of the coupled to the uncoupled natural frequency for (a) the resistive load and (b) driving frequency.

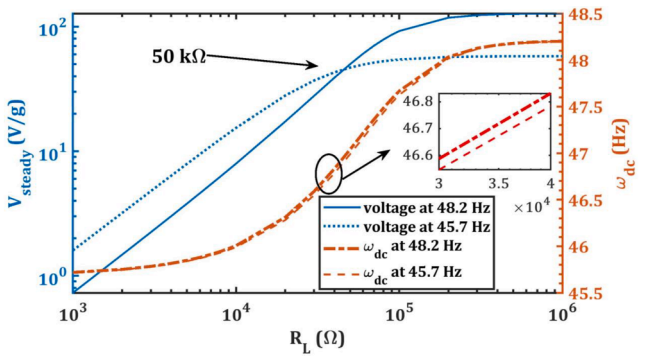


**Fig. 16.** Steady-state voltage and $\omega_{dc}$ for 45.7 and 48.2 Hz driving frequencies corresponding to the harvester coupled natural frequency in short-circuit and open-circuit conditions, respectively.

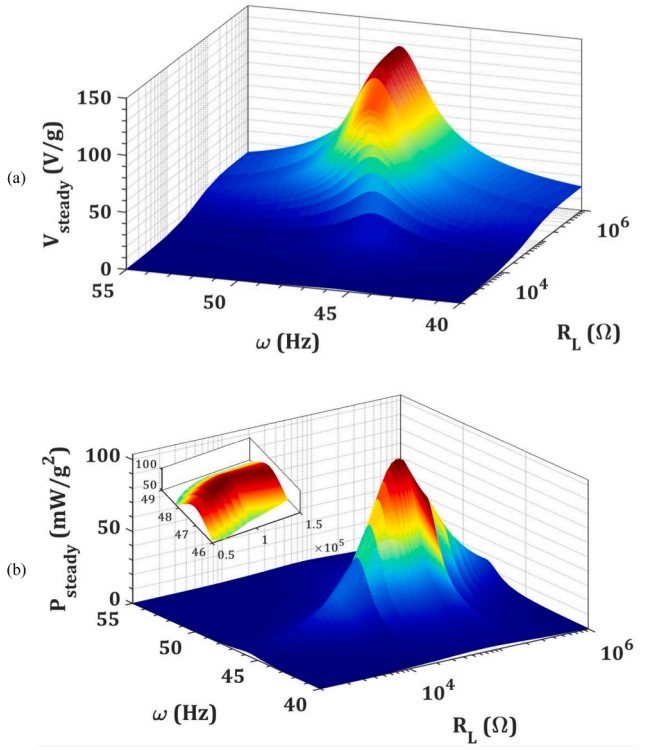


**Fig. 17.** The steady-state (a) voltage and (b) power versus the resistive electrical load ($R_L$) and the excitation frequency ($\omega$).

frequencies are close to each other, the output voltage curves are not identical and have considerable differences. Before the resistive load reaches 50kΩ, the 45.7 Hz-driving frequency generates a greater voltage, while the 48.2 Hz-driving frequency generates a greater voltage after this resistive load, emphasizing that the selection of the resistive load is also a function of the driving frequency. From the zoomed-in view in Fig. 16, a slight difference in the $\omega_{dc}$ can be seen between the two different driving frequencies. The analytical model in Eq. (22) showed this dependency. According to the findings above in Fig. 16, the output voltage and the power generation are simultaneously dependent on the driving frequency and resistive load.

The voltage and power dependencies to the electrical load ($R_L$) and driving frequency ($\omega$) are respectively shown in Fig. 17 (a) and (b). The voltage increases substantially by the $R_L$-increase and reaches to the open-circuit voltage, $V_{OC}$, at great resistive loads. The frequency at which voltage is maximum shifts forward by increasing $R_L$ demonstrating a strong coupling between the mechanical vibration and the connected electrical load. In the maximum power condition, the output voltage and current are 91.12 V/g and 1.14 mA/g, respectively corresponding to the maximum output power of 103.9 mW/g$^2$. As shown in Fig. 17 (b), the power has a strong dependency on the driving frequency, and, for each resistive load, a driving frequency associated with the maximum power exists. Because of the electromechanically coupled equations, the optimum resistive load is different for different driving frequencies.

### 6.3. Evaluation of the approach for damping determination

This section investigates the damping determination method and its relevant setting parameters.

#### 6.3.1. Effect of the excitation frequency

The excitation frequency can affect the results of the current damping determination method. Therefore, the method is applied to the transient responses from different excitation frequencies, and the damping coefficients will be compared.

The voltage outputs made on the piezoelectric bimorph are shown in Fig. 18 for $\Omega = 0.4$, 0.7, 0.8, and 0.9 harmonic excitations. These voltage responses are employed for the damping identification process. All the responses reach a steady-state harmonic after 0.4 s applying the harmonic excitation. During the transient stage, i.e., 0 to 0.4 s, the voltage response has a maximum peak value. The time associated with the maximum transient voltage, the maximum transient voltage, and the steady-state voltage is called $T_1$, $V(T_1)$ and $V_{steady}$, respectively. By substituting these parameters into Eq. (33) and Eq. (34), the damping coefficients can be obtained. Table 5 presents the transient peak times and values and the identified damping coefficients for the mentioned harmonic excitations. The damping coefficient is identified with <5% error in all excitation cases. The 5% error in damping identification using this simple approach, which does not require any pre-knowledge about the system, is a good accuracy as damping extraction is a complex process requiring numerical curve fittings and optimizations [25]. It can also be seen that the method can calculate the damping coefficient accurately in any harmonic excitation frequency and is not limited to the resonant case. The damping coefficient identification error is smaller if the energy harvester is subjected to a resonant or near-resonant harmonic excitation than off-resonant excitations. Therefore, one should excite the harvester with the frequency as close as possible to its resonant frequency for the most accurate damping determination.

#### 6.3.2. Comparison with the other methods

The half-power bandwidth [39] and logarithmic decay [33] methos are also applied to the bimorph example for comparing the current study results.

The half-power bandwidth method is based on the steady voltage responses over a range of frequencies. Without installing any additional sensor, the voltage output is needed to be measured in different frequency steps. Then, by plotting the voltage-frequency curve, the damping coefficient can be measured. Fig. 19 (a) shows the voltage

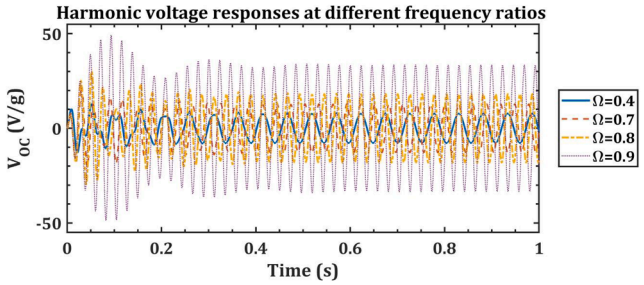


**Fig. 18.** The voltage responses for the bimorph under the harmonic excitation at different frequency ratios.

**Table 5**
The estimation of damping coefficient at different harmonic excitations for the bimorph example.

| | $T_1$(ms) | $V(T_1)$(V/g) | $V_{steady}$(V/g) | $\zeta$ | Exact $\zeta$ value | Error |
|---|---|---|---|---|---|---|
| $\Omega$ = 0.4 | 52.01 | 13 | 7.8 | 2.57% | 2.7% | 4.8% |
| $\Omega$ = 0.7 | 30.81 | 22.53 | 12.82 | 2.82% | | 4.4% |
| $\Omega$ = 0.8 | 52.21 | 30.07 | 18.06 | 2.58% | | 4.4% |
| $\Omega$ = 0.9 | 93.41 | 49.04 | 33.41 | 2.64% | | 2.2% |
| $\Omega$ = 1.0 | 502.9 | 125.30 | 127.83 | 2.71% | | 0.3% |

responses over the 45–55 Hz frequency range with a 0.25 Hz frequency step. The damping coefficient is then calculated as:

$$\zeta \cong \frac{\Delta\omega}{2\omega_{dc}} = \frac{2.4}{2 \times 48.25} = 2.49\%$$

In the logarithmic decay method, the time-domain voltage response to an impact excitation is recorded. Fig. 19(b) shows the voltage response of the bimorph to a 1 g impact force. The damping coefficient is calculated based on the value of any two successive positive peaks, as given by:

$$\zeta = \frac{1}{\sqrt{1 + \left(\frac{2\pi}{\frac{1}{N}\ln\frac{V_{peak-1}}{V_{peak-N}}}\right)^2}} \quad (35)$$

The comparison of the damping coefficient with three different methods are given in Table 6. In either of $\Omega \approx 1$ or $\Omega = 0.9$ cases, the current method has considerably better accuracy than the other methods. The current method can have an accuracy of 2% with the harmonic excitation around the resonance, while the accuracy for the half-power and logarithmic decay methods are respectively 7.8% and 10.4%.

### 6.3.3. *Effect of added white noise*

As the present approach uses the time-domain voltage responses, the noise effect on the HTVR performance should be determined since the experimental data is always polluted with noise. The damping determination method is tested with 2% and 5% white noise data. Fig. 20 presents the identified damping coefficients in the presence of noise. Added noise increases the damping identification error; yet the method

**Table 6**
The comparison of the present study results with half-power bandwidth and logarithmic decay method for the bimorph example.

| Method | Determined damping coefficient | Exact damping coefficient | Error (%) |
|---|---|---|---|
| present method ($\Omega \approx 1$) | 2.71% | 2.7% | 0.0 |
| present method ($\Omega$ = 0.9) | 2.64% | | 2.2% |
| half-power bandwidth method | 2.49% | | 7.8% |
| logarithmic decay method- N = 2 | 2.37% | | 12.2% |
| logarithmic decay method- N = 3 | 2.98% | | 10.4% |

calculated the damping coefficient with reasonable accuracy. The most significant estimation error is for $\Omega$ = 0.7 excitation, while low frequency and near-resonant harmonic excitations have identified the damping very accurately, even with the added noise. This finding recommends the low frequency or near-resonant excitations for the extraction of the damping coefficient.

## 7. Conclusion

In the presented study, the transient voltage response of unimorph and bimorph piezoelectric harvesters are presented. The model considers a fully electromechanical coupling and the Euler beam theory. The dependencies of the energy harvester resonant frequency and the output power to the resistive load and the driving frequency are shown. A simple method for the determination of damping coefficient, the harmonic transient voltage response (HTVR), is presented that can be applied on only the voltage measurements made on piezoelectric harvesters at any harmonic excitation and resistive load. The main outcomes of this study can be summarized as:

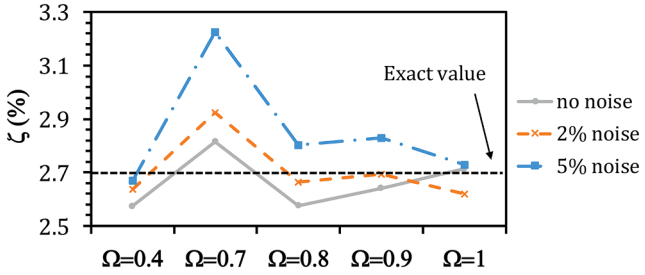


**Fig. 20.** The identified damping from the transient voltage response at different excitations considering added white noise.

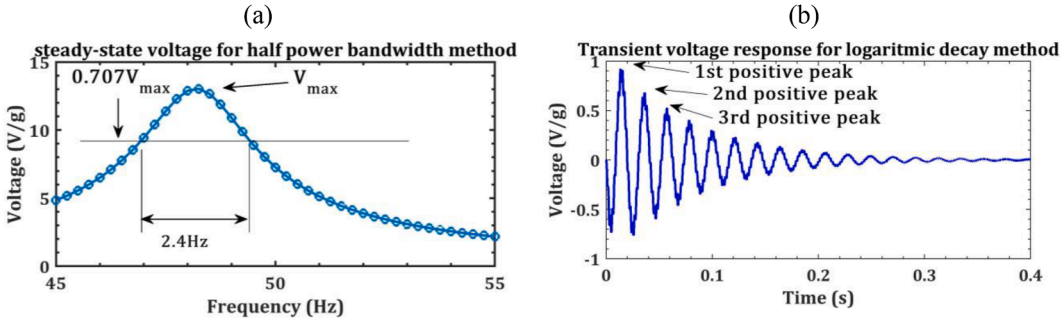


**Fig. 19.** (a) The steady-state voltage response versus frequency for the half-power bandwidth method (b) the impact transient voltage response for the logarithmic decay method.

- The electromechanical-coupled natural frequency should be used for frequency matching of a piezoelectric harvester instead of the uncoupled natural frequency. A factor of 1.025 can be used for considering the electromechanical effects on the natural frequency for around resonant excitations and the electrical load in the range 10-60kΩ.
- The present damping determination method calculates the damping coefficient accurately from only the transient voltage responses without any limitation on the excitation frequency.
- The accuracy of the damping determination method is higher for around the resonant excitations.
- Noise on the transient signal can decrease the damping determination performance by 3.5%.

## CRediT authorship contribution statement

**Majid Khazaee:** Conceptualization, Methodology, Writing - original draft, Software, Data curation, Visualization, Software. **Alireza Rezaniakolaie:** Methodology, Investigation, Writing - review & editing, Supervision. **Lasse Rosendahl:** Methodology, Supervision.

## Declaration of Competing Interest

The authors declare that they have no known competing financial interests or personal relationships that could have appeared to influence the work reported in this paper.

## Appendix A. .

For the clamped-free boundary conditions, beam mode shapes is given by Eq. (A1) [40]:

$$\phi_i(x) = \chi_i[cosh\lambda_i x - cos\lambda_i x + \alpha_i(sinh\lambda_i x - sin\lambda_i x)\,] \tag{A1}$$

where $\lambda_i$ is the solution of Eq. (A2), $\alpha_i$ is a constant given by Eq. (A2), and $\chi_i$ is a constant for satisfying mass normalization of the mode shapes, e.g. $\int_0^l m^* \phi_i^2(x)dx + m_a\phi_i^2(L) = 1$.

$$1 + \cos\lambda_i\cosh\lambda_i + \lambda_i\frac{m_a}{m^*L}(\cos\lambda_i\sinh\lambda_i - \sin\lambda_i\cosh\lambda_i) = 0 \tag{A2}$$

$$\alpha_i = \frac{\sin\lambda_i - \sinh\lambda_i + \lambda_i\frac{m_a}{m^*L}[\cos\lambda_i - \cosh\lambda_i]}{\cos\lambda_i + \cosh\lambda_i - \lambda_i\frac{m_a}{m^*L}[\sin\lambda_i - \sinh\lambda_i]} \tag{A3}$$

## References


[1] Nakamura K. Ultrasonic transducers: Materials and design for sensors, actuators and medical applications. Woodhead Publishing Limited; 2012.
[2] Anton SR, Sodano HA. A review of power harvesting using piezoelectric materials (2003–2006). Smart Mater Struct 2007;16:R1–21. https://doi.org/10.1088/0964-1726/16/3/R01.
[3] Safaei M, Sodano HA, Anton SR. A review of energy harvesting using piezoelectric materials: State-of-the-art a decade later (2008-2018). Smart Mater Struct 2019;28. https://doi.org/10.1088/1361-665X/ab36e4.
[4] Ilyas MA, Swingler J. Piezoelectric energy harvesting from raindrop impacts. Energy 2015;90:796–806. https://doi.org/10.1016/j.energy.2015.07.114.
[5] Guo L, Lu Q. Numerical analysis of a new piezoelectric-based energy harvesting pavement system: Lessons from laboratory-based and field-based simulations. Appl Energy 2019;235:963–77. https://doi.org/10.1016/j.apenergy.2018.11.037.
[6] Zou H-X, Zhao L-C, Gao Q-H, Zuo L, Liu F-R, Tan T, et al. Mechanical modulations for enhancing energy harvesting_ Principles, methods and applications _ Elsevier Enhanced Reader.pdf. Appl Energy 2019;255:113871.
[7] Wang W, Cao J, Bowen CR, Zhou S, Lin J. Optimum resistance analysis and experimental verification of nonlinear piezoelectric energy harvesting from human motions. Energy 2017;118:221–30. https://doi.org/10.1016/j.energy.2016.12.035.
[8] Kong N, Ha DS, Erturk A, Inman DJ. Resistive impedance matching circuit for piezoelectric energy harvesting. J Intell Mater Syst Struct 2010;21:1293–302. https://doi.org/10.1177/1045389X09357971.
[9] Liao Y, Sodano HA. Optimal parameters and power characteristics of piezoelectric energy harvesters with an RC circuit. Smart Mater Struct 2009;18.. https://doi.org/10.1088/0964-1726/18/4/045011.
[10] Dicken J, Mitcheson PD, Stoianov I, Yeatman EM. Power-extraction circuits for piezoelectric energy harvesters in miniature and low-power applications. IEEE Trans Power Electron 2012;27:4514–29. https://doi.org/10.1109/TPEL.2012.2192291.
[11] DuToit NE, Wardle BL. Experimental verification of models for microfabricated piezoelectric vibration energy harvesters. AIAA J 2007;45:1126–37. https://doi.org/10.2514/1.25047.
[12] Khazaee M, Rezaniakolaie A, Moosavian A, Rosendahl L. A novel method for autonomous remote condition monitoring of rotating machines using piezoelectric energy harvesting approach. Sensors Actuators A Phys 2019;295:37–50. https://doi.org/10.1016/j.sna.2019.05.016.
[13] Noel AB, Abdaoui A, Elfouly T, Ahmed MH, Badawy A, Shehata MS. Structural Health Monitoring Using Wireless Sensor Networks: A Comprehensive Survey. IEEE Commun Surv Tutorials 2017;19:1403–23. https://doi.org/10.1109/COMST.2017.2691551.
[14] Li H, Tian C, Deng ZD. Energy harvesting from low frequency applications using piezoelectric materials. 2014. https://doi.org/10.1063/1.4900845.
[15] Khazaee M, Rezaniakolaei A, Rosendahl L. An experimental study on macro Piezoceramic fiber composites for energy harvesting. Mater Sci Forum 2019;951:3–8. https://doi.org/https://doi.org/10.4028/www.scientific.net/MSF.951.3.
[16] Yang Y, Upadrashta D. Modeling of geometric, material and damping nonlinearities in piezoelectric energy harvesters. Nonlinear Dyn 2016;84:2487–504. https://doi.org/10.1007/s11071-016-2660-1.
[17] Khazaee M, Rezaniakolaei A, Rosendahl L. A broadband Macro-Fiber-Composite piezoelectric energy harvester for higher energy conversion from practical wideband vibrations. Nano Energy 2020;76:104978.
[18] DuToit NE, Wardle BL, Kim SG. Design considerations for MEMS-scale piezoelectric mechanical vibration energy harvesters. Integr Ferroelectr 2005;71:121–60. https://doi.org/10.1080/10584580590964574.
[19] Lallart M, Zhou S, Yang Z, Yan L, Li K, Chen Y. Coupling mechanical and electrical nonlinearities: The effect of synchronized discharging on tristable energy harvesters. Appl Energy 2020;266.. https://doi.org/10.1016/j.apenergy.2020.114516.
[20] Hosaka H, Itao K, Kuruda S. Damping characteristics of beam-shaped micro-oscillators. Sensors Actuators, A Phys 1995;49:87–95. https://doi.org/10.1016/0924-4247(95)01003-J.
[21] Khazaee M, Rezania A, Rosendahl L. Effect of damage and support damping mechanisms on unimorph piezoelectric energy harvester. JVC/Journal Vib. Control 2019;25.. https://doi.org/10.1177/1077546319855162.
[22] Dayou J, Kim J, Im J, Zhai L, How ATC, Liew WYH. The effects of width reduction on the damping of a cantilever beam and its application in increasing the harvesting power of piezoelectric energy harvester. Smart Mater Struct 2015;24:045006. https://doi.org/10.1088/0964-1726/24/4/045006.
[23] Hentschel OP, Von SLP, Wallaschek J, Denk M. Introduction and evaluation of a damping determination method based on the Short-Term fourier transform and Resampling (STFR). J Theor Appl Mech 2015;53:439–52. https://doi.org/10.15632/jtam-pl.53.2.395.
[24] Ewins DJ. Modal Testing : Theory. RSP: Practice and Application. Second; 2000.
[25] Khazaee M, Nobari AS, Aliabadi MHF. Experimental Investigation of Delamination Effects on Modal Damping of a CFRP Laminate, Using a Statistical Rationalization Approach. Comput. Exp. Methods Struct. 2018;10:75–103. https://doi.org/10.1142/9781786344977_0003.
[26] Liang J-W. Damping estimation via energy dissipation method. J Sensors 2007;307:349–64.
[27] Ju S, Ji CH. Impact-based piezoelectric vibration energy harvester. Appl Energy 2018;214:139–51. https://doi.org/10.1016/j.apenergy.2018.01.076.
[28] De Marqui JC, Erturk A, Inman DJ. An electromechanical finite element model for piezoelectric energy harvester plates. J Sound Vib 2009;327:9–25. https://doi.org/10.1016/j.jsv.2009.05.015.
[29] Khazaee M, Rezaniakolaei A, Rosendahl L. A comprehensive electromechanically coupled model for non-uniform piezoelectric energy harvesting composite laminates. Mech Syst Signal Process 2020;145:106927.

[30] Erturk A, Inman DJ. An experimentally validated bimorph cantilever model for piezoelectric energy harvesting from base excitations. Smart Mater Struct 2009;18:025009. https://doi.org/10.1088/0964-1726/18/2/025009.
[31] Paknejad A, Rahimi G, Farrokhabadi A, Khatibi MM. Analytical solution of piezoelectric energy harvester patch for various thin multilayer composite beams. Compos Struct 2016;154:694–706. https://doi.org/10.1016/j.compstruct.2016.06.074.
[32] Wei C, Jing X. A comprehensive review on vibration energy harvesting: Modelling and realization. Renew Sustain Energy Rev 2017;74:1–18. https://doi.org/10.1016/j.rser.2017.01.073.
[33] He J, Fu Z-F. Modal analysis. 1st ed. Butterworth-Heinemann; 2001.
[34] Erturk A. Piezoelectric energy harvesting for civil infrastructure system applications: Moving loads and surface strain fluctuations. J Intell Mater Syst Struct 2011;22:1959–73. https://doi.org/10.1177/1045389X11420593.
[35] Erturk A, Inman DJ. On Mechanical Modeling of Cantilevered Piezoelectric Vibration Energy Harvesters. J Intell Mater Syst Struct 2008;19:1311–25. https://doi.org/10.1177/1045389X07085639.
[36] Roundy S, Wright PK, Rabaey JM. Energy scavenging for wireless sensor networks. 1st ed. Springer Science; 2004. https://doi.org/10.1007/978-1-4615-0485-6_1.
[37] Material S. https://www.smart-material.com n.d.
[38] Roundy S, Wright PK, Rabaey J. A study of low level vibrations as a power source for wireless sensor nodes. Comput Commun 2003;26:1131–44. https://doi.org/10.1016/S0140-3664(02)00248-7.
[39] Papagiannopoulos GA, Hatzigeorgiou GD. On the use of the half-power bandwidth method to estimate damping in building structures. Soil Dyn Earthq Eng 2011;31:1075–9. https://doi.org/10.1016/j.soildyn.2011.02.007.
[40] Young D, Felgar RP. Tables of characteristic functions representing normal modes of vibration of a beam. Univ Texas Eng Res Ser 1949;44:1–31.

# Appendix I. Paper 9: Reference [187]

## An optimum practical piezoelectric energy-harvesting device for energy scavenging from car vibration

M. Khazaee, A. Rezaniakolaei, L. Rosendahl.

This paper is ready to be submitted.

# Appendix J. Paper 10: Reference [177]

## Power generation from a DC motor at defect-free and misaligned shaft conditions by piezoelectric energy harvester attached to the shaft bearing

M. Khazaee, A. Rezaniakolaei, L. Rosendahl.

This paper is ready to be submitted.

ISSN (online): 2446-1636
ISBN (online): 978-87-7210-924-4 AALBORG UNIVERSITY PRESS